# INVESTIGATING THE USE OF FIRST-PRINCIPLES CALCULATIONS FOR NMR STUDIES OF DISORDER IN THE SOLID STATE

Robert Moran

A Thesis Submitted for the Degree of PhD
at the
University of St Andrews

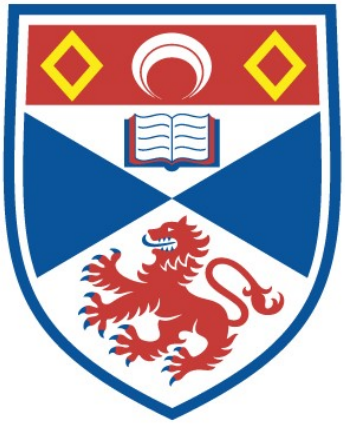

2019

# Investigating the use of first-principles calculations for NMR studies of disorder in the solid state

Robert Moran

University of
St Andrews

This thesis is submitted in partial fulfilment for the degree of Doctor of Philosophy (PhD) at the University of St Andrews

March 2019

## Candidate's declaration

I, Robert Moran, do hereby certify that this thesis, submitted for the degree of PhD, which is approximately 80,000 words in length, has been written by me, and that it is the record of work carried out by me, or principally by myself in collaboration with others as acknowledged, and that it has not been submitted in any previous application for any degree.

I was admitted as a research student at the University of St Andrews in September 2014.

I received funding from an organisation or institution and have acknowledged the funder(s) in the full text of my thesis.

Date Signature of candidate

## Supervisor's declaration

I hereby certify that the candidate has fulfilled the conditions of the Resolution and Regulations appropriate for the degree of PhD in the University of St Andrews and that the candidate is qualified to submit this thesis in application for that degree.

Date Signature of supervisor

## Permission for publication

In submitting this thesis to the University of St Andrews we understand that we are giving permission for it to be made available for use in accordance with the regulations of the University Library for the time being in force, subject to any copyright vested in the work not being affected thereby. We also understand, unless exempt by an award of an embargo as requested below, that the title and the abstract will be published, and that a copy of the work may be made and supplied to any bona fide library or research worker, that this thesis will be electronically accessible for personal or research use and that the library has the right to migrate this thesis into new electronic forms as required to ensure continued access to the thesis.

I, Robert Moran, confirm that my thesis does not contain any third-party material that requires copyright clearance.

The following is an agreed request by candidate and supervisor regarding the publication of this thesis:

**Printed copy**

No embargo on print copy.

**Electronic copy**

No embargo on electronic copy.

Date Signature of candidate

Date Signature of supervisor

**Underpinning Research Data or Digital Outputs**

**Candidate's declaration**

I, Robert Moran, understand that by declaring that I have original research data or digital outputs, I should make every effort in meeting the University's and research funders' requirements on the deposit and sharing of research data or research digital outputs.

Date Signature of candidate

**Permission for publication of underpinning research data or digital outputs**

We understand that for any original research data or digital outputs which are deposited, we are giving permission for them to be made available for use in accordance with the requirements of the University and research funders, for the time being in force.

We also understand that the title and the description will be published, and that the underpinning research data or digital outputs will be electronically accessible for use in accordance with the license specified at the point of deposit, unless exempt by award of an embargo as requested below.

The following is an agreed request by candidate and supervisor regarding the publication of underpinning research data or digital outputs:

No embargo on underpinning research data or digital outputs.

Date Signature of candidate

Date Signature of supervisor

**Acknowledgements**

I would first like to thank my supervisor, Sharon Ashbrook, for giving me this fantastic opportunity to complete a PhD with her. Throughout my PhD she has been more than willing to provide me with support, guidance and on occasion, a very well-deserved sarcastic comment, all of which I am very grateful for.

I would also like to thank David McKay, who has attempted to educate me in the dark art of computational chemistry and all things DFT during my project. I can honestly say that working with you over the last four years has been one of the most enjoyable aspects of my PhD, from bouncing ideas off one another in the pub, to doing our best to drunkenly find our hotel after a night of "networking" at a German conference.

I must also thank Daniel Dawson for all his assistance with all things solid-state NMR spectroscopy, as well as all his input and ideas regarding the challenge of computationally modelling disordered materials. Despite his best efforts to always appear irascible and aloof, Daniel is in fact a lovely person, although I'm sure he'll do his best to vehemently deny any such claims.

I also need to thank fellow Ashbrook Group member, Arantxa Fernandes, for recording many of the NMR spectra that are presented in this thesis.

I would like to thank members of the Ashbrook Group, both past and present, for their friendship and support, especially Joseph Hooper, Suzi Pugh and David McKay, who have helped to keep me sane during my PhD. I also need to thank Daniel Twist and Alison Lightfoot for their enthusiasm and hard work during their undergraduate research projects.

Special thanks must also go to the academics I've collaborated with, namely Chris Pickard, Jonathan Yates, John Griffin and Ricardo Grau-Crespo, all of whom have provided support and guidance in one way or another.

Finally, I need to thank my family and friends, especially my parents, Paul and Norma Moran, my sister Emily Moran, my incredible girlfriend Amy Sheader, and my long suffering flatmate Andrew Neal.

This work was supported by the ERC (EU FP7 Consolidator Grant 614290 "EXONMR").

The Collaborative Computational Project for NMR Crystallography (CCP-NC) also supported this work.

Research data underpinning this thesis are available at https://doi.org/10.17630/24ae94ef-3de0-4d96-8ec9-045f60b9606b

**Abstract**

In this thesis, the use of first-principles calculations to assist solid-state NMR spectroscopic studies of disordered inorganic materials has been investigated, with emphasis placed on understanding the most relevant and efficient methods for computationally modelling a system. The first class of materials studied are oxide ceramics, more specifically $Y_2Sn_xTi_{2-x}O_7$, $La_2Sn_xZr_{2-x}O_7$, $Y_2Zr_2O_7$ and $Y_2Hf_2O_7$; the first two of which are pyrochlore solid solutions, while the latter adopt the disordered defect fluorite phase. Both pyrochlore systems exhibit configurational disorder in the form of B-site cation mixing, which leads to the overlapping and complex experimental solid-state NMR spectra being challenging to assign. By considering several methods to generate structural models computationally, the site occupancy disorder (SOD) method was found to be particularly well suited to producing a set of structural models capable of representing the configurational disorder in these materials with the predicted $^{89}Y$, $^{119}Sn$ and $^{17}O$ NMR parameters able to assist the assignment of the experimental NMR spectra and provide significant structural insight. Investigation into $Y_2Zr_2O_7$ and $Y_2Hf_2O_7$ defect fluorites proved considerably more challenging, with the high level of structural disorder preventing easy implementation of SOD-based approaches, and necessitating a less sophisticated and more manual modelling approach being employed. Although some understanding of the origin of the signals seen in the NMR spectra was able to be obtained in this way, the limited scope of this computational investigation prevents a more detailed and quantitative analysis.

The second class of materials investigated in this thesis are hydrous silicate minerals found in the inner-Earth, specifically, hydrous Fe-free wadsleyite ($\beta$-$Mg_2SiO_4$), a system that is challenging to study experimentally due to the positional disorder of the incorporated protons (and of the charge-balancing associated cation vacancies). In combination with experimental solid-state NMR spectra and the first-principles calculation of NMR parameters, the *ab initio* random structure searching (AIRSS) approach was used to probe the structure of hydrous wadsleyite, by identifying many possible protonation

arrangements for semi- and fully-hydrous wadsleyite. Through this investigation, enthalpically stable protonation arrangements were identified for both semi- and fully-hydrous wadsleyite, with predicted NMR parameters for the AIRSS-generated structures used to assist assignment of the solid-state NMR spectra of a sample of wadsleyite containing ~3 wt% $H_2O$. By using the experimental NMR spectra to validate the accuracy and relevance of AIRSS-generated structural models, a new structural picture of the disorder in fully-hydrous wadsleyite was proposed, highlighting the success with which first-principles calculations can be used to assist the assignment of the solid-state NMR spectra of disordered inorganic materials.

**Publications**

S. E. Ashbrook, M. R. Mitchell, S. Sneddon, R. F. Moran, M. de los Reyes, G. R. Lumpkin, and K. R. Whittle, *New insights into phase distribution, phase composition and disorder in $Y_2(Zr,Sn)_2O_7$ ceramics from NMR spectroscopy, Phys. Chem. Chem. Phys.*, 2015, **17**, 9049-9059.

R. F. Moran, D. McKay, C. J. Pickard, A. J. Berry, J. M. Griffin and S. E. Ashbrook, *Hunting for hydrogen: random structure searching and prediction of NMR parameters of hydrous wadsleyite, Phys. Chem. Chem. Phys.*, 2016, **18**, 10173-10181.

R. F. Moran, D. M. Dawson and S. E. Ashbrook, *Exploring NMR spectroscopy for the study of disorder in solids, Int. Rev. Phys. Chem.*, 2017, **36**, 39-115.

D. M. Dawson, R. F. Moran and S. E. Ashbrook, *A computational investigation of the empirical relationship between the crystal structure and $^{29}Si$ isotropic chemical shift in silica zeolites, J. Phys. Chem. C*, 2017, **121**, 15198-15210.

A. Fernandes, R. F. Moran, S. Sneddon, D. M. Dawson, D. McKay, G. P. M. Bignami, F. Blanc, K. R. Whittle and S. E. Ashbrook, *$^{17}O$ solid-state NMR spectroscopy of $A_2B_2O_7$ oxides: quantitative isotopic enrichment and spectral acquisition, RSC Advances*, 2018, **8**, 7089-7101.

D. M. Dawson, R. F. Moran, S. Sneddon and S. E. Ashbrook, *Is the $^{31}P$ chemical shift anisotropy of aluminophosphates a useful parameter for NMR Crystallography, Magn. Reson. Chem.*, 2018, in press.

D. McKay, R. F. Moran, D. M. Dawson, J. M. Griffin, S. Sturniolo, C. J. Pickard, A. J. Berry and S. E. Ashbrook, *A picture of disorder in hydrous wadsleyite – under the combined microscope of solid-state NMR spectroscopy and ab initio random structure searching, J. Am. Chem. Soc.*, 2019, **141**, 3024-3036.

**Table of content**


**1 General overview** **1**
1.1 Introduction 1
1.2 Thesis overview 7
1.3 References 11

**2 Solid-state NMR spectroscopy** **13**
2.1 Introduction 13
2.2 Essentials of NMR spectroscopy 14
2.3 NMR interactions 22
2.3.1 The chemical shift 23
2.3.2 Chemical shift anisotropy 24
2.3.3 Dipolar coupling 27
2.3.4 Scalar coupling 29
2.3.5 Quadrupolar interactions 30
2.4 Experimental methods 33
2.4.1 Signal, sensitivity and resolution enhancement methods 33
2.4.1.1 Magic-angle spinning 34
2.4.1.2 Decoupling 36
2.4.1.3 Cross-polarisation 36
2.4.2 Relevant NMR experiments 38
2.4.2.1 Pulse-acquire 38
2.4.2.2 Spin-echo 39
2.4.2.3 CPMG 39
2.4.2.4 HETCOR 40
2.4.2.5 DQ MAS 41
2.4.2.6 STMAS 42
2.5 References 42

**3 Computational chemistry** **47**
3.1 An introduction to computational chemistry 47
3.2 Fundamentals of first-principles calculations 48
3.3 The Hartree-Fock method 53

3.4 Density functional theory 58
3.5 Basis sets 72
3.5.1 Atom-centred basis sets 72
3.5.2 Planewave basis sets 74
3.6 Pseudopotentials 76
3.7 k-point sampling 79
3.8 Calculating solid-state NMR parameters 80
3.8.1 Relativistic effects 81
3.8.2 Geometry optimisation 82
3.8.3 Semi-empirical dispersion corrections 84
3.8.4 Referencing calculated shieldings 87
3.8.5 Quadrupolar interactions 88
3.9 Convergence 89
3.10 General computational methodology 91
3.11 References 95

**4 Computational modelling of disorder in materials 100**
4.1 Introduction 100
4.2 Ordered materials 103
4.3 Disordered materials 106
4.3.1 Configurational and compositional disorder 108
4.3.2 Positional disorder 121
4.3.3 Dynamic disorder 132
4.4 Summary 134
4.5 References 135

**5 Investigating structural disorder in ceramic materials 142**
5.1 Materials 142
5.1.1 Pyrochlores 142
5.1.2 Defect fluorites 144
5.2 Applications 145
5.3 Previous work 151
5.4 Acknowledgements 159
5.5 $Y_2Sn_xTi_{2-x}O_7$: using NMR spectroscopy and first-principles 161

calculations to investigate B-site cation disorder
5.5.1 Introduction 161
5.5.2 Experimental NMR spectra 161
5.5.2.1 $^{89}$Y MAS NMR spectra 162
5.5.2.2 $^{119}$Sn MAS NMR spectra 164
5.5.2.3 $^{17}$O MAS NMR spectra 164
5.5.3 Cluster models 167
5.5.4 Models with randomised B-site cations 180
5.5.4.1 Repeatability of geometry optimisation calculations 193
5.5.5 SOD-generated structural models 196
5.5.5.1 SOD-generated structural models: series 1 197
5.5.5.2 SOD-generated structural models: series 2 209
5.5.5.3 SOD-generated structural models: series 3 218
5.5.6 Summary 248
5.6 $La_2Sn_xZr_{2-x}O_7$: using NMR spectroscopy and first-principles calculations to investigate B-site cation disorder 250
5.6.1 Introduction 250
5.6.2 Experimental NMR spectra 251
5.6.2.1 $^{119}$Sn MAS NMR spectra 251
5.6.2.2 $^{17}$O MAS NMR spectra 252
5.6.3 Cluster models 254
5.6.4 SOD-generated structural models 261
5.6.5 Summary 278
5.7 $Y_2Zr_2O_7$ and $Y_2Hf_2O_7$: probing cation disorder and anion randomisation using NMR spectroscopy and first-principles calculations 281
5.7.1 Introduction 281
5.7.2 Experimental NMR spectra 282
5.7.2.1 $^{89}$Y MAS NMR spectra 282
5.7.2.2 $^{17}$O MAS NMR spectra 284
5.7.3 Models with cation mixing and randomised anion positions 285
5.7.4 Summary 296
5.8 Outlook 298

5.9 References 300

**6 Investigating proton disorder in hydrous wadsleyite, an inner-Earth mineral** **307**

6.1 Introduction 307
6.2 Fe-free wadsleyite 310
6.3 Previous work 311
6.4 Acknowledgements 317
6.5 Experimental NMR spectra 318
6.5.1 Anhydrous Fe-free wadsleyite 319
6.5.2 Hydrous Fe-free wadsleyite 321
6.6 Investigating the structure of semi-hydrous wadsleyite 327
6.6.1 AIRSS-generated structural models 327
6.6.2 Mg3 vacant structural models 331
6.6.3 Mg1, Mg2 and Mg3 vacant structural models 347
6.6.4 Summary 358
6.7 Investigating the structure of fully-hydrous wadsleyite 360
6.7.1 AIRSS-generated structural models 360
6.7.2 Post *k*-means clustering analysis 363
6.7.3 Summary 378
6.8 Outlook 380
6.9 References 382

**7 Conclusions and outlook** **387**

**Appendices** **393**

**List of symbols and abbreviations**

| | |
|---|---|
| Å | angstrom |
| $B_0$ | magnetic field strength |
| $C_Q$ | quadrupolar coupling constant |
| eV | electron volts |
| $E_{cut}$ | cut-off energy |
| $E_{xc}$ | exchange-correlation energy |
| h | Plancks' constant |
| **I** | spin angular momentum vector |
| I | spin quantum number |
| $m_I$ | magnetic spin quantum number |
| $\mathbf{M}_0$ | bulk magnetisation vector |
| ppm | parts per million |
| r | ionic radius |
| $r_{core}$ | core radius |
| rf | radiofrequency |
| Ry | Rydberg |
| T | kinetic energy |
| V | potential energy |
| **V** | EFG tensor |
| $\gamma$ | gyromagnetic ratio |
| $\boldsymbol{\delta}$ | chemical shift tensor |
| $\delta_{iso}$ | isotropic chemical shift |
| $\Delta H$ | relative enthalpy |
| $\boldsymbol{\sigma}$ | chemical shielding tensor |
| $\sigma_{iso}$ | isotropic chemical shielding |
| $\sigma_{ref}$ | reference shielding |
| $\Omega$ | span |
| $\kappa$ | skew |
| $\lambda$ | wavelength |
| $\rho(\mathbf{r})$ | electron density |

| | |
|---|---|
| $\Psi$ | wavefunction |
| $\omega_0$ | Larmor frequency (in rads $s^{-1}$) |
| AIRSS | *ab initio* random structure searching |
| AO | atomic orbital |
| CASTEP | Cambridge serial total energy package |
| CP | cross-polarisation |
| CPMG | Carr-Purcell-Meiboom-Gill |
| CPU | central processing unit |
| CSA | chemical shift anisotropy |
| CT | central transition |
| DFT | density functional theory |
| DQ | double-quantum |
| EFG | electric field gradient |
| HETCOR | heteronuclear correlation |
| HF | Hartree-Fock |
| HPC | high-performance computing |
| FID | free induction decay |
| FT | Fourier transform |
| GIPAW | gauge-including projector augmented wave |
| GGA | general gradient approximation |
| LDA | local density approximation |
| MAS | magic-angle spinning |
| MD | molecular dynamics |
| MO | molecular orbital |
| NAM | nominally anhydrous mineral |
| NMR | nuclear magnetic resonance |
| NNN | next nearest neighbour |
| PAS | principal axis system |
| PAW | projector augmented wave |
| PBE | Perdew-Burke-Ernzerhof |
| PDF | pair distribution function |
| PES | potential energy surface |
| POSAMP | position amplitude |

| | |
|---|---|
| SCF | self-consistent field |
| SDA | structure-directing agent |
| SEDC | semi-empirical dispersion correction |
| SOD | site occupancy disorder |
| SQ | single-quantum |
| ST | satellite transition |
| VASP | Vienna *ab initio* simulation package |
| XRD | X-ray diffraction |
| ZORA | zero-order relativity approximation |

# Chapter 1: General overview

## 1.1 Introduction

Given the many and seemingly ever-changing social, economic and environmental challenges that humanity faces, including a growing global population, widespread food and water shortages, and increasing demand for cheap and renewable sources of energy, scientists are constantly searching for new materials, or finding alternative uses for existing materials, to help address some of these concerns. Identifying a material as having the desired chemical and/or physical properties required to solve a particular problem is only part of the challenge: it is also necessary to understand what it is about a material that is responsible for a specific property, something that is typically only possible once the structure has been determined. Despite the periodicity typically displayed by the solid state, *i.e.*, solids usually possess long-range order, it is often a deviation or variation in this structural ordering that leads to useful physical and chemical properties being exhibited. Structural disorder, even in the form of small variations in atom position or composition can result in large changes in the properties of a material and ultimately, therefore, in its end use. This tunability in properties, through the careful manipulation of composition and atomic ordering has led to disordered materials being used for a wide range of applications, including in catalysis, as pharmaceuticals, in the electronics industry and the world of energy materials.[1]

Characterisation methods based on Bragg diffraction are routinely used to investigate the structure of solid-state materials, with single-crystal or powder X-ray diffraction (XRD) data able to provide an accurate structural description of solids that have long-range order in both atomic positions and site occupancies, *i.e.*, an ideal solid such as that shown schematically in Figure 1.1(a). Any breakdown in long-range ordering reduces the effectiveness of Bragg diffraction-based techniques, providing only a description of the *average* structure. For example, the schematic crystal

structure shown in Figure 1.1(b) retains the periodicity of the atomic positions, but there is a variation in the species occupying the B site, *i.e.*, compositional disorder. In this case, diffraction would be able to accurately determine the atomic coordinates and suggests the B site has a fractional occupancy of $B_{0.5}C_{0.5}$, but is not able to describe how these atoms are arranged throughout the material, *i.e.*, whether there is clustering of like atoms, or a random distribution of each type of atom. A solid exhibiting positional disorder is shown in Figure 1.1(c), with one quarter of the B sites now vacant, leading to a fractional occupancy of $B_{0.75}$. However, this fractional occupancy description could perhaps be interpreted in two ways, either that throughout the material 25% of the B site are vacant, or that any one site is vacant for 25% of the time. The former interpretation is shown in Figure 1.1(c), and represents static positional disorder, whereas the latter results from dynamic disorder, where atoms within a solid are moving as a function of time. Without knowing which of these situations is present, *i.e.*, static or dynamic disorder, the fractional occupancy description of a crystallographic site is of limited use. Compounding the disorder caused by the fractional occupancy of crystallographic sites, non-ideal solids can also exhibit variations in local geometry, *e.g.*, a distribution of bond lengths and bond angles. The more pronounced this geometrical variation is from ideality, the less the long-range is maintained, causing difficulties for may diffraction-based techniques. As shown in Figure 1.1(d), amorphous solids, such as glasses, display this type of disorder and crystallographic sites can no longer be defined, leading to significant differences in long-range structure, even though the local structure around a particular atom may remain relatively unchanged in comparison to an ordered solid of equivalent composition.

Given that Bragg diffraction techniques probe the long-range ordering of a system, as the level of disorder in a solid increases the less adept these approaches become at describing a structure reflecting the unit cell length scale, rather than simply a description of the average structure. Therefore, to more accurately describe the structure of a disordered material it is necessary to combine information relating to any periodicity, *i.e.*, any remaining long-range order with information on the local structure, including the bonding

geometry, the number and type of directly coordinating species, as well as the type of atoms on the next nearest neighbour (NNN) sites. With this in mind, nuclear magnetic resonance (NMR) spectroscopy[2–4] is perfectly suited for investigating the structure of disordered solids. The chemical shift (change in resonance frequency of a nuclear spin) is very sensitive to changes in the local structure, while through-bond and through-space couplings between nuclear spins provide information on covalent bonding and

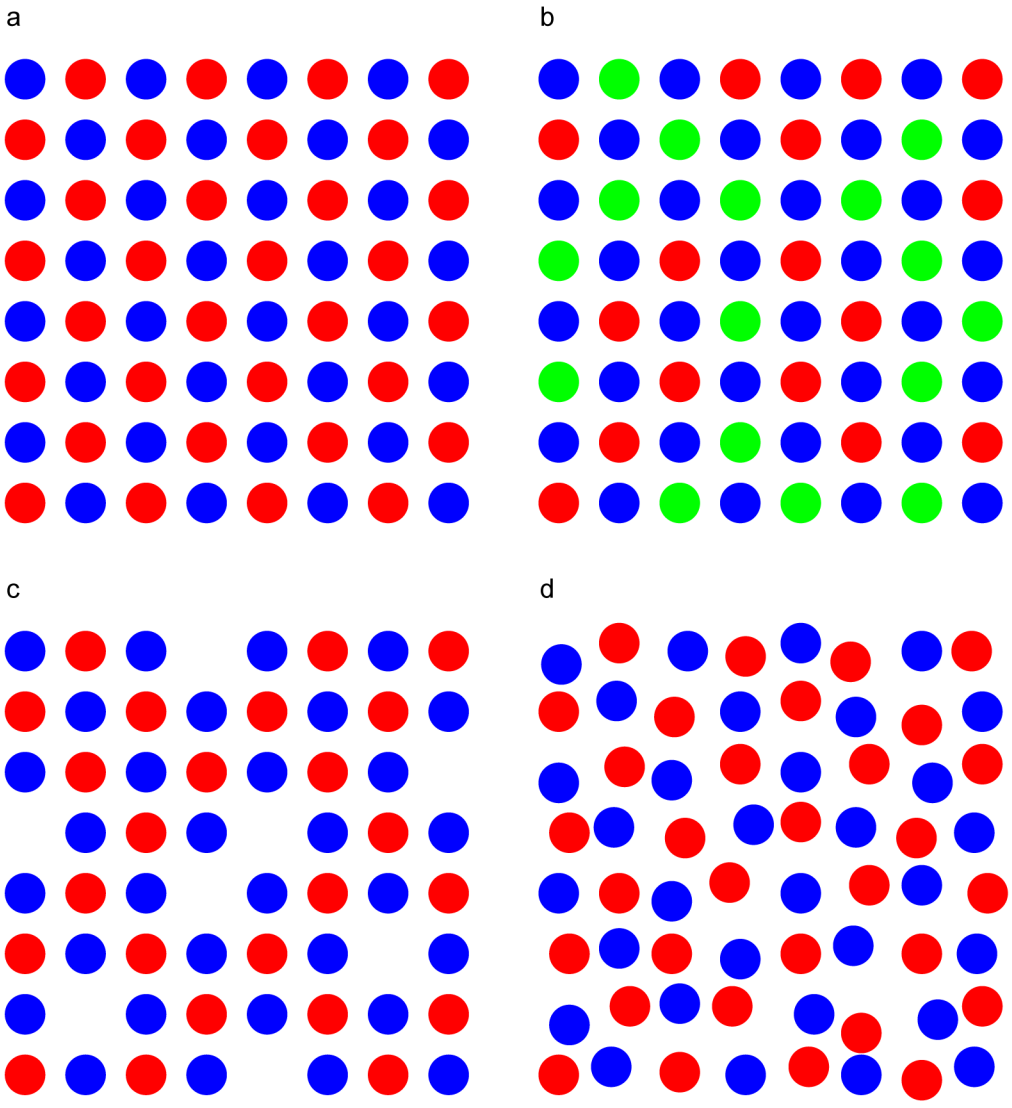


**Figure 1.1:** Schematic showing (a) an ordered crystalline AB material, (b) $A(B_{0.5}C_{0.5})$ with the B and C atoms randomly distributed throughout the crystal lattice, (c) $AB_{0.75}$ with a random distribution of B site vacancies and (d) amorphous AB. A, B and C atoms are shown in blue, red and green, respectively.

distances between atoms.[5] This sensitivity to *local* structure has resulted in NMR spectroscopy becoming one of the most versatile and widely used analytical approaches today. In solution-state NMR lineshapes are characteristically narrow due to the rapid molecular tumbling that occurs naturally in liquids. This isotropic tumbling motion has the effect of averaging many interactions that contribute to spectral line broadening, including chemical shift anisotropy (CSA) and dipolar coupling.[6] In contrast, the NMR spectra of solids are associated with broad, often featureless lineshapes caused by broadening from anisotropic interactions. As these anisotropic interactions are orientationally dependent, a number of approaches, including magic angle spinning (MAS)[7–9] have been developed to improve the resolution of solid-state NMR spectra by physical manipulation of the sample. Figure 1.2 shows the effectiveness of using MAS to remove the anisotropic broadening in a $^{31}$P solid-state NMR spectrum of $(NH_4)_2HPO_4$, with a significant difference observed between the spectrum acquired for a static sample and those recorded using MAS. In addition to the CSA and dipolar coupling mentioned previously, the NMR spectra of quadrupolar nuclei, *i.e.*, those with spin quantum number $I > 1/2$, also exhibit quadrupolar broadening, resulting from the interaction between the quadrupolar moment and the electric field gradient (EFG). This interaction cannot be fully removed by MAS, necessitating more complex approaches to acquire high-resolution spectra.[10–13]

Despite the development of numerous signal and resolution enhancement techniques, solid-state NMR spectra are often far more complex than those seen in solution, particularly if the system is disordered. The effect of configurational disorder in the solid-state is illustrated in Figure 1.3, where the $^{89}$Y ($I = 1/2$) MAS NMR spectra for $Y_2Sn_2O_7$ and $Y_2Ti_2O_7$, (Figure 1.3(a) and (b), respectively), each consist of a single sharp resonance, whereas the corresponding MAS spectrum of $Y_2SnTiO_7$ (where the B site has fractional occupancy $Sn_{0.5}Ti_{0.5}$) (Figure 1.3(c)) consists of several broad overlapping resonances. Overlapping features, as seen in Figure 1.3(c), often make it difficult to confidently assign individual resonances in solid-state NMR

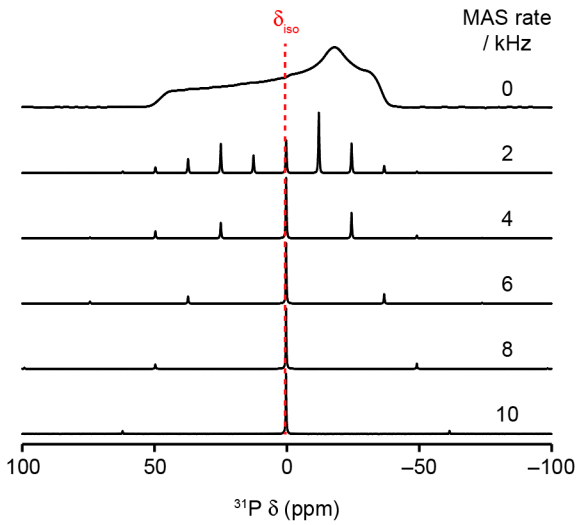


**Figure 1.2:** Effect of MAS on the 9.4 T $^{31}$P (I = 1/2) NMR spectrum of $(NH_4)_2HPO_4$, showing how the anisotropic lineshape observed for a static sample is broken up into a series of spinning sidebands, with the intensity of the centreband (at ~0 ppm) and sidebands increasing and decreasing, respectively, as the MAS rate increases. This figure has been modified from that presented by Moran *et al*.[1]

spectra. In fact, the very nature of the solid phase complicates matters, with samples containing not only chemically-distinct but also crystallographically-distinct species as a result of crystal packing.

The significant challenges associated with the acquisition, assignment and interpretation of solid-state NMR spectra for disordered inorganic materials has led to the rise in popularity of first-principles calculations being used to predict NMR parameters for a structure or series of structural models.[14,15] It has only been relatively recently that the solid-state NMR community has been able to benefit from the use of first-principles calculations to accurately predict NMR parameters for both finite and infinitely periodic systems, made possible through the Gauge Including Projector Augmented-Wave (GIPAW) approach, developed by Pickard and Mauri in 2001.[16] In the case of ordered solids, first-principles calculations can be used to confirm peak assignments and predict parameters that are challenging to measure experimentally, such as tensor orientations and anisotropic couplings. As such, first-principles calculations play a key role in the emerging field of NMR crystallography, which is the use of NMR spectroscopy, in tandem

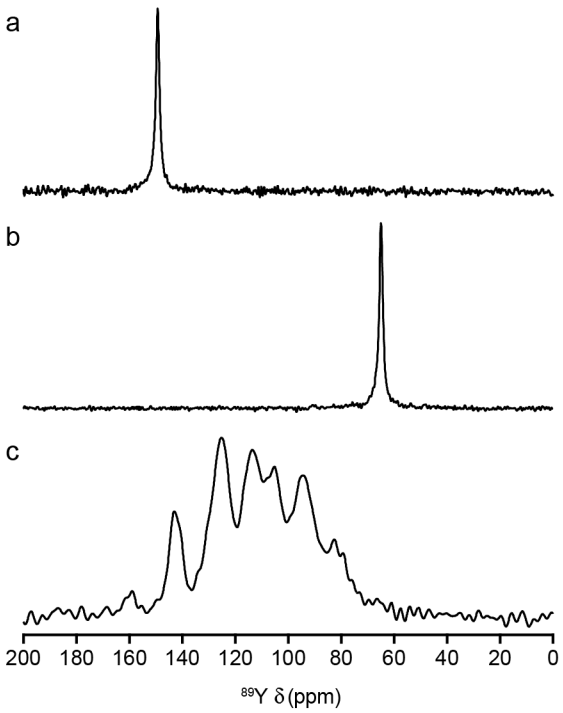


**Figure 1.3:** 14.1 T $^{89}$Y (I = 1/2) MAS spectrum of (a) $Y_2Sn_2O_7$, (b) $Y_2Ti_2O_7$ and (c) $Y_2SnTiO_7$, showing the effect of configurational disorder on the number and width of resonances. All spectra were recorded by Arantxa Fernandes.

with diffraction measurements to characterise structures.[17–19] The deviation from periodicity associated with disordered materials makes computational approaches significantly more challenging, often necessitating the use of supercells or a set of related structural models to represent a disordered system, both of which can require a large amount of computational resources. The main difficulty with using first-principles calculations to provide insight into the structure of disordered materials is that a simple initial structural model is often not available. If structural variation leads to diffraction-based models no longer being a realistic representation of a disordered system, the predicted NMR parameters associated with such an initial structural model will be of little use when comparing to experiment and guiding spectral interpretation. In order to predict meaningful solid-state NMR parameters for a disordered material, the most important step to verify is that the structural model(s) being used are a realistic representation of the system. To this end, significant effort is currently being expended into

developing computational approaches to generate sets of possible periodic models that could be used to gain insight into the structure of disordered inorganic materials. Although many methods exist to model both static and dynamic disorder, the two approaches most important for the work presented in this thesis are site occupancy disorder (SOD)[20,21] and *ab initio* random structure searching (AIRSS),[22,23] which are discussed in more detail in subsequent chapters. These approaches have been employed extensively in this thesis to generate structural models that were used to represent various inorganic materials which exhibit configurational, compositional or positional disorder, structural variations that make these systems very challenging to explore experimentally.

## 1.2 Thesis overview

The work presented in this thesis focuses on using first-principles density functional theory (DFT) calculations to generate a series of possible structural models for disordered inorganic materials including hydrated inner-Earth minerals and mixed-metal ceramics. Predicted solid-state NMR parameters for these possible structures were subsequently compared to experimental measurements to validate the accuracy of the computationally generated structural models.

To this end, Chapter 2 introduces the NMR phenomenon and the theory behind nuclear magnetism, concepts that are crucial to understanding the experimental solid-state NMR spectra presented in this thesis (and therefore the evaluation of any theoretical predictions). A description of the interactions that affect NMR spectra, and methods for removing these (for acquiring high-resolution spectra) are also covered, along with a brief description of how simple NMR experiments are performed.

In Chapter 3, the theoretical principles of quantum-chemical calculations are introduced, highlighting the growing role they play in the chemical sciences. The theory underlying first-principles calculations is explained, including a brief description of the Hartree-Fock approximation and DFT, before moving

onto the general approximations used to simplify the mathematics of calculations, the types of basis sets that can be used and the concept of a pseudopotential. Finally, the GIPAW method, by which solid-state NMR parameters can be predicted is discussed, along with ways in which the accuracy of predicted solid-state NMR parameters can be improved, by geometry optimising structures, *i.e.*, minimising the forces acting on atoms by allowing them to move, or by considering additional effects like relativity or dispersion interactions.

Being able to predict accurate and meaningful solid-state NMR parameters and ultimately explain the appearance of complex experimental NMR spectra requires a suitable way of modelling disordered materials. In Chapter 4, a description of the various ways in which structural models can be generated to investigate systems that exhibit different types of structural disorder is presented. These include approaches that use simple atomic substitution, systematic changes in atom configurations (describes how the atoms are arranged in a unit cell, *i.e.*, ABC, ACB, BAC, BCA, CAB or CBA), variations in local geometry (bond lengths and bond angles), as well as more complicated methods, including SOD and AIRSS, both used extensively in this thesis.

Chapter 5 investigates the local structure and B site cation ordering in $Y_2(Sn,Ti)_2O_7$ pyrochlore ceramics (general formula $A_2B_2O_7$), important materials that have chemical and physical properties that makes them widely applicable in areas such as catalysis, energy materials, as components in electronics and semiconductors and as potentially stable, long-term radioactive wasteforms. In order to assist the assignment of the often-complex solid-state $^{89}Y$, $^{119}Sn$ and $^{17}O$ NMR spectra of these pyrochlores ceramics, a number of theoretical approaches to model the changes in local structure and B site cation ordering have been explored. These approaches vary in their complexity, and importantly, how closely the predicted solid-state NMR parameters for the resulting structural models compare to experimental measurements. These modelling approaches ranged from a series of models produced by systematic and manual manipulation of the

NNN B site cations, random variation of B site cations over the relevant crystallographic sites in a unit cell, to the use of SOD to identify every symmetrically inequivalent B site cation arrangement and their corresponding configurational degeneracy for a series of B site cation composition. Comparing the predicted solid-state NMR parameters with experimental $^{89}Y$ and $^{119}Sn$ solid-state NMR spectra allowed for new information on the local structure and B site cation ordering in $Y_2(Sn,Ti)_2O_7$ pyrochlores to be determined. Additionally, these approaches enabled the relationship between geometrical features (bond lengths, bond angles and interatomic distances), and solid-state NMR parameters to be investigated, facilitating a more complete and confident assignment of experimental solid-state NMR spectra for the $Y_2(Sn,Ti)_2O_7$ pyrochlore ceramics.

Also within Chapter 5, the effectiveness and limitations of approaches for the modelling of additional disordered ceramics is explored, including generating structural models by systematically manipulating th NNN B site cations, using the SOD approach and by randomising the positions of cation and anions over the relevant crystallographic sites in the unit cell. These include $La_2(Sn,Zr)_2O_7$ ceramics, which like the $Y_2(Sn,Ti)_2O_7$ system, adopt the pyrochlore structure throughout the entire compositional range (*i.e.*, from $La_2Sn_2O_7$ to $La_2Zr_2O_7$) and exhibit B site cation disorder. The SOD approach is again shown to be a powerful tool capable of providing significant insight into the structure of these disordered materials and, most importantly, is able to guide the interpretation and assignment of the $^{119}Sn$ solid-state NMR spectra. Also in this chapter, first-principles calculations have been used to assist in the assignment of the more complex $^{89}Y$ and $^{17}O$ solid-state NMR spectra of $Y_2Zr_2O_7$ and $Y_2Hf_2O_7$ ceramics. These materials adopt a defect fluorite structure which exhibits cation mixing and positional disorder of O and vacancies on the anion sub lattice, making them challenging to study experimentally.

In Chapter 6, the "hydration" of wadsleyite ($\beta$-$Mg_2SiO_4$), a normally anhydrous, dense-phase silicate mineral is investigated. It has been speculated that wadsleyite can accommodate stoichiometric amounts of

"water", in the form of hydroxyls, leading to the possible existence of vast water reservoirs deep within the Earth, with the proton incorporation mechanism believed to be charge balanced by the removal of $Mg^{2+}$ and/or $Si^{4+}$ cations. Despite a number of theoretical and experimental studies, there is still no general consensus regarding the detailed hydration mechanism or the preferred protonation positions. The challenges associated with synthesising even a few milligrams of these hydrated minerals in a repeatable fashion, procedures that involve extreme temperatures and pressures (~1200 ºC and ~14 GPa), are no doubt responsible for some of the ambiguity surrounding the mechanism of hydration. These materials are also not trivial to analyse using either diffraction-based or solid-state NMR spectroscopic techniques given XRD struggles to identify the position of light atoms such as protons (particularly when disordered) and solid-state NMR spectra of these hydrated samples often consist of many overlapping resonances. In this chapter, AIRSS was used to understand hydrogen incorporation, by generating a large number of candidate structures for different hydration mechanisms. Starting initially from an anhydrous wadsleyite unit cell. The prediction of solid-state NMR parameters for these models and subsequent comparison to experimental solid-state NMR spectra has provided new insight into the energetically favourable protonation motifs and, hence, the most likely hydration mechanisms for hydrous wadsleyite.

In Chapter 7, the overarching conclusions of this thesis are discussed, with particular emphasis placed on the ways in which disordered inorganic materials can and should be modelled computationally, highlighting how the optimum modelling strategy is often dependant on the type of structural disorder exhibited by a particular material. The general challenges associated with modelling disordered materials is also discussed, including the current limitations of DFT accuracy, the need to consider systems on a length scale greater than a single unit cell, as well as the need for more widely accessible high-performance computing (HPC) resources, in order to facilitate the investigation of larger and more disordered systems. Within this chapter, possible directions for future work are also discussed, including use of the

SOD approach to investigate additional systems that exhibit some form of configurational disorder, such as pyrochlores or perovskites. Considering how the AIRSS approach could be used to provide structural insight into system with positional disorder is also discussed, with a seemingly natural progression being to use AIRSS in conjunction with GIPAW calculations to investigate the stability of potential fuel cell or battery materials.

## 1.3 References


1. R. F. Moran, D. M. Dawson, and S. E. Ashbrook, *Int. Rev. Phys. Chem.*, 2017, **36**, 39–115.
2. F. Bloch, *Phys. Rev.*, 1946, **70**, 460–474.
3. F. Bloch, W. W. Hansen, and M. Packard, *Phys. Rev.*, 1946, **70**, 474–485.
4. E. M. Purcell, H. C. Torrey, and R. V. Pound, *Phys. Rev.*, 1946, **69**, 37–38.
5. J. Keeler, *Understanding NMR Spectroscopy*, Wiley-Blackwell, 2nd edn., 2010.
6. S. E. Ashbrook, D. M. Dawson, and J. M. Griffin, in *Local Structural Characterisation*, eds. D. W. Bruce, D. O'Hare, and R. I. Walton, John Wiley & Sons, Ltd, 2014.
7. E. R. Andrew, A. Bradbury, and R. G. Eades, *Nature*, 1958, **182**, 1659.
8. E. R. Andrew, A. Bradbury, and R. G. Eades, *Nature*, 1959, **183**, 1802–1803.
9. L. J. Lowe, *Phys. Rev. Lett.*, 1959, **2**, 285–287.
10. S. E. Ashbrook and S. Sneddon, *J. Am. Chem. Soc.*, 2014, **136**, 15440−15456.
11. A. Samoson, E. Lippman, and A. Pines, *Mol. Phys.*, 1988, **65**, 1013–1018.
12. K. T. Mueller, B. Q. Sun, G. C. Chingas, J. W. Zwanziger, T. Terao, and A. Pines, *J. Magn. Reson.*, 1990, **86**, 470–487.
13. L. Frydman and J. S. Harwood, *J. Am. Chem. Soc.*, 1995, **117**, 5367–5368.
14. S. E. Ashbrook and D. McKay, *Chem. Commun.*, 2016, **52**, 7186–7204.
15. C. Bonhomme, C. Gervais, F. Babonneau, C. Coelho, F. Pourpoint, T. Azaïs, S. E. Ashbrook, J. M. Griffin, J. R. Yates, F. Mauri, and C. J. Pickard, *Chem. Rev.*, 2012, **112**, 5733–5779.
16. C. J. Pickard and F. Mauri, *Phys. Rev. B*, 2001, **63**, 245101.

17. E. Salager, G. M. Day, R. S. Stein, C. J. Pickard, B. Elena, and L. Emsley, *J. Am. Chem. Soc.*, 2010, **132**, 2564–2566.
18. M. Baias, J. N. Dumez, P. H. Svensson, S. Schantz, G. M. Day, and L. Emsley, *J. Am. Chem. Soc.*, 2013, **135**, 17501–17507.
19. R. K. Harris, R. E. Wasylishen, and M. J. Duer, *NMR Crystallography*, Wiley, Chichester, 1st edn., 2009.
20. R. Grau-Crespo, S. Hamad, C. R. A. Catlow, and N. H. De Leeuw, *J. Phys. Condens. Matter*, 2007, **19**, 256201.
21. J. González-López, S. E. Ruiz-Hernández, Á. Fernández-González, A. Jiménez, N. H. de Leeuw, and R. Grau-Crespo, *Geochim. Cosmochim. Acta*, 2014, **142**, 205–216.
22. C. J. Pickard and R. J. Needs, *Phys. Rev. Lett.*, 2006, **97**, 45504.
23. C. J. Pickard and R. J. Needs, *J. Phys. Condens. Matter*, 2011, **23**, 53201.

# Chapter 2: Solid-state NMR spectroscopy

## 2.1 Introduction

NMR spectroscopy is widely accepted as one of the most important and powerful analytical approaches for determining the molecular-level structure of materials and the dynamic processes occurring within them.[1,2] The modern-day success and widespread application of NMR spectroscopy stems from ground-breaking research carried out independently in the mid 1940s by Edward Purcell[3] and Felix Bloch,[4,5] who are considered to be the pioneers of the technique and as such were both awarded the 1952 Nobel Prize in Physics, for their "development of new ways and methods for nuclear magnetic precision methods".[6] NMR spectroscopy is a very sensitive probe of local structure, meaning it can provide information on geometry and atomic ordering and as such, is routinely used to study complex systems in both the solid and solution state. This sensitivity to short-range structural variation is in contrast to other analytical approaches, such as Bragg diffraction-based techniques, which provide structural information averaged over time and length scales. This makes diffraction-based approaches good for investigating the periodicity of materials, but is a disadvantage when looking at subtle structural variations that lead to a breakdown in long-range ordering. With more sophisticated NMR experiments and methodologies continuously being developed and improved, and with most stable elements in the periodic table possessing at least one NMR-active isotope, it is no surprise that NMR spectroscopy continues to be integral in the structure elucidation of an ever-increasing variety of systems. Given the widely applicable nature and extensive use of NMR spectroscopy, it is unsurprising that since its initial development over seventy years ago, numerous books, reviews and journal articles concerning the theory and application of this technique have been published. In addition to the references cited throughout this chapter, several textbooks were used extensively,[7–13] to which the reader is referred to for a more detailed discussion of the theory and application of NMR spectroscopy.

## 2.2 Essentials of NMR spectroscopy

Central to NMR spectroscopy is spin angular momentum, an intrinsic quantum-mechanical property that is described by the spin angular momentum vector, **I**, and associated spin quantum number, I. As both neutrons and protons are fermions, *i.e.*, they have I = 1/2, depending on the number of each of these present, atomic nuclei can also possess a net spin. It follows that nuclei with a spin I > 0 will have an overall spin angular momentum vector, **I**, which causes a nuclear magnetic dipole moment, $\boldsymbol{\mu}$, given by

$$\boldsymbol{\mu} = \gamma \mathbf{I} \ , \tag{2.1}$$

where $\gamma$, the gyromagnetic ratio, is the measure of angular momentum polarisability by an external magnetic field and therefore unique to each nucleus. The magnitude of the spin angular momentum for a given nuclide is

$$|\mathbf{I}| = \hbar\sqrt{I(I+1)} \ , \tag{2.2}$$

where $\hbar$ is the reduced Planck's constant ($h/2\pi = 1.0546 \times 10^{-34}$ J s). When there is no applied magnetic field, **I** is quantised along an arbitrary axis, the *z*-axis by convention, such that

$$I_z = m_I \hbar \ , \tag{2.3}$$

where $m_I$ is the magnetic spin quantum number, which can take any value between –I and +I, in steps of 1, leading to spin states with degeneracy 2I + 1. From Equation 2.1, $\boldsymbol{\mu}$ must also be quantised along the *z*-axis, *i.e.*,

$$\mu_z = \gamma I_z = \gamma m_I \hbar \ . \tag{2.4}$$

In the absence of an external magnetic field, there is no energetic preference for a particular spin state, and all orientations are degenerate. In a phenomenon known as the Zeeman interaction, nuclear magnetic moments interact with an external magnetic field, with the energy, $E_0$, of each spin state then dependent on its orientation relative to the magnetic field vector, $\mathbf{B}_0$, (which has magnitude $B_0$ and by convention lies along the *z*-axis), lifting the degeneracy of the spin states, as shown in Figure 2.1. The energy of the spin states only depends on the *z*-component of the nuclear magnetic dipole moment and the external magnetic field vector,

$$E_0 = -\mu_z B_0 \ . \tag{2.5}$$

From Equations 2.4 and 2.5 it can be inferred that the energy difference between two spin states in the presence of an external magnetic field is,

$$\Delta E = \Delta m_I \hbar \gamma B_0 \ . \tag{2.6}$$

As only single-quantum (*i.e.*, $\Delta m_I = \pm 1$) transitions are allowed by the NMR selection rules, all observable transitions in a system are degenerate, with an energy difference equal to

$$\left| E \right| = -\gamma \hbar B_0 \ . \tag{2.7}$$

These transitions appear at the Larmor frequency, $\omega_0$, which represents the resonant frequency of a free (bare) nucleus in a vacuum, and is given by

$$\omega_0 = -\gamma B_0 \ , \tag{2.8}$$

in rad $s^{-1}$, or

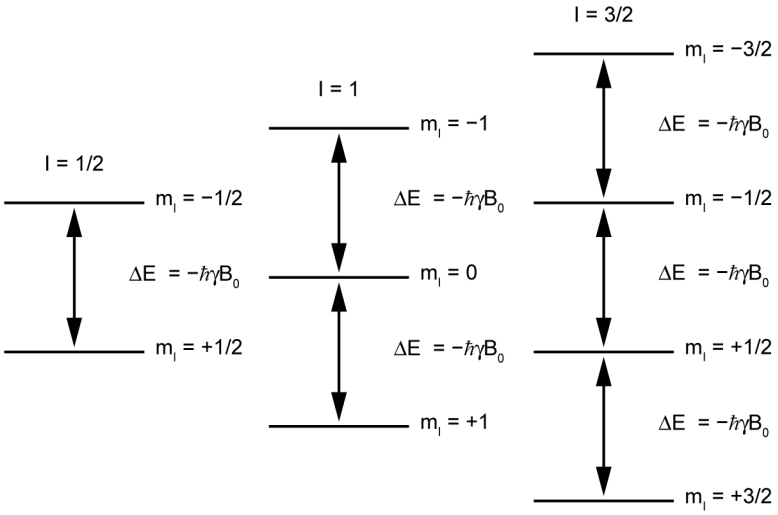


**Figure 2.1:** Schematic showing the effect of the Zeeman interaction on the nuclear energy levels of spin I = 1/2, I = 1 and I = 3/2 nuclei. The order of the energy levels assumes a positive γ.

$$\upsilon_0 = \frac{-\gamma B_0}{2\pi}\ , \tag{2.9}$$

in Hz. As most NMR spectroscopy experiments employ external magnetic field strengths between 5-25 T, the Larmor frequency falls within the radiofrequency (rf) range, meaning transitions can be effected by the application of electromagnetic radiation in this frequency range.

For a macroscopic system consisting of an ensemble of spins, the population of nuclear energy levels will be given according to the Boltzmann distribution, with the difference in population between two adjacent energy levels expressed as

$$\frac{N_{m_I+1}}{N_{m_I}} = e^{\frac{-\gamma\hbar B_0}{k_B T}}\ , \tag{2.10}$$

where $N_{m_I}$ and $N_{m_I+1}$ are the nuclear populations of the $m_I$ and $m_I+1$ states, respectively (for spin I = 1/2 nuclei, these are the $m_I = +1/2$ and $m_I = -1/2$ nuclear spin states, aligned parallel and antiparallel to $\mathbf{B}_0$,

respectively, if $\gamma$ is positive), T is the absolute temperature and $k_B$ is Boltzmann's constant ($1.3806 \times 10^{-23}$ J $K^{-1}$). As NMR spectroscopy is related to the population difference between spin states, which is often quite small, it is often considered to be an insensitive technique. For example, as the $^1H$ nucleus (I = 1/2) has a $\gamma$ of $26.7513 \times 10^7$ $s^{-1}$ $T^{-1}$, at 298 K with $B_0$ = 9.4 T, the population difference between the two adjacent energy levels would be 0.999936, showing that at this temperature and field strength there are almost an equal number of spins in the upper and lower state. By studying Equation 2.10, it can be seen that increasing $B_0$ and decreasing T are the only ways to increase the population difference, as all other quantities are either constants or nucleus dependent.

For nuclei with I = 1/2, the macroscopic magnetisation can easily be defined in terms of a bulk magnetisation vector, $\mathbf{M}_0$, which is the sum of all individual magnetic moments that align parallel to $\mathbf{B}_0$, along the *z*-axis, as shown in Figure 2.2. Therefore, the magnitude of $\mathbf{M}_0$ depends on the equilibrium population difference between the two nuclear spin states,

$$\Delta N_{equilib} = N_{m_I} - N_{m_I+1} \ . \qquad (2.11)$$

The vector model, conceived by Bloch,[4] is used to visualise the effect of a rf pulse on the bulk magnetisation vector. This representation is a convenient classical framework that describes an NMR experiment. Though more elegant and concise methods for describing the ensemble of nuclear spins

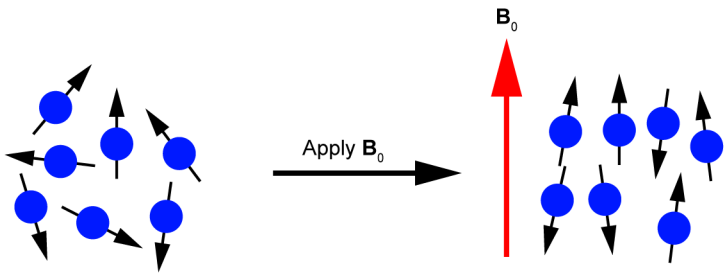


**Figure 2.2:** Schematic showing the alignment of nuclear spins upon the application of an external magnetic field, $\mathbf{B}_0$.

during an NMR experiment exist, such as the density operator formalism,[14,15] which is a quantum mechanical description of the macroscopic number of spins, these more complex frameworks are not discussed here.

If somehow $\mathbf{M}_0$ is moved away from the external magnetic field, it would precess around the *z*-axis at the Larmor frequency,[4,5] tracing a cone with $\mathbf{B}_0$ at its centre. It is easier to consider the effects of a pulse using a rotating frame, where the *x* and *y* axes rotate about *z* at a frequency $\omega_{rf}$. In the laboratory frame a rf pulse, applied at frequency $\omega_{rf}$, is described by an oscillating field with two separate components counter-rotating with angular frequencies of $\pm\omega_{rf}$, as shown in Figure 2.3. In the rotating frame, the component rotating at $+\omega_{rf}$ appears static, and the other component has a frequency of $-2\omega_{rf}$, far enough away for it to be neglected. The result of this is that the time dependence is removed, allowing the rf pulse to be thought of as a fixed field $\mathbf{B}_1$, of magnitude $B_1$. As $\mathbf{B}_1$ has no prerequisite orientation, other than needing to be perpendicular to $\mathbf{B}_0$, theoretically it can be applied anywhere within the *xy* plane. It is important that the phase ($\phi$) of the rf field, a quantity which describes the orientations of $\mathbf{B}_1$ and the *x* and *y* axes, be specified.

In the rotating frame, Larmor precession will occur at an offset frequency ($\Omega$) given by

$$\Omega = \omega_0 - \omega_{rf} \ . \tag{2.12}$$

If $\omega_0 = \omega_{rf}$, the rf pulse is said to be "on resonance" and the bulk magnetisation is static in the rotating frame as $\Omega = 0$. In the rotating frame an apparent magnetic field, $\Delta B_0$, remains aligned along the *z* axis, such that

$$\Omega = -\gamma \Delta B_0 \ . \tag{2.13}$$

A short burst or "pulse" of rf radiation nutates the bulk magnetisation away from $\mathbf{B}_0$, about the static $\mathbf{B}_1$ field, at a rate of

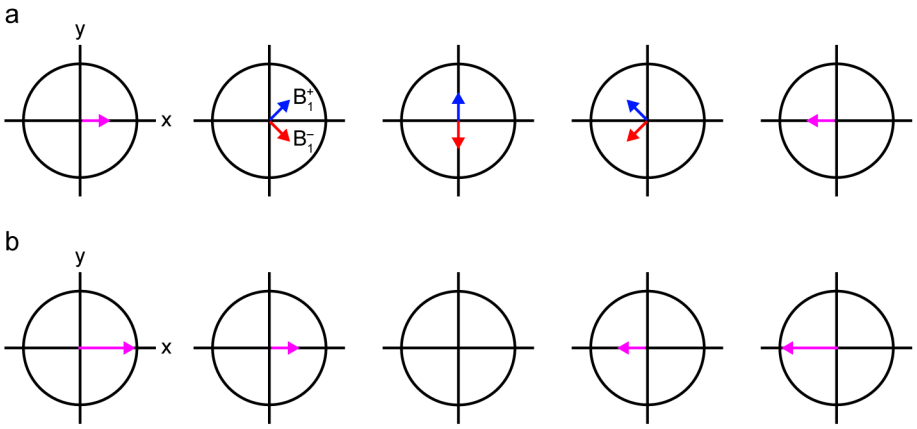


**Figure 2.3:** Schematic showing how (a) two counter-rotating fields denoted by $B_1^+$ and $B_1^-$, combine to give (b) an oscillating field in the laboratory frame.

$$\omega_1 = -\gamma B_1 \ . \tag{2.14}$$

The degree to which $\mathbf{M}_0$ nutates is described by the flip angle (β) of the pulse, which is dependent on the pulse duration, $\tau_p$, and $\omega_1$,

$$\beta = \tau_p \omega_1 \ . \tag{2.15}$$

Although any are possible, typical flip angles used in NMR experiments are β = 90°, where $\mathbf{M}_0$ lies in the transverse (*xy*) plane, and β = 180°, which leads to an inversion of the bulk magnetisation, causing $\mathbf{M}_0$ to lie along –*z*. When there are two static fields being applied, $\Delta\mathbf{B}_0$ along the *z*-axis and $\mathbf{B}_1$ in the

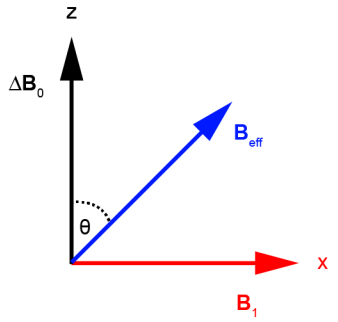


**Figure 2.4:** Schematic showing the effective field vector, $\mathbf{B}_{eff}$, and the tilt angle, θ, between the apparent and effective field.

transverse plane, the nuclear magnetic moments will experience an effective magnetic field, $\mathbf{B}_{eff}$, as shown in Figure 2.4, given by

$$\mathbf{B}_{eff} = \sqrt{\Delta\mathbf{B}_0^2 + \mathbf{B}_1^2} \ . \tag{2.16}$$

$\mathbf{M}_0$ nutates about this field at a frequency of

$$\omega_{eff} = -\gamma B_{eff} \ . \tag{2.17}$$

As shown in Figure 2.5, once the rf pulse is stopped, the bulk magnetisation vector precesses in the transverse plane. The process by which the *z*-component of $\mathbf{M}_0$ returns to thermal equilibrium is termed longitudinal or spin-lattice relaxation and is characterised by the time constant, $T_1$. $T_1$ is sample dependent and in solids can span many orders of magnitude, from milliseconds to hours. Transverse, or spin-spin relaxation, characterised by the time constant, $T_2$, is the dephasing of magnetisation in the transverse plane. This dephasing is caused by inhomogeneous relaxation rates, with different components of the bulk magnetisation vector precessing at frequencies $\Omega \pm \Delta\Omega$, meaning after time period, t, $\mathbf{M}_{xy}$ (the transverse component of the bulk magnetisation vector) will have a frequency distribution of $2\Delta\Omega t$. There are many dynamic (motional), nuclear-electron and nuclear-nuclear interactions that can affect both spin-lattice and spin-spin relaxation, but it is typically seen that in solids, $T_1 >> T_2$.

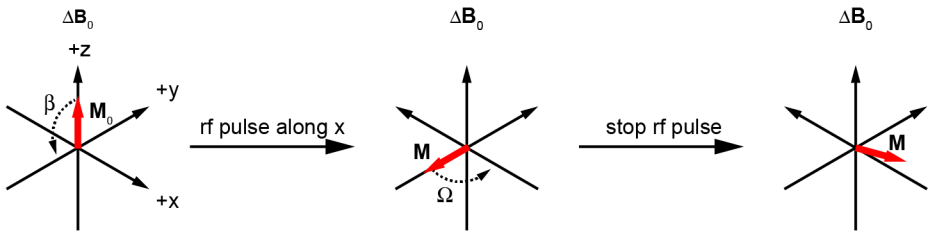


**Figure 2.5:** Vector model showing the effect of a rf pulse applied along the *x* axis on the bulk magnetisation vector.

The precession of the magnetisation vector is the quantity that is measured during an NMR experiment. Mounting a coil of wire round the sample and aligning it in the *xy*-plane allows the current generated when the magnetisation vector interacts with the coil to be detected. Once amplified, this induced current is recorded, giving the so-called free induction signal, which oscillates at the Larmor frequency. As this signal eventually decays away due to relaxation processes, it is often referred to as free induction decay, or FID. As shown in Figure 2.6, a Fourier transformation (FT)[16] can be used to produce a frequency-domain spectrum from the (time-domain) FID. The sign of precession in the rotating frame, (*i.e.*, the sign of Ω) can be determined using quadrature detection[17,18] where two detectors are used to simultaneously measure both the *x* and *y* components of the FID. This gives a time-dependent signal, s(t),

$$s(t) = \left[\cos \Omega t + i \sin \Omega t\right] e^{-t/T_2} \ , \tag{2.18}$$

$$s(t) = e^{i\Omega t} e^{-t/T_2} \ \ t \geq 0 \ , \tag{2.19}$$

$$s(t) = 0 \ \ t < 0 \ . \tag{2.20}$$

The signal is then Fourier transformed into a frequency-domain spectrum, S(ω), which contains both real and imaginary components

$$S(\omega) = \int_0^\infty s(t) e^{i\omega t} \, dt \ , \tag{2.21}$$

$$S(\omega) = A(\Delta\omega) - iD(\Delta\omega) \ . \tag{2.22}$$

These real and imaginary components, defined in Equation 2.23 and 2.24, respectively, correspond to absorptive and dispersive Lorentzian lineshape,

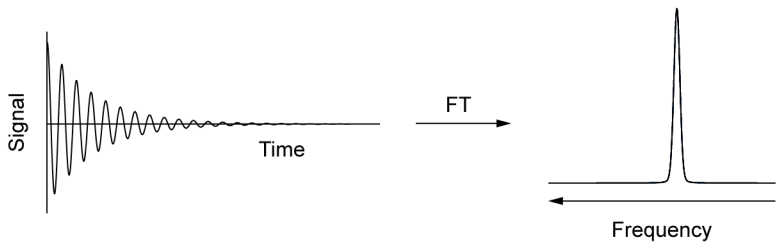


**Figure 2.6:** Time-domain FID and the frequency-domain spectrum produced after a Fourier transformation.

$$A(\Delta\omega) = \frac{1/T_2}{(1/T_2)^2 + (\Delta\omega)^2} \ , \tag{2.23}$$

$$D(\Delta\omega) = \frac{\Delta\omega}{(1/T_2)^2 + (\Delta\omega)^2} \ . \tag{2.24}$$

As spectral resonances are the sum of both real and imaginary parts, after Fourier transforming the signal, the final spectrum is usually "phased" to ensure the real component contains only the purely absorptive signal.

## 2.3 NMR interactions

As discussed in the previous section, every NMR-active nuclide in a sample will produce a resonance at the corresponding Larmor frequency. If this level of detail is all that NMR spectroscopy could provide, it would be of limited use. However, interactions between the nucleus being investigated and other nuclei, electric field gradients, unpaired electrons and nearby electron density, affect the local magnetic field at a nuclear site and therefore, result in a change in resonance frequency. Hence, species with different chemical, or even crystallographic environments give separate resonances within an NMR spectrum. This makes NMR spectroscopy an invaluable technique for studying local structure, dynamics and disorder.

### 2.3.1 The chemical shift

The presence and motion of electrons surrounding a nucleus, either in atomic or molecular orbitals, causes a small magnetic field, **B**′, to be produced. This small local magnetic field can oppose or augment the external magnetic field, $\mathbf{B}_0$, leading to nuclei experiencing an effective field at the nucleus, **B** (different from $\mathbf{B}_{\text{eff}}$ described in the previous section) of

$$\mathbf{B} = \mathbf{B}_0 - \mathbf{B}' \ , \tag{2.25}$$

or

$$\mathbf{B} = \mathbf{B}_0(1-\sigma) \ , \tag{2.26}$$

where σ is the field-independent shielding constant. This magnetic shielding interaction causes a change in the observed resonance frequency, such that

$$\omega = \omega_0(1-\sigma) \ . \tag{2.27}$$

It is usual to report the observed resonant frequency, ω of a nucleus as a chemical shift, δ, as the absolute σ is hard to measure. This is achieved by relating the resonance frequency to that of a reference compound ($\omega_{\text{ref}}$)

$$\delta = \frac{\omega - \omega_{\text{ref}}}{\omega_{\text{ref}}} \ . \tag{2.28}$$

The denominator causes the chemical shift to be both dimensionless and field independent. This latter property is particularly useful as it enables spectra acquired at different $B_0$ to be directly compared. The chemical shift is related to chemical shielding according to

$$\delta = \frac{\sigma_{ref} - \sigma}{1 - \sigma_{ref}} , \tag{2.29}$$

where $\sigma_{ref}$ is the shielding associated with the reference compound (and gives rise to $\omega_{ref}$). As typically $\sigma_{ref} << 1$, the relationship between $\delta$ and $\sigma$ can usually be simplified to

$$\delta = \sigma_{ref} - \sigma . \tag{2.30}$$

Unlike $\sigma$, which describes the shielding of the nucleus, $\delta$ is a deshielding parameter meaning that the $\delta$ and $\sigma$ scales are of opposite sign. Given that the observed chemical shift is often very small, by convention $\delta$ is reported in parts per million, 1 ppm = $10^{-6}$.

### 2.3.2 Chemical shift anisotropy

As the electron density surrounding a nucleus is seldom spherical (except for nuclei in highly symmetrical environments), the chemical shielding scalar, $\sigma$, is not sufficient. Instead, the chemical shielding tensor, $\boldsymbol{\sigma}$, a second-rank tensor, described by nine coefficients in a 3×3 matrix is required to describe the orientation dependence. In the laboratory frame the chemical shielding tensor is given by

$$\boldsymbol{\sigma}^{lab} = \begin{pmatrix} \sigma_{xx} & \sigma_{xy} & \sigma_{xz} \\ \sigma_{yx} & \sigma_{yy} & \sigma_{yz} \\ \sigma_{zx} & \sigma_{zy} & \sigma_{zz} \end{pmatrix} , \tag{2.31}$$

or when transformed into its principal axis system (PAS) by choosing axes in which $\boldsymbol{\sigma}$ is diagonal,

$$\boldsymbol{\sigma}^{\mathrm{PAS}} = \begin{pmatrix} \sigma_{11} & 0 & 0 \\ 0 & \sigma_{22} & 0 \\ 0 & 0 & \sigma_{33} \end{pmatrix}, \tag{2.32}$$

where $\sigma_{11}$, $\sigma_{22}$ and $\sigma_{33}$ represent the principal components of the symmetric part of the shielding tensor. The analogous chemical shift tensor, $\boldsymbol{\delta}$, is then expressed as

$$\boldsymbol{\delta}^{\mathrm{PAS}} = \begin{pmatrix} \delta_{11} & 0 & 0 \\ 0 & \delta_{22} & 0 \\ 0 & 0 & \delta_{33} \end{pmatrix}, \tag{2.33}$$

where

$$\delta_{ii} = \sigma_{ref} - \sigma_{ii} \ . \tag{2.34}$$

According to the IUPAC convention, $\delta_{11} \geq \delta_{22} \geq \delta_{33}$,[19] whereas in the Haeberlen notation,[20] the components are ordered such that $|\delta_{33} - \delta_{iso}| \geq |\delta_{11} - \delta_{iso}| \geq |\delta_{22} - \delta_{iso}|$, where $\delta_{iso}$, the isotropic chemical shift, is the trace of $\delta^{\mathrm{PAS}}$,

$$\delta_{iso} = \frac{\delta_{11} + \delta_{22} + \delta_{33}}{3} \ . \tag{2.35}$$

The orientation of the PAS relative to the laboratory frame is defined by the three Euler angles, $\alpha$, $\beta$, $\gamma$, which are unique for each crystallite orientation. Alternatively, the two polar angles, $\theta$ and $\phi$, which describe a rotation about and a tilt away from the laboratory *z*-axis, respectively, as shown in Figure 2.7, can be used to relate the orientation of $\boldsymbol{\delta}$ relative to $\mathbf{B}_0$. The chemical shift for a nucleus in a specific crystallite depends on these two angles, with

$$\delta = \delta_{iso} + \frac{\Delta_{CS}}{2}\left[(3\cos^2\theta - 1) + \eta_{CS}(\sin^2\theta\cos 2\phi)\right] , \quad (2.36)$$

where $\Delta_{CS}$ and $\eta_{CS}$ are the chemical shift anisotropy (sometimes termed the reduced anisotropy) and asymmetry, respectively, equal to

$$\Delta_{CS} = \delta_{33} - \delta_{iso} , \quad (2.37)$$

and

$$\eta_{CS} = \frac{\delta_{22} - \delta_{11}}{\Delta_{CS}} . \quad (2.38)$$

when following the Haeberlen notation.

Another popular notation is the Herzfeld-Berger convention,[21] which orders the $\delta_{ii}$ in the same way as the IUPAC convention. However, as shown in Figure 2.8a, the shielding is described by its span ($\Omega_{CS}$) and skew ($\kappa_{CS}$), which denote the width and shape of a lineshape, respectively,

$$\Omega_{CS} = \delta_{11} - \delta_{33} \quad (\Omega_{CS} \geq 0) , \quad (2.39)$$

and

$$\kappa_{CS} = \frac{3(\delta_{22} - \delta_{iso})}{\Omega_{CS}} \quad (-1 \leq \kappa_{CS} \leq +1) . \quad (2.40)$$

It is clear that for a single crystallite the anisotropic component of the chemical shift tensor causes an orientation dependence for the observed frequency, whereas for a powdered system, the presence of crystallites with every possible orientation with respect to $\mathbf{B}_0$ results in a distribution of frequencies, leading to a broadened lineshape, with $\delta_{11}$ and $\delta_{33}$ representing

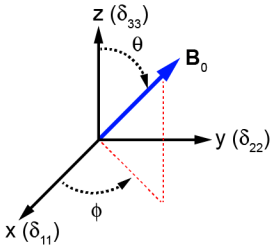


**Figure 2.7:** Schematic showing how the polar angles, θ and ϕ, relate the PAS to the external magnetic field $\mathbf{B}_0$.

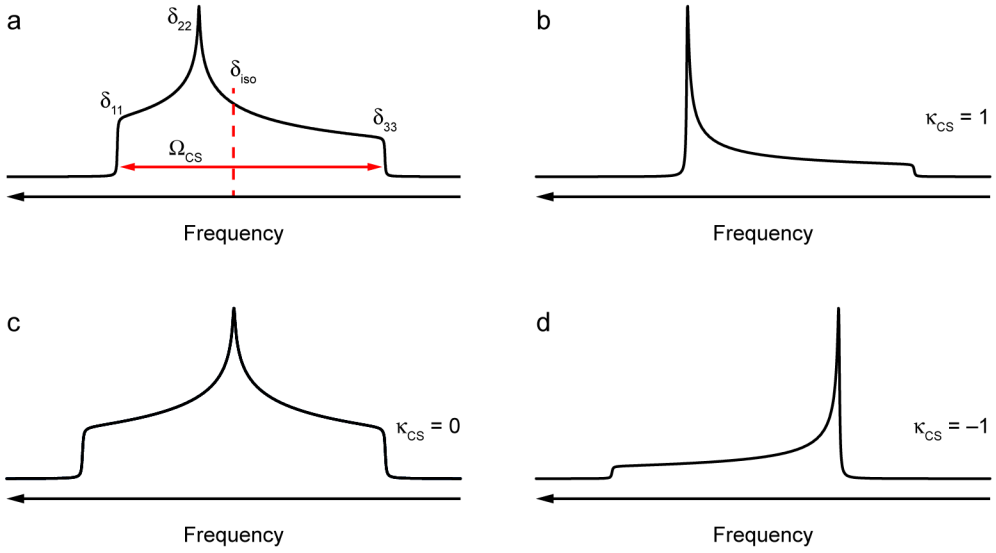


**Figure 2.8:** Schematic powder pattern lineshape showing (a) the components of the chemical shift tensor, **δ**, $\delta_{11}$, $\delta_{22}$, $\delta_{33}$, the isotropic chemical shift, $\delta_{iso}$ and the span, $\Omega_{CS}$, and (b-d) the powder pattern lineshape resulting from (b) $\kappa_{CS} = 1$, (c) $\kappa_{CS} = 0$ and (d) $\kappa_{CS} = -1$. The figures have been modified from those presented by Moran *et al*.[22]

the frequency extremes. In the solution state, rapid molecular tumbling averages the orientation of the molecule with respect to $B_0$, leaving only the isotropic shift.

### 2.3.3 Dipolar coupling

In addition to interactions with the electrons surrounding a nucleus, the position of a spectral resonance can also be affected by interactions with nearby nuclei. The dipolar interaction refers to the direct coupling of nuclear dipole moments "through space", where one spin is affected by the local

magnetic field produced by a second spin. For an isolated system containing two nuclei, I and S, the dipolar interaction results in a doublet in the spectrum (for a single crystal). This interaction, which is dependent on the internuclear distance and the orientation of the spins relative to $\mathbf{B}_0$, is described by the dipolar coupling tensor, **D**. In the PAS, the dipolar coupling tensor ($\mathbf{D}^{PAS}$) is traceless and axially symmetric. The magnitude of the dipolar coupling, $\omega_D$, is equal to

$$\omega_D = \omega_D^{PAS}\frac{1}{2}\left(3\cos^2\theta_{IS}-1\right) = -\frac{\mu_0\hbar\gamma_I\gamma_S}{4\pi r_{IS}^3}\left(3\cos^2\theta_{IS}-1\right), \qquad (2.41)$$

where $\gamma_I$ and $\gamma_S$ are the gyromagnetic ratios of I and S, $\mu_0$ is the permittivity of a vacuum, $r_{IS}$ is the magnitude of the internuclear vector $\mathbf{r}_{IS}$ and $\theta_{IS}$ is the angle between $\mathbf{r}_{IS}$ and $\mathbf{B}_0$, as shown in Figure 2.9. The dipolar interaction is strongly dependent on the gyromagnetic ratios and the internuclear distance, meaning the largest couplings will be observed for two high-$\gamma$ spins close in space.

A system containing an isolated pair of spins will result in a doublet with a width of $2\omega_D$ or $3\omega_D$ for the heteronculear or homonuclear dipolar interaction, respectively. In a polycrystalline sample where all crystallite orientations are present simultaneously, a Pake doublet is observed (shown schematically in Figure 2.10a).[23] However, in most cases there is a practically

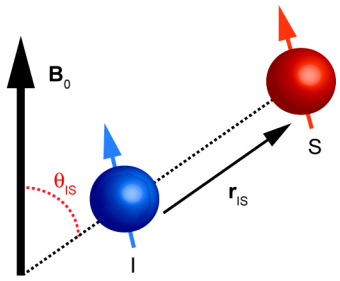


**Figure 2.9:** Schematic showing the dipolar interaction between two spins, I and S.

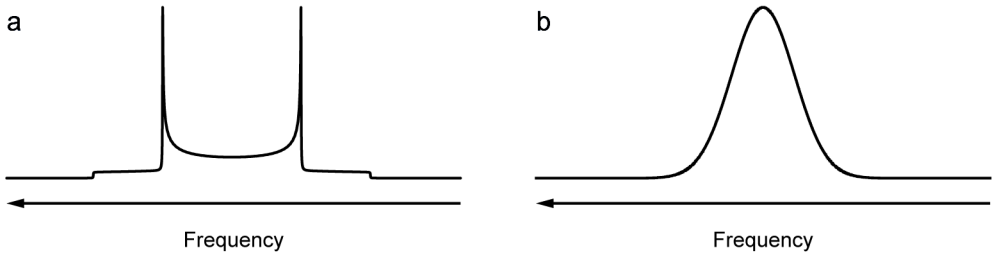


**Figure 2.10:** Schematic (a) Pake doublet lineshape resulting from the dipolar interaction between I and S, two spin I = 1/2 nuclei, (b) the Gaussian-type lineshape resulting from the combination of many dipolar interactions. The figures have been modified from those presented by Moran *et al*.[22]

infinite number of dipole interactions present in a powder sample, each with a particular internuclear distance and nuclear spin orientation relative to $\mathbf{B}_0$.

The overall effect of dipolar coupling is often a Gaussian-like broadening of the resonance, as shown in Figure 2.10b. Whereas for solid samples dipole interactions can have a magnitude of $10^3$-$10^5$ Hz, often resulting in noticeable line broadening, rapid molecular tumbling in the solution state averages this interaction to zero.

### 2.3.4 Scalar coupling

In addition to the internuclear dipolar interaction that occurs through space, neighbouring or nearby nuclear spins can also interact through chemical bonds. This interaction, termed scalar, indirect spin-spin or simply J coupling occurs *via* a mechanism facilitated by the transfer of magnetisation through regions of shared electron density, *e.g.*, hydrogen or covalent bonds.[24,25] The scalar coupling is represented by a second-rank tensor, denoted **J**, whose isotropic component, $J_{iso}$, is the observed "coupling constant"equal to

$$J_{iso} = \frac{J_{11} + J_{22} + J_{33}}{3} \quad . \tag{2.42}$$

The anisotropic and asymmetric components of **J**, are given by

$$\Delta_J = J_{33} - J_{iso} \ , \tag{2.43}$$

and

$$\eta_J = \frac{J_{22} - J_{11}}{\Delta_J} \ , \tag{2.44}$$

respectively. Given the scalar coupling provides information regarding the way in which nearby nuclear spins interact, it is not surprising that this internuclear coupling has been exploited to assist spectral assignment and structural characterisation.[26–32] However, scalar coupling constants are very small, usually several orders of magnitude smaller than the other interactions that affect solid-state spectra, and so are rarely resolved in a spectrum, although they can still be exploited for magnetisation transfer.

### 2.3.5 Quadrupolar interactions

Quadrupolar nuclei, *i.e.*, those with a spin quantum number, $I > 1/2$, make up 74% of the periodic table, with over 63% of all elements only possessing a quadrupolar NMR-active isotope.[33] Quadrupolar nuclei are of interest in a range of scientific disciplines, from chemistry, materials science and physics, to geology, as these elements are present in minerals, ceramics, catalysts and energy materials, as well as many other important systems.[34–48] However, the NMR spectra of quadrupolar nuclei are additionally broadened by the interaction between the nuclear electric quadrupole moment, eQ, (resulting from the non-spherical nuclear charge distribution), and the electric field gradient (EFG), present at the nucleus. The EFG is described by a tensor, **V**, which is traceless, and which is diagonalised in the principal axis system to give

$$\mathbf{V}^{\mathrm{PAS}} = \begin{pmatrix} V_{xx} & 0 & 0 \\ 0 & V_{yy} & 0 \\ 0 & 0 & V_{zz} \end{pmatrix}, \tag{2.45}$$

with the components ordered $|V_{zz}| \geq |V_{yy}| \geq |V_{xx}|$. The magnitude of the quadrupolar coupling is given by

$$C_Q = \frac{eQV_{zz}}{h}, \tag{2.46}$$

with the shape, or asymmetry of the interaction, given by

$$\eta_Q = \frac{V_{xx} - V_{yy}}{V_{zz}}. \tag{2.47}$$

The geometry of a system will have a large effect on the EFG and, therefore on $C_Q$, with very symmetrical systems such as those with tetrahedral or octahedral geometries often having very small (or even zero) quadrupolar coupling constants, whereas larger values of $C_Q$ (up to several MHz) can be observed for systems with lower point symmetry. Though the quadrupolar interaction can be very large, for most practically relevant cases its effect can be treated as a perturbation to the Zeeman energy levels. As there are 2I + 1 Zeeman energy levels, it follows that there will be 2I degenerate transitions at the Larmor frequency, $\omega_0$, *i.e.*, 3 transitions for a spin I = 3/2 nucleus, as shown in Figure 2.11. To a first-order approximation, the quadrupolar coupling lifts the degeneracy of the 2I transitions, resulting in a central transition (CT), with $m_I = \pm 1/2 \leftrightarrow \mp 1/2$, and satellite transitions (STs), with $m_I = \pm n/2 \leftrightarrow \pm m/2$. For a nucleus with half-integer spin quantum number, the CT is unaffected by the first-order quadrupolar interaction, but the frequencies of the STs now depend upon the quadrupolar splitting parameter, $\omega_Q$,

$$\omega_Q = \frac{\omega_Q^{PAS}}{2}[(3\cos^2\theta - 1) + \eta_Q(\sin^2\theta\cos 2\phi)], \quad (2.48)$$

where

$$\omega_Q^{PAS} = \frac{3\pi C_Q}{2I(2I+1)}, \quad (2.49)$$

in units of rad $s^{-1}$. For a single crystal this interaction would produce 2I resonances. In a powdered sample the CT resonance would remain sharp but the ST would exhibit powder-patter lineshapes, due to the orientation dependence of $\omega_Q$, as shown in Figure 2.12a. For large EFGs, a second-order perturbation must also be considered, which affects every transition in the spectrum as shown in Figure 2.11. Even though the second-order quadrupolar interaction is much smaller than the first-order interaction, the former can still cause significant line broadening, as shown in Figure 2.12b, where the CT is broadened by several kHz. As nuclei with integer spin quantum number, *i.e.*, $^2$H, $^6$Li, $^{10}$B, $^{14}$N, have no CT, all transitions are affected

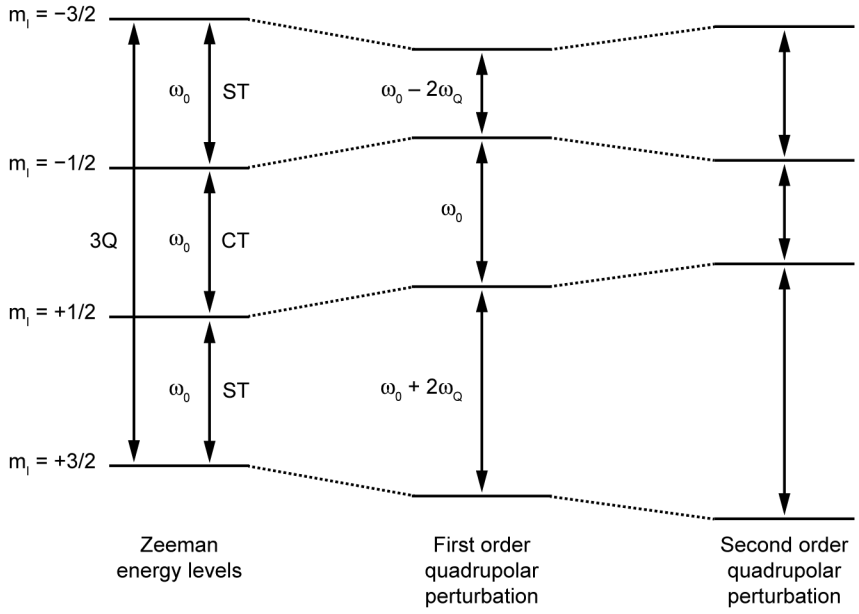


**Figure 2.11:** Schematic showing the perturbation of the 2I Zeeman energy levels of a spin I = 3/2 nucleus.

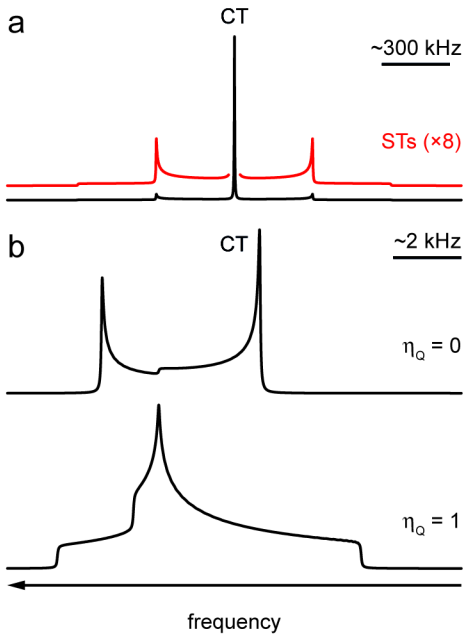


**Figure 2.12:** Schematic showing (a) the effect of the first-order quadrupolar interaction on the satellite transitions (STs), for $\eta_Q = 0$ and (b) expansions showing the anisotropic broadening of the central transition (CT) by the second-order quadrupolar interaction, for $\eta_Q = 0$ and 1 for a spin I = 3/2 nucleus. The figures have been modified from those presented by Moran *et al.*[22]

by the first-order quadrupolar interaction, often making it difficult to acquire and interpret spectra unless $C_Q$ is very small.

## 2.4 Experimental methods

### 2.4.1 Signal, sensitivity and resolution enhancement methods

The key limitation of solid-state NMR spectroscopy is that it is often difficult to acquire high-resolution spectra, as the anisotropic interactions discussed in the previous section cause resonances to be broad and frequently overlapped, making spectral interpretation (and the extraction of structural information) challenging. As a result it is not surprising that there is a constant drive to develop new approaches that can improve resolution and sensitivity, the most common of which are outlined briefly below.

### 2.4.1.1 Magic-angle spinning

One common approach for acquiring high-resolution solid-state NMR spectra involves rapid sample rotation in order to mimic the rapid molecular tumbling present in the solution-state; an approach that in principle removes orientation dependence, thus leaving only the isotropic components. As the chemical shielding, dipolar, scalar and first-order quadrupolar interactions all exhibit a similar orientation dependence, $(3\cos^2\theta - 1)/2$, when $\theta$ is equal to 54.736°, the anisotropic components from these interactions would be removed. Given it is not possible to manipulate the orientation of each individual crystallite in a sample simultaneously, this is achieved practically by physically rotating the entire sample about an axis inclined at an angle, $\chi$, 54.736° to $\mathbf{B}_0$ (see Figure 2.13), an approach called magic-angle spinning (MAS) developed in the late 1950s.[49–51] MAS is achieved by packing a powdered sample into a cylindrical "rotor", usually made of yttrium-stabilised zirconia, a material that can withstand the high forces generated during MAS. The greater the rotation rate required, the smaller the rotor diameter (and hence, volume) has to be, meaning there is a trade-off between resolution enhancement and sensitivity loss. Recently, it has been shown that using a 0.75 mm diameter rotor, rotation rates over 100 kHz are possible.[52–56] Despite this, most systems do not require such rapid spinning, with MAS rates of 10-60 kHz and rotor diameters between 4.0 and 1.3 mm more commonly used. When the sample rotation rate is too slow to fully remove the anisotropic components, additional signals termed spinning sidebands (SSBs) appear at integer multiples of the MAS rate, $\omega_R$, away from the

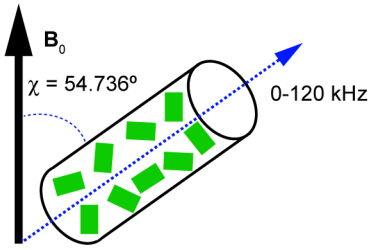


**Figure 2.13:** Schematic representation of the MAS, with individual crystallites shown by green rectangles.

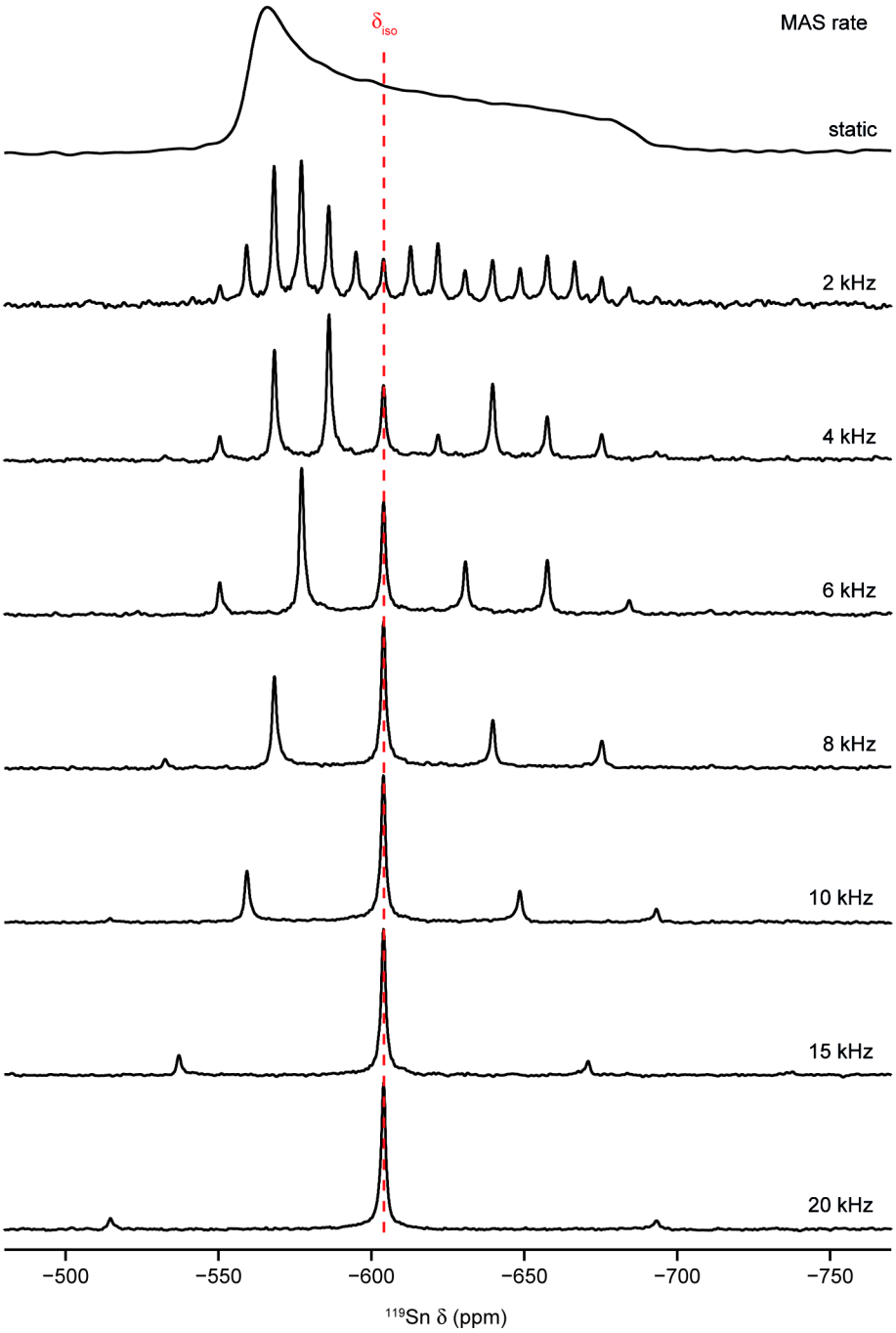


**Figure 2.14:** Effect of MAS upon the $^{119}$Sn (14.1 T) NMR spectra of $SnO_2$, containing a lineshape broadened by the CSA interaction, with spectra the result of averaging 16 transients, with a recycle interval of 30 s. At low MAS rates the spinning sideband manifold mirrors the static lineshape. As the MAS rate increases, the isotropic peak begins to dominate and the sidebands decrease in number and intensity. This figure have been modified from that presented by Ashbrook *et al*.[11]

isotropic resonance. As shown in Figure 2.14, the number of SSBs (and their intensities) decrease as the MAS rate increases. In order to record a spectrum

free of SSBs it is necessary to spin the sample at a rate greater than the width of the static lineshape.

### 2.4.1.2 Decoupling

In comparison to MAS, which, by rotating the sample at an angle of 54.736° to $\mathbf{B}_0$ alters the orientation of the interaction tensors, decoupling uses rf pulses to achieve similar averaging, allowing the dipolar and scalar couplings to be removed.[57,58] The most basic way of achieving decoupling between two different spins, I and S, *i.e.*, heteronuclear decoupling, is achieved by the continuous application of a rf pulse at the Larmor frequency of one species, whilst the FID for the second nucleus is acquired. High-power pulses are necessary to remove strong interactions, meaning care must be taken not to overheat the sample or damage the spectrometer hardware when performing heteronuclear decoupling. Homonuclear decoupling (*i.e.*, the removal of interactions between two I spins) is more challenging as this requires the same spin to be observed and manipulated simultaneously. This is achieved by acquiring an FID at particular points between decoupling pulses, where the coupling interaction is averaged instantaneously, rather than continuously irradiating the sample.[59,60]

### 2.4.1.3 Cross-polarisation

Unlike MAS or decoupling, which are employed primarily to improve signal resolution (although this does result in a concomitant increase in sensitivity), cross-polarisation (CP)[61,62] is used purely to improve sensitivity, and is one of the most common sensitivity enhancement techniques used today. CP works by transferring magnetisation from a highly abundant spin with a high γ, ($\gamma^H$) such as $^1$H, to a less abundant, lower γ, ($\gamma^L$) nucleus such as $^{13}$C or $^{15}$N. In addition to improving sensitivity through the transfer of magnetisation, the high γ, highly abundant species tends to relax more rapidly, meaning experiments can be recorded more quickly, with the summation of the

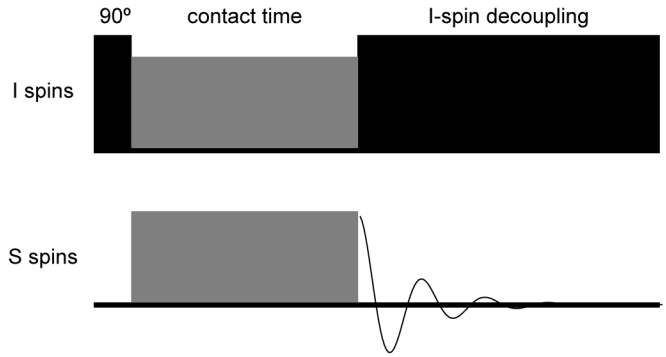


**Figure 2.15:** Pulse sequence for the CP experiment in which magnetisation is transferred from spin I to spin S.

experiments, *i.e.*, signal averaging, leading to an improved signal-to-noise ratio per unit time.

In CP, magnetisation transfer occurs *via* the heteronuclear dipolar coupling, meaning that in addition to improving sensitivity, CP also provides structural information on the spatial proximity of the I and S spins. However, this reliance on the dipolar coupling does mean that spectra acquired using CP will be non-quantitative, meaning that the detailed interpretation of relative peak intensities can be misleading.

As shown in Figure 2.15, the CP pulse sequence involves the creation of I-spin magnetisation by an initial 90º rf pulse, with the magnetisation transferred to the S spin during a contact time, where low-power pulses are applied to both spins simultaneously to "lock" the magnetisation along a particular direction while transfer occurs. The contact time is chosen to maximise the amount of magnetisation transferred, meaning it depends on the relaxation rate of the two spins during the spin lock, described by time constant, $T_{1\rho}$, and the magnetisation transfer rate, which is proportional to the dipolar coupling. After the contact time, decoupling of spin I is typically employed, while the FID for spin S is acquired.

In order for magnetisation transfer to occur in the CP experiment, the rf fields used during the spin-lock period must fulfil the Hartmann-Hahn condition[63]

$$\gamma_I B_{1I} = \gamma_S B_{1S} \ , \tag{2.50}$$

which has to be adapted when CP is performed in conjunction with MAS, such that

$$\gamma_I B_{1I} = \gamma_S B_{1S} \pm n\ \omega_R \ , \tag{2.51}$$

where n is an integer and $\omega_R$ is the MAS rate in rad $s^{-1}$.

### 2.4.2 Relevant NMR experiments

Although the work carried out for this thesis is purely computational, involving the use of first-principles calculations to assist the structural characterisation of disordered inorganic materials, throughout Chapters 5 and 6 experimental solid-state NMR spectra will be shown. As a result, this section briefly introduces some specific NMR experiments that have been used to study the materials discussed later in this thesis.

#### 2.4.2.1 Pulse-acquire

The pulse-acquire or "one pulse" experiment, shown in Figure 2.16a is the simplest pulse sequence used to record NMR spectra, and involves a single rf pulse followed by the acquisition of the resulting FID. This is repeated N times with each individual FID summed together to give the final spectrum. Repeating the experiment N times improves the signal-to-noise ratio by a factor of $N^{1/2}$, meaning that averaging more transients improves sensitivity, crucial when dealing with insensitive or low abundant nuclei. To ensure that unwanted probe ringing does not affect the spectrum, a time

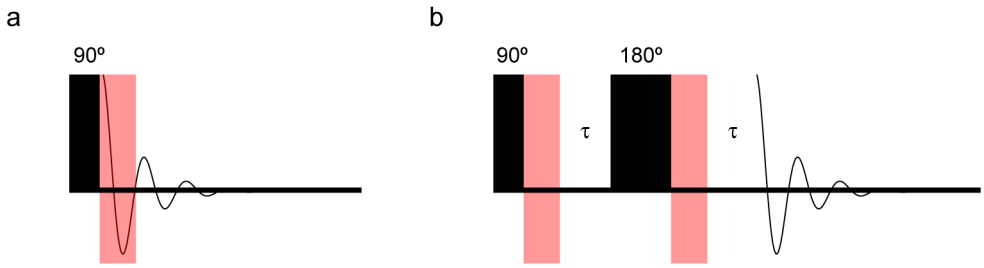


**Figure 2.16:** Pulse sequence for (a) one pulse and (b) spin echo experiments. Pulses are shown as black rectangles, with the dead time, $\tau_D$ marked in red.

delay, $\tau_D$, termed the dead time, is left between the end of the rf pulse and the start of FID acquisition.

### 2.4.2.2 Spin-echo

The spin-echo experiment,[64] shown in Figure 2.16b, consists of 90° and 180° pulses separated by time, τ, with the FID then acquired after a second τ. During the first τ time the nuclear spins will precess in the transverse plane at slightly different rates, leading to dephasing of the magnetisation. The 180° pulse inverts the magnetic moments about in the *xy* plane and after the second τ time, the spins will be refocused, allowing the full FID to be acquired, without any signal being lost during the dead time. This is most important for broad lines, where significant portion of the signal can be lost in the dead time, leading to loss of intensity and distortion of the spectra lineshapes. When used under MAS, the time period between the pulses should be synchronised with the rotor period.

### 2.4.2.3 CPMG

The Carr-Purcell-Meiboom-Gill (CPMG) echo-train experiment[65] is a very popular approach to overcome sensitivity issues associated with large anisotropic broadening that may be too significant for current MAS rotation rates to remove. CPMG can also be used in conjunction with MAS provided the pulses are applied synchronously with the sample rotation. In the CPMG

experiment, a series of spin echoes are used to repeatedly refocus the magnetisation, throughout acquisition, resulting in an FID comprised of multiple echoes. Upon Fourier transformation this results in a spectrum containing discrete 'spikelets'. The spikelet manifold in the CPMG spectrum mirrors that of the static lineshape, but as the intensity is restricted to discrete regions in the spectrum (the spikelets) the peak-height signal is increased significantly, leading to improved sensitivity.

#### 2.4.2.4 HETCOR

HETCOR is the general term for any heteronuclear correlation experiment that uses either the through-bond (scalar coupling) or through-space (dipolar coupling) interaction to transfer magnetisation between I and S spins, where I ≠ S. The CP HETCOR experiment, analogous to the CP method, transfers magnetisation between different spins *via* the dipolar coupling interaction, however, as shown in Figure 2.17, a time period, $t_1$, is included for the I spins before the spin-lock pulses are applied, allowing the I spins to evolve before magnetisation transfer. By varying $t_1$, the magnetisation available for transfer during the spin-lock process can be modulated, allowing for the acquisition of a two-dimensional dataset.

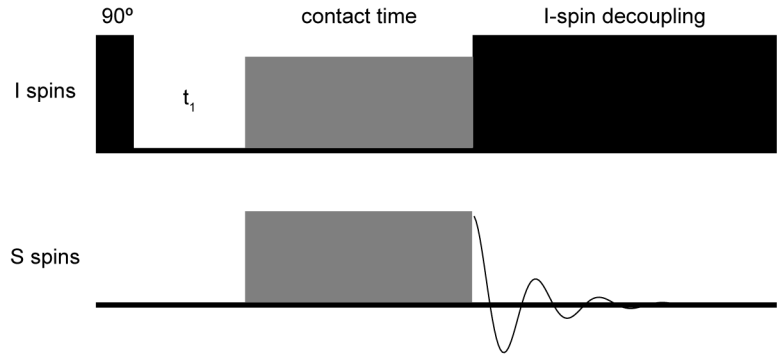


**Figure 2.17:** Pulse sequence for the CP HETCOR experiment in which magnetisation is transferred from spin I to spin S.

### 2.4.2.5 DQ MAS

The double-quantum (DQ) MAS experiment correlates coherence between homonuclear or heteronuclear species *via* the through-space (dipolar) or through-bond (scalar) interaction, producing a two-dimensional spectrum. As the dipolar coupling is strongly dependent on interatomic distances, these experiments are able to provide insight into the spatial arrangement of atoms within a system. In a DQ MAS spectrum, coupled nuclear spins are represented as a pair of cross peaks. For two coupled spins, A and B, the peaks would have single-quantum, double-quantum coordinates ($\delta_A$,$\delta_{A+B}$) and ($\delta_B$,$\delta_{A+B}$), respectively. Nuclei in the same magnetic environment appear as a single auto-correlation peak, appearing at δ,2δ, *i.e.*, along the diagonal of the spectrum. A schematic DQ MAS spectrum resulting

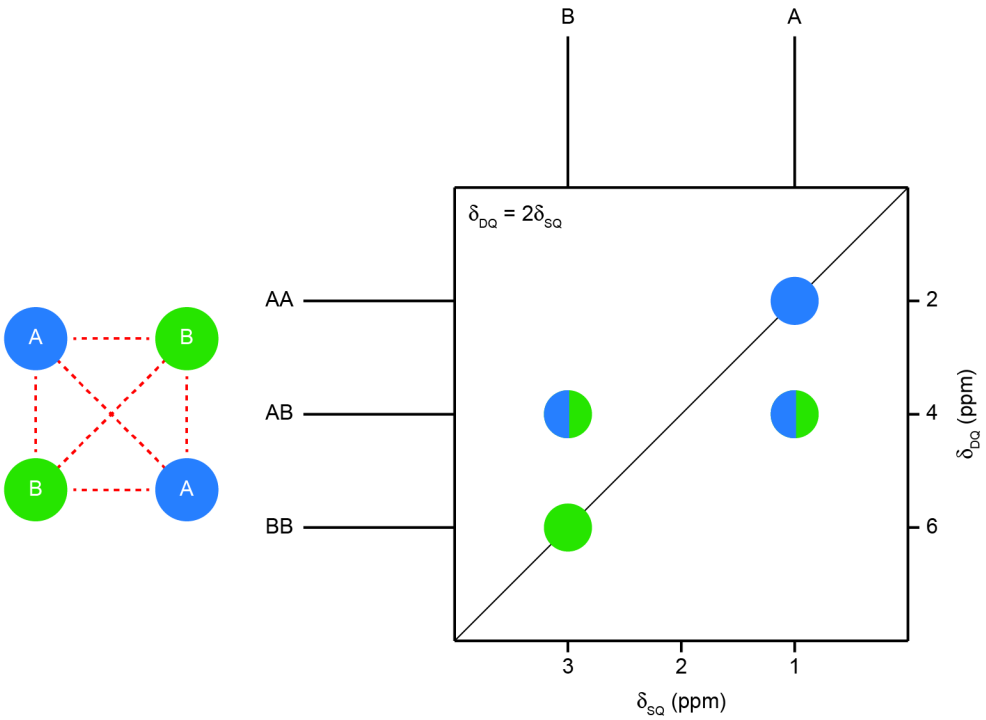


**Figure 2.18:** Schematic representation of a DQ MAS spectrum for the hypothetical $A_2B_2$ spin system, showing cross-peaks between the A and B spins, as well as auto-correlation peaks that lie along the diagonal of the spectrum, with A and B spins shown as blue and green circles, respectively.

from a hypothetical AB system showing dipolar interactions between all spins, is shown in Figure 2.18.

#### 2.4.2.6 STMAS

Introduced in 2000 by Gan, the satellite-transition (ST) MAS NMR experiment[66,67] is a method of acquiring high-resolution NMR spectra of half-integer quadrupolar nuclei.[68] This is a two-dimensional experiment involving the correlation of single-quantum STs in the $t_1$ ($F_1$) dimension and CT in the $t_2$ ($F_2$) dimension. Spectral acquisition requires precise angle setting (to one thousandth of a degree), as well as performing the experiment under rotor-synchronised conditions to remove the first-order quadrupolar broadening that also affects the STs.[68] The experiment exploits the fact that the second-order quadrupolar broadening that affects the ST and CT is related by a simple scaling factor, while the factor that relates the isotropic terms is different, leading to these being retained in the indirect dimension of the experiment. Although similar in principle to the much more widely applied multiple-quantum (MQ) MAS experiment,[69,70] the purely single-quantum nature of STMAS provides a significant sensitivity advantage. Therefore, STMAS is often employed when sensitivity is poor, *e.g.*, for nuclei with low natural abundance or low $\gamma$, for systems subject to larger quadrupolar interactions, or for samples with low sample volume.

## 2.5 References


1. D. C. Apperley, R. K. Harris, and P. Hodgkinson, *Solid State NMR: Basic Principles and Practice*, Momentum Press, LLC, New York, 2nd edn., 2012.
2. K. J. D. MacKenzie and M. E. Smith, in *Multinuclear Solid-State NMR of Inorganic Materials*, Pergamon Press, Oxford, 1st edn., 2002.
3. E. M. Purcell, H. C. Torrey, and R. V. Pound, *Phys. Rev.*, 1946, **69**, 37–38.
4. F. Bloch, *Phys. Rev.*, 1946, **70**, 460–474.
5. F. Bloch, W. W. Hansen, and M. Packard, *Phys. Rev.*, 1946, **70**, 474–485.

6. *Nature*, 1952, **170**, 911–912.
7. M. J. Duer, *Introduction to Solid-State NMR Spectroscopy*, Blackwell Publishing Ltd, 1st edn., 2004.
8. T. D. W. Claridge, *High-Resolution NMR Techniques in Organic Chemistry*, Elsevier, 2nd edn., 2008.
9. P. J. Hore, *Nuclear Magnetic Resonance*, Oxford University Press, Oxford, 1st edn., 1995.
10. P. J. Hore, J. A. Jones, and S. Wimperis, *NMR: The Toolkit*, Oxford University Press, Oxford, 1st edn., 2000.
11. S. E. Ashbrook, D. M. Dawson, and J. M. Griffin, in *Local Structural Characterisation*, eds. D. W. Bruce, D. O'Hare, and R. I. Walton, John Wiley & Sons, Ltd, 2014.
12. J. Keeler, *Understanding NMR Spectroscopy*, Wiley-Blackwell, 2nd edn., 2010.
13. M. H. Levitt, *Spin Dynamics: Basics of Nuclear Magnetic Resonance*, John Wiley & Sons, Ltd, 2nd edn., 2008.
14. O. W. Sorensen, G. W. Eich, M. H. Levitt, G. Bodenhausen, and R. R. Ernst, *Prog. Nucl. Magn. Reson. Spectrosc.*, 1984, **16**, 163–192.
15. D. P. Goldenberg, *Concepts Magn. Reson. Part A. Bridg. Educ. Res.*, 2010, **88**, 49–83.
16. R. R. Ernst and W. A. Anderson, *Rev. Sci. Instrum.*, 1966, **37**, 93–102.
17. J. D. Ellett, M. G. Gibby, U. Haeberlen, L. M. Huber, M. Mehring, A. Pines, and J. S. Waugh, *Adv. Magn. Opt. Reson.*, 1971, **5**, 117–176.
18. G. Bodenhausen, R. Freeman, G. A. Morris, R. Niedermeyer, and D. L. Turner, *J. Magn. Reson.*, 1977, **25**, 559–562.
19. R. K. Harris, E. D. Becker, S. M. De Cabral Menezes, P. Granger, R. E. Hoffman, and K. W. Zilm, *Magn. Reson. Chem.*, 2008, **46**, 582–598.
20. U. Haeberlen, *High Resolution NMR in Solids Selective Averaging*, Academic Press, New York, 1st edn., 1976.
21. J. Herzfeld and A. E. Berger, *J. Chem. Phys.*, 1980, **73**, 6021–6030.
22. R. F. Moran, D. M. Dawson, and S. E. Ashbrook, *Int. Rev. Phys. Chem.*, 2017, **36**, 39–115.
23. G. E. Pake, *J. Chem. Phys.*, 1948, **16**, 327–336.
24. E. L. Hahn and D. E. Maxwell, *Phys. Rev.*, 1952, **88**, 1070–1084.

25. R. E. Wasylishen, in *Encyclopedia of Magnetic Resonance*, eds. R. K. Harris and R. E. Wasylishen, John Wiley, Chichester, 2007.
26. J. Vaara, J. Jokisaari, R. E. Wasylishen, and D. L. Bryce, *Prog. Nucl. Magn. Reson. Spectrosc.*, 2002, **41**, 233–304.
27. J. M. Griffin, J. R. Yates, A. J. Berry, S. Wimperis, and S. E. Ashbrook, *J. Am. Chem. Soc.*, 2010, **132**, 15651–15660.
28. P. Sanz Camacho, D. McKay, D. M. Dawson, C. Kirst, J. R. Yates, T. F. G. Green, D. B. Cordes, A. M. Z. Slawin, J. D. Woollins, and S. E. Ashbrook, *Inorg. Chem.*, 2016, **55**, 10881–10887.
29. D. Massiot, F. Fayon, B. Alonso, J. Trebose, and J. P. Amoureux, *J. Magn. Reson.*, 2003, **164**, 160–164.
30. P. Florian, F. Fayon, and D. Massiot, *J. Phys. Chem. C*, 2009, **113**, 2562–2572.
31. A. Lesage, M. Bardet, and L. Emsley, *J. Am. Chem. Soc.*, 1999, **121**, 10987–10993.
32. S. Cadars, A. Lesage, M. Trierweiler, L. Heux, and L. Emsley, *Phys. Chem. Chem. Phys.*, 2007, **9**, 92–103.
33. S. E. Ashbrook and S. Sneddon, *J. Am. Chem. Soc.*, 2014, **136**, 15440−15456.
34. C. Fernandez and M. Pruski, *Top. Curr. Chem.*, 2012, **306**, 119–188.
35. S. E. Ashbrook and M. E. Smith, *Chem. Soc. Rev.*, 2006, **35**, 718–735.
36. S. E. Ashbrook and M. J. Duer, *Concepts Magn. Reson.*, 2006, **28**, 183–248.
37. F. Pourpoint, C. C. Diogo, C. Gervais, C. Bonhomme, F. Fayon, S. L. Dalicieux, I. Gennero, J.-P. Salles, A. P. Howes, R. Dupree, J. V. Hanna, M. E. Smith, F. Mauri, G. Guerrero, P. H. Mutin, and D. Laurencin, *J. Mater. Res.*, 2011, **26**, 2355–2368.
38. J. M. Griffin, A. J. Berry, and S. E. Ashbrook, *Solid State Nucl. Magn. Reson.*, 2011, **40**, 91–99.
39. K. E. Johnston, J. M. Griffin, R. I. Walton, D. M. Dawson, P. Lightfoot, and S. E. Ashbrook, *Phys. Chem. Chem. Phys.*, 2011, **13**, 7565–7576.
40. J. P. Amoureux, F. Bauer, C. Fernandez, D. Freude, D. Michel, and U. T. Pingel, *Chem. Phys. Lett.*, 1998, **285**, 10–14.
41. O. P. Lapina, A. A. Shubin, D. F. Khabibulin, V. V. Terskikh, P. R.

Bodart, and J. P. Amoureux, *Catal. Today*, 2003, **78**, 91–104.
42. V. Montouillout, C. M. Morais, A. Douy, F. Fayon, and D. Massiot, *Magn. Reson. Chem.*, 2006, **44**, 770–775.
43. P. Florian, E. Veron, T. F. G. Green, J. R. Yates, and D. Massiot, *Chem. Mater.*, 2012, **24**, 4068–4079.
44. K. M. N. Burgess, Y. Xu, M. C. Leclerc, and D. L. Bryce, *Inorg. Chem.*, 2014, **53**, 552–561.
45. C. Leroy, R. Johannson, and D. L. Bryce, *J. Phys. Chem. A*, 2019, **123**, 1030–1043.
46. H. Hamaed, J. M. Pawlowski, B. F. T. Cooper, R. Fu, S. H. Eichhorn, and R. W. Schurko, 2008, 11056–11065.
47. D. A. Hirsh, Y. Su, H. Nie, W. Xu, D. Stueber, N. Variankaval, and R. W. Schurko, *Mol. Pharm.*, 2018, **15**, 4038–4048.
48. D. Laurencin, C. Gervais, A. Wong, C. Coelho, F. Mauri, D. Massiot, M. E. Smith, and C. Bonhomme, *J. Am. Chem. Soc.*, 2009, **131**, 13430–13440.
49. E. R. Andrew, A. Bradbury, and R. G. Eades, *Nature*, 1958, **182**, 1659.
50. E. R. Andrew, A. Bradbury, and R. G. Eades, *Nature*, 1959, **183**, 1802–1803.
51. L. J. Lowe, *Phys. Rev. Lett.*, 1959, **2**, 285–287.
52. K. H. Mroue, Y. Nishiyama, M. Kumar Pandey, B. Gong, E. McNerny, D. H. Kohn, M. D. Morris, and A. Ramamoorthy, *Sci. Rep.*, 2015, **5**, 11991–12000.
53. R. Zhang, K. H. Mroue, and A. Ramamoorthy, *Acc. Chem. Res.*, 2017, **50**, 1105–1113.
54. S. Penzel, A. Oss, M.-L. Org, A. Samoson, A. Bockmann, M. Ernst, and B. H. Meier, *J. Biomol. NMR*, 2019, **73**, 19–29.
55. V. Agarwal, K. Penzel, S. Szekely, R. Cadalbert, E. Testori, A. Oss, J. Past, A. Samoson, M. Ernst, A. Bockmann, and B. H. Meier, *Angew. Chem. Int. Ed.*, 2014, **53**, 12253–12256.
56. G. David, M.-L. Fogeron, M. Schledorn, R. Montserret, U. Haselmann, S. Penzel, A. Badillo, L. Lecoq, P. Andre, R. Nassal, M. Bartenschlager, B. H. Meier, and A. Bockmann, *Angew. Chem. Int. Ed.*, 2018, **57**, 4787–4791.
57. P. Hodgkinson, *Prog. Nucl. Magn. Reson. Spectrosc.*, 2005, **46**, 197–222.

58. M. Ernst, *J. Magn. Reson.*, 2003, **162**, 1–34.
59. D. Sakellariou, A. Lesage, P. Hodgkinson, and L. Emsley, *Chem. Phys. Lett.*, 2000, **319**, 253–260.
60. P. K. Madhu, *Solid State Nucl. Magn. Reson.*, 2009, **35**, 2–11.
61. A. Pines, M. G. Gibby, and J. S. Waugh, *J. Chem. Phys.*, 1972, **56**, 1776–1777.
62. M. H. Levitt, D. Suter, and R. R. Ernst, *J. Chem. Phys.*, 1986, **84**, 4243–4255.
63. S. R. Hartmann and E. L. Hahn, *Phys. Rev.*, 1962, **128**, 2042–2053.
64. E. Hahn, *Phys. Rev.*, 1950, **80**, 580–594.
65. S. Meiboom and D. Gill, *Rev. Sci. Instrum.*, 1958, **29**, 688–691.
66. Z. Gan, *J. Am. Chem. Soc.*, 2000, **112**, 3242–3243.
67. Z. Gan, *J. Chem. Phys.*, 2001, **114**, 10845–10853.
68. S. E. Ashbrook and S. Wimperis, *J. Magn. Reson.*, 2002, **156**, 269–281.
69. A. Medek, J. S. Harwood, and L. Frydman, *J. Am. Chem. Soc.*, 1995, **117**, 12779–12787.
70. P. K. Madhu, A. Goldbourt, L. Frydman, and S. Vega, *Chem. Phys. Lett.*, 1999, **307**, 41–47.

# Chapter 3: Computational chemistry

## 3.1 An introduction to computational chemistry

As a result of major advances in theoretical codes, which have been extensively improved over the last few decades, the use of quantum-chemical calculations within solid-state chemistry has exploded. The popularity and widespread use of first-principles calculations is due not only to the improved accuracy and reliability of computational codes, but also to the ever-reducing cost of processors (Moore's law),[1] combined with the increasing availability of resources, often in the form of national-level high-performance supercomputing facilities. As a result, it is more convenient and economical to use first-principles calculations than ever before. In addition, given the level of accuracy they have achieved and that they can consider systems or conditions that cannot (currently at least) be replicated experimentally, first-principles calculations have become predictive, meaning they can act as a guide for future experiments.

Solid-state NMR spectroscopy is one area where the advancement of first-principles calculations has been particularly beneficial. As discussed in Chapter 2, the NMR spectra of solids are often far more complicated than their solution-state counterparts, due to the presence of anisotropic interactions that broaden the spectra of solids.[2,3] Furthermore, for solution-state NMR spectra, extensive databases of NMR parameters for common nuclei help to facilitate rapid and accurate spectral assignment. In contrast, relatively little information of this type is available for solids. Additionally, in many systems, more than one resonance is observed for a single chemical species. The combination of these factors complicates the assignment of solid-state NMR spectra for even simple systems with the presence of structural disorder, be it compositional, configurational, positional, temporal or a combination of these only magnifying the challenge. As a result, it is becoming increasingly common to use first-principles calculations in combination with experiment, with the former capable of accurately

predicting NMR parameters, including $\delta_{iso}$ and $C_Q$. Indeed, quantum-chemical calculations can easily provide information on tensor orientations and anisotropic components of interactions, information that is often challenging to extract experimentally. The widespread use of first-principles calculations in combination with experimental measurements has led to the emergence of a new discipline, termed NMR crystallography,[4–7] where NMR spectroscopy and other techniques (including X-ray or neutron diffraction) are used in conjunction with calculations to solve the structure of materials. Within this thesis, first-principles, or more accurately, DFT calculations have been used to predict the NMR parameters for a variety of disordered inorganic solids, with the overall goal being to understand how these can be used to inform on variations in local structure and atomic ordering. DFT calculations also represent a convenient way to explore different structural models, something crucial to this project as the materials of interest are highly disordered and often have unknown or only partially understood structures, meaning before any desirable quantities can be calculated, a reasonable structural model or set of models must be generated, which will be the focus of Chapter 4.

## 3.2 Fundamentals of first-principles calculations

In addition to the references cited specifically throughout this chapter, several sources,[8–11] to which the reader is referred were consulted extensively.

The key purpose of quantum-chemical calculations is to find the electronic ground state of whatever many-electron system is under investigation. From this information any quantity or observable of the system can be determined using the relevant operators. The energy of the system, E, is a fundamental quantity in quantum mechanics. Often the goal of performing quantum-chemical calculations is to find E through the approximate solution to the time-independent non-relativistic Schrödinger equation,

$$\hat{H}\Psi_i(\mathbf{x}_1, \mathbf{x}_2, ..., \mathbf{x}_N, \mathbf{R}_1, \mathbf{R}_2, ..., \mathbf{R}_M) = E_i\Psi_i(\mathbf{x}_1, \mathbf{x}_2, ..., \mathbf{x}_N, \mathbf{R}_1, \mathbf{R}_2, ..., \mathbf{R}_M) \ , \quad (3.1)$$

often abbreviated to

$$\hat{H}\Psi_i = E_i\Psi_i \ , \quad (3.2)$$

where is the Hamiltonian operator, for a system with M nuclei and N electrons in the absence of an electric or magnetic field, and $\Psi_i$ and $E_i$ are the wavefunction and total energy of the system, respectively. The wavefunction contains all the information for the system, including the N spin and 3N spatial coordinates of each electron and the 3M spatial coordinates of each nucleus. The Hamiltonian operator shown in Equation 3.2 can be expressed as

$$\hat{H} = -\frac{1}{2}\sum_{i=1}^{N}\nabla_i^2 - \frac{1}{2}\sum_{A=1}^{M}\frac{1}{M_A}\nabla_A^2 - \sum_{i=1}^{N}\sum_{A=1}^{M}\frac{Z_A}{r_{iA}} + \sum_{i=1}^{N}\sum_{j>i}^{N}\frac{1}{r_{ij}} + \sum_{A=1}^{M}\sum_{B>A}^{M}\frac{Z_A Z_B}{R_{AB}} \ , \quad (3.3)$$

where A and B refer to the M nuclei and i and j, the N electrons in the system. The first two terms in Equation 3.3 represent the kinetic energy of the electrons and nuclei, respectively, with $M_A$ representing the mass of nucleus A, given in multiples of the mass of an electron and where $\nabla_q$ (q = i or A), the Laplacian operator, is defined as the sum of differential operators given in Cartesian coordinates, as shown in Equation 3.4,

$$\nabla_q^2 = \frac{\partial^2}{\partial x_q^2} + \frac{\partial^2}{\partial y_q^2} + \frac{\partial^2}{\partial z_q^2} \ . \quad (3.4)$$

The final three terms of Equation 3.3 represent the potential energy component of the Hamiltonian operator, with the third term denoting the attractive electrostatic interaction between the nuclei and electrons, whereas the fourth and fifth terms represent the repulsive potentials due to the

electron-electron and nucleus-nucleus interactions, respectively. A more compact way of writing Equation 3.3 is shown below,

$$\hat{H} = \hat{T}_e + \hat{T}_n + \hat{V}_{ne} + \hat{V}_{ee} + \hat{V}_{nn} \ . \tag{3.5}$$

By accounting for the large mass difference between nuclei and electrons, the Schrödinger equation can be simplified further. As an electron is 1800 times lighter than a proton, electrons have much higher velocities as compared to nuclei. As a result, the Born-Oppenheimer approximation[12] can be applied, where the nuclei are considered stationary, with the electrons then moving through a fixed field. When this approximation is applied, the kinetic energy of the nuclei will be zero and the potential energy of nucleus-nucleus repulsion is simply a constant. Therefore the complete Hamiltonian shown in Equation 3.3 is reduced to the electronic Hamiltonian,

$$\hat{H}_{elec} = -\frac{1}{2}\sum_{i=1}^{N}\nabla_i^2 - \sum_{i=1}^{N}\sum_{A=1}^{M}\frac{Z_A}{r_{iA}} + \sum_{i=1}^{N}\sum_{j>i}^{N}\frac{1}{r_{ij}} = \hat{T}_e + \hat{V}_{ne} + \hat{V}_{ee} \ . \tag{3.6}$$

Using the electronic Hamiltonian to solve the now time-independent Schrödinger equation gives the electronic wavefunction, $\Psi_{elec}$, and the electronic energy, $E_{elec}$, with the former only depending on the electronic spin and coordinates,

$$\hat{H}_{elec}\Psi_{elec} = E_{elec}\Psi_{elec} \ . \tag{3.7}$$

Summing the electronic energy and the nuclear repulsion terms, $E_{nuc}$, gives the total energy,

$$E_{tot} = E_{elec} + E_{nuc} \ , \tag{3.8}$$

where

$$E_{nuc} = \sum_{i=1}^{M} \sum_{B>A}^{M} \frac{Z_A Z_B}{r_{AB}} . \quad (3.9)$$

Although the wavefunction, $\Psi$, of a system cannot be observed directly, the square of the wavefunction allows for a physical description of the system, where

$$\left|\Psi(\mathbf{x}_1, \mathbf{x}_2, ..., \mathbf{x}_N)\right|^2 d\mathbf{x}_1, d\mathbf{x}_2, ..., d\mathbf{x}_N , \quad (3.10)$$

represents the probability of simultaneously finding all electrons within a volume element. Given that within a wavefunction electrons are indistinguishable, a switch in the coordinates of any two electrons (here i and j), cannot lead to a change in probability, *i.e.*,

$$\left|\Psi(\mathbf{x}_1, \mathbf{x}_2, ..., \mathbf{x}_i, \mathbf{x}_j, ..., \mathbf{x}_N)\right|^2 = \left|\Psi(\mathbf{x}_1, \mathbf{x}_2, ..., \mathbf{x}_j, \mathbf{x}_i, ..., \mathbf{x}_N)\right|^2 . \quad (3.11)$$

In nature there are only two possibilities: either swapping the position of two electrons in a wavefunction leads to an identical function, which is the case for bosons, *i.e.*, particles with integer (including zero) spin or swapping the position of two electrons results in the wavefunction changing sign, which is observed for half-integer spin particles, known as fermions. As electrons are fermions, possessing a spin quantum number of 1/2, swapping the spatial and spin coordinates of any two electrons must lead to a change in sign, indicating that the wavefunction for electrons is antisymmetric,

$$\Psi(\mathbf{x}_1, \mathbf{x}_2, ..., \mathbf{x}_i, \mathbf{x}_j, ..., \mathbf{x}_N) = -\Psi(\mathbf{x}_1, \mathbf{x}_2, ..., \mathbf{x}_j, \mathbf{x}_i, ..., \mathbf{x}_N) . \quad (3.12)$$

This satisfies the Pauli exclusion principle,[13] which states that no two electrons within a system can have the same four quantum numbers. By considering the square of the wavefunction, *i.e.*, the probability, it follows that the integral of Equation 3.10 over all space is one, meaning the

probability of finding N electrons, in all space, is one as shown in Equation 3.13,

$$\int \cdots \int \left|\Psi(\mathbf{x}_1, \mathbf{x}_2, ..., \mathbf{x}_N)\right|^2 d\mathbf{x}_1, d\mathbf{x}_2, ..., d\mathbf{x}_N = 1 \, . \tag{3.13}$$

A wavefunction that satisfies this condition is considered normalised. To solve the time-independent Schrödinger equation (Equation 3.7) for a system, the Hamiltonian operator, $\hat{H}$, must be constructed, which requires knowing which components of this are system specific. Equation 3.6 shows that only the number of electrons, N, and the external potential – which can be determined through the positions and charges of all nuclei in the system – are system dependent. Next, the eigenfunctions, $\Psi_i$, and resulting eigenvalues, $E_i$, of the Hamiltonian must be determined, with all properties of a system being able to be extracted by applying the relevant operators to the wavefunction. Notwithstanding its apparent simplicity, following this procedure is of little practical use as the exact solution to the Schrödinger equation for all but the simplest of systems is unknown. Instead, the *variational principle* provides a construct to systematically approach the ground state wavefunction, $\Psi_0$, which is the wavefunction that gives the lowest possible value of the energy, $E_0$, termed the ground state energy. The value of an observable, represented by the operator $\hat{O}$, using a normalised trial wavefunction $\Psi_{trial}$, is given by

$$\left\langle \hat{O} \right\rangle = \int \cdots \int \Psi^*_{trial} \, \hat{O} \, \Psi_{trial} d\mathbf{x}_1, d\mathbf{x}_2, ..., d\mathbf{x}_N = \left\langle \Psi_{trial} \middle| \hat{O} \middle| \Psi_{trial} \right\rangle \, , \tag{3.14}$$

shown using the bracket notation for integrals, where * denotes the complex conjugate. The variational principle states that the energy determined from Equation 3.14 will be greater than the true ground state energy, *i.e.*,

$$\left\langle \Psi_{trial} \middle| \hat{H} \middle| \Psi_{trial} \right\rangle = E_{trial} \geq E_0 \left\langle \Psi_0 \middle| \hat{H} \middle| \Psi_0 \right\rangle \, . \tag{3.15}$$

In Equation 3.15 a function, $\Psi_{trial}$ is assigned an energy, $E_{trial}$, making $\Psi_{trial}$ a *functional*, *i.e.*, a function whose input is also a function. It follows that in order to find the ground state wavefunction and energy, $E_{trial}$ must be minimised, achieved by searching through all N-electron wavefunctions that are allowed, *i.e.*, wavefunctions that are quadratically integrable functions that are continuous everywhere, without which normalisation would be impossible. Therefore the wavefunction that leads to $E_0$ will be the ground state wavefunction, $\Psi_0$, such that

$$E_0 = \min_{\Psi \to N} E[\Psi] = \min_{\Psi \to N} \left\langle \Psi \middle| \hat{T}_e + \hat{V}_{ne} + \hat{V}_{ee} \middle| \Psi \right\rangle . \tag{3.16}$$

Above, $\Psi \to N$ simply indicates that the N-electron wavefunction is allowed, *i.e.*, satisfies the requirements of being continuous and quadratically integrable. Considering all possible wavefunctions is not feasible, as there are simply too many possibilities, so in reality, only a small subset is considered. Through application of the variational principle in a quantum-chemical calculation, the energy of a wavefunction tends towards $E_0$, meaning the best outcome that can be expected from any energy minimisation procedure is a close approximation of $E_0$.

## 3.3 The Hartree-Fock method

The Hartree-Fock (HF) method is the quintessential wavefunction-based electronic structure approach, attempting to find $E_0$ by solving the electronic Schrödinger equation. However, as mentioned previously, solving Equation 3.16 by considering all allowed N-electron wavefunctions is impossible for all but the simplest of systems. As a result, it is necessary to identify a suitable subset of one-electron wavefunctions that can serve as a reasonable approximation of the exact wavefunction. In HF theory, an antisymmetric product of N one-electron wavefunctions, $\chi_i(\mathbf{x}_i)$, is used to represent the total wavefunction, with the product of these termed a Slater determinant, $\Phi_{SD}$,

$$\Psi_0 = \Phi_{SD} = \frac{1}{\sqrt{N!}} \begin{vmatrix} \chi_1(\mathbf{x}_1) & \chi_2(\mathbf{x}_1) & \cdots & \chi_N(\mathbf{x}_1) \\ \chi_1(\mathbf{x}_2) & \chi_2(\mathbf{x}_2) & \cdots & \chi_N(\mathbf{x}_2) \\ \vdots & \vdots & & \vdots \\ \chi_1(\mathbf{x}_N) & \chi_2(\mathbf{x}_N) & \cdots & \chi_N(\mathbf{x}_N) \end{vmatrix} , \tag{3.17}$$

where $1/\sqrt{N!}$ ensures the Slater determinant is normalised. As all one-electron wavefunctions are orthogonal, the Slater determinant can be rewritten in a form where only the diagonal elements are considered, giving

$$\Phi_{SD} = \frac{1}{\sqrt{N!}} \{ \chi_1(\mathbf{x}_1)\, \chi_2(\mathbf{x}_2) \cdots \chi_N(\mathbf{x}_N) \} . \tag{3.18}$$

For fermions, an antisymmetric product of N one-electron wavefunctions is required as a straightforward product assigns a particular wavefunction to a specific electron, an impossible assignment given that the electrons are indistinguishable. Also, as shown in Equation 3.19, interchange of two particles does not result in the antisymmetric product being observed, *i.e.*, swapping the position of two electrons does not result in a change in the sign of the wavefunction

$$\begin{aligned} &\chi_1(\mathbf{x}_1)\, \chi_2(\mathbf{x}_2) \cdots \chi_i(\mathbf{x}_i)\, \chi_j(\mathbf{x}_j) \cdots \chi_N(\mathbf{x}_N) \\ &\neq -\chi_1(\mathbf{x}_1)\, \chi_2(\mathbf{x}_2) \cdots \chi_i(\mathbf{x}_j)\, \chi_j(\mathbf{x}_i) \cdots \chi_N(\mathbf{x}_N) . \end{aligned} \tag{3.19}$$

The $\chi_i(\mathbf{x}_i)$ functions are referred to as *spin orbitals*, comprising a spatial orbital $\phi_i(\mathbf{r})$ and one of the two possible spin functions, $\sigma(s)$, $\alpha$ or $\beta$, *i.e.*, spin up or spin down,

$$\chi_i(\mathbf{x}_i) = \phi_i(\mathbf{r})\, \sigma(s) . \tag{3.20}$$

$\sigma(s)$ must be orthogonal to each other, with the spin orbitals usually also selected to be orthonormal, in an effort to simplify the mathematics

associated with the wavefunction construction. It follows that the square of the spin orbital represents the probability of finding the electron within a given volume. Although a Slater determinant of the form shown in Equation 3.17 satisfies the need for an antisymmetric function (as the exchange of two rows or two columns results in a change of sign), the process of representing the full N-electron wavefunction as the antisymmetric product of N one-electron wavefunctions is an extreme approximation. As a result, it is necessary to find the best possible Slater determinant by using the variational principle to find the $\Phi_{SD}$ that gives the lowest energy, termed the Hartree-Fock energy, $E_{HF}$. This is achieved by varying the spin orbitals (whilst ensuring they remain orthonormal) until the lowest energy Slater determinant has been found,

$$E_{HF} = \min_{\Phi_{SD} \to N} E\left[\Phi_{SD}\right] . \tag{3.21}$$

By expanding the Slater determinant, $E_{HF}$ can be derived

$$E_{HF} = \left\langle \Phi_{SD} \middle| \hat{H} \middle| \Phi_{SD} \right\rangle = \sum_{i}^{N} \left( i \left| \hat{h} \right| i \right) + \frac{1}{2} \sum_{i}^{N} \sum_{j}^{N} \left( ii \mid jj \right) - \left( ij \mid ji \right) , \tag{3.22}$$

from which it can be seen that the energy is a functional of the spin orbitals, and it is the variation of these orbitals that allows the energy to be minimised. In Equation 3.22, the $(i \mid \hat{h} \mid i)$ term, expressed as

$$(i \mid \hat{h} \mid i) = \int \chi_i^*(\mathbf{x}_1) \left\{ -\frac{1}{2} \nabla^2 - \sum_{A}^{M} \frac{Z_A}{r_{1A}} \right\} \chi_i(\mathbf{x}_1) \, d\mathbf{x}_1 , \tag{3.23}$$

represents the kinetic energy and electron-nucleus attraction terms, whereas

$$(ii \mid jj) = \int \int \left| \chi_i(\mathbf{x}_1) \right|^2 \frac{1}{r_{12}} \left| \chi_j(\mathbf{x}_2) \right|^2 \, d\mathbf{x}_1 d\mathbf{x}_2 \tag{3.24}$$

and

$$(ij \mid ji) = \int\int \chi_i(\mathbf{x}_1)\chi_j^*(\mathbf{x}_1)\frac{1}{r_{12}}\chi_j(\mathbf{x}_2)\chi_i^*(\mathbf{x}_2)\, d\mathbf{x}_1 d\mathbf{x}_2 \tag{3.25}$$

are the Coulomb and exchange interactions, respectively, between two electrons. Equation 3.26, commonly known as the Hartree-Fock equation, is used to find the spin orbitals that lead to the lowest value of $E_{HF}$,

$$\hat{f}\,\chi_i = \varepsilon_i\,\chi_i,\ i = 1,\ 2,\ ...,\ N\ , \tag{3.26}$$

where $\varepsilon_i$, the Lagrangian multipliers, are the orbital energy eigenvalues for the one-electron operator $\hat{f}$, expressed as

$$\hat{f}_i = -\frac{1}{2}\nabla_i^2 - \sum_A^M \frac{Z_A}{r_{iA}} + V_{HF}(i)\ . \tag{3.27}$$

In Equation 3.27, the negative terms represent the kinetic and potential energy components due to the attractive electron-nucleus interaction. The final term, $V_{HF}(i)$, is the Hartree-Fock potential, which describes the average repulsion felt by one electron interacting with the remaining N – 1 electrons in the system. Representing the electron-electron repulsion by $V_{HF}(i)$, a one-electron operator, removes the need to include the two-electron repulsion operator, $1/r_{ij}$ in the Hamiltonian. The Hartree-Fock potential is comprised of two components,

$$V_{HF}(\mathbf{x}_1) = \sum_j^N (\hat{J}_j(\mathbf{x}_1) - \hat{K}_j(\mathbf{x}_1))\ , \tag{3.28}$$

where, the Coulomb operator, $\hat{J}_j$, is

$$\hat{J}_j(\mathbf{x}_1) = \int \left|\chi_j(\mathbf{x}_2)\right|^2 \frac{1}{r_{12}} d\mathbf{x}_2 \ , \tag{3.29}$$

This term describes the repulsive potential an electron at one position experiences due to the average charge distribution of another electron in spin orbital $\chi_j$. The term $\hat{K}_j$ in Equation 3.28 is the exchange contribution to $V_{HF}(i)$,

$$\hat{K}_j(\mathbf{x}_1)\chi_i(\mathbf{x}_1) = \int \chi_j^*(\mathbf{x}_2)\frac{1}{r_{12}}\chi_i(\mathbf{x}_2)\, d\mathbf{x}_2\ \chi_j(\mathbf{x}_1) \ . \tag{3.30}$$

an effect that leads to the variables in the two spin orbitals being exchanged. As operating on $\chi_i(\mathbf{x}_1)$ with $\hat{K}_j(\mathbf{x}_1)$ depends on the value of $\chi_i$ at position $\mathbf{x}_2$, the exchange operator and the corresponding potential are called non-local. As applying the Coulomb operator to a spin orbital only depends on the value of $\chi_i$ at one position $\mathbf{x}_1$, this interaction is considered to be a local potential. Given that *via* the Hartree-Fock potential, the Fock operator depends on the spin orbitals, which themselves must be approximated, Equation 3.26 is considered a *pseudo-eigenvalue* problem, which is solved using the self-consistent field (SCF) method, this procedure involves starting with a set of orbitals that are used to solve the Hartree-Fock equations, with the new set of spin orbitals thus generated being used in the subsequent iteration. This iterative process continues until the energy difference between iterations falls below a predetermined threshold value.

As discussed above, although approximating a wavefunction using a single Slater determinant $\Phi_{SD}$ provides a reasonable representation of a many electron system, it will never correspond to the exact wavefunction. Due to the variational principle, $E_{HF}$ will always be larger than $E_0$, with the difference between these two energies being known as the electron correlation energy,[14]

$$E_C^{HF} = E_0 - E_{HF} \ . \tag{3.31}$$

The electron correlation energy is a measure of the error associated with the Hatree-Fock approach for finding the ground state wavefunction. The electron correlation phenomenon is predominantly caused by the instantaneous repulsion of the electrons, which is not considered in the HF potential. The treatment of the electrostatic interactions as an average potential causes the electrons to be too close to one another, ultimately causing the HF approach to overestimate the electron-electron repulsion.

## 3.4 Density functional theory

The implication of Equation 3.10, that the square of the wavefunction represents the probability of finding all N electrons simultaneously in the specified volume feeds directly into the concept of the electron density, $\rho(\mathbf{r})$, which, as shown in Equation 3.32, depends on the spin and spatial coordinates of N and N – 1 electrons, respectively,

$$\rho(\mathbf{r}) = N\int\cdots\int \left|\Psi(\mathbf{x}_1, \mathbf{x}_2, ..., \mathbf{x}_N)\right|^2 ds_1, d\mathbf{x}_2, ..., d\mathbf{x}_N \ . \tag{3.32}$$

Unlike a wavefunction, $\rho(\mathbf{r})$ is an observable quantity, *i.e.*, it can be measured experimentally. $\rho(\mathbf{r})$ describes the probability of finding one of the N electrons within a volume element, $d\mathbf{r}_1$, but without determining its spin orientation, while the remaining N – 1 electrons in the system have arbitrary spin and positions. As electrons are indistinguishable from one another, the probability of finding multiple electrons within a volume element is simply N times the probability for one electron in the same volume. The electron density is a function of the three spatial variables of the electrons, which integrates to the total number of electrons and which tends to zero as the volume element approaches infinity, *i.e.*,

$$\int \rho(\mathbf{r})\ d\mathbf{r}_1 = N \ , \tag{3.33}$$

and

$$\rho(\mathbf{r} \to \infty) = 0 \ . \tag{3.34}$$

As a result of the attractive electron-nucleus interaction, at atomic positions $\rho(\mathbf{r})$ exhibits a maximum with a finite value. At these positions there is a discontinuity in the gradient of the electron density, leading to a cusp, the result of the singularity in the $Z_A / r_{iA}$ term in $\hat{H}$ as $r_{iA}$ approaches zero. The properties of this cusp in electron density are related to Z, the nuclear charge of the nucleus as shown below,

$$\lim_{r_{iA} \to 0} \left[ \frac{\partial}{\partial r} + 2Z_A \right] \overline{\rho}(\mathbf{r}) = 0 \ , \tag{3.35}$$

where $\overline{\rho}(\mathbf{r})$ is the spherical average of $\rho(\mathbf{r})$. At large distances from all nuclei the electron density decays asymptotically exponentially

$$\rho(\mathbf{r}) \propto e^{-2\sqrt{2I_e}|\mathbf{r}|} \ , \tag{3.36}$$

where $I_e$ represents the first ionisation energy of the system.

It is possible to extend the idea of electron density to simultaneously find two electrons with spins $\sigma_1$ and $\sigma_2$ in two different volume elements $d\mathbf{r}_1$ and $d\mathbf{r}_2$, whilst not considering the position and spins of the remaining N – 2 electrons. This can be achieved by using the pair density function, $\rho_2(\mathbf{x}_1,\mathbf{x}_2)$, which is equal to

$$\rho_2(\mathbf{x}_1, \mathbf{x}_2) = N(N-1) \int \cdots \int \left| \Psi(\mathbf{x}_1, \mathbf{x}_2, ..., \mathbf{x}_N) \right|^2 \, d\mathbf{x}_3 ... d\mathbf{x}_N \ , \tag{3.37}$$

a function that holds all information relating to the electron correlation interaction. As in this idealised model the electrons are considered as points of mass with no volume, it is possible that two electrons are simultaneously occupying the same spatial coordinates, a scenario that reduces the complexity of the pair density to a product of the individual probabilities,

$$\rho_2(\mathbf{x}_1,\mathbf{x}_2)=\frac{N-1}{N}\rho\mathbf{x}_1,\rho\mathbf{x}_2\ , \tag{3.38}$$

with the indistinguishable nature of electrons necessitating the $(N-1)/N$ term. However, the pair density is complicated by the fact that electrons do not behave like ideal particles; their wavefunctions must be antisymmetric, and, as they are charged particles, electrons exhibit Coulomb repulsion with other electrons. Additionally, due to the Pauli principle, the probability of two electrons with the same spin occupying the same space is zero, meaning electrons cannot move independently of one another, an effect termed Fermi correlation or, exchange. Unrelated to the spin of electrons, the electrostatic repulsion (represented in Equation 3.29 by the $1/r_{12}$ term) that stops electrons getting too close to each other is referred to as the Coulomb correlation, allowing a distinction to be made between this effect and the Fermi correlation. The HF approach accounts exactly for exchange, but it does not include the effect of Coulomb correlation. By splitting the pair density function into two parts, where the first is just the product of the two individual electron densities, and the second is the result of the exchange and Coulomb correlations effects, the influence of the latter interactions can be seen

$$\rho_2(\mathbf{x}_1,\mathbf{x}_2)=\rho(\mathbf{x}_1)\ \rho(\mathbf{x}_2)\left[1+f(\mathbf{x}_1;\mathbf{x}_2)\right]\ , \tag{3.39}$$

where $f(\mathbf{x}_1;\mathbf{x}_2)$ is the correlation factor. If one electron is known to be at position one, the probability of finding any electron at a second position is known as the conditional probability density, $\Omega$, given by

$$\Omega(\mathbf{x}_2;\mathbf{x}_1)=\frac{\rho_2(\mathbf{x}_1,\mathbf{x}_2)}{\rho(\mathbf{x}_1)}\ , \tag{3.40}$$

an expression that contains all but the one electron already known to be at position $\mathbf{x}_1$. As the conditional probability density concerns all electrons except the one known to be at position $\mathbf{x}_1$, it integrates to $N-1$ electrons,

$$\int \Omega(\mathbf{x}_2;\mathbf{x}_1)\ \mathrm{d}\mathbf{x}_2 = \mathrm{N}-1\ . \tag{3.41}$$

The corrections needed to account for exchange and Coulomb correlation can be seen by comparing the conditional probability with the uncorrelated probability of finding an electron at a second position

$$\mathrm{h}_{\mathrm{XC}}(\mathbf{x}_1;\mathbf{x}_2) = \frac{\rho_2(\mathbf{x}_1,\mathbf{x}_2)}{\rho(\mathbf{x}_1)} - \rho(\mathbf{x}_2) = \rho(\mathbf{x}_2)\mathrm{f}(\mathbf{x}_1,\mathbf{x}_2)\ . \tag{3.42}$$

where $\mathrm{h}_{\mathrm{XC}}(\mathbf{x}_1;\mathbf{x}_2)$ is the *exchange-correlation hole*. An abstract way of thinking about the effect of the exchange-correlation hole is to picture an electron surrounding itself with a hole or moat, where the probability of finding another electron is decreased. From Equation 3.43 it can be seen that the exchange-correlation hole integrates to a value of –1, meaning it contains the charge of one electron,

$$\int \mathrm{h}_{\mathrm{XC}}(\mathbf{x}_1;\mathbf{x}_2)\ \mathrm{d}\mathbf{x}_2 = -1\ . \tag{3.43}$$

Now that the phenomenon of electron density has been introduced, whether the N-electron wavefunction can be replaced by $\rho(\mathbf{r})$, must be considered. The idea of extracting information relating to atomic and molecular systems using the electron density is over 90 years old, being initiated by work from Thomas[15] and Fermi[16,17] that led to what is now known as the Thomas-Fermi (TF) method.[18,19] This was based on a purely quantum statistical approach, where only the kinetic energy component of the Schrödinger equation was considered explicitly, with the nuclear-electron and electron-electron terms treated classically, and exchange and Coulomb correlation omitted. To determine the kinetic energy, the TF model relies on the concept of a uniform electron gas to simplify the problem, where the electron density is considered constant throughout the system, leading to the following expression

$$T_{TF}[\rho(\mathbf{r})] = \frac{3}{10}(3\pi^2)^{2/3}\int \rho^{5/3}(\mathbf{r})\, d(\mathbf{r}) \,, \tag{3.44}$$

where $T_{TF}$ is the Thomas-Fermi kinetic energy. By combining this with the attractive and repulsive terms for the nucleus-electron and electron-electron interactions, respectively, the resulting expression, shown in Equation 3.45, represents the kinetic energy for an atom

$$\begin{aligned} T_{TF}[\rho(\mathbf{r})] = \frac{3}{10}(3\pi^2)^{2/3}\int \rho^{5/3}(\mathbf{r})\, d(\mathbf{r}) \; - Z\int \frac{\rho(\mathbf{r})}{r}\, d(\mathbf{r}) \\ + \frac{1}{2}\int\int \frac{\rho(\mathbf{r}_1)\rho(\mathbf{r}_2)}{r_{12}}\, d(\mathbf{r}_1)d(\mathbf{r}_2) \,. \end{aligned} \tag{3.45}$$

In order to find the appropriate electron density to use in Equation 3.45, the input electron density is minimised using the variational principle. Although the TF model does not determine the energy of an atom particularly accurately, it nevertheless is being expressed as a functional of the electron density.

In work to approximate the non-local exchange using $\rho(\mathbf{r})$,[20] which led to the Hartree-Fock-Slater (HFS) method, Slater also succeeded in pushing forward the field of DFT. Using the idea of the uniform electron gas,[21] a modification can be made to the TF model, leading to the Thomas-Fermi-Dirac (TFD) approach, which unlike HFS relies purely on $\rho(\mathbf{r})$. Although (as with the original TF method), this expansion was not particularly successful, the TFD approximation did highlight that $\rho(\mathbf{r})$ could be used to express additional interactions.

The research performed by Hohenberg and Kohn represents the foundation on which modern DFT has been built. Kohn was awarded the 1998 Nobel Prize in Chemistry for his development of this field. A full proof of the Hohenberg-Kohn (HK) theorem can be found in their 1964 *Phys. Rev.* paper.[22] The HK theorem showed that the ground state electron density, $\rho_0$, describes

the Hamiltonian operator, from which all other properties can be inferred. As the total ground state energy is a functional of the ground state electron density, it follows that this must also hold for the individual components of the total energy, which can be written as

$$E_0[\rho_0] = T[\rho_0] + E_{ee}[\rho_0] + E_{ne}[\rho_0] \ , \tag{3.46}$$

where $E_0$, T, $E_{ee}$ and $E_{ne}$ refer to the total, kinetic, potential electron-electron and potential nucleus-electron energy terms, respectively. Equation 3.46 can be separated according into terms which are independent of the system (*i.e.*, independent of the number of electrons, interatomic distances and atom species), and terms which are system dependent, with only $E_{ne}$ falling into the latter category. Therefore, by combining the terms that are independent of the system into a single term, the HK functional, $F_{HK}[\rho_0]$, Equation 3.46 can be rewritten as

$$E_0[\rho_0] = \int \rho_0(\mathbf{r})\, V_{ne}\, d\mathbf{r} + F_{HK}[\rho_0] \ . \tag{3.47}$$

This means that an input electron density will output the sum of the kinetic and electron-electron repulsion energy operators for the wavefunction, yielding the ground state wavefunction,

$$F_{HK}[\rho] = T[\rho] + E_{ee}[\rho] = \left\langle \Psi \middle| \hat{T} + \hat{V}_{ee} \middle| \Psi \right\rangle \ . \tag{3.48}$$

If the HK functional was known explicitly, the Schrödinger equation could be solved for any system as it has already been shown that the energy components that make up this quantity are independent of the system in question. However, the correct expressions for the kinetic energy and electron-electron repulsion functions are unknown. Despite this, the classical interpretation of the Coulombic electron-electron interaction, J[ρ], is known, allowing for a partial decomposition of $E_{ee}$, as shown in Equation 3.49,

$$E_{ee} = J[\rho] + E_{ncl} = \frac{1}{2}\iint \frac{\rho(\mathbf{r}_1)\rho(\mathbf{r}_2)}{r_{12}}\, d\mathbf{r}_1 d\mathbf{r}_2 + E_{ncl} \ , \tag{3.49}$$

where the subscript 'ncl' in $E_{ncl}$ does not relate to nuclei, but instead, denotes the non-classical component of the electron-electron interaction, including the self-interaction correction, Coulomb correlation and exchange effects.

A second, equally important theorem that came out of this approach is that the HK functional, which outputs the ground state energy, will only do so if the true ground state electron density is inputted. This means that the variational principle can be employed to find the HK functional that leads to the lowest energy, which will represent the upper limit of the true ground state energy, $E_0$. It is therefore clear that although the proofs presented by Hohenberg and Kohn were a crucial step in the development of density functional theory, the HK functional is unknown, with no strategy laid out to determine it.

A paper by Kohn and Sham, published in 1965, represents a second milestone in the development of DFT. This work, known now as the Kohn-Sham (KS) approach[23] showed how the HK method could be implemented in practice, by proposing a way of approaching the unknown HK functional. The HK approach showed that the energy of a system can be written in terms of its electron density

$$E_0 = \min_{\rho \to N} \left( F[\rho(\mathbf{r})] + \int \rho(\mathbf{r})\, V_{ne}\, d\mathbf{r} \right) , \tag{3.50}$$

where

$$F[\rho(\mathbf{r})] = T[\rho(\mathbf{r})] + J[\rho(\mathbf{r})] + E_{ncl}[\rho(\mathbf{r})] \ , \tag{3.51}$$

and where only $J[\rho(\mathbf{r})]$, the Coulomb electron-electron interaction is known exactly. As a result the KS approach attempts to find a way to more

accurately calculate the kinetic energy, something that previous methods fail to do. To do this, Kohn and Sham turned to the HF approach, where a Slater determinant of N one-electron spin orbitals was used to approximate the wavefunction of a system. $T_{HF}$ can be calculated explicitly from a Slater determinant by

$$T_{HF} = -\frac{1}{2}\sum_{i}^{N}\left\langle \chi_i \middle| \nabla^2 \middle| \chi_i \right\rangle . \tag{3.52}$$

DFT can use this to calculate the kinetic energy of a system made up of non-interacting electrons, which makes up a significant proportion of the total kinetic energy, described by the operator $\hat{H}_S$, equal to

$$\hat{H}_S = -\frac{1}{2}\sum_{i}^{N}\nabla_i^2 + \sum_{i}^{N} V_S(\mathbf{r}_i) , \tag{3.53}$$

where $V_S$ is an effective local potential. As electron-electron interactions are absent, a Slater determinant ($\Theta_S$) of spin orbitals ($\varphi$) (note the different notation compared to HF theory) can be used to represent the ground state wavefunction of this non-interacting system,

$$\Theta_S = \frac{1}{\sqrt{N!}}\begin{vmatrix} \varphi_1(\mathbf{x}_1) & \varphi_2(\mathbf{x}_1) & \cdots & \varphi_N(\mathbf{x}_1) \\ \varphi_1(\mathbf{x}_2) & \varphi_2(\mathbf{x}_2) & \cdots & \varphi_N(\mathbf{x}_2) \\ \vdots & \vdots & & \vdots \\ \varphi_1(\mathbf{x}_N) & \varphi_2(\mathbf{x}_N) & \cdots & \varphi_N(\mathbf{x}_N) \end{vmatrix} . \tag{3.54}$$

In analogy to HF theory, the spin orbitals, termed Kohn-Sham or KS orbitals in this approach, are given by

$$\hat{f}^{KS}\,\varphi_i = \varepsilon_i \varphi_i , \tag{3.55}$$

where $\hat{f}^{KS}$ refers to the Kohn-Sham operator, expressed as

$$\hat{f}^{KS} = -\frac{1}{2}\nabla^2 + V_S(\mathbf{r}) \ . \tag{3.56}$$

By manipulating $V_S$ until the sum of the electron density for the moduli of the squared KS orbitals in the non-interacting system, $\rho_S$, equals the ground state electron density of the real system, $\rho_0$, (*i.e.*, where electron-electron interactions occur), a link between the idealised and the target system can be established. This relationship is expressed in Equation 3.57.

$$\rho_S(\mathbf{r}) = \sum_i^N \sum_s \left|\varphi_i(\mathbf{r},s)\right|^2 = \rho_0(\mathbf{r}) \ . \tag{3.57}$$

The brilliance of the KS approach was its acceptance that explicitly determining the kinetic energy of an N-electron system is unfeasible, instead settling for accurately calculating as much of this quantity as possible and approximating the remaining components. To this end, Kohn and Sham showed that, by assuming it has the same electron density as the true system, where electron-electron interactions do occur, the kinetic energy of the non-interacting system ($T_S$) can be calculated exactly using KS orbitals

$$T_S = -\frac{1}{2}\sum_i^N \left\langle \varphi_i \middle| \nabla^2 \middle| \varphi_i \right\rangle \ . \tag{3.58}$$

Even if the idealised and the true systems share the same electron density, they will not have the same kinetic energy, something that the KS approach accounts for by separating $F[\rho(\mathbf{r})]$, the universal functional, as shown below

$$F[\rho(\mathbf{r})] = T_S[\rho(\mathbf{r})] + J[\rho(\mathbf{r})] + E_{XC}[\rho(\mathbf{r})] \ . \tag{3.59}$$

The final term in Equation 3.59, $E_{XC}$ is the exchange-correlation energy, a functional where all the terms and interactions that cannot be quantified explicitly, are collected. $E_{XC}$ is given by

$$E_{XC}[\rho] = (T[\rho] - T_S[\rho]) + (E_{ee}[\rho] - J[\rho]) = T_C[\rho] + E_{ncl}[\rho] \ , \tag{3.60}$$

where $T_C$ is the remainder of the true kinetic energy that is not accounted for by $T_S$. As $T_S$ must have the same electron density as the ground state electron density of the real system, finding a way to determine the value of the effective potential $V_S$, is important. This is achieved by first expressing the energy of the real system in terms of its component parts,

$$\begin{aligned} E[\rho(\mathbf{r})] &= T_S[\rho] + J[\rho] + E_{ne}[\rho] + E_{XC}[\rho] \\ &= T_S[\rho] + \frac{1}{2}\iint \frac{\rho(\mathbf{r}_1)\rho(\mathbf{r}_1)}{r_{12}} d\mathbf{r}_1\, d\mathbf{r}_2 + \int \rho(\mathbf{r}) V_{ne}\, d\mathbf{r} + E_{XC}[\rho] \\ &= -\frac{1}{2}\sum_i^N \left\langle \varphi_i \middle| \nabla^2 \middle| \varphi_i \right\rangle + \frac{1}{2}\sum_i^N \sum_j^N \iint |\varphi_i(\mathbf{r}_1)|^2 \frac{1}{r_{12}} |\varphi_j(\mathbf{r}_2)|^2 \, d\mathbf{r}_1 d\mathbf{r}_2 \\ &\quad - \sum_i^N \int \sum_A^M \frac{Z_A}{r_{1A}} |\varphi_i(\mathbf{r}_1)|^2 \, d\mathbf{r}_1 + E_{XC}[\rho(\mathbf{r})] \ . \end{aligned} \tag{3.61}$$

As expected, the one component that cannot be described explicitly is $E_{XC}$. It can be seen from Equation 3.61 that the KS orbitals are key to being able to accurately determine the energy of a system. In order to apply the variational principle, the KS orbitals must satisfy the following conditions

$$\begin{aligned} \varphi_i &= \left( -\frac{1}{2}\nabla^2 + \left[ \int \frac{\rho(\mathbf{r}_2)}{r_{12}} d\mathbf{r}_2 + V_{XC}(\mathbf{r}_1) - \sum_A^M \frac{Z_A}{r_{1A}} \right] \right) \varphi_i \\ &= \left( -\frac{1}{2}\nabla^2 + V_{eff}(\mathbf{r}_1) \right) \varphi_i = \varepsilon_i \varphi_i \ , \end{aligned} \tag{3.62}$$

where $V_{XC}$ is the potential from the exchange-correlation energy and $V_{eff}$ is the effective potential. As $E_{XC}$ is unknown, it follows that $V_{XC}$ also does not have a known solution, and so $V_{XC}$ is expressed as the functional derivative

of the exchange-correlation energy with respect to $\rho(\mathbf{r})$. By comparing Equation 3.62 to Equation 3.56, it can be seen that $V_{eff}$ is equivalent to $V_S$, meaning the latter can be expressed in the same way,

$$V_S = V_{eff} = \left[ \int \frac{\rho(\mathbf{r}_2)}{r_{12}} d\mathbf{r}_2 + V_{XC}(\mathbf{r}_1) - \sum_A^M \frac{Z_A}{r_{1A}} \right] . \tag{3.63}$$

This now means a procedure to determine $V_S$ exists, all be it an iterative one. This one realisation has a cascade effect, as $V_S$ must be included in the one-electron equation (see Equation 3.56), which determines the orbitals in the Slater determinant and in turn the ground state electron density, allowing the ground state energy to be determined through the use of Equation 3.61. It follows that, if the value of $E_{XC}$ was known, the KS approach could be used to find the exact solution to the time-independent Schrödinger equation. As it stands, the only approximation that has to be made during the KS approach is the functional that should be used to represent $E_{XC}$. With this in mind, it seems apt to highlight how important the progress made by Hohenberg, Kohn and later Sham was for DFT, as their contributions laid the foundations for an area of computational chemistry that continues to go from strength to strength.

As $E_{XC}$ cannot be determined explicitly, searching for more accurate functionals is still a major goal of DFT today. The original set of functionals used to estimate $E_{XC}$ are known as local density approximation (LDA) functionals,[24–27] which are based on the idealised uniform electron gas model, as this is the only system where the $E_{XC}$ can be calculated exactly. In LDA functionals, it is assumed that locally the electron density of a system can be considered equivalent to that of a uniform electron gas of the same electron density, *i.e.*, $\rho(\mathbf{r})$ is assumed to be constant at each spatial position. In this simplified model, $E_{XC}$ can be written as

$$E_{XC}^{LDA}[\rho] = \int \rho(\mathbf{r})\, \varepsilon_{XC}(\rho(\mathbf{r}))\, d\mathbf{r} , \tag{3.64}$$

where $\varepsilon_{XC}$ represents the exchange-correlation energy per particle, which is weighted by the probability of an electron occupying a particular point in space, *i.e.*, $\rho(\mathbf{r})$. By inputting the spin densities, $\rho_\alpha(\mathbf{r})$ and $\rho_\beta(\mathbf{r})$, which representing the electron density of the α- and β-spin electrons, respectively, instead of the overall electron density, the local spin-density approximation (LSDA) is obtained

$$E_{XC}^{LSDA}\left[\rho_\alpha,\rho_\beta\right]=\int\rho(\mathbf{r})\varepsilon_{XC}(\rho_\alpha(\mathbf{r}),\rho_\beta(\mathbf{r}))\,d\mathbf{r}\ , \tag{3.65}$$

where $\rho(\mathbf{r})=\rho_\alpha(\mathbf{r})+\rho_\beta(\mathbf{r})$. As this approximation is a poor model of a true chemical system, where $\rho(\mathbf{r})$ varies rapidly, the LDA is known to underestimate interatomic distances leading to overbinding.[9,28] Nevertheless, it is still used to investigate systems that closely resemble a uniform electron gas, such as metals (which have mobile electrons).

In the early 1980s, the first improvement upon the LDA opened up DFT to be used by computational chemists, as up until this point, the limitations associated with approximating the exchange-correlation functional hindered its application to chemical systems. It suggests that as well as using the information about the electron density at a particular spatial coordinate, a better description of the non-uniformity of the true electron density could be achieved by also considering the gradient of the electron density, $\nabla\rho(\mathbf{r})$. To do this, a Taylor expansion of the uniform electron density is constructed, with LDA representing the first term. The resulting expression shown in Equation 3.66, is a gradient expansion approximation (GEA) functional

$$\begin{aligned}E_{XC}^{GEA}\left[\rho_\alpha,\rho_\beta\right]&=\int\rho\varepsilon_{XC}(\rho_\alpha,\rho_\beta)\,d\mathbf{r}\\&+\sum_{\sigma,\sigma'}\int C_{XC}^{\sigma,\sigma'}(\rho_\alpha,\rho_\beta)\frac{\nabla\rho\sigma}{\rho_\sigma{}^{2/3}}\frac{\nabla\rho\sigma'}{\rho_{\sigma'}{}^{2/3}}\,d\mathbf{r}+\dots\ ,\end{aligned} \tag{3.66}$$

where the α and β spins are represented by σ and σ′, respectively. Despite the inclusion of the gradient of $\rho(\mathbf{r})$, the GEA does not represent a significant

improvement compared to the LDA, as the former does not contain restraints that cause the resulting exchange-correlation hole to make physical sense. By ensuring that the exchange and correlation holes integrate to –1 and 0, respectively, the issue of the GEA producing spurious results can be resolved. The result of these modifications are generalised gradient approximation (GGA) functionals,[29–33] which are still widely used today, with the functional developed by Perdew, Burke and Ernzerhof (PBE)[29] used exclusively in this thesis. In general terms, this type of functional can be written in the following form

$$E_{XC}^{GGA}\left[\rho_\alpha,\rho_\beta\right]=\int f(\rho_\alpha,\rho_\beta,\nabla\rho_\alpha,\nabla\rho_\beta)\,d\mathbf{r}\ . \tag{3.67}$$

In reality, a GGA functional is split into its two constituent parts

$$E_{XC}^{GGA}=E_X^{GGA}+E_C^{GGA}\ , \tag{3.68}$$

with the exchange component being the larger of the two. By expanding the Taylor series further, and considering higher-order derivatives of the electron density, $\nabla^2\rho(\vec{r})$, the GGA method can be extended, leading to so-called meta-GGA functionals, which can also depend on a number of parameters, including the kinetic energy density.[34–36]

Given the apparent hierarchy of accuracy associated with functionals, it should come as no surprise that each type is commonly represented as a separate rung of a ladder, as shown schematically in Figure 3.1. The fourth rung up the proverbial Jacob's ladder of $E_{XC}$ approximations[37] is home to the hybrid functionals, which involve an exact calculation of the exchange energy by representing this term as a Slater determinant, as in HF theory, and mixing a percentage of this quantity with the remaining percentage of the exchange-correlation energy approximated using LDA or GGA.[38–41] For instance, a hybrid GGA functional that mixes 50% of the exact exchange energy, calculated using a Slater determinant, with 50% of the exchange-

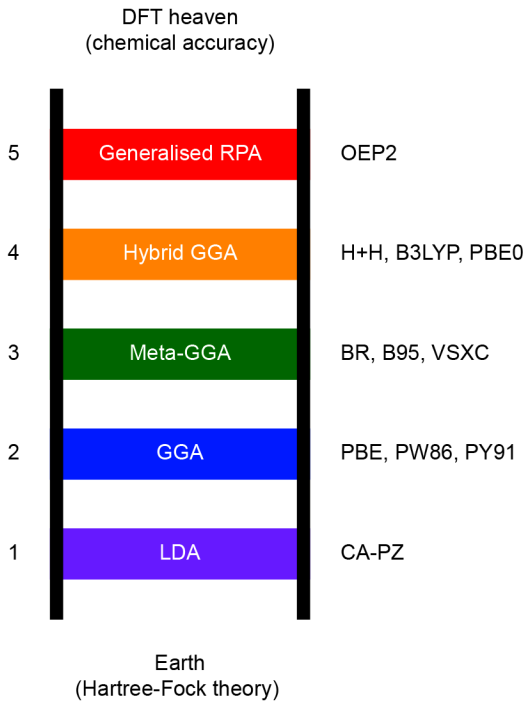


**Figure 3.1:** Jacob's ladder schematic representing the hierarchical nature of exchange-correlation energy functional approximations.

correlation energy approximated using a GGA functional would be expressed as

$$E_{XC} = 0.5E_X^{exact} + 0.5E_X^{GGA} + E_C^{GGA} \quad , \tag{3.69}$$

although, as in DFT $E_X$ contains some correlation and $E_C$ contain some exchange, this procedure is not seamless.

Functionals based on the generalised random phase approximation (RPA) represent the fifth rung of the hierarchical functional scheme. Expanding upon hybrid GGA methods, these functionals include information from the unoccupied, virtual KS orbitals as well as the occupied orbitals, in an attempt to better account for interactions including dispersion. The optimised effective potential (OEP) method falls into this classification of high-level, highly parameterised functional.[42–44]

## 3.5 Basis sets

Regardless of the computational approach employed, it is clear that finding the ground state energy (and thus all other properties of interest) of a system is neither trivial nor cheap. As a result, it is often necessary to rely on further approximations, such as a basis set, to improve the efficiency of a calculation. A basis set is the term used to describe a series of basis functions, $\varphi_i$, that have a known mathematical solution, allowing an unknown quantity, such as the wavefunction of a system, to be decomposed into a series of simpler problems. Basis functions are used to represent individual atomic orbitals (AOs), with a linear combination of the AOs representing the full wavefunction. The choice of basis set is heavily dependent on the type of system being investigated, meaning factors including the atomic species, system size and the type of chemical interactions that may be present (methodology, dispersion forces, covalent/ionic bond character, properties of interest, *etc*) should be considered. With this in mind, basis sets can in general be divided into two categories, atom-centred and planewave.

### 3.5.1 Atom-centred basis sets

The Slater-type orbitals (STOs)[45] of the form shown in Equation 3.70 are typical basis functions used to represent the wavefunction during an electronic structure calculation,

$$\varphi_i^{STO} = Nr^{n-1}e^{-\zeta r}Y_{lm_l}(\Theta,\phi) \ , \tag{3.70}$$

where N is a normalisation constant (ensuring that the AO integrates to one electron), r is the distance between the nucleus and the electron, n is the principal quantum number, $\zeta$ is the effective nuclear charge and $Y_{lm_l}(\Theta,\phi)$ represents spherical harmonic functions that are dependent on the orbital and angular momentum numbers l and $m_l$, respectively. The STOs decay exponentially as the nucleus-electron distance increases, reaching zero as r

tends to infinity, as shown in Figure 3.2a, ideally modelling an AO. Although STOs can represent the one-electron wavefunctions reasonably accurately, when an overlap of STOs is required, to calculate the electron-electron interaction present in a non-idealised system, a large flaw is revealed. This flaw is that it is only possible to solve the overlap of two STOs numerically, rather than analytically, meaning their practical use is often prohibitively expensive.

Alternatively, Gaussian-type orbitals (GTOs),[46] of the form

$$\varphi_i^{GTO} = Nr^L e^{-\alpha r^2} Y_{lm_l}(\Theta,\phi) \ , \tag{3.71}$$

may be adopted, where L represents an integer for every dimension of the GTO, meaning there will be two and three integers, each corresponding to a different Cartesian axes for a two- and three-dimensional GTO, respectively. The square dependence in the exponential term of the GTO means it is a less realistic representation of a single-electron wavefunction, relative to a STO in two main respects. Firstly, when $r = 0$, *i.e.*, at the nucleus, a STO has a cusp, whereas a GTO has a gradient of zero, meaning the latter does not accurately represent the behaviour of a wavefunction close to the nucleus as shown in Figure 3.2a. Additionally this squared dependence in the exponential also causes the GTO to decay too rapidly at large distances, compared to an AO. In order to overcome these problems and achieve a good level of accuracy, many more GTOs than STOs are required to model an AO. Although on their own GTOs are less accurate than STOs, in one respect, GTOs are undoubtedly superior; the overlap of two Gaussians, is a third Gaussian, meaning their linear combination has an exact mathematical solution. This makes using GTOs a more sensible choice when dealing with systems larger than a few atoms. A reasonable approximation of an AO can be achieved by forming a contracted Gaussian function (CGF), is simply the sum of several GTOs, with the inclusion of more GTOs leading to a better representation of a single STO, as shown in Figure 3.2b.

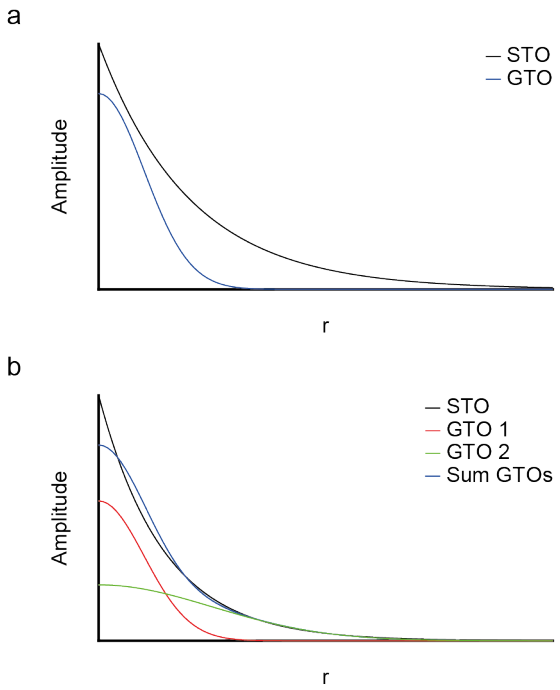


**Figure 3.2:** (a) Schematic showing a STO and a GTO, showing that the latter decay much faster as the nucleus-electron distance increases. (b) Schematic showing the sum of two GTOs to give better description of a STO.

Basis sets are highly parameterised, with many families of atom-centred basis sets developed for different systems, with some being highly optimised for one specific compound, and others developed to be more general. As a result, the choice of basis set can be an arduous one, involving literature research, testing, and fine tuning of parameters although often the choice is heavily influenced by the trade-off between calculation cost and accuracy. Nevertheless, it is important to ensure that the selected basis set is properly converged, *i.e.*, increasing the number of basis functions does not lead to a significant change in the calculated result.

### 3.5.2 Planewave basis sets

Instead of using basis functions designed to model individual atomic orbitals, such as STOs and GTOs, which can then be linearly combined to describe molecular orbitals for the entire system, it is possible to use functions that are able to represent the whole system directly. Using atom-

centred basis functions may not be practical when investigating systems such as extended solids, which would require an infinite number of AOs to model the entire structure. For these types of crystalline materials both the atom positions and the electron potential energy are periodic, *i.e.*,

$$V(\mathbf{r}) = V(\mathbf{r} + R) \ , \tag{3.72}$$

where R represent the unit cell length (the lattice vector), meaning they satisfy Bloch's theorem.[47] As the square of the wavefunction is equal to the electron density, it follows that if one quantity is periodic the other must be too. In fact, the magnitude of the wavefunction is indeed periodic but its phase is not, leading to wavefunctions being termed "quasi-periodic".

Investigating systems such as extended solids suggests the need for basis functions that are equally periodic. Constructing basis functions on the solution of the Schrödinger equation for free electrons was suggested after it was noted that the outer valence electrons in metals behave similarly to a uniform electron gas, which allows their behaviour to be approximated. As shown in Equation 3.73, complex exponentials, or equally, a combination of sine and cosine functions can be used to represent the solution to the Schrödinger equation for a free electron in one dimension

$$\begin{gathered} \varphi(x) = Ae^{ikx} + Be^{-ikx} = A\cos(kx) + B\sin(kx) \\ E = \frac{1}{2}k^2 \ , \end{gathered} \tag{3.73}$$

where k, the wavevector, refers to the momentum of the function. In an infinitely repeating system the energy gap between individual molecular orbitals disappears, leading to the formation of bands of electrons, which can be represented by a basis set made up of planewave functions. In three dimensions, planewaves can be written in the form

$$\varphi(\mathbf{r}) = e^{ikr} \ . \tag{3.74}$$

As individual planewave functions do a poor job of representing the electronic wavefunction for a system, basis sets based on these tend to be many times larger than the equivalent GTO-based basis sets. However, as the size of planewave basis set is only dependent on the size of the unit cell, and not on the contents of the unit cell, the larger the system, the more favourable it becomes to use planewaves compared to atom-centred basis sets. The wavefunction is simply expressed as the sum of the individual planewaves,

$$\psi_{n,k}(\mathbf{r}) = \sum_{G} C_{n,k}(\mathbf{G})\, e^{i(\mathbf{G}+k)\mathbf{r}} \quad , \tag{3.75}$$

where $C_{n,k}$ are Fourier coefficients of **G**, the reciprocal lattice vector. The Fourier coefficients are summed up to a maximum value, $G_{max}$, which in turn determines $E_{cut}$, the kinetic energy cut-off, expressed as

$$E_{cut} = \frac{h^2}{2m}(G_{max} + k)^2 \quad , \tag{3.76}$$

where m is the mass of an electron. This means that the size (and ultimately the accuracy) of a planewave basis set is determined by a single parameter, $E_{cut}$. The control of planewave basis sets through this one quantity represents a sizeable advantage over atom-centred counterparts.

## 3.6 Pseudopotentials

It has already been highlighted in previous sections of this chapter that given the complexity associated with electronic-structure calculations, the need to maximise calculation efficiency, without sacrificing computational accuracy, is key. It is widely accepted that most chemical properties are dominated by valence electrons, with the behaviour of the core electrons being almost independent of the chemical system. As a result, it is often seen as unnecessary to explicitly consider all the electrons in a system. Therefore, the frozen-core approximation (FCA)[48] is often employed to improve calculation efficiency. In this approximation, core electrons,

classified as all electrons with an energy below a specified level, are treated as part of the background potential of the system, with only the electrons above the specified energy, *i.e.*, the valence electrons, being calculated explicitly. As long as the energy cut-off is not too high, applying the FCA can still yield accurate results, but at a significantly reduced cost compared to the explicitly consideration of all electrons within a system.

As electronic wavefunctions must be orthogonal to each other, the explicit treatment of all core and valence electrons results in a wavefunction that contains numerous nodes (*i.e.*, where the magnitude of the wavefunction is zero). Representing such a wavefunction would require a large basis set. In addition to removing the need to explicitly describe the core electrons by applying the FCA, it is also possible to replace the wavefuncion for the valence electrons close to the nucleus (which is rapidly oscillating and therefore complex to represent) with a "pseudised" wavefunction. This is a nodeless function to describe the valence electrons within a core radius ($r_{core}$) of the nucleus, whilst continuing to explicitly describe these electrons beyond $r_{core,}$ (see Figure 3.3), allowing a smaller basis set to be used to represent the wavefunction.

The most common type of pseudopotentials used in condensed matter calculations are norm-conserving pseudopotentials (NCPs).[49] A drawback of NCPs is that they require the norm of the orbitals to be conserved, leading to a lack of flexibility or transferability in NCPs requiring a high $E_{cut}$ and hence

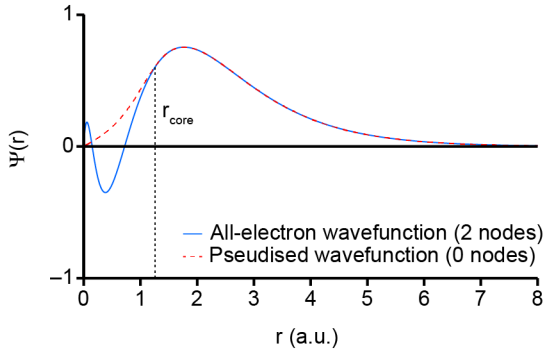


**Figure 3.2:** Schematic representation of the AE and pseudised Si 3s wavefunctions.

a large basis set. As a result, a different class of potentials, termed ultrasoft pseudopotentials (USPs) were developed.[50] In USPs the norm-conserving condition, which requires the total pseudocharge inside $r_{core}$ to match that of the total all-electron (AE) wavefunction, is relaxed, giving them increased transferability relative to NCPs. Despite this, the implementation of USPs into DFT codes is not trivial, and thus their widespread use has been slow. The on-the-fly generated USPs in the CASTEP code,[51] which are available for NMR calculations,[52] as well as the calculation of energies, forces and other properties, have been shown to produce accurate results compared to other DFT codes.[53]

For some chemical properties, including the NMR chemical shift, the AE wavefunction (and particularly its behaviour close to the nucleus) is important. As a result, it is important to reconstruct the AE wavefunction from a pseudopotential before calculating any properties that are particularly sensitive to the behaviour of electrons close to the nucleus. A procedure to use a psuedopotential to reconstruct the AE wavefunction, termed the projector augmented wave (PAW)[54] approach was set out by van de Walle and Blöchl, and is given by

$$\psi^{AE}(\mathbf{r}) = T\psi^{PS}(\mathbf{r}) \ , \tag{3.77}$$

where $\psi^{AE}$, $\psi^{PS}$ and T represent the AE wavefunction, the pseudised wavefunction and the transformation operator, respectively. An important extension of this theory that has revolutionised the use of first-principle calculations by the solid-state NMR spectroscopy is the development of the gauge including projector augmented wave (GIPAW) method[55] and its successful compatibility with USPs.[52,56] If a system is in a uniform magnetic field, the PAW transformation operator is unable to reconstruct the core region of a wavefunction without losing translational symmetry, introducing the so-called "gauge origin problem". The GIPAW method[55] overcomes this by including a magnetic field dependent phase to the translated waves, causing translational symmetry to be retained and allowing properties such

as the chemical shift, which is dependent on the external magnetic field, to be accurately calculated.

## 3.7 k-point sampling

A grid of equally spaced points, termed k-points, are used to sample the first Brillouin zone in reciprocal space. The k-points are usually placed on a Monkhorst-Pack (MP) grid,[57] an unbiased approach to choose points in reciprocal space. The number of k-points used can be easily controlled by setting the k-point spacing parameter, given in units of $2\pi$ Å$^{-1}$, with more k points selected as the k-point spacing decreases, leading to a more accurate approximation of the wavefunction. In principle, to determine the electron density it is necessary to integrate the wavefunction at every position, *i.e.*, every value of k, however, it is possible to approximate the integral with a sum,

$$\rho(\mathbf{r}) = \int \left|\Psi_k(\mathbf{r})\right|^2 d^3\mathbf{k} \approx \sum_k \left|\Psi_k(\mathbf{r})\right|^2 . \tag{3.78}$$

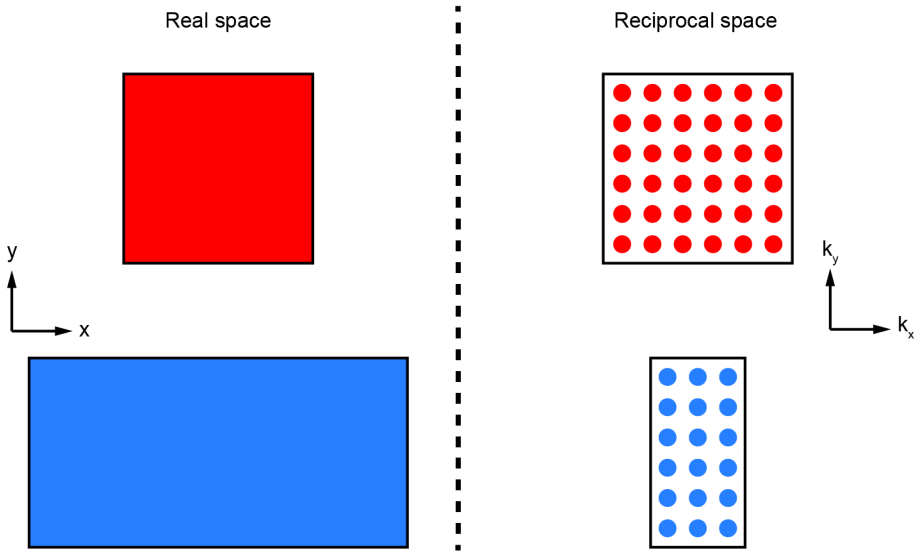


**Figure 3.4:** Schematic showing the effect that increasing the x-vector of a unit cell in real space causes the reciprocal x-vector, $k_x$, to decrease.

This means that the total electron density can be approximated as the sum of the square of the wavefunction determined at each k-point, giving a finite number of points. It is important to remember that dimensions in reciprocal space are the inverse of the real space dimensions, meaning that if a unit cell is lengthened in real space, the corresponding cell in reciprocal space will decrease in size, as highlighted in Figure 3.4.

## 3.8 Calculating solid-state NMR parameters

To calculate the NMR magnetic shielding for a nucleus it is necessary to first determine the electronic current created following the application of an external magnetic field. This can be achieved by considering how a magnetic field can be generated from an electronic current, a relationship laid out in the Biot-Savart law

$$\mathbf{B}(\mathbf{r}) = \frac{\mu_0}{4\pi}\int \frac{\mathrm{Id}\mathbf{L}\mathbf{r}'}{|\mathbf{r}'|^3} \,, \tag{3.79}$$

where **B** is the magnetic field, $\mu_0$ is the permeability of a vacuum, I is the current (in amperes), **L** is the length of the current carrying conductor, **r** is the distance from the conductor and **r′** is the displacement vector, *i.e.*, $\mathbf{r}' = \mathbf{r} - \mathbf{L}$ . With respect to the magnetic shielding, the effective Hamiltonian for this interaction is given as

$$\hat{\mathrm{H}} = -\frac{1}{2\pi}\sum \gamma_{\mathrm{K}}\mathbf{I}_{\mathrm{K}}(1-\boldsymbol{\sigma}_{\mathrm{K}})\mathbf{B}_{\mathrm{ext}} \,, \tag{3.80}$$

where $\gamma_K$ is the gyromagnetic ratio of nucleus K, $\mathbf{I}_K$ is the spin angular momentum of this species, $\boldsymbol{\sigma}_K$ is the chemical shielding tensor that represents the response of the electrons to the external magnetic field, $\mathbf{B}_{ext}$. The electronic response to $\mathbf{B}_{ext}$ results in an induced magnetic field, $\mathbf{B}_{in}$, that is caused by the orbital currents j(**r′**) computed using perturbation theory. $\mathbf{B}_{in}$ can be expressed as

$$\mathbf{B}_{\text{in}}(\mathbf{r}) = \frac{1}{c}\int d^3\mathbf{r}'\, j(\mathbf{r}')\frac{\mathbf{r}-\mathbf{r}'}{|\mathbf{r}-\mathbf{r}'|^3}\ , \tag{3.81}$$

and as

$$\mathbf{B}_{\text{in}}(\mathbf{R}_K) = -\boldsymbol{\sigma}_K \mathbf{B}_{\text{ext}}\ . \tag{3.82}$$

The magnetic shielding tensor can be stated as

$$\boldsymbol{\sigma}_K = -\frac{\mathbf{B}_{\text{in}}(\mathbf{R}_K)}{\mathbf{B}_{\text{ext}}}\ . \tag{3.83}$$

As alluded to in Section 3.6, the ability to accurately calculate $\boldsymbol{\sigma}$ for nuclei in extended materials using planewave-based DFT codes was only made feasible after the development of the GIPAW method, with its subsequent application using USPs making this process more efficient. The advantages of the ability to routinely and accurately calculate solid-state NMR parameters for periodic systems cannot be overstated. GIPAW calculations have assisted and guided the assignment of complex experimental NMR spectra, providing invaluable insight into the structure and ordering of a range of periodic materials.[4,58–62]

### 3.8.1 Relativistic effects

Recently the importance of including scalar relativistic effects when predicting solid-state NMR parameters has been considered. As the nuclear mass of a species increases, the effect of relativity also increases, as the speed of electrons close to heavy nuclei approaches the speed of light. As a result, it is unsurprising that relativity can have a significant effect on the shielding of heavy nuclei as these parameters are dominated by the behaviour of these electrons. The zero-order relativity approximation (ZORA)[63–65] can be used to account for relativistic effects. Table 3.1 shows the isotropic magnetic

**Table 3.1:** Calculated isotropic shielding values for a series of structures, calculated with no relativistic correction and with ZORA, with the magnitude of the difference in isotropic shielding ($\Delta\sigma_{iso}$) also shown. All calculations were performed using CASTEP 8.0, the GGA PBE functional, an $E_{cut}$ of 60 Ry and a k-point spacing of 0.04 $2\pi$ Å$^{-1}$. The structures were not geometry optimised prior to the prediction of NMR parameters.

| Structure | Nucleus | $\sigma_{iso}$ with no relativistic scheme (ppm) | $\sigma_{iso}$ with ZORA (ppm) | $\Delta\sigma_{iso}$ (ppm) |
|---|---|---|---|---|
| Al-MIL-53[66] | $^{1}$H | 26.61 | 26.60 | 0.01 |
| | $^{13}$C | 31.15 | 31.21 | 0.07 |
| | $^{17}$O | 86.34 | 86.15 | 0.19 |
| | $^{27}$Al | 550.67 | 552.99 | 2.32 |
| β-cristobalite[67] | $^{17}$O | 234.55 | 234.64 | 0.09 |
| | $^{29}$Si | 450.44 | 453.13 | 2.69 |
| AlPO-53(C)[68] | $^{17}$O | 177.88 | 177.04 | 0.84 |
| | $^{27}$Al | 507.75 | 510.19 | 2.44 |
| | $^{31}$P | 304.22 | 305.97 | 1.75 |
| $Y_2Ti_2O_7$[69] | $^{49}$Ti | –215.26 | –167.69 | 47.56 |
| | $^{89}$Y | 2535.81 | 2669.50 | 133.69 |

shielding, $\sigma_{iso}$, for a series of compounds, calculated with no relativistic correction scheme, and with ZORA. From this data it can be seen that there is very little difference in $\sigma_{iso}$ for light species, including $^{1}$H and $^{13}$C, whereas for the heavier nuclei such as $^{49}$Ti and $^{89}$Y, the difference in $\sigma_{iso}$ calculated with and without relativistic corrections is much larger. Ensuring that relativistic effects are considered becomes particularly important when predicting quantities that rely heavily on accurately modelling the core-valence electron interactions, such as NMR J-couplings.[70,71]

### 3.8.2 Geometry optimisation

In Chapter 2 the sensitivity of solid-state NMR parameters with respect to subtle changes in local geometry was stressed. This indicates that prior to predicting NMR parameters, it is essential to have high confidence in

the structural model(s) being used. Whether structural models have been generated computationally or from experimental data, initially predicted NMR parameters rarely agree well with experiment. This is because the structures often do not reflect an energy minimum on the DFT potential energy surface (PES). In the case where structures have been generated computationally, poor agreement with experiment could stem from the partial modification of an existing structure (*e.g.*, by changing composition, unit cell size or atom positions). Alternatively using low level DFT during the structure generation process could also lead to inconsistencies between predicted and experimental quantities. Structural models based on experimental data are typically constructed from diffraction measurements, meaning they can suffer from their own set of limitations. The accuracy of experimentally determined structures will depend on both the radiation source, *e.g.*, X-ray, synchrotron or neutron radiation, and on whether the sample is in powder or single-crystal form. Additionally, as DFT calculations are typically performed at zero Kelvin, the atom positions or overall unit cell size of structures optimised under DFT can differ from one constructed directly from experimental diffraction measurements, which are often performed closer to room temperature than absolute zero. Given these points, to minimise any discrepancies between DFT-predicted and experimentally determined parameters, it is advisable to perform a geometry optimisation prior to the prediction of quantities such as solid-state NMR parameters. This allows the atomic positions and unit cell vectors to vary to minimise the forces and stresses, and, as a consequence, the total energy. The importance of performing a geometry optimisation calculation prior to the prediction of solid-state NMR parameters is well documented in the literature, with improved agreement between predicted and experimental NMR parameters typically seen.[56,58,72–77] Table 3.2 shows the calculated and experimental isotropic chemical shieldings/shifts for the two crystallographically distinct $^{89}$Y sites in $Y_2O_3$. From this data it can be seen that the relative shielding difference between the two Y sites is much closer to the relative shift difference seen experimentally following geometry optimisation.

**Table 3.2:** Calculated and experimental isotropic shielding and shift values for $Y_2O_3$,[78] with the magnitude of the difference in isotropic shielding and shift also shown. All calculations were performed using CASTEP 8.0, the GGA PBE functional, an $E_{cut}$ of 60 Ry and a k-point spacing of 0.04 $2\pi$ Å$^{-1}$, with ZORA applied for the NMR parameter calculations.

| | Y1 site (ppm) | Y2 site (ppm) | Magnitude of difference (ppm) |
|---|---|---|---|
| Calculated (unoptimised) | $\sigma_{iso}$ = 2442 | $\sigma_{iso}$ = 2380 | 62 |
| Calculated (optimised) | $\sigma_{iso}$ = 2432 | $\sigma_{iso}$ = 2388 | 44 |
| Experimental[79] | $\delta_{iso}$ = 273 | $\delta_{iso}$ = 314 | 41 |

### 3.8.3 Semi-empirical dispersion correction

The recent introduction of semi-empirical dispersion correction (SEDC) schemes[80] into DFT codes has represented another significant improvement in the accuracy of quantum chemical calculations, allowing for even closer agreement between experimental and predicted NMR parameters. Dispersion interactions, sometimes referred to as London dispersion forces, arise from long-range electron correlation effects. As such, they represent the attractive $r^{-6}$ term in the 12-6 Lennard-Jones potential

$$V_{LJ} = 4\varepsilon\left[\left(\frac{\sigma}{r}\right)^{12} - \left(\frac{\sigma}{r}\right)^{6}\right], \tag{3.84}$$

where ε is the potential energy well depth, σ represents the distance at which the inter-particle potential is zero, and r is the distance between two particles. Failure to consider longer-range attractive interactions can have a significant effect on the accuracy of geometry optimisation, particularly if the crystal packing is strongly dependent on non-covalent interactions such as hydrogen bonding or π-π stacking interactions. Given their apparent importance, several DFT methods that include dispersion effects have been

**Table 3.3:** The unit cell volume for a series of structures, which were geometry optimised with no SEDC scheme and with the TS SEDC scheme. All calculations were performed using CASTEP 8.0, the GGA PBE functional, an $E_{cut}$ of 60 Ry and a k-point spacing of 0.04 2π Å$^{-1}$. The relative difference in unit cell volumes for the structures optimised in the two separate ways is also given (expressed as a percentage).

| | Unit cell volume / Å$^3$ | | |
|---|---|---|---|
| Structure | Optimised with no SEDC scheme | Optimised with TS SEDC scheme | Relative difference (%)[a] |
| Urea[81] | 160.33 | 144.66 | 10.83 |
| Al-MIL-53[66] | 2008.73 | 1816.18 | 10.60 |
| AlPO-53(C)[68] | 1238.55 | 1110.51 | 11.53 |
| β-$Mg_2SiO_4$[82] | 555.45 | 542.50 | 2.39 |
| β-cristobalite[67] | 415.22 | 412.67 | 0.62 |
| $SnO_2$[83] | 75.18 | 74.50 | 0.91 |
| $Y_2O_3$[78] | 1208.84 | 1176.35 | 2.76 |
| $Y_2Sn_2O_7$[84] | 1151.56 | 1128.33 | 2.06 |
| $Y_2Ti_2O_7$[69] | 1046.23 | 1018.68 | 2.70 |

[a] The relative difference in unit cell volume was determined by $[((V_{no\ SEDC} - V_{TS}) / V_{TS}) \times 100]$ where $V_{no\ SEDC}$ and $V_{TS}$ are the unit cell volumes of the structures geometry optimised with no SEDC scheme and with the TS SEDC scheme, respectively.

developed for periodic systems, including the Grimme (D2) and the Tkatchenko and Scheffler (TS) schemes.[85,86] In these SEDC schemes, an isotropic potential is used to describe the dispersion interactions, which at long range can be expressed using a sum of the London potentials over all N atoms in the system,

$$V = s_6 \sum_{i=1}^{N} \sum_{j>i}^{N} C_{6,ij} R_{ij}^{-6} \ , \qquad (3.85)$$

where $s_6$ is a scaling factor, $C_{6,ij}$ is a dispersion coefficient between any two atoms, *i* and *j*, separated by interatomic distance $R_{ij}$. At short range, a damping function $f(R_{ij}^0, R_{ij})$ is applied to the long-range expression in Equation 3.85. By specifying an interatomic distance cut-off, $R_{ij}^0$, which

depends on the van der Waals radii of the atom pairs (i and j), the dampening function reduces the excess dispersion interactions to zero. When this potential is added to the original DFT energy, the dispersion-corrected total energy, $E_{tot}$ can be expressed as

$$E_{tot} = E_{DFT} + s_6 \sum_{i=1}^{N} \sum_{j>i}^{N} f(S_R R_{ij}^0, R_{ij}) C_{6,ij} R_{ij}^0 \ , \qquad (3.86)$$

where $S_R$ is a scaling factor dependent on the $E_{XC}$ functional, used to match the dampening function to the DFT potential. The factors, $s_6$ and $S_R$, which scale the dispersion coefficients are parameterised according to the particular SEDC scheme used, *i.e.*, in D2 $s_6 = 0.75$, and in TS $S_R = 0.94$. Table 3.3 shows the unit cell volumes for a series of structures optimised with no SEDC and with the TS SEDC scheme. It is clear that the decision to omit or include dispersion corrections during the calculation is of more importance for systems such as molecular crystals, which are held together by long-range van der Waals interactions. Applying a SEDC scheme when optimising materials such as aluminophosphates (AlPOs) and metal-organic frameworks (MOFs), systems that exhibit significant structural flexibility, also has a large effect on the resulting unit cell volume. In comparison, the unit cell volume of dense-phase materials, usually held together by strong covalent or ionic interactions, are less dependent on the inclusion of a SEDC scheme during the geometry optimisation. The data in Table 3.3 highlights how the decision whether to include a SEDC scheme or not is highly system-dependent. Any variations in atomic position or unit cell volume can affect the predicted NMR parameters, and it has previously been shown that geometry optimisation using a SEDC scheme such as D2 or TS prior to the calculation of NMR parameters yields better agreement with experimental NMR measurements.[87–89]

### 3.8.4 Referencing calculated shieldings

It is extremely difficult, if not impossible to determine absolute shieldings experimentally. It is more common to reference shieldings relative to a known compound, and report the value as a chemical shift (see Section 2.3.1). Therefore, in order to compare to experiment, it is necessary to convert calculated shieldings to shifts using a reference shielding, $\sigma_{ref}$, given by

$$\sigma_{ref} = \sigma_{iso}^{calc} + \delta_{iso}^{exp} \ , \tag{3.87}$$

for one reference compound. Therefore, the calculated isotropic chemical shift, $\delta_{iso}^{calc}$, is equal to

$$\delta_{iso}^{calc} \approx \sigma_{ref} - \sigma_{iso}^{calc} \ . \tag{3.88}$$

Alternatively, instead of using a reference shielding determined from one system, a potentially more robust referencing approach is to compare calculated shielding and experimental shift data for a set of compounds. As shown in Figure 3.5, the line of best fit produced from plotting $\delta_{iso}^{exp}$ against $\sigma_{iso}^{calc}$ allows $\delta_{iso}^{calc}$, to be determined by

$$\delta_{iso}^{calc} = m\sigma_{iso}^{calc} + c \ , \tag{3.89}$$

where m and c represent the gradient and intercept of the line, respectively. Depending on the system being investigated the most appropriate referencing approach can vary. For example, if the experimental $\delta_{iso}$ for the compound being investigated is known, it can be used to internally reference the corresponding calculated $\sigma_{iso}$ value, but, if no experimental $\delta_{iso}$ data is available for the material being studied, the calculated $\sigma_{iso}$ may need to be referenced by comparing the experimental $\delta_{iso}$ and calculated $\sigma_{iso}$ values for a

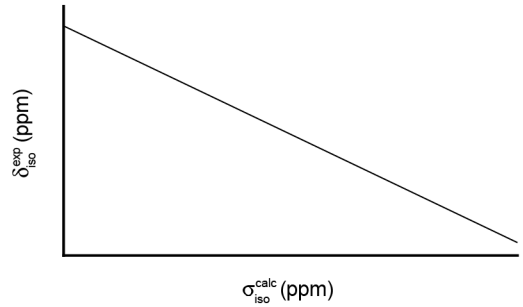


**Figure 3.5:** Schematic plot of experimental isotropic chemical shift ($\delta_{iso}^{exp}$) against calculated isotropic shielding ($\sigma_{iso}^{calc}$), showing the equation of the line of best fit, which can be used to generate calculated isotropic shifts ($\delta_{iso}^{calc}$).

series of related compounds that have known experimental values. As a result, through this thesis, the various reference approaches used will be described explicitly for each system being investigated.

### 3.8.5 Quadrupolar interactions

In contrast to dealing with experimental spectra, the process of calculating quadrupolar NMR parameters is relatively straightforward as the EFG can be expressed as a function of the total charge density, n(**r**). This allows the quadrupolar coupling constant, $C_Q$ and asymmetry parameter, $\eta_Q$, to be determined.[90] This involves first defining the traceless EFG tensor, V(**r**),

$$V_{\alpha\beta}(\mathbf{r}) = \frac{\partial E_\alpha(\mathbf{r})}{\partial r_\beta} - \frac{1}{3}\delta_{\alpha\beta}\sum_\gamma \frac{\partial E_\gamma(\mathbf{r})}{\partial r_\gamma} \quad , \tag{3.90}$$

where α, β, and γ represent the x, y, and z Cartesian coordinates and $E_\alpha(\mathbf{r})$ denotes the local electric field at position **r**. $E_\alpha(\mathbf{r})$ can be calculated using n(**r**),

$$E_\alpha(\mathbf{r}) = \int d^3r' \frac{n(\mathbf{r}')}{|\mathbf{r}-\mathbf{r}'|}(r_\alpha - r_\alpha') \, , \tag{3.91}$$

from which the EFG tensor can be determined

$$V_{\alpha\beta}(\mathbf{r}) = \int d^3r' \frac{n(\mathbf{r}')}{|\mathbf{r}-\mathbf{r}'|^3}\left[\delta_{\alpha\beta} - 3\frac{(r_\alpha - r_\alpha')(r_\beta - r_\beta')}{|\mathbf{r}-\mathbf{r}'|^2}\right]. \quad (3.92)$$

After ordering the eigenvalues of the EFG tensor so that $|V_{zz}| > |V_{yy}| > |V_{xx}|$, the quadrupolar NMR parameters can be determined as

$$C_Q = \frac{eQV_{zz}}{h} \quad (3.93)$$

and

$$\eta_Q = \frac{V_{xx} - V_{yy}}{V_{zz}}, \quad (3.94)$$

where e, Q and h are the charge of an electron, the electric quadrupole moment (published in date tables[91]) and Planck's constant, respectively.

## 3.9 Convergence

The accuracy of planewave DFT calculations (using a chosen $E_{XC}$ functional) is primarily determined by two factors, the energy cut-off, $E_{cut}$, which determines the number of planewave functions in the basis set, and the sampling of the first Brillouin zone in reciprocal space, *i.e.*, the number of k-points used. Values for $E_{cut}$ and k-point spacing are obtained by ensuring the calculations are converged. This involves varying each parameter independently whilst monitoring the effect on a relevant calculated property. Figure 3.6 shows the results of such convergence tests for α-quartz, a polymorph of $SiO_2$, where the total energy of the system is monitored as $E_{cut}$ and k-point spacing were independently varies. It can be seen that from 45 Ry and 0.07 $2\pi$ $Å^{-1}$ no appreciable variation in total energy is observed with increasing accuracy of $E_{cut}$ or k-point spacing. In contrast, from Figure 3.7,

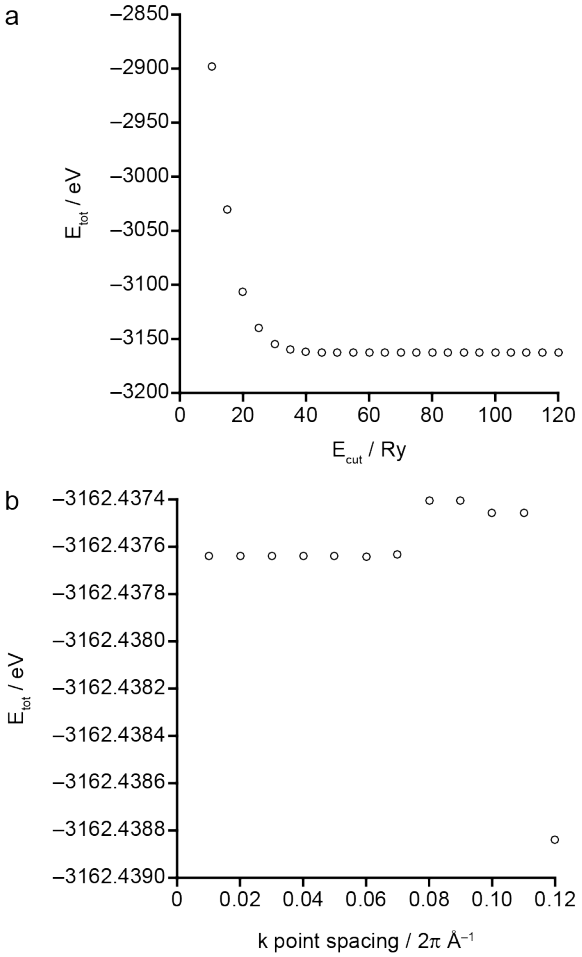


**Figure 3.6:** Plots showing the total energy, $E_{tot}$, for α-quart, against (a) energy cut-off, $E_{cut}$ and (b) k-point spacing. When $E_{cut}$ was varied the k-point spacing was fixed at 0.04 2π $Å^{-1}$, whilst $E_{cut}$ was fixed at 60 Ry (1 Ry = 13.61 eV) when k-point spacing was varied.

which shows similar plots of calculated $^{29}Si$ $\sigma_{iso}$ with varying $E_{cut}$ and k-point spacing values, it can be seen that this quantity only converges when $E_{cut}$ is 55-60 Ry and very small k-point spacing. Figure 3.7 also shows the calculation time for these calculations, with the time increasing reasonably consistently with $E_{cut}$ but exponentially as the k-point spacing is decreased. As with most aspects of DFT calculations, when determining the values of $E_{cut}$ and k-point spacing to be used, the computational cost is a large factor. As shown in Figure 3,7, increasing the accuracy of these parameters results in longer calculations. Therefore, the choice of $E_{cut}$ and k-point spacing is a balancing act between computational cost and accuracy, something that must

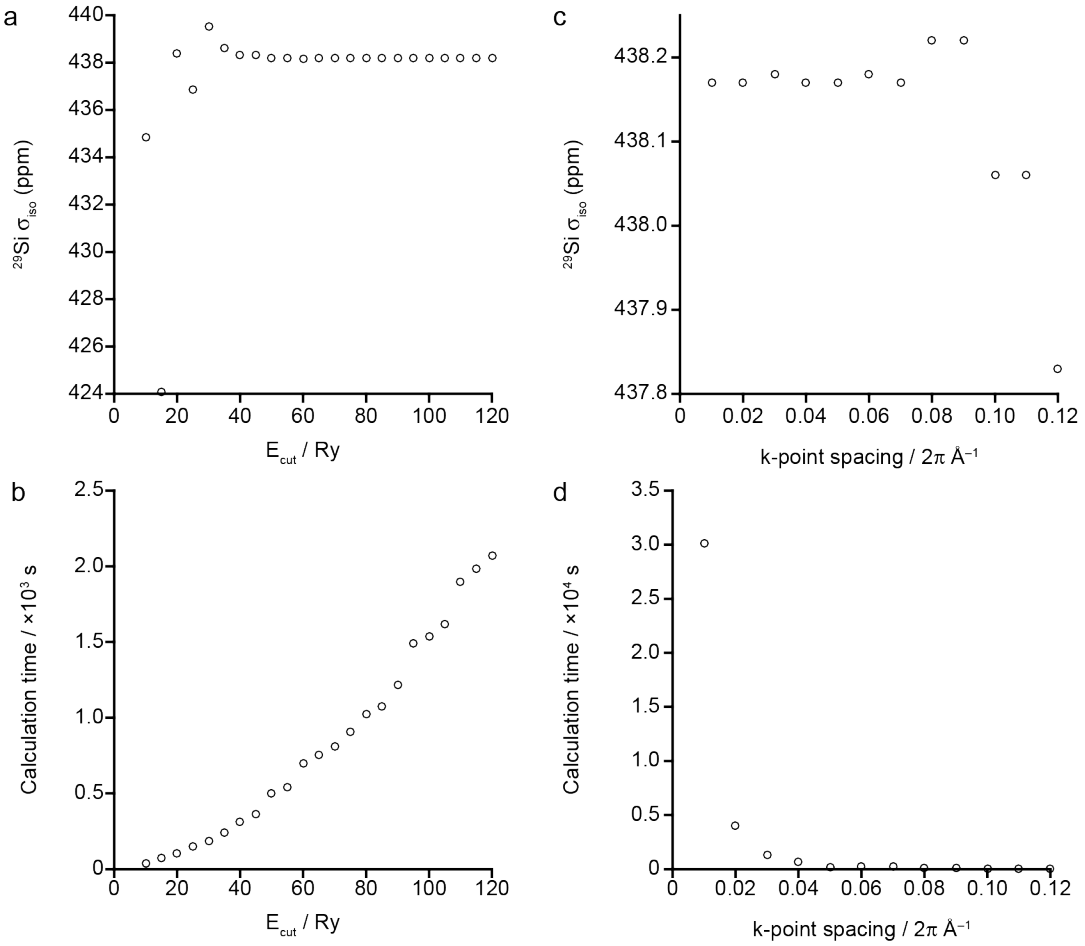


**Figure 3.7:** Plots showing (a and c) calculated $^{29}$Si $\sigma_{iso}$ for α-quartz, and (b and d) calculation time (on one 32 core node) for α-quartz against (a and b) energy cut-off, $E_{cut}$, and (c and d) k-point spacing. When $E_{cut}$ was varied the k-point spacing was fixed at 0.04 2π Å$^{-1}$, whilst $E_{cut}$ was fixed at 60 Ry when k-point spacing was varied.

be seriously considered, especially if a project is going to require a large number of calculations. A compromise in accuracy may be required in order to complete a large project within a realistic timeframe.

## 3.10 General computational methodology

Over the course of this thesis a number of computing resources were used to run planewave DFT calculations. These resources included Wardlaw and Kennedy, local clusters at the EaStCHEM computing facility at the University of St Andrews, the UK national tier-2 high performance computing hub in materials and molecular modelling (Thomas) hosted at

**Table 3.4:** Summary of the hardware specifics for the computing resources used for this work presented in this thesis.

| Cluster | Number of nodes | Cores per node | CPU type | Memory per core / GB | Interconnect |
|---|---|---|---|---|---|
| Wardlaw | 290 | 12 | Intel Westmere | 2 | InfiniBand |
| Kennedy | 90 | 32 | Intel Broadwell | 4 | FDR InfiniBand |
| Thomas | 720 | 24 | Intel Broadwell | 4 | InfiniBand |
| ARCHER | 4290 | 24 | Ivy Bridge | 4 | Cray Aries |

UCL, and the national ARCHER facility, based in Edinburgh. A brief summary of the cluster specifics is given in Table 3.4.

Unless explicitly stated otherwise, all DFT calculations carried out for this thesis were performed using CASTEP version 7.01, 8.0 or 16.11. For CASTEP calculations, two input files, a `.cell` and a `.param` file, are required. The `.cell` file contains all the structural information on the system, including the unit cell size and shape, and fractional coordinates for all atoms, in addition to the k-point spacing to be implemented and the pseudopotentials used. In all geometry optimisations and all calculations of NMR parameters the recommended ultrasoft pseudopotentials were used, with CASTEP on-the-fly pseudopotentials used for calculations performed in versions 8.0 or 16.11 of the code, and generated from a stated pseudopotential string in calculations with version 7.01. The calculation type (geometry optimisation, single-point energy, NMR parameter, phonon *etc.*), exchange-correlation functional, $E_{cut}$, and all other parameters were specified in the `.param` file.

Within this thesis the predicted solid-state NMR parameters for $^{1}$H, $^{2}$H, $^{17}$O, $^{29}$Si, $^{89}$Y and $^{119}$Sn were investigated in detail. In all calculations the electric quadrupole moment, Q, for $^{2}$H and $^{17}$O were 0.00286 and –0.02558 Barn, respectively. Typically parameters used for geometry optimisation and the calculation of NMR parameters were $E_{cut}$ of 50-60 Ry and k-point spacing of 0.04-0.05 $2\pi$ Å$^{-1}$. For all calculations performed using CASTEP versions 8.0 or 16.11, ZORA was employed. The TS SEDC scheme was used during the geometry optimisation of hydrous minerals (see Chapter 6) when CASTEP

version 8.0 was used. Over the course of this thesis, the importance of the electronic energy tolerance (defined as `elec_energy_tol` in the `.param` file), the parameter that determines the tolerance to be used when determining the convergence of the total energy of a system during an electronic energy minimisation, was investigated and will be discussed in Chapter 5. Table 3.5 contains a summary of the typical parameters used in typical CASTEP geometry optimisation and the calculation of NMR parameter using CASTEP during this thesis. Depending on the computational resource being used, the type of calculation, size, atomic species and complexity of the system, calculation times varied significantly, with geometry optimisation and calculation of NMR parameter typically taking between 8 and 48 hours on two nodes of Kennedy, *i.e.*, using 64 cores.

**Table 3.5:** Selected input options (from `.cell` and `.param` files) used during a typical geometry optimisation or calculation of NMR parameters using CASTEP.

| CASTEP option | Description | Typical value(s) |
|---|---|---|
| `task` | defines the type of calculation to be performed | geometryoptimisation, magres |
| `xc_functional` | controls which functional is used to calculate the exchange-correlation potential | PBE |
| `opt_strategy` | determines the optimisation strategy | speed |
| `opt_method` | determines the optimiser used | LBFGS, BFGS |
| `calculate_stress` | determines whether or not a stress calculation will be performed | true |
| `max_SCF_cycles` | determines the maximum number of SCF cycles performed during an electronic minimisation | 50 |
| `geom_max_iter` | determines the maximum number of steps in a geometry optimisation | 200 |
| `geom_energy_tol` | controls the tolerance for accepting convergence of the free energy per atom during a geometry optimisation | $1 \times 10^{-4}$, $1 \times 10^{-5}$ eV / atom |
| `kpoints_mp_spacing` | specifies the maximum distance between k-points | 0.04, 0.05 $2\pi$ Å$^{-1}$ |
| `cut_off_energy` | specifies the cut-off energy for the planewave basis set | 50, 60 Ry |
| `SEDC_scheme` | specifies the semi-empirical dispersion correction scheme | TS |
| `relativistic_treatment` | specifies the relativistic treatment scheme | ZORA |
| `elec_energy_tol` | controls the tolerance for accepting convergence of the total energy in an electronic minimisation | $1 \times 10^{-5}$, $1 \times 10^{-9}$ eV / atom |

## 3.11 References


1. G. E. Moore, *Electronics*, 1965, **38**, 114–117.
2. R. F. Moran, D. M. Dawson, and S. E. Ashbrook, *Int. Rev. Phys. Chem.*, 2017, **36**, 39–115.
3. S. E. Ashbrook, D. M. Dawson, and J. M. Griffin, in *Local Structural Characterisation*, eds. D. W. Bruce, D. O'Hare, and R. I. Walton, John Wiley & Sons, Ltd, 2014.
4. S. E. Ashbrook and D. McKay, *Chem. Commun.*, 2016, **52**, 7186–7204.
5. E. Salager, G. M. Day, R. S. Stein, C. J. Pickard, B. Elena, and L. Emsley, *J. Am. Chem. Soc.*, 2010, **132**, 2564–2566.
6. M. Baias, J. N. Dumez, P. H. Svensson, S. Schantz, G. M. Day, and L. Emsley, *J. Am. Chem. Soc.*, 2013, **135**, 17501–17507.
7. R. K. Harris, S. Cadars, L. Emsley, J. R. Yates, C. J. Pickard, R. K. R. Jetti, and U. J. Griesser, *Phys. Chem. Chem. Phys.*, 2007, **9**, 360–8.
8. F. Jensen, *Introduction to Computational Chemistry*, John Wiley & Sons, Ltd, Chichester, 2nd edn., 2007.
9. W. Koch and M. C. Holthausen, *A Chemist's Guide to Density Functional Theory*, Wiley-VCH, Chichester, 2nd edn., 2001.
10. C. J. Cramer, *Essentials of Computational Chemistry Theories and Models*, John Wiley & Sons, Ltd, Chichester, 2nd edn., 2004.
11. M. Kaupp, M. Bühl, and V. G. Malkin, *Calculation of NMR and EPR Parameters: Theory and Applications*, Wiley-VCH, Weinheim, 1st edn., 2004.
12. M. Born and J. R. Oppenheimer, *Ann. Phys.*, 1927, **389**, 457–484.
13. W. Pauli, *Zeitschrift für Phys.*, 1925, **31**, 765–783.
14. P. Lowdin, *Int. J. Quantum Chem.*, 1995, **55**, 77–102.
15. L. H. Thomas, *Math. Proc. Camb. Phil. Soc.*, 1927, **23**, 542–548.
16. E. Fermi, *Rend. Accad. Naz. Lincei*, 1927, **6**, 602–607.
17. E. Fermi, *Zeitschrift für Phys.*, 1928, 48, 73–79.
18. E. H. Lieb and B. Simon, *Adv. Math.*, 1977, **23**, 22–116.
19. R. G. Parr and W. Yang, *Density-Functional Theory of Atoms and Molecules*, Oxford University Press, New York, 1989.
20. J. C. Slater, *Phys. Rev.*, 1951, **81**, 385–390.

21. P. A. M. Dirac, *Math. Proc. Camb. Phil. Soc.*, 1930, **26**, 376–385.
22. P. Hohenberg and W. Kohn, *Phys. Rev.*, 1964, **136**, B864–B871.
23. W. Kohn and L. J. Sham, *Phys. Rev.*, 1965, **140**, A1133–A1138.
24. S. H. Vosko, L. Wilk, and M. Nusair, *Can. J. Phys.*, 1980, **58**, 1200–1211.
25. D. M. Ceperley and B. J. Alder, *Phys. Rev. Lett.*, 1980, **45**, 566–569.
26. J. P. Perdew and A. Zunger, *Phys. Rev. B*, 1981, **23**, 5048–5079.
27. J. P. Perdew and Y. Wang, *Phys. Rev. B*, 1992, **45**, 13244–13249.
28. M. Ernzerhof, J. P. Perdew, and K. Burke, *Int. J. Quantum Chem.*, 1997, **64**, 285–295.
29. J. P. Perdew, K. Burke, and M. Ernzerhof, *Phys. Rev. Lett.*, 1996, **77**, 3865–3868.
30. J. P. Perdew, J. A. Chevary, S. A. Vosko, K. A. Jackson, M. R. Pederson, D. J. Singh, and C. Fiolhais, *Phys. Rev. B*, 1992, **46**, 6671–6687.
31. B. Hammer, L. B. Hansen, and J. K. Nørskov, *Phys. Rev. B*, 1999, **59**, 7413–7421.
32. Z. Wu and R. E. Cohen, *Phys. Rev. B*, 2006, **73**, 235116.
33. J. P. Perdew, A. Ruzsinszky, G. I. Csonka, O. A. Vydrov, G. E. Scuseria, L. A. Constantin, X. Zhou, and K. Burke, *Phys. Rev. Lett.*, 2008, **100**, 136406.
34. A. D. Becke and M. R. Roussel, *Phys. Rev. A*, 1989, **39**, 3761–3767.
35. A. D. Becke, *J. Chem. Phys.*, 1996, **104**, 1040–1046.
36. J. Tao, J. P. Perdew, V. N. Staroverov, and G. E. Scuseria, *Phys. Rev. Lett.*, 2003, **91**, 146401.
37. J. P. Perdew and K. Schmidt, *AIP Conf. Proc.*, 2001, **577**, 1–20.
38. A. D. Becke, *J. Chem. Phys.*, 1993, **98**, 1372–1377.
39. A. D. Becke, *J. Chem. Phys.*, 1993, **98**, 5648–5652.
40. A. D. Becke, *J. Chem. Phys.*, 1997, **107**, 8554–8560.
41. A. D. Boese and N. C. Handy, *J. Chem. Phys.*, 2002, **116**, 9559–9569.
42. T. Kotani, *J. Phys. Condens. Matter*, 1998, **10**, 9241–9261.
43. S. Kümmel and J. P. Perdew, *Phys. Rev. Lett.*, 2003, **90**, 43004.
44. S. Kümmel and J. P. Perdew, *Phys. Rev. B*, 2003, **68**, 35103.
45. J. C. Slater, *Phys. Rev.*, 1930, **36**, 57–64.
46. S. F. Boys, *Proc. R. Soc. A*, 1950, **200**, 542–554.
47. F. Bloch, *Zeitschrift für Phys.*, 1929, **52**, 555–600.

48. U. von Barth and C. D. Gelatt, *Phys. Rev. B*, 1980, **21**, 2222–2228.
49. D. R. Hamann, M. Schlüter, and C. Chiang, *Phys. Rev. Lett.*, 1979, **43**, 1494–1497.
50. D. Vanderbilt, *Phys. Rev. B*, 1990, **41**, 7892–7895.
51. S. J. Clark, M. D. Segall, C. J. Pickard, P. J. Hasnip, M. I. J. Probert, K. Refson, and M. C. Payne, *Z. Kristallogr.*, 2005, **220**, 567–570.
52. J. R. Yates, C. J. Pickard, and F. Mauri, *Phys. Rev. B*, 2007, **76**, 24401.
53. K. Lejaeghere, G. Bihlmayer, T. Björkman, P. Blaha, S. Blügel, V. Blum, D. Caliste, I. E. Castelli, S. J. Clark, A. Dal Corso, S. De Gironcoli, T. Deutsch, J. K. Dewhurst, I. Di Marco, C. Draxl, M. Dułak, O. Eriksson, J. A. Flores-Livas, K. F. Garrity, L. Genovese, P. Giannozzi, M. Giantomassi, S. Goedecker, X. Gonze, O. Grånäs, E. K. U. Gross, A. Gulans, F. Gygi, D. R. Hamann, P. J. Hasnip, N. A. W. Holzwarth, D. Iuşan, D. B. Jochym, F. Jollet, D. Jones, G. Kresse, K. Koepernik, E. Küçükbenli, Y. O. Kvashnin, I. L. M. Locht, S. Lubeck, M. Marsman, N. Marzari, U. Nitzsche, L. Nordström, T. Ozaki, L. Paulatto, C. J. Pickard, W. Poelmans, M. I. J. Probert, K. Refson, M. Richter, G. M. Rignanese, S. Saha, M. Scheffler, M. Schlipf, K. Schwarz, S. Sharma, F. Tavazza, P. Thunström, A. Tkatchenko, M. Torrent, D. Vanderbilt, M. J. Van Setten, V. Van Speybroeck, J. M. Wills, J. R. Yates, G. X. Zhang, and S. Cottenier, *Science*, 2016, **351**, aad3000.
54. C. G. Van de Walle and P. E. Blöchl, *Phys. Rev. B*, 1993, **47**, 4244–4255.
55. C. J. Pickard and F. Mauri, *Phys. Rev. B*, 2001, **63**, 245101.
56. T. Charpentier, *Solid State Nucl. Magn. Reson.*, 2011, **40**, 1–20.
57. H. J. Monkhorst and J. D. Pack, *Phys. Rev. B*, 1976, **13**, 5188–5192.
58. C. Bonhomme, C. Gervais, F. Babonneau, C. Coelho, F. Pourpoint, T. Azaïs, S. E. Ashbrook, J. M. Griffin, J. R. Yates, F. Mauri, and C. J. Pickard, *Chem. Rev.*, 2012, **112**, 5733–5779.
59. M. Profeta, F. Mauri, and C. J. Pickard, *J. Am. Chem. Soc.*, 2003, **125**, 541–548.
60. M. Profeta, M. Benoit, F. Mauri, and C. J. Pickard, *J. Am. Chem. Soc.*, 2004, **126**, 12628–12635.
61. J. R. Yates, T. N. Pham, C. J. Pickard, F. Mauri, A. M. Amado, A. M. Gil, and S. P. Brown, *J. Am. Chem. Soc.*, 2005, **127**, 10216–10220.

62. A. Fernandes, R. F. Moran, S. Sneddon, D. M. Dawson, D. McKay, G. P. M. Bignami, F. Blanc, K. R. Whittle, and S. E. Ashbrook, *RSC Adv.*, 2018, **8**, 7089–7101.
63. S. K. Wolff, T. Ziegler, E. Van Lenthe, and E. J. Baerends, *J. Chem. Phys.*, 1999, **110**, 7689–7698.
64. R. Bouten, E. J. Baerends, E. van Lenthe, L. Visscher, G. Schreckenbach, and T. Ziegler, *J. Phys. Chem. A*, 2000, **104**, 5600–5611.
65. J. R. Yates, C. J. Pickard, M. C. Payne, and F. Mauri, *J. Chem. Phys.*, 2003, **118**, 5746.
66. G. Ortiz, G. Chaplais, J.-L. Paillaud, H. Nouali, J. Patarin, J. Raya, and C. Marichal, *J. Phys. Chem. C*, 2014, **118**, 22021–22029.
67. W. W. Schmahl, I. P. Swainson, M. T. Dove, and A. Graeme-Barber, *Z. Kristallogr.*, 1992, **201**, 125–145.
68. R. M. Kirchner, R. W. Grosse-kunstleve, J. J. Pluth, S. T. Wilson, R. W. Broach, and J. V. Smith, *Microporous Mesoporous Mater.*, 2000, **39**, 319–332.
69. O. Knop, F. Brisse, and L. Castelliz, *Can. J. Chem.*, 1969, **47**, 971–990.
70. T. F. G. Green and J. R. Yates, *J. Chem. Phys.*, 2014, **140**, 234106.
71. P. Sanz Camacho, D. McKay, D. M. Dawson, C. Kirst, J. R. Yates, T. F. G. Green, D. B. Cordes, A. M. Z. Slawin, J. D. Woollins, and S. E. Ashbrook, *Inorg. Chem.*, 2016, **55**, 10881–10887.
72. J. R. Yates, S. E. Dobbins, C. J. Pickard, F. Mauri, P. Y. Ghi, and R. K. Harris, *Phys. Chem. Chem. Phys.*, 2005, **7**, 1402–1407.
73. R. K. Harris, P. Hodgkinson, C. J. Pickard, J. R. Yates, and V. Zorin, *Magn. Reson. Chem.*, 2007, 45, S174–S186.
74. S. E. Ashbrook and D. M. Dawson, *Acc. Chem. Res.*, 2013, **46**, 1964–1974.
75. S. E. Ashbrook, M. Cutajar, C. J. Pickard, R. I. Walton, and S. Wimperis, *Phys. Chem. Chem. Phys.*, 2008, **10**, 5754–5764.
76. C. J. Pickard, E. Salager, G. Pintacuda, B. Elena, and L. Emsley, *J. Am. Chem. Soc.*, 2007, **129**, 8932–8933.
77. S. Sneddon, D. M. Dawson, C. J. Pickard, and S. E. Ashbrook, *Phys. Chem. Chem. Phys.*, 2014, **16**, 2660–2673.
78. M. G. Paton and E. N. Maslen, *Acta Crystallogr.*, 1965, **19**, 307–310.
79. P. Florian, M. Gervais, A. Douy, D. Massiot, and J.-P. Coutures, *J. Phys.*

*Chem. B*, 2001, **105**, 379–391.
80. E. R. McNellis, J. Meyer, and K. Reuter, *Phys. Rev. B*, 2009, **80**, 205414.
81. N. Sklar, M. E. Senko, and B. Post, *Acta Crystallogr.*, 1961, **14**, 716–720.
82. H. Horiuchi and H. Sawamoto, *Am. Mineral.*, 1981, **66**, 568–575.
83. W. H. Baur and A. A. Khan, *Acta Crystallogr. Sect. B*, 1971, **27**, 2133–2139.
84. F. Brisse and O. Knop, *Can. J. Chem.*, 1968, **46**, 859–873.
85. S. Grimme, *J. Comput. Chem.*, 2006, **27**, 1787–1799.
86. A. Tkatchenko and M. Scheffler, *Phys. Rev. Lett.*, 2009, **102**, 73005.
87. D. V. Dudenko, J. R. Yates, K. D. M. Harris, and S. P. Brown, *CrystEngComm*, 2013, **15**, 8797–8807.
88. N. Folliet, C. Gervais, D. Costa, G. Laurent, F. Babonneau, L. Stievano, J. F. Lambert, and F. Tielens, *J. Phys. Chem. C*, 2013, **117**, 4104–4114.
89. S. T. Holmes and R. W. Schurko, *J. Phys. Chem. C*, 2018, **122**, 1809–1820.
90. M. Profeta, F. Mauri, and C. J. Pickard, *J. Am. Chem. Soc.*, 2003, **125**, 541–548.
91. P. Pyykkö, *Mol. Phys.*, 2018, **116**, 1328–1338.

# Chapter 4: Computational modelling of disorder in materials

## 4.1 Introduction

Although the presence of disorder in solids often leads to interesting physical and chemical properties being exhibited, any deviation from periodicity, *i.e.*, a loss of some component of long-range order, can make structure determination significantly more challenging in comparison to that for a periodically ordered structure. While Bragg-based techniques such as XRD can provide an accurate description of solids in which the long-range order of atoms is maintained, once periodicity is disrupted many of these approaches are less effective, and provide either an incomplete structural model or only an average picture of the structure and the atom positions. Additionally, it is known that XRD struggles to accurately determine the position of light atoms, or to provide a clear distinction between species with the same, or a similar number of electrons, *i.e.*, XRD cannot distinguish between the positions of isoelectronic species such as $F^-$ and $HO^-$ (hydroxide), or $Al^{3+}$ and $Si^{4+}$. The crystal structure of GaPO-34A(mim),[1] shown in Figure 4.1, is a gallium phosphate framework where the structure directing agent (SDA) is 1-methylimidizolium. This structural model was produced from data acquired using single-crystal XRD, and illustrates the difficulties diffraction techniques often face when attempting to determine the structure of disordered materials. In the crystal structure of GaPO-34A(mim), three separate SDA orientations are identified, with 55, 30 and 15% occupancy, respectively, the positions of all H atoms are not refined, no distinction is made between the position of C and N atoms in the SDA, and plus there are Ga and O sites with fractional occupancies. Although diffraction measurements were able to determine information on the unit cell parameters more easily, the exact positions and connectivity of many of the atoms remain unknown or ambiguous.

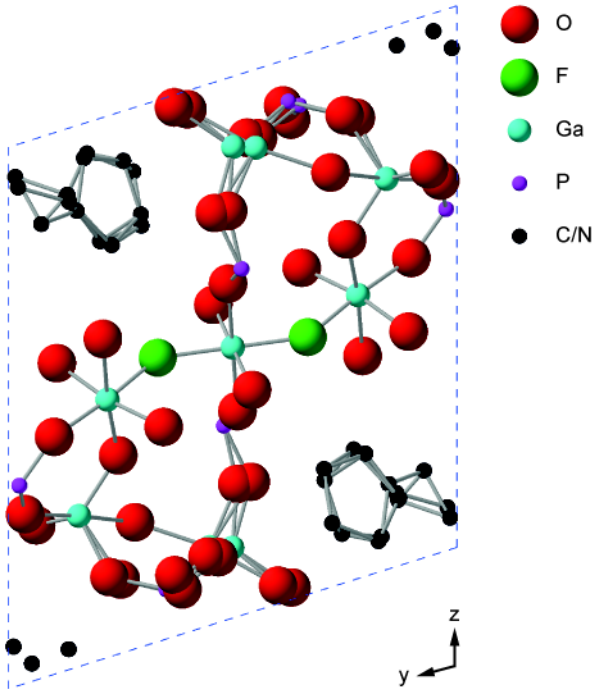


**Figure 4.1:** Schematic crystal structure of GaPO-34A(mim), determined using single-crystal XRD measurements,[1] illustrating the challenges many Bragg diffraction techniques encounter when investigating disordered materials.

As discussed in Chapter 2, NMR spectroscopy is very sensitive to changes in the local environment of atoms, seemingly making it the ideal approach for studying disordered materials. However, in some respects, NMR spectroscopy could be considered too sensitive to short-range structural variations, as the resulting NMR spectra often contain broad, overlapping lineshapes from chemically different environments, which are challenging to assign. Given the challenges associated with interpreting experimental solid-state NMR spectra, it is not surprising that first-principles calculations are often used to predict NMR parameters and ultimately assist structure determination.

In early work on the prediction of solid-state NMR parameters, periodic solids were represented as a "molecular cluster", where a discrete arrangement of a small number of atoms are "cut out" of the periodic structure and considered independently. In this type of structural model, any atoms that have their coordination environment affected by the creation of a

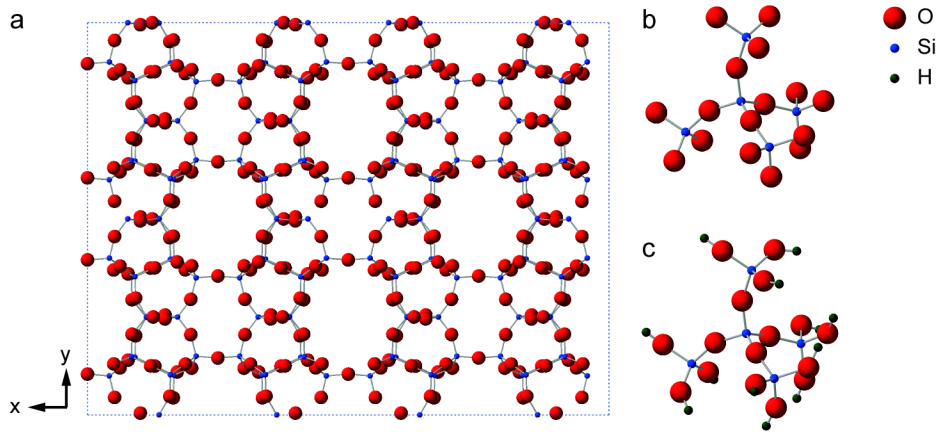


**Figure 4.2:** Schematic showing (a) a 2 × 2 × 1 supercell of ferrierite,[2] (b) a model cluster centred on Si and (c) the cluster in (b) with the dangling Si–O bonds terminated by H.

discrete cluster, *i.e.*, the atoms around the perimeter will have their valences completed usually by H atoms, giving a terminated cluster model. The general process of creating a molecular cluster from a periodic system is shown in Figure 4.2, where a Si centred model cluster is created from ferrierite,[2] a periodic pure silica zeolite framework, with hydrogen atoms then added to terminate the cluster. This approach results in efficient calculations (as only relatively few atoms have to be considered in the calculation), of the solid-state NMR parameters for the atom in the centre of the cluster. However, this modelling approach does have its limitations, as for many materials, representing the "true" periodic structure using a discrete number of atoms, is too extreme an approximation, and one that could lead to inaccurate solid-state NMR parameters being predicted. In addition, as only the predicted NMR parameters for the central atom in the cluster can be accurately calculated, this process can be quite inefficient as multiple calculations might have to be performed. The development of the GIPAW approach,[3] signified a step change in the use of first-principles calculations for solids, as it allowed the NMR parameters of all atoms in a periodically repeating structure solid to be predicted simultaneously, all to a high level of accuracy. As a result, this approach has become very popular in the experimental solid-state NMR community, being applied to a wide range of systems, including ceramics, pharmaceuticals, minerals and glasses.[4–7]

For an ordered system, the calculation of solid-state NMR parameters can aid the assignment and interpretation of experimental NMR spectra by providing information on the number of crystallographically different sites present. In addition, the magnitude of quantities including quadrupolar coupling constants ($C_Q$) and chemical shift anisotropies (CSAs), can be challenging to determine experimentally, can be predicted, again, potentially aiding spectral assignment. When attempting to understand the structure of disordered materials, first-principles calculations can play an even more important role, providing insight into how the predicted NMR parameters change in response to structural variations. Additionally, predicted solid-state NMR parameters can be used to guide the interpretation of NMR spectra for disordered materials, which tend to contain complex lineshapes that can be difficult to unambiguously assign.

Arguably the most important prerequisite for calculating solid-state NMR parameters (or in fact any quantity) is a realistic structural model, or series of models that contain within them the different local structural environments that could lead to the resonance(s) observed in the experimental NMR spectra. This chapter focuses on different possible ways of constructing structural models computationally, ensuring that the chosen approach results in models that accurately reflect the different local chemical environments present in the material. This discussion is crucial as the ultimate goal of this thesis is to describe how first-principles calculations can assist the interpretation of the solid-state NMR spectra of disordered materials, the success of which will depend in no small part on the relevance or completeness of the structural models used to represent the material.

## 4.2 Ordered materials

When the system being investigated is known, or suspected to be ordered, the process of constructing the structural model and predicting the solid-state NMR parameters is relatively straightforward. The simplest case is when there is already a known crystal structure (usually determined by

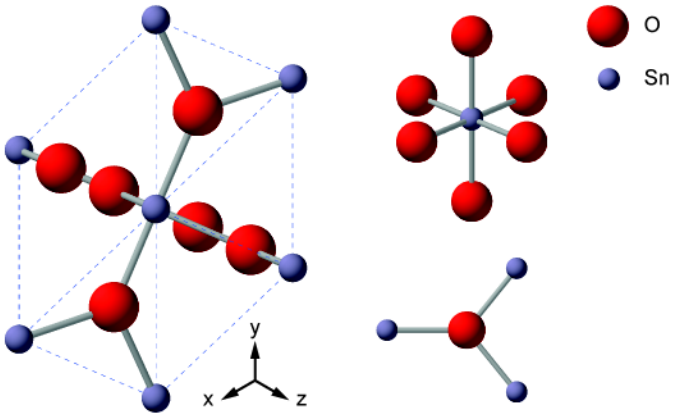


**Figure 4.3:** Unit cell for the $SnO_2$ structure (viewed down the 111 axis),[8] and the local coordination environment of Sn and O.

prior experimental measurements, often by diffraction) for the system being investigated. In this case, the NMR parameters can be predicted directly from the crystal structure, although as discussed in Chapter 3, optimising the geometry prior to the prediction of NMR parameters is recommended as this usually results in closer agreement to experiment. Additionally, through simple structural modifications, such as atom substitution, the crystal structure of one ordered solid can be used as the template for a whole series of related systems. For example, the tin dioxide ($SnO_2$) structure,[8] shown in Figure 4.3, could be used to generate an extended series of related input structures, simply by changing the two tin atoms in the unit cell to a different tetravalent species, giving structures with the same $AO_2$ formula, where A could represent any tetravalent cation. Modifying the unit cell (*i.e.*, the size and shape or its contents) of a structure known to possess long-range order is a way to represent similar systems that may themselves not yet have a known crystal structure, thus allowing the solid-state NMR parameters for these related systems to be predicted and ultimately allowing at least a qualitative comparison with experimental measurements. In addition, varying an existing ordered crystal structure by simple atom substitution can be a way of investigating trends between structural and/or chemical features and predicted NMR parameters, *i.e.*, substituting Sn in $SnO_2$ for a series of

**Table 4.1:** Calculated $^{17}O$ $\sigma_{iso}$, $C_Q$, unit cell volume and average A–O bond lengths for a series of $AO_2$ systems based on $SnO_2$.[8] Only the magnitude of the $^{17}O$ $C_Q$ is considered. All calculations were performed using CASTEP 8.0, the GGA PBE functional, an $E_{cut}$ of 60 Ry and a k-point spacing of 0.04 $2\pi$ $Å^{-1}$, with all structures geometry optimised prior to calculation of the solid-state NMR parameters.

| Structure | $^{17}O$ $\sigma_{iso}$ (ppm) | $^{17}O$ $C_Q$ / MHz | Unit cell volume / $Å^3$ | Average A–O bond length / Å |
|---|---|---|---|---|
| $SnO_2$ | 114.08 | 6.95 | 75.18 | 2.09 |
| $GeO_2$ | 48.71 | 8.37 | 58.53 | 1.92 |
| $PbO_2$ | –20.07 | 8.29 | 88.67 | 2.21 |
| $TiO_2$ | –398.33 | 1.49 | 63.80 | 1.98 |
| $ZrO_2$ | –191.58 | 0.73 | 78.18 | 2.12 |
| $HfO_2$ | –102.2 | 1.18 | 77.29 | 2.11 |

different cations can show how the predicted $^{17}O$ NMR parameters are affected by factors including cation size, cation electronegativity, unit cell volume, bond lengths, *etc.* Table 4.1 shows the calculated (using CASTEP 8.0) $^{17}O$ $\sigma_{iso}$, $C_Q$, unit cell volume and average A–O bond length values for a series of $AO_2$ systems based on the $SnO_2$ crystal structure, where A = Sn, Ge, Pb, Ti, Zr or Hf. From Table 4.1 it can be seen that the predicted $^{17}O$ $\sigma_{iso}$ values are more negative (less shielded) and $^{17}O$ $C_Q$ values much smaller in the three structures where A is a group 4 transition metal, compared to a group 14 main group element. Whether or not the starting crystal structure is modified, the typical procedure for calculating the corresponding solid-state NMR parameters for an ordered, periodic system is relatively facile, with Figure 4.4 showing a flowchart outlining the general steps involved. It is important to note that poor agreement between predicted and experimental NMR parameters could indicate that either, the model does not represent the structure adopted by the real system (*i.e.*, the real systems adopts a different polymorph), or, that the model does not account for the presence of some form of structural (static or dynamic) disorder.

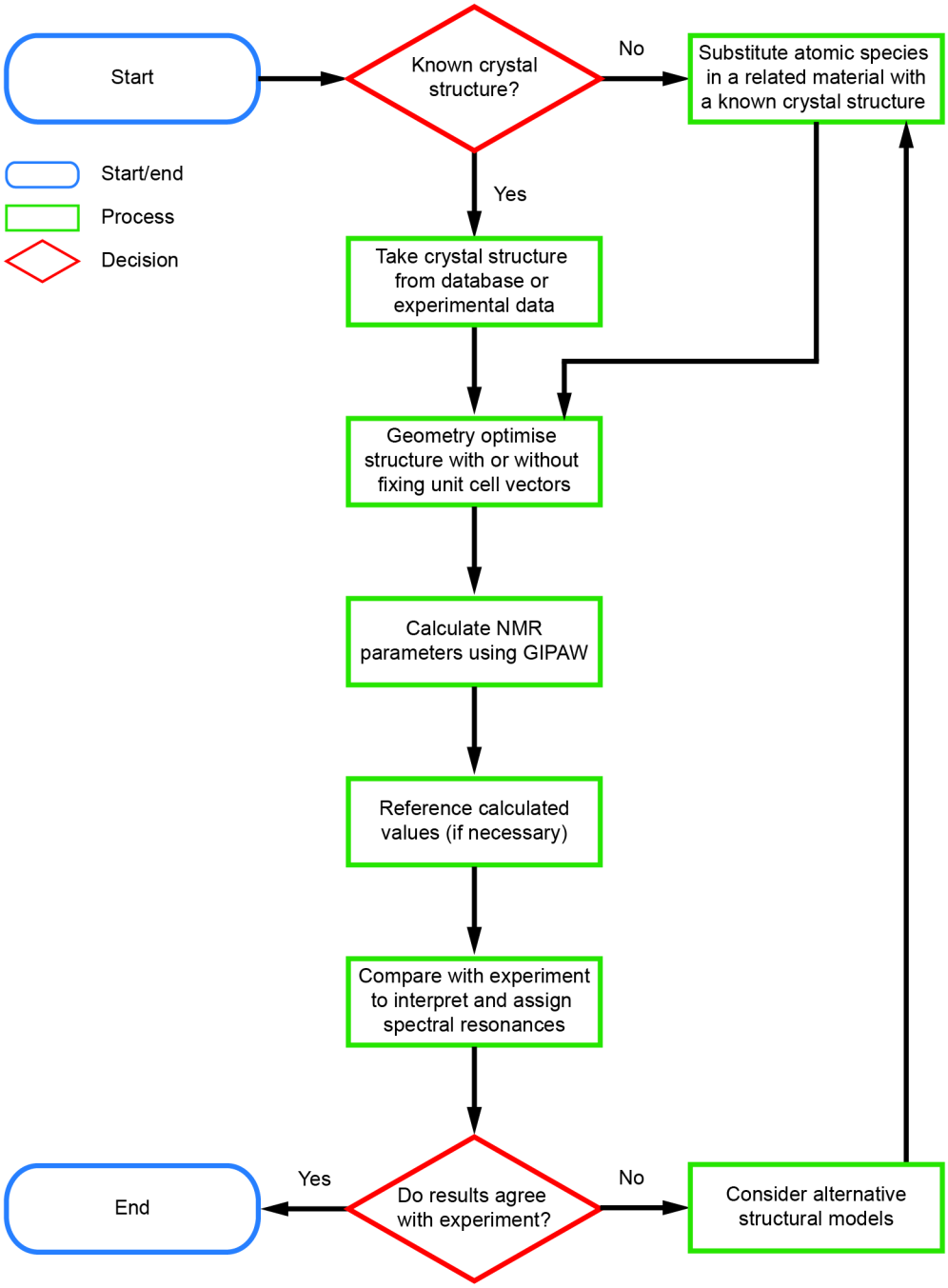


**Figure 4.4:** Flowchart outlining the general steps involved in calculating the solid-state NMR parameters for a system, where the crystal structure is known or suspected to be ordered.

## 4.3 Disordered materials

A breakdown in the long-range ordering of atoms in a solid caused by local structural changes often leads to the corresponding solid-state NMR spectra containing broad, overlapping lineshapes, indicative of the presence

of many chemical environments being present. The computational modelling of disordered materials is challenging as it often involves significant effort to create a series of structural models that together contain the set of local chemical environments that are present in the real material (although it may not be possible to distinguish each chemical environment individually, in the NMR spectrum). Additionally, the way in which structural models are produced or modified is heavily dependent on the type of disorder that a particular system exhibits. In this section, different methods for constructing sets of structural models, designed to represent the local chemical environments present in disorder materials are discussed, with the eventual goal being to use the solid-state NMR parameters predicted for these models to guide the interpretation and assignment of experimental NMR spectra. As discussed in Section 4.2, the importance of geometry optimisation (using DFT) prior to the prediction of solid-state NMR parameters cannot be overstressed, especially if the structure in question has been modified in some way.

One common approach for generating structural models for disordered materials is to modify the structure of a related, ordered material. By doing this, any changes in the value of predicted solid-state NMR parameters, arising from structural modifications can be investigated and compared to experimental NMR spectra, allowing a picture of the type(s) of disorder present to be formed. In order to visualise the various structural modifications that can be made (to attempt to represent the local chemical environments potentially present in a particular disordered material), the pyrochlore structure, shown in Figure 4.5, with general formula $A_2B_2O_7$, adopting the space group $Fd\overline{3}m$, will be used as a specific example.[9,10] The pyrochlore unit cell is based on a superstructure of fluorite ($AO_2$) with an ordered cation arrangement and the ordered removal of 1/8 of the oxygen atoms, and contains 16 A, 16 B and 56 O sites, respectively, with two crystallographic unique O sites, labelled here as $O_{8a}$ and $O_{48f}$, which have different local environment $O(A_4)$ and $O(A_2B_2)$, respectively.

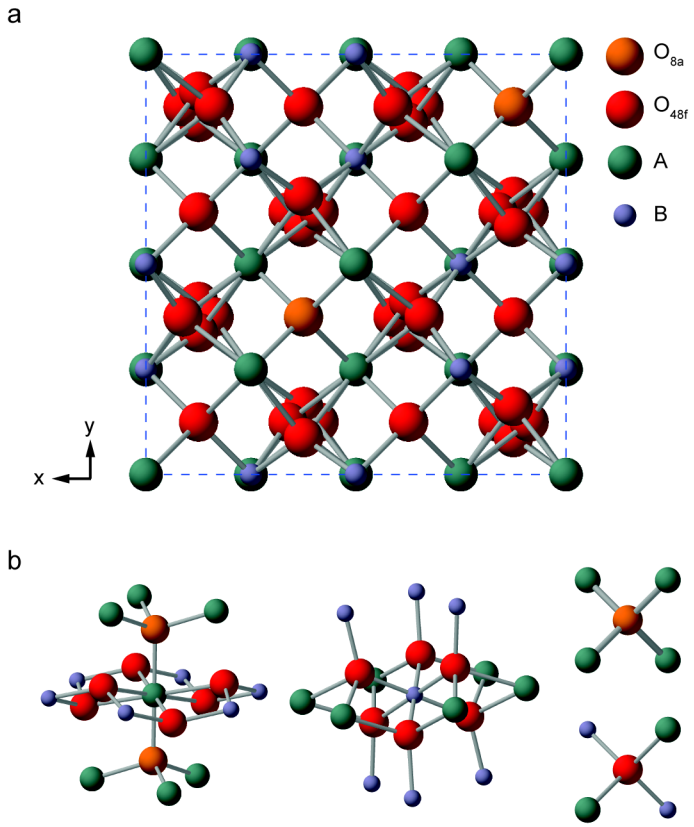


**Figure 4.5:** (a) Unit cell structure of a general ($A_2B_2O_7$) pyrochlore, (b) showing the local coordination of the A, B, $O_{8a}$ and $O_{48f}$ sites, based on the structural model for yttrium stannate ($Y_2Sn_2O_7$).[11]

### 4.3.1 Configurational and compositional disorder

Configurational disorder, *i.e.*, a variation in atomic arrangements, leading to a breakdown in long-range ordering, can lead to additional crystallographically distinct sites being created, which ultimately can cause NMR spectral lineshapes to become overlapped and more challenging to interpret. One reasonably simple way to investigate the effect configurational disorder in the pyrochlore structure has on the predicted solid-state NMR parameters could be to exchange the position of one A-, and one B-site cation, which in an unmodified structure are exclusively eight and six coordinate, respectively. This modification would lead to a structural model containing one six-coordinate A and one eight-coordinate B cation, respectively, with these modified local environments shown in Figure 4.6.

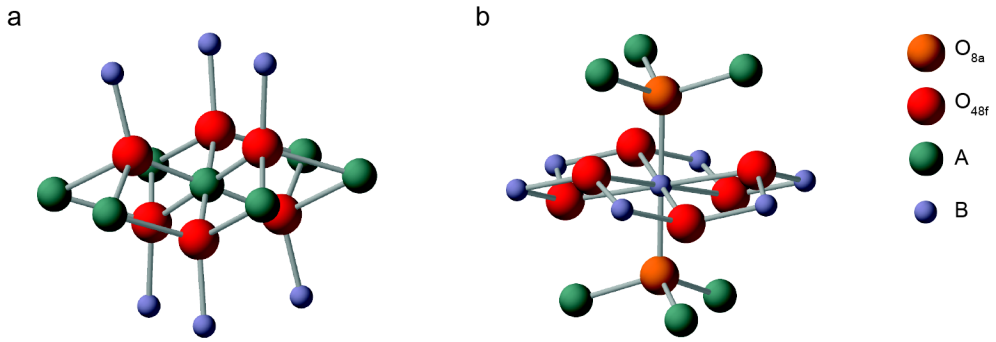


**Figure 4.6:** Schematic of the (a) six-coordinate A and (b) eight-coordinate B cation, resulting from the substation of an A cation onto a B site and the substitution of a cation onto an A site, respectively.

Investigating how this change in coordination environment affects predicted NMR parameters for the A and B species involved in the configurational exchange, and comparing with experimental spectra could indicate whether these types of local cation environments are present in the real material.

Structural models can also be constructed in a way that allows compositional disorder, and the effects this may have on local structure and solid-state NMR parameters, to be investigated. Compositional disorder, common in many minerals, as well as frameworks and ceramic materials arises when the species occupying a specific crystallographic site varies, even though the periodic ordering of the site positions is not lost, *i.e.*, the species changes but the position does not. By varying the arrangement of atoms on specified sites within a unit cell, a set of possible structural models can be produced, with the comparison between predicted and experimental NMR parameters allowing the effects of compositional disorder to be investigated. For a low level of substitution, a sensible structural model can be generated by substituting a single atom into the structure of a pure end member, with DFT calculations providing insight into the NMR parameters of the substituted atom itself and the changes in the NMR parameters of the surrounding atoms as a result of the species substitution. For instance, the effect that varying composition has on the predicted NMR parameters for an A-site species (*e.g.*, Y) in a pyrochlore structure could be probed by exchanging the original atom occupying a nearby B site, for a different but isovalent species,

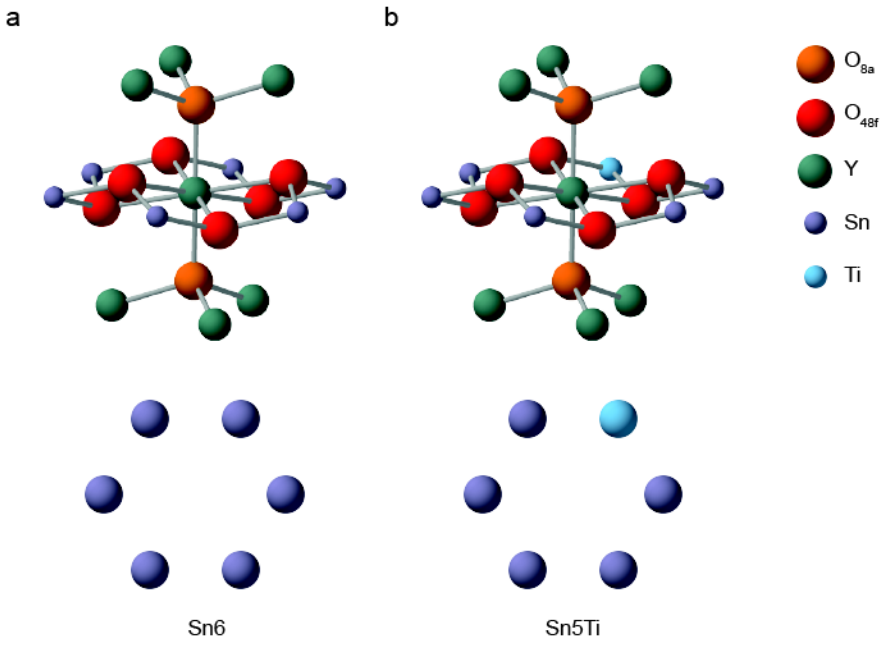


**Figure 4.7:** The local environment of Y when occupying the eight-coordinate A site in the pyrochlore structure, with (a) Sn6 and (b) Sn5Ti NNN environments. Two-dimensional representations of these environments where only the six NNN B sites surrounding the specified A site are also shown.

to give an eight-coordinate A site cation with an altered NNN environment. Figure 4.7a shows the local environment of an eight-coordinate pyrochlore A site with six Sn on the NNN B sites, giving a Y(Sn6) environment. The exchange of one Sn for one Ti leads to a Y(Sn5Ti) environment, as shown in Figure 4.7b. Figure 4.7 highlights how models representing different local structural environments can be created, with subsequent DFT calculations enabling the effect of compositional changes on the predicted solid-state NMR parameters of the nearby atoms to be evaluated. In the pyrochlore structure there is only one type of B site; however, in structures where there is more than one crystallographically unique site that a given species might occupy, more than one structural model will be required. This was illustrated by Fernandes *et al.*,[12] who used solid-state NMR spectroscopy and DFT calculations to investigate the phase composition and disorder in $La_2(Sn,Ti)_2O_7$ series. In this series, the $La_2Sn_2O_7$ end member adopts a pyrochlore phase with one distinct B site, whereas the $La_2Ti_2O_7$ end member adopts a monoclinic layered structure, with four separate

crystallographically distinct B sites, requiring the generation of four different structural models to investigate the substitution of one Ti for Sn on each of the four unique B sites.

When considering very low levels of substitution, or when dealing with small unit cells, to prevent substituted atoms being too close together it is sometimes necessary to construct a supercell, in which substituted atoms can then be sufficiently isolated. This is illustrated in Figure 4.8, where the result of substituting one atom, C, into a hypothetical AB system when a single unit cell and a 3 × 3 supercell are used, is shown in Figure 4.8a and Figure 4.8b, respectively. This shows that when the unit cell is used, substituting one existing B site cation for a different species results in the substitution of all the atoms on this crystallographic site (owing to the small unit cell size), changing the chemical formula to AC, meaning low levels of substitution cannot be studied. However, when a 3 × 3 supercell is used, a much lower

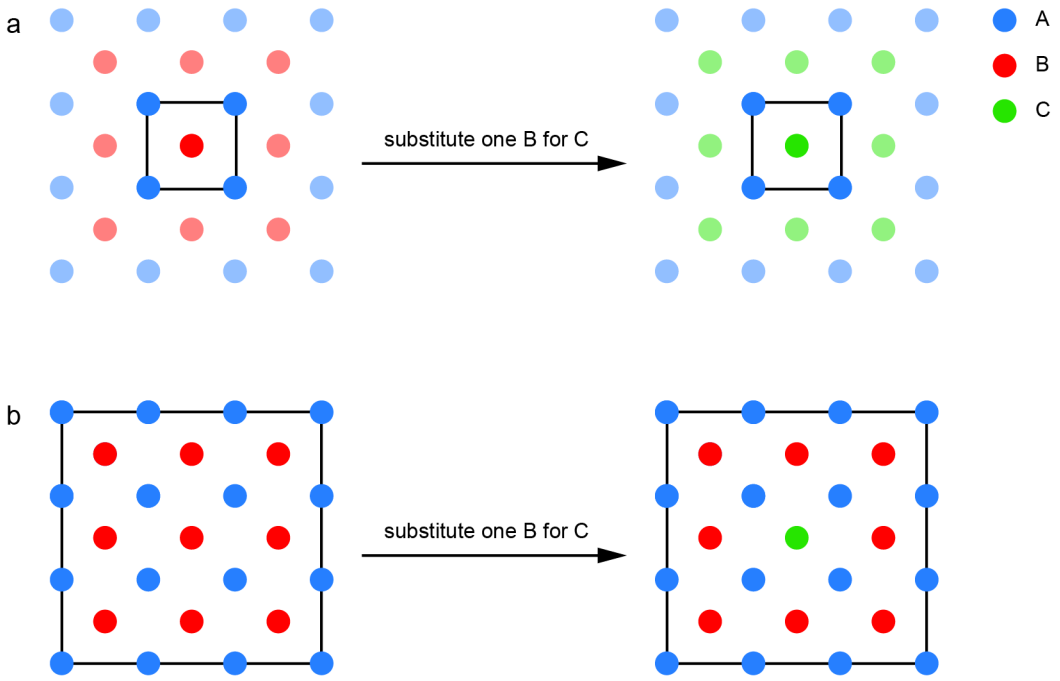


**Figure 4.8:** Schematic showing the result of substituting one C atom into a hypothetical AB system using (a) a single unit cell and (b) a 3 × 3 supercell. This figure illustrates that due to the periodicity of the solid, when a single unit cell is used all B atoms are substituted by C, whereas when a 3 × 3 supercell is used, the substituted atom is isolated, with C only occupying $1/9^{th}$ of the B sites.

level of substitution can be achieved, with substitution on only 1/9th of the B sites. Using this 3 × 3 supercell also ensures that the substituted species are well separated, allowing them to be considered as isolated defects in the material. Using a supercell to achieve these lower levels of substitution and to ensure the substituted atoms are isolated from each other is an approach that has previously been used successfully by Laurencin *et al*. to study doping of Mg into the calcium mineral, hydroxyapatite, where some of the most energetically favourable substituted models agreed well with $^{43}$Ca NMR spectra.[13] Similarly, Buannic *et al*. used solid-state NMR spectroscopy, combined with DFT calculations to investigate cation and vacancy ordering in Y-substituted $BaSnO_3$ perovskites, with structural models based on a 3 × 3 × 3 supercell of $BaSnO_3$ showing preferential substitution of Y onto the six-coordinate Sn site, rather than the twelve- coordinate Ba site.[14] In an attempt to understand $F^-/HO^-$ anion ordering in clinohumite, $4Mg_2SiO_4{\cdot}Mg(OH)_2$, Griffin *et al*.[15] constructed a series of structural models in which the anion composition and configuration were varied. GIPAW calculations revealed that the $^{19}$F chemical shift was sensitive to the nature of the species on the two closest anion sites, at distances of 2.7 and 3.2 Å, with the four possible ways of arranging these two anions (*i.e.*, two $F^-$, two $HO^-$ or the two different arrangements of one $F^-$ and one $HO^-$) on the two closest anion sites to fluorine giving four distinct $^{19}$F chemical shifts, in good agreement with the $^{19}$F MAS NMR spectrum, which contained four well-resolved resonances. The calculations allowed the resonances in the experimental NMR spectrum to be assigned, while the relative intensities of the four resonances provided information on the preferential ordering of anions in clinohumite.

The general procedure, where a finite number of structural models are manually constructed, with varying atomic arrangements has also been used to study metal carbides including $YB_2C$, with comparison to experimental $^{11}$B NMR spectra used to validate structural models with particular arrangements of B and C.[16] In a similar approach, Seymour *et al*. used the comparison between experimental and predicted $^{27}$Al and $^{31}$P solid-state NMR parameters to investigate the cation ordering in Mg-substituted STA-2, an aluminophosphate (AlPO) framework.[17] In this study, structural models

were constructed by substituting $Al^{3+}$ for $Mg^{2+}$ at various crystallographic sites in a reduced unit cell of STA-2, with cation substitutions encompassing several different internuclear distances. The GIPAW calculations for structural models confirmed the presence of preferential substitution of Mg onto the Al1 site, with the calculations also revealing that the $^{31}P$ chemical shift was dependent on the number of Mg species on the NNN sites, as well as on the specific site geometry in the STA-2 structure.

In some solids, the degree of structural disorder, or the size of the unit cell, may result in a large number of possible atomic arrangements, far more than can be reasonably considered. When this is the case, it is often necessary to identify a subset of structural models that can be studied computationally. This can be achieved by creating a series of structures where the local environment of a specific site is systematically varied, to consider the effect of compositional changes on neighbouring atoms, NNNs, or even more distant sites. Although using a subset of all the possible atomic arrangements, and restricting the structural variation to being centred around one particular species may result in structural models that do not show perfect agreement with experiment, the changes in predicted NMR parameters resulting from systematic structural modifications should at least show qualitative agreement with experimental and, therefore, aid the assignment of NMR spectra. Using this simplified approach, it is possible that the subset of structural models designed to represent a disordered solid may not include certain atomic arrangements that are present in the real material, seen experimentally, or may include structures that could be

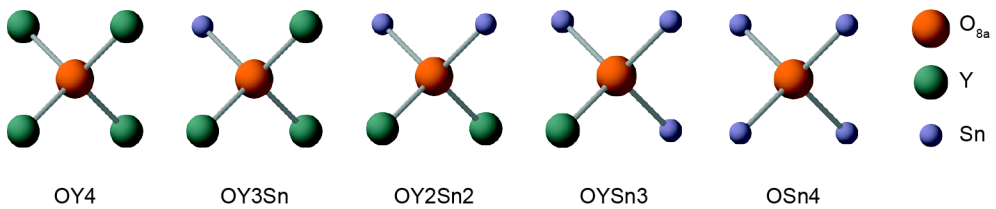


**Figure 4.9:** Schematic of the five $O_{8a}$ centred environments resulting from the systematic modification of the four atoms directly neighbouring oxygen on the $O_{8a}$ site in the pyrochlore structure, where the environment is systematically changed from OY4 to OSn4.

chemically unfeasible and thus not seen experimentally. Systematically altering the nature of the species directly neighbouring an $O_{8a}$ oxygen site in the pyrochlore structure is an example of a modification resulting in a subset of structural models that could be used to investigate how local structural changes affect predicted NMR parameters. The five unique local environments resulting from systematically substituting the four A species (*e.g.* Y) originally coordinated to the $O_{8a}$ oxygen, for four B species (*e.g.* Sn), are shown in Figure 4.9. In order to maintain charge neutrality in the unit cell, when constructing these models it is necessary to retain the A to B cation ratio (*i.e.*, A:B = 1:1), meaning the $A^{3+}$ cations originally occupying the four A sites around the selected $O_{8a}$ site must be relocated elsewhere else in the structure. This can be achieved by simply exchanging the A and B atoms involved in the substitution so the A species originally surrounding the selected $O_{8a}$ site will now be on six-coordinate B sites.

The approach of representing a disordered solid using a series of structural models that systematically alter the local environment around a selected species has been demonstrated by Ashbrook and co-workers in a series of studies focussing on the $Y_2(Sn,Ti)_2O_7$ pyrochlore solid solution.[18–20] In these studies, $^{89}Y$ and $^{119}Sn$ MAS NMR spectroscopy was used to investigate the effect of NNN cation substitution on the six B sites surrounding either Y or Sn, occupying the eight-coordinate A and six-coordinate B site, respectively. To aid the assignment of NMR spectra, a series of DFT calculations were performed where the atoms on the six B sites surrounding a single Y or Sn atom were varied, while the rest of the cell was unaltered. This results in a Sn rich series of structural models where an initial $Y_2Sn_2O_7$ structure was used to generate the subset of structures, in which a maximum of six Sn on the NNN sites around either a Y or a Sn atom were substituted for Ti (isovalent to Sn). Similarly, a Ti rich series of structures was created from an initial $Y_2Ti_2O_7$ structure, which contain a maximum of six or seven Sn atoms (six in the case where the species on the NNN sites around Y were varied and seven where the species on the NNN sites around Sn were varied, as an additional Ti was substituted in this series to act as the central Sn cation). Factoring in the different arrangements for certain B site cation compositions, this approach

results in 13 Y-centred Sn rich, 13 Y-centred Ti rich, 13 Sn-centred Sn rich and 13 Sn-centred Ti rich arrangements, giving a total of 52 structural models. Figure 4.10a shows the Y-centred $Y_2Sn_2O_7$ extreme of these structural models, where the six NNN B sites surrounding Y are all occupied by Sn, whereas Figure 4.10b shows the other extreme, where six Ti atoms surround Y. Figure 4.10c shows the 13 different ways in which Sn and Ti atoms can occupy the six NNN B sites surrounding a specified Y (or Sn) atom, giving environments ranging from Y(Sn6) to Y(Ti6). Using these structural models, it was observed that the substitution of Sn for Ti was accompanied by a systematic change in the calculated $^{89}Y$ $\delta_{iso}$, whereas the change in calculated $^{119}Sn$ $\delta_{iso}$ was much smaller, leading to similar predicted NMR parameters for Sn with different NNN environments, seen experimentally as the overlap of individual resonances in the spectrum. Even with the limited number of structural models, the information obtained from the DFT calculations was key to the assignment of the $^{89}Y$ MAS NMR spectra, with the comparisons between calculated and experimental NMR parameters suggesting the arrangement of B-site cations in this system are randomly distributed on the pyrochlore B site.[18–20] More recently, a similar study into phase distribution, phase composition and cation disorder in $Y_2(Sn,Zr)_2O_7$ ceramics relied on computational models in order to guide the assignment of $^{89}Y$ and $^{119}Sn$ MAS NMR spectra.[21]

When attempting to model some disordered systems, tens if not hundreds of structural models may be required to ensure all chemical environments are represented. At some point, the method by which structures are generated must be considered; after a certain point, manually modifying a starting structure to create a set of different local chemical environments will cease to be the most sensible or efficient way to produce potential structural models of a disordered system. For the pyrochlore example discussed above, modelling the disorder of the B site cations by varying just the six NNN B sites around a single A site cation resulted in the generation of thirteen unique structural models, between which every possible combination and arrangement of Sn and Ti on the six sites is considered. However, if all sixteen of the B sites in a pyrochlore unit cell were considered, both the

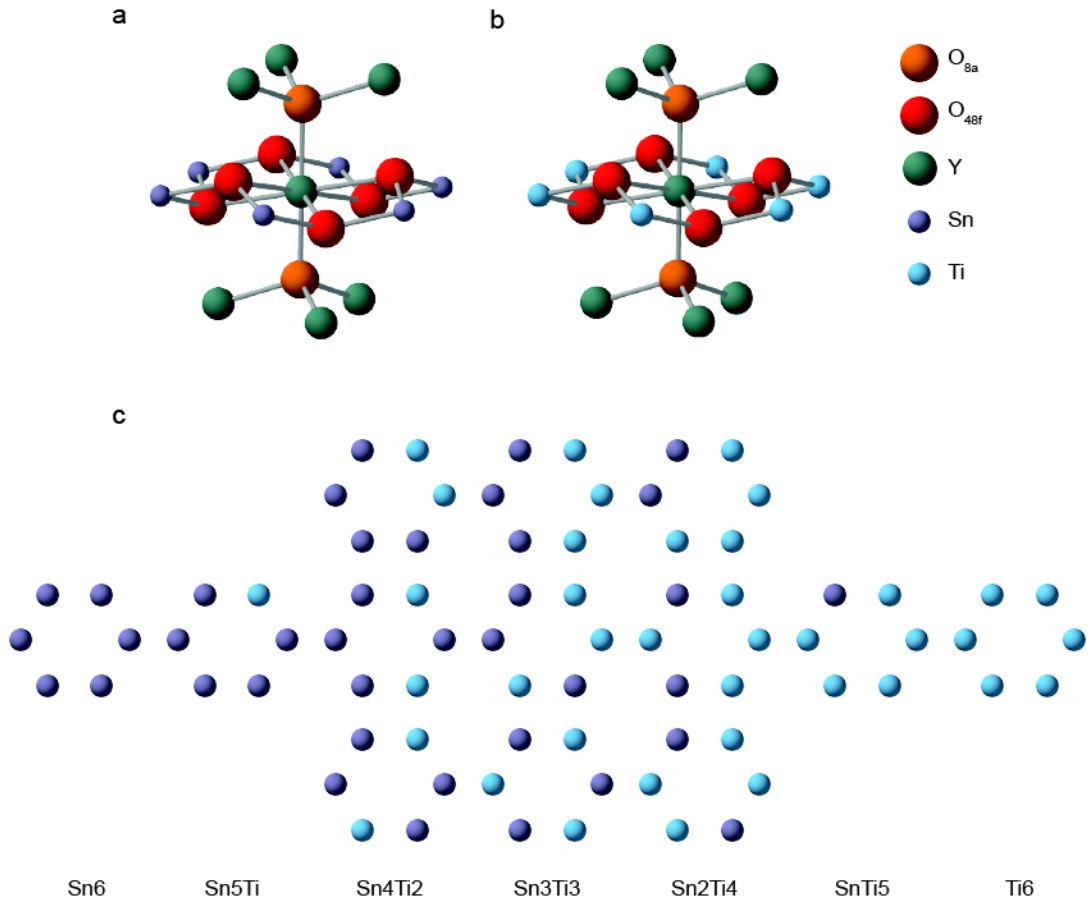


**Figure 4.10:** The thirteen possible arrangements of Sn and Ti on the six NNN B sites that surround the eight-coordinate pyrochlore A site.

compositional range, and the number of possible atom substitutions and, more importantly, their possible combinations, would increase significantly. In this case, generating a series of structural models by systematically modifying all B site cation within the pyrochlore unit cell would be a complex and extremely labour intensive task, particularly as the high-symmetry, cubic pyrochlore unit cell will result in many of the structural models created manually to be identical (*i.e.*, related by a symmetry operation), something that may not be initially obvious. The highly likely possibility of generating identical structural models through manual modification of an ordered pyrochlore structure indicates that attempting to investigate this form of configurational disorder, even for one composition, could be highly inefficient.

When considering systems that exhibit complex forms of structural disorder, more sophisticated approaches to generate structural models may need to be considered. One such approach, capable of efficiently generating a series of computational models that, when combined, represent all possible local chemical environments in a system that exhibits configurational disorder over known, well-defined crystallographic sites, is the site occupancy disorder (SOD) method.[22,23] The generation of structural models is achieved using a multiconfigurational supercell approach, in which an infinite site-disordered solid is modelled by a set of configurations with various site occupancies in a supercell designed to represent the disordered solid. Each site occupancy configuration corresponds to a specific atomic arrangement within the supercell, meaning an ensemble of configurations is used to represent the site-disordered system. By determining all possible atom configurations the SOD method aims to provide a complete description of the atom distribution and degree of site occupancy disorder in solid systems. For a fixed composition (or more strictly a fixed number of each type of atom), the total number of configurations that make up the supercell (the total number of site occupancy combinations possible for a given composition), W, is given by

$$W = \frac{N!}{(N-x)!\ x!}\ , \tag{4.1}$$

where N is the number of exchangeable sites in the system and x represents the number of atoms of one of the species that can occupy these sites. For the pyrochlore example discussed above a mixture of two species occupy the six-coordinate B site. For example, if the sixteen B sites are occupied by a total of four Sn and twelve Ti, the total number of atom configurations, *i.e.*, the total number of different ways the four Sn and twelve Ti can be arranged on the sixteen B sites, is equal to

$$W = \frac{16!}{4!\ 12!} = 1820\ . \tag{4.2}$$

It can be appreciated that this may be an unreasonably large number of structural models to consider for a single composition, especially if no significant HPC resources are available. However, the SOD approach is able to identify symmetry equivalent atomic arrangements, which significantly reduces the number of structural models that need to be considered for a given composition. This method for determining whether two or more atomic configurations are symmetry equivalent is based on the concept of isometric transformations,[24] which are geometric operations such as translations, rotations or reflections that do not affect the distances or angles between atoms during the transformation. Therefore, two configurations are considered symmetry equivalent if an isometric transformation can convert one configuration into the other. An illustration of isometric transformations causing two seemingly different configurations to be identified as identical is shown in Figure 4.11, where Figures 4.11a, b and c show a reflection, a 180° rotation and a reflection followed by a translation, respectively, cause two configurations to be identical. By considering isometric transformations, SOD is able to reduce the total number of configurations, W, for a given composition, to a subset of structures consisting of only the symmetry inequivalent configurations, M, where M << W. By identifying the number of equivalents that exist for each configuration, a corresponding configurational degeneracy, Ω, for each symmetry unique atomic arrangement can be determined. The magnitude of this configurational degeneracy will depend on the symmetry of the particular configuration, with higher symmetry arrangements resulting in a larger degeneracy. Accounting for the number of symmetry equivalent configurations, the 1820 ways of arranging the four Sn and twelve Ti atoms on the sixteen pyrochlore B sites discussed above reduces to only 22 symmetry inequivalent configurations.

The W and M values for a series of pyrochlore systems where the occupancy of the B site varies from purely Sn to purely Ti (*i.e.*, where the Sn/Ti composition systematically varies through the series) are shown in Table 4.2. This data shows how the number of structural models dramatically decreases when the symmetry equivalency of specific atomic arrangements are considered, particularly in systems where the Sn to Ti ratio is 1. The data

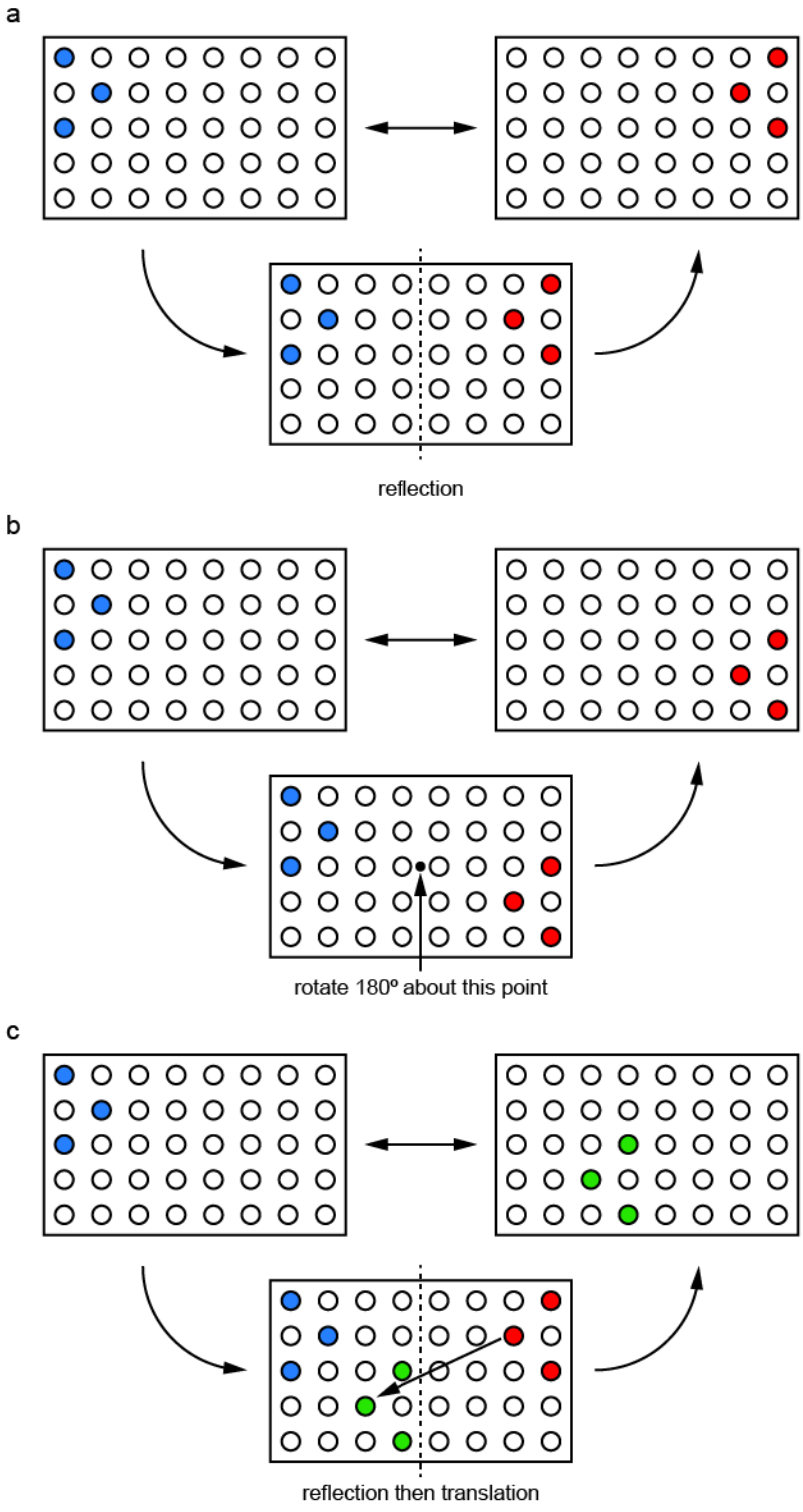


**Figure 4.11:** Illustration of atom configurations related by isometric transformations, in the form of (a) a reflection, (b) a 180° rotation and (c) a reflection and a translation, where the circles represent atoms.

**Table 4.2:** The total number of atom configurations (W) and the number of symmetry inequivalent configurations (M) for a series of $A_2B_2O_7$ pyrochlore systems, where the number of Sn/Ti ions occupying the sixteen B sites in the unit cell varies.

| B site composition | W | M |
|---|---|---|
| Sn16 | 1 | 1 |
| Sn15Ti | 16 | 1 |
| Sn14Ti2 | 120 | 3 |
| Sn13Ti3 | 560 | 8 |
| Sn12Ti4 | 1820 | 22 |
| Sn11Ti5 | 4368 | 35 |
| Sn10Ti6 | 8008 | 65 |
| Sn9Ti7 | 11440 | 82 |
| Sn8Ti8 | 12870 | 97 |
| Sn7Ti9 | 11440 | 82 |
| Sn6Ti10 | 8008 | 65 |
| Sn5Ti11 | 4368 | 35 |
| Sn4Ti12 | 1820 | 22 |
| Sn3Ti13 | 560 | 8 |
| Sn2Ti14 | 120 | 3 |
| SnTi15 | 16 | 1 |
| Ti16 | 1 | 1 |

in Table 4.2 also highlights how difficult it would be to manually generate a complete series of symmetry inequivalent structural models for a specific composition. The ability of SOD to identify every possible atomic configuration for a given composition, and then reduce this number to a subset of the symmetry inequivalent configurations, for which energies and other properties can be extracted using computation, makes it an extremely attractive option for investigating solid systems that exhibit site disorder. SOD has the potential to be even more useful as knowing the degeneracy associated with configuration in principle allows thermodynamic quantities to be obtained using Boltzmann's statistics, with the degeneracy of each unique configuration representing a proxy of the entropy. As a result, the SOD program has previously been used to investigate site disorder in a

range of minerals, including carbonates,[25–27] oxides,[28,29] and sulfides,[30–32] as well as zeolite and zeotype structures.[33,34]

### 4.3.2 Positional disorder

In some materials, positional (or topological) disorder, *i.e.*, uncertainty regarding the position of atoms or groups of atoms within the solid may be present. The level of positional disorder in a solid can vary significantly, from small localised structural variations, in the form of changes in bond distances and angles, leading to the position of surrounding atoms being altered, all the way to glasses, where there is a complex breakdown in any long-range ordering, whilst local structure may be retained. Even for ordered structures, such as AlPO frameworks, where diffraction techniques are able to determine the unit cell dimensions and specific atom connectivity, the precise position of the atoms are often not totally accurate. The GaPO-34A(mim) structure (discussed in Section 4.1), has previously been used to highlight the limitations of diffraction, with positional disorder leading to some Ga and O sites exhibiting fractional occupancy. As NMR spectroscopy is extremely sensitive to changes in local structure, caution must be taken when using structural models based on diffraction measurements, even when the structure appears ordered, as very small variations in local geometry can lead to poor correlation between predicted and experimental NMR measurements. Therefore, even if the number of resonances in an NMR spectrum match the number of crystallographic sites in a framework, it is not always possible to attribute individual spectral resonances to specific crystallographic sites.

The general task of assigning spectral resonances to specific crystallographic sites was approached in most early work using empirical relationships between geometrical and NMR parameters. For example, correlations between $^{31}$P $\delta_{iso}$ and average P–O–Al bond angle ($\theta_{POAl}$),[35] in AlPOs were used to assist the assignment of $^{31}$P spectra of many phosphate materials.[36–40] This approach was investigated further by Dawson and Ashbrook.[41] By using a

model cluster of an AlPO framework centred on P, with H atoms terminating the $AlO_4$ tetrahedra, the authors constructed a series of structural models where $\theta_{POAl}$ and the average P–O bond length ($r_{PO}$) were systematically varied, determining that the (calculated) $^{31}P$ $\delta_{iso}$ was dependent on both geometrical parameters. More recently, Dawson and co-workers used a similar cluster-based approach to investigate the relationship between structure and $^{29}Si$ $\delta_{iso}$ in silica zeolites, concluding that this parameter is dependent on the average Si–O bond length, the average Si–O–Si angle and the standard deviation of both parameters,[42] determining how simple empirical relationships can be used to help assign NMR spectra for some systems. This study shows that, despite its simplicity, this modelling approach can provide good agreement between calculated and experimental $^{29}Si$ NMR parameters. Similar studies of correlations between NMR parameters and changes in local geometry have been shown in the literature for a range of materials.[43–47]

For most materials that exhibit positional disorder, many aspects of the translational symmetry are retained, but the position of some atoms or molecules, such as $H^+$, $F^-$, or $H_2O$ may vary and thus cannot be well defined in an average structural picture. Indeed, as a result, diffraction techniques can struggle to accurately determine all atomic positions in the solid. This means that instead of being able to accurately determine the position of every atom within a system, diffraction can often only narrow down the location of an atom to a set of possible sites, each with some stated fractional occupancy. An example of this is shown schematically in Figure 4.12, where the B site in a $A_4B_3$ system has a fractional occupancy of 0.75, meaning that only six of the eight B sites in a unit cell are occupied. Figure 4.12a shows the average typical structural picture obtained from most diffraction-based approaches, where all eight B sites have a fractional occupancy of 0.75, indicating that the exact position of the six B species is unknown. Figure 4.12b shows a 2 × 2 supercell (with a different arrangement of occupied B sites in each of the four unit cells), giving the same overall B site occupancy as in Figure 4.12a, but with the fractional occupancy of the B site explicitly

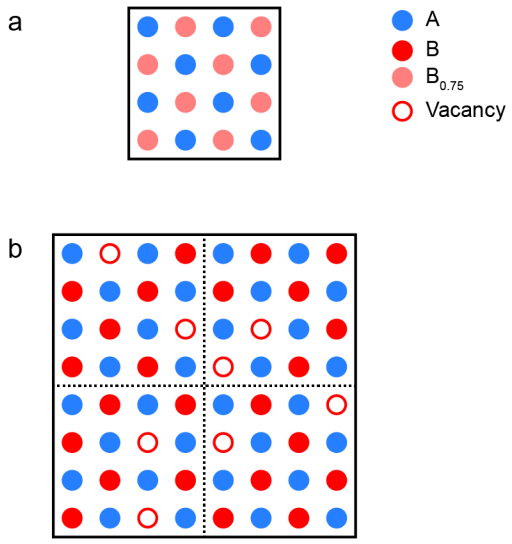


**Figure 4.12:** Schematic showing a hypothetical $A_4B_3$ system where positional disorder is represented in the form of (a) all 8 B sites having a fractional occupancy of 0.75, *i.e.*, the average diffraction picture, and (b) a 2 × 2 supercell where only 24 of the 32 B sites are occupied.

defined as 1 or 0 (*i.e.*, fully occupied or vacant). This indicates that while the average occupancy is well defined by diffraction, information on the preferred local environments, or relative arrangements of atoms is lost.

As is the case for solids that exhibit compositional or configurational disorder, it is often possible to construct a series of model structures for DFT calculations (including prediction of NMR parameters) by varying the positions of specific atoms or molecules, resulting in a set of models, each with a different distribution of atoms. For example, it was discussed in Section 4.1 that the GaPO-34A(mim) framework possesses significant structural disorder, including three specific SDA orientations.[1] In order to investigate this, a set of three structural models could be created, where a different orientation of 1-methylimidizole, the SDA, is imposed in each model. As the diffraction analysis was unable to distinguish between the carbon and nitrogen atoms in the SDA (although as one nitrogen is directly bonded to a methyl group, this atom can be identified unambiguously), for each of the three orientations, there will also be two possible positions for the second N atom in the SDA. Therefore, six separate structural models are

required when attempting to account for the different orientations of the SDA in GaPO-34A(mim). As it was assumed that all SDAs within the unit cell have the same orientation, additional structural models would need to be constructed if a unit cell containing a combination of SDA orientations needed to be considered. Comparing experimental NMR spectra with NMR parameters from GIPAW calculations for the six models could provide insight into the orientation of the SDA in this framework, with poor agreement to experiment for any models suggesting they do not represent the real structure of the material. However, poor agreement between predicted and experimental NMR parameters would also be obtained if the SDA was dynamic, *i.e.*, its position varied with time, with no one structural model then a good representation of the real material.

In many materials, there are only a few, well-defined sites that have fractional occupancies, meaning often the structure, and thus the NMR spectrum can be approximated by a small number of structural models. This approach has been used to study positional disorder in both the AlPO-STA-2 framework[48] and the perovskite-based $Ba_2In_2O_4(OH)_2$ structure,[49] where in both cases, the number of possible atom positions (well-defined crystallographic sites identified as having fractional occupancy) is small, meaning the possible atom/vacancy arrangements could be investigated with a finite number of models on a reasonable timescale.

When dealing with molecular systems, variations in the packing or layering of individual molecules can cause a breakdown in long-range periodically, often leading to NMR spectra that are challenging to assign, meaning DFT calculations are frequently used to interpret NMR spectra and provide structural insight. As an example, when investigating the transformation of 10-hydroxy-10,9-boroxophenanthrene to its anhydride form, the use of computational models, in which the orientation of the B–O–B bridges were varied, allowed Carnevale *et al.*,[50] to elucidate the reaction pathway and assign the complex $^{13}C$ solid-state NMR spectra. Similarly, Cadars *et al*. relied on DFT calculations, and the generation of a series of structural models to understand the structure of a layered silicate material of composition

$[Si_5O_{11}H][C_9N_2H_{15}]\cdot 1.9(H_2O)$, that exhibited stacking disorder.[51] In this investigation, solid-state NMR spectroscopy was able to provide information on the number of crystallographic Si sites, their multiplicities and an insight into the Si–O–Si connectivity, whereas XRD identified several possible space groups for the layered structure. However, full structure solution was not possible due to disorder in the sheet assembly. Using the $C_{2/c}$ space group, which was the only option that satisfied the long- and short-range structural information provided by XRD and NMR spectroscopy, respectively, resulted in three very similar framework structure solutions. Using these frameworks, a series of structural models, in which different positions and orientations of the SDA between the silicate layers were considered using DFT calculations, with comparisons to experimental NMR and XRD data enabling the structure determination of this layered silicate framework. DFT calculations have also been used to assist the structure determination for $CaSi_{1/3}B_{2/3}O_{8/3}$, a crystalline calcium borosilicate material that exhibits positional disorder.[52] The average diffraction-based description of the structure suggests fractional occupancy of a bridging O site, in addition to chains of $SiO_4$ tetrahedral and $BO_3$ trigonal units, with the Si and B species occupying the same crystallographic site, with occupancies of 1/3 and 2/3, respectively. DFT calculations were used to explore the possible distributions of Si and B within the chains, producing a series of structural models with different Si/B atomic arrangements and thus, polyhedral connectivity. Comparison with $^{11}$B MAS NMR spectra suggested that the $CaSi_{1/3}B_{2/3}O_{8/3}$ structure is made up of $BO_3$–$SiO_4$–$BO_3$ units, with no B–O–B linkages.

For some disordered materials, X-ray diffraction-based techniques may struggle to identify the position of some atoms or molecules if two or more species have similar atomic masses, *e.g.*, C and N, isoelectronic species such as $F^-$ and $HO^-$, or light atoms (such as H) in dense structures. When this is the case, simple structural models can be constructed by manually placing atoms at chemically sensible positions, or at positions deemed likely by prior NMR measurements, which can give information relating to the number, nature and position (local geometry) of the surrounding atoms, in addition to interatomic distances, *via* the through-space and through-bond coupling

interactions. Using $^{1}H$, $^{2}H$, $^{17}O$ and $^{29}Si$ NMR measurements, and information from previous experimental and theoretical studies,[53–56] in their study of the hydration of wadsleyite (β-$Mg_2SiO_4$), Griffin *et al*. followed this procedure and placed H atoms in chemically-sensible locations, giving a series of candidate structures for the hydrous mineral.[57] Through the comparison of predicted and experimental NMR parameters, likely protonation positions were identified (and others deemed less likely to be occupied by H) in hydrous wadsleyite. In similar work, Grüninger *et al*. used this approach to manually place H atoms on a series of positions adjacent to O atoms (leading to the formation of hydroxyl ions) in a 2 × 1 × 1 ringwoodite (γ-$Mg_2SiO_4$) supercell, to create a series of candidate hydrous ringwoodite structures. Subsequent DFT calculations then provided insight into favourable protonation sites and importantly, assisted the assignment of $^{1}H$ one- and two-dimensional MAS NMR spectra.[58] Naturally, manual positioning of atoms or molecules within a structure restricts the number of models considered to a predetermined subset (chosen using chemical intuition or insight from NMR measurements). However, this selection could also introduce unwanted bias into the type(s) of positions chosen, meaning less likely, yet potentially important, atom positions could be completely overlooked.

Using computational approaches to automate the generation of structural models is becoming more popular, as large sets of structures can be produced easily and efficiently. These methods can potentially remove some, if not all of the bias that can result when the position of atoms are chosen manually. The use of crystal structure prediction (CSP) methods has become more widespread in recent years. Substantial effort has been expended into developing computational methods that can efficiently predict the structure of organic molecules, with several blind tests conducted.[59–61] These tests assess the ability of different CSP methodologies to accurately predict the structure of a set of small organic molecules. One CSP method that has recently generated interest, and which is of particular importance to the work presented in this thesis, is *ab initio* random structure searching, or

AIRSS,[62,63] developed by Pickard and Needs in 2006. Unlike many other structure prediction methods,[61] AIRSS is designed to be unbiased, generating (in the simplest case) candidate structures using randomised unit cell vectors with atoms also placed randomly. DFT is subsequently used to optimise the geometry of the AIRSS-generated structures. A schematic of the general AIRSS method is shown in Figure 4.13, with the potential energy surface (PES) of a system explored by the unbiased construction of candidate structures using DFT to find energy minima. The minimisation of the stresses and forces acting on the atoms is achieved by using DFT rather than forcefields, a decision that increases computational cost. However, in comparison to most forcefields, DFT is able to cope better with structures that are far from an energy minimum (further from equilibrium), helping AIRSS to study systems subjected to extreme conditions, *i.e.*, high temperatures or pressures, and to find potentially metastable but plausible structures.[63] Given these advantages, AIRSS has been used to study the phase stability of a number of systems subjected to extreme pressures (ranging from GPa to TPa), including silane,[62] hydrogen,[64–67] nitrogen,[68] water,[69] ammonia and its hydrated forms,[70–72] tellurium dioxide,[73] lithium,[74] iron,[75] aluminium,[76] hydrogen sulfide[77] and calcium carbonate,[78] with further examples found in the literature. Using DFT to geometry optimise models

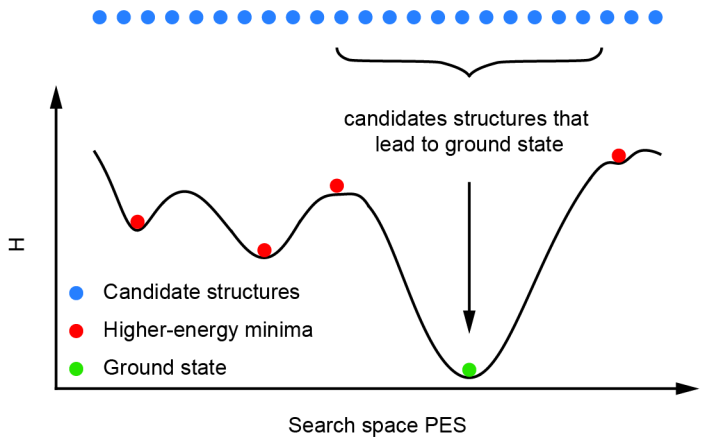


**Figure 4.13:** Schematic showing the AIRSS method, where candidate structures are generated without bias to explore the PES of search space, with DFT geometry optimisation used to find energy minima.

also results in a more accurate description of the PES, which would be less smooth if forcefields were used to locate energy minima.[79,80] As the AIRSS method is designed to be random in its structure searching approach, generating structures by randomly positioning atoms into a box that has dimensions that have also been randomly determined, the ability for AIRSS to successfully navigate search space in an efficient manor, is surprising and perhaps somewhat counter intuitive. AIRSS overcomes any structure searching inefficiencies associated with generating structures randomly (an approach that in theory could increase significantly the potentialsearch space), by capitalising on the nature of the PES. It has been shown that basins (wells in the PES) with low energy minima tend to have larger hyper-volumes in the "structure space" than the higher energy minima.[63,81,82] This phenomenon causes the probability of finding low energy minima, during a random structure search, is generally higher than the probability of locating higher energy structures.

AIRSS was designed to be a straightforward, simple to use and, crucially, an unbiased structure searching method, meaning candidate structures can even be generated for systems that have little to no experimental data available to assist the structure search. This means even from just a chemical formula, a series of potential structures can be generated using AIRSS. Although AIRSS does not necessarily require any information other than a chemical formula, pertinent information, such as experimental measurements or observations, can be included to bias the investigation and reduce the search space if desired. AIRSS has built-in functionality, in the form of parameterisable constraints, some of which are described in Table 4.3, that allow the search process to be modified in a way that ensures the generated structures satisfy certain criteria, For example, searches can be parameterised so that only candidate structures that agree with experimental data, such as having a particular space group, number of symmetry operations, unit cell volume or interatomic distances (all of which can be specified), are considered, with any structures that fail to meet these predetermined requirements discarded. This ability to bias structure

**Table 4.3:** Some of the built-in AIRSS commands that allow bias to be introduced to the structure searching process, with these commands applied prior to geometry optimisation.

| Command | Description |
|---|---|
| NFORM | Number of formula units to be placed in a unit cell, where one formula unit is defined in the `position` block of the `.cell` file |
| SUPERCELL | Size of the supercell being generated, defined by the number of unit cells it contains (one number), the number of unit cell lattice vectors in each direction (3 numbers) or the full matrix (9 numbers) |
| SLAB | Prevents repeat units being made in the *z*-direction, giving two- rather than three-dimensional structures |
| SYMMOPS | Specify the number of symmetry operations the generated structure must possess |
| POSAMP | Maximum position amplitude (in Å) to move atoms, each in a different, random direction |
| MINAMP | Minimum position amplitude (in Å) to move atoms, each in a different, random direction |
| ZAMP | Minimum position amplitude (in Å) to move atoms, each in a different, random direction along the *z*-axis |
| ANGAMP | Rotate a subset of atoms in the cell by a specified angle (in degrees) |
| MINSEP | Minimum separation (in Å) between all or a subset of atoms, which can be used to define specific distances between different species |
| FIX | Fixes unit cell size and shape |
| NUM | Number of atoms, molecules or fragments placed randomly in a unit cell |

searching lies at the heart of the AIRSS philosophy, which is to input all known structural information and then allow AIRSS to randomise the remaining aspects of the system.

In theory, the AIRSS approach could be used to generate millions of candidate structures for a particular system, which would be an extremely computationally expensive undertaking. This means that it is important to determine at what point a PES has been satisfactorily searched, *i.e.*, how many candidates must be generated before the ground state and other potentially relevant, metastable structures have been found. Typically,

structure searching continues until multiple candidate structures with the same energy have been found, which leads to the appearance of distinct plateaus in the energy profile for the AIRSS-generated structures. Figure 4.14a shows the energy profile for a typical AIRSS study, with the candidate structures ranked according to their relative enthalpy. It can be seen that when only 50 or 100 structures are generated, no plateaus are present at low energy, whereas when 250 structures are generated, such plateaus are clearly present. When a total of 500 structures are generated, represented by the blue points in Figure 4.14b, several plateaus are clearly defined, especially at low energy, with approximately twenty structures comprising the lowest energy plateau. The number of structures in the lowest plateau is a strong indication that for an AIRSS run consisting 500 structures, the ground state has been located. The energy profile plots for the AIRSS runs containing 250 and 500 structures, in Figure 4.14a and 4.14b, respectively, look very similar,

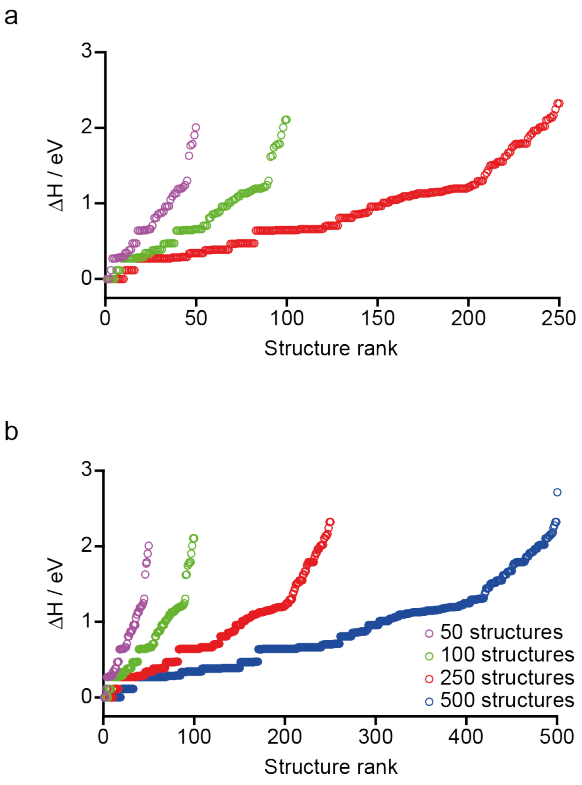


**Figure 4.14:** Energy ranking for a typical AIRSS run consisting of (a) 50, 100 and 250 candidate structures, with (b) also including the full AIRSS run of 500 candidate structures. From the full AIRSS run the presence of multiple plateaus, corresponding to the generation of numerous structurally similar low energy candidate structures is clearly shown.

suggesting that generating the additional 250 structures results in few new low energy structures being found. With this in mind, for the AIRSS run shown in Figure 4.14(b), it seems unnecessary to generate additional structures as finding a lower energy structure (lower than all 500 structures previously generated) is unlikely, although, it is possible that additional, higher energy candidates not represented by the 500 shown in Figure 4.14(b) could be found.

In some cases, the complexity of a system, or the size of search space that must be investigated by AIRSS may limit the appearance of energy plateaus unless extremely large numbers of candidate structures are generated. Figure 4.15 shows the energy profile for a set of 1754 AIRSS-generated structures, where there is a clear lack of well-defined plateaus at lower energy, with the plot instead showing a steady increase in energy with structure rank. The appearance of this energy profile suggests that there is still significant structural variation in the candidate structures, with few candidates being structurally very similar, in contrast to the AIRSS-generated series shown in Figure 4.14b. This indicates that for some systems, the point at which it could be considered reasonable to stop an AIRSS run is not always clear. In these cases the decision becomes more about the computational cost associated with continuing an AIRSS run that may or may not yield any structures that are noticeably different to those that have already been generated.

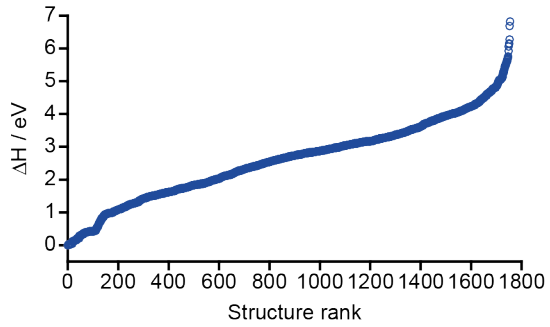


**Figure 4.15:** Energy ranking of the 1754 AIRSS-generated structures for a system that has more structural variables, leading to a more complex PES. From the gradual increase in energy, rather than the presence a set of well-defined plateaus, the plot suggests that few of the AIRSS-generated candidates are structurally very similar.

As AIRSS is compatible with DFT codes such as CASTEP,[83] NMR parameters for the generated candidates can be easily predicted using the GIPAW approach,[3] allowing a direct connection between AIRSS-generated structures and experimental NMR spectra. So far, this combinatorial approach, consisting of AIRSS and GIPAW calculations has been used to study the structure of molecular solids,[84] as well as to extensively investigate the structure, chemical stability and conductivity of battery materials.[85–90] The success of these studies indicates that forming a bridge between structure prediction and experimental data by combining AIRSS with GIPAW calculations could represent a new approach for studying disordered materials.

### 4.3.3 Dynamic disorder

In contrast to configurational, compositional or positional disorder, dynamic (or temporal) disorder is a variant resulting from the position of atoms or molecules within a material fluctuating over time. As a result, for techniques that produce an average structural picture, *i.e.*, diffraction, it can often be difficult to distinguish between dynamic disorder, where motion leads to atomic positions changing over time, and static positional disorder, where atoms are stationary but their positions can vary throughout a structure. As many Bragg-diffraction techniques provide information on a structure that has been averaged over both a time and lengthscale, attempting to distinguish between dynamic and static positional disorder using these methods can be extremely challenging, as both types of disorder scenarios can lead to fractional occupancies being assigned to crystallographic sites. As an example, Figure 4.16 shows a 1 × 2 supercell of a hypothetical $A_4B_2C$ system, where half the C sites are vacant. Bragg diffraction approaches would give the average structural picture, where all eight C site have a fractional occupancy of 0.5, as shown in Figure 4.16a. However, this could arise due to either dynamic or static positional disorder. Figure 4.16b shows the effect dynamic disorder could have on the structure, where the occupancy of the C sites changes over time, whereas Figure 4.16c shows the result of static positional disorder, where the occupancies of the C

sites do not change with time, In this case, both dynamic and static positional disorder will yield the same result, a structure with four C site vacancies, with diffraction often unable to identify the nature of the disorder. In contrast, NMR spectroscopy can distinguish between dynamic and static positional disorder, as different experimental techniques can be exploited to detect motion on timescales spanning fifteen orders of magnitude,[91] with materials that exhibit dynamic disorder tending to have solid-state NMR spectra that show a significant variation (*e.g.*, in line position, lineshape or relaxation time) with temperature.[7,92–94]

As the NMR spectra of materials that exhibit atomic or molecular motion, *i.e.*, dynamic disorder, can be difficult to interpret (particularly as small temperature changes can significantly alter their appearance), computation is often used to assist spectral assignment, with molecular dynamics (MD) approaches frequently used. In classical MD, Newton's equations of motion are used to propagate the system, using forcefields to represent the forces, which often require careful parameterisation. In contrast, *ab initio* MD relies on DFT to propagate the forces acting upon atoms. Both approaches generate an ensemble of atomic arrangements, each of which represents a snapshot of the dynamic system. The use of forcefields in classical MD provides an inexpensive way to investigate potential dynamics on a short timescale (*i.e.*, very fast motion), whereas *ab initio* MD is usually more accurate but considerably more expensive, meaning fewer structural snapshots can be obtained. By combining MD with GIPAW calculations, the time-averaged NMR parameters for a dynamically disordered material can be predicted, allowing for comparison with experimental NMR spectra to be made. The use of MD in combination with GIPAW calculations, has proven particularly important in the structural elucidation of glasses, as the experimental spectra for these highly-disordered materials are often too challenging to fully assign without the generation of potential structural models or predicted NMR parameters for these.[95–101] As the materials central to this thesis (see Chapter 5 and Chapter 6) are not believed to exhibit significant dynamics on timescales relevant to the NMR experiments, this form of structural disorder is not discussed further.

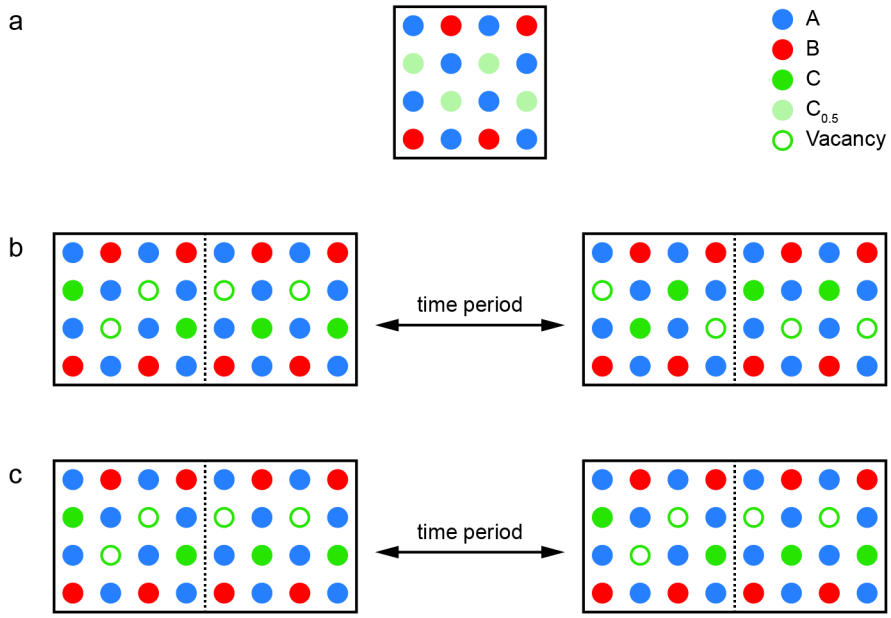


**Figure 4.16:** Schematic of a 1 × 2 supercell of a hypothetical $A_4B_2C$ system where (a) all eight of the C sites have a fractional occupancy of 0.5, *i.e.*, the average picture (as obtained from many diffraction experiments), (b) four of the C sites are vacant at any one time but the location of the occupied C sites changes over time, *i.e.*, dynamic disorder, and (c) the same four C sites are vacant at all times, *i.e.*, static positional disorder. In (a to c) the dotted line represents the divide between the two unit cells making up the formal 1 × 2 supercell of the average structure.

## 4.4 Summary

Generating structural models capable of accurately representing the local structure of disordered inorganic materials is a complicated process. However, being able to construct realistic structural models is vital if accurate NMR parameters (that can assist the understanding and aid assignment of experimental NMR spectra) are to be predicted. The work in Chapter 5 and 6 will use many of the approaches outlined here to investigate compositional and configurational disorder in ceramics, as well as positional disorder in hydrous minerals.

## 4.5 References


1. L. K. Broom, G. J. Clarkson, N. Guillou, J. E. Hooper, D. M. Dawson, C. C. Tang, S. E. Ashbrook, and R. I. Walton, *Dalt. Trans.*, 2017, **46**, 16895–16904.
2. R. E. Morris, S. J. Weigel, N. J. Henson, L. M. Bull, A. K. Cheetham, M. T. Janicke, and B. F. Chmelka, *J. Am. Chem. Soc.*, 1994, **116**, 11849–11855.
3. C. J. Pickard and F. Mauri, *Phys. Rev. B*, 2001, **63**, 245101.
4. C. Bonhomme, C. Gervais, F. Babonneau, C. Coelho, F. Pourpoint, T. Azaïs, S. E. Ashbrook, J. M. Griffin, J. R. Yates, F. Mauri, and C. J. Pickard, *Chem. Rev.*, 2012, **112**, 5733–5779.
5. T. Charpentier, *Solid State Nucl. Magn. Reson.*, 2011, **40**, 1–20.
6. S. E. Ashbrook and D. McKay, *Chem. Commun.*, 2016, **52**, 7186–7204.
7. R. F. Moran, D. M. Dawson, and S. E. Ashbrook, *Int. Rev. Phys. Chem.*, 2017, **36**, 39–115.
8. W. H. Baur and A. A. Khan, *Acta Crystallogr. Sect. B*, 1971, **27**, 2133–2139.
9. M. A. Subramanian, G. Aravamudan, and G. V. Subba Rao, *Prog. Solid State Chem.*, 1983, **15**, 55–143.
10. B. C. Chakoumakos, *J. Solid State Chem.*, 1984, **53**, 120–129.
11. F. Brisse and O. Knop, *Can. J. Chem.*, 1968, **46**, 859–873.
12. A. Fernandes, D. McKay, S. Sneddon, D. M. Dawson, S. Lawson, R. Veazey, K. R. Whittle, and S. E. Ashbrook, *J. Phys. Chem. C*, 2016, **120**, 20288–20296.
13. D. Laurencin, N. Almora-Barrios, N. H. de Leeuw, C. Gervais, C. Bonhomme, F. Mauri, W. Chrzanowski, J. C. Knowles, R. J. Newport, A. Wong, Z. Gan, and M. E. Smith, *Biomaterials*, 2011, **32**, 1826–1837.
14. L. Buannic, F. Blanc, D. S. Middlemiss, and C. P. Grey, *J. Am. Chem. Soc.*, 2012, **134**, 14483–14498.
15. J. M. Griffin, J. R. Yates, A. J. Berry, S. Wimperis, and S. E. Ashbrook, *J. Am. Chem. Soc.*, 2010, **132**, 15651–15660.
16. J. Cuny, S. Messaoudi, V. Alonzo, E. Furet, J. F. Halet, E. Le Fur, S. E. Ashbrook, C. J. Pickard, R. Gautier, and L. Le Polles, *J. Comput. Chem.*, 2008, **29**, 2279–2287.

17. V. R. Seymour, E. C. V. Eschenroeder, P. A. Wright, and S. E. Ashbrook, *Solid State Nucl. Magn. Reson.*, 2015, **65**, 64–74.
18. S. Reader, M. R. Mitchell, K. E. Johnston, C. J. Pickard, K. R. Whittle, and S. E. Ashbrook, *J. Phys. Chem. C*, 2009, **113**, 18874–18883.
19. M. R. Mitchell, S. W. Reader, K. E. Johnston, C. J. Pickard, K. R. Whittle, and S. E. Ashbrook, *Phys. Chem. Chem. Phys.*, 2011, **13**, 488–497.
20. M. R. Mitchell, D. Carnevale, R. Orr, K. R. Whittle, and S. E. Ashbrook, *J. Phys. Chem. C*, 2012, **116**, 4273–4286.
21. S. E. Ashbrook, M. R. Mitchell, S. Sneddon, R. F. Moran, M. de los Reyes, G. R. Lumpkin, and K. R. Whittle, *Phys. Chem. Chem. Phys.*, 2015, **17**, 9049–9059.
22. R. Grau-Crespo, S. Hamad, C. R. A. Catlow, and N. H. De Leeuw, *J. Phys. Condens. Matter*, 2007, **19**, 256201.
23. R. Grau-Crespo and U. V. Waghmare, in *Molecular Modeling for the Design of Novel Performance Chemicals and Materials*, ed. B. Rai, CRC Press, Boca Raton, Florida, 1st edn., 2012.
24. C. Giacovazzo, H. L. Monaco, G. Artioli, D. Viterbo, G. Ferraris, G. Gilli, G. Zanotti, and M. Catti, *Fundamentals of Crystallography*, Oxford University Press, Oxford, 2nd edn., 2002.
25. S. E. Ruiz-Hernandez, R. Grau-Crespo, A. R. Ruiz-Salvador, and N. H. De Leeuw, *Geochim. Cosmochim. Acta*, 2010, **74**, 1320–1328.
26. Q. Wang, R. Grau-Crespo, and N. H. De Leeuw, *J. Phys. Chem. B*, 2011, **115**, 13854–13861.
27. J. González-López, S. E. Ruiz-Hernández, Á. Fernández-González, A. Jiménez, N. H. de Leeuw, and R. Grau-Crespo, *Geochim. Cosmochim. Acta*, 2014, **142**, 205–216.
28. S. Benny, R. Grau-Crespo, and N. H. de Leeuw, *Phys. Chem. Chem. Phys.*, 2009, **11**, 808–815.
29. R. Grau-Crespo, A. Y. Al-Baitai, I. Saadoune, and N. H. De Leeuw, *J. Phys. Condens. Matter*, 2010, **22**, 255401.
30. S. Haider, R. Grau-Crespo, A. J. Devey, and N. H. De Leeuw, *Geochim. Cosmochim. Acta*, 2012, **88**, 275–282.
31. Y. Seminovski, P. Palacios, P. Wahnon, and R. Grau-Crespo, *Appl. Phys. Lett.*, 2012, **100**, 102112.

32. J. Corps, P. Vaqueiro, A. Aziz, R. Grau-Crespo, W. Kockelmann, J. C. Jumas, and A. V. Powell, *Chem. Mater.*, 2015, **27**, 3946–3956.
33. A. R. Ruiz-Salvador, R. Grau-Crespo, A. E. Gray, and D. W. Lewis, *J. Solid State Chem.*, 2013, **198**, 330–336.
34. J. Arce-Molina, R. Grau-Crespo, D. W. Lewis, and A. R. Ruiz-Salvador, *Phys. Chem. Chem. Phys.*, 2018, **20**, 18047–18055.
35. D. Müller, E. Jahn, G. Ladwig, and U. Haubenreisser, *Chem. Phys. Lett.*, 1984, **109**, 332–336.
36. Z. Yan, B. Chen, and Y. Huang, *Solid State Nucl. Magn. Reson.*, 2009, **35**, 49–60.
37. M. Hartmann, A. M. Prakash, and L. Kevan, *J. Chem. Soc., Faraday Trans.*, 1998, **94**, 723–727.
38. P. J. Byrne, J. E. Warren, R. E. Morris, and S. E. Ashbrook, *Solid State Sci.*, 2009, **11**, 1001–1006.
39. S. E. Ashbrook, M. Cutajar, C. J. Pickard, R. I. Walton, and S. Wimperis, *Phys. Chem. Chem. Phys.*, 2008, **10**, 5754–5764.
40. D. E. Akporiaye, A. Andersen, I. M. Dahl, H. B. Mostad, and R. Wendelbo, *J. Phys. Chem.*, 1995, **99**, 14142–14148.
41. D. M. Dawson and S. E. Ashbrook, *J. Phys. Chem. C*, 2014, **118**, 23285–23296.
42. D. M. Dawson, R. F. Moran, and S. E. Ashbrook, *J. Phys. Chem. C*, 2017, **121**, 15198–15210.
43. A.-R. Grimmer and R. Radaglia, *Chem. Phys. Lett.*, 1984, **106**, 262–265.
44. A.-R. Grimmer, *Chem. Phys. Lett.*, 1985, **119**, 416–420.
45. N. M. Trease, T. M. Clark, P. J. Grandinetti, J. F. Stebbins, and S. Sen, *J. Chem. Phys.*, 2017, **146**, 184505.
46. D. J. Srivastava, P. Florian, J. H. Baltisberger, and P. J. Grandinetti, *Phys. Chem. Chem. Phys.*, 2018, **20**, 562–571.
47. I. Ponomarev and P. Kroll, *Materials*, 2018, **11**, 1646.
48. V. R. Seymour, E. C. V. Eschenroeder, M. Castro, P. A. Wright, and S. E. Ashbrook, *CrystEngComm*, 2013, **15**, 8668–8679.
49. R. Dervişoğlu, D. S. Middlemiss, F. Blanc, Y.-L. Lee, D. Morgan, and C. P. Grey, *Chem. Mater.*, 2015, **27**, 3861–3873.
50. D. Carnevale, V. Del Amo, D. Philp, and S. E. Ashbrook, *Tetrahedron*,

2010, **66**, 6238–6250.

51. S. Cadars, M. Allix, D. H. Brouwer, R. Shayib, M. Suchomel, M. N. Garaga, A. Rakhmatullin, A. W. Burton, S. I. Zones, D. Massiot, and B. F. Chmelka, *Chem. Mater.*, 2014, **26**, 6994–7008.
52. E. Véron, M. N. Garaga, D. Pelloquin, S. Cadars, M. Suchomel, E. Suard, D. Massiot, V. Montouillout, G. Matzen, and M. Allix, *Inorg. Chem.*, 2013, **52**, 4250–4258.
53. J. Tsuchiya and T. Tsuchiya, *J. Geophys. Res.*, 2009, **114**, B02206.
54. S. C. Kohn, R. A. Brooker, D. J. Frost, A. E. Slesinger, and B. J. Wood, *Am. Mineral.*, 2002, **87**, 293–301.
55. S. D. Jacobsen, S. Demouchy, D. J. Frost, T. B. Ballaran, and J. Kung, *Am. Mineral.*, 2005, **90**, 61–70.
56. F. Deon, M. Koch-Müller, D. Rhede, M. Gottschalk, R. Wirth, and S. M. Thomas, *Am. Mineral.*, 2010, **95**, 312–322.
57. J. M. Griffin, A. J. Berry, D. J. Frost, S. Wimperis, and S. E. Ashbrook, *Chem. Sci.*, 2013, **4**, 1523–1538.
58. H. Grüninger, K. Armstrong, D. Greim, T. Boffa-Ballaran, D. J. Frost, and J. Senker, *J. Am. Chem. Soc.*, 2017, **139**, 10499–10505.
59. G. M. Day, T. G. Cooper, A. J. Cruz-Cabeza, K. E. Hejczyk, H. L. Ammon, S. X. M. Boerrigter, J. S. Tan, R. G. Della Valle, E. Venuti, J. Jose, S. R. Gadre, G. R. Desiraju, T. S. Thakur, B. P. Van Eijck, J. C. Facelli, V. E. Bazterra, M. B. Ferraro, D. W. M. Hofmann, M. A. Neumann, F. J. J. Leusen, J. Kendrick, S. L. Price, A. J. Misquitta, P. G. Karamertzanis, G. W. A. Welch, H. A. Scheraga, Y. A. Arnautova, M. U. Schmidt, J. Van De Streek, A. K. Wolf, and B. Schweizer, *Acta Crystallogr. Sect. B Struct. Sci.*, 2009, **65**, 107–125.
60. D. A. Bardwell, C. S. Adjiman, Y. A. Arnautova, E. Bartashevich, S. X. M. Boerrigter, D. E. Braun, A. J. Cruz-Cabeza, G. M. Day, R. G. Della Valle, G. R. Desiraju, B. P. Van Eijck, J. C. Facelli, M. B. Ferraro, D. Grillo, M. Habgood, D. W. M. Hofmann, F. Hofmann, K. V. J. Jose, P. G. Karamertzanis, A. V. Kazantsev, J. Kendrick, L. N. Kuleshova, F. J. J. Leusen, A. V. Maleev, A. J. Misquitta, S. Mohamed, R. J. Needs, M. A. Neumann, D. Nikylov, A. M. Orendt, R. Pal, C. C. Pantelides, C. J. Pickard, L. S. Price, S. L. Price, H. A. Scheraga, J. Van De Streek, T. S.

Thakur, S. Tiwari, E. Venuti, and I. K. Zhitkov, *Acta Crystallogr. Sect. B Struct. Sci.*, 2011, **67**, 535–551.

61. A. M. Reilly, R. I. Cooper, C. S. Adjiman, S. Bhattacharya, A. D. Boese, J. G. Brandenburg, P. J. Bygrave, R. Bylsma, J. E. Campbell, R. Car, D. H. Case, R. Chadha, J. C. Cole, K. Cosburn, H. M. Cuppen, F. Curtis, G. M. Day, R. A. DiStasio, A. Dzyabchenko, B. P. Van Eijck, D. M. Elking, J. A. Van Den Ende, J. C. Facelli, M. B. Ferraro, L. Fusti-Molnar, C. A. Gatsiou, T. S. Gee, R. De Gelder, L. M. Ghiringhelli, H. Goto, S. Grimme, R. Guo, D. W. M. Hofmann, J. Hoja, R. K. Hylton, L. Iuzzolino, W. Jankiewicz, D. T. De Jong, J. Kendrick, N. J. J. De Klerk, H. Y. Ko, L. N. Kuleshova, X. Li, S. Lohani, F. J. J. Leusen, A. M. Lund, J. Lv, Y. Ma, N. Marom, A. E. Masunov, P. McCabe, D. P. McMahon, H. Meekes, M. P. Metz, A. J. Misquitta, S. Mohamed, B. Monserrat, R. J. Needs, M. A. Neumann, J. Nyman, S. Obata, H. Oberhofer, A. R. Oganov, A. M. Orendt, G. I. Pagola, C. C. Pantelides, C. J. Pickard, R. Podeszwa, L. S. Price, S. L. Price, A. Pulido, M. G. Read, K. Reuter, E. Schneider, C. Schober, G. P. Shields, P. Singh, I. J. Sugden, K. Szalewicz, C. R. Taylor, A. Tkatchenko, M. E. Tuckerman, F. Vacarro, M. Vasileiadis, A. Vazquez-Mayagoitia, L. Vogt, Y. Wang, R. E. Watson, G. A. De Wijs, J. Yang, Q. Zhu, and C. R. Groom, *Acta Crystallogr. Sect. B Struct. Sci. Cryst. Eng. Mater.*, 2016, **72**, 439–459.
62. C. J. Pickard and R. J. Needs, *Phys. Rev. Lett.*, 2006, **97**, 45504.
63. C. J. Pickard and R. J. Needs, *J. Phys. Condens. Matter*, 2011, **23**, 53201.
64. C. J. Pickard and R. J. Needs, *Nat. Phys.*, 2007, **3**, 473–476.
65. C. J. Pickard and R. J. Needs, *Phys. Status Solidi B*, 2009, **246**, 536–540.
66. C. J. Pickard, M. Martinez-Canales, and R. J. Needs, *Phys. Rev. B*, 2012, **85**, 214114.
67. B. Monserrat, R. J. Needs, E. Gregoryanz, and C. J. Pickard, *Phys. Rev. B*, 2016, **94**, 134101.
68. C. J. Pickard and R. J. Needs, *Phys. Rev. Lett.*, 2009, **102**, 125702.
69. C. J. Pickard and R. J. Needs, *J. Chem. Phys.*, 2007, **127**, 244503.
70. C. J. Pickard and R. J. Needs, *Nat. Mater.*, 2008, **7**, 775–759.
71. G. I. G. Griffiths, A. D. Fortes, C. J. Pickard, and R. J. Needs, *J. Chem. Phys.*, 2012, **136**, 174512.

72. G. I. G. Griffiths, A. J. Misquitta, A. D. Fortes, C. J. Pickard, and R. J. Needs, *J. Chem. Phys.*, 2012, **137**, 64506.
73. G. I. G. Griffiths, R. J. Needs, and C. J. Pickard, *Phys. Rev. B*, 2009, **80**, 184115.
74. C. J. Pickard and R. J. Needs, *Phys. Rev. Lett.*, 2009, **102**, 146401.
75. C. J. Pickard and R. J. Needs, *J. Phys. Condens. Matter*, 2009, **21**, 452205.
76. C. J. Pickard and R. J. Needs, *Nat. Mater.*, 2010, **9**, 624–627.
77. I. Errea, M. Calandra, C. J. Pickard, J. Nelson, R. J. Needs, Y. Li, H. Liu, Y. Zhang, Y. Ma, and F. Mauri, *Phys. Rev. Lett.*, 2015, **114**, 157004.
78. D. Smith, K. V. Lawler, A. W. Daykin, Z. Fussell, G. A. Smith, C. Childs, J. S. Smith, C. J. Pickard, and A. Salamat, *Phys. Rev. Mater.*, 2018, **2**, 13605.
79. J. Nyman, O. S. Pundyke, and G. M. Day, *Phys. Chem. Chem. Phys.*, 2016, **18**, 15828–15837.
80. I. Y. Kanal, J. A. Keith, and G. R. Hutchison, *Int. J. Quantum Chem.*, 2018, **118**, e25512.
81. J. P. K. Doye, D. J. Wales, and M. A. Miller, *J. Chem. Phys.*, 1998, **109**, 8143–8153.
82. J. P. K. Doye and C. P. Massen, *J. Chem. Phys.*, 2005, **122**, 84105.
83. S. J. Clark, M. D. Segall, C. J. Pickard, P. J. Hasnip, M. I. J. Probert, K. Refson, and M. C. Payne, *Z. Kristallogr.*, 2005, **220**, 567–570.
84. M. Zilka, D. V. Dudenko, C. E. Hughes, P. A. Williams, S. Sturniolo, W. T. Franks, C. J. Pickard, J. R. Yates, K. D. M. Harris, and S. P. Brown, *Phys. Chem. Chem. Phys.*, 2017, **19**, 25949–25960.
85. K. A. See, M. Leskes, J. M. Griffin, S. Britto, P. D. Matthews, A. Emly, A. Van Der Ven, D. S. Wright, A. J. Morris, C. P. Grey, and R. Seshadri, *J. Am. Chem. Soc.*, 2014, **136**, 16368–16377.
86. H. Jung, P. K. Allan, Y. Y. Hu, O. J. Borkiewicz, X. L. Wang, W. Q. Han, L. S. Du, C. J. Pickard, P. J. Chupas, K. W. Chapman, A. J. Morris, and C. P. Grey, *Chem. Mater.*, 2015, **27**, 1031–1041.
87. J. M. Stratford, M. Mayo, P. K. Allan, O. Pecher, O. J. Borkiewicz, K. M. Wiaderek, K. W. Chapman, C. J. Pickard, A. J. Morris, and C. P. Grey, *J. Am. Chem. Soc.*, 2017, **139**, 7273–7286.
88. K. Ogata, E. Salager, C. J. Kerr, A. E. Fraser, C. Ducati, A. J. Morris, S.

Hofmann, and C. P. Grey, *Nat. Commun.*, 2014, **5**, 3217–3227.

89. A. J. Morris, R. J. Needs, E. Salager, C. P. Grey, and C. J. Pickard, *Phys. Rev. B - Condens. Matter Mater. Phys.*, 2013, **87**, 174108.
90. M. Mayo, K. J. Griffith, C. J. Pickard, and A. J. Morris, *Chem. Mater.*, 2016, **28**, 2011–2021.
91. S. E. Ashbrook, D. M. Dawson, and J. M. Griffin, in *Local Structural Characterisation*, eds. D. W. Bruce, D. O'Hare, and R. I. Walton, John Wiley & Sons, Ltd, 2014.
92. M. R. Hampson, J. S. O. Evans, and P. Hodgkinson, *J. Am. Chem. Soc.*, 2005, **127**, 15175–15181.
93. M. Dračínský, M. Šála, and P. Hodgkinson, *CrystEngComm*, 2014, **16**, 6756–6764.
94. L. Buannic, F. Blanc, D. S. Middlemiss, and C. P. Grey, *J. Am. Chem. Soc.*, 2012, **134**, 14483–14498.
95. T. Charpentier, S. Ispas, M. Profeta, F. Mauri, and C. J. Pickard, *J. Phys. Chem. B*, 2004, **108**, 4147–4161.
96. T. Charpentier, M. C. Menziani, and A. Pedone, *RSC Adv.*, 2013, **3**, 10550–10578.
97. M. Benoit, M. Profeta, F. Mauri, C. J. Pickard, and M. E. Tuckerman, *J. Phys. Chem. B*, 2005, **109**, 6052–6060.
98. A. Pedone, E. Gambuzzi, G. Malavasi, and M. C. Menziani, *Theor. Chem. Acc.*, 2012, **131**, 1147.
99. A. Pedone, T. Charpentier, and M. C. Menziani, *Phys. Chem. Chem. Phys.*, 2010, **12**, 6054–6066.
100. A. Pedone, T. Charpentier, G. Malavasi, and M. C. Menziani, *Chem. Mater.*, 2010, **22**, 5644–5652.
101. E. Gambuzzi, A. Pedone, M. C. Menziani, F. Angeli, P. Florian, and T. Charpentier, *Solid State Nucl. Magn. Reson.*, 2015, **68**, 31–36.

# Chapter 5: Investigating structural disorder in ceramic materials

## 5.1 Materials

### 5.1.1 Pyrochlores

The structure of $A_2B_2O_7$ (or more specifically, $A_2B_2O_6O'$) pyrochlore,[1–4] which adopts the $Fd\bar{3}m$ space group, is closely related to the fluorite structure, $AX_2$ (typically X = halogen or O), shown in Figure 5.1, which adopts the $Fm\bar{3}m$ space group. A pyrochlore can be formed by the ordered removal of $1/8^{th}$ of the O atoms from the fluorite structure, leading to two different cation sites, an eight-coordinate A site, occupied by 2+ or 3+ species such as $Cd^{2+}$, $Y^{3+}$, $La^{3+}$ or $Sc^{3+}$, and a six-coordinate B site, where smaller, 4+ or 5+ species, including $Ti^{4+}$, $Sn^{4+}$, $Zr^{4+}$, $Hf^{4+}$ or $Nb^{5+}$ reside. Using the Wyckoff notation,[5,6] where A is placed at the origin (termed origin choice two), the A and B cations occupy the 16c (0, 0, 0) and 16d (1/2, 1/2, 1/2) positions, respectively, with 16 denting the number of these sites in the pyrochlore unit cell. This produces three crystallographically-unique oxygen positions, with only the 8a (1/8, 1/8, 1/8) and the 48f ($x_{48f}$, 1/8, 1/8) occupied, accounting for one and six O in the formula units, respectively, leaving the 8b (3/8, 3/8, 3/8) site vacant. The creation of the oxygen vacancy at this site allows the $O_{48f}$ positions to vary, moving from its position in the ideal fluorite structure (3/8, 1/8, 1/8) towards the 8b vacancy. As shown in Figure 5.2, in the pyrochlore structure the A site cation has scalenohedral geometry, being surrounded by six $O_{48f}$ and two $O_{8a}$ anions, with $O_{8a}$ typically closer. The B site cation is surrounded by six $O_{48f}$ anions, giving trigonal prismatic coordination. The O occupying the 8a (O1) site, is surrounded by four A cations whereas the O occupying the 48f (O2) site is coordinated by two A and two B cations, with both O sites adopting tetrahedral coordination. In the literature the nomenclature of O1 and O2 can sometimes be reversed, such that O1 is 48f and O2 is 8a, however, in this thesis the crystallographic

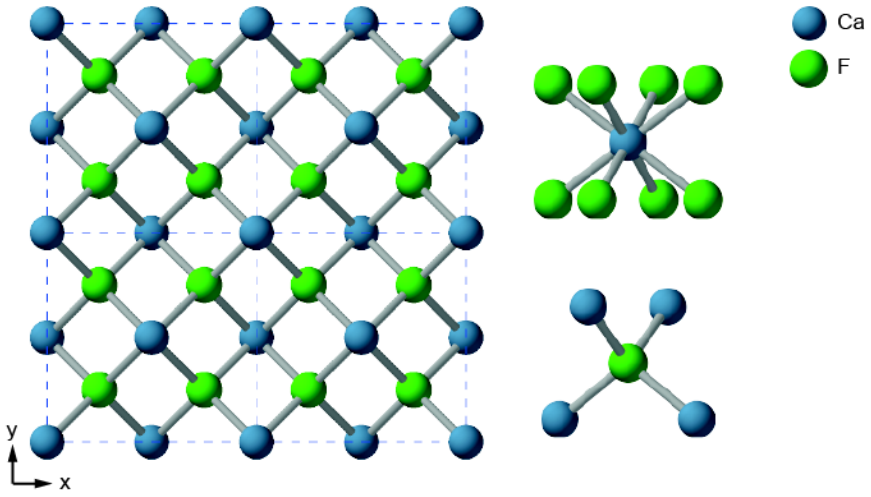


**Figure 5.1:** Structure of a 2 × 2 × 2 supercell of the fluorite $CaF_2$,[7] with expansions of the Ca and F local environments also shown.

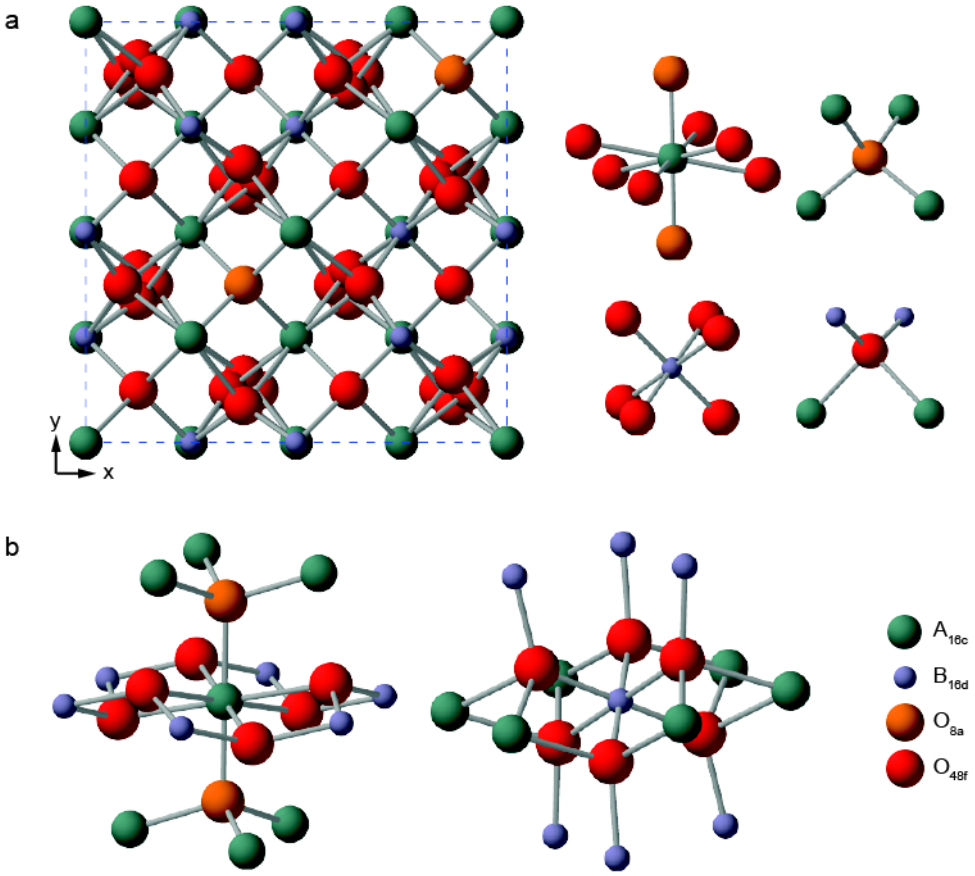


**Figure 5.2:** (a) Structure of a typical $A_2B_2O_7$ pyrochlore, formed by the ordered removal of $1/8^{th}$ of the oxygen anions from a fluorite structure, with expansions of the local environments of the 16c, 16d, 8a and 48f sites. (b) Expansions of the NNN environments for the A and B site cations.

notation used by Brisse and Knop has been followed.[8] It should be noted that in other literature, the B site is placed at the origin, in which case the Wyckoff positions of the $A_{16c}$ and $B_{16d}$ cations, and the occupied $O_{8a}$ and vacant $O_{8b}$ sites are swapped, leading to $A_{16d}$, $B_{16c}$, $O_{8b}$ and $O_{8a}$, the last being vacant.

The preferential formation of a pyrochlore structure is though to be linked to the relative ratio of the ionic radii for the A and B cations ($r_A/r_B$).[4] If this ratio lies between 1.46-1.78, a pyrochlore structure is favourable, whereas outside of this range, alternative phases are formed. If $r_A/r_B$ is below 1.46 a defect fluorite structure (see Section 5.1.2) is thought to be favoured, whereas above 1.78, the movement of the $O_{48f}$ anion alone can no longer compensate for the large size discrepancy, forcing other atoms to also move. This leads to the formation of a monoclinic layered perovskite-related structure with space group $P2_1$, a phase only formed for a relatively small number of materials, including $Ca_2Nb_2O_7$,[9] $Sr_2Nb_2O_7$[10] and $La_2Ti_2O_7$,[11,12] the latter of which has previously been studied using solid-state NMR spectroscopy,[13] and more recently by NMR crystallography.[14]

### 5.1.2 Defect fluorites

When the $r_A/r_B$ cation ratio of $A_2B_2O_7$ systems falls below 1.46, the formation of a defect fluorite structure (formally $A_4O_7$), with space group $Fm\bar{3}m$, is favoured. This disordered structure is adopted by a series of materials, including $La_2Ce_2O_7$,[15] and $Y_2Hf_2O_7$,[16,17] as well as several zirconates, $M_2Zr_2O_7$, where M = Gd, Ho, Er or Y.[18–20] The defect fluorite structure is closely related to that of fluorite ($AX_2$) discussed above, but with O atoms distributed randomly on $7/8^{th}$ of the anion sites, *i.e.*, all anion sites have a formal fractional occupancy of 0.875. This is in contrast to the pyrochlore structure, where all the vacancies are ordered on a single type of anion site. In addition, due to the similarity in size between the A and B cations (which leads to a reduction in the preference for a type of cation to have a specific O coordination, *i.e.*, A and B cations being exclusively eight- and six-coordinate, respectively), there is also mixing of the two cations, with the average cation

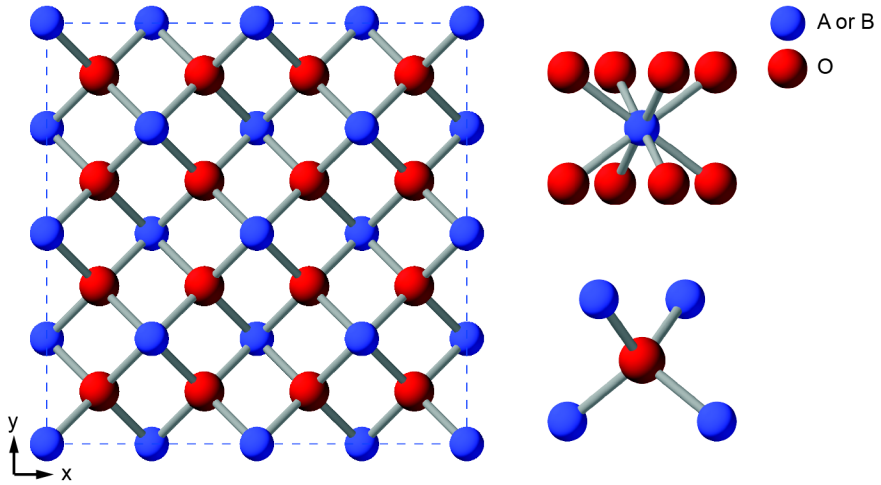


**Figure 5.3:** Structure of a typical $A_4O_7$ defect fluorite material, where $1/8^{th}$ of all anion sites will be vacant. An expansion of the cation and anion coordination environments is also shown, where $1/8^{th}$ of the O surrounding the cation site are vacant and where the four sites surrounding O can be occupied by either A or B.

coordination number remaining seven, as found in the pyrochlore structure.

## 5.2 Applications

Materials that adopt the pyrochlore structure tend to generate significant interest from the scientific community as their diverse chemistry leads to a wide range of chemical and physical properties, including interesting magnetic[21–23] and luminescent[24] behaviour, in addition to ionic and electrical conductivity.[25–29] The wide variety of properties exhibited by pyrochlores is due to the high level of structural flexibility afforded by this structure type, allowing the incorporation of many combinations of cations, and tolerance of different oxidation states, resulting in the known preparation of over 500 pyrochlores with different compositions.[1] With the highly tuneable nature of the pyrochlore structure allowing different properties to be selected by varying structure and composition, it is unsurprising that many are used for important technological and industrial applications, including in energy materials, catalysis, sensors, and thermal barrier coatings.[30–38]

A particularly important industrial application of pyrochlore ceramics is as

components of potential wasteform for radioactive lanthanides and actinides, including plutonium, uranium and thorium.[39–44] Finding a way to safely immobilise radioactive waste for a prolonged period of time is particularly important given the current social climate, where the need for safe and affordable energy will only increase with the rise in human population, and where there is a need to find a solution to address economic, environmental and security concerns. The UK was one of the first nations to use nuclear fission to produce electricity, meaning that since the 1950s radioactive waste has been accumulating, with the 15 reactors currently operational continuing to add to this dangerous stockpile. The UK government divides radioactive waste into four categories according to the degree of possible contamination: high level waste (HLW) such as spent nuclear fuel which, due to the high level of radioactivity, generates significant amounts of heat; intermediate level waste (ILW), which encompasses a wide array of materials including reactor components, filters and glove boxes; low level waste (LLW), denoting items that have low levels of radioactive contamination, including protective equipment and resins, with the majority of LLW resulting from dismantled nuclear reactors; and very low level waste (VLLW), which includes items from hospitals or universities that have only been contaminated with very low levels of radiation.[45] The HLW, generated as a highly acidic liquid, is heated to dryness then mixed with glass in a furnace, producing a molten substance that is poured into corrosion resistant cylindrical stainless steel canisters and allowed to cool and solidify. This process, known as vitrification, reduces the volume of HLW by approximately one third. However, as of yet there is no strategy for the safe disposal of HLW, only a storage procedure.

In a recent report produced by the Department of Business, Energy and Industrial Strategy (BEIS) and the Nuclear Decommissioning Authority (NDA), it was concluded that based on existing stores as of 1st April 2016, and based on future forecasts, by 2125 the amount of packed radioactive waste produced by the UK will be 4.77 million cubic metres, equivalent to the volume of Wembley Stadium. Although only 0.03% (1,500 $m^3$) of the total volume is attributed to HLW, this corresponds to a mass of UK-owned spent

uranium and plutonium of approximately 200,000 and 114 tonnes, respectively. As the highly radioactive isotopes $^{235}U$ and $^{239}Pu$, used and produced during the fission process have half-lives of 700 million and 24,100 years, respectively,[40] it is worryingly clear that if it is not feasible to dispose of these radioactive waste sources, at the very least a long-term containment and storage strategy needs to be implemented.

The first class of materials employed to immobilise HLW materials, termed first-generation wasteforms were based on borosilicate or aluminophosphate glasses.[40,46–48] Depending on the nature of the cation being immobilised, the composition of the glass would vary to maximise durability and minimise phase separation. Though they are still being used to this day, glass-based wasteforms have several shortcomings, namely, low levels of waste loading and reactivity towards moisture that reduces durability. In addition, radiation damage from the immobilised cations can lead to deformation that can compromise structural integrity. Therefore, it seems that rather than the glasses themselves exhibiting high chemical or physical durability, it is the combination of this immobilisation matrix, surrounded by the additional containment measures, *i.e.*, the reinforced, corrosion resistant steel containers, that together are designed to prevent any leaching of the radioactive cations and contamination of the local ecosystem. In order to ensure the safe long-term encapsulation of radioactive materials, it is clear that alternative wasteforms, with improved chemical and physical durability, must be found.

A potential second-generation wasteform for radioactive cations is synthetic inorganic rock (SYNROC) systems, first developed by Ringwood *et al.* in the late 1970s.[49–51] This material was designed to mimic naturally occurring minerals that have successfully immobilised radioactive cations for millions of years. For example, natural zirconolite ($CaZrTi_2O_7$) can contain up to 20 wt% (weight present) $ThO_2$ and 14 wt% $UO_2$,[52] while natural pyrochlores have been seen to contain as much as 9 wt% $ThO_2$ and 30 wt% $UO_2$.[53] The crystalline nature of ceramics mean that the radioactive cations should in principle be distributed homogenously through the material, and occupy

distinct crystallographic sites, in contrast to the potential cation distribution in amorphous glass-based encapsulation systems. This bodes well for the chemical durability of ceramic-based waseforms which, in order to be effective at safely encapsulating radioactive species for centuries, must be thermodynamically stable and highly resistant to any variation in pH, temperature, moisture levels, as well as many other conditions. Compared to other wasteforms, titanium-containing ceramics have shown particularly good chemical durability,[54,55] with the excellent resistance to leaching exhibited by SYNROC due predominantly to the presence of titanium oxide.[46] Hollandite ($BaAl_2Ti_6O_{16}$), zirconolite ($CaZrTi_2O_7$) and perovskite ($CaTiO_3$) were the main mineral components of the first synthetic rock material, SYNROC-C, which was developed to immobilise liquid HLW from used nuclear reactor fuel. Cations including $Cs^+$, $K^+$, $Rb^+$ and $Ba^{2+}$ can be immobilised within the hollandite phase, whereas the zirconolite and perovskite minerals primarily immobilise radioactive species including Sr and Pu, with SYNROC-C capable of storing up to 30 wt% HLW.[52]

The advantage of SYNROC over earlier wasteforms is its compositional flexibility, which allows it to be tuned for the particular HLW species needing to be immobilised. This tailoring has led to a series of SYNROC variations, including SYNROC-D, which contains nepheline ($(Na,K)AlSiO_4$) rather than hollandite, and SYNROC-F, a compositional variant containing pyrochlore ($(Ca,Gd,U,Pu,Hf)_2Ti_2O_7$), with zirconolite-rich materials specifically developed for the immobilisation of excess Pu.[56–58]

The immobilisation of radioactive species will expose the wasteform to α-decay, β-decay and γ-irradiation processes, which can lead to the generation of excess heat, species transmutation and atomic displacement through collisions.[59] The α-decay process involves the ejection of an α-particle (He nucleus) from a radioactive species, causing the parent nucleus to transmutate, for example, converting $^{239}Pu$ to $^{235}U$, with the daughter species known as an α-recoil ion. The energy from emitted α-particles is dispersed through ionisation processes, leading to heat being generated in the

wasteform. The α-particle also causes minor displacement of the atoms in its path. However, more localised and therefore more severe atomic displacement is caused by the much heavier α-recoil ion, causing a cascade of perturbation in atomic positions and thus significant amorphisation of the structure.[60,61] The release of He during the α-decay process can cause the pressure within the material to increase, meaning wasteforms must exhibit good mechanical strength, to minimise structural damage.[62] In addition, as the daughter species formed during α-decay may have different properties to the parent atom, wasteforms designed to immobilise HLW must also possess the structural flexibility that enables them to cope with the structural change resulting from this radiation damage process.

β-decay involves an electron being ejected from a radioactive species, causing transmutation of the parent cation. As an electron is significantly lighter than an α-particle, this radiation process results in much less structural disruption compared to the 1500 atom displacements resulting from a single α-decay process.[59] The emitted β-particle triggers ionisation processes, leading to heat generation and structural damage. Indeed, β-decay is responsible for the majority of wasteform heating during the first 500 years of HLW immobilisation.[63]

Radioactive species can also damage wasteforms through γ-irradiation, where highly energetic γ-rays are emitted. As this process does not involve the ejection of a particle, the γ-irradiation process has a negligible effect on the displacement of atoms in a wasteform.[63] However, as γ-rays are highly energetic, their release does contribute to wasteform heating.

The compositional range and resulting structural flexibility exhibited by pyrochlore ceramics has made them potentially promising radioactive wasteforms. The response to ion-beam irradiation for a series of rare-earth $A_2B_2O_7$ pyrochlores, in which B = Ti, Sn and Zr has previously been investigated.[64] Pyrochlores containing Sn and Zr were found to be far more

resistant to radiation damage compared to Ti-bearing pyrochlores. It was concluded that the relative cation size ($r_A/r_B$) was a significant factor in determining how a particular material responds to irradiation. As $Sn^{4+}$ and $Zr^{4+}$ are both larger than $Ti^{4+}$, the Sn- and Zr-bearing pyrochlores have lower $r_A/r_B$, meaning these structures are closer to the threshold where a defect fluorite phase may form and thus are more able to account for radiation damage by adopting this alternative crystalline phase, in preference to amorphisation.[64] A relationship between radiation resistance and $r_A/r_B$ has also been observed for $Ga_2Zr_xTi_{2-x}O_7$ pyrochlores, where systematically increasing the Zr content results in a reduction in susceptibility to radiation-induced amorphisation.[65] The difference in radiation tolerance for $Er_2Ti_2O_7$ and $Er_2Zr_2O_7$,[66] which adopt pyrochlore and defect fluorite structures, respectively, further highlights how key the $r_A/r_B$ ratio is in determining the response of a ceramic material to radiation-induced defects. This study again showed that structures containing A and B cations with highly disparate sizes, *i.e.*, $Er_2Ti_2O_7$, are less resistant to radiation damage, leading to amorphisation, whereas compounds for which $r_A/r_B$ is smaller, such as $Er_2Zr_2O_7$, have a higher radiation tolerance.[66] In a more recent study of a $Y_2Sn_xTi_{2-x}O_7$ pyrochlore solid solution, it was observed that susceptibility to radiation damage decreased linearly with increasing Sn content, again showing how materials with lower $r_A/r_B$ are more capable of accommodating radioactive species.[67] A similar trend was seen during an investigation in which a series of $Ln_2Sn_2O_7$ pyrochlores (Ln = Y and La-Lu) were irradiated. It was found that the response of these stannate pyrochlores to ion beam radiation varied greatly, with La-, Nd- and Gd- bearing compounds becoming amorphous following irradiation, whereas the Y and Er pyrochlore derivatives, which both have lower $r_A/r_B$, instead adopt the crystalline defect fluorite structure.[68]

The seemingly linear relationship between the ionic radius ratio ($r_A/r_B$) and the radiation resistance of a ceramic indicates that it should be possible to synthesise ceramic-based materials that have the correct balance of high chemical durability, as exhibited by Ti-containing materials, combined with the impressive radiation resistance of Zr- and Sn-containing materials, to

produce wasteforms capable of safely immobilising HLW species for thousands of years.

## 5.3 Previous work

As discussed above, the $r_A/r_B$ ratio plays a significant role in determining the phase adopted by $A_2B_2O_7$ ceramics, an outcome that can affect the physical and chemical properties exhibited by a material. Table 5.1, gives $r_A$, $r_B$, and the $r_A/r_B$, ratio for a selection of $A_2B_2O_7$ ceramics, along with the phase adopted in each case, and highlights how small changes in cation radii can have a large effect on phase stability. As illustrated in Figure 5.4, which shows $r_A/r_B$ for a series of $A_2Sn_xB_{2-x}O_7$ (A = Y and La, B = Ti, Zr and Hf) systems, at a particular B-site cation composition, materials are expected to undergo a phase transition, which can make structural characterisation significantly more challenging. From Figure 5.4 it can be seen that $Y_2Sn_xTi_{2-x}O_7$ is expected to adopt a pyrochlore phase throughout, as $r_A/r_B$ remains between 1.78 and 1.46. However, several phase transitions are expected for several other systems, with either the layered perovskite-like, or the disordered defect fluorite structures becoming more favourable as the composition varies. As NMR spectroscopy is extremely sensitive to small changes in local structure, it has proven to be particularly successful for understanding the number and type of phases formed for ceramic materials, particularly when experimental NMR measurements are combined with information from diffraction and first-principles calculations.

Although $^{89}Y$ is 100% abundant and has spin quantum number I = 1/2, poor sensitivity (owing to the very low $\gamma$) and long relaxation times (in some cases up to 10,000 s) cause the acquisition of NMR spectra to be extremely challenging. Grey *et al*. published the first $^{89}Y$ solid-state NMR investigation of Y-containing pyrochlores in 1990,[69] in which $^{89}Y$ MAS NMR spectra for a series of pyrochlores, $Y_{2-y}Ln_yM_2O_7$ (Ln = Ce, Pr, Nd, Sm, Eu and Yb, M = Sn and Ti), were obtained, in order to observe the effect of incorporating

**Table 5.1:** The A and B site ionic radii, $r_A/r_B$ ratio and phase adopted for selected $A_2B_2O_7$ ceramics. The ionic radii quoted were taken from the table of Ionic Radii in Crystals in the 2005 Internet version of the CRC Handbook of Chemistry and Physics.[70]

| Structure | $r_A$ / Å | $r_B$ / Å | $r_A/r_B$ | Phase |
|---|---|---|---|---|
| $Y_2Sn_2O_7$ | 1.02 | 0.69 | 1.48 | Pyrochlore |
| $Y_2Ti_2O_7$ | 1.02 | 0.61 | 1.67 | Pyrochlore |
| $Y_2Zr_2O_7$ | 1.02 | 0.72 | 1.42 | Defect fluorite |
| $Y_2Hf_2O_7$ | 1.02 | 0.71 | 1.44 | Defect fluorite |
| $La_2Sn_2O_7$ | 1.16 | 0.69 | 1.68 | Pyrochlore |
| $La_2Ti_2O_7$ | 1.16 | 0.61 | 1.90 | Perovskite-like |
| $La_2Zr_2O_7$ | 1.16 | 0.72 | 1.61 | Pyrochlore |
| $La_2Hf_2O_7$ | 1.16 | 0.71 | 1.63 | Pyrochlore |

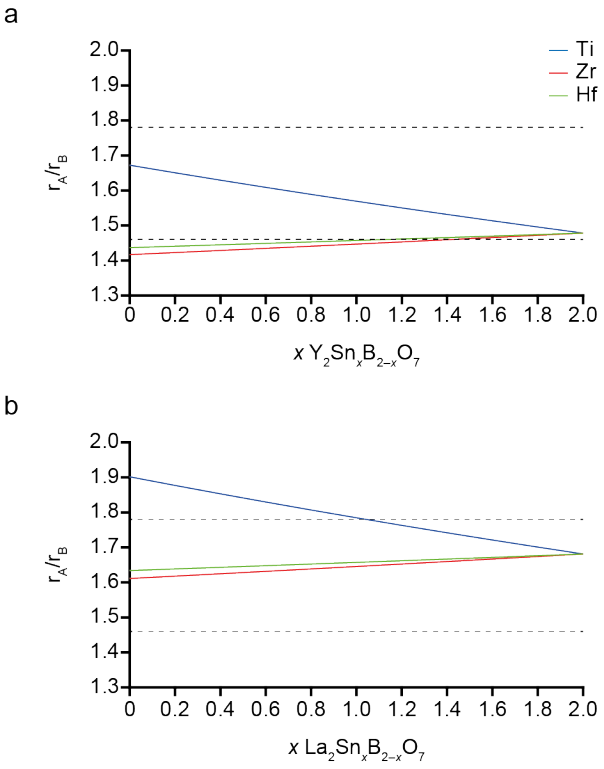


**Figure 5.4:** Plot showing the variation in $r_A/r_B$ with B site composition for a series of (a) $Y_2Sn_xB_{2-x}O_7$ and (b) $La_2Sn_xB_{2-x}O_7$, systems where B = Ti, Zr or Hf. The horizontal dashed lines at 1.78 and 1.46 describe the boundaries between which the pyrochlore structure is expected. Above 1.78, a layered perovskite-like structure is expected and below 1.46 a disordered defect fluorite phase is predicted to be formed. The ionic radii values used to make these plots were taken from the table of Ionic Radii in Crystals in the 2005 Internet version of the CRC Handbook of Chemistry and Physics.[70]

paramagnetic ions into the diamagnetic system. A single resonance was observed in the $^{89}$Y MAS NMR spectra of $Y_2Sn_2O_7$ and $Y_2Ti_2O_7$, agreeing with the one crystallographically unique Y site identified in the crystal structures. The $^{89}$Y isotropic chemical shift ($\delta_{iso}$) was 150 and 65 ppm for $Y_2Sn_2O_7$ and $Y_2Ti_2O_7$, respectively, with the difference in shift attributed to the difference in polarisability between the cations occupying the six NNN B sites surrounding each Y in both structures, with the lower $^{89}$Y $\delta_{iso}$ for $Y_2Ti_2O_7$ believed to be due to the more polarising nature of $Ti^{4+}$ compared to $Sn^{4+}$.

Ashbrook *et al*. later used $^{89}$Y MAS NMR experiments to study $Y_2Sn_xTi_{2-x}O_7$, where $x$ = 2.0, 1.6, 1.2, 0.8, 0.4 and 0.0,[71] showing that $^{89}$Y NMR provides an excellent probe of local structure. The study confirmed that this system remains pyrochlore phase throughout, with a single phase formed in all cases. It was also shown (within the detection level of the spectrum) that Y occupies only the eight-coordinate A site, with the six-coordinate B site exclusively occupied by Ti and/or Sn. Although the $^{89}$Y MAS NMR spectra of the two end members each contain a single sharp resonance, the incorporation of Ti into $Y_2Sn_2O_7$ leads to the appearance of additional resonances at lower shifts, as a result of the presence of the more polarising $Ti^{4+}$ cation in the local coordination environment.[72] With most of the observed resonances separated by ~15 ppm, it was possible to tentatively assign these to Y species with different numbers of Sn (*n* Sn) on the six surrounding NNN B sites, *i.e.*, Sn6, Sn5Ti, Sn4Ti2, *etc,*. However, more than seven resonances could be resolved, with smaller splittings tentatively assumed to be due to different spatial arrangements of Sn and Ti on the surrounding NNN B sites. In addition, smaller changes in chemical shift for resonances in samples with different compositions were thought to be due to the decrease in unit cell size as $x$ decreased. Finally, Ashbrook *et al*. concluded that based on the good agreement between the peak intensities for the different *n* Sn NNN environments (based on their tentative assignment described above) and intensities predicted assuming a random distribution of B site cations, there was no evidence of any preferential clustering into Sn- and Ti-rich regions.[71]

Many of the conclusions from Ashbrook *et al*.[71] were supported in a later study by Reader *et al*.,[73] which combined experiment with first-principles calculations to investigate the cation disorder in $Y_2Sn_xTi_{2-x}O_7$. It was confirmed that the Sn/Ti distribution over the B sites appears random and that upfield shifts associated with the incorporation of Ti into $Y_2Sn_2O_7$ are a result of changes to the *n* Sn NNN environment. By constructing an alternative structural model where one Y was placed on the six-coordinate B site (and correspondingly a Sn cation was placed on the A site), this study confirmed that there was no evidence for any cation mixing between the sites (at the NMR detection level), with Y exclusively occupying the eight-coordinate A site in $Y_2Sn_xTi_{2-x}O_7$.[73] In addition, by analysing the Y–O bond lengths and O–Y–O angles in their structural models, Reader *et al*. showed how first-principles calculations could be used to relate variations in $^{89}$Y NMR parameters directly to changes in local geometry.

In 2012, Ashbrook and co-workers continued their investigation into $Y_2Sn_xTi_{2-x}O_7$, this time using $^{89}$Y CSA measurements, combined with first-principles calculations.[74] Implemented for $^{89}$Y for the first time, the two-dimensional CSA-amplified phase adjusted spinning sideband (PASS)[75,76] experiment was used to obtain experimental $^{89}$Y CSA values for the solid solution. The good agreement between the experimental and calculated CSA values supported the original (tentative) assignment of the $^{89}$Y MAS NMR spectra for $Y_2Sn_xTi_{2-x}O_7$.[71,73] The $^{89}$Y span ($\Omega$) proved to be particularly sensitive to changes in the *n* Sn NNN environment, as well as exhibiting a strong correlation with the average Y–$O_{8b}$ bond length.[74] Note that as Sn was placed at the origin in this study the $O_{8b}$ and $O_{8a}$ sites are classified as occupied and vacant, respectively.

Pyrochlores have also been studied using $^{119}$Sn (I = 1/2) NMR spectroscopy,[77] with Mitchell *et al*. demonstrating that the combination of $^{119}$Sn MAS NMR experiments with first-principles calculations is very effective at probing local structure and cation disorder in $Y_2Sn_xTi_{2-x}O_7$.[78] First-principles calculations confirmed that in the $Y_2Sn_xTi_{2-x}O_7$ pyrochlores Sn only occupies the six-coordinate B site, and showed that the $^{119}$Sn chemical shift is also

sensitive to the nature of the species (*i.e.*, the number of Sn and Ti) on the six NNN B sites. When the Ti content was low, distinct resonances could be resolved in the $^{119}$Sn MAS NMR spectra, whereas for Ti-rich compositions a small number of broader resonances are observed, suggesting either ordering/clustering of Sn (in contrast to the conclusions from $^{89}$Y NMR[71,73]) or an overlap of resonances from species with different NNN environments, Using first-principles calculations it was shown that the latter conclusion was correct and the authors attributed the significant overlap of $^{119}$Sn resonances to two competing factors; first the upfield shift caused by incorporation of the more polarising $Ti^{4+}$ cation, and second, a downfield shift (of similar size) resulting from the unit cell contraction that results from Ti incorporation. Despite the challenges associated with assignment of the broader and overlapped spectral lines, it was shown that the relative intensities of peaks in the $^{119}$Sn MAS NMR spectra were consistent with a random distribution of Sn and Ti on the six-coordinate B sites, in agreement with conclusions from the $^{89}$Y MAS NMR spectra.[71]

More recently, Ashbrook and co-workers have used $^{89}$Y and $^{119}$Sn solid-state MAS NMR spectroscopy, combined with XRD and first-principles calculations to investigate the phase composition, phase distribution and cation disorder in $Y_2Sn_xZr_{2-x}O_7$ ceramics, where $x$ = 2, 1.8, 1.6, 1.4, 1.2, 1, 0.8, 0.6, 0.4, 0.2 and 0.[79] The $^{89}$Y MAS NMR spectra of the two end members, $Y_2Sn_2O_7$ and $Y_2Zr_2O_7$, shown in Figure 5.5a and 5.5b, respectively, are strikingly different, with the ordered pyrochlore phase adopted by $Y_2Sn_2O_7$ resulting in a single, sharp resonance. In contrast, the $^{89}$Y MAS NMR spectrum for $Y_2Zr_2O_7$, known to adopt the defect fluorite structure, contains three broad resonances, corresponding to Y coordinated by six, seven and eight O atoms, respectively, with the higher coordination leading to a more upfield shift.[79,80] The $^{89}$Y MAS NMR spectra showed the appearance of additional resonances with the incorporation of Zr into $Y_2Sn_2O_7$, similar to those observed when Sn was substituted for Ti in $Y_2Sn_xTi_{2-x}O_7$,[71] allowing these to be attributed to Y in the pyrochlore phase with different $n$ Sn (and therefore Zr) NNNs. As $x$ decreases, broad resonances appear in the $^{89}$Y MAS spectra and grow in intensity, confirming the increasing proportion of a

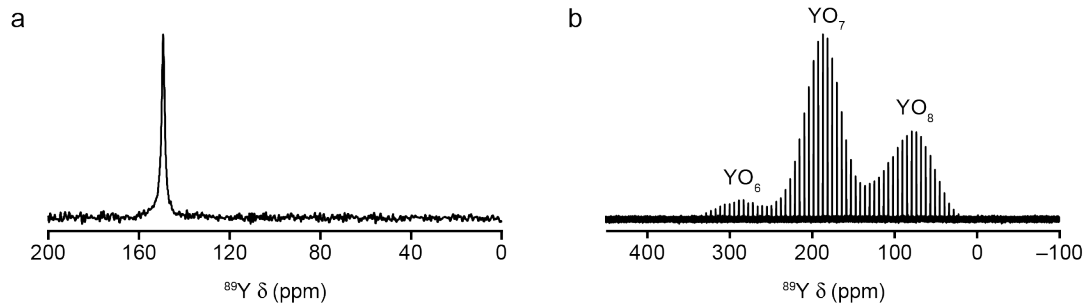


**Figure 5.5:** $^{89}$Y (14.1 T, 14 kHz) MAS NMR spectra of (a) $Y_2Sn_2O_7$ using a spin echo pulse sequence and (b) $Y_2Zr_2O_7$ using a CPMG pulse sequence.

defect fluorite phase as the Zr content increases. Interestingly, a two-phase region (*i.e.*, with co-existence of ordered pyrochlore and disordered defect fluorite phases) are observed for $x$ = 0.8 to 1.8, with a pure pyrochlore phase observed only for $Y_2Sn_2O_7$ and a single defect fluorite phase only for $x$ = 0.6 to 0. The relative intensities of the $^{89}$Y pyrochlore resonances was used to determine the cation composition in each sample, *i.e.*, to determine the composition of the pyrochlore phase and, subsequently, of the defect fluorite phase, and the proportions of each phase present. It was shown that the pyrochlore phase is Sn rich, with a solid solution limit of 13% (*i.e.*, $Y_2Sn_{1.74}Zr_{0.26}O_7$) Using the relative intensities of the $^{89}$Y resonances corresponding to six- seven- and eight- coordinate Y in the defect fluorite phase, Ashbrook *et al*. also concluded that O vacancies are more likely to be associated with Zr, with $Y^{3+}$ cations having a greater preference for a higher average coordination number compared to $Zr^{4+}$, which is unsurprising given the difference in ionic radii ratio. The $^{119}$Sn MAS NMR spectra for $Y_2Sn_xZr_{2-x}O_7$ also confirms the presence of a significant two-phase region from $x$ = 1.8 to 0.8.[79] As for $Y_2Sn_xTi_{2-x}O_7$, for $Y_2Sn_xZr_{2-x}O_7$ the $^{119}$Sn NMR resonances are significantly overlapped, with the presence of two phases for most compositions exacerbating the challenge of spectral assignment. Despite this, distinct $^{119}$Sn resonances believed to be due to Sn in different $n$ Sn NNN environments (Sn6, Sn5Zr, Sn4Zr2, *etc*.) in the ordered pyrochlore phase could be resolved in Sn-rich compositions, from $x$ = 1.8 to 1.4.

In an earlier study, de los Reyes *et al*. used a series of analytical techniques, including $^{119}$Sn MAS NMR spectroscopy, to investigate the pyrochlore to

defect fluorite phase transition in $Y_2Zr_xSn_{2-x}O_7$.[81] In this study de los Reyes *et al*. used a different notation for composition, with $x = 2$ referring to $Y_2Zr_2O_7$, (the reverse of the notation used by Ashbrook and co-workers).[79] It was shown that a pyrochlore phase was present up to $x = 1.2$ ($Y_2Zr_{1.2}Sn_{0.8}O_7$), meaning this phase extends to a higher Zr content than is expected based on the classical $r_A/r_B$ ratio analysis which, as seen in Figure 5.4a, predicts the absence of the pyrochlore phase in $Y_2Zr_{0.6}Sn_{1.4}O_7$ and all other samples with a higher Zr content. The apparent stability of the pyrochlore phase in Zr-rich structures was attributed to the highly covalent nature of Sn–O bond and the strong preference for the $Sn^{4+}$ cations to be six coordinate.[81]

As by definition all metal oxides must contain O, it is unsurprising that $^{17}O$ (I = 5/2), has been used to study pyrochlore ceramics. However, as $^{17}O$ (the only NMR-active isotope) has a very low natural abundance, 0.037%,[82] in order to ensure NMR spectra are recorded within a sensible timeframe, it is necessary to first enrich most samples. In 2003, Kim and Grey used $^{17}O$ MAS NMR spectroscopy to investigate the local structure of a set of Y-based pyrochlore and defect fluorite structures, $Y_2Ti_{2-x}B_xO_7$ (B = Sn, Zr), with the small $^{17}O$ $C_Q$ observed allowing resonances to be resolved using MAS.[83] Different numbers of resonances were observed for the different systems, showing that $^{17}O$ is a sufficiently sensitive probe of the number and nature of the metal cations surrounding O. This information was used to provide insight into the cation mixing and disorder in these ceramic materials. In Figure 5.6a and 5.6b the $^{17}O$ MAS NMR spectra of $Y_2Sn_2O_7$ and $Y_2Zr_2O_7$, respectively, are shown, highlighting the considerable differences between materials that adopt the pyrochlore or the defect fluorite structures. While the $^{17}O$ MAS NMR spectrum of $Y_2Sn_2O_7$ contains two distinct resonances at ~385 and ~165 ppm, corresponding to the $O_{8a}$ (OY4) and $O_{48f}$ (OY2Sn2) environments, respectively, the $^{17}O$ MAS NMR spectrum of $Y_2Zr_2O_7$ consists of a very broad resonance, which Kim and Grey attribute to the overlap of several distinct chemical environments, *i.e.*, OY4, OY3Zr, OY2Zr2, OYZr3 and OZr4.[83]

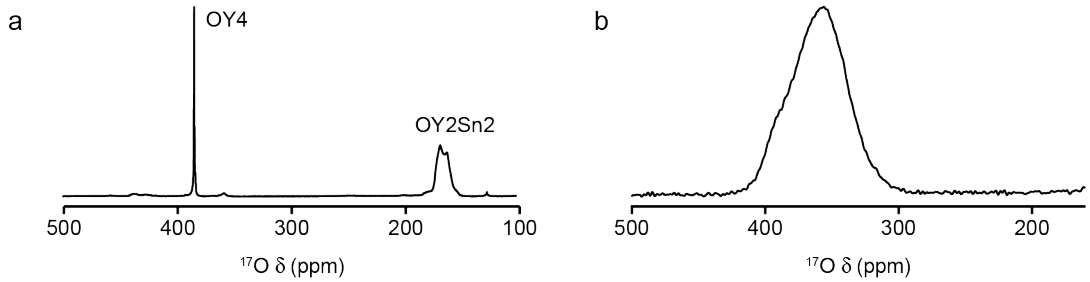


**Figure 5.6:** $^{17}O$ (14.1 T, 21 kHz) MAS NMR spectra of (a) $Y_2Sn_2O_7$ and (b) $Y_2Zr_2O_7$.

$^{17}O$ MAS NMR spectroscopy has also been used to investigate the local structure, cation ordering and the phase evolution for materials in the $Y_2Ti_2O_7$-$ZrTiO_4$ binary system.[84] In this study, the effect of synthesising the materials at either 800, 1000 or 1300 °C, prior to $^{17}O$ gas enrichment, on the local and long-range ordering of $Y_{1.6}Zr_{0.4}Ti_2O_{7.2}$ and $Y_{1.2}Zr_{0.8}Ti_2O_{7.4}$, was investigated, using both XRD and $^{17}O$ MAS NMR spectroscopy. The $^{17}O$ MAS NMR spectra of the materials synthesised at low temperature were dominated by broad resonances, indicative of a disordered phase, with XRD measurements suggests the formation of a metastable $Y_{2-x}Zr_xTi_{2-y}Zr_yO_7$ structure, with Zr found on both the A and B sites, but located predominantly on the eight-coordinate A site, *i.e.*, $x > y$. In contrast, XRD of samples synthesised at higher temperatures showed a reduction in eight-coordinate Zr, until at the highest temperatures the ordered pyrochlore phase dominates. The $^{17}O$ MAS NMR spectra of the samples synthesised at 1300 °C are dominated by sharp resonances attributed to the ordered $Y_2Ti_2O_7$ pyrochlore, further evidence suggesting that as the synthesis temperature increases, the phase evolves from a disordered, fluorite-like structure to being dominated by a more ordered pyrochlore phase.[84]

In this chapter the local structure of several ceramic materials that adopt the pyrochlore or defect fluorite structures are investigated using $^{89}Y$, $^{119}Sn$ and $^{17}O$ solid-state NMR spectroscopy and first-principles calculations. The cation and/or anion site disorder present in these types of materials often makes the interpretation of the solid-state NMR spectra challenging. As a result, first-principles calculations are often used to provide structural insight and guide spectral assignment.[85–87] Here, various methods for the construction of

structural models for disordered materials are considered, with subsequent prediction of NMR parameters and comparison to experimental measurements used to evaluate their accuracy and relevance. In addition to demonstrating how first-principles calculations can be effectively used to assist the assignment of challenging NMR spectra, this chapter also aims to develop procedures for generating structural models that can be applied to other inorganic materials that exhibit similar types of structural disorder.

## 5.4 Acknowledgements

The ceramic oxide materials investigated in this chapter were synthesised by the group of Dr Karl Whittle at the University of Liverpool, or by Dr Martin Mitchell, Dr Scott Sneddon, or Miss Arantxa Fernandes, former or current members of the Ashbrook group at the University of St Andrews.

The $^{17}O$ enrichment of $Y_2Sn_xTi_{2-x}O_7$, $La_2Sn_xZr_{2-x}O_7$, $Y_2Zr_2O_7$ and $Y_2Hf_2O_7$ was performed by Miss Arantxa Fernandes at the University of St Andrews. This involved heating the samples at 600-900 °C for 12-24 hours in the presence of 70% $^{17}O_2$ gas.

$^{89}Y$, $^{119}Sn$ and $^{17}O$ solid-state NMR spectra were acquired by Miss Arantxa Fernandes at the Solid-State NMR Facility at the University of St Andrews, using Bruker Avance III spectrometers.

$^{89}Y$ MAS (14 kHz) NMR spectra of $Y_2Sn_xTi_{2-x}O_7$, $Y_2Zr_2O_7$ and $Y_2Hf_2O_7$ were acquired on a 14.1 T wide-bore magnet, using a 4 mm $Si_3N_4$ rotor and 4 mm HX low-γ probe. Chemical shifts are shown in ppm relative to the primary reference 1 M $YCl_3$ (aq), measured using a secondary solid reference of $Y_2Ti_2O_7$ (δ = 65 ppm) for all spectra. An rf nutation rate of ~23 kHz was used for all experiments (power level of 380 W) and measured on $Y_2Ti_2O_7$. For $Y_2Sn_xTi_{2-x}O_7$, single pulse and spin echo experiments were performed, with spectra the result of averaging between 256 and 4480 transients, with a typical recycle interval of 30 s. For $Y_2Zr_2O_7$ and $Y_2Hf_2O_7$ CPMG spectra were

acquired by averaging 2448 and 4320 transients, with recycle intervals of 11 and 10 s, respectively.

$^{119}$Sn MAS (14 kHz) NMR spectra of $Y_2Sn_xTi_{2-x}O_7$ and $La_2Sn_xZr_{2-x}O_7$ were acquired on a 9.4 T wide-bore magnet, using a 4 mm $ZrO_2$ rotor and 4 mm HX probe, using spin echo experiments. Chemical shifts are shown in ppm relative to the primary reference tetramethyl tin, $Sn(CH_3)_4$ (l), measured using a secondary solid reference of $SnO_2$ at –604.3 ppm for all spectra. An rf nutation rate of 111 kHz was employed, measured using $SnO_2$ at a power level of 250 W. Spectra are a result of averaging between 32 and 2994 transients, with a recycle interval of 30 s.

$^{17}$O MAS (21 kHz) NMR spectra of $Y_2Sn_xTi_{2-x}O_7$, $La_2Sn_xZr_{2-x}O_7$, $Y_2Zr_2O_7$ and $Y_2Hf_2O_7$ were acquired on a 14.1 T wide-bore magnet, using a 3.2 mm $ZrO_2$ rotor and 3.2 mm HX probe. Chemical shifts are shown in ppm relative to the primary reference of distilled $H_2O$ (l) at 0 ppm. An rf nutation rate of 71 kHz was used, measured on $H_2O$ at a power level of 300 W. Spectra were acquired using a conventional single pulse experiment, and are the result of averaging 1024, 2048, 4096 and 4096 transients (with recycle intervals of 5, 30, 1 and 1 s,) for $Y_2Sn_xTi_{2-x}O_7$, $La_2Sn_xZr_{2-x}O_7$ $Y_2Zr_2O_7$ and $Y_2Hf_2O_7$, respectively.

During a summer research project, Mr Ben Griffiths, a chemistry undergraduate at the University of St Andrews also assisted in the investigation of the $La_2Sn_xZr_{2-x}O_7$ ceramics.

I would also like to thank Dr Ricardo Grau-Crespo and his research group at the University of Reading for the generation of a series of input structures for $Y_2Sn_xTi_{2-x}O_7$ and $La_2Sn_xZr_{2-x}O_7$ using the SOD program.[88]

I must also thank Dr David McKay, a postdoctoral research fellow in the Ashbrook group at the University of St Andrews, for his assistance setting up and performing CASTEP calculations, as well as helping to develop Python scripts to analyse output data from first-principles calculations.

## 5.5 $Y_2Sn_xTi_{2-x}O_7$: using NMR spectroscopy and first-principles calculations to investigate B-site cation disorder

### 5.5.1 Introduction

The $Y_2Sn_xTi_{2-x}O_7$ series has been investigated previously using NMR spectroscopy, with studies using $^{89}Y$ and $^{119}Sn$ experiments, often in combination with first-principles calculations, to explain the changes in local structure resulting from B-site cation disorder.[71,73,74,78,89] From these investigations it was concluded that $Y_2Sn_xTi_{2-x}O_7$ forms a solid solution, adopting a single pyrochlore phase through the entire compositional series, that Y and Sn reside exclusively (at least to the detection limits) on the eight- and six-coordinate A and B sites, respectively, and the distribution of Sn and Ti occupying the B sites is essentially random, *i.e.*, there is no evidence for any significant clustering or ordering. Despite these important insights, the challenges associated with completely assigning the $^{89}Y$ and $^{119}Sn$ MAS NMR spectra, the latter showing significant overlap of the spectral resonances, combined with the relatively simple (and potentially unrealistic) structural models used to predict NMR parameters means there is still a need to investigate this system further. The work presented in this section focuses on investigating whether using alternative, potentially more sophisticated approaches to generate structural models of disordered $Y_2Sn_xTi_{2-x}O_7$ can provide additional information that ultimately could help assign the $^{89}Y$, $^{119}Sn$ and $^{17}O$ MAS NMR spectra with more confidence, and gain any further insight into the detailed cation distribution.

### 5.5.2 Experimental NMR spectra

As described in Section 5.4, all $^{89}Y$, $^{119}Sn$ and $^{17}O$ MAS NMR spectra were recorded by Miss Arantxa Fernandes using Bruker Avance III spectrometers equipped with either a 9.4 T ($^{119}Sn$) or 14.1 T ($^{89}Y$ and $^{17}O$) wide-bore magnet at the Solid-State NMR Facility at the University of St Andrews. In previous studies, $Y_2Sn_xTi_{2-x}O_7$ was synthesised in steps of $x$ =

0.4,[71,73,74,78,89] whereas here, a new series of $Y_2Sn_xTi_{2-x}O_7$ samples, with $x$ = 2, 1.75, 1.5, 1.25, 1, 0.75, 0.5, 0.25 and 0 are studied. The smaller changes in composition should enable a more detailed examination of how NMR parameters and NMR spectra change with composition, and the exact compositions chosen will facilitate comparison with the computational predictions, and the compositions used in the generation of $Y_2Sn_xTi_{2-x}O_7$ structural models by Dr Ricardo Grau-Crespo, using the SOD program,[88] the results of which are discussed in Section 5.5.5.

### 5.5.2.1 $^{89}$Y MAS NMR spectra

The $^{89}$Y MAS NMR spectra of $Y_2Sn_xTi_{2-x}O_7$ are shown in Figure 5.7, with the spectra of $Y_2Sn_2O_7$ and $Y_2Ti_2O_7$ each containing one sharp resonance, at 150 and 65 ppm, respectively, in good agreement with previous literature.[69,71] Upon incorporation of Ti into $Y_2Sn_2O_7$, additional resonances are again observed, appearing upfield of the peak corresponding to Y with Sn6 NNN. As the additional resonances that appear with increasing Ti content (decreasing $x$) are reasonably well separated, with ~15 ppm between each, it is possible to tentatively assign each to Y with a specific $n$ Sn NNN environment,[71] *i.e.*, Sn6, Sn5Ti, Sn4Ti2, *etc*, as shown in Figure 5.7. The effect of the change in unit cell size that accompanies the incorporation of Ti into $Y_2Sn_2O_7$ can also clearly be seen from Figure 5.7, as the resonance assigned to Y with Sn6 NNN moves ~10 ppm downfied as $x$ decreases from 2 to 1, *i.e.*, from $Y_2Sn_2O_7$ to $Y_2SnTiO_7$. As shown in Table 5.1, there is over a 10% difference in the ionic radii of six-coordinate $Ti^{4+}$ (0.61 Å) and six-coordinate $Sn^{4+}$ (0.69 Å), with the Sn/Ti content having a noticeable effect on the unit cell size; lattice parameters ($a$) for $Y_2Sn_2O_7$ and $Y_2Ti_2O_7$ are 10.3725 Å and 10.0949 Å, respectively.[8,90] However, as neighbouring resonances generally appear to be separated by ~15 ppm for all spectra of the $Y_2Sn_xTi_{2-x}O_7$ compositional series, it suggests that the $^{89}$Y chemical shift is more determined by $n$ Sn NNN. The $^{89}$Y MAS NMR spectra also show that the resonance assigned to environments with 3 Sn NNN (Sn3Ti3) exhibits a clear splitting in several compositions, being most apparent in spectra for $x$ = 1.25

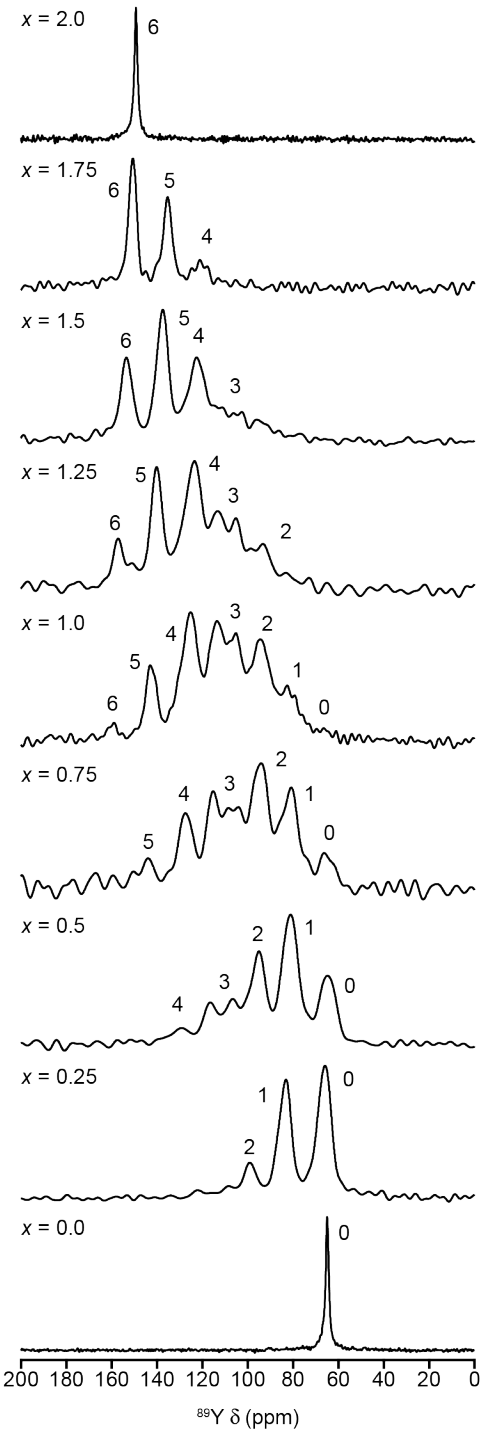


**Figure 5.7:** $^{89}$Y (14.1 T, 14 kHz) MAS NMR spectra of $Y_2Sn_xTi_{2-x}O_7$, with the tentative assignment of the *n* Sn NNN shown.

to 0.75. A similar splitting was observed for compositions $x$ = 1.2 and 0.8 in the original $Y_2Sn_xTi_{2-x}O_7$ series,[71,89] although the exact origin of this has yet to be conformed conclusively.

### 5.5.2.2 $^{119}$Sn MAS NMR spectra

The $^{119}$Sn MAS NMR spectra of $Y_2Sn_xTi_{2-x}O_7$ are shown in Figure 5.8, with the spectrum for $Y_2Sn_2O_7$ ($x = 2$), containing one sharp resonance at –582 ppm, characteristic of six coordinate Sn, and in good agreement with previous $^{119}$Sn NMR studies.[77,78] The result of Ti incorporation can be seen in the $^{119}$Sn spectrum of $Y_2Sn_{1.75}Ti_{0.25}O_7$, which exhibits two additional peaks at a lower (upfield) chemical shift. Although these spectra compare well with those presented in previous $^{119}$Sn NMR studies of $Y_2Sn_xTi_{2-x}O_7$,[78] as the Ti content increases, the $^{119}$Sn spectra begin to appear very different to the corresponding $^{89}$Y spectra. Whereas the $^{89}$Y spectra (see Figure 5.7) contain a series of reasonably well-separated peaks, the $^{119}$Sn spectra are dominated by broad, overlapping lineshapes, with a maximum of three distinct resonances observed when $x$ = 1.75 to 1.25. From Figure 5.8 it can also be seen (most clearly at high $x$) that the unit cell contraction that accompanies Ti incorporation causes a downfield shift of the $^{119}$Sn resonances as $x$ decreases, the same effect seen in the $^{89}$Y spectra of $Y_2Sn_xTi_{2-x}O_7$, shown in Figure 5.7. As observed in previous work,[78] the extensive overlap means that most resonances in the $^{119}$Sn spectra, especially those for Ti-rich samples, cannot be confidently assigned to specific NNN environments, making these spectra more challenging to assign compared to the corresponding $^{89}$Y spectra.

### 5.5.2.3 $^{17}$O MAS NMR spectra

As shown in Figure 5.9, the $^{17}$O MAS NMR spectra of $Y_2Sn_2O_7$ and $Y_2Ti_2O_7$, both contain two distinct resonances, in good agreement with the $^{17}$O MAS NMR spectra in a previous study.[83] These resonances are attributed to the OY4 and OY2Sn2 environments in $Y_2Sn_2O_7$ and the OY4 and OY2Ti2 environments in $Y_2Ti_2O_7$. The $^{17}$O spectra of the $Y_2Sn_xTi_{2-x}O_7$ series, shown in Figure 5.9 reveal that while the position of the OY4 resonance ($O_{8a}$ site) remains relatively unchanged, as $x$ decreases, the OY2Sn2 peak is shifted slightly upfield (to a lower chemical shift), as is the peak for the OY2Ti2

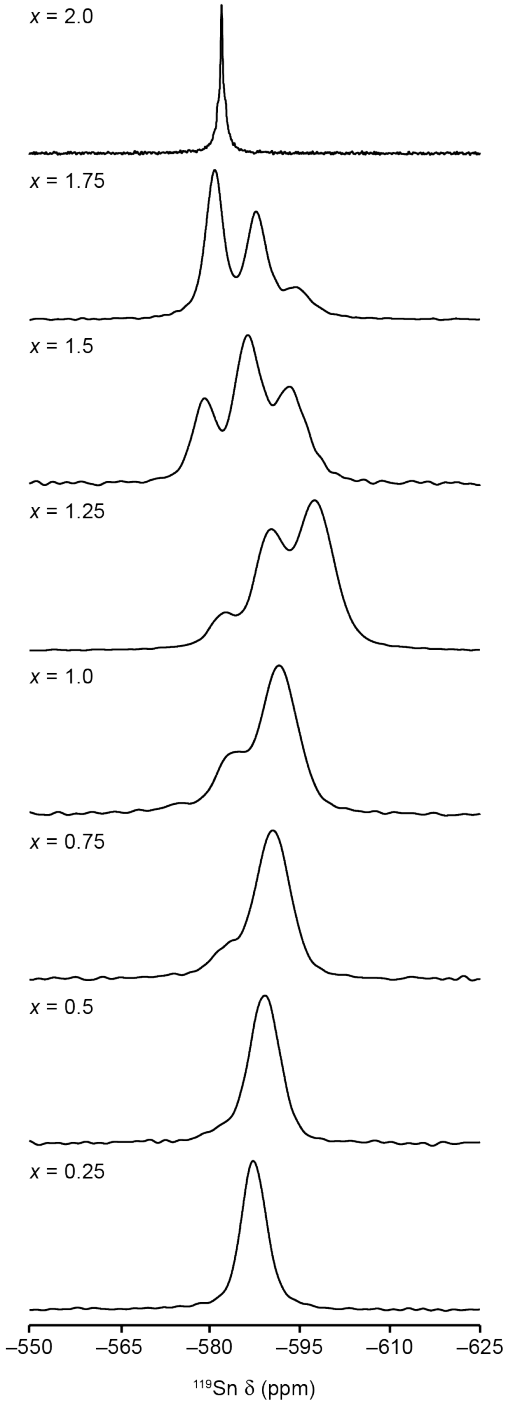


**Figure 5.8:** $^{119}$Sn (9.4 T, 14 kHz) MAS NMR spectra of $Y_2Sn_xTi_{2-x}O_7$.

environment. It can also be seen that as soon as Ti is introduced into $Y_2Sn_2O_7$, *i.e.*, when $x = 1.75$, an additional peak appears, growing in intensity as $x$ decreases further, and appearing to be most intense when $x = 1$, before decreasing with a further decrease in $x$. As this peak appears in the $^{17}$O spectra of all but the compositional end members, it was assigned to an

OY2SnTi environment, which of course only occurs when both Sn and Ti are present. The $^{17}O$ spectra also show that as the $Y_2Ti_2O_7$ end member composition is approached (as $x$ approaches 0) the OY2Ti2 peak becomes sharper, indicating the increase in long-range order.

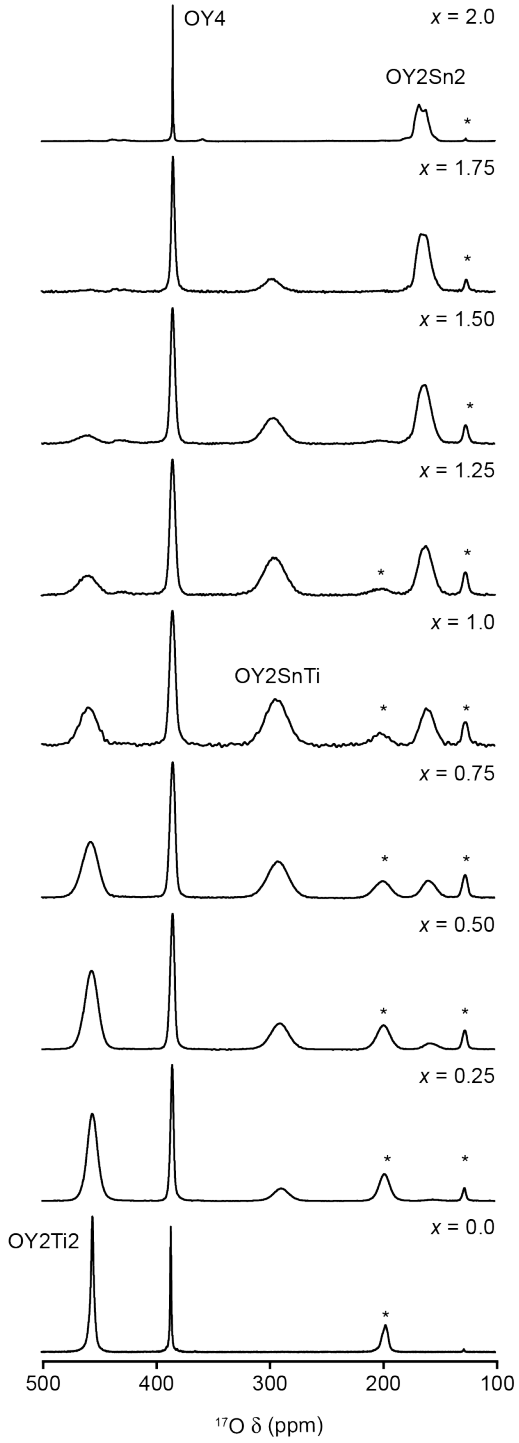


**Figure 5.9:** $^{17}O$ (14.1 T, 21 kHz) MAS NMR spectra of $Y_2Sn_xTi_{2-x}O_7$, showing the different O environments. Spinning sidebands denoted by asterisks (*).

### 5.5.3 Cluster models

The first step in the process of investigating how first-principles calculations can assist the assignment of the NMR spectra of $Y_2Sn_xTi_{2-x}O_7$ involved generating a series of structural models based on an approach detailed in previous studies,[73,78] but using a more recent version of CASTEP,[91] to take advantage of the various advances in DFT, including the development of new, more accurate and transferrable pseudopotentials, and the implementation of ZORA for the calculation of NMR parameters.[92,93]

In this approach, the NNN environment for a single cation (Y or Sn) is systemically varied, by constructing a series of models, each with a different number and arrangement of Sn and Ti on the six NNN B sites, leading to 13 unique structural models. To generate a series of Y-centred models, the $Y_2Sn_2O_7$ unit cell[8] was used, with the environment of one Y atom varied, as shown in Figure 5.10a. The Sn cations on the six NNN B sites surrounding the selected Y are then systematically substituted for Ti, leading to a set of structures with different numbers of Sn NNN and arrangements of these. This approach results in 13 unique structures based on $Y_2Sn_2O_7$ as shown in Figure 5.10b, (a series subsequently referred to as Y-centred, Sn-rich models). This process was repeated using the $Y_2Ti_2O_7$ unit cell,[90] leading to 13 Y-centred Ti-rich models, and a total of 26 structural models.

An equivalent series of Sn-rich and Ti-rich Sn-centred structural models were generated, again starting from either $Y_2Sn_2O_7$ or $Y_2Ti_2O_7$, but now systematically varying the NNN environment of a selected Sn cation. As Ti occupies all the B sites in $Y_2Ti_2O_7$, the first step in constructing the Ti-rich models, involved an initial substitution of one Ti for Sn, before the NNN environment of this Sn species was then systematically modified. In the Y-centred clusters the six NNN B sites are arranged in a hexagon around the Y (*i.e.*, all lie in a similar structural plane), making it straightforward to represent the NNN arrangements using a two-dimensional projection, as shown in Figure 5.10b. As the six NNN B sites in the Sn-centred cluster form a triangular antiprism, with three cations above and three cations below the

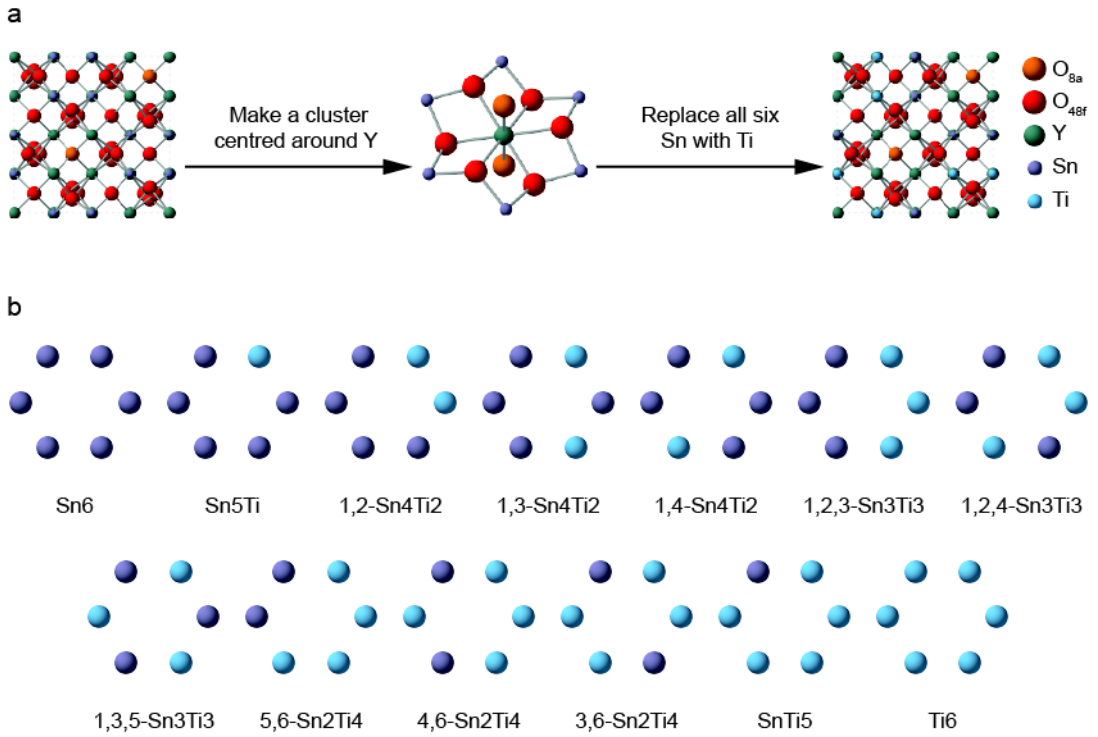


**Figure 5.10:** (a) Schematic showing the modification of the NNN environment of a single Y species in $Y_2Sn_2O_7$ to give a Y-centred cluster within the final unit cell. (b) Two-dimensional projection of the 13 unique ways of arranging Sn and Ti cations on the NNN B sites surrounding Y.

central Sn, each in a triangular arrangement (see Figure 5.2b), the Sn-centred cluster must be orientated to show the six B site cations in the same two-dimensional representation as seen for the Y-centred clusters. This involves aligning the Sn-centred cluster along the three-fold rotation axis. As shown in Figure 5.11, reorientation causes the six NNN B site cations to appear in a hexagonal arrangement around the central Sn, allowing the same numbering system, *i.e.*, 1,2,3-, 1,2,4- or 1,3,5-Sn3Ti3, to be used for both Y-centred and Sn-centred cluster models. However, it is important to note that in the two-dimensional representation of the 1,3,5-Sn3Ti3 arrangement shown in Figure 5.11, the cations on adjacent NNN positions, *e.g.*, position 1 and position 2, are actually on different faces of the triangular antiprism, with the cations on positions 3 and 5 on the same face as the cation on position 1. Figure 5.12 shows how the bond angle between two cations on the NNN B sites, joined through the central atom (Y or Sn) differs depending on whether a Y-centred or an Sn-centred cluster is being considered.

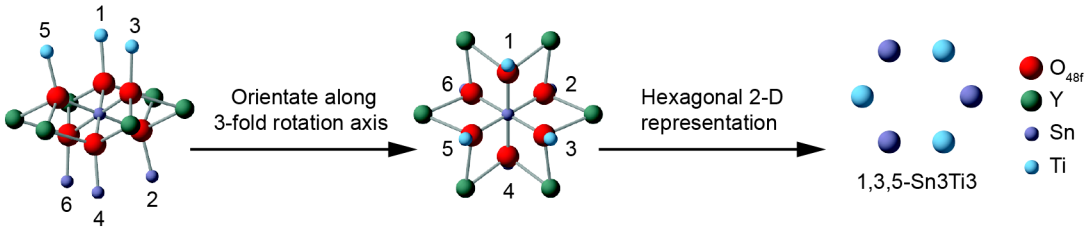


**Figure 5.11:** Schematic showing how an Sn-centred cluster is orientated such that the same NNN nomenclature for the Y-centred models can be used for the Sn-centred models.

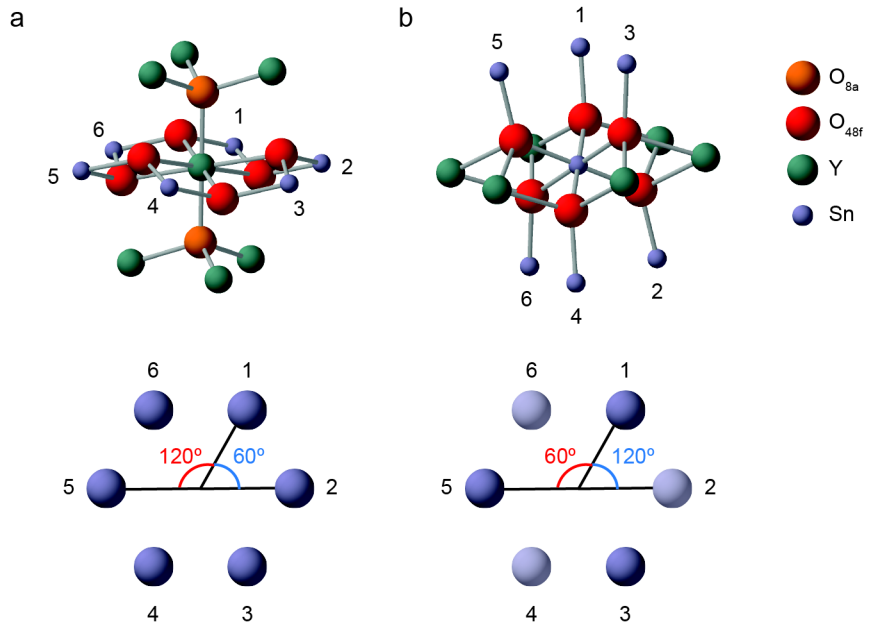


**Figure 5.12:** The local environment of (a) a Y-centred and (b) a Sn-centred cluster model, with a two-dimensional representation of the NNN B site arrangement, showing the bond angles linking cations on positions 1 and 2, and positions 1 and 5 (same as the angle between positions 1 and 3) to one another in three-dimensions, *i.e.*, through the central atom (note the central cation (Y or Sn) is not shown). In (b) the three cations on positions 2, 4 and 6 have been faded to represent them being arranged below the central Sn, whereas the three cations on positions 1, 3 and 5 are arranged above the central cation.

In summary, by manually modifying the $Y_2Sn_2O_7$ and $Y_2Ti_2O_7$ structures, a series of structural models designed to investigate how the systematic change in *n* Sn NNN environment effects the calculated NMR parameters. These models consist of 13 Y-centred Sn-rich, 13 Y-centred Ti-rich, 13 Sn-centred Sn-rich and 13 Sn-centred Ti-rich structures, giving a total of 52 unique models, each of which can be investigated separately.

All first-principles calculations were performed using CASTEP 8.0, with an $E_{cut}$ of 60 Ry, a k-point spacing of 0.04 $2\pi$ Å$^{-1}$ (see Appendix A1 for convergence testing), the PBE $E_{XC}$ functional,[94] default on-the-fly ultrasoft pseudopotentials,[95] a `geom_energy_tol` value of $1 \times 10^{-4}$ eV / atom and an `elec_energy_tol` value of $1 \times 10^{-5}$ eV / atom used (see Table 3.5 for a definition of `geom_energy_tol` and `elec_energy_tol`, which are also discussed in detail in Section 5.5.1.4). The CASTEP 8.0 convergence criteria used were $5 \times 10^{-2}$ eV / Å, $1 \times 10^{-3}$ Å and $1 \times 10^{-1}$ GPa for the maximum forces, atomic displacement and stress, respectively. All structural models were geometry optimised to reduce the forces acting upon the atoms, with the subsequent calculations of NMR parameters carried out using ZORA correction. As described in Chapter 3, a reference shielding ($\sigma_{ref}$) was used to convert calculated isotropic shieldings ($\sigma_{iso}$) to isotropic shifts ($\delta_{iso}$). For $^{89}$Y a comparison of $\sigma_{iso}$ and $\delta_{iso}$ for the two Y sites in $Y_2O_3$ gave a $\sigma_{ref}$ of 2705.64 ppm. For $^{119}$Sn a comparison of $\sigma_{iso}$ and $\delta_{iso}$ for the single Sn site in $Y_2Sn_2O_7$ gave a $\sigma_{ref}$ of 2601.93 ppm. However, in order to provide better agreement with experimental NMR measurements, the calculated $^{89}$Y $\delta_{iso}$ and $\Omega$ values were scaled by comparing the calculated and experimental NMR parameters for $Y_2Sn_2O_7$ and $Y_2Ti_2O_7$, *i.e.*, the two compositional end-members of the 26 Y-centred cluster models, as described in Appendix A2. Calculated NMR parameters were analysed using in-house Python scripts extending the CCP-NC MagresPython module.[96]

The calculated $^{89}$Y $\delta_{iso}$ for all Y cations in each Y-centred cluster models are plotted as a function of *n* Sn NNN in Figure 5.13a, with the points coloured according to model set, *i.e.*, Sn-rich or Ti-rich structural models in Figure 5.13b. Figure 5.13 indicates that the incorporation of Ti, *i.e.*, a decrease in *n* Sn NNN, is accompanied by a noticeable (~15 ppm) upfield shift. There is also little overlap between calculated $^{89}$Y $\delta_{iso}$ for Y with different *n* Sn NNN, in agreement with previous first-principles calculations[73] and supporting the initial assignment of the $^{89}$Y MAS NMR spectra of $Y_2Sn_xTi_{2-x}O_7$.[71] While there is a generally clear, systematic change in calculated $^{89}$Y $\delta_{iso}$ with decreasing *n*,

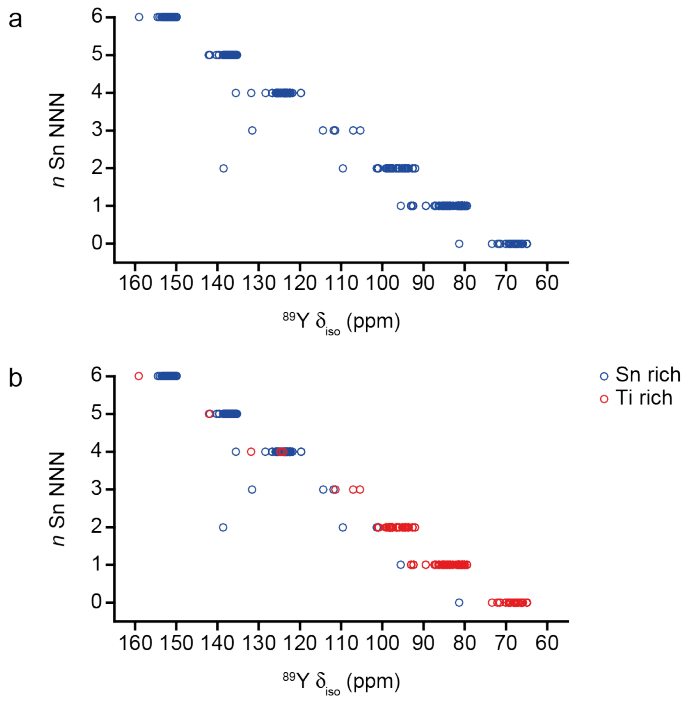


**Figure 5.13:** Plot of (a) calculated $^{89}$Y $\delta_{iso}$ as a function of *n* Sn NNN for the 26 Y-centred cluster models of $Y_2Sn_xTi_{2-x}O_7$, and (b) with the data points coloured by the model type.

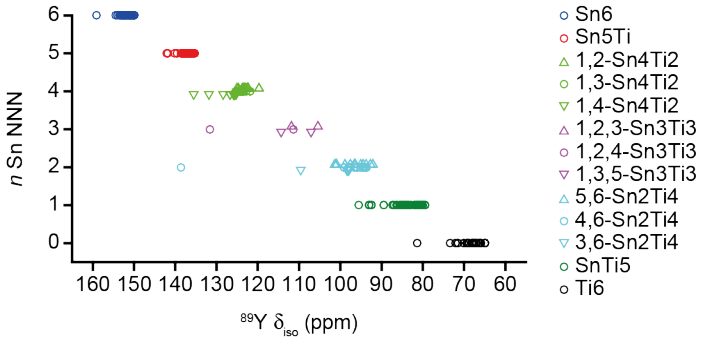


**Figure 5.14:** Plot of calculated $^{89}$Y $\delta_{iso}$ as a function of *n* Sn NNN for the 26 Y-centred cluster models of $Y_2Sn_xTi_{2-x}O_7$, with the type of NNN environment indicated. For *n* Sn NNN = 4, 3 and 2, data points for the different arrangements have been vertically offset to facilitate comparison.

Figure 5.13 shows several outlying points, for Y with Sn3Ti3 or Sn2Ti4 NNN environments. Figure 5.14 shows calculated $^{89}$Y $\delta_{iso}$ plotted as a function of *n* Sn NNN, with the data points coloured by *n* and shaped according to the specific NNN arrangements (see Figure 5.10b), with the outlying points corresponding to Y with either a 1,2,4-Sn3Ti3 or a 4,6-Sn2Ti4 arrangement.

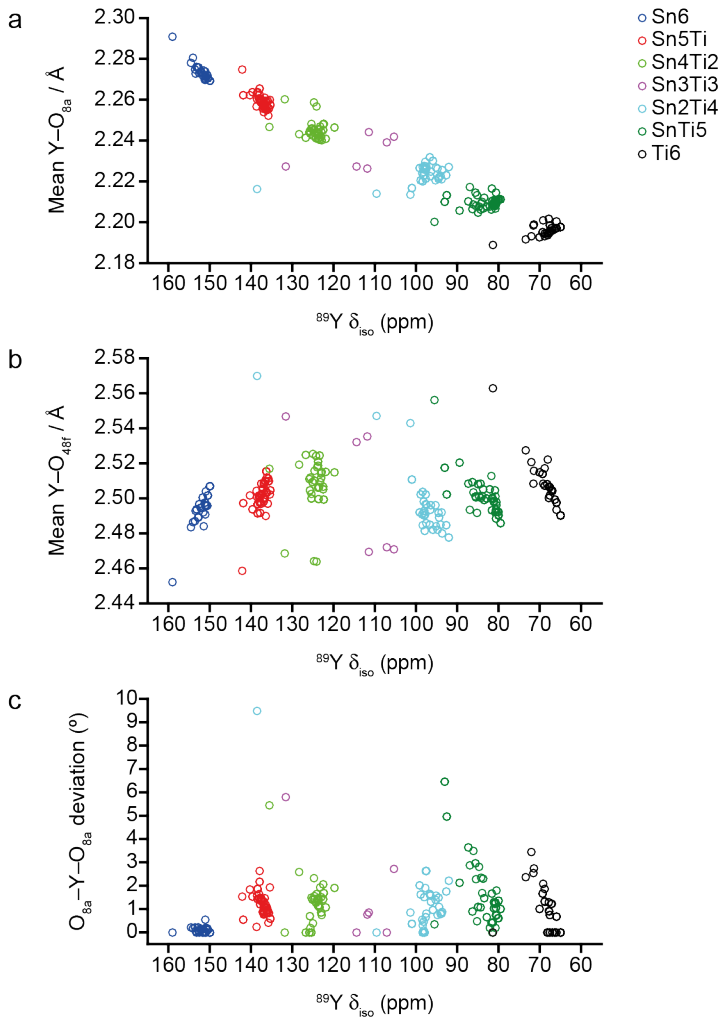


**Figure 5.15:** Plot of calculated $^{89}Y$ $\delta_{iso}$ as a function of (a) mean Y–$O_{8a}$ bond length, (b) mean Y–$O_{48f}$ bond length and (c) deviation of the$O_{8a}$–Y–$O_{8a}$ bond angle from 180°, for the 26 Y-centred cluster models of $Y_2Sn_xTi_{2-x}O_7$, with data points coloured by *n* Sn NNN.

Figure 5.15a shows that a systematic decrease in both calculated $^{89}Y$ $\delta_{iso}$ and mean Y–$O_{8a}$ bond length results from the successive substitution of Sn for Ti.

The data points for Y species with unexpectedly high $^{89}Y$ $\delta_{iso}$ have very, similar mean Y–$O_{8a}$ bond lengths to other Y with the same *n* Sn NNN indicating that this is determined primarily by the nature of the species occupying the six NNN B sites. When the calculated $^{89}Y$ $\delta_{iso}$ is plotted against the corresponding mean Y–$O_{48f}$ bond length, as shown in Figure 5.15b, there seems to be a general increase in mean bond length with increasing Ti incorporation. It also appears that the data points in Figure 5.15b can be split

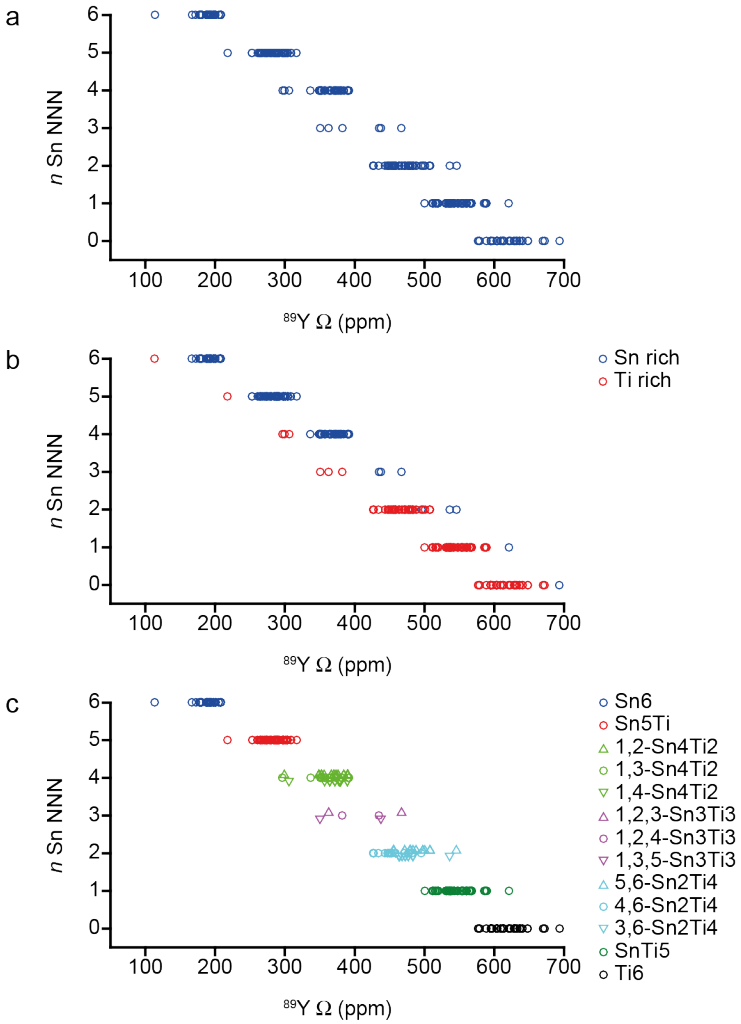


**Figure 5.16:** Plot of (a) calculated $^{89}$Y Ω as a function of *n* Sn NNN for 26 Y-centred cluster models of $Y_2Sn_xTi_{2-x}O_7$, with data points (b) coloured by model type and (c) shaped according to NNN cation arrangement. For *n* Sn NNN = 4, 3 and 2 in (c) the data points for the different NNN arrangements have been offset slightly to facilitate comparison.

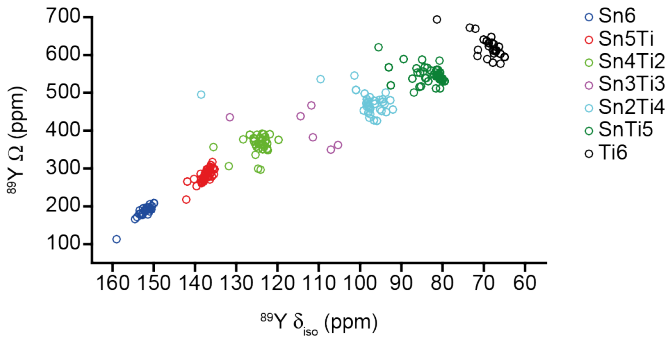


**Figure 5.17:** Plot of calculated $^{89}$Y Ω against calculated $^{89}$Y $\delta_{iso}$ for the 26 Y-centred cluster models of $Y_2Sn_xTi_{2-x}O_7$, with the data points coloured by *n* Sn NNN.

into two separate series, corresponding to the Sn-rich and Ti-rich structural models, respectively, with the latter exhibiting the shorter mean Y–$O_{48f}$ bond lengths irrespective of the *n* Sn NNN. In addition, Y with unusually high $^{89}$Y $\delta_{iso}$ have noticeably longer mean Y–$O_{48f}$ bonds compared to Y with the same *n* Sn NNN. As shown in Figure 5.15c, the strongest correlation seems to be between calculated $^{89}$Y $\delta_{iso}$ and the deviation in the $O_{8a}$–Y–$O_{8a}$ bond angle from 180°, the angle in an ideal pyrochlore structure.

From Figure 5.16a, it is apparent that as seen for $^{89}$Y $\delta_{iso}$, as the number of Sn NNN decreases, $^{89}$Y Ω increases, with Sn-rich structural models yielding the

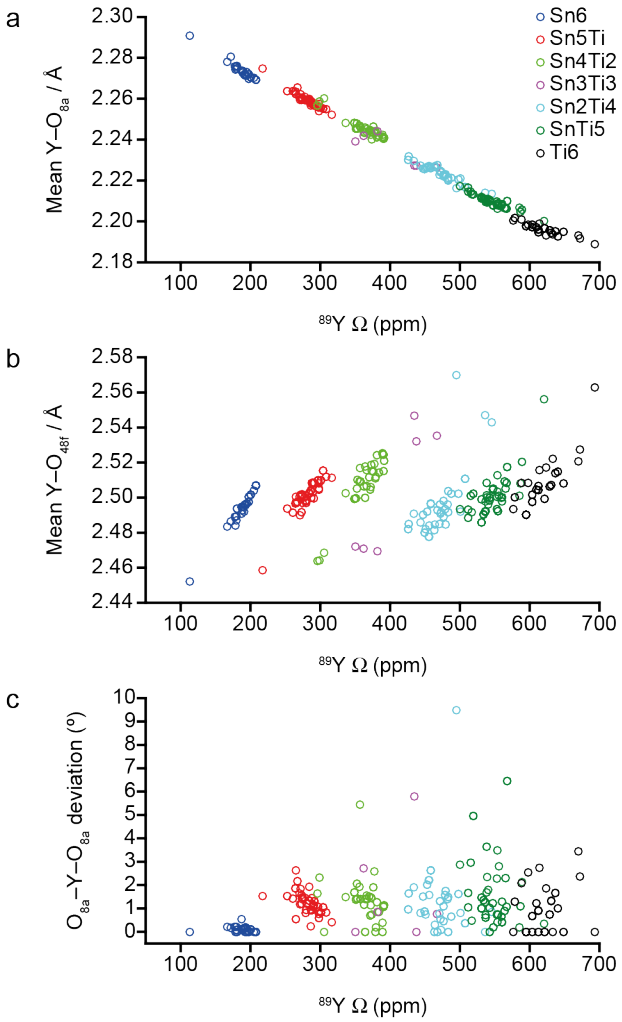


**Figure 5.18:** Plot of calculated $^{89}$Y Ω as a function of (a) mean Y–$O_{8a}$ bond length, (b) mean Y–$O_{48f}$ bond length and (c) deviation of the $O_{8a}$–Y–$O_{8a}$ bond angle from 180°, for the 26 Y-centred cluster models of $Y_2Sn_xTi_{2-x}O_7$, with the data points coloured by *n* Sn NNN.

largest values, particularly apparent for the Sn3Ti3 NNN environments, as shown in Figure 5.16b. Environment with *n* Sn NNN have a reasonably well-defined predicted range of $^{89}$Y Ω, with this parameter appearing to be a reasonably sensitive probe of changes in the NNN environment. However, as shown in Figure 5.16c, calculated $^{89}$Y Ω for different arrangements of cations for a particular value of *n*, *i.e.*, 1,2-Sn4Ti2, 1,3-Sn4Ti2 and 1,4-Sn4Ti2, are too similar to allow them to be separated using this NMR parameter alone. As shown in Figure 5.17, when both the calculated $^{89}$Y $\delta_{iso}$ and Ω are considered simultaneously, it can be seen that each environment with *n* Sn NNN generally has a reasonably well-defined range for both NMR parameters, although several Y have noticeably high $^{89}$Y $\delta_{iso}$, despite $^{89}$Y Ω being well within the expected range for that particular *n* Sn NNN environment.

The relationship between calculated $^{89}$Y Ω and local geometrical parameters for the 26 Y-centred cluster models have also been investigated, as shown in Figure 5.18, with Figure 5.18a highlighting a very strong correlation between mean Y–$O_{8a}$ bond length and $^{89}$Y Ω. Figure 5.18b shows that irrespective of *n* Sn NNN, Y in Sn-rich models have longer mean Y–$O_{48f}$ bond lengths, resulting in an increase in $^{89}$Y Ω. In contrast to $^{89}$Y $\delta_{iso}$, Figure 5.18c indicates that there is no strong correlation between the $O_{8a}$–Y–$O_{8a}$ bond angle deviation from 180° and $^{89}$Y Ω, with even significant angle variations of up to ~10° having little effect on Ω. This suggests that the magnitude of $^{89}$Y Ω is dominated by *n*, with the deviation in $O_{8a}$–Y–$O_{8a}$ bond angle having little effect on this NMR parameter. Something evident in all three of the plots in Figure 5.18 is that as *n* decreases, the overlap in $^{89}$Y Ω for neighbouring environments increases, with the largest range of $^{89}$Y Ω seen for the Sn2Ti4, SnTi5 and Ti6 environments.

How the predicted $^{119}$Sn NMR parameters for the 26 Sn-centred cluster models vary with local geometry has also been investigated. When calculated $^{119}$Sn $\delta_{iso}$ is plotted as a function of *n* Sn NNN (see Figure 5.19), it is apparent that as NNN Ti content increases, the range of $^{119}$Sn $\delta_{iso}$ for Sn with

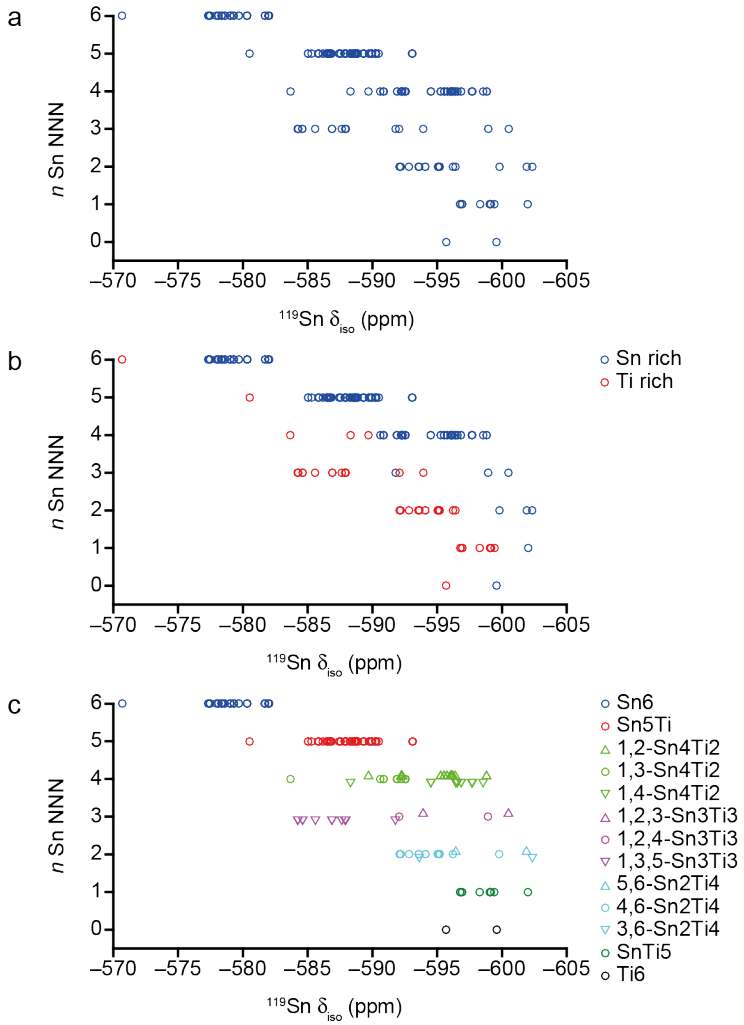


**Figure 5.19:** Plot of (a) calculated $^{119}$Sn $\delta_{iso}$ as a function of *n* Sn NNN for the 26 Sn-centred cluster models of $Y_2Sn_xTi_{2-x}O_7$, with the data points (b) coloured by model type and (c) shaped by NNN arrangement. For *n* Sn NNN = 4, 3 and 2 in (c) the data points for the different arrangements have been offset slightly, to facilitate comparison.

different *n* begin to converge, with significant overlap seen for all but the *n* = 6 (Sn6) environment. This significant overlap in $^{119}$Sn $\delta_{iso}$ for species with different *n* Sn NNN is generally consistent with the appearance of the $^{119}$Sn MAS NMR spectra of $Y_2Sn_xTi_{2-x}O_7$, shown in Figure 5.8, which are dominated by a maximum of three, very broad resonances. This perhaps indicates that in comparison to $^{89}$Y $\delta_{iso}$, the $^{119}$Sn $\delta_{iso}$ is relatively more strongly affected by the unit cell contraction caused by Ti incorporation, *i.e.*, the upfield shift associated with the incorporation of subsequent Ti is roughly balanced by the downfield shift caused by the unit cell contraction. When, as shown in

Figure 5.19c, the data points are separated according to specific NNN arrangements, it is apparent that, in general, ranges of $^{119}$Sn $\delta_{iso}$ for environments that have the same *n* but different cation arrangements, *i.e.*, 1,2-Sn4Ti2, 1,3-Sn4Ti2 and 1,4-Sn4Ti2, overlap significantly. The only exception to this seems to be is the 1,3,5-Sn3Ti3 arrangement, where the three NNN Sn cations occupy the same face of the Sn-centred antiprism, with the three Ti occupying the opposite face (see Figure 5.11), leading to an increase in $^{119}$Sn $\delta_{iso}$, over that seen for 1,2,3- or 1,2,4-Sn3Ti3 environments. It should, however, be noted that there are a relatively small number of structural models considered for some environment types, which may pose a particular problem when defining a typical range for a parameter. The extensive overlap in calculated $^{119}$Sn $\delta_{iso}$ for Sn-centred structural models indicates that it will not be possible to unambiguously assign resonances in the $^{119}$Sn MAS NMR spectra for many $Y_2Sn_xTi_{2-x}O_7$ compositions.

The relationship between calculated $^{119}$Sn $\delta_{iso}$ and the mean Sn–$O_{48f}$ bond

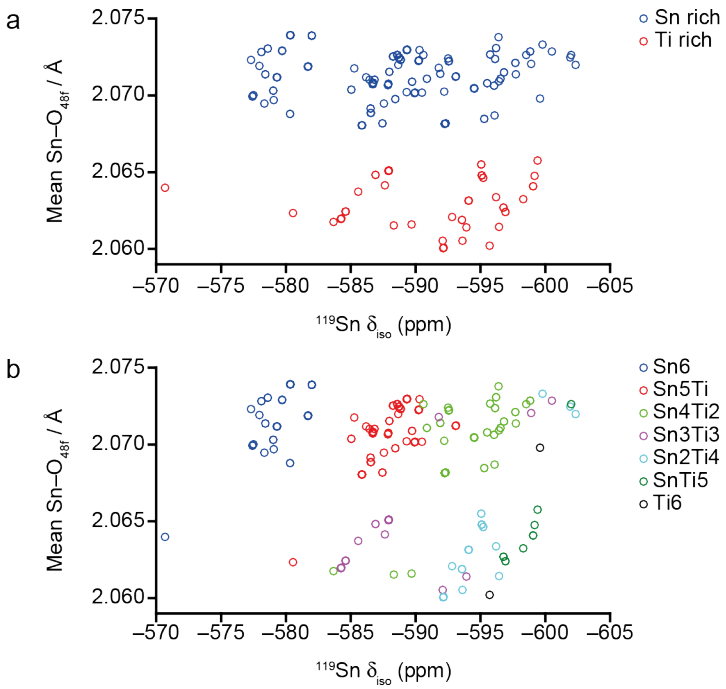


**Figure 5.20:** Plot of calculated $^{119}$Sn $\delta_{iso}$ as a function of mean Sn–$O_{48f}$ bond length for the 26 Sn-centred cluster models of $Y_2Sn_xTi_{2-x}O_7$, with the data points coloured by (a) model type and (b) *n* Sn NNN.

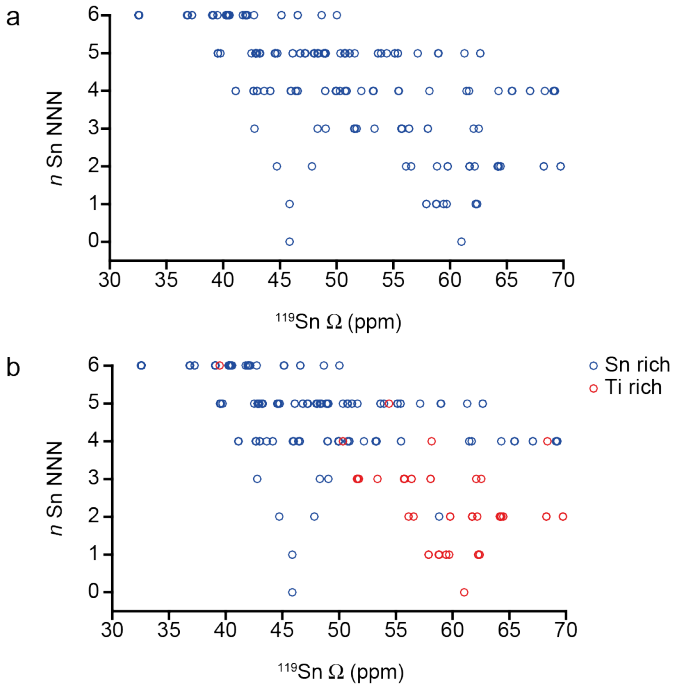


**Figure 5.21:** Plot of calculated $^{119}$Sn Ω as a function of *n* Sn NNN for the 26 Sn-centred cluster models of $Y_2Sn_xTi_{2-x}O_7$, with (b) the data points coloured by model type.

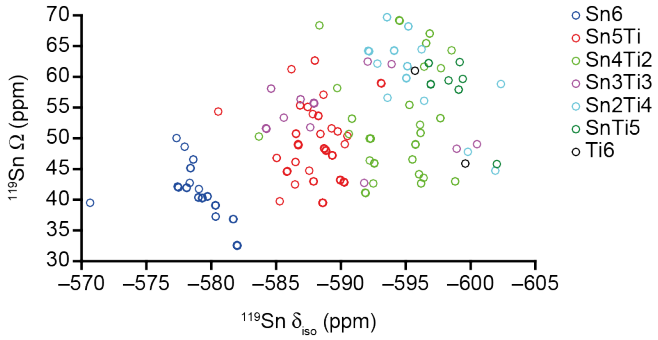


**Figure 5.22:** Plot of calculated $^{119}$Sn Ω against calculated $^{119}$Sn $\delta_{iso}$ for the 26 Sn-centred cluster models of $Y_2Sn_xTi_{2-x}O_7$, with the data points coloured by *n* Sn NNN.

length has also been considered, with Figure 5.20a showing that the mean Sn–$O_{48f}$ bond length is significantly different in the Sn-rich and Ti-rich structural models, with the latter having much shorter bond lengths. Figure 5.20b indicates that within each model type, the mean Sn–$O_{48f}$ bond lengths are very similar for all environments with the same *n* Sn NNN. Figure 5.21 shows that there is an increase in $^{119}$Sn Ω with decreasing *n*, but that (unlike for $^{89}$Y, as shown in Figure 5.16), the range of Ω values predicted also increases, and there is significant overlap between ranges observed for

environments with different values of *n*. Indeed, there appears to be more overlap in $^{119}$Sn Ω than in $^{119}$Sn $\delta_{iso,}$ as shown in Figure 5.19, meaning that this anisotropic NMR parameter is less sensitive to small variations in local geometry than the isotropic component of the shielding tensor. As shown in Figure 5.22, considering the combination of calculated $^{119}$Sn $\delta_{iso}$ and Ω values is not sufficient to separate Sn species according to specific *n* Sn NNN environments, supporting the assumption that the broad resonances seen in many of the $^{119}$Sn MAS NMR spectra of $Y_2Sn_xTi_{2-x}O_7$ (see Figure 5.8) result from overlap between peaks from Sn species with different NNN B-site environments.

The Y- and Sn-centred cluster models provide good insight into the relationship between predicted NMR parameters and changes in local geometry, helping to explain many of the observations made from the $^{89}$Y and $^{119}$Sn MAS NMR spectra of $Y_2Sn_xTi_{2-x}O_7$. For example, the calculated $^{89}$Y $\delta_{iso}$ for the Y-centred structural models show a systematic decrease in shift with increasing Ti content on the NNN B site. This confirms that the additional resonances upfield of the peak seen in the $^{89}$Y MAS NMR spectrum of $Y_2Sn_2O_7$, which appear when Ti is introduced, can be attributed to Y with different *n* Sn NNNs, generally supporting the initial assignment of the $^{89}$Y MAS NMR spectra for $Y_2Sn_xTi_{2-x}O_7$.[71] It was also shown that the small number of Y species that seemed to have anomalously high $\delta_{iso}$, have noticeably longer mean Y–$O_{48f}$ bond lengths and a much more distorted $O_{8a}$–Y–$O_{8a}$ bond angle than other Y with the same *n* Sn NNN. The decrease in *n* Sn NNN also results in a systematic increase in calculated $^{89}$Y Ω, a parameter that also showed a strong correlation with mean Y–$O_{8a}$ bond length, as reported in previous studies of $Y_2Sn_xTi_{2-x}O_7$ pyrochlores.[74]

The calculated $^{119}$Sn NMR parameters for the Sn-centred cluster models also provide information relating to the structure of $Y_2Sn_xTi_{2-x}O_7$ pyrochlores, with the significant overlap in calculated $^{119}$Sn $\delta_{iso}$ and Ω helping to explain the appearance of the $^{119}$Sn MAS NMR spectra of these materials (see Figure 5.8). First-principles calculations indicate that the broad resonances in the

$^{119}$Sn NMR spectra result from Sn species with different *n* Sn NNN having very similar $^{119}$Sn NMR parameters, causing them to overlap significantly and ultimately making it impossible to unambiguously assign the signals seen experimentally for the majority of the $^{119}$Sn MAS NMR spectra of $Y_2Sn_xTi_{2-x}O_7$.

Although the cluster models generally provide valuable insight into the NMR spectra of $Y_2Sn_xTi_{2-x}O_7$ pyrochlores, they are a very simplistic representation of the disorder in these systems. Indeed, localising structural changes around only one atom (Y or Sn), with the longer-range structure still resembling either $Y_2Sn_2O_7$ or $Y_2Ti_2O_7$ may introduce undesirable, and possibly unrealistic structural constraints, that could negatively impact the accuracy and reliability of the predicted NMR parameters. The structural constraints imposed by the cluster models could be responsible for the large deviation in $O_{8a}$–Y–$O_{8a}$ bond angles away from 180°, seen for several Y species in the Y-centred models, and in turn the extreme, downfield $^{89}$Y $\delta_{iso}$ that result. These observations raise the question of whether more realistic structural models are required, and if so, could they provide insight into the relationship between local geometry and predicted NMR parameters that could be used to guide a more detailed assignment of the NMR spectra of $Y_2Sn_xTi_{2-x}O_7$.

### 5.5.4 Models with randomised B-site cations

In an attempt to generate structural models that more closely resemble the disordered $Y_2Sn_xTi_{2-x}O_7$ pyrochlores, with B-site cation disorder is not limited to the six NNN sites surrounding a single Y or Sn, an in-house Fortran90 script was written to randomise Sn and Ti cations over the 16 B sites in a single pyrochlore unit cell. As with the cluster models described above, this approach involved starting from an initial ideal and ordered pyrochlore structure, namely $Y_2Sn_2O_7$[8] or $Y_2Ti_2O_7$.[90] Five individual $Y_2Sn_xTi_{2-x}O_7$ compositions, $x$ = 1.5, 1.25, 1, 0.75 and 0.5, were chosen, with $Y_2Sn_2O_7$ used as the input structure for $x$ = 1.5 and 1.25 models and $Y_2Ti_2O_7$ used for

**Table 5.2:** Summary of the randomised structural models of $Y_2Sn_xTi_{2-x}O_7$, generated using an in-house script.

| $x$ $Y_2Sn_xTi_{2-x}O_7$ | Number of Sn | Number of Ti | Input structure | $a$ / Å | Number of structures generated |
|---|---|---|---|---|---|
| 1.5 | 12 | 4 | $Y_2Sn_2O_7$ | 10.3725 | 20 |
| 1.25 | 10 | 6 | $Y_2Sn_2O_7$ | 10.3725 | 20 |
| 1.0 | 8 | 8 | $Y_2Ti_2O_7$ | 10.1385 | 20 |
| 0.75 | 6 | 10 | $Y_2Ti_2O_7$ | 10.0949 | 20 |
| 0.5 | 4 | 12 | $Y_2Ti_2O_7$ | 10.0949 | 20 |

the remaining compositions ($x$ = 1, 0.75 and 0.5). A total of twenty structures were generated for each composition, with Sn and Ti randomly assigned to B sites. For example, for the $x$ = 1.5 structural models, using the fractional atomic coordinates and unit cell lengths for $Y_2Sn_2O_7$, the script randomly positioned 12 Sn and 4 Ti on the 16 B sites. This was repeated twenty times, giving structures with the same composition but different B-site cation arrangements. For the $x$ = 1 structures, the original $Y_2Ti_2O_7$ unit cell length, $a$, was increased from 10.0949 Å to 10.1385 Å, in an attempt to account for eight Ti being substituted for eight larger, Sn cations, in an attempt to increase the efficiency of the geometry optimisation. A summary of the randomised models, including the initial unit cell used to generate the structures and the specific B-site compositions investigated, is given in Table 5.2.

All first-principles calculations were performed using CASTEP 8.0, with an $E_{cut}$ of 60 Ry, a k-point spacing of 0.04 2π Å$^{-1}$ (see Appendix A1 for convergence testing), the PBE $E_{XC}$ functional,[94] default on-the-fly ultrasoft pseudopotentials,[95] a `geom_energy_tol` value of 1 × 10$^{-4}$ eV / atom and an `elec_energy_tol` value of 1 × 10$^{-5}$ eV / atom used. The CASTEP 8.0 convergence criteria used were 5 × 10$^{-2}$ eV / Å, 1 × 10$^{-3}$ Å and 1 × 10$^{-1}$ GPa for the maximum forces, atomic displacement and stress, respectively. All structural models were geometry optimised to reduce the forces acting on the atoms, with the subsequent calculation of the NMR parameter carried out with ZORA correction applied. The reference shielding values discussed in

Section 5.5.3 were used to convert calculated $^{89}$Y and $^{119}$Sn $\sigma_{iso}$ to $\delta_{iso}$, and the same scaling approach was applied to calculated $^{89}$Y $\delta_{iso}$ and $\Omega$ (see Appendix A2). A comparison of the calculated chemical shielding and experimental chemical shift values for the two O sites in both $Y_2Sn_2O_7$ and $Y_2Ti_2O_7$ were used to convert calculated $^{17}$O $\sigma_{iso}$ to $\delta_{iso}$. See Appendix A3 for a full description of this process. In this section only the magnitude of the $^{17}$O $C_Q$ value is considered.

The changes in calculated $^{89}$Y $\delta_{iso}$ and $\Omega$ that accompany a decrease in the number *n* of Sn NNN are in good agreement with those seen for the Y-centred cluster models (see Figures 5.13 and 5.16), with this decrease resulting in an upfield shift of $^{89}$Y $\delta_{iso}$ and an increase in $^{89}$Y $\Omega$, as shown in Figure 5.23. From Figure 5.23a it is clear that when *n* Sn NNN < 4, the range of calculated $^{89}$Y $\delta_{iso}$ for Y species with the same *n* Sn NNN is very large, extending into regions of chemical shift more typical of neighbouring, more Sn rich NNN environments. The presence of a number of Y species with more extreme downfield $^{89}$Y $\delta_{iso}$ moved downfield suggests that the few seemingly outlying points present in the corresponding plots for the Y-centred cluster models are far from rare in the 100 randomised B-site cation structural models. Importantly, the significant overlap in $^{89}$Y $\delta_{iso}$ for Y species with different *n* Sn NNN environments shown in Figure 5.23a could suggest that the relative intensities of individual resonances in the $^{89}$Y MAS NMR spectra of $Y_2Sn_xTi_{2-x}O_7$ (see Figure 5.7) do not give an accurate representation of the true ratio of different *n* Sn NNN environments present in the real materials,, *i.e.*, intensity from multiple Y environment could be contributing to a single resonance. In contrast to the large range in $^{89}$Y $\delta_{iso}$ for Y cations with Ti-rich NNN environments, Figure 5.23b shows that there is a steady increase in calculated $^{89}$Y $\Omega$ with the systematic substitution of Sn for Ti. These observations are in good agreement with the calculated $^{89}$Y $\Omega$ for the Y-centred cluster models shown in Figure 5.16.

As illustrated in Figure 5.24, when both calculated $^{89}$Y $\Omega$ and $\delta_{iso}$ parameters

are considered simultaneously, it is quite clear that while there is a range of $^{89}$Y $\delta_{iso}$ for environments where *n* Sn NNN < 4, the $^{89}$Y Ω remains reasonably similar for environments with *n* Sn NNN, even if $^{89}$Y $\delta_{iso}$ is at the more extreme end of the range observed. One possible explanation for this increase in the range of $^{89}$Y $\delta_{iso}$ seen for Y environments with a low number of Sn NNN could be the significant size difference between Sn and Ti. Ti may be less able to satisfactorily occupy the B site compared to the larger Sn cation,

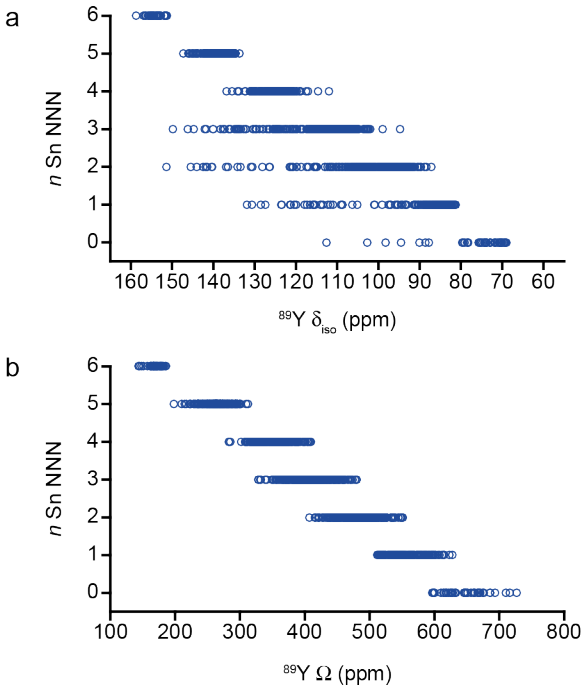


**Figure 5.23:** Plot of calculated $^{89}$Y (a) $\delta_{iso}$ and (b) Ω as a function of *n* Sn NNN for the 100 randomised structural models of $Y_2Sn_xTi_{2-x}O_7$.

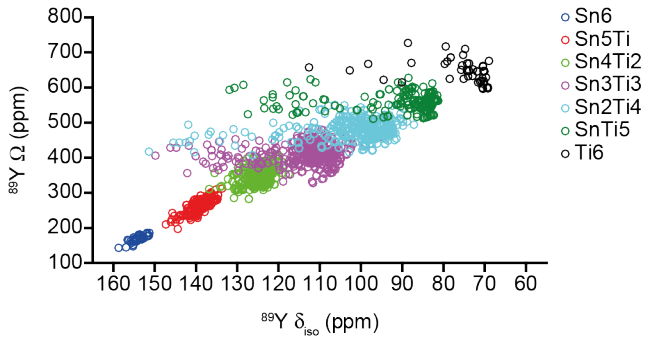


**Figure 5.24:** Plot of calculated $^{89}$Y Ω against calculated $^{89}$Y $\delta_{iso}$ for the 100 randomised structural models of $Y_2Sn_xTi_{2-x}O_7$, with data points coloured by *n* Sn NNN.

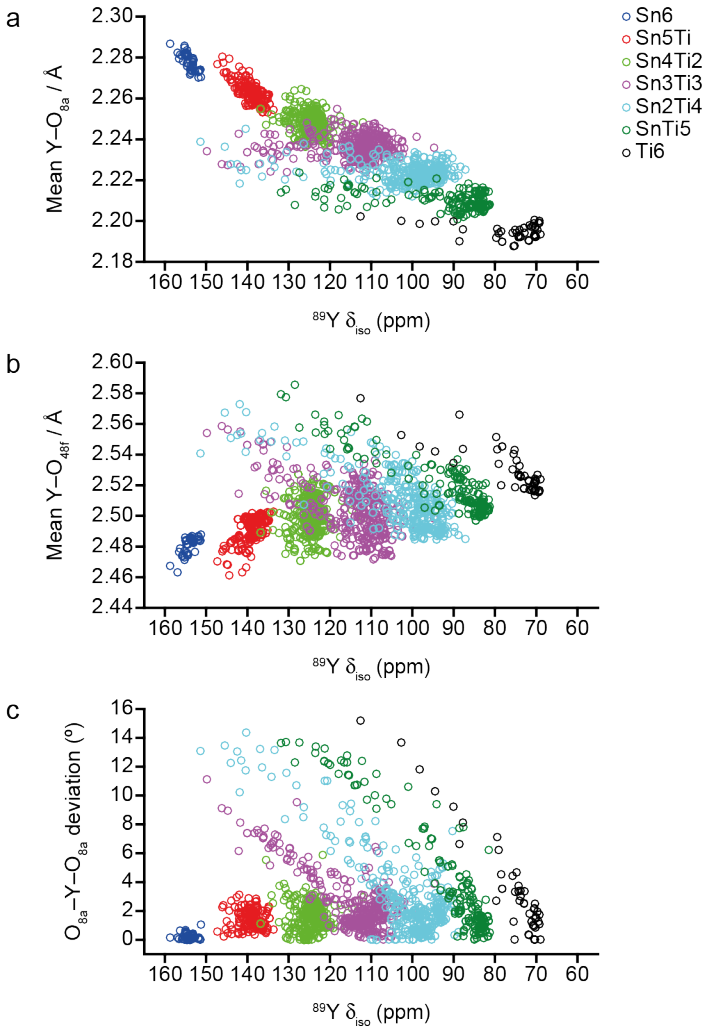


**Figure 5.25:** Plot of calculated $^{89}Y$ $\delta_{iso}$ as a function of (a) mean Y–$O_{8a}$ bond length, (b) mean Y–$O_{48f}$ bond length and (c) deviation of the $O_{8a}$–Y–$O_{8a}$ bond angle from 180°, for the 100 randomised structural models of $Y_2Sn_xTi_{2-x}O_7$, with data points coloured by *n* Sn NNN.

with the former possibly unable to provide the same level of bonding stability to the surrounding atoms, allowing for more structural flexibility, ultimately leading to a larger variation in $^{89}Y$ $\delta_{iso}$ for Ti-rich environments.

For the randomised models, the relationship between calculated $^{89}Y$ $\delta_{iso}$ and mean Y–O bond lengths is very similar to those seen for the 26 Y-centred cluster models (see Figure 5.15). Figure 5.25a shows that decreasing *n* Sn NNN results in a decrease in the mean Y–$O_{8a}$ bond length. However, for Y with the same *n*, this mean bond length is very similar, demonstrating that there is little correlation between $^{89}Y$ $\delta_{iso}$ and mean Y–$O_{8a}$ bond length.

The Y species with more extreme calculated $^{89}$Y $\delta_{iso}$ relative to other Y species with the same *n* Sn NNN do however, seem to have a slightly longer mean Y–$O_{48f}$ bond length, as shown in Figure 5.25b. It can also be seen that longer mean Y–$O_{48f}$ bond lengths are observed for Y with lower *n* Sn NNN, *i.e.*, as the number of NNN B sites occupied by Sn decreases, this mean bond length increases. This is likely due to the presence of shorter Ti–$O_{48f}$ bonds relative to Sn–$O_{48f}$ bonds, caused by the smaller ionic radii of $Ti^{4+}$ which forces the corresponding Y–$O_{48f}$ bonds to elongates as *n* Sn NNN decreases.

Although the small number of data points corresponding to Y with much higher than expected $^{89}$Y $\delta_{iso}$ (the small number of outlying points) in the Y-centred cluster models made it difficult to confidently identify a strong correlation between $\delta_{iso}$ and the deviation in the $O_{8a}$–Y–$O_{8a}$ bond angle from 180$^o$ (see Figure 5.15c), using the larger dataset resulting from the 1,600 Y species in the 100 randomised models, Figure 5.25c shows that these two parameters are strongly correlated. From Figure 5.25, Y with outlying $^{89}$Y $\delta_{iso}$ clearly have the most distorted local geometries, with Y in environments where $n < 4$ showing the largest ranges of $^{89}$Y $\delta_{iso}$, and biggest variation in local geometry. This indicates that as *n* Sn NNN decreases, the level of structural flexibility around Y increases, allowing the mean Y–$O_{48f}$ bond lengths and $O_{8a}$–Y–$O_{8a}$ bond angles to vary most significantly for Y with Ti-rich NNN environments.

The correlations seen between calculated $^{89}$Y Ω and structural parameters for the 100 randomised models look very similar to those seen for the 26 Y-centred cluster models (see Section 5.5.3), with Figure 5.26a showing a very strong correlation between $^{89}$Y Ω and mean Y–$O_{8a}$ bond length. Both the calculated $^{89}$Y Ω and the mean Y–$O_{48f}$ bond length increase as *n* Sn NNN decreases, with the $^{89}$Y Ω for Y with the same *n* appearing relatively similar, although as *n* decreases, the range of $^{89}$Y Ω observed, increases, likely reflecting the increase in structural flexibility that accompanies increased Ti substitution. Figure 5.26c suggests that there is no correlation between the

deviation in $O_{8a}$–Y–$O_{8a}$ bond angle 180° and calculated $^{89}$Y **Ω**, with all Y with the same *n* exhibiting similar $^{89}$Y **Ω**, irrespective of the degree of $O_{8a}$–Y–$O_{8a}$ bond angle distortion.

In general, the calculated $^{89}$Y NMR parameters for the 100 randomised models agree with those produced from the 26 Y-centred localised cluster models, as well as the results of previous studies.[73,74,89] The $^{89}$Y $\delta_{iso}$ value shows a strong correlation with the degree of $O_{8a}$–Y–$O_{8a}$ angle deviation from

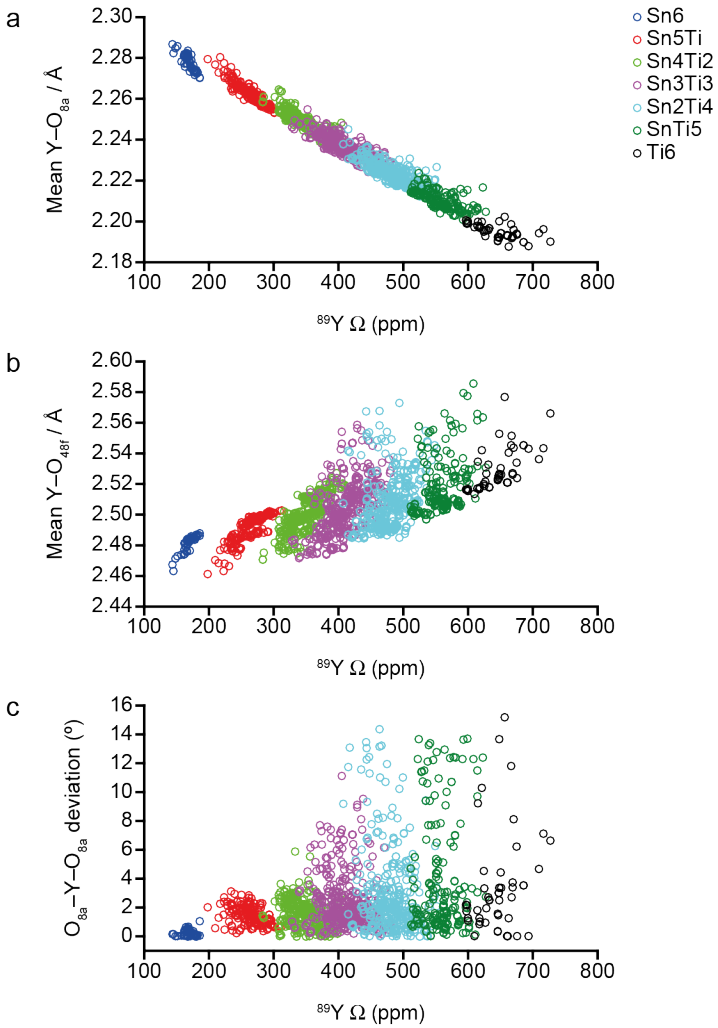


**Figure 5.26:** Plot of calculated $^{89}$Y **Ω** as a function of (a) mean Y–$O_{8a}$ bond length, (b) mean Y–$O_{48f}$ bond length and (c) deviation of the $O_{8a}$–Y–$O_{8a}$ bond angle from 180°, for the 100 randomised structural models of $Y_2Sn_xTi_{2-x}O_7$, with data points coloured by *n* Sn NNN.

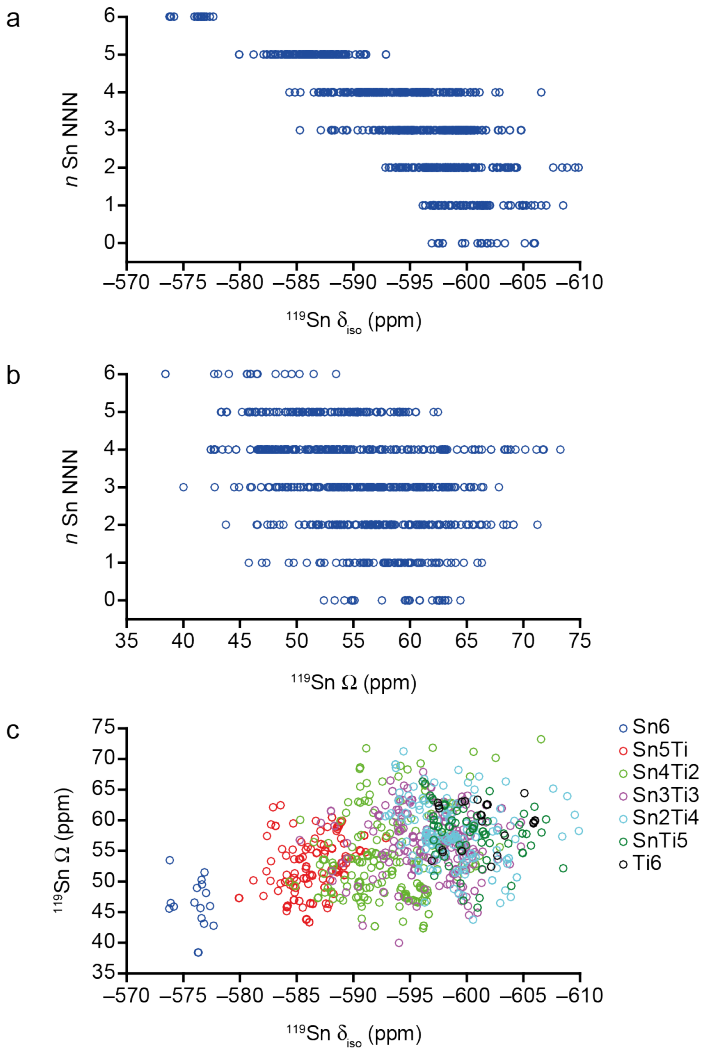


**Figure 5.27:** Plot of calculated $^{119}$Sn (a) $\delta_{iso}$ and (b) Ω as a function of *n* Sn NNN for the 100 randomised structural models of $Y_2Sn_xTi_{2-x}O_7$. (c) Plot of calculated $^{119}$Sn Ω against calculated $^{119}$Sn $\delta_{iso}$ for the 100 randomised structural models of $Y_2Sn_xTi_{2-x}O_7$, with data points coloured by *n* Sn NNN.

180°, whereas the magnitude of Ω seems most strongly correlated with mean Y–$O_{8a}$ bond length. The increase in dataset size associated with investigating 100 $Y_2Sn_xTi_{2-x}O_7$ models also allows trends between calculated NMR and structural parameters to be more clearly identified.

As shown in Figure 5.27a, calculated $^{119}$Sn $\delta_{iso}$ for all Sn in the 100 randomised models show a similar trend with decreasing *n* Sn NNN to that observed for the Sn-centred cluster models. Although a small decrease in the average $\delta_{iso}$

is observed as *n* decreases, this change is much smaller than the range of $\delta_{iso}$ seen, and becomes smaller still with increasing Ti content. This results in a significant overlap of the range of $\delta_{iso}$ observed for different *n* as this value decreases. Very similar ranges of $\delta_{iso}$ are seen for Sn4Ti2, Sn3Ti3, Sn2Ti4, SnTi5 and Ti6. Figure 5.27b shows that the calculated $^{119}$Sn Ω is not structural particularly sensitive to any B-site cation disorder in $Y_2Sn_xTi_{2-x}O_7$, as the average value and range of Ω observed is very similar regardless of the specific NNN environment. As shown in Figure 5.27c, given the significant overlap in both $^{119}$Sn $\delta_{iso}$ and Ω values, considering both parameters simultaneously does not enable Sn with different *n* Sn NNN to be resolved, as the $^{119}$Sn NMR parameters are too poorly correlated with the number of Sn/Ti occupying the six NNN B sites.

The $^{119}$Sn $\delta_{iso}$ appears to be reasonably correlated with the mean Sn–$O_{48f}$ bond length, with a longer bond seeming to result in a small decrease in shift, as shown in Figure 5.28, although significant overlap of the ranges seen means that this structural parameter is not indicative of a specific *n* Sn NNN. The degree of overlap in $^{119}$Sn $\delta_{iso}$ for Sn with different *n* Sn NNN means that these first-principles calculations are of little help in assigning the $^{119}$Sn MAS NMR spectra of $Y_2Sn_xTi_{2-x}O_7$.

The calculated $^{17}$O NMR parameters for the 56,000 O atoms in the 100 randomised structural models were also investigated, with the hope that they can provide insights into the $^{17}$O MAS NMR spectra of the disordered $Y_2Sn_xTi_{2-x}O_7$ materials. As shown in Figure 5.29, the calculated $^{17}$O $\delta_{iso}$ and $C_Q$ values for the four different O environments are all fairly distinct, with the more covalent character of the O–Sn bonds leading to O in the OY2Sn2 environment exhibiting the lowest $^{17}$O $\delta_{iso}$ and the highest $^{17}$O $C_Q$. Conversely, the highly symmetrical (and more ionic) OY4 environment is characterised by extremely low $^{17}$O $C_Q$ values. A reasonably small range of $^{17}$O $\delta_{iso}$ is seen for the OY4 and OY2Sn2 environments, with noticeably larger ranges seen for the Ti-containing (OY2SnTi and OY2Ti2) environments, again, indicative

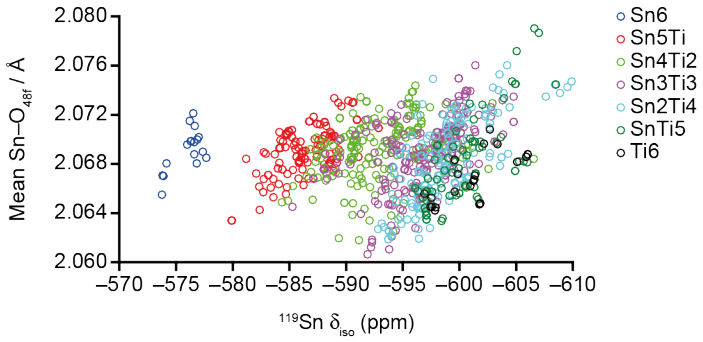


**Figure 5.28:** Plot of calculated $^{119}$Sn $\delta_{iso}$ as a function of mean Sn–$O_{48f}$ bond length for the 100 randomised structural models of $Y_2Sn_xTi_{2-x}O_7$, with the data points coloured by *n* Sn NNN.

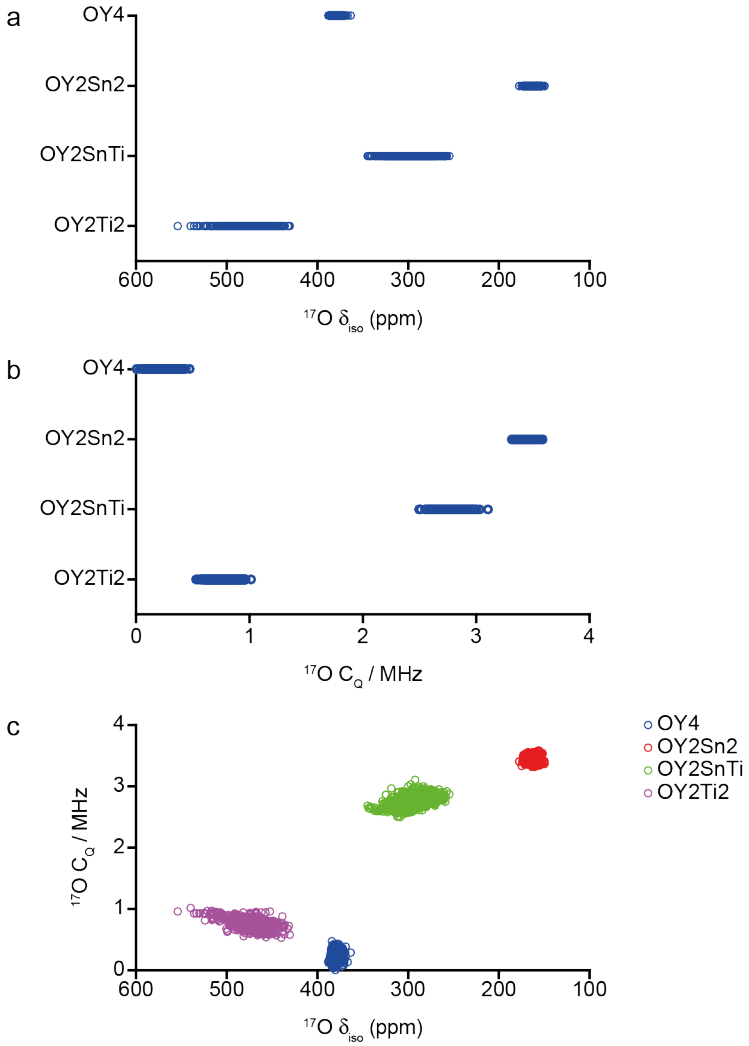


**Figure 5.29:** Plot of calculated $^{17}$O (a) $\delta_{iso}$ and (b) $C_Q$ as a function of O environment for the 100 randomised structural models of $Y_2Sn_xTi_{2-x}O_7$. (c) Plot of calculated $^{17}$O $C_Q$ against $^{17}$O $\delta_{iso}$ for the 100 randomised structural models of $Y_2Sn_xTi_{2-x}O_7$, with data points coloured by the type of O environment.

of Ti being insufficiently large to fully stabilise the six-coordinate B site.

Considering the range of mean O–cation bond distance (where cation = Y, Sn or Ti) shown in Figure 5.30a, highlights how much more structural flexibility appears to be possible when one or more of the four cations surrounding O are Ti, with far less variation in the mean bond length seen for the OY4 and OY2Sn2 environments. A similar trend is seen in Figure 5.30b, where the variation in distortion index for the four O environments is plotted against $^{17}O$ $\delta_{iso}$. The distortion index is a measure of the O local geometry distortion relative to an idealised tetrahedron (where all six M–O–M bonds are equal to 109.47°), and is given by the average of the differences of this ideal angle with the six actual M–O–M angles present. In both Figure 5.30a and Figure 5.30b there is also a clear trend between the structural parameter and calculated $^{17}O$ $\delta_{iso}$, for the OY2SnTi and OY2Ti2 environments. When the data points are coloured according to the composition of the overall models, *i.e.*, coloured according to $x$ in $Y_2Sn_xTi_{2-x}O_7$, as shown by the corresponding plots in Figure 5.31, it can be seen that a decrease in $x$, and therefore unit cell size, is associated with data points shifted more upfield, matching the trend seen in the $^{17}O$ MAS NMR spectra of $Y_2Sn_xTi_{2-x}O_7$ in Figure 5.9. As shown in Figures 5.32 and 5.33, very similar trends are observed when these two structural parameters are plotted against $^{17}O$ $C_Q$ and when the data points are again coloured according to $x$ composition.

The structural models used in this section to model B-site cation disorder in $Y_2Sn_xTi_{2-x}O_7$ pyrochlores, should correspond to a more accurate representation of these disordered materials as, unlike the cluster models, here the B-site cation disorder is not limited to the six NNN sites surrounding a central Y or Sn cation. These first-principles calculations have undoubtedly helped to understand how predicted NMR parameters depend on local structure, relationships that may help assign of the NMR spectra of $Y_2Sn_xTi_{2-x}O_7$ materials.

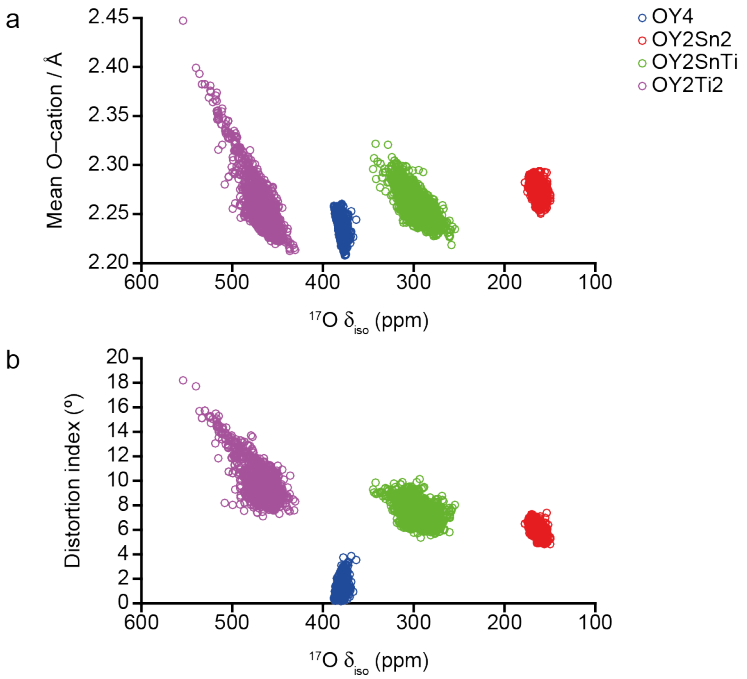


**Figure 5.30:** Plot of calculated $^{17}$O $\delta_{iso}$ as a function of mean O–cation bond length and (b) distortion index for the 100 randomised structural models of $Y_2Sn_xTi_{2-x}O_7$, with data points coloured by O environment.

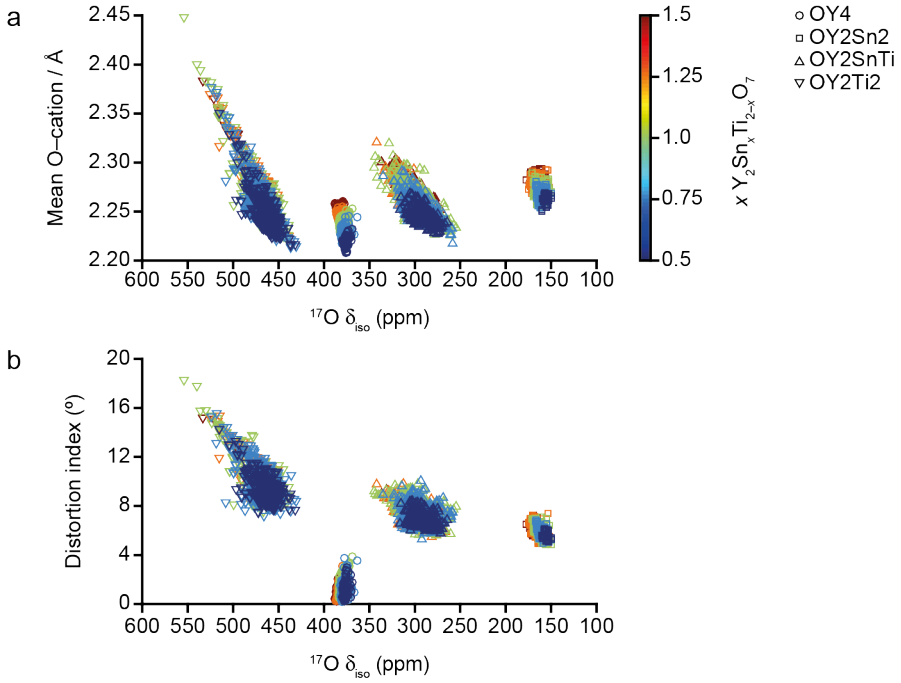


**Figure 5.31:** Plot of calculated $^{17}$O $\delta_{iso}$ as a function of mean O–cation bond length and (b) distortion index for the 100 randomised structural models of $Y_2Sn_xTi_{2-x}O_7$, with data points shaped according to the type of O environment and coloured by $x$.

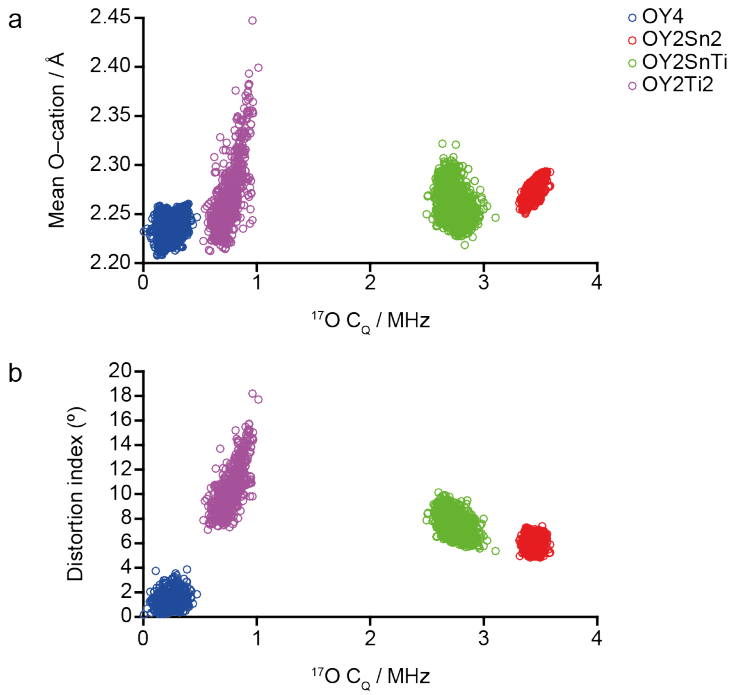


**Figure 5.32:** Plot of calculated $^{17}$O $C_Q$ as a function of mean O–cation bond length and (b) distortion index for the 100 randomised structural models of $Y_2Sn_xTi_{2-x}O_7$, with data points coloured by O environment.

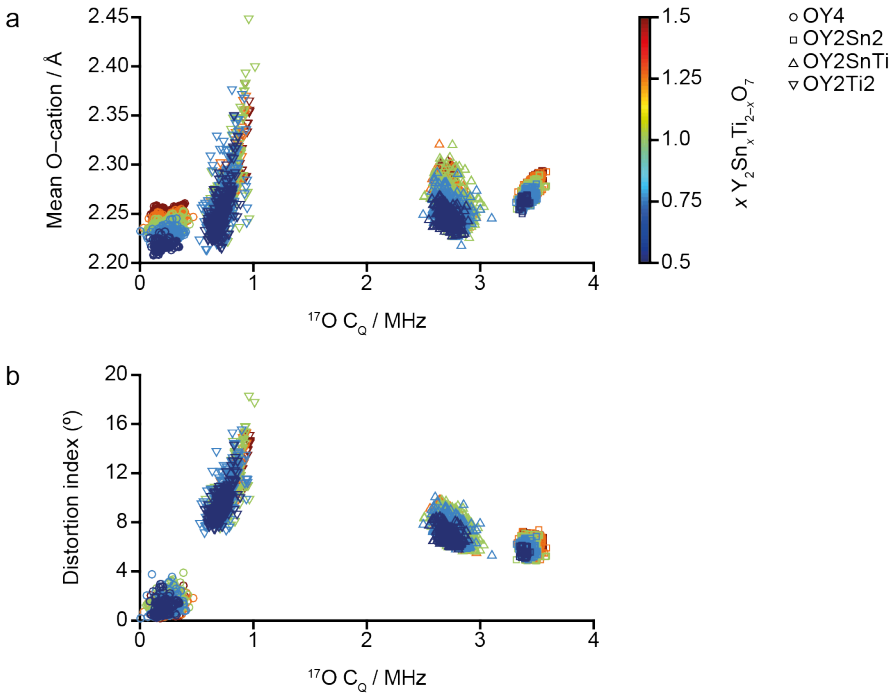


**Figure 5.33:** Plot of calculated $^{17}$O $C_Q$ as a function of mean O–cation bond length and (b) distortion index for the 100 randomised structural models of $Y_2Sn_xTi_{2-x}O_7$, with data points shaped according to the type of O environment and coloured by $x$.

### 5.5.4.1 Repeatability of geometry optimisation calculations

During the investigation of the $Y_2Sn_xTi_{2-x}O_7$ models with randomised B-site cation disorder described above, and given the significant structural variation seen for some types of local environments, the repeatability of geometry optimisation calculations was also considered. In order to probe the repeatability of a geometry optimisation calculation, a single $Y_2Sn_{1.5}Ti_{0.5}O_7$ pyrochlore structure (*i.e.*, a unit cell containing 12 Sn and 4 Ti on the B sites), was generated using the same in-house Fortran90 script used to generate the series of structural models discussed in Section 5.5.4. This initial structure was optimised from the same starting point a number of times while the effect of varying the value of different optimisation parameters (namely `geom_energy_tol` and `elec_energy_tol` were considered. The first of these parameters controls the acceptable tolerance for the convergence of the free energy per atom during a geometry optimisation, and the latter controls the accepted tolerance for convergence of the total energy during the minimisation of the energy (carried out within each step of the geometry optimisation). Two series of geometry optimisations were carried out, allowing the effect of varying `geom_energy_tol` and `elec_energy_tol` to be investigated independently. The value of these two parameters was systematically decreased (or "tightened") in order to see if this had a significant effect on the overall accuracy and repeatability of a CASTEP 8.0 geometry optimisation. In each case, the initial $Y_2Sn_{1.5}Ti_{0.5}O_7$ structural model was geometry optimised twice, with the root-mean-square deviation (RMSD) between the two structures (both geometry optimised using the exact same input calculation parameters) providing an indication of the level of repeatability when specified values of `geom_energy_tol` or `elec_energy_tol` value were used. A summary of the RMSD results from this repeatability testing is given in Table 5.3, with the data also represented in bar chart form in Figure 5.34. In Table 5.3, a small RMSD value indicates that following the geometry optimisation, the two structural models under consideration bear a closer resemblance to each other compared to if a larger RMSD value was observed. The results shown in Table 5.3 indicate that as

**Table 5.3:** Summary of the testing of the repeatability of geometry optimisation, with all calculations performed using CASTEP 8.0. For every value of `geom_energy_tol` or `elec_energy_tol`, the same initial $Y_2Sn_{1.5}Ti_{0.5}O_7$ structure was geometry optimised twice (using the same parameters), with the RMSD representing the structural difference between the two models. When `geom_energy_tol` was varied `elec_energy_tol` was fixed at $1 \times 10^{-5}$ eV / atom, whilst `geom_energy_tol` was fixed at $1 \times 10^{-4}$ eV / atom when `elec_energy_tol` was varied.

| `Geom_energy_tol` / eV / atom | RMSD / Å | `Elec_energy_tol` / eV / atom | RMSD / Å |
|---|---|---|---|
| $1 \times 10^{-4}$ | $1.50 \times 10^{-2}$ | $1 \times 10^{-5}$ | $9.19 \times 10^{-3}$ |
| $1 \times 10^{-5}$ | $2.32 \times 10^{-3}$ | $1 \times 10^{-6}$ | $3.06 \times 10^{-3}$ |
| $1 \times 10^{-6}$ | $1.99 \times 10^{-2}$ | $1 \times 10^{-7}$ | $7.27 \times 10^{-5}$ |
| $1 \times 10^{-7}$ | $7.72 \times 10^{-2}$ | $1 \times 10^{-8}$ | $5.03 \times 10^{-5}$ |
| | | $1 \times 10^{-9}$ | $1.07 \times 10^{-5}$ |

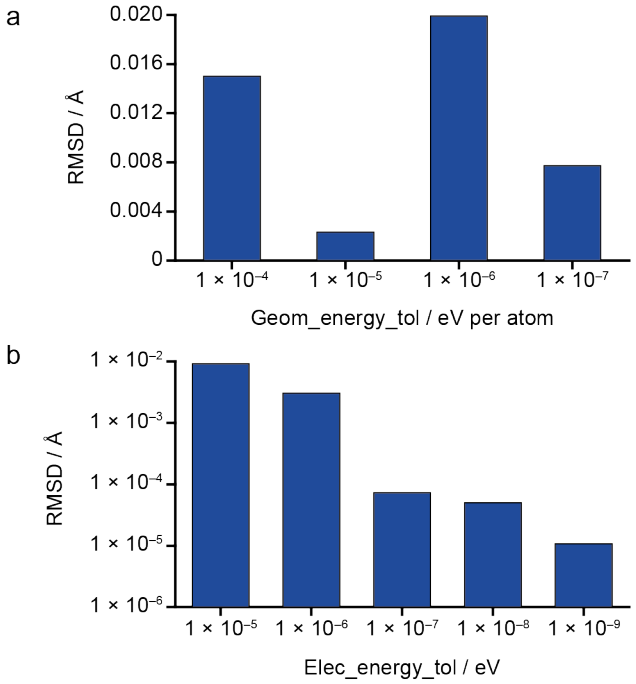


**Figure 5.34:** Bar chart showing the RMSD for two geometry optimisations of an initial $Y_2Sn_{1.5}Ti_{0.5}O_7$ structural model of $Y_2Sn_{1.5}Ti_{0.5}O_7$, optimised using the same input parameters, plotted as a function of (a) `geom_energy_tol` and (b) `elec_energy_tol`.

the magnitude of the `elec_energy_tol` is reduced, the RMSD steadily decreases, indicating that the repeatability of a geometry optimisation calculation is dependent on the accuracy of this parameter. In contrast, the

RMSD fluctuates as `geom_energy_tol` is tightened, suggesting that the relationship between this parameter and the overall accuracy and repeatability of a geometry optimisation calculation is less straightforward.

To further test the importance of the `elec_energy_tol` parameter on the repeatability of a geometry optimisation, in two separate sets of calculations an initial (randomly generated) $Y_2SnTiO_7$ ($x = 1$) structural model was geometry optimised twenty times. In the first set of twenty optimisations, the CASTEP default `elec_energy_tol` value, $1 \times 10^{-5}$ eV / atom, was used, with a tighter value of $1 \times 10^{-9}$ eV / atom used for the second set of twenty optimisations. The same initial $Y_2SnTiO_7$ structural model was used for all forty calculations, with the only difference between the two sets of calculations being the value of the `elec_energy_tol` used. The calculated $^{89}Y$ $\delta_{iso}$ were converted from $\sigma_{iso}$ using the same reference shielding approach described and discussed in Appendix A2). As shown in Figure 5.35, the calculated $^{89}Y$ $\delta_{iso}$ corresponding to the set of twenty structures geometry

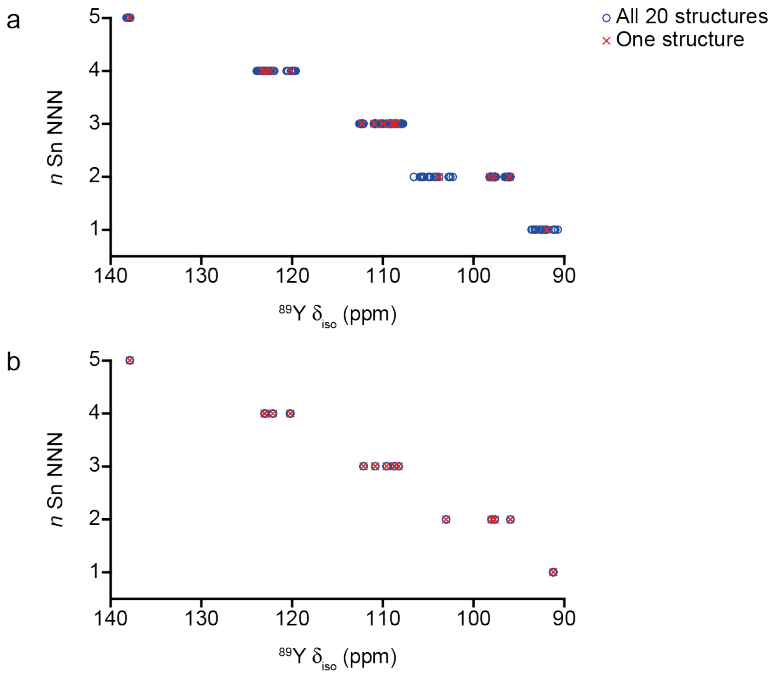


**Figure 5.35:** Plot of calculated $^{89}Y$ $\delta_{iso}$ as a function of *n* Sn NNN for a set of 20 identical structural models of $Y_2SnTiO_7$ geometry optimised using an `elec_energy_tol` values of (a) $1 \times 10^{-5}$ eV / atom and (b) $1 \times 10^{-9}$ eV / atom.

optimised with the default `elec_energy_tol` (Figure 5.35a) show a larger range than seen for the set geometry optimised using the tighter (*i.e.*, lower) `elec_energy_tol` (Figure 5.35b), indicating that the latter set have geometries that are more converged, leading to practically identical $^{89}$Y $\delta_{iso}$.

These results indicate that (at least for this disordered pyrochlore), using a lower value of `elec_energy_tol` for the geometry optimisation calculations is vital in obtaining more consistent optimised structures and accurate calculated $^{89}$Y $\delta_{iso}$. As a result, all subsequent geometry optimisation calculations discussed in the remainder of this chapter, and in Chapter 6, were performed (using CASTEP 8.0 or 16.11), using `geom_energy_tol` and `elec_energy_tol` values of $1 \times 10^{-5}$ eV / atom and $1 \times 10^{-9}$ eV / atom, respectively, whereas all calculations discussed previously were performed using `geom_energy_tol` and `elec_energy_tol` values of $1 \times 10^{-4}$ eV / atom and $1 \times 10^{-5}$ eV / atom, respectively.

### 5.5.5 SOD-generated structural models

The local structure and cation disorder in $Y_2Sn_xTi_{2-x}O_7$ pyrochlores has also been investigated through a collaboration with Ricardo Grau-Crespo at the University of Reading. The SOD program[88] (see Chapter 4, Section 4.3.1) was used to generate all symmetry inequivalent structural models for a series of $Y_2Sn_xTi_{2-x}O_7$ compositions. A summary of the number of structural models generated is given in Table 5.4. An initial pyrochlore structure with $Fd\bar{3}m$ space group was used to generate all SOD structures, with the only variation being the number of Sn and Ti present in the unit cell. In contrast to the cluster and randomised models discussed previously, the SOD approach is far more sophisticated, using isometric transformations to identify symmetry equivalent cation arrangements and produce a complete series of symmetry unique structural models, accompanied by individual configurational degeneracies. For the 279 symmetry unique SOD-generated $Y_2Sn_xTi_{2-x}O_7$ structural models the corresponding solid-state NMR parameters were calculated and used to gain insight into, and aid more

**Table 5.4:** The total number of B site configurations (W) and the number of symmetry inequivalent configurations (M) for $Y_2Sn_xTi_{2-x}O_7$ structures generated using SOD.

| Structural formula | $x$ | B site composition | W | M |
|---|---|---|---|---|
| $Y_2Sn_2O_7$ | 2.0 | Sn16 | 1 | 1 |
| $Y_2Sn_{1.75}Ti_{0.25}O_7$ | 1.75 | Sn14Ti2 | 120 | 3 |
| $Y_2Sn_{1.5}Ti_{0.5}O_7$ | 1.5 | Sn12Ti4 | 1820 | 22 |
| $Y_2Sn_{1.25}Ti_{0.75}O_7$ | 1.25 | Sn10Ti6 | 8008 | 65 |
| $Y_2SnTiO_7$ | 1.0 | Sn8Ti8 | 12870 | 97 |
| $Y_2Sn_{0.75}Ti_{1.25}O_7$ | 0.75 | Sn6Ti10 | 8008 | 65 |
| $Y_2Sn_{0.5}Ti_{1.5}O_7$ | 0.5 | Sn4Ti12 | 1820 | 22 |
| $Y_2Sn_{0.25}Ti_{1.75}O_7$ | 0.25 | Sn2Ti14 | 120 | 3 |
| $Y_2Ti_2O_7$ | 0.0 | Ti16 | 1 | 1 |
| Total | | | 32768 | 279 |

detailed assignment of the $^{89}Y$, $^{119}Sn$ and $^{17}O$ MAS NMR spectra (see Figures 5.7-5.9).

### 5.5.5.1 SOD-generated structural models: series 1

The 279 $Y_2Sn_xTi_{2-x}O_7$ SOD-generated structures were initially geometry optimised (by Dr Grau-Crespo), using VASP 5.[97–100] The geometry optimisation calculations involved using the PBE+U (U = 3 eV and only applied for Ti) $E_{XC}$ functional, an $E_{cut}$ of 520 eV (38 Ry), k-sampling for the gamma point only (referring to the point at 0, 0, 0 in the Brillouin zone) and PAW pseudopotentials,[101,102] with 11, 4, 4, and 6 valence electrons for Y, Sn, Ti and O, respectively. This set of structures will be exclusively referred to as series 1. The NMR parameters for the 279 series 1 structures were performed using CASTEP 8.0, with an $E_{cut}$ of 60 Ry, a k-point spacing of 0.04 2π Å$^{-1}$ (see Appendix A1 for convergence testing), the PBE $E_{XC}$ functional,[94] default on-the-fly ultrasoft pseudopotentials,[95] a `geom_energy_tol` value of $1 \times 10^{-4}$ eV / atom and an `elec_energy_tol` value of $1 \times 10^{-5}$ eV / atom used, with the ZORA correction applied. A description of the referencing used for $^{89}Y$ and $^{119}Sn$ (the former using information from both pyrochlore end members and

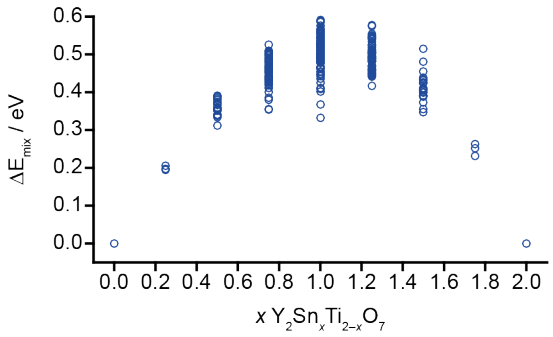


**Figure 5.36:** Plot of relative energy of mixing ($\Delta E_{mix}$) as a function of Sn composition, $x$, for the 279 series 1 structural models of $Y_2Sn_xTi_{2-x}O_7$.

the latter from $Y_2Sn_2O_7$ only) NMR parameters is given in Appendix A4.

The relative energy of mixing ($\Delta E_{mix}$) for the mixed B-site cation structural models in series 1 was determined by using the total energy values (equivalent to enthalpy, H = U + PV, where internal energy (U) is approximated to the electronic potential energy and where pressure (P) is a constant) from the CASTEP 8.0 NMR calculations for the pyrochlore end members, $Y_2Sn_2O_7$ and $Y_2Ti_2O_7$. This involved first determining the energy of mixing for each $Y_2Sn_xTi_{2-x}O_7$ composition, by multiplying the total energy of $Y_2Sn_2O_7$ and $Y_2Ti_2O_7$ by $x/2$ and $(2-x)/2$ respectively, and summing the resulting values together, as shown in Equation 5.1

$$E_{mix}(x) = \left(\frac{x}{2}\right)E_{Y_2Sn_2O_7} + \left(\frac{2-x}{2}\right)E_{Y_2Ti_2O_7} \quad . \tag{5.1}$$

Therefore, when $x = 0.5$ ($Y_2Sn_{0.5}Ti_{1.5}O_7$), $E_{mix}$ is equal to

$$E_{mix} = (0.25E_{Y_2Sn_2O_7}) + (0.75E_{Y_2Ti_2O_7}) \, . \tag{5.2}$$

The difference between this energy of mixing and the total energy for any individual structural model of the same composition gives $\Delta E_{mix}$ for that particular structure. This is a measure of the stability of the mixed B-site cation pyrochlore structures in comparison to stoichiometrically identical

proportions of amount of $Y_2Sn_2O_7$ and $Y_2Ti_2O_7$. A negative $\Delta E_{mix}$ would indicate that a structural model is predicted to be more stable than phase separation. From Figure 5.36 it can be seen that all of the structural models have a positive $\Delta E_{mix}$, meaning all the mixed-metal structures are predicted to be less favourable than the formation of two pure phases. Although the series 1 $\Delta E_{mix}$ suggest phase separation is more favourable than the formation of a solid solution, entropy is not accounted for, meaning these values represent enthalpies rather than Gibbs free energies. The largest variation in $\Delta E_{mix}$ for any one composition is seen for the 97 $x = 1$ ($Y_2SnTiO_7$) structural models, with a smaller spread in $\Delta E_{mix}$ observed for the 22 $x = 0.5$, relative to the same number of $x = 1.5$ structures. This suggests that the Ti-rich structural models are more similar in energy to each other compared to the corresponding Sn-rich models. The $\Delta E_{mix}$ for the three $x = 0.25$ and 1.75 structures also seems to indicate that it is energetically more favourable to incorporate a small amount of Sn into $Y_2Ti_2O_7$ than it is to substitute an equally small amount of Ti into $Y_2Sn_2O_7$. This observation is likely be a result of the difference in ionic radii between $Sn^{4+}$ and $Ti^{4+}$, with the larger Sn more suitable to stabilising the six-coordinate pyrochlore B site compared to Ti, leading to less structural and thus energy variation in the three $x = 0.25$ models.

As shown in Figure 5.37, the decrease in calculated $^{89}Y$ $\delta_{iso}$ and the increase in $\Omega$ that coincide with a reduction in $n$ Sn NNN agree well with the trends seen for other sets of $Y_2Sn_xTi_{2-x}O_7$ structural models (see Sections 5.5.3 and 5.5.4). Figure 5.37a reveals there is a significant number of Y with abnormally high $\delta_{iso}$ compared to others with the same NNN environment, as observed earlier for both the cluster and randomised B-site cation models. In contrast, Figure 5.37b shows that the increase in calculated $^{89}Y$ $\Omega$ that accompanies the decrease in $n$ Sn NNN is once again systematic, agreeing well with results from previous models. Figure 5.37c reinforces this, showing that all Y with a specific $n$ Sn NNN environment have calculated $^{89}Y$ $\Omega$ values that fall within a reasonably well-defined range, but that there is much greater variation in

$^{89}$Y $\delta_{iso}$, particularly for Y in *n* Sn NNN = 3, 2 and 1 environments.

As shown in Figure 5.38, the correlations between calculated $^{89}$Y Ω and local structural parameters for the 279 series 1 structures are similar to those trends seen for the two sets of models previously discussed in Sections 5.5.3 and 5.5.4. Most noticeably, it is clear that there is a strong correlation between calculated $^{89}$Y Ω and mean Y–$O_{8a}$ bond length. Figure 5.38b shows that a decrease in *n* Sn NNN results in a slight increase in mean Y–$O_{48f}$ bond length. As seen in Figure 5.38c, the deviation in the $O_{8a}$–Y–$O_{8a}$ bond angle

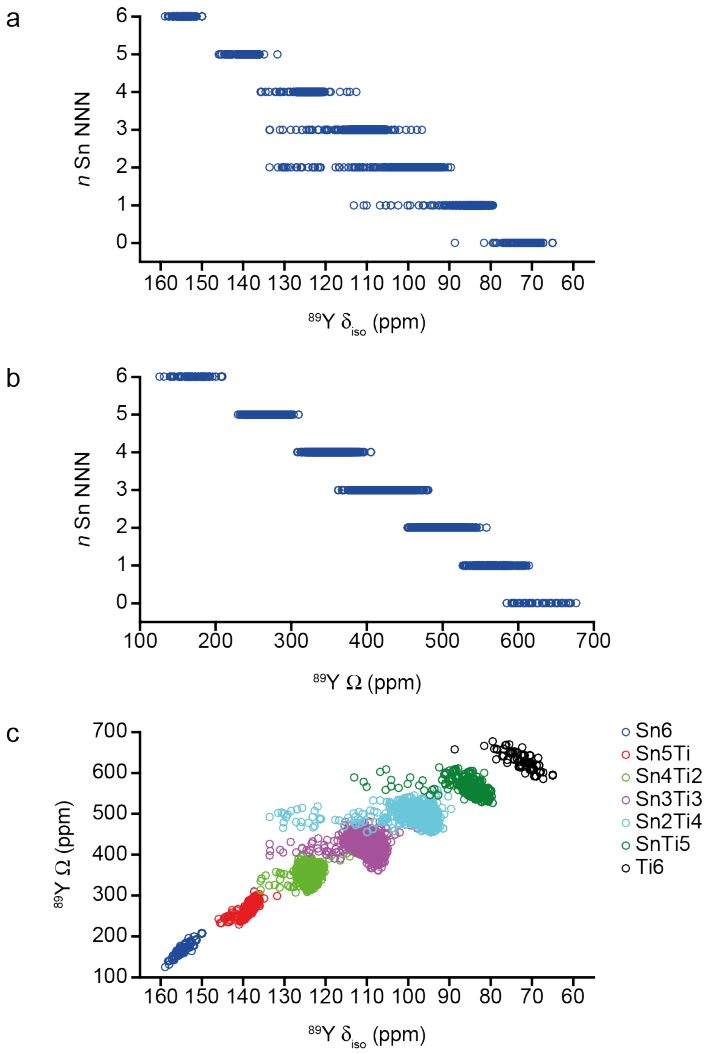


**Figure 5.37:** Plot of calculated $^{89}$Y (a) $\delta_{iso}$ and (b) Ω as a function of *n* Sn NNN and (c) plot of calculated $^{89}$Y $\delta_{iso}$ as a function of calculated $^{89}$Y Ω, for all 279 series 1 structural models of $Y_2Sn_xTi_{2-x}O_7$, with data points coloured by *n* Sn NNN in (c).

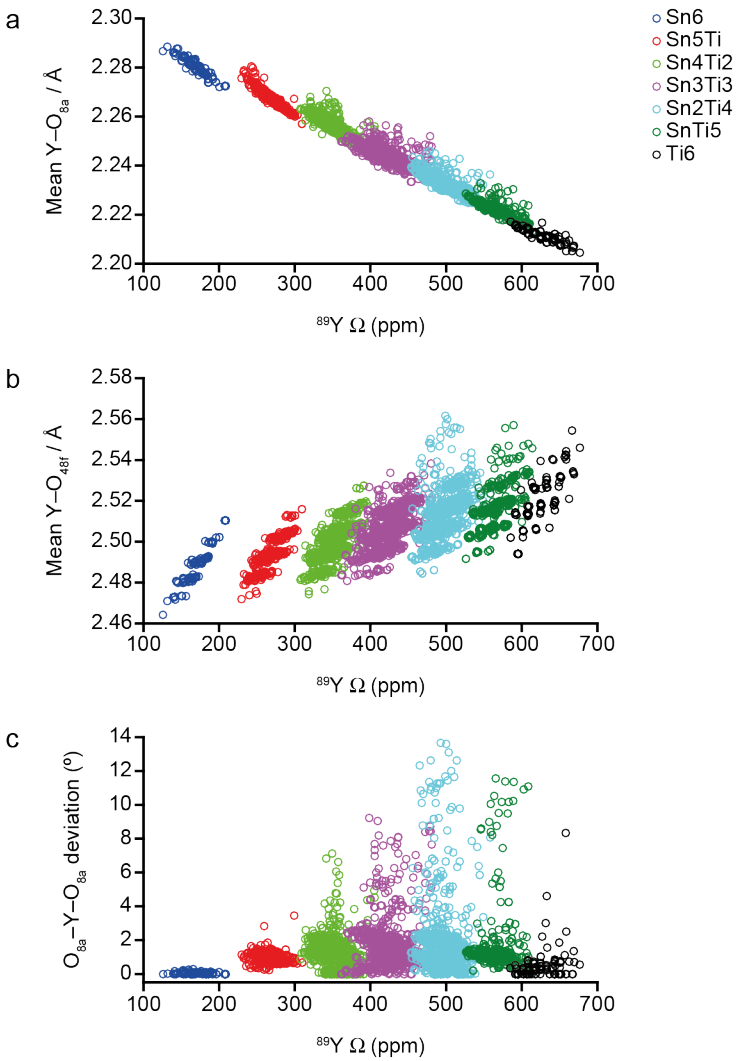


**Figure 5.38:** Plot of calculated $^{89}$Y Ω as a function of (a) mean Y–$O_{8a}$ bond length, (b) mean Y–$O_{48f}$ bond length and (c) deviation of the $O_{8a}$–Y–$O_{8a}$ bond angle from 180°, for all 279 series 1 structural models of $Y_2Sn_xTi_{2-x}O_7$, with data points coloured by *n* Sn NNN.

from 180° does not strongly influence the calculated $^{89}$Y Ω, with the nature of the species occupying the closest B sites, most important in determining the magnitude of this parameter.

As seen for $^{89}$Y Ω, the correlations between calculated $^{89}$Y $\delta_{iso}$ and local structural parameters, shown in Figure 5.39, also agree well with the trends seen for the sets of structural models previously discussed in Sections 5.5.3 and 5.5.4. In contrast to $^{89}$Y Ω, there are a significant number of Y with outlying, downfield $\delta_{iso}$, particularly for *n* Sn NNN = 3, 2 and 1. As *n* Sn

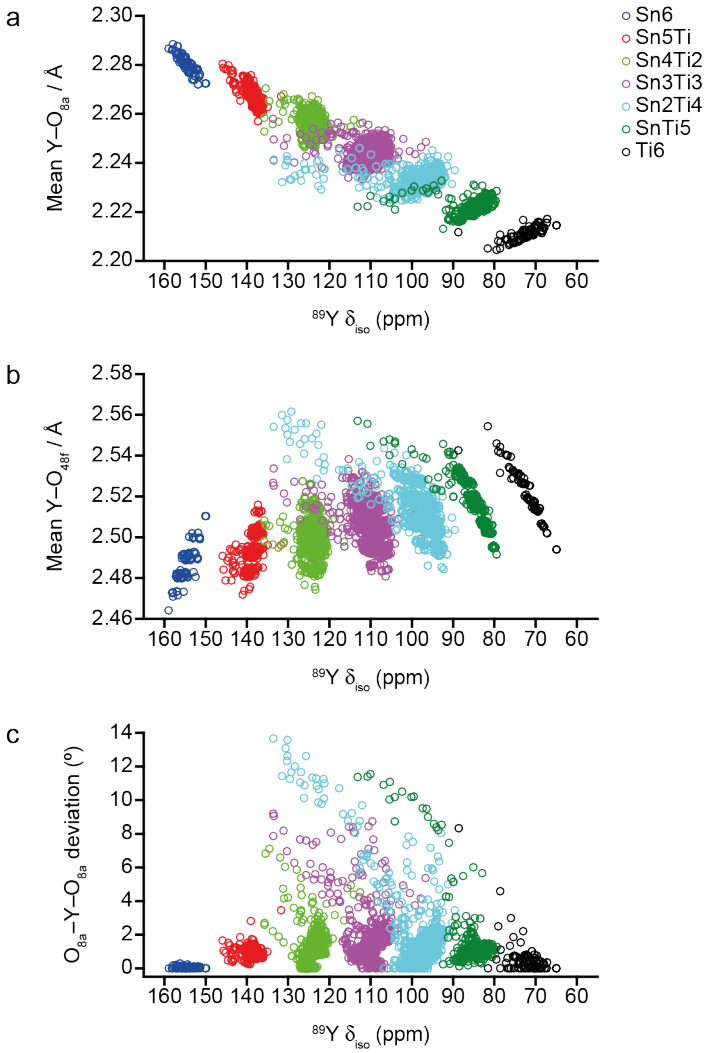


**Figure 5.39:** Plot of calculated $^{89}Y$ $\delta_{iso}$ as a function of (a) mean Y–$O_{8a}$ bond length, (b) mean Y–$O_{48f}$ bond length and (c) deviation of the $O_{8a}$–Y–$O_{8a}$ bond angle from 180°, for all 279 series 1 structural models of $Y_2Sn_xTi_{2-x}O_7$, with the data points coloured by *n* Sn NNN.

NNN decreases, the mean Y–$O_{8a}$ and Y–$O_{58f}$ bond lengths shorten and lengthen, respectively. In addition, from Figure 5.39c it is clear that a strong correlation between the deviation in the $O_{8a}$–Y–$O_{8a}$ bond angle from 180° and $^{89}Y$ $\delta_{iso}$, with extremely high $^{89}Y$ $\delta_{iso}$ resulting from species with particularly large deviations. Indeed, as shown in Figure 5.40a, if the data points are coloured according to the deviation of the $O_{8a}$–Y–$O_{8a}$ bond angle, the strength of this correlation is more apparent. From Figure 5.40b, it can be seen that the majority of Y with a Sn2Ti4 (*i.e.*, *n* Sn NNN = 2) environments that have unusually large $^{89}Y$ $\delta_{iso}$ have a 3,6-Sn2Ti4 arrangement, whereas the more outlying $^{89}Y$ $\delta_{iso}$ seen for the Sn3Ti3 (*i.e.*, *n* Sn NNN = 3) environments

exclusively correspond to the 1,2,4-Sn3Ti3 arrangement. Figure 5.40b indicates that the most asymmetric way of arranging three Sn and three Ti on six NNN B sites results in the largest deviation in $O_{8a}$–Y–$O_{8a}$ bond angle, which in turn causes an increase in a $^{89}$Y $\delta_{iso}$.

As the SOD procedure not only identifies every symmetry inequivalent atomic arrangement for a fixed pyrochlore composition, but also determines the configurational degeneracy associated with each structural model it was concluded that by representing each $^{89}$Y $\delta_{iso}$ into an individual Gaussian function, a spectrum based on calculated $^{89}$Y $\delta_{iso}$ for each composition can be generated. Each individual Gaussian (for each Y species in a particular model) was weighted by configurational degeneracy of the structural model in which it is found, before all were summed to produce the final spectrum. In principle, this allows a direct comparison to the experimental $^{89}$Y MAS

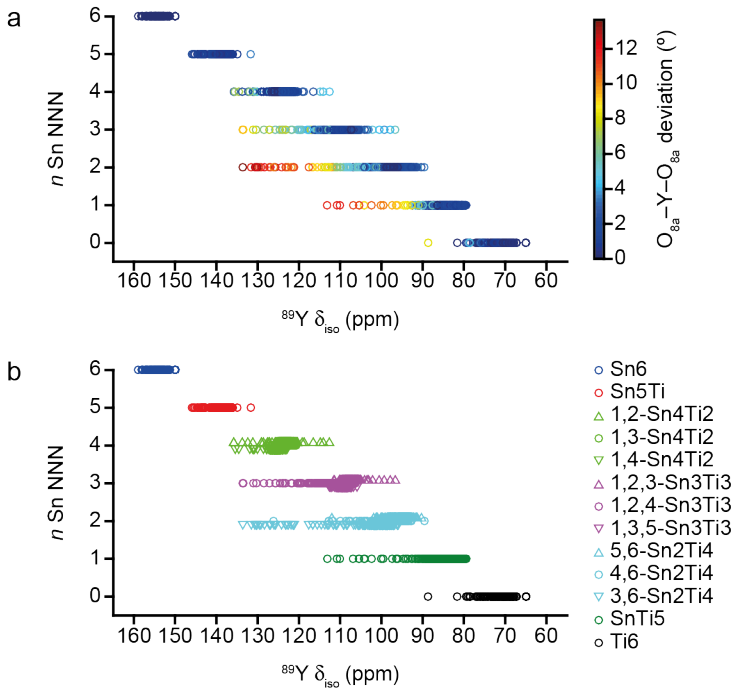


**Figure 5.40:** Plot of calculated $^{89}$Y $\delta_{iso}$ as a function of *n* Sn NNN for all 279 series 1 structural models of $Y_2Sn_xTi_{2-x}O_7$, with (a) the data points coloured by the deviation in the$O_{8a}$–Y–$O_{8a}$ bond angle from 180° and (b) the shape of the data points denoting the specific Sn NNN arrangement. Where *n* Sn NNN = 4, 3 and 2 in (b) the data points for the different arrangements have been offset slightly to facilitate comparison.

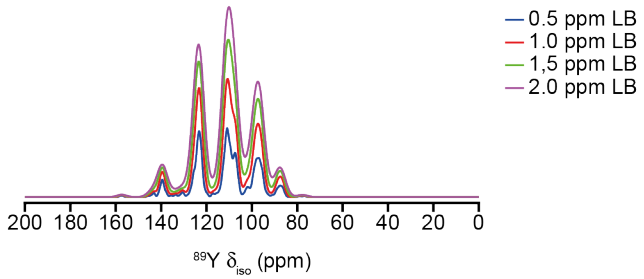


**Figure 5.41:** Calculated $^{89}Y$ $\delta_{iso}$ Gaussian spectrum of series 1 $Y_2SnTiO_7$, with the lineshapes coloured according to the Gaussian line broadening (LB).

NMR spectra of $Y_2Sn_xTi_{2-x}O_7$ (see Figure 5.7) to be made, potentially enabling insight into the local structure and B-site cation ordering in the real materials to be obtained. As shown in Figure 5.41, spectra for the $Y_2SnTiO_7$, $x$ = 1.0 composition were generated using four possible Gaussian line broadening (LB) values, with LB =1.0 ppm giving best overall agreement with the experimental spectrum.

Using a LB of 1.0 ppm, calculated $^{89}Y$ $\delta_{iso}$ spectra were generated for all nine series 1 $Y_2Sn_xTi_{2-x}O_7$ compositions and are shown in Figure 5.42 along with the corresponding experimental $^{89}Y$ MAS NMR spectra for comparison. Figure 5.42 shows fairly good agreement between the simulated and experimental $^{89}Y$ MAS NMR spectra, with the former perhaps containing more well-defined resonances that can be easily assigned to $^{89}Y$ with different $n$ Sn NNN environments. For most of the compositions, especially those closest to $x$ = 1.0, the relative intensities of the resonances in the predicted $^{89}Y$ NMR spectra agree well with their experimental equivalents, with the noticeable exceptions being for $x$ = 1.75 and 0.25, where the intensities of the resonances assigned to $n$ Sn NNN = 6 and 5 in the former and 1 and 0 in the latter composition are inverted relative to the corresponding experimental spectra. For structural models based on a single unit cell, where $x$ = 1.75 and 0.25 only three symmetry unique atomic arrangements are possible. Clearly, the relative intensities predicted for the (weighted) combination of these three do not match those seen experimentally, suggesting either (i) that not all contribute equally to the experimental spectrum of (ii) that disorder on a greater length scale (*i.e.*, a larger supercell) needs to be considered.

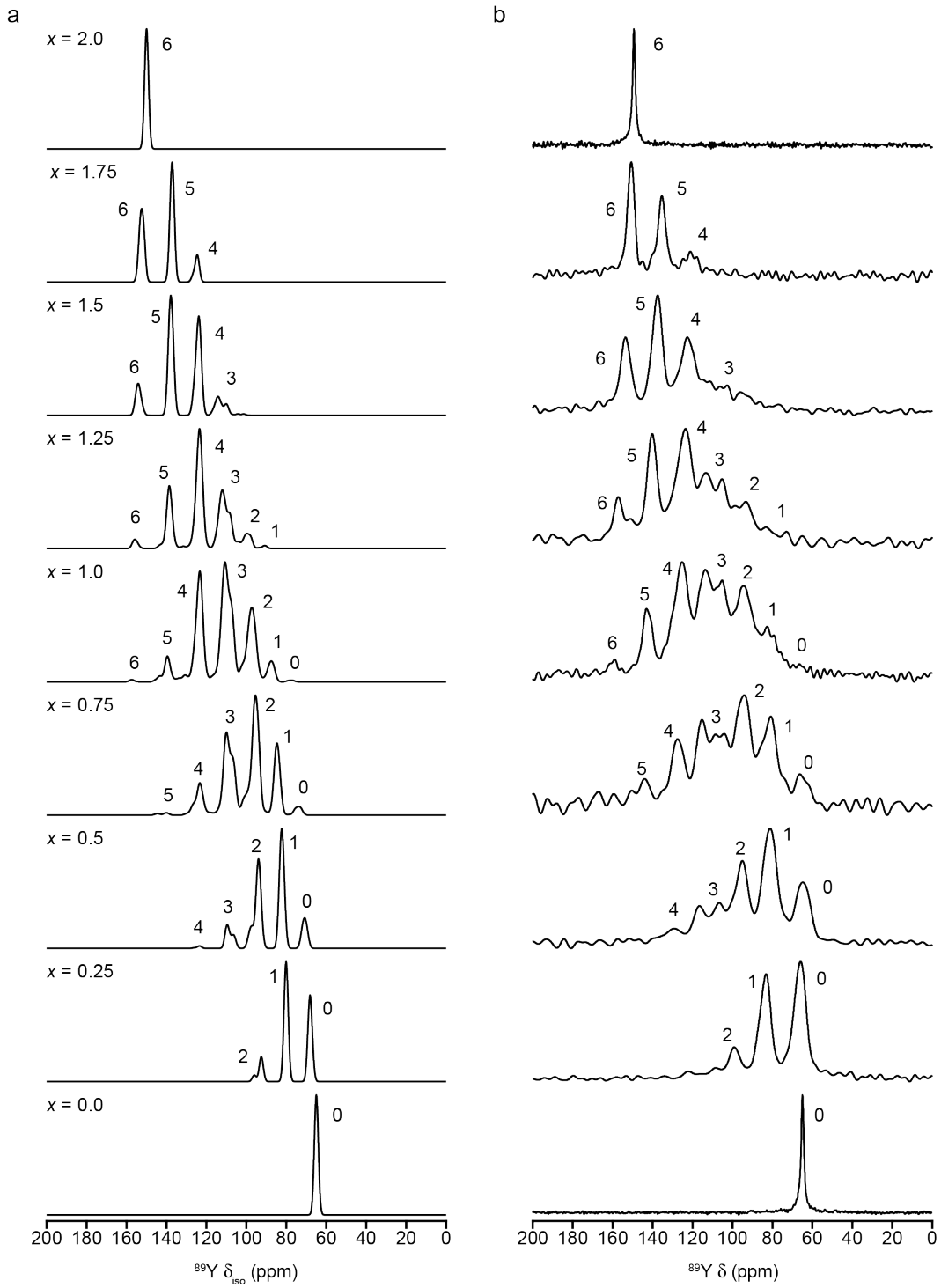


**Figure 5.42:** (a) Simulated $^{89}$Y NMR spectra for series 1 structural models and (b) experimental $^{89}$Y (14.1 T, 14 kHz) MAS NMR spectra of $Y_2Sn_xTi_{2-x}O_7$, with the results from (a) used to assign resonances to $^{89}$Y with a particular *n* Sn NNN environment.

Other than providing a means of directly comparing calculated $^{89}$Y $\delta_{iso}$ values to the $^{89}$Y MAS NMR spectra of $Y_2Sn_xTi_{2-x}O_7$, an additional a benefit of

generating simulated spectra is that more specific information on local structure and disorder can in principle, be extracted. For the $x$ = 1.0 composition, the simulated $^{89}$Y $\delta_{iso}$ spectrum was decomposed (as shown in Figure 5.43) to highlight the contributions from the seven $n$ Sn NNN environments, and secondly, those from the individual NNN cation arrangements for $n$ Sn NNN = 4, 3, and 2 environments. From Figure 5.43a, it is more noticeable that the peak attributed to $n$ Sn NNN = 3 is asymmetric, with a clear shoulder to low δ, which could be interpreted as a less pronounced version of the clear splitting seen in the experimental $^{89}$Y MAS NMR spectrum of $Y_2SnTiO_7$. Figure 5.43b indicates that the vast majority of intensity contributing to individual peaks in the simulated spectra comes from Y with the same $n$ Sn NNN, *i.e.*, the bulk of the $n$ Sn NNN = 3 peak comes from the Y with the Sn3Ti3 environment. This also indicates that the Y species that have abnormally high $^{89}$Y $\delta_{iso}$ (relative to the majority with the same $n$) result in a very small contribution to the intensity of neighbouring, more Sn-rich (more downfield) resonances resulting from more Sn-rich NNN

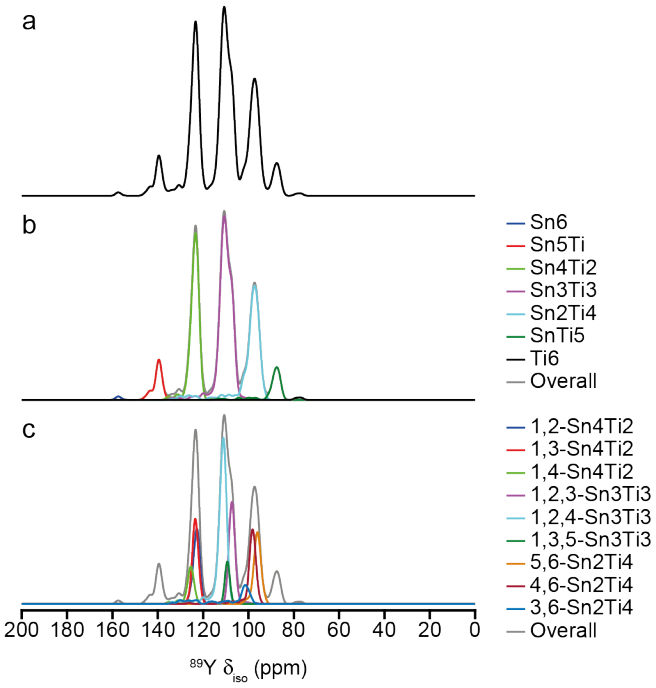


**Figure 5.43:** (a) Simulated $^{89}$Y NMR spectrum resulting from series 1 structural models of $Y_2SnTiO_7$, with the spectrum decomposed according to (b) $n$ Sn NNN and (c) the specific Sn NNN arrangements for $n$ = 4, 3 and 2.

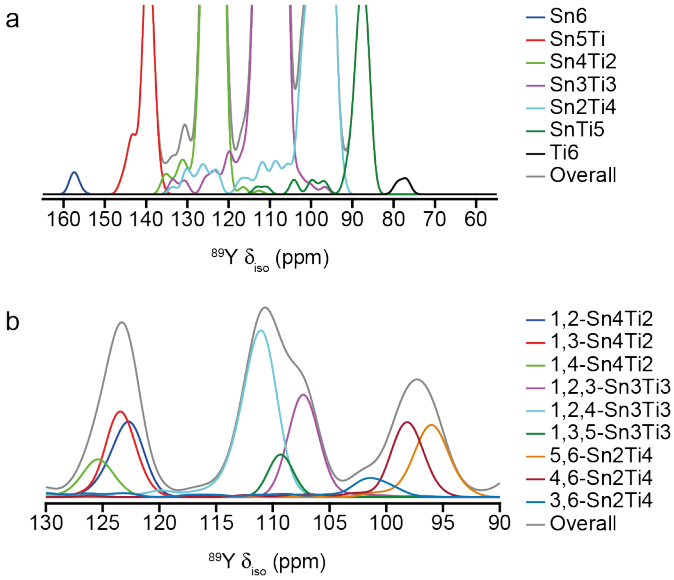


**Figure 5.44:** (a) Vertical and horizontal expansion of the simulated $^{89}$Y spectrum of series 1 structural models of $Y_2SnTiO_7$, decomposed according to *n* Sn NNN. (b) Horizontal expansion of the simulated $^{89}$Y spectrum of series 1 structural models of $Y_2SnTiO_7$, decomposed according to the specific Sn NNN arrangements for the $n$ = 4, 3 and 2.

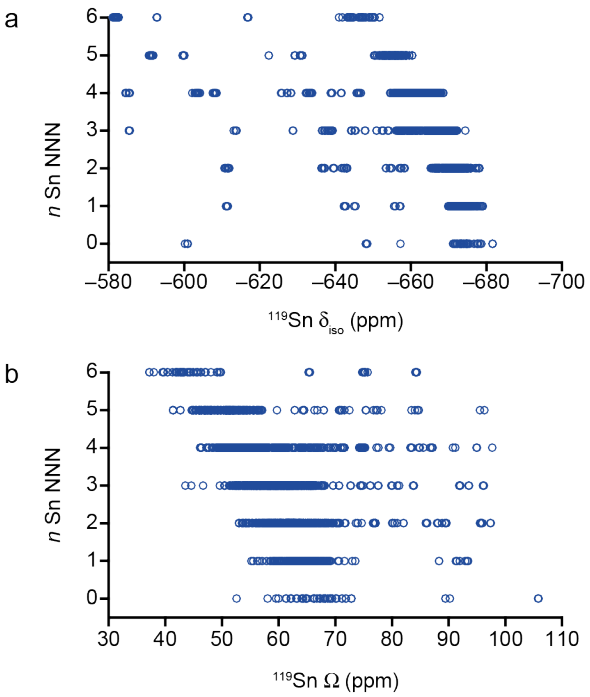


**Figure 5.45:** Plot of calculated $^{119}$Sn (a) $\delta_{iso}$ and (b) Ω as a function of *n* Sn NNN for series 1 structural models of $Y_2Sn_xTi_{2-x}O_7$.

environments. For example, although some Y species with a Sn2Ti4 NNN

environment have very high $^{89}$Y $\delta_{iso}$, their contribution to the intensity of the resonances from Y species with Sn3Ti3 and Sn4Ti2 environments is very small, as shown in the expansion in Figure 5.44a.

The contributions of the nine arrangements with *n* Sn NNN = 4, 3 and 2 to the simulated spectrum is shown in Figure 5.43c. This figure shows that Y with the 1,2,3-Sn3Ti3 and 1,2,4-Sn3Ti3 arrangements have noticeably different $^{89}$Y $\delta_{iso}$, (with the latter arrangement shifted ~5 ppm downfield relative to the former), with signal from the 1,3,5-Sn3Ti3 arrangement appearing in the centre of the two. From the expansion of Figure 5.43c, shown in Figure 5.44b, it is clearer that this $^{89}$Y $\delta_{iso}$ difference could explain why a prominent splitting of the Sn3Ti3 resonance is observed in the experimental $^{89}$Y MAS NMR spectra. Similarly, the $^{89}$Y $\delta_{iso}$ for Y with a 1,4-Sn4Ti2 or 3,6-Sn2Ti4 arrangement are shifted downfield relative to the remaining *n* Sn NNN = 4 or 2 environments, respectively. However, these more downfield shifted resonances have low intensity and so in comparison to the 1,2,4-Sn3Ti3 arrangement, do not contribute to the experimental $^{89}$Y MAS NMR spectra as significant shoulders or peak splittings.

As with the previous two sets of $Y_2Sn_xTi_{2-x}O_7$ structural models (see Sections 5.5.3 and 5.5.4), the calculated $^{119}$Sn NMR parameters for the series 1 structural models were also investigated, as shown in Figure 5.45. Although it is possible to see the same general trends in these calculated $^{119}$Sn NMR parameters with changing *n* as observed for the cluster and randomised models, Figure 5.45 shows that there are a large number of data points that appear to be somewhat anomalous, *i.e.*, appearing at very different values of $\delta_{iso}$ and $\Omega$ than seen experimentally or in any of the calculations so far, leading to some doubt over the accuracy of these values, and therefore over the structural models used (and making it challenging to extract any useful information). One possible reason for the poor agreement between the calculated $^{119}$Sn NMR parameters for series 1 and the sets of structures previously discussed in Sections 5.5.3 and 5.5.4 could be that the use of VASP (rather than CASTEP) for geometry optimisation has resulted in different

structural models, or that the accuracy of optimisation could be affected by the Sn pseudopotential used during the optimisation process. As NMR parameters are extremely sensitive to local structure, even very small variations in atomic positions can cause significant changes in calculated NMR parameters (as shown in Section 5.5.4.1)

### 5.5.5.2 SOD-generated structural models: series 2

Using the geometry optimised series 1 models as the input structures, a second geometry optimisation (involving more precise pseudopotentials) was performed using VASP 5.[97–100] The geometry optimisation calculations involved using the PBE+U (U = 3 eV and only applied for Ti) $E_{XC}$ functional, an $E_{cut}$ of 520 eV (38 Ry), k-sampling for the gamma point only and PAW pseudopotentials,[101,102] with 11, 14, 12, and 6 valence electrons for Y, Sn, Ti and O, respectively. This set of structures will be exclusively referred to as series 2. CASTEP 8.0 was then used to calculate the NMR parameters for the 279 VASP-optimised $Y_2Sn_xTi_{2-x}O_7$ structures, using an $E_{cut}$ of 60 Ry, a k-point spacing of 0.04 2π Å$^{-1}$ (see Appendix A1 for convergence testing), the PBE $E_{XC}$ functional,[94] default on-the-fly ultrasoft pseudopotentials,[95] a `geom_energy_tol` value of $1 \times 10^{-4}$ eV / atom and an `elec_energy_tol` value of $1 \times 10^{-5}$ eV / atom, with the ZORA correction applied. A description of the referencing used for $^{89}$Y and $^{119}$Sn (the former using information from both series 2 pyrochlore end members and the latter from $Y_2Sn_2O_7$ only) NMR parameters is given in Appendix A5.

The relative energy of mixing ($\Delta E_{mix}$) for the series 2 structures was determined as described above for series 1 (see Section 5.5.5.1). Figure 5.46 shows that the $\Delta E_{mix}$ for the series 2 models appear very similar to the values seen for series 1 (see Figure 5.36), with the largest variation seen for the 97 $x$ = 1.0 models, which span ~0.3 eV. As for series 1, the $\Delta E_{mix}$ values suggest that it is energetically more favourable to substitute a small amount of Sn into $Y_2Ti_2O_7$ than it is to incorporate the same amount of Ti into $Y_2Sn_2O_7$, with the $\Delta E_{mix}$ for the $x$ = 0.25 models slightly lower than those for $x$ = 1.75.

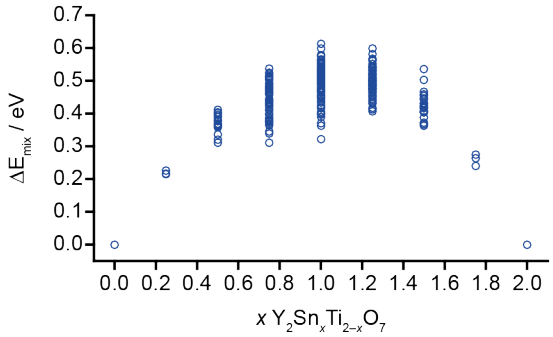


**Figure 5.46:** Plot of relative energy of mixing ($\Delta E_{mix}$) as a function of Sn composition, *x*, for the 279 series 2 structural models of $Y_2Sn_xTi_{2-x}O_7$.

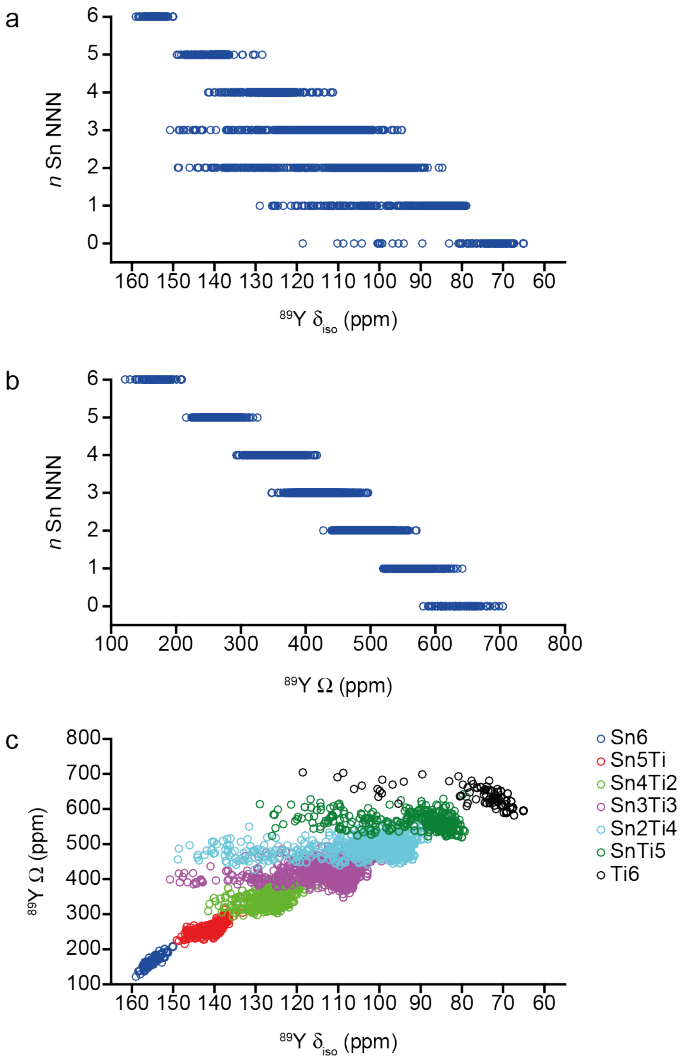


**Figure 5.47:** Plot of calculated $^{89}Y$ (a) $\delta_{iso}$ and (b) $\Omega$ as a function of *n* Sn NNN, and (c) calculated $^{89}Y$ $\delta_{iso}$ as a function of calculated $^{89}Y$ $\Omega$ for all 279 series 2 structural models of $Y_2Sn_xTi_{2-x}O_7$, with data points coloured by *n* Sn NNN in (c).

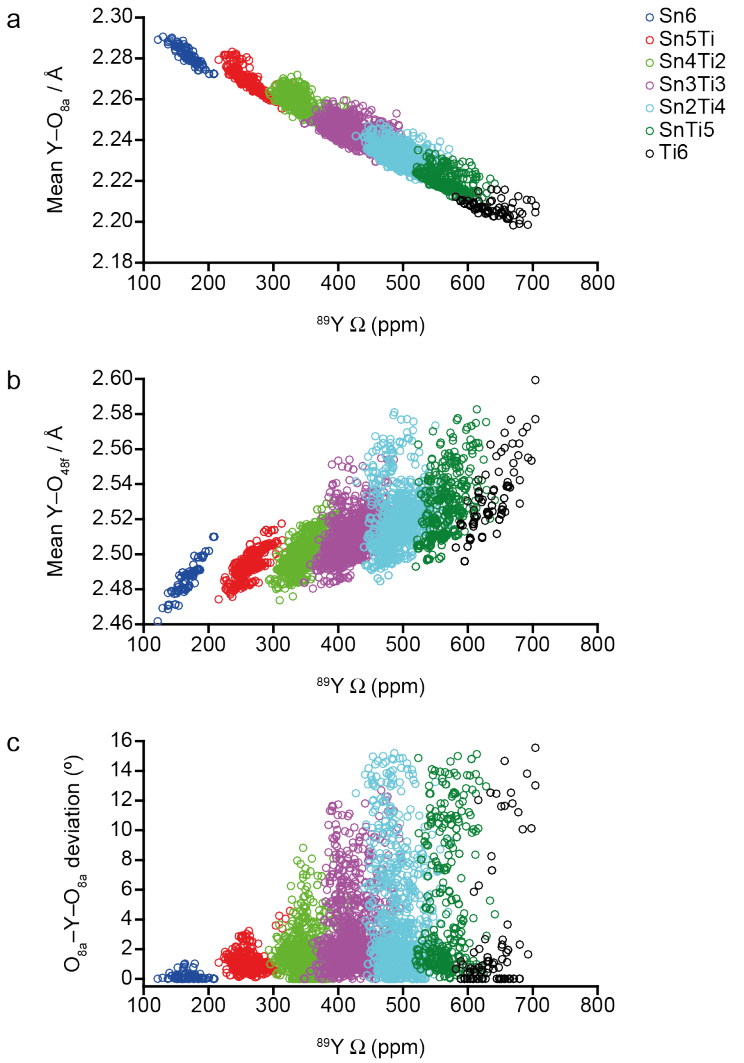


**Figure 5.48:** Plot of calculated $^{89}$Y Ω as a function of (a) mean Y–$O_{8a}$ bond length, (b) mean Y–$O_{48f}$ bond length and (c) deviation of the $O_{8a}$–Y–$O_{8a}$ bond angle from 180°, for all 279 series 2 structural models of $Y_2Sn_xTi_{2-x}O_7$, with data points coloured by *n* Sn NNN.

As shown in Figure 5.47, similar trend in calculated $^{89}$Y $\delta_{iso}$ and Ω are observed with changing *n* Sn NNN, to those seen for series 1, although a larger number of Y with extremely high $^{89}$Y $\delta_{iso}$, are present, causing large shift ranges for all $n < 4$ environments.

Figures 5.48 and 5.49 show that the trends in calculated $^{89}$Y Ω and $\delta_{iso}$ with the local structural parameters considered earlier are very similar for series 2 structural models to those seen for series 1 (see Section 5.5.5.1). Particularly strong correlations are observed between mean Y–$O_{8a}$ bond length and $^{89}$Y Ω,

in addition to correlations between the deviation in the $O_{8a}$–Y–$O_{8a}$ bond angle from 180° and $^{89}$Y $\delta_{iso}$. In general the series 2 models exhibit a larger range in the $O_{8a}$–Y–$O_{8a}$ bond angle deviation than seen for the series 1 structural models.

When $^{89}$Y $\delta_{iso}$ is plotted against *n* Sn NNN and the data points coloured according to the deviation in the $O_{8a}$–Y–$O_{8a}$ bond angle, as shown in Figure 5.50a, it is clear that an increase in this deviation results in an increase in $^{89}$Y $\delta_{iso}$, regardless of the *n* Sn NNN, although this correlation is strongest for Y in

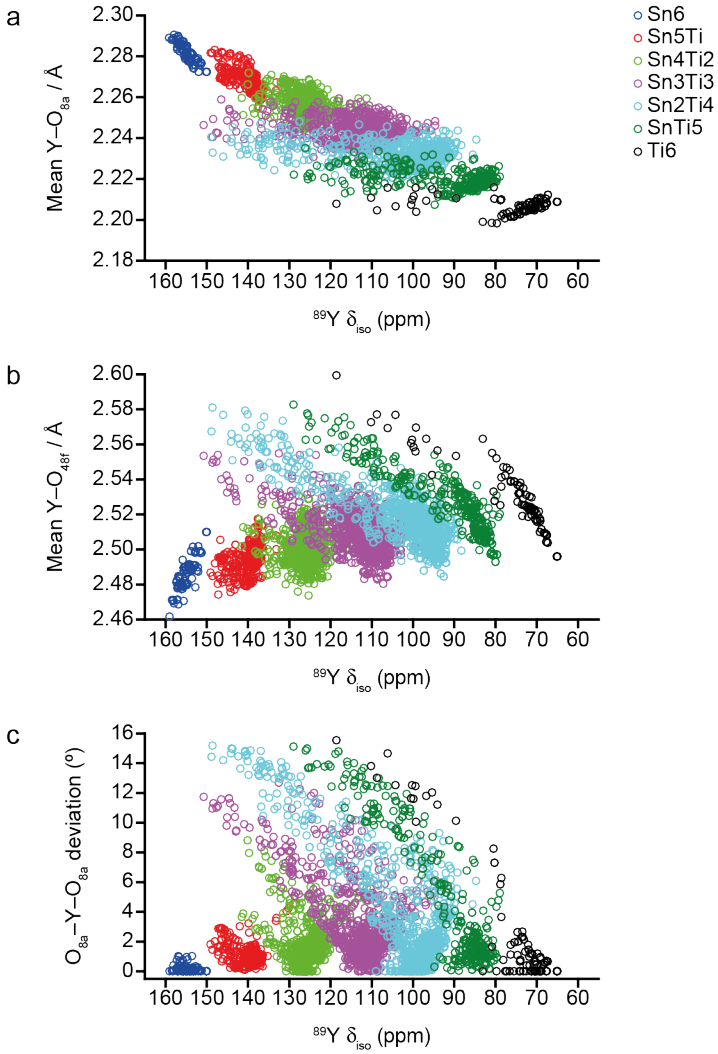


**Figure 5.49:** Plot of calculated $^{89}$Y $\delta_{iso}$ as a function of (a) mean Y–$O_{8a}$ bond length, (b) mean Y–$O_{48f}$ bond length and (c) deviation of the $O_{8a}$–Y–$O_{8a}$ bond angle from 180°, for all 279 series 2 structural models of $Y_2Sn_xTi_{2-x}O_7$, with data points coloured by *n* Sn NNN.

environments where three or more of the surrounding NNN B sites are occupied by Ti. Figure 5.50b shows that the $^{89}$Y $\delta_{iso}$ for the three different *n* Sn NNN = 4 arrangements are all reasonably similar with no particularly unusual or outlying data points observed, whereas for *n* Sn NNN = 3 there is a much clearer distinction between the shifts seen for different arrangements. It is apparent that the most extreme $^{89}$Y $\delta_{iso}$ are exhibited by Y with a 1,2,4-Sn3Ti3 arrangement, while Y with either of the two remaining arrangements, 1,2,3-Sn3Ti3 and 1,3,5-Sn3Ti3 do not have particularly large values of $^{89}$Y $\delta_{iso}$, in any structural models. For the Sn2Ti4 environment there are examples of extreme $^{89}$Y $\delta_{iso}$ values for Y with all three of the different Sn2Ti4 arrangements, especially 4,6-Sn2Ti4 and 3,6-Sn2Ti4. This indicate that as *n* Sn NNN decreases, the specific NNN arrangement becomes less important in determining whether an unusually large $^{89}$Y $\delta_{iso}$ is observed, similar to what was seen for the series 1 models.

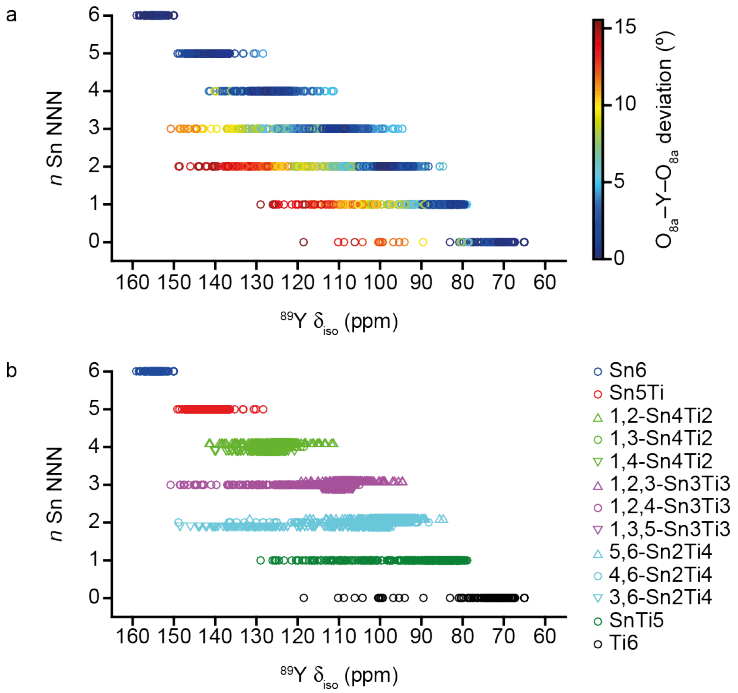


**Figure 5.50:** Plot of calculated $^{89}$Y $\delta_{iso}$ as a function of *n* Sn NNN for all 279 series 2 structural models of $Y_2Sn_xTi_{2-x}O_7$, with (a) the data points coloured by the deviation in the $O_{8a}$–Y–$O_{8a}$ bond angle from 180° and (b) the shape of the data points denoting the specific Sn NNN arrangement. Where *n* Sn NNN = 4, 3 and 2 in (b) the data points for the different arrangements have been offset slightly to facilitate comparison.

As described above, simulated spectra were generated (using a Gaussian with LB = 1.0 ppm centred on each $^{89}Y$ $\delta_{iso}$ and weighted by the configurational degeneracy for each individual structural model) for all

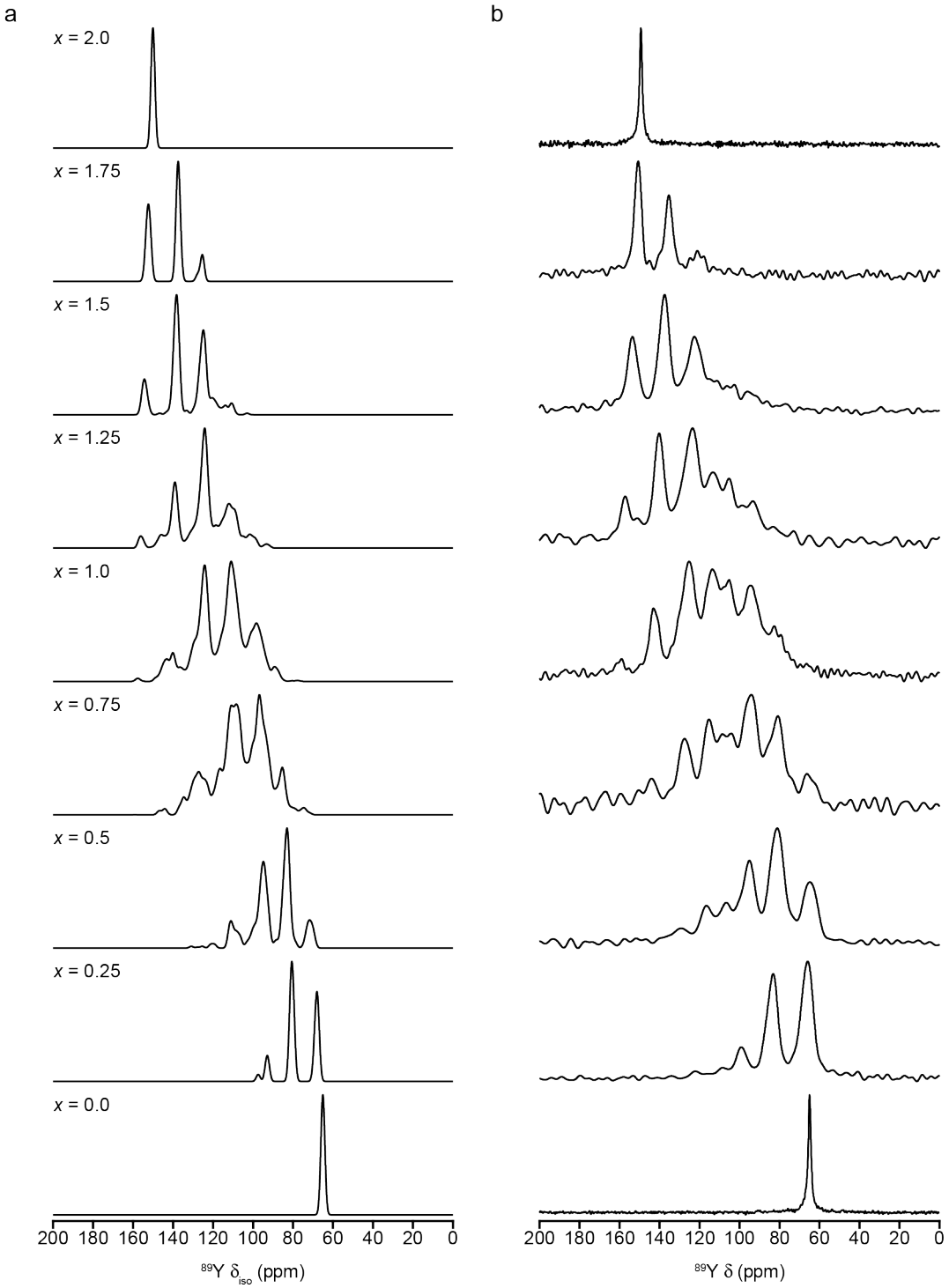


**Figure 5.51:** (a) Simulated $^{89}Y$ NMR spectra for series 2 structural models and (b) experimental $^{89}Y$ (14.1 T, 14 kHz) MAS NMR spectra of $Y_2Sn_xTi_{2-x}O_7$.

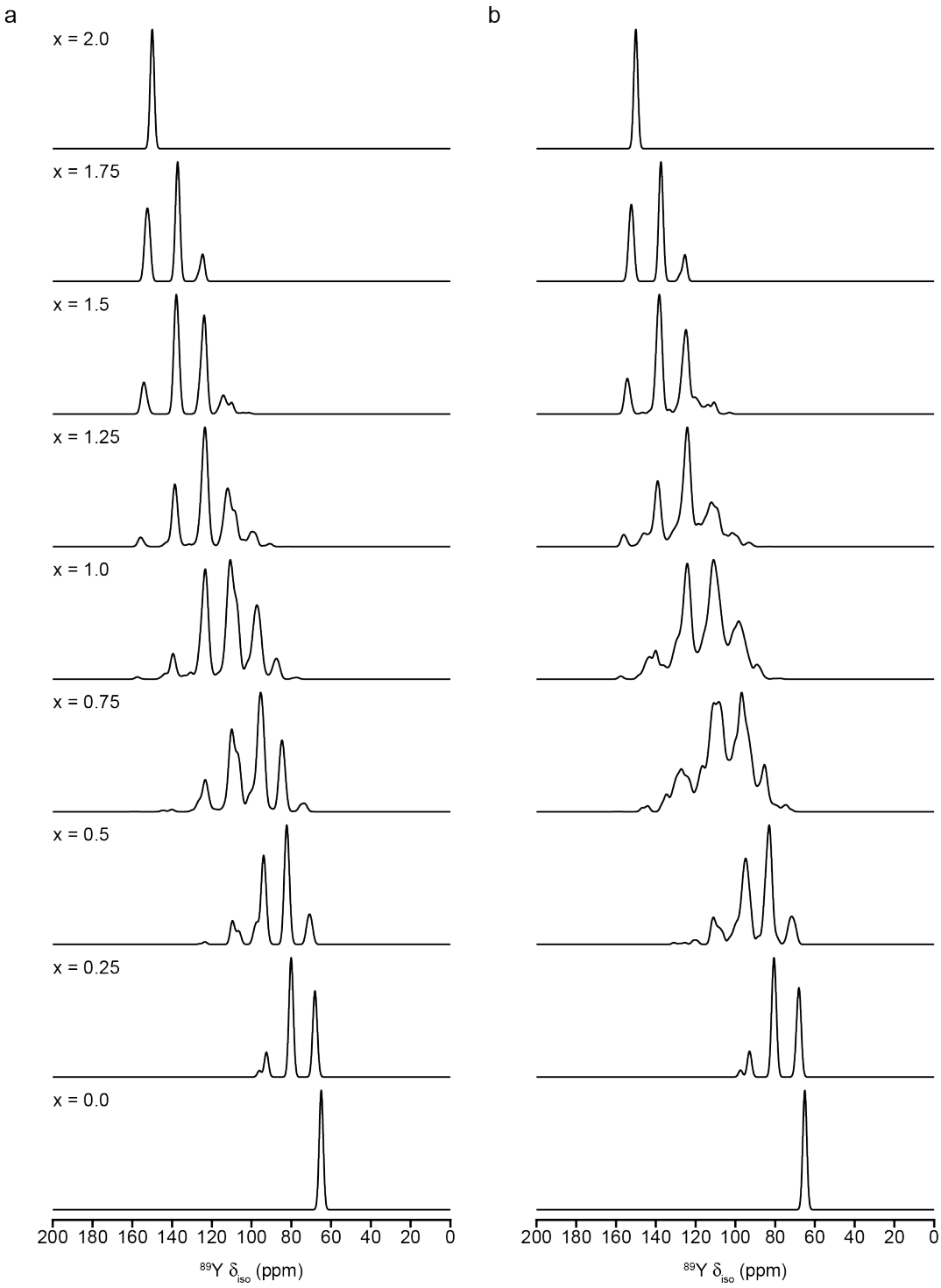


**Figure 5.52:** Simulated $^{89}$Y NMR spectra of (a) series 1 and (b) series 2.

compositions and are shown in Figure 5.51. Good agreement between simulated and experimental NMR spectra are seen (again with the exception of the relative resonance intensities in the spectra for $x$ = 1.75 and 0.25, as observed for the series 1 models).

A direct comparison of the simulated $^{89}$Y spectra for series 1 and series 2 models shown in Figure 5.52 shows that, in general, the resonances in the latter series are broader and more overlapped. As the same LB was used this reflects a larger distribution of shifts (and presumably of local structure) for each *n* Sn NNN. Although at first glance the increased resonance overlap present in series 2 makes the simulated $^{89}$Y spectra seem more complicated and perhaps less "aesthetically pleasing" than those for series 1, these spectra do agree much better with the experimental $^{89}$Y MAS NMR spectra (see Figure 5.51), where significant overlap between neighbouring resonances is observed in many cases.

As discussed earlier for series 1 models, the contributions of different NNN environments to the simulated spectra in series 2 can also be investigated in more detail, as shown in Figure 5.53. Figure 5.53b shows that the extent of overlap in the shifts observed for Y species with different *n* is much more significant than seen for the equivalent spectra in series 1 (see Figure 5.43). For example, some intensity from Y with Sn2Ti4 and Sn3Ti3 NNN environments contributes to the signals seen for Y with Sn4Ti2 and even Sn5Ti environments. This observation could have implications for the accuracy of the integrated intensities determined from experimental $^{89}$Y MAS NMR spectra (or more specifically of the assignment and interpretation of these). When contributions from the nine Sn NNN arrangements for the *n* = 4, 3 and 2 environments are included, as shown in Figure 5.53c (expansion shown in Figure 5.54), it can be seen that there is a clear difference in shift (of ~5 ppm) for 1,2,3-Sn3Ti3 and 1,2,4-Sn3Ti3 arrangements, again resulting in a small shoulder (less clear than in the simulated spectrum of series 1 models) on the spectral resonance.

The calculated $^{119}$Sn $\delta_{iso}$ and $\Omega$ for the 279 series 2 structural models were also investigated, with Figure 5.55 showing these parameters plotted as a function of *n* Sn NNN. Surprisingly, both plots are similar to those seen for the series 1 models (see Figure 5.45), with a significant number of unusually large $^{119}$Sn $\delta_{iso}$ and significant overlap of the shift ranges seen for Sn species

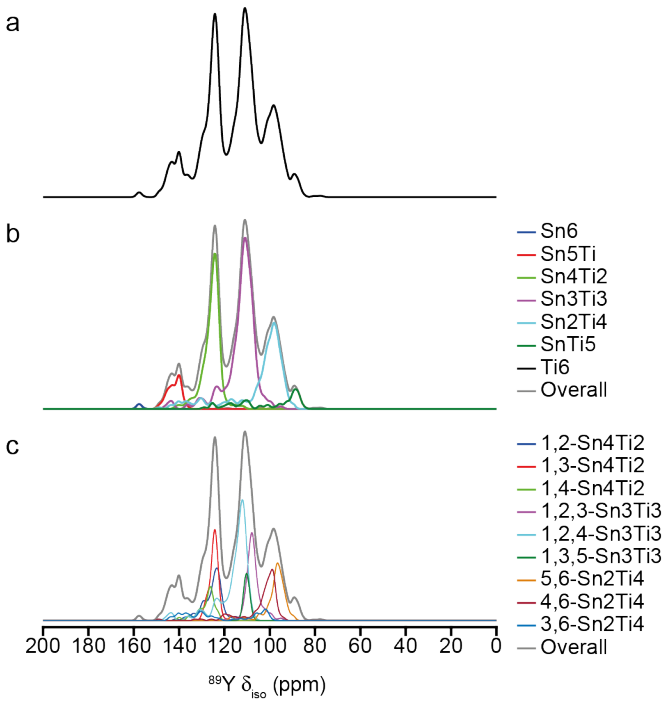


**Figure 5.53:** (a) Simulated $^{89}$Y NMR spectrum resulting from series 2 structural models of $Y_2SnTiO_7$, with the spectrum decomposed according to (b) *n* Sn NNN and (c) the specific Sn NNN arrangements for *n* = 4, 3 and 2 environments.

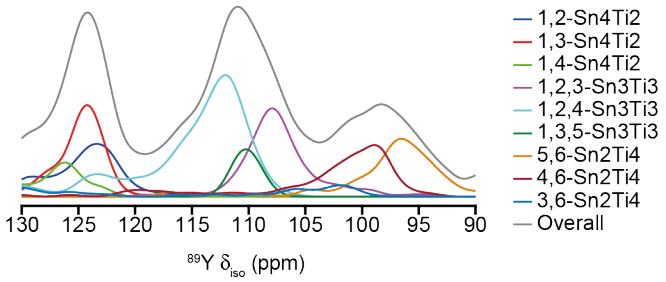


**Figure 5.54:** Horizontal expansion of the simulated $^{89}$Y NMR spectrum resulting from series 2 structural models of $Y_2SnTiO_7$, decomposed according to the specific Sn NNN arrangements for *n* = 4, 3 and 2 environments.

with different *n* Sn NNN. This suggests that even with the more accurate Sn pseudopotential used during the VASP 5 geometry optimisations of the series 2 structural models, there is still some variation in the optimised models leading to inaccurate predicted NMR parameters and poor agreement with experiment.

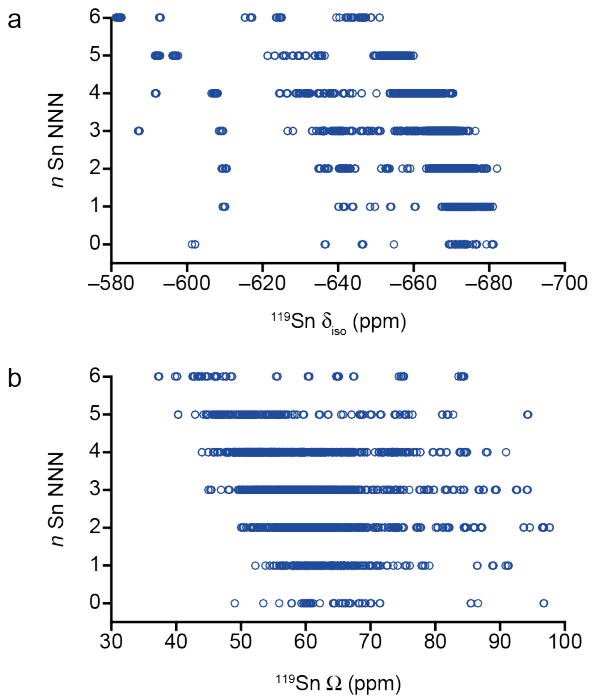


**Figure 5.55:** Plot of calculated $^{119}$Sn (a) $\delta_{iso}$ and (b) **Ω** as a function of *n* Sn NNN for series 2 structural models of $Y_2Sn_xTi_{2-x}O_7$.

In summary, the calculated $^{89}$Y NMR parameters for the series 2 structural models are in better agreement with experiment than those for series 1, and the simulations are able to provide additional insight into the assignment and interpretation of the experimental NMR spectra. However, surprisingly poor agreement is obtained for $^{119}$Sn NMR parameters, raising concerns about the accuracy of the optimised models and suggesting a different approach may be required.

### 5.5.5.3 SOD-generated structural models: series 3

In order to investigate the accuracy of the optimised structural models discussed above, a further set of 279 models were produced. The series 1 structural models, initially geometry optimised, using VASP 5 (see Section 5.5.5.1) were used as the input structures for a second geometry optimisation, this time using CASTEP 8.0. This set of structures will be referred to as series 3. All geometry optimisations and subsequent NMR parameter calculations were performed using CASTEP 8.0, with an $E_{cut}$ of 60 Ry, a k-point spacing of

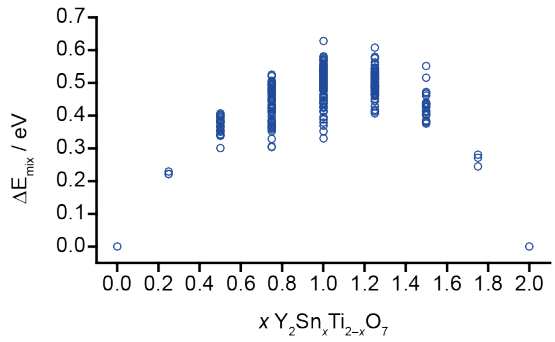


**Figure 5.56::** Plot of relative energy of mixing ($\Delta E_{mix}$) as a function of Sn composition, $x$, for the 279 series 3 structural models of $Y_2Sn_xTi_{2-x}O_7$.

0.04 2π Å$^{-1}$ (see Appendix A1 for convergence testing), the PBE $E_{XC}$ functional,[94] default on-the-fly ultrasoft pseudopotentials,[95] a `geom_energy_tol` value of 1 × 10$^{-5}$ eV / atom and an `elec_energy_tol` value of 1 × 10$^{-9}$ eV / atom (see Section 5.5.4.1) used, with the ZORA correction applied for both calculations. A description of the referencing of $^{89}$Y, $^{119}$Sn and $^{17}$O NMR parameters, which are based on either one ($^{119}$Sn) or both ($^{89}$Y and $^{17}$O) pyrochlore end members, $Y_2Sn_2O_7$ and $Y_2Ti_2O_7$, is given in Appendix A6. In this section only the magnitude of the $^{17}$O $C_Q$ value is considered.

As shown in Figure 5.56, the $\Delta E_{mix}$ for series 3 are very similar to the corresponding plots for both series 1 and series 2, with the asymmetric shape apparent. As for both of the previous series, all 279 SOD-generated $Y_2Sn_xTi_{2-x}O_7$ structures have a positive $\Delta E_{mix}$ although as discussed above, $\Delta E_{mix}$ does not account for the effects of entropy for the mixed-metal materials. Based on the series 3 $\Delta E_{mix}$ for the $x$ = 0.25 and 1.75 structural models, it appears that it is energetically favourable to substitute a small amount of Sn into $Y_2Ti_2O_7$, compared to substitute an equal amount of Ti into $Y_2Sn_2O_7$, in agreement with the $\Delta E_{mix}$ for Series 1 and 2.

Figure 5.57 shows the calculated $^{89}$Y $\delta_{iso}$, Ω and κ plotted against $n$ Sn NNN, with Figure 5.57a confirming that as $n$ Sn NNN decreases, there is a general upfield shift in $\delta_{iso}$, with very large ranges in shift seen for $n$ Sn NNN < 4. Of

the three SOD-generated series discussed in Section 5.5.5, it is clear that the series 3 models have the largest number of outlying data points with higher $^{89}$Y $\delta_{iso}$ than perhaps expected given the average values. Indeed, a number of Y with Sn3TI3, Sn2Ti4, SnTi5 or Ti6 environments exhibit calculated $^{89}$Y $\delta_{iso}$ more typical of Y surrounded by five or six Sn, *i.e.*, Sn5Ti or Sn6 environments. In contrast, the calculated $^{89}$Y Ω exhibits a systematic increase as the number of Sn occupying the six NNN B sites decreases, in good agreement with previous results for season 1 and season 2 structural models. Figure 5.57c indicates that there is a reasonably large variation in $^{89}$Y κ, regardless of the specific *n* Sn NNN, as perhaps expected given the local

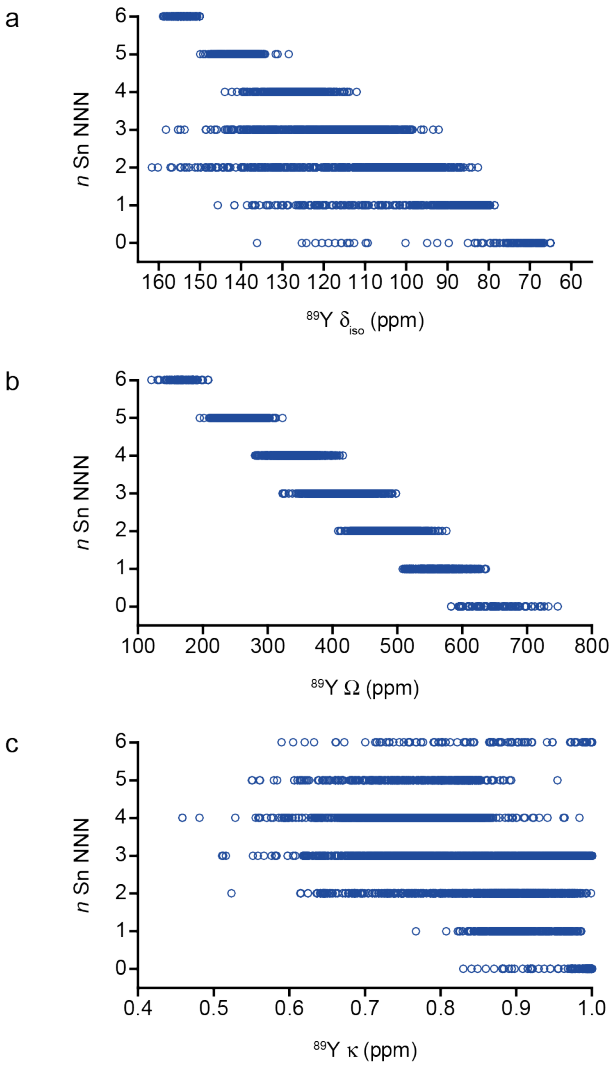


**Figure 5.57:** Plot of calculated $^{89}$Y (a) $\delta_{iso}$, (b) Ω and (c) κ as a function of *n* Sn NNN for all 279 series 3 structural models of $Y_2Sn_xTi_{2-x}O_7$.

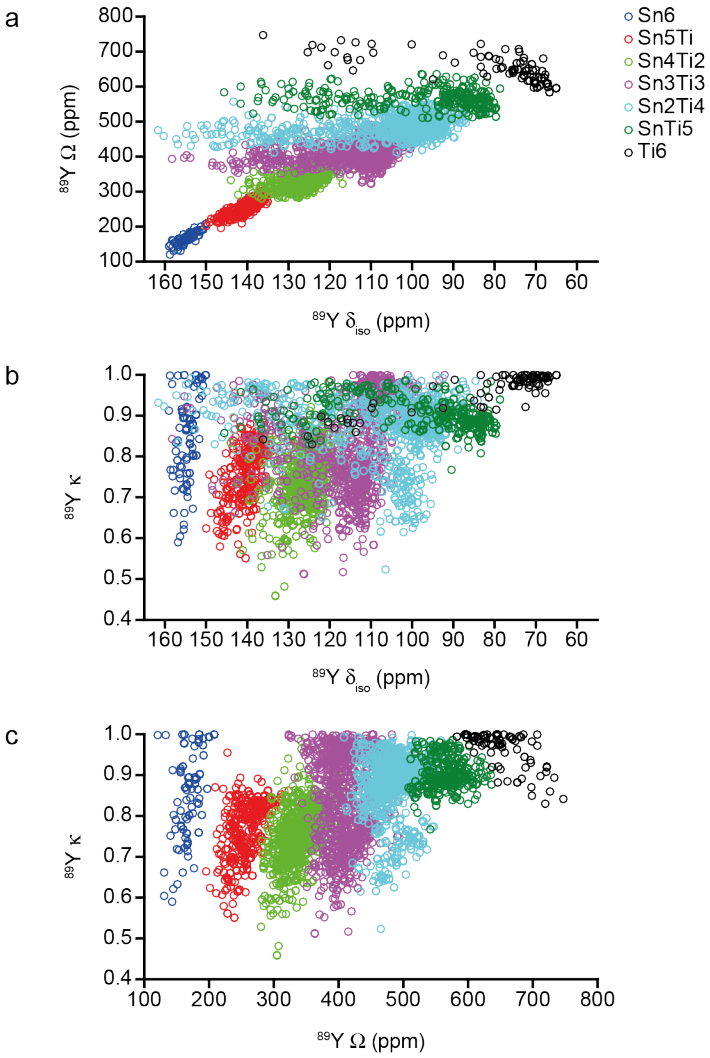


**Figure 5.58:** Plot of calculated $^{89}$Y $\delta_{iso}$, as a function of (a) Ω and (b) κ, (c) plot of calculated $^{89}$Y Ω as a function of κ for all 279 series 3 structural models of $Y_2Sn_xTi_{2-x}O_7$, with data points coloured by *n* Sn NNN.

symmetry associated with the different arrangements of Sn and Ti on the neighbouring sites. When these three NMR parameters are plotted against each other, as shown in Figure 5.58, the strong dependence of $^{89}$Y Ω on *n* Sn NNN, as well the lack of similar dependence for $\delta_{iso}$ and κ, which both show large variations for Y with the same *n* Sn NNN environment are clear.

As shown in Figure 5.59, the Series 3 structural models exhibit the largest range of structural parameters seen for the three sets, *i.e.*, the most significant variation in mean bond lengths and deviations in bond angles. Despite this,

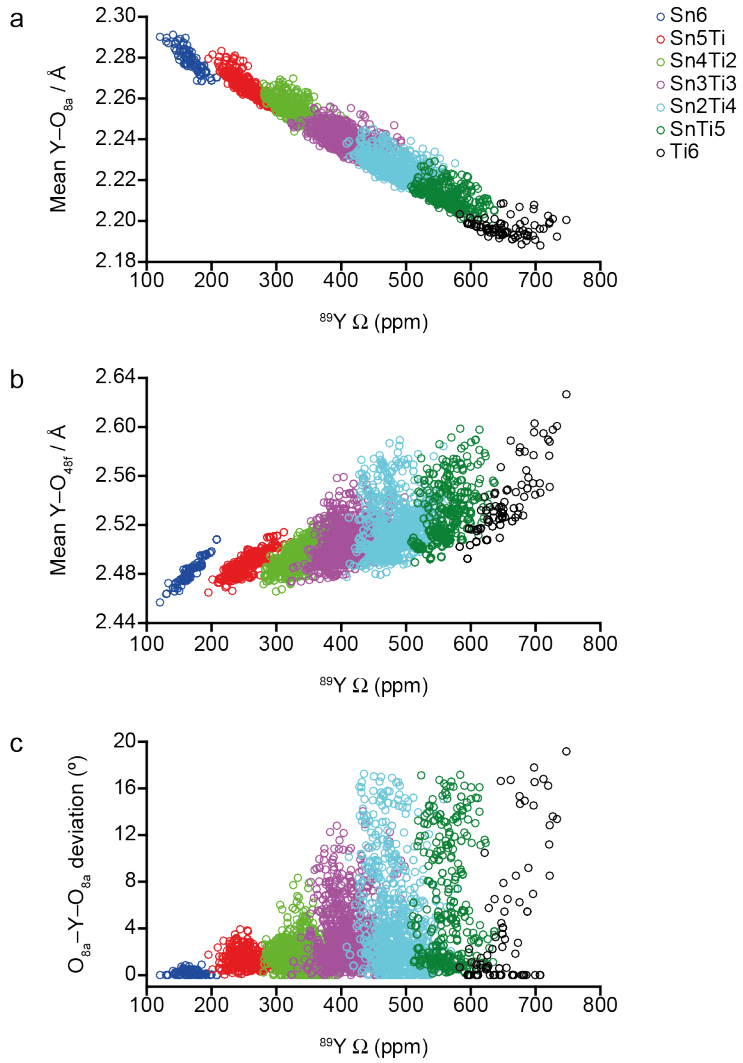


**Figure 5.59:** Plot of calculated $^{89}$Y Ω as a function of (a) mean Y–$O_{8a}$ bond length, (b) mean Y–$O_{48f}$ bond length and (c) deviation in the $O_{8a}$–Y–$O_{8a}$ bond angle from 180°, for all 279 series 3 structural models of $Y_2Sn_xTi_{2-x}O_7$, with data points coloured by *n* Sn NNN.

similar trends between the local structural parameters and calculated $^{89}$Y Ω and those seen for series 1 and 2 models are also observed here, with a particularly strong correlation with the mean Y–$O_{8a}$ bond length and calculated $^{89}$Y Ω, as shown in Figure 5.59a. An increase in $^{89}$Y Ω is accompanied by a general lengthening of the mean Y–$O_{48f}$ bond length, a trend that can be seen in the entire data set as a whole, as well as for species with the same *n* Sn NNN environments. From Figure 5.59c it is clear that calculated $^{89}$Y Ω is not strongly affected by variations in $O_{8a}$–Y–$O_{8a}$ bond angle, as even Y exhibiting deviations of almost 20° still lie within the region

of Ω common to species with *n* Sn NNN. Figure 5.60 indicates that calculated $^{89}$Y κ is perhaps as expected, not strongly correlated to mean Y–$O_{8a}$, Y–$O_{48f}$ bond lengths, or to the degree of deviation in the $O_{8a}$–Y–$O_{8a}$ bond angle.

The relationships between local structural parameters and calculated $^{89}$Y $\delta_{iso}$ for Series 3 have also been investigated. From Figure 5.61a it is clear that although a decrease in *n* Sn NNN results in a shortening of the mean Y–$O_{8a}$ bond length, all Y species with the same *n* are affected in a similar way, regardless of their $^{89}$Y $\delta_{iso}$, indicating there is not a strong correlation between

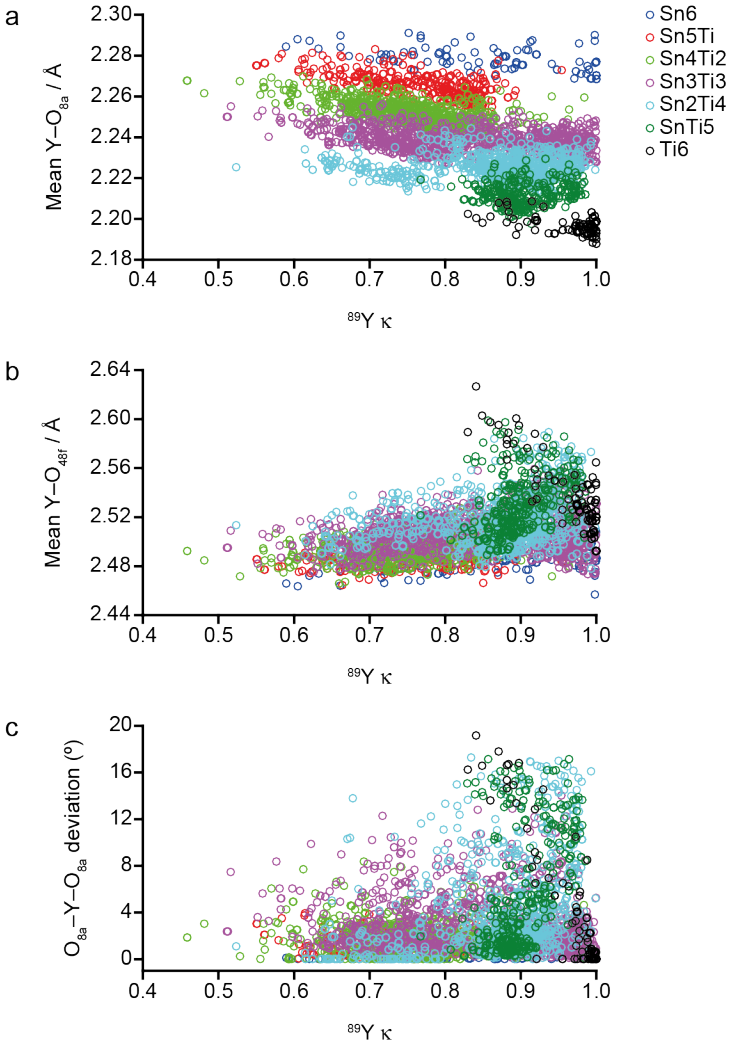


**Figure 5.60:** Plot of calculated $^{89}$Y κ as a function of (a) mean Y–$O_{8a}$ bond length, (b) mean Y–$O_{48f}$ bond length and (c) deviation in the $O_{8a}$–Y–$O_{8a}$ bond angle from 180°, for all 279 series 3 structural models of $Y_2Sn_xTi_{2-x}O_7$, with data points coloured by *n* Sn NNN.

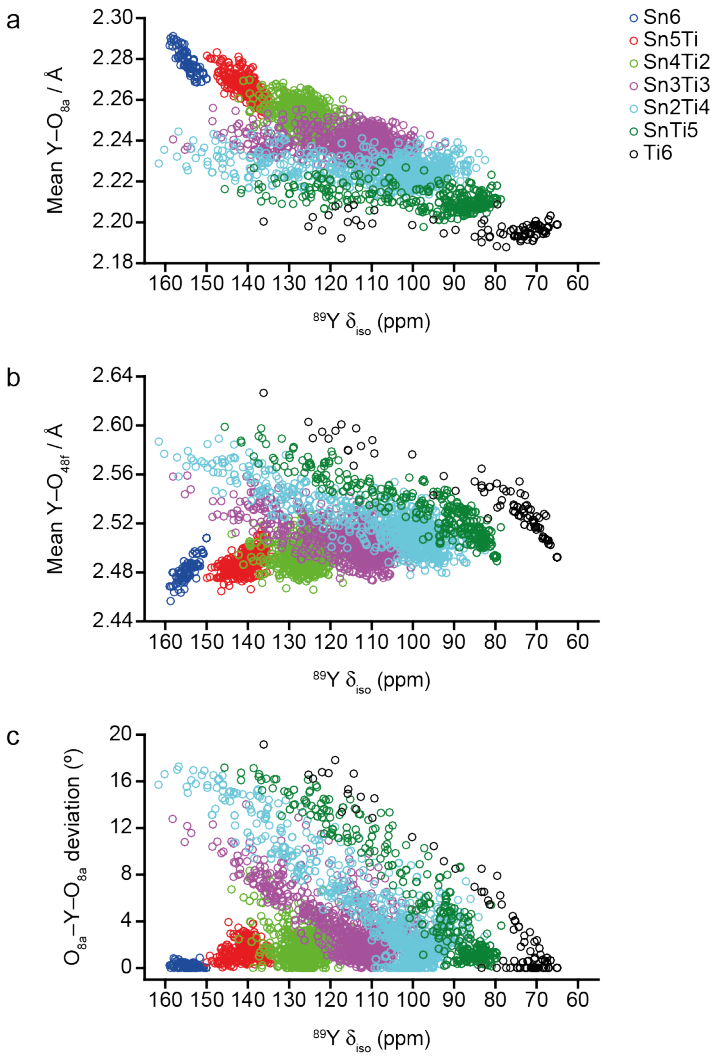


**Figure 5.61:** Plot of calculated $^{89}Y$ $\delta_{iso}$ as a function of (a) mean Y–$O_{8a}$ bond length, (b) mean Y–$O_{48f}$ bond length and (c) deviation in the $O_{8a}$–Y–$O_{8a}$ bond angle from 180°, for all 279 series 3 structural models of $Y_2Sn_xTi_{2-x}O_7$, with data points coloured by *n* Sn NNN.

this and mean Y–$O_{8a}$ bond length. Figure 5.61b suggests there is a reasonable correlation between the mean Y–$O_{48f}$ bond length and $^{89}Y$ $\delta_{iso}$, with Y that have abnormally high shifts for a particular *n*, also exhibiting the longest mean Y–$O_{48f}$ bond lengths. The strongest correlation however is between the $O_{8a}$–Y–$O_{8a}$ bond angle deviation and $^{89}Y$ $\delta_{iso}$ as shown in Figure 5.62c, with the larger shifts associated with Y species that have more distorted bond angles. The magnitude of these deviations is greatest for the series 3 structural models.

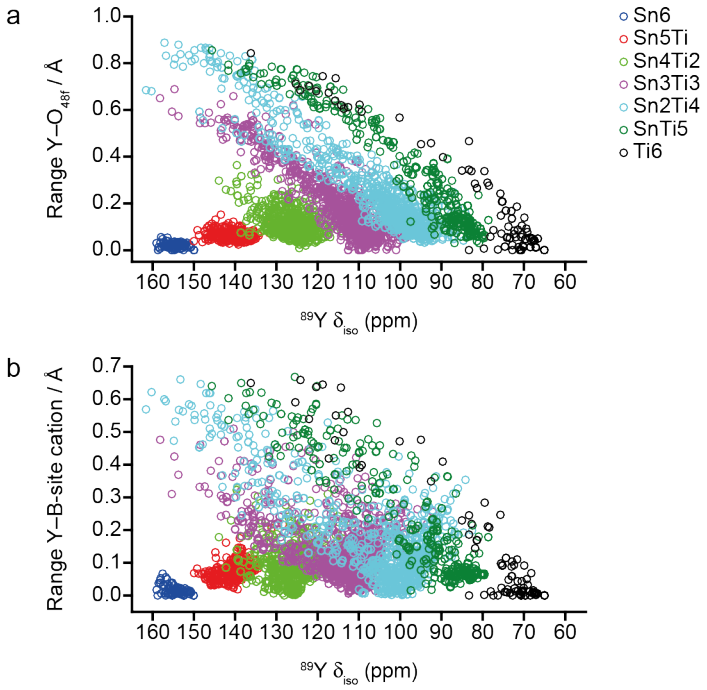


**Figure 5.62:** Plot of calculated $^{89}$Y $\delta_{iso}$ as a function of (a) the range in Y–$O_{48f}$ bond lengths and (b) the range in Y–B-site cation interatomic distances for all 279 series 3 structural models of $Y_2Sn_xTi_{2-x}O_7$, with data points coloured by *n* Sn NNN.

The relationships between calculated $^{89}$Y $\delta_{iso}$ and the range in Y–$O_{48f}$ bond length and Y–B-site interatomic distances found for the series 3 structural models were also considered, as shown in Figure 5.62. A strong correlation is clear for both parameters, with Y species that have larger variations in the Y–$O_{48f}$ bond lengths and the Y–B-site cation interatomic distances also having larger $^{89}$Y $\delta_{iso}$. This further indicates that Y with unusually large $^{89}$Y $\delta_{iso}$ relative to that expected shift for *n* Sn NNN, have extremely distorted local environments, including large deviation in $O_{8a}$–Y–$O_{8a}$ bond angles and large ranges in both Y–$O_{48f}$ bond lengths and Y–B-site cation interatomic distances. Indeed, as shown in Figure 5.63, there seems to be a direct correlation between the range of Y–$O_{48f}$ bond lengths and the degree of deviation in the$O_{8a}$–Y–$O_{8a}$ bond angle, irrespective of the number of Sn NNN. Figure 5.64 confirms that the range of deviation observed in the $O_{8a}$–Y–$O_{8a}$ bond angle increases significantly with the number of Ti occupying the six NNN B sites, most likely, as discussed above, as a result of the small ionic radius of $Ti^{4+}$.

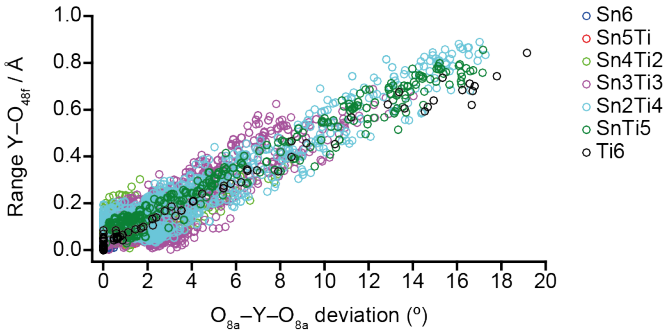


**Figure 5.63:** Plot of the deviation in the $O_{8a}$–Y–$O_{8a}$ bond angle from 180°, as a function of the range in Y–$O_{48f}$ bond lengths for all 279 series 3 structural models of $Y_2Sn_xTi_{2-x}O_7$, with data points coloured by *n* Sn NNN.

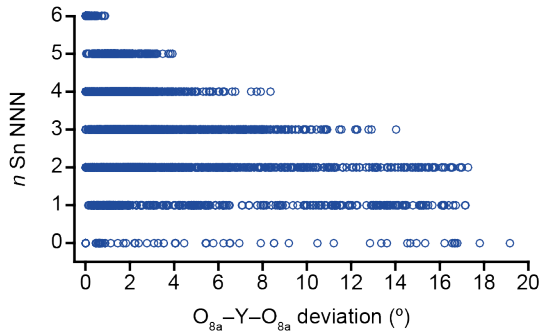


**Figure 5.64:** Plot of the deviation in the $O_{8a}$–Y–$O_{8a}$ bond angle from 180°, as a function of *n* Sn NNN for all 279 series 3 structural models of $Y_2Sn_xTi_{2-x}O_7$.

The effect of the deviation in the $O_{8a}$–Y–$O_{8a}$ bond angle upon $^{89}Y$ $\delta_{iso}$ is even more apparent in Figure 5.65a, which also illustrates how the range of bond angles seen increases with decreasing *n* (*i.e.*, an increasing number of Ti NNN). Figure 5.65b confirms (as seen for series 1 and 2 structural models) that the deviation in the $O_{8a}$–Y–$O_{8a}$ bond angle (and the unusual shift that accompanies this) affects some NNN arrangements more than others. While the $^{89}Y$ $\delta_{iso}$ for all three $n = 4$ (Sn4Ti2) arrangements are very similar, the same is not true for the three $n = 3$ (Sn3Ti3) arrangements.

The 1,2,3-Sn3Ti3 and 1,3,5-Sn3Ti3 arrangements all have very similar $^{89}Y$ $\delta_{iso}$, whereas Y species with a 1,2,4-Sn3Ti3 arrangement are solely responsible for the highest $^{89}Y$ $\delta_{iso}$ seen for the Sn3Ti3 environment. In contrast, all three types of Sn2Ti4 arrangements have Y species with extremely high $^{89}Y$ $\delta_{iso}$,

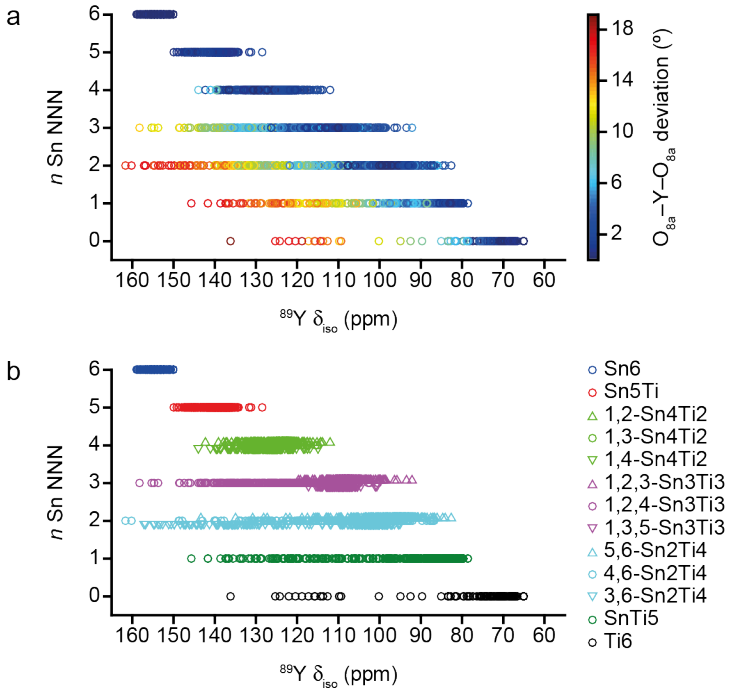


**Figure 5.65:** Plot of calculated $^{89}Y$ $\delta_{iso}$ as a function of *n* Sn NNN for all 279 series 3 structural models of $Y_2Sn_xTi_{2-x}O_7$, with (a) the data points coloured by the deviation in the $O_{8a}$–Y–$O_{8a}$ bond angle from 180° and (b) the shape of the data points denoting the specific Sn NNN arrangement. Where *n* = 4, 3 and 2 in (b) the data points for the different arrangements have been offset slightly to facilitate comparison.

supporting the previous suggestion that the increasing structural flexibility associated with larger numbers of smaller Ti cations produces more distorted local geometries.

Following the same approach used for series 1 and 2, *i.e.*, using a Gaussian with a LB of 1.0 ppm, simulated spectra based on the calculated $^{89}Y$ $\delta_{iso}$ were generated for all series 3 compositions, with the comparison between these and the corresponding experimental $^{89}Y$ MAS NMR spectra shown in Figure 5.66. In general, there is very good agreement between the two sets of spectra, with even the splitting in the Sn3Ti3 peak in the spectrum of $Y_2SnTiO_7$, now clearly apparent. As shown in Figure 5.67, when the simulated $^{89}Y$ spectra are decomposed according to contributions from species with different *n* Sn NNN, significant overlap between neighbouring resonances is apparent for many compositions, and resulting in better agreement with the more overlapped experimental spectra. A direct

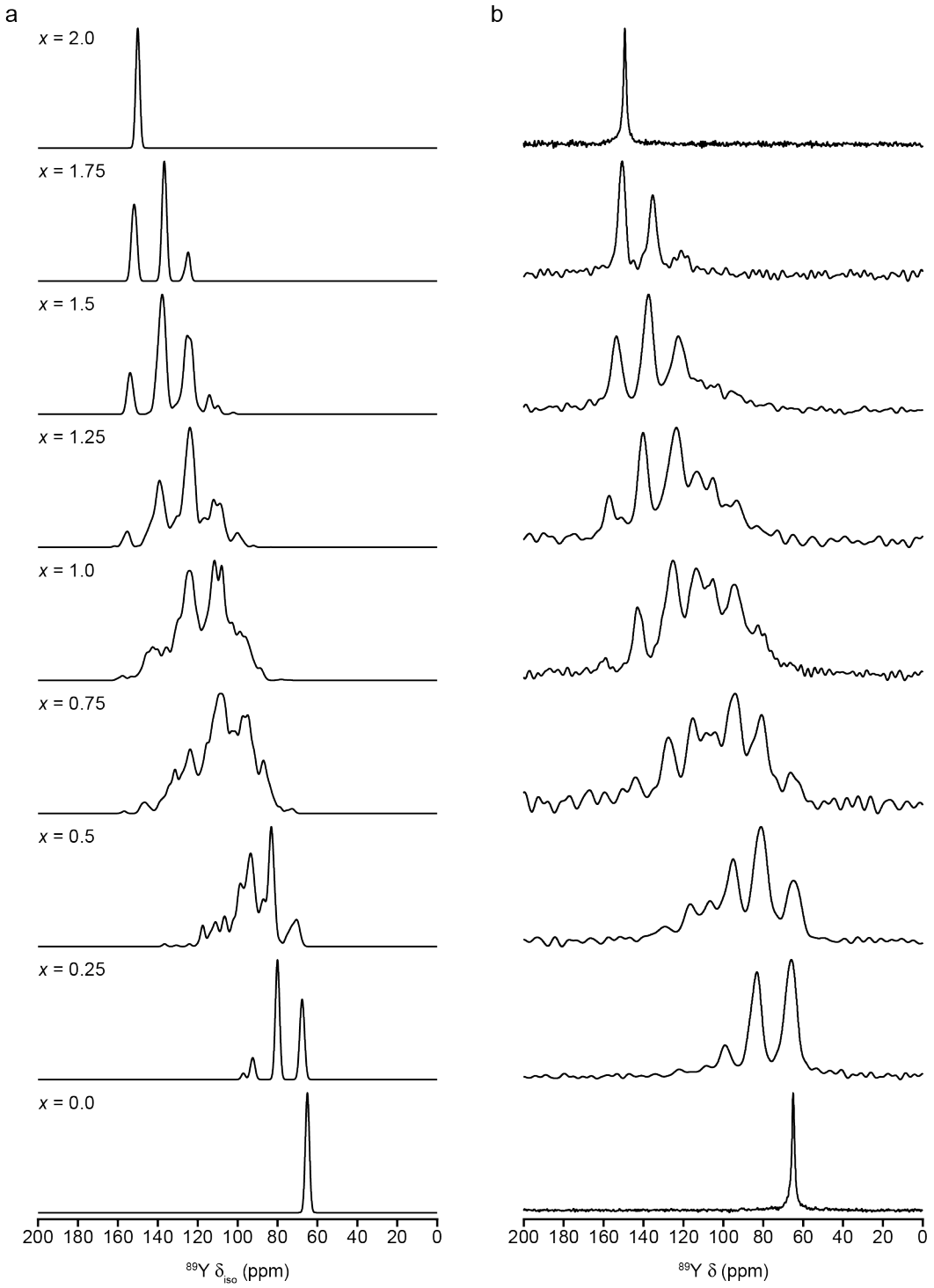


**Figure 5.66:** (a) Simulated $^{89}Y$ NMR spectra for series 3 structural models and (b) experimental $^{89}Y$ (14.1 T, 14 kHz) MAS NMR spectra of $Y_2Sn_xTi_{2-x}O_7$.

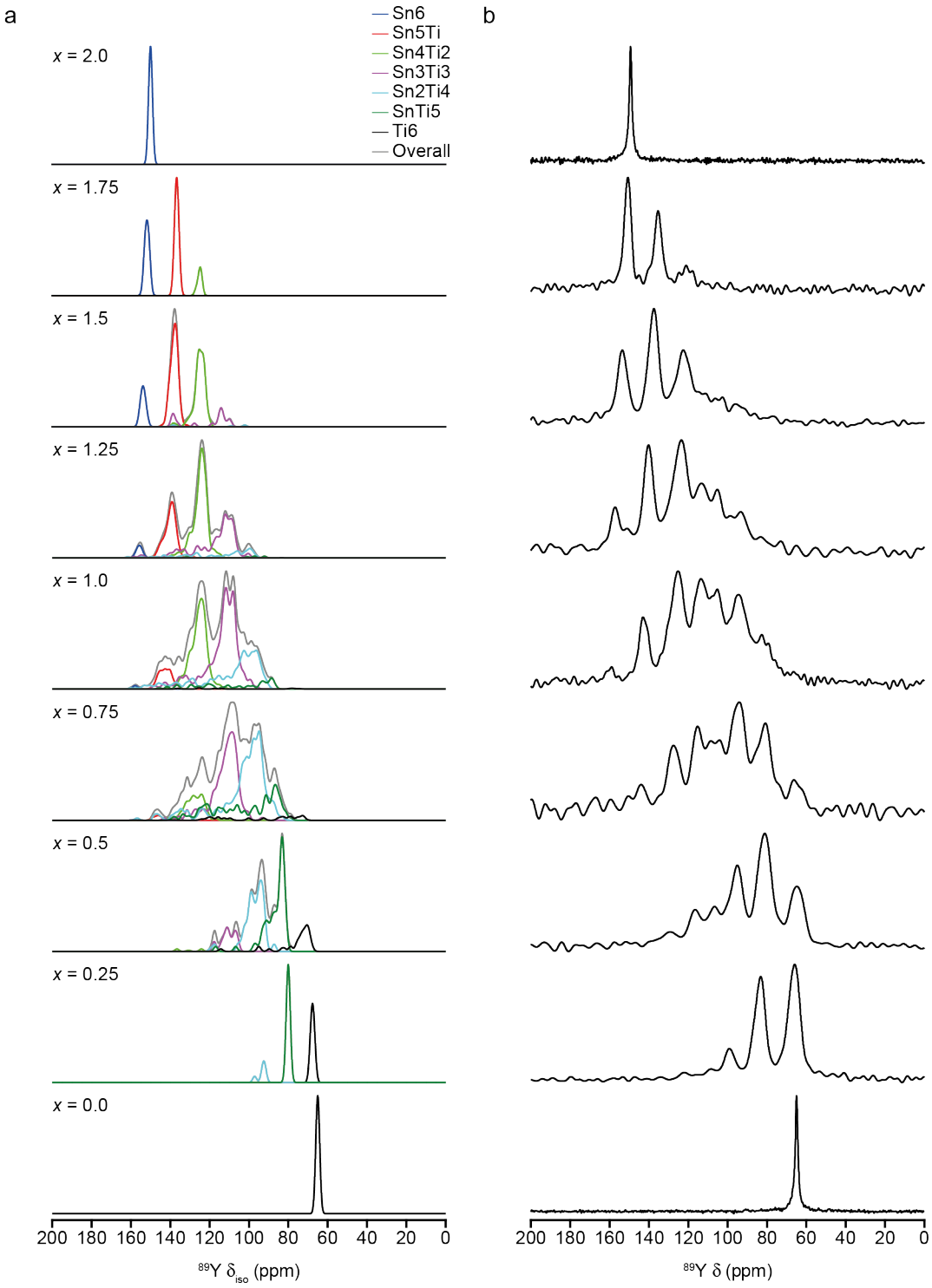


**Figure 5.67:** (a) Simulated $^{89}$Y NMR spectra for series 3 structural models with the spectra decomposed according to *n* Sn NNN, and (b) experimental $^{89}$Y (14.1 T, 14 kHz) MAS NMR spectra of $Y_2Sn_xTi_{2-x}O_7$.

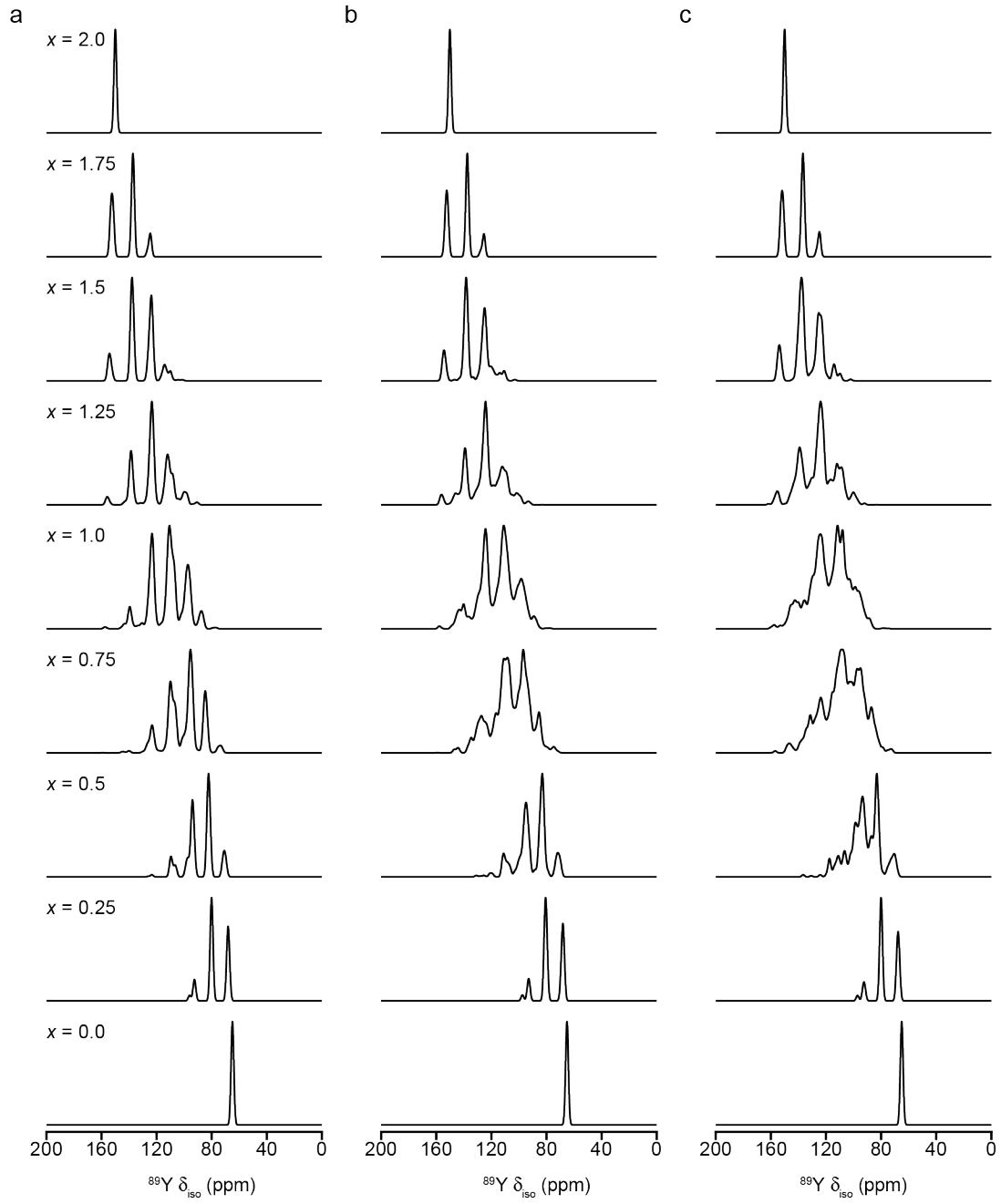


**Figure 5.68:** Simulated $^{89}$Y NMR spectra for (a) series 1, (b) series 2 and (c) series 3 structural models.

comparison of the three sets of simulated $^{89}$Y spectra (*i.e.*, for the three series of $Y_2Sn_xTi_{2-x}O_7$ structural models) is shown in Figure 5.68. This shows that the degree of overlap of the spectral resonances increases significantly on moving from series 1 to series 3, reducing the resolution (but resulting in closer agreement with experiment). Owing to the much smaller overlap between neighbouring resonances for the series 1 models, many spectra

appear somewhat artificially idealised, bearing much less resemblance to the experimental $^{89}$Y spectral lineshapes.

The simulated $^{89}$Y spectrum of $Y_2SnTiO_7$ ($x$ = 1.0), is decomposed according to $n$ Sn NNN, and the specific B-site cation arrangement for $n$ = 4, 3 and 2, in Figure 5.69. it can be seen that the signals resulting from Sn2Ti4

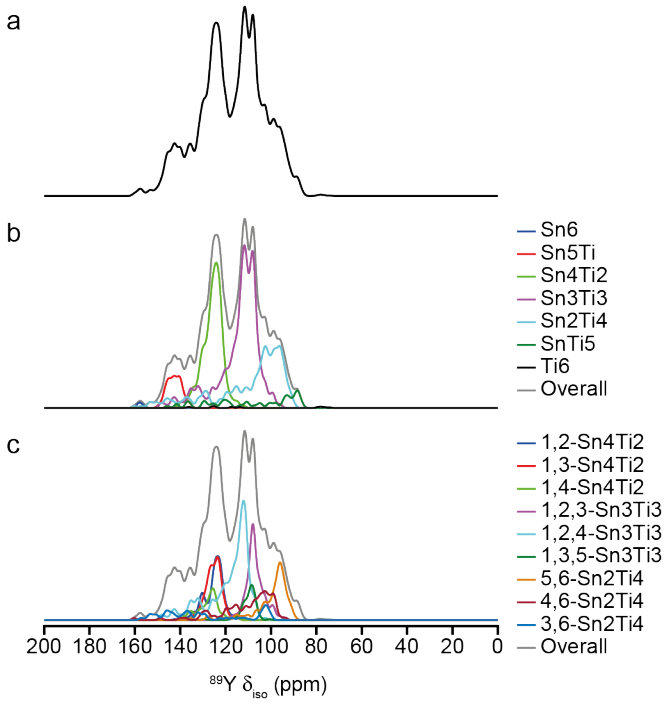


**Figure 5.69:** (a) Simulated $^{89}$Y NMR spectrum of series 3 structural models of $Y_2SnTiO_7$, with the spectrum decomposed according to (b) $n$ Sn NNN and (c) the specific NNN arrangements for the $n$ = 4, 3 and 2 environments.

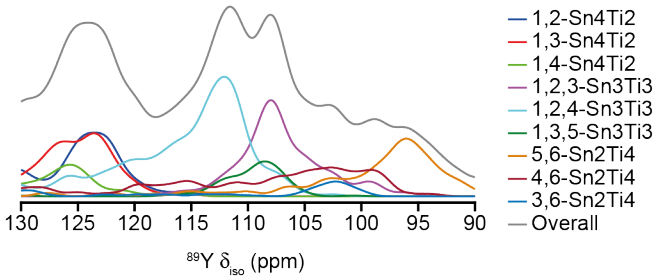


**Figure 5.70:** Horizontal expansion of the simulated $^{89}$Y NMR spectrum of series 3 structural models of $Y_2SnTiO_7$, with the spectrum decomposed according to the specific NNN arrangements for the $n$ = 4, 3 and 2 environments.

environments contribute intensity to several resonances in the spectrum, each representing Y in more Sn-rich NNN environments, especially with a noticeable proportion of the overall intensity in the peak at ~115 ppm (largely resulting from Sn3Ti3 environments) actually supplied by Y with Sn2Ti4 environments with large $^{89}$Y $\delta_{iso}$, no doubt resulting from distortions in their local geometries. In addition, despite significant overlap between the $^{89}$Y $\delta_{iso}$ of Y with different NNN arrangements, Figure 5.69c indicates that the signals resulting from Y with a 1,2,3-Sn3Ti3 or 1,2,4-Sn3Ti3 arrangements, are still separated by ~5 ppm, with the latter exclusively exhibiting a larger shift than the former. The difference in $^{89}$Y $\delta_{iso}$, between these two

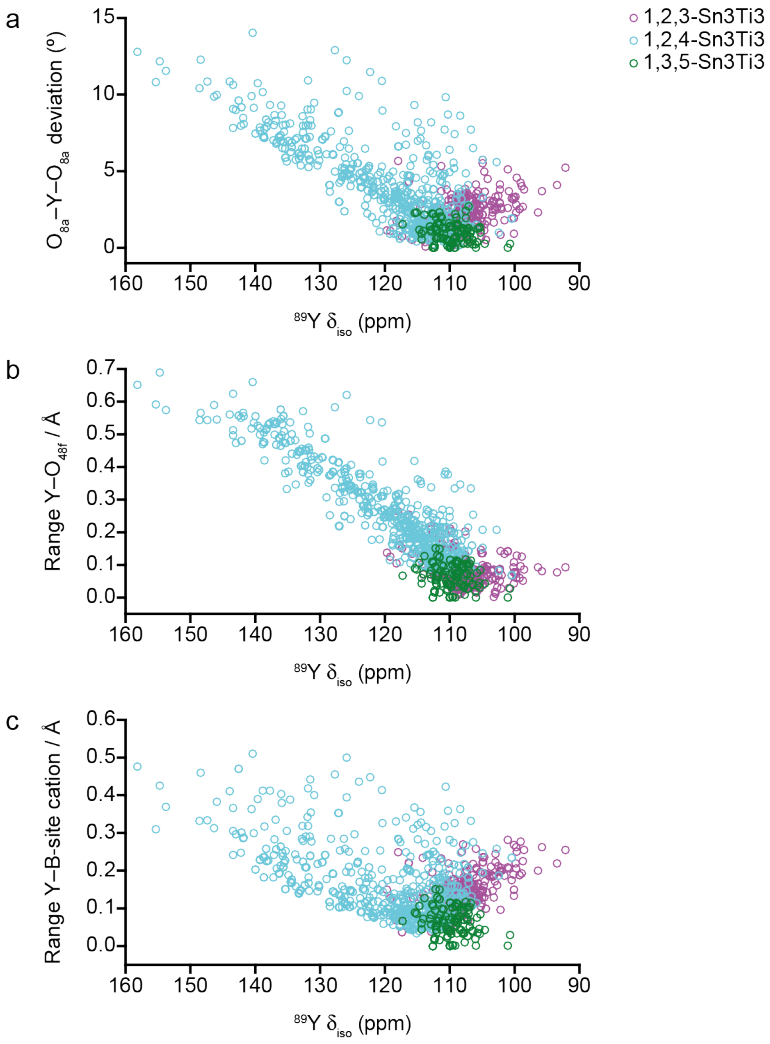


**Figure 5.71:** Plot of calculated $^{89}$Y $\delta_{iso}$ as a function of (a) deviation in the $O_{8a}$–Y–$O_{8a}$ bond angle from 180°, (b) the range of Y–$O_{48f}$ bond lengths and (c) the range of Y–B-site cation interatomic distances, for all 279 series 3 structural models of $Y_2Sn_xTi_{2-x}O_7$, for $n = 3$.

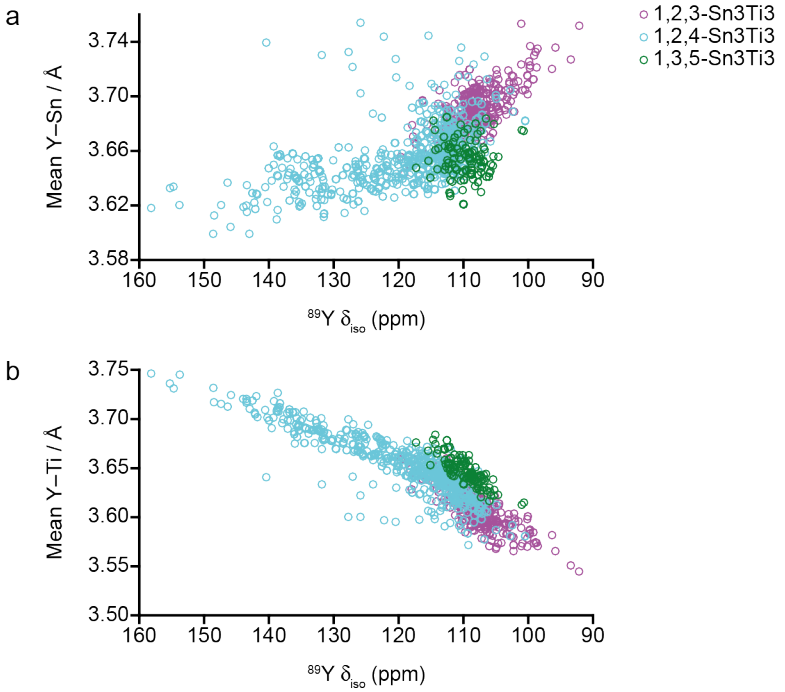


**Figure 5.72:** Plot of calculated $^{89}$Y $\delta_{iso}$ as a function of (a) mean Y–Sn interatomic distance and (b) mean Y–Ti interatomic distance, for all 279 series 3 structural models of $Y_2Sn_xTi_{2-x}O_7$, for $n$ = 3.

Sn3Ti3 arrangements, as well as the significant contribution that many Y with the 1,2,4-Sn3Ti3 arrangement make to the signal at this point is highlighted in the horizontal expansion of Figure 5.69c, shown in Figure 5.70.

In an attempt to understand the different $^{89}$Y $\delta_{iso}$ exhibited by Y with different types of $n$ = 3 B-site cation arrangements, the variation in local geometry surrounding the central Y cation, resulting from the specific way in which the six NNN B sites are occupied by three Sn and three Ti was investigated. From Figure 5.71 it is clear that the 1,2,4-Sn3Ti3 arrangement often results in Y with a more distorted local structure, with Figure 5.72 indicating that the calculated $^{89}$Y $\delta_{iso}$ is strongly dependent on the mean Y–Sn and particularly the mean Y–Ti interatomic distances. As shown in Figure 5.72, for the 1,2,4-Sn3Ti3 arrangement, shorter mean Y–Sn and longer mean Y–Ti interatomic distances are observed. In contrast for 1,2,3-Sn3Ti3 and 1,3,5-Sn3Ti3 arrangements, the mean Y–Ti interatomic distance is shorter than the mean Y–Sn interatomic distance.

Up to this point, all simulated $^{89}$Y NMR spectra have been generated assuming all B-site cation arrangements, *i.e.*, all structural models within a given $x$ $Y_2Sn_xTi_{2-x}O_7$ composition, are equally probable irrespective of any differences, *i.e.*, equivalent to assuming an infinite temperature. It is possible to investigate the effects of any energy differences between the different cation arrangements by weighting the relative populations of each of the 97 individual structural models for $Y_2SnTiO_7$ ($x$ = 1.0) using a temperature-related parameter. This was achieved by multiplying the intensity of the Gaussian signals generated for each individual Y species by the partition function shown in Equation 5.3,

$$P = \frac{g_i \, e^{-\Delta E/k_B T}}{\sum g_i \, e^{-\Delta E/k_B T}} \, , \tag{5.3}$$

where P represents the probability that a particular structural model occurs, $g_i$ is the configurational degeneracy associated with the specific structural model, $\Delta E$ is the energy of that model relative to the model with the lowest energy for that composition, $k_B$ is the Boltzmann constant and T is the temperature. All Gaussians (each representing a single Y) were then constructed using Equation 5.1, with the intensity of each Gaussian summed to give the overall simulated $^{89}$Y NMR spectrum. This process was repeated four times, for "nominal" temperatures of 298, 500, 1000 and 2000 K, respectively. The resulting simulated $^{89}$Y NMR spectra of $Y_2SnTiO_7$, along with the spectrum simulated assuming infinite temperature and the corresponding experiential spectrum are shown in Figure 5.73. From Figure 5.73 it appears that the simulated $^{89}$Y NMR spectrum with the best agreement with the experimental $^{89}$Y MAS NMR spectrum of $Y_2SnTiO_7$ was generated when a finite temperature of 2000 K was used, which also closely resembles the spectrum simulated using an infinite temperature shown in Figure 5.74b. When the finite temperature is reduced, reducing the relative proportions of higher energy structural models, the intensity of the resonance at ~115 ppm (largely from Sn3Ti3 NNN) decreases noticeably, whereas the intensities of signals from Sn5Ti and SnTi5 environments increase significantly. This

suggests that the lowest energy arrangements of B-site cations have increased tendency for B-site cation clustering.

It is clear that the simulated $^{89}$Y NMR spectrum shown in Figure 5.73b gives the best agreement with the experimental $^{89}$Y MAS NMR spectrum of $Y_2SnTiO_7$. This agrees well with previous $^{89}$Y MAS NMR studies into the cation ordering in $Y_2Sn_xTi_{2-x}O_7$,[71,73] which concluded that the B-site cation ordering is best described by a random distribution, *i.e.*, that there is no significant evidence for ordering or clustering. Although Figure 5.73a indicates that the lowest energy arrangements (at 0 K) for $Y_2SnTiO_7$ involve B-site cation clustering, it should be noted that the experimental synthesis temperature is much higher. This might suggest that the relative energies of the different structural models are more similar at higher temperature, or could indicate that there is quenching of atomic arrangements as the sample cools. However, it is also possible that the poor agreement between NMR

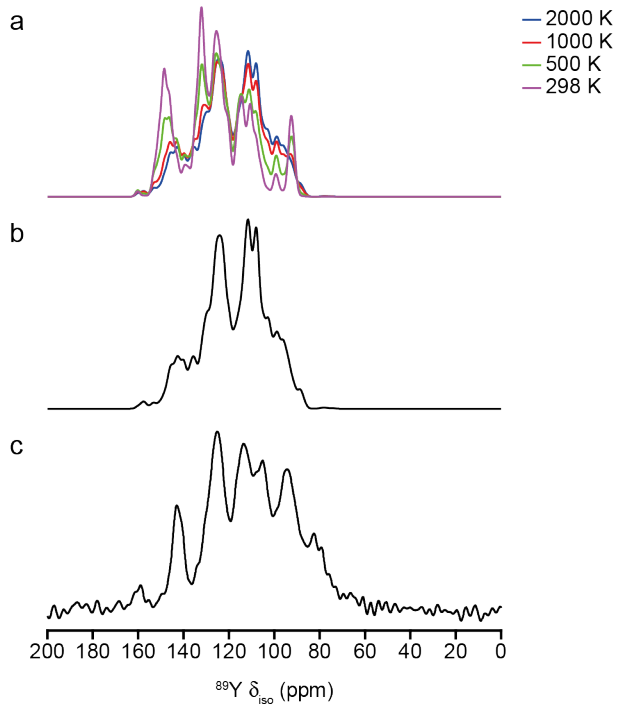


**Figure 5.73:** Simulated $^{89}$Y NMR spectra for series 3 structural models of$Y_2SnTiO_7$, with (a) the lineshape coloured by the temperature used in Equation 5.3, (b) assuming an infinite temperature (*i.e.*, all structural models presumed equally occupied) and (c) experimental $^{89}$Y (14.1 T, 14 kHz) MAS NMR spectrum of $Y_2SnTiO_7$.

spectra simulated using a finite temperature arises due to the accuracy with which the DFT energies can be currently determined. In addition, the weightings considered here reflect differences in calculated enthalpy (and the additional contribution of configurational entropy) rather than differences in free energy.

In summary, DFT calculations of the $^{89}$Y NMR parameters for series 3 structural models have provided insight into the changes in local geometry and the nature of B-site cation ordering in $Y_2Sn_xTi_{2-x}O_7$ pyrochlores. The $^{89}$Y $\delta_{iso}$ provides a sensitive probe of the local geometry, including the variation in Y–$O_{48f}$ bond lengths, Y–B-site cation interatomic distances and deviation in the $O_{8a}$–Y–$O_{8a}$ bond angle. The simulated $^{89}$Y NMR spectra for the series 3 models showed better agreement with the experimental $^{89}$Y MAS NMR spectra of $Y_2Sn_xTi_{2-x}O_7$, than the corresponding spectra for series 1 or series 2. In particular, the splitting in the signal largely arising from Sn3Ti3 environments (most prominent for the $x$ = 1.0 composition) is well reproduced and results from the difference in shift for different arrangements of the three Sn and three Ti cation on the neighbouring B sites. After investigating the use of a finite temperature parameter on the simulated spectra of $Y_2SnTiO_7$, it was seen that best agreement with experiment was obtained when all 97 B-site cation arrangements are equally weighted, *i.e.*, assuming an infinite temperature, suggesting that the B site cations are effectively randomly distributed in the real material.

The calculated $^{119}$Sn NMR parameters, for all 278 (*i.e.*, all excluding $Y_2Ti_2O_7$) Sn-containing series 3 structural models were investigated. Figure 5.74 shows the $^{119}$Sn $\delta_{iso}$, $\Omega$ and $\kappa$ plotted as functions of $n$ Sn NNN. A similar trend with decreasing $n$ is seen for $^{119}$Sn $\delta_{iso}$ as was observed for the cluster models (see Season 5.5.3), with the predicted shifts in good agreement with the spectra seen experimentally (Figure 5.8), where broad and overlapped resonances are observed. The predicted shifts are different to those for the season 1 and 2 structural models, with much narrower ranges in $\delta_{iso}$ found for species with the same value of $n$, suggesting the geometry optimisation

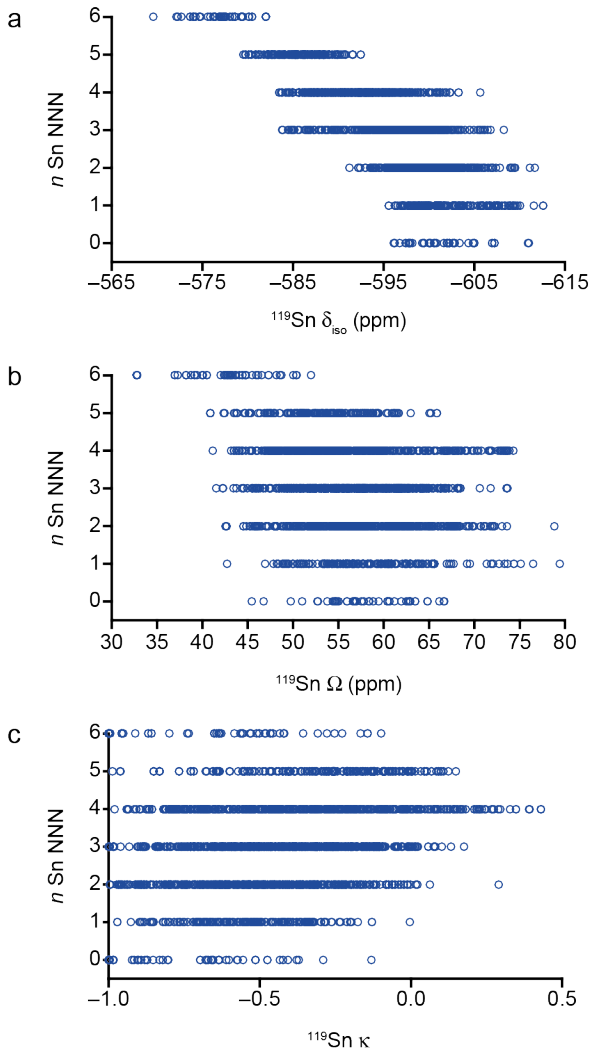


**Figure 5.74:** Plot of calculated $^{119}$Sn (a) $\delta_{iso}$, (b) Ω and (c) κ as a function of *n* Sn NNN for series 3 structural models of $Y_2Sn_xTi_{2-x}O_7$.

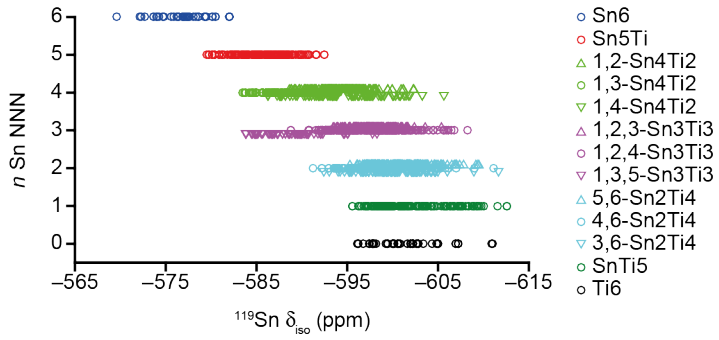


**Figure 5.75:** Plot of calculated $^{119}$Sn $\delta_{iso}$ as a function of *n* Sn NNN for series 3 structural models of $Y_2Sn_xTi_{2-x}O_7$, separated by Sn NNN arrangement. For *n* = 4, 3 and 2, the data points for the different arrangements have been offset slightly to facilitate comparison.

using CASTEP has produced more accurate models. Very similar values of Ω and κ are observed for all Sn species, irrespective of *n*.

Even though there is significant overlap in the range of $^{119}$Sn $\delta_{iso}$ observed especially as *n* decreases, as shown in Figure 5.75, the potential effects that specific NNN arrangements could have on the $^{119}$Sn $\delta_{iso}$ were also considered. Despite most Sn with 1,3,5-Sn3Ti3 arrangements having slightly higher $^{119}$Sn $\delta_{iso}$ than those for the other two types of Sn3Ti3 environments, Figure 5.75 indicates that regardless of the specific NNN B-site cation arrangement, the range of $\delta_{iso}$ for Sn with the same *n* is very similar, and this parameter cannot be used to provide clear distinction between these.

From Figure 5.76 it can be seen that $^{119}$Sn $\delta_{iso}$, while very weakly correlated to mean Sn–$O_{48f}$ bond length, is overall more strongly correlated with either the mean Sn–Y or mean Sn–B-site cation interatomic distances. For a specific *n* Sn NNN, an increase in mean Sn–$O_{48f}$ bond length is accompanied by a decrease in $^{119}$Sn $\delta_{iso}$, a trend that is most noticeable for $n = 6$ or 5 data points, where the overlap between $\delta_{iso}$ for Sn with different NNN environments is not too extensive. A similar, but less pronounced trend is seen in Figure 5.76b and 5.76c, with larger interatomic distances resulting in lower $^{119}$Sn $\delta_{iso}$, however, the *n* Sn NNN is clearly the dominant factor in determining both the mean Sn–Y and Sn–B-site cation interatomic distances.

As better agreement with experiment is obtained for series 3 (as opposed to series 1 or 2) structural models, and given these models predict shifts that are also in good agreement to those observed for the cluster and randomised B-site cation models, discussed earlier, the series 3 models were used to simulate $^{119}$Sn NMR spectra for all eight Sn-containing $Y_2Sn_xTi_{2-x}O_7$ compositions. The same process used to generate the simulated $^{89}$Y NMR spectra was followed; *i.e.*, each individual $^{119}$Sn $\delta_{iso}$ was represented by an individual Gaussian function with 1.0 ppm LB, multiplied by the configurational degeneracy of the specific structural model and summed

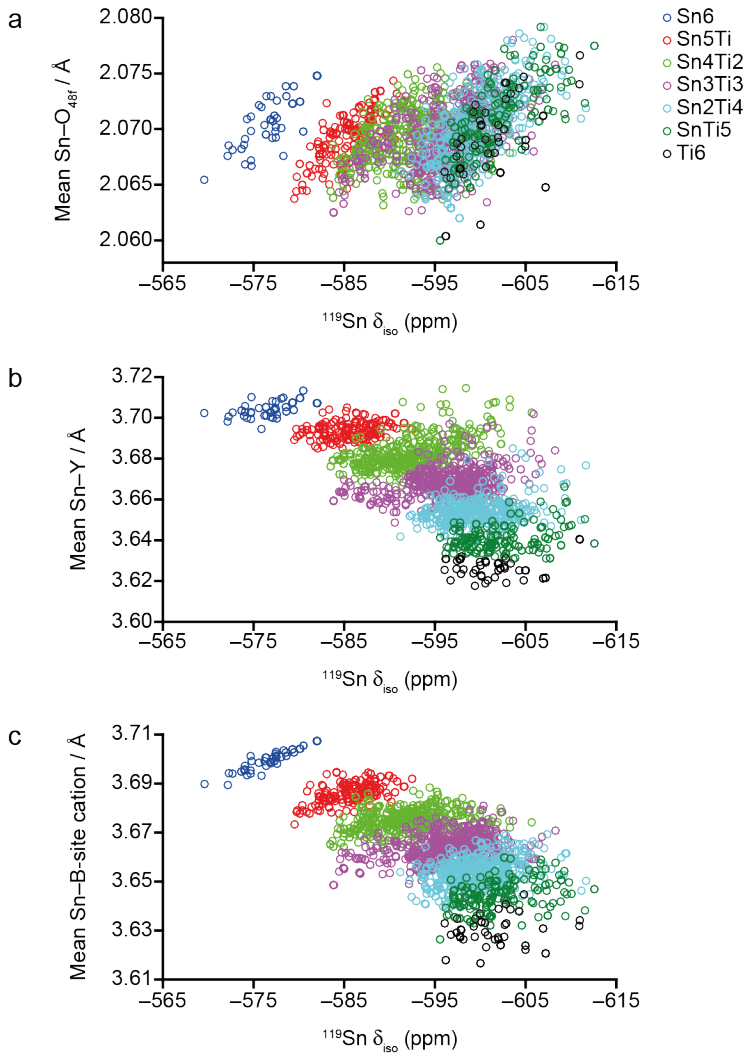


**Figure 5.76:** Plot of calculated $^{119}$Sn $\delta_{iso}$ as a function of (a) mean Sn–$O_{48f}$ bond length, (b) mean Sn–Y interatomic distance and (c) mean Sn–B-site cation interatomic distance for series 3 structural models of $Y_2Sn_xTi_{2-x}O_7$, with data points coloured by *n* Sn NNN.

over all structures for a specific composition. Figure 5.77 shows the simulated $^{119}$Sn NMR spectra alongside the experimental $^{119}$Sn MAS NMR spectra of $Y_2Sn_xTi_{2-x}O_7$. There is reasonable agreement in the overall appearance of the two sets of spectra, although it is possible that an alternative method of referencing (and scaling) of the $^{119}$Sn $\sigma_{iso}$ could result in an even closer match with experiment. Regardless of the small chemical shift differences between the simulated and experimental $^{119}$Sn NMR spectra, in general the two contain the same number of resonances, with the peak intensities also showing relatively good agreement. As seen in the simulated $^{89}$Y NMR spectra, the poorest agreement in peak intensity is seen for the $x$ =

1.75 and 0.25 compositions. As discussed above, this might result from the use of only a single cell (thereby restricting the number of symmetry inequivalent structural models used, and imposing order on lengh scales that are longer than this). For example, in contrast to the unit cell $x = 1.75$ system, which can only contain two Ti cations (thereby only resulting in Sn species

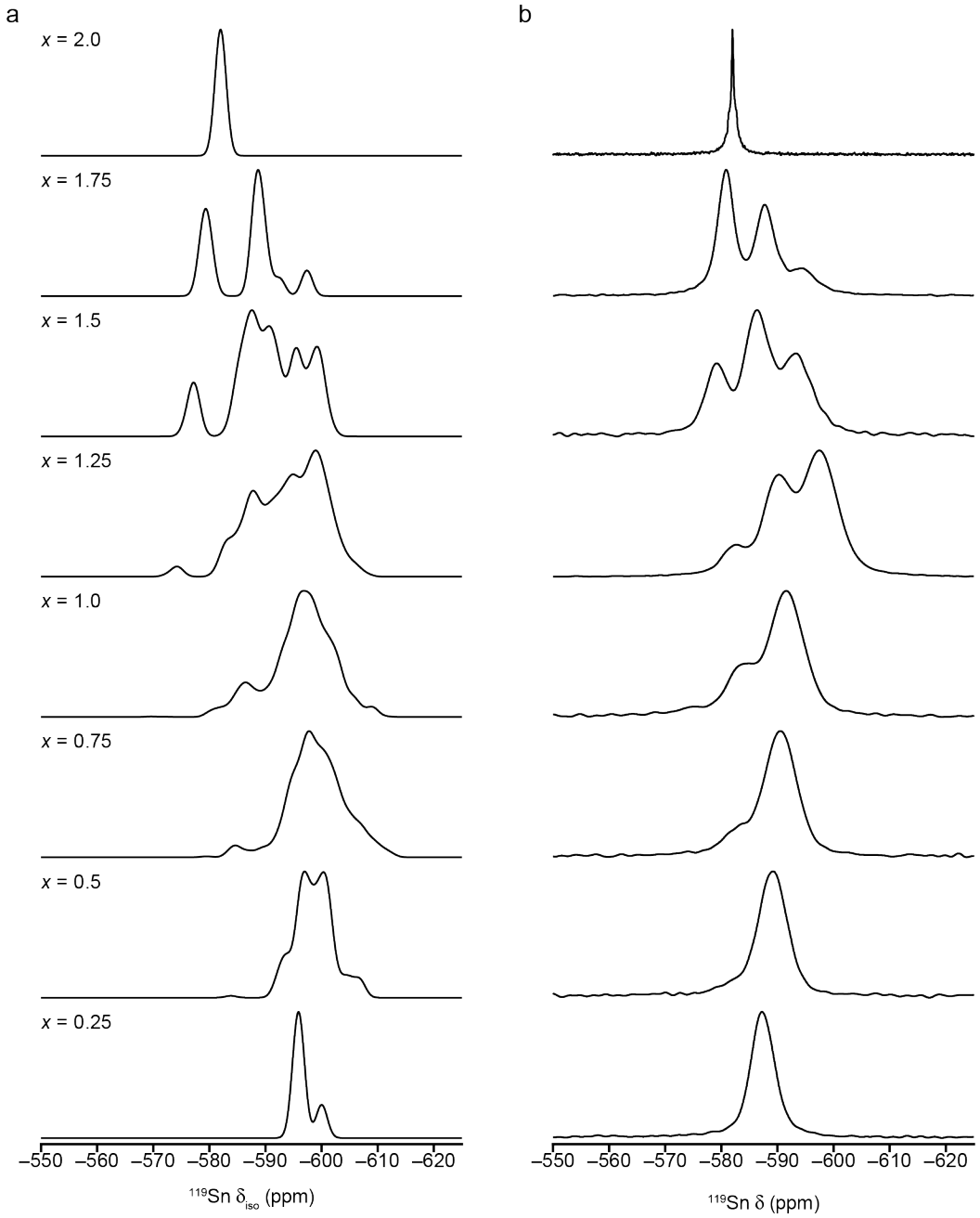


**Figure 5.77:** (a) Simulated $^{119}$Sn NMR spectra for series 3 structural models. (b) $^{119}$Sn (9.4 T, 14 kHz) MAS NMR spectra of $Y_2Sn_xTi_{2-x}O_7$.

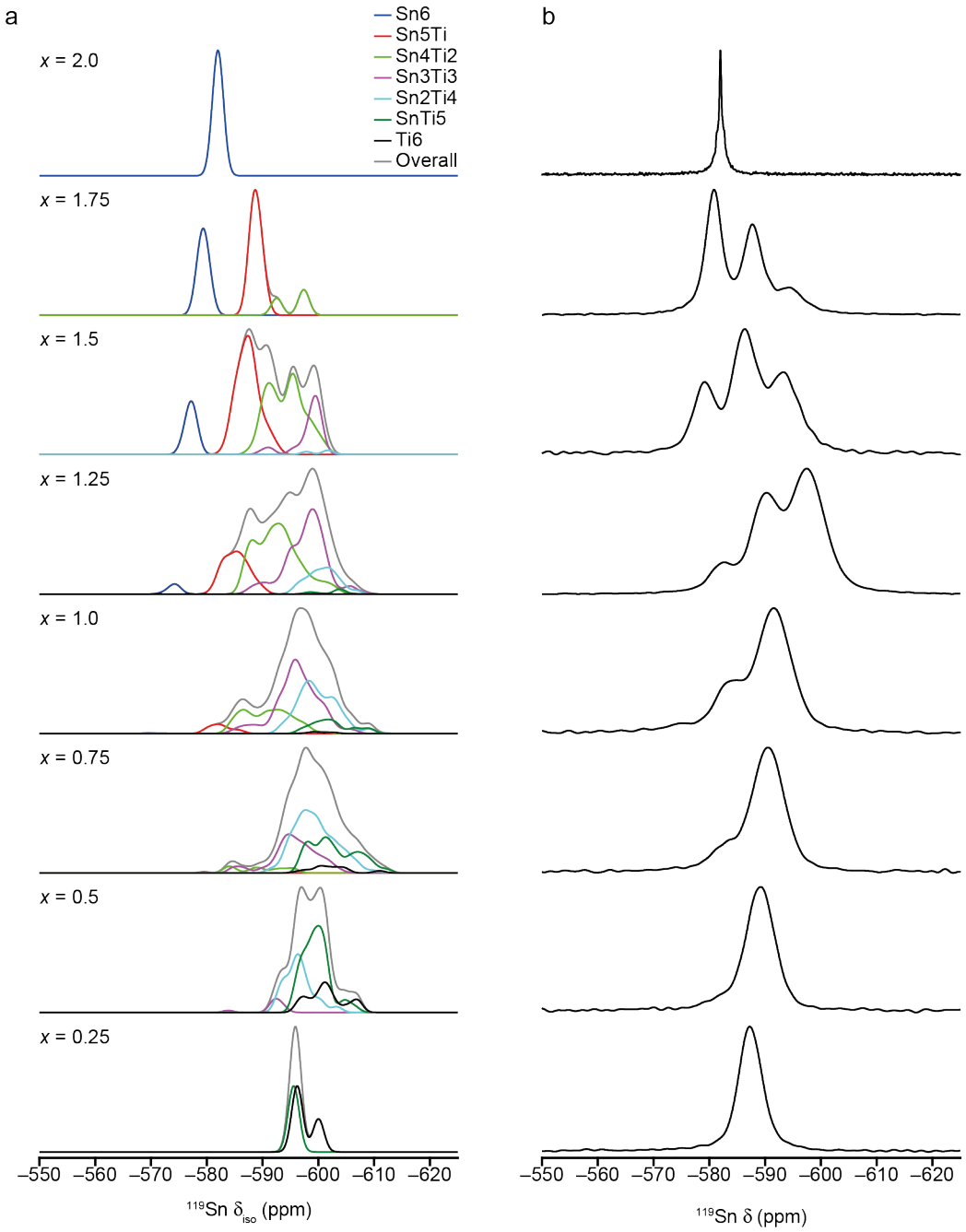


**Figure 5.78:** (a) Simulated $^{119}$Sn NMR spectra for series 3 structural models, decomposed according to *n* Sn NNN. (b) $^{119}$Sn (9.4 T, 14 kHz) MAS NMR spectra of $Y_2Sn_xTi_{2-x}O_7$.

with 0, 1 and 2 Sn NNN), in a larger system with the same composition, *i.e.*, a 2 × 2 × 2 supercell containing 16 Ti, it would in principle, be possible for some structural models to have Sn species present that have more than two Ti on the NNN B sites. Given the overall composition is fixed, for these models there would also be an increase in *e.g.*, Sn with $n = 6$. This lifting of the restriction on long-range order on the scale of the unit cell size may well

then result in better overall agreement with experiment, at the cost of course, of increased computational time.

Figure 5.78, shows that although there is significant overlap between signals from Sn with different *n* Sn NNN, which is seemingly the main cause for the observation of three broad resonances in the experimental $^{119}$Sn MAS NMR spectra of $Y_2Sn_xTi_{2-x}O_7$, it is clear that a decrease in *n* corresponds to a general decrease in $^{119}$Sn $\delta_{iso}$, a trend that is perhaps not obvious from the plot of calculated $^{119}$Sn $\delta_{iso}$ against *n* Sn NNN in Figure 5.74.

The simulated $^{119}$Sn NMR spectrum of $Y_2SnTiO_7$ was investigated in more detail, as shown in Figure 5.79, where it is separated according to *n* (Figure 5.79b) and into the nine individual B-site cation arrangements for the Sn4Ti2, Sn3Ti3 and Sn2Ti4 environments (Figure 5.79c). From Figure 5.79b it is clear that as *n* decreases, so does $^{119}$Sn $\delta_{iso}$ although significant overlap of the signals prevents individual resonances being resolved. It is this overlap that

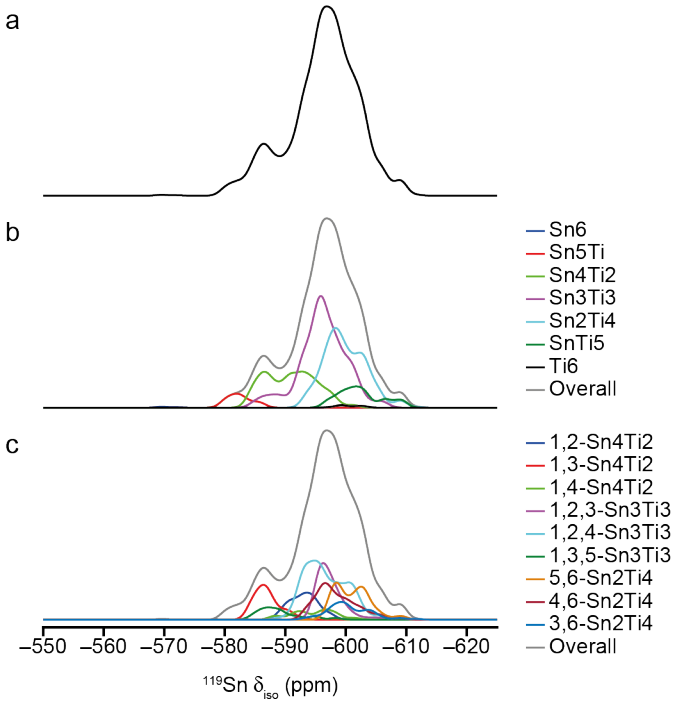


**Figure 5.79:** (a) Simulated $^{119}$Sn NMR spectrum for series 3 structural models of $Y_2SnTiO_7$, decomposed according to (b) *n* Sn NNN and (c) the specific Sn NNN arrangements for the *n* = 4, 3 and 2 environments.

limits the ability to assign (or decompose accurately) the $^{119}$Sn MAS NMR spectra of $Y_2Sn_xTi_{2-x}O_7$ (in contrast to the corresponding $^{89}$Y MAS NMR spectra, where resonances from individual *n* Sn NNN environments are more well resolved. It is clear from Figure 5.79c that decomposing the simulated $^{119}$Sn NMR spectrum of $Y_2SnTiO_7$ so only intensity from $n$ = 4, 3 and 2 environments, coloured according to the specific B-site cation arrangement is shown, does not provide any additional information that could be used to aid interpretation or assignment of the experimental spectra, with significant overlap of most signals predicted

In contrast to series 1 and series 2, the calculated $^{119}$Sn $\delta_{iso}$ for the Sn-containing series 3 structural models show increased overlap with decreasing *n* Sn NNN, in good agreement with the results seen for the Sn-centred cluster and the randomised cation models. The simulated $^{119}$Sn NMR spectra also aid interpretation of the experimental $^{119}$Sn MAS NMR spectra of $Y_2Sn_xTi_{2-x}O_7$ with reasonably good agreement observed for most compositions. However, decomposition of these simulated $^{119}$Sn NMR spectra according to *n* Sn NNN (see Figure 5.79) shows that, despite significant overlapping, there is a general trend for a decrease in $^{119}$Sn $\delta_{iso}$ as *n* Sn NNN decreases, *i.e.*, as the number Ti occupying the six B sites surrounding Sn increases. Despite this, the extent of overlap prevents any detailed analysis of $^{119}$Sn NMR spectra, preventing the level of insight into the local structure of $Y_2Sn_xTi_{2-x}O_7$ obtained from the corresponding $^{89}$Y NMR spectra, where individual resonances are more resolved.

As a result of the insight gained from the calculated $^{89}$Y and $^{119}$Sn NMR parameters for the series 3 structural models, the $^{17}$O NMR parameters, specifically $\delta_{iso}$ and $C_Q$, for this series were also considered (although $^{17}$O NMR spectra have only been published for the two end member compositions).[83,103] Figure 5.80 shows that the four types of O local environment (OY4, OY2Sn2, OY2SnTi and OY2Ti2) have reasonably well-defined ranges of $^{17}$O $\delta_{iso}$ and $C_Q$, with OY2SnTi and OY2Ti2 showing the

**Table 5.5:** Experimental and calculated $^{17}O$ $\delta_{iso}$ and $C_Q$ values for $Y_2Sn_2O_7$ and $Y_2Ti_2O_7$.

| Structure | Site | Experimental $^{17}O$ $\delta_{iso}$[103] (ppm) | Experimental $^{17}O$ $C_Q$[103] / MHz | Calculated $^{17}O$ $\delta_{iso}$ (ppm) | Calculated $^{17}O$ $C_Q$ / MHz |
|---|---|---|---|---|---|
| $Y_2Sn_2O_7$[a] | O1 | 384.0 | ~0.02 | 387.6 | 0.0 |
| | O2 | 172.5 | 3.2 (1) | 167.8 | 3.5 |
| $Y_2Ti_2O_7$[a] | O1 | 386.1 | ~0.02 | 373.5 | 0.0 |
| | O2 | 454.6 | 0.7 (1) | 461.1 | 0.6 |

[a] Compositional end members of the series 3 structural models.

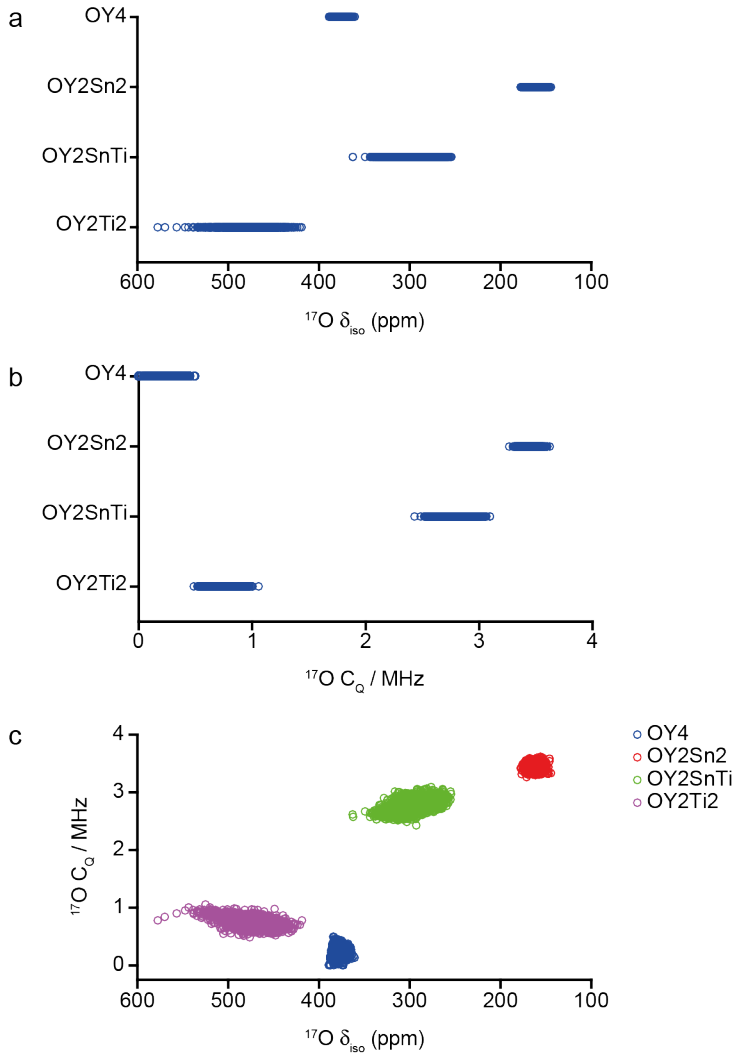


**Figure 5.80:** Plot of calculated $^{17}O$ (a) $\delta_{iso}$ and (b) $C_Q$ as a function of O environment and (c) plot of calculated $^{17}O$ $\delta_{iso}$ against $^{17}O$ $C_Q$ for all 279 series 3 structural models of $Y_2Sn_xTi_{2-x}O_7$, with data points coloured by the type of O environment.

largest variation in $^{17}O$ $\delta_{iso}$, with significantly less variation within the remaining two environments. It is also apparent that while the highly symmetric OY4 environment results in very small $^{17}O$ $C_Q$, as perhaps would be expected, the more covalent nature of the Sn–O bond causes larger $C_Q$ values to be exhibited by O with an OY2Sn2 environment, with an increase in the number of neighbouring Ti atoms causing the magnitude of $C_Q$ to decrease. The calculated and experiment $^{17}O$ $\delta_{iso}$ and $C_Q$ values are shown in Table 5.5, with the reasonable agreement providing confidence in the accuracy of the calculated $^{17}O$ NMR parameters for the series 3 structures.

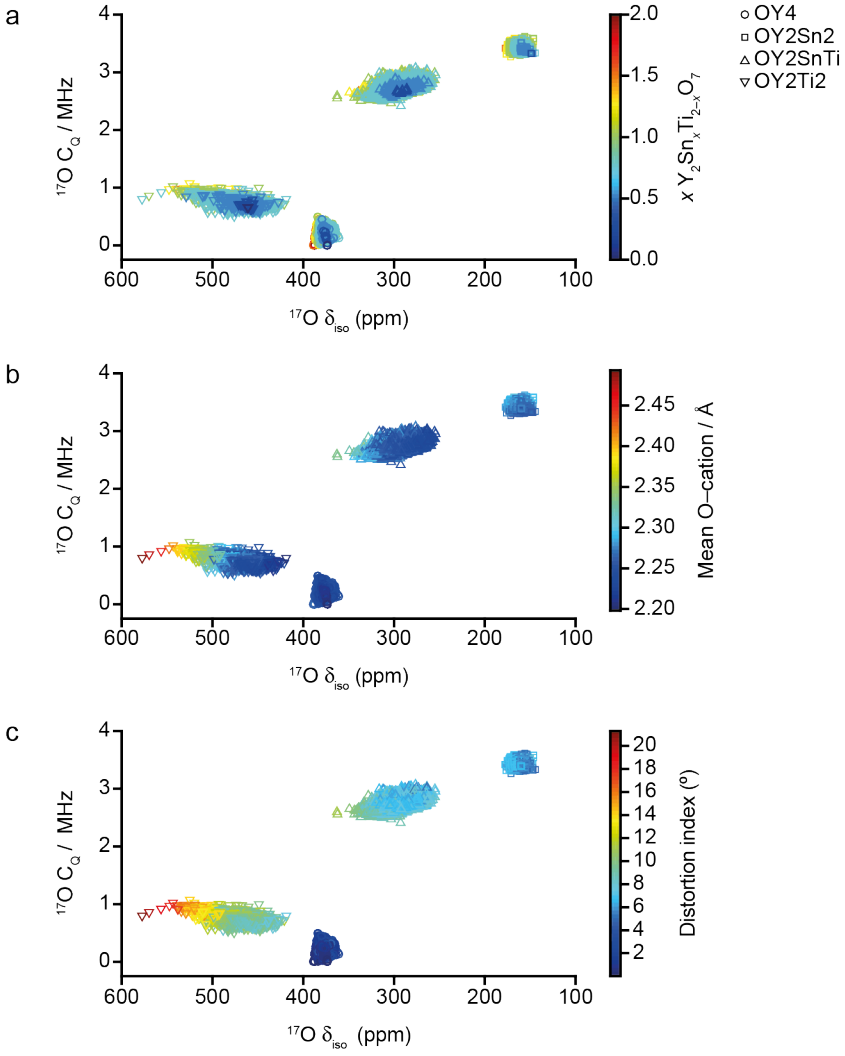


**Figure 5.81:** Plot of calculated $^{17}O$ $C_Q$ against $^{17}O$ $\delta_{iso}$ for all 279 series 3 structural models of $Y_2Sn_xTi_{2-x}O_7$, with the data points coloured by (a) $x$ (in $Y_2Sn_xTi_{2-x}O_7$) (b) mean O–cation bond length and (c) distortion index.

Figure 5.81a shows a similar plot to that in Figure 5.80c but with the data points coloured by $x$ (*i.e.*, by $Y_2Sn_xTi_{2-x}O_7$ composition), from which it can be seen that as the Ti content increases, $^{17}O$ $\delta_{iso}$, exhibits very little change. matching the general variation in peak position with $x$ seen in the $^{17}O$ MAS NMR spectra shown in Figure 5.9. In addition, from Figures 5.81b and 5.81c, where the data points are coloured according to their O–cation bond length and distortion index (previously described in Section 5.5.4), respectively, it is clear that the OY2SnTi and OY2Ti2 environments with the highest $^{17}O$ $\delta_{iso}$ correspond to O with extremely distorted local environments, where the distortion index especially seems to be strongly correlated with $\delta_{iso}$.

From Figure 5.82 and Figure 5.83 it is apparent that the $^{17}O$ $\delta_{iso}$ is strongly correlated with both mean O–cation bond length and distortion index, with OY2Ti2 environments exhibiting the largest variations in both NMR and structural parameters, whereas the highly symmetrical OY4 environment is characterised by much less structural variation. In addition, Figure 5.84 shows that these two structural parameters are inherently related, with a longer mean O–cation bond length correlating to O that also exhibit the largest distortion indices, *i.e.*, the largest distortion from an idealised tetrahedral geometry. Figure 5.84 also shows that of the three OY2B2 environments, where B = Sn or Ti, as the Ti content increases the structural variation becomes more extreme. This is consistent with the previous suggestion that the smaller Ti is perhaps being unable to satisfactorily occupy the six-coordinate B site in comparison to Sn, leading to more local structural flexibility being exhibited.

Based on the results discussed in this section, it is clear that the calculated $^{17}O$ NMR parameters for the 279 series 3 structural models are sensitive to changes in local structure The calculated $^{17}O$ NMR parameters also indicated that the degree of structural variation exhibited by O is strongly dependent on the particular environment, with the OY2Ti2 exhibiting the greatest structural variation. These results also indicate that predicted $^{17}O$ NMR parameters can be used to assist assignment of experimental NMR spectra,

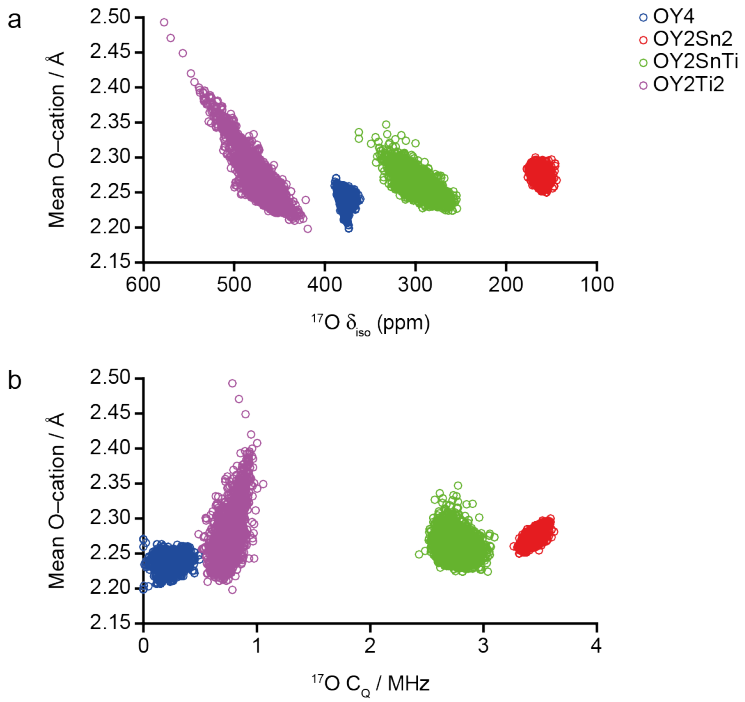


**Figure 5.82:** Plot of calculated $^{17}$O (a) $\delta_{iso}$ and (b) $C_Q$ against mean O–cation bond length for all 279 series 3 structural models of $Y_2Sn_xTi_{2-x}O_7$, with data points coloured by the type of O environment.

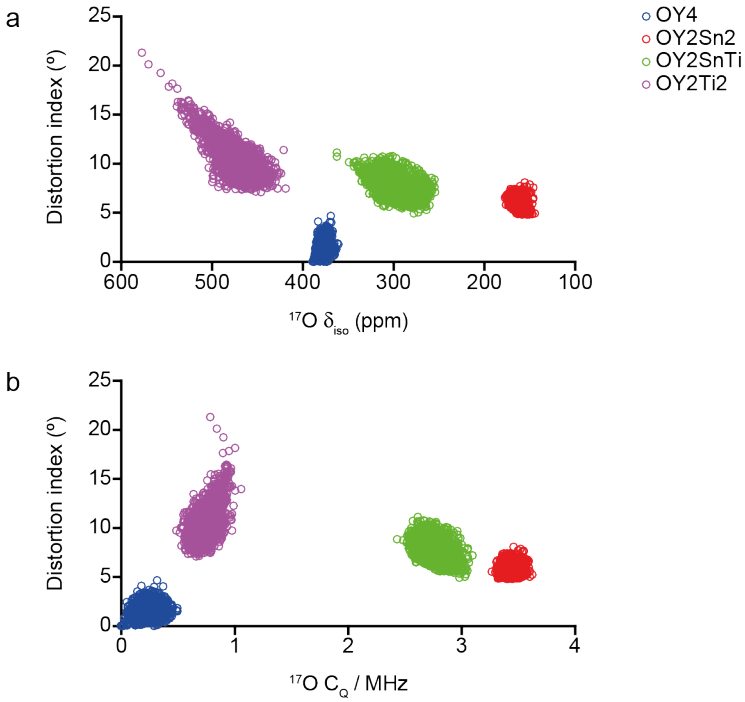


**Figure 5.83:** Plot of calculated $^{17}$O (a) $\delta_{iso}$ and (b) $C_Q$ against distortion index for all 279 series 3 structural models of $Y_2Sn_xTi_{2-x}O_7$, with data points coloured by the type of O environment.

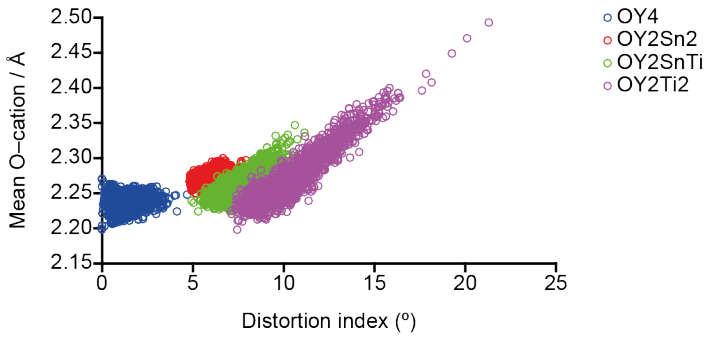


**Figure 5.84:** Plot of mean O–cation bond length against distortion index for all 279 series 3 structural models of $Y_2Sn_xTi_{2-x}O_7$, with data points coloured by the type of O environment.

meaning that, despite the high cost and complexity associated with $^{17}O$ enrichment of inorganic materials, $^{17}O$ NMR spectra, especially in combination with first-principles calculations, can provide useful insights that can assist structure elucidation.

### 5.5.6 Summary

In this section the ability for NMR spectroscopy to provide insights into the local structure and B-site cation disorder in $Y_2Sn_xTi_{2-x}O_7$ pyrochlore ceramics, as well as how first-principles calculations can help with interpretation and assignment of NMR spectra, has been investigated. Within this study a variety of methods to generate structural models, designed to represent a range of local environments in $Y_2Sn_xTi_{2-x}O_7$ pyrochlores have been investigated.

Despite representing a rather simple way of modelling B-site cation disorder in $Y_2Sn_xTi_{2-x}O_7$, with only the local structure around one atom (Y or Sn) in a unit cell being systematically varied, the Y- and Sn-centred localised cluster models provide important insight into the changes in NMR parameters expected. The results presented in this thesis agree well with previous studies,[71,73,78] confirming that the additional sharper resonances that appear in the $^{89}Y$ MAS NMR spectra upon Ti incorporation correspond to Y with different numbers of Sn NNN. Although the calculated NMR parameters for these cluster models provided some insight into the interpretation of the

experimental spectra, there are some downsides. Firstly, the variation in structure is very local, *i.e.*, *n* Sn NNN only changed for one Y or Sn, meaning changes in longer-range structure is not considered, meaning by definition, not all possible environments are being considered. In addition, due to the relatively small number of structural models considered, it is difficult to understand trends in NMR parameters with local geometry, meaning it is unclear whether the few outlying data points (*i.e.*, Y species with unusually large $^{89}$Y $\delta_{iso}$), are a result of real geometrical variations, or due to local distortions imposed by unrealistic long-range structures.

The 100 structures generated with randomised B-site cations provided a larger, and arguably less simplistic or idealised set of models, with the variation in B-site species no longer restricted to the six NNN B sites surrounding a single Y or Sn. From this set of structural models, relationships between calculated NMR and structural parameters were much more apparent, with the larger data set enabling trends that were not clearly apparent from the cluster models to be identified, most noticeably the strong correlation between $^{89}$Y $\delta_{iso}$ and the deviation in $O_{8a}$–Y–$O_{8a}$ bond angle from 180°.

With the built-in functionality allowing every symmetry inequivalent atomic arrangement for a particular $Y_2Sn_xTi_{2-x}O_7$ composition to be identified, and the configurational degeneracy for each arrangement to be determined, the SOD program represents the best approach considered here for generating structural models that can accurately represent the B-site cation disorder in $Y_2Sn_xTi_{2-x}O_7$. In particular, the simulated $^{89}$Y and $^{119}$Sn NMR spectra generated from series 3 models provided new insight into the interpretation (and for Y also the assignment) of the experimental MAS NMR spectra. Noticeably, the simulated $^{89}$Y NMR spectra provided evidence that the splitting in the resonance largely resulting from Sn3Ti3 environments results from the differences in the $^{89}$Y $\delta_{iso}$ for the 1,2,3-Sn3Ti3 and 1,2,4-Sn3Ti3 arrangements.

The variation in the calculated NMR parameters for series 1, 2 and 3

highlights the importance of ensuring structures are accurately geometry optimised prior to the calculation of NMR parameters. Series 3 models (optimised using CASTEP) showed the best agreement with the NMR parameters calculated for both the cluster and randomised models, and most importantly with the $^{89}Y$, $^{119}Sn$ and $^{17}O$ MAS NMR spectra of $Y_2Sn_xTi_{2-x}O_7$.

Based on the extensive investigation presented in this section, it is possible to conclude that using SOD to generate the full set of symmetry inequivalent structural models, combined with an accurate geometry optimisation prior to the calculation of NMR parameters, represents the most effective way of aiding the interpretation and assignment of experimental NMR spectra and ultimately help probe disorder in $Y_2Sn_xTi_{2-x}O_7$ pyrochlore ceramics.

## 5.6 $La_2Sn_xZr_{2-x}O_7$: using NMR spectroscopy and first-principles calculations to investigate B-site cation disorder

### 5.6.1 Introduction

From the simple radius ratio considerations discussed above, it is expected that $La_2Sn_xZr_{2-x}O_7$ would also adopt a pyrochlore phase throughout the compositional range. In this section, first-principles calculations are combined with multinuclear MAS NMR spectroscopy to investigate the local structure and B-site cation disorder in this series, which has not previously been studied using NMR spectroscopy. Unlike $Y_2Sn_xTi_{2-x}O_7$, for $La_2Sn_xZr_{2-x}O_7$ only $^{119}Sn$ and $^{17}O$ are easily accessible (with both La and Zr exhibiting large quadrupole moments resulting in extremely broad spectral lines), meaning that structural characterisation may prove to be more challenging. The detailed studies presented in Section 5.5 informed the methodology and approaches used in the investigation into local structure and B-site cation disorder in $La_2Sn_xZr_{2-x}O_7$, with cluster models and SOD-generated structural models (geometry optimised using CASTEP) used to assist the interpretation and assignment of $^{119}Sn$ and $^{17}O$ MAS NMR spectra.

### 5.6.2 Experimental NMR spectra

As described in Section 5.4, all $^{119}$Sn and $^{17}$O MAS NMR spectra were recorded by Miss Arantxa Fernandes using Bruker Avance III spectrometers equipped with either a 9.4 T ($^{119}$Sn) or 14.1 T ($^{17}$O) wide-bore magnet at the Solid-State NMR Facility at the University of St Andrews. A series of $La_2Sn_xZr_{2-x}O_7$ samples, with $x$ = 2, 1.75, 1.5, 1.25, 1, 0.75, 0.5, 0.25 and 0 were studied. The compositions were chosen to facilitate comparison with the computational predictions, and were also used in the generation of $La_2Sn_xZr_{2-x}O_7$ structural models by Dr Ricardo Grau-Crespo, using the SOD program,[88] the results of which are discussed in Section 5.6.4.

#### 5.6.2.1 $^{119}$Sn MAS NMR spectra

The $^{119}$Sn MAS NMR spectra of $La_2Sn_xZr_{2-x}O_7$ are shown in Figure 5.85, with the spectrum of $La_2Sn_2O_7$ ($x$ = 2.0), containing one sharp resonance at approximately –642 ppm, characteristic of six-coordinate Sn, in good agreement with previous work.[77] The result of Zr incorporation can be seen in the $^{119}$Sn spectrum of $La_2Sn_{1.75}Zr_{0.25}O_7$, which exhibits two additional peaks at a lower (upfield) chemical shift. However, the majority of the $^{119}$Sn spectra are dominated by broad, more overlapping lineshapes, with a maximum of three resonances observed when $x$ < 2.0. The similarity in ionic radius of $Sn^{4+}$ and $Zr^{4+}$ (0.69 Å and 0.72 Å, respectively) appears to lead to very little change in the chemical shifts of a resonance as $x$ decreases, in contrast to the $^{119}$Sn MAS NMR spectra of $Y_2Sn_xTi_{2-x}O_7$ (shown in Figure 5.8), where the incorporation of Ti causes a clear upfield shift in any one resonance as $x$ decreases. However, in agreement with the behaviour seen for the $Y_2Sn_xTi_{2-x}O_7$ series, the overlap of the spectral resonances means that the majority of signals in the $^{119}$Sn MAS NMR spectra of $La_2Sn_xZr_{2-x}O_7$ cannot be definitively assigned to Sn species with specific NNN environments.

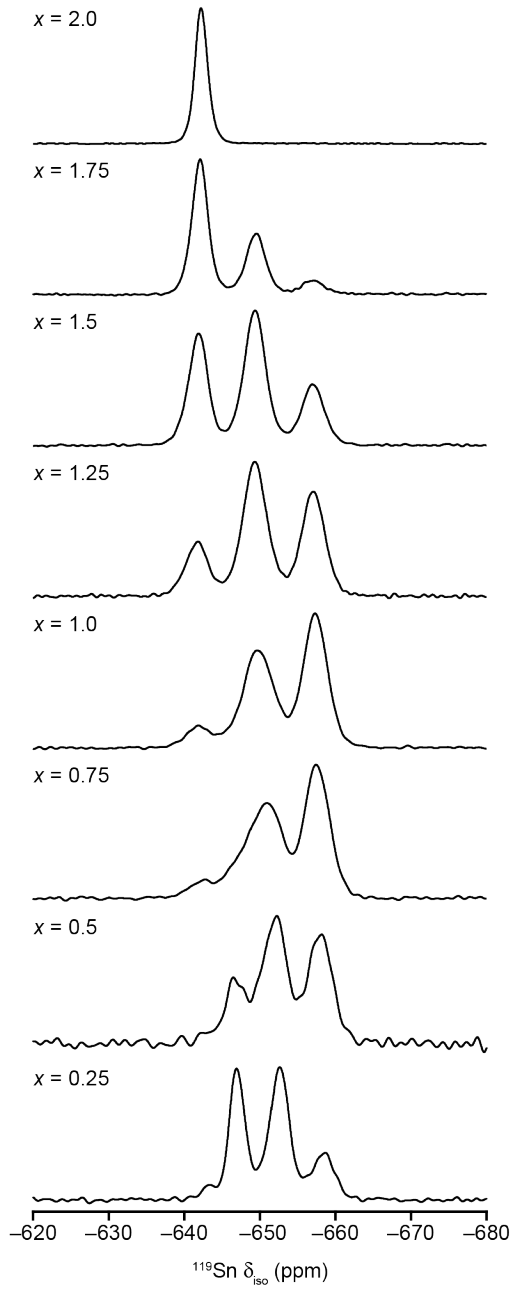


**Figure 5.85:** $^{119}$Sn (9.4 T, 14 kHz) MAS NMR spectra of $La_2Sn_xZr_{2-x}O_7$

### 5.6.2.2 $^{17}$O MAS NMR spectra

As shown in Figure 5.86, the $^{17}$O MAS NMR spectra of $La_2Sn_2O_7$ and $La_2Zr_2O_7$ both contain two distinct resonances. By comparison of the two spectra the signal at ~640 ppm can be attributed to an OLa4 (O1) species, with those at ~220 ppm and ~390 ppm to OLa2Sn2 and OLa2Zr2 environments, respectively. The $^{17}$O spectra of the mixed-metal materials,

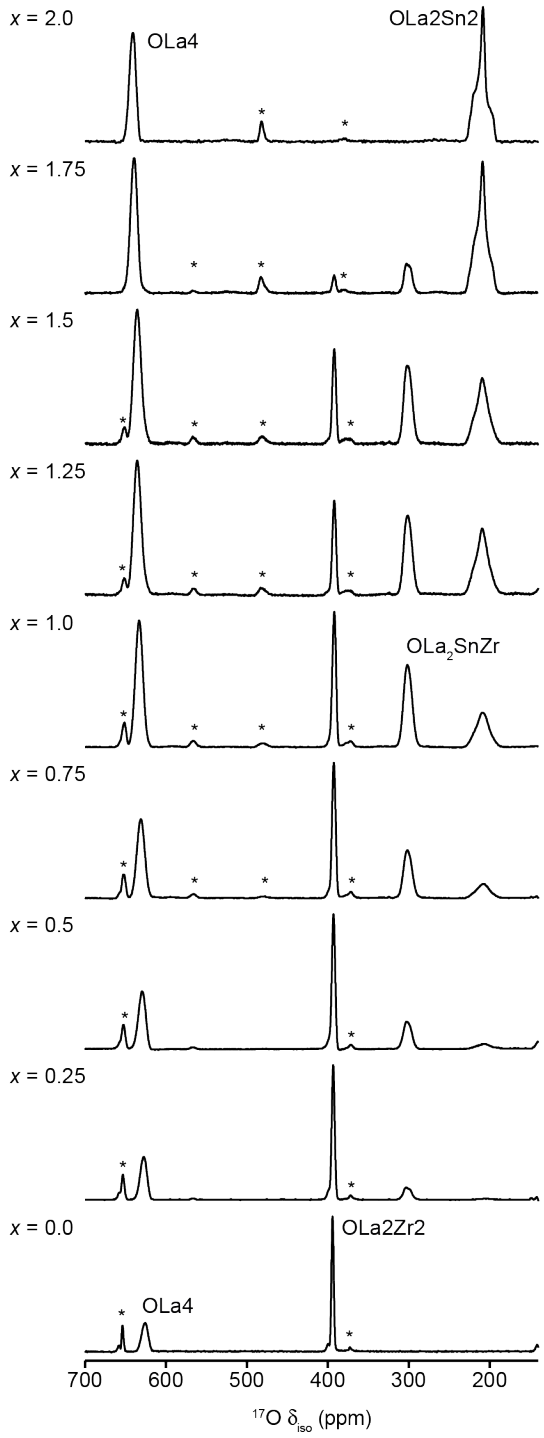


**Figure 5.86:** $^{17}O$ (14.1 T, 21 kHz) MAS NMR spectra of $La_2Sn_xZr_{2-x}O_7$, showing the different O environments. Spinning sidebands denoted by asterisks (*).

shown in Figure 5.86 reveal that while the position of the OLa4 resonance moves to a slightly lower (upfield) chemical shift as $x$ decreases, the positions of the remaining signals appears relatively unaffected. It can also be seen that as Zr is introduced into $La_2Sn_2O_7$, *i.e.*, when $x$ = 1.75, an additional peak

appears at ~300 ppm, which grows in intensity as $x$ decreases, is most intense when $x$ = 1.0 before decreasing in intensity with as $x$ decreases further. As this peak appears in the $^{17}O$ spectra of all but the two end members, it can be tentatively assigned to an OLa2SnZr environment, which can only occur when both Sn and Zr are present. The $^{17}O$ spectra also show that as the $La_2Zr_2O_7$ end member is approached, *i.e.*, as $x$ approaches 0.0, the OLa2Zr2 peak becomes sharper, highlighting the increase in long-range order.

### 5.6.3 Cluster models

As described previously for $Y_2Sn_xTi_{2-x}O_7$ (see Section 5.5.3), in a cluster based approach the NNN environment for a single cation (in this case Sn) is systematically varied by constructing a series of models, each with a different number and arrangement of Sn and Zr on the six NNN B sites, leading to 13 unique structural models. The $La_2Sn_2O_7$ unit cell determined

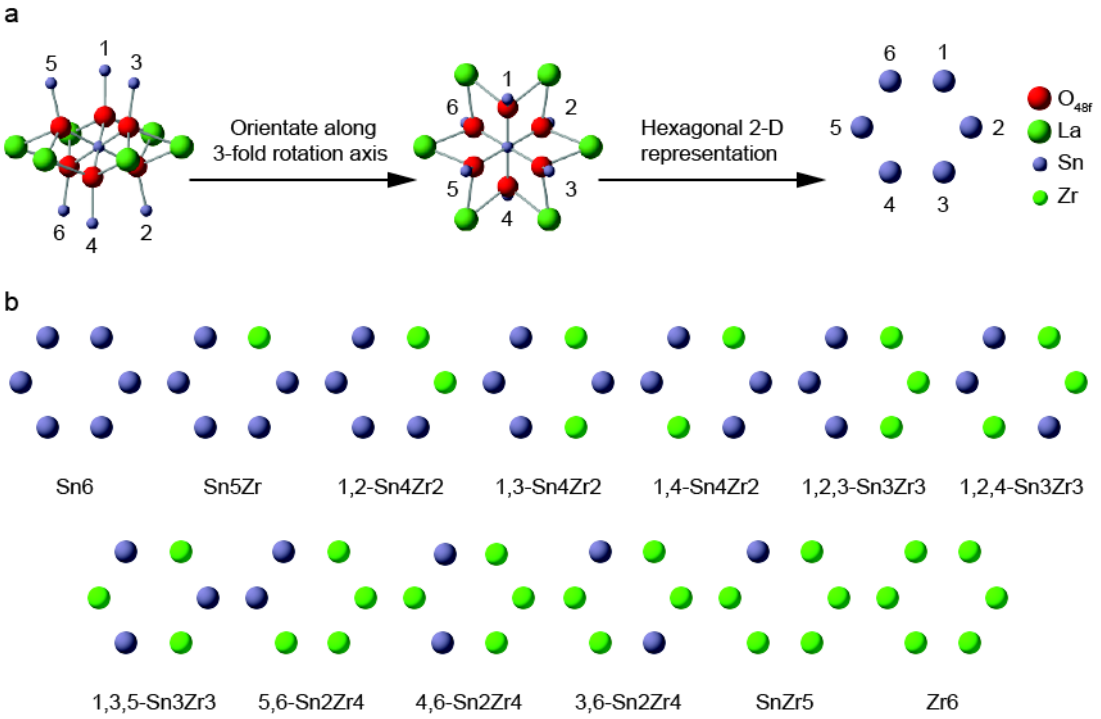


**Figure 5.87:** (a) Schematic showing spatial arrangement of NNN B sites and the nomenclature used for the $Y_2Sn_xTi_{2-x}O_7$ series can be used for the $La_2Sn_xZr_{2-x}O_7$ cluster models. (b) Two-dimensional projection of the 13 unique ways of arranging Sn and Zr cations on the NNN B sites surrounding Sn.

experimentally by diffrraction[104] was used to generate a series of Sn-centred, Sn-rich structural models, with this process then repeated using the corresponding $La_2Zr_2O_7$ unit cell,[105] to give 13 Sn-centred, Zr-rich models and 26 models in total. Figure 5.87 shows the spectral arrangement of the NNN B sites and the nomenclature used for the Sn centred models.

All first-principles calculations were performed using CASTEP 16.11, with an $E_{cut}$ of 60 Ry, a k-point spacing of 0.04 $2\pi$ $Å^{-1}$ (see Appendix B1 for convergence testing), the PBE $E_{XC}$ functional,[94] default on-the-fly ultrasoft pseudopotentials,[95] a `geom_energy_tol` value of $1 \times 10^{-5}$ eV / atom and an `elec_energy_tol` value of $1 \times 10^{-9}$ eV / atom (see Section 5.5.4.1). All structural models were geometry optimised to reduce the forces acting upon the atoms, with the subsequent calculation of NMR parameter carried out using the ZORA correction. A reference shielding ($\sigma_{ref}$) was used to convert calculated isotropic shieldings ($\sigma_{iso}$) to isotropic shifts ($\delta_{iso}$). A description of the referencing of calculated $^{119}$Sn and $^{17}$O shieldings, based on comparisons between experimental and calculated NMR parameters for $La_2Sn_2O_7$ for $^{119}$Sn and both $La_2Sn_2O_7$ and $La_2Zr_2O_7$, for $^{17}$O, is given in Appendix B2.

The predicted $^{119}$Sn $\delta_{iso}$, $\Omega$ and $\kappa$ for the Sn-centred $La_2Sn_xZr_{2-x}O_7$ cluster models of $La_2Sn_xZr_{2-x}O_7$ are plotted as a function of *n* Sn NNN in Figure 5.88. Figure 5.88a indicates that $^{119}$Sn $\delta_{iso}$ decreases (moves upfield) as *n* decreases, although for the Sn4Zr2, Sn3Zr3 and Sn2Zr4 environments in particular, the data points are split into two distinct groups with significantly different $\delta_{iso}$. This splitting is particularly apparent for Sn3Zr3, where the two sets of points are separated by ~15 ppm. Figure 5.88b shows that as *n* decreases, so does the calculated $^{119}$Sn $\Omega$, with significant overlap apparent, especially when $n > 2$. Again, the distribution of $^{119}$Sn $\Omega$ values observed for several *n* leads to Sn species being separated into two groups, each with distinct ranges of $^{119}$Sn $\Omega$, with this particularly pronounced for the Sn4Zr2 and Sn3Zr3 environments. In contrast, Figure 5.88c indicates that (as expected) there is no strong correlation between $^{119}$Sn $\kappa$ and *n*.

Figure 5.89 shows the calculated $^{119}$Sn $\delta_{iso}$ plotted against *n*, now with data points coloured according to the model set, *i.e.*, Sn-rich or Zr-rich structural models. Significant overlap in the calculated $^{119}$Sn NMR parameters for the two sets of structural models can be seen. However, in general, Sn species in Sn-rich models tend to have higher (more downfield) $^{119}$Sn $\delta_{iso}$ and smaller **Ω**, relative to similar species in Zr-rich structural models. This is particularly apparent when *n* is low, *i.e.*, for Sn2Zr4, SnZr5 and Zr6 NNN environments.

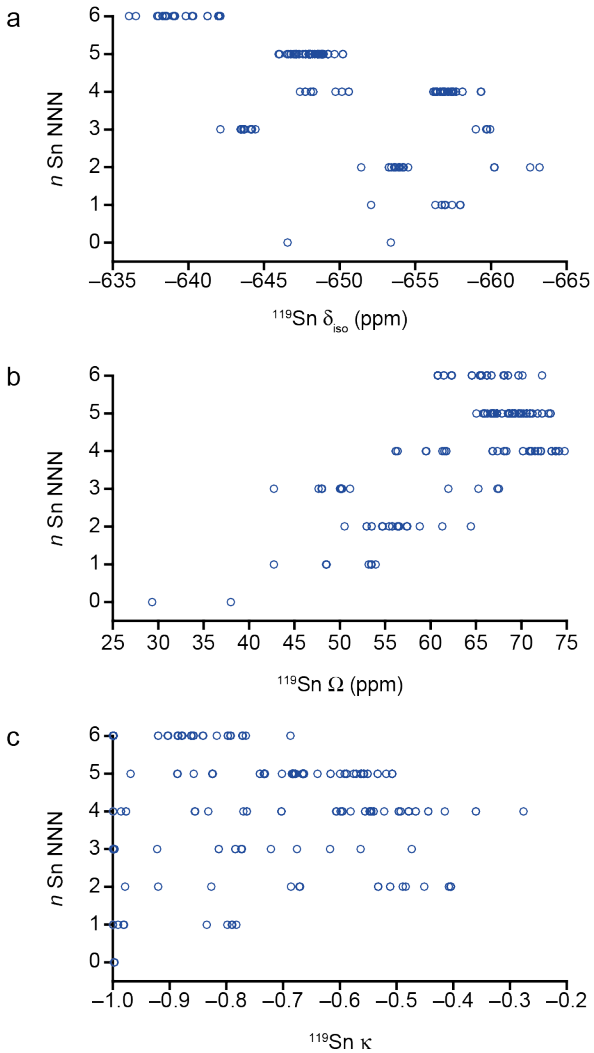


**Figure 5.88:** Plot of calculated $^{119}$Sn (a) $\delta_{iso}$, (b) **Ω** and (c) **κ** as a function of *n* Sn NNN for the 26 Sn-centred cluster models of $La_2Sn_xZr_{2-x}O_7$.

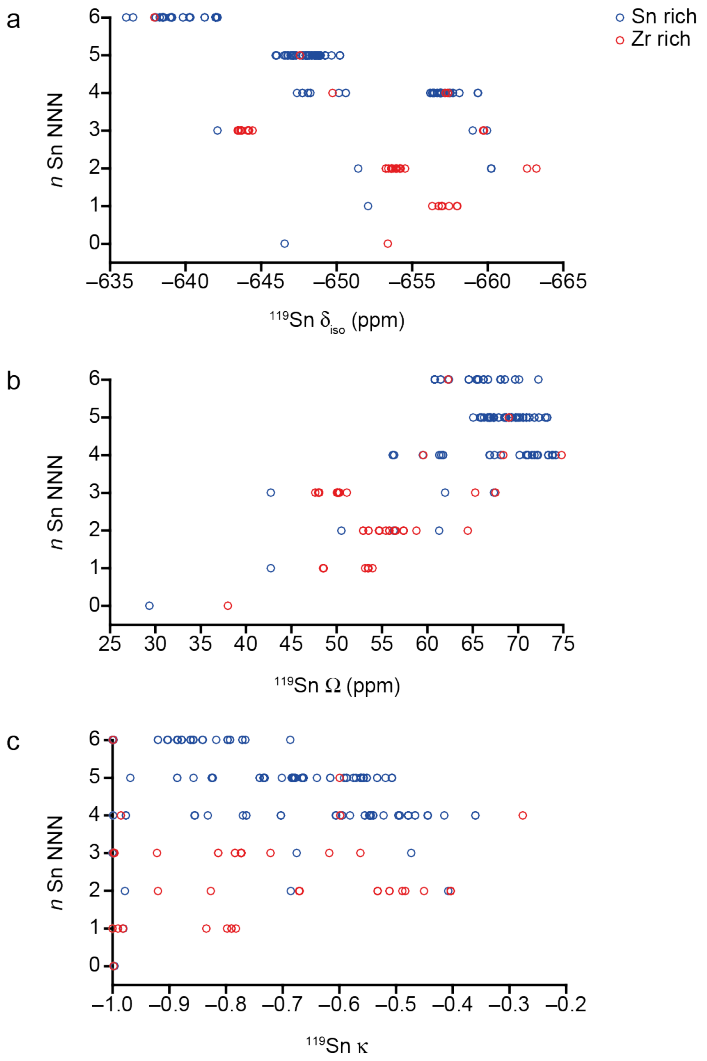


**Figure 5.89:** Plot of calculated $^{119}$Sn (a) $\delta_{iso}$, (b) Ω and (c) κ as a function of *n* Sn NNN for the 26 Sn-centred cluster models of $La_2Sn_xZr_{2-x}O_7$, with data points coloured by model type.

When calculated $^{119}$Sn $\delta_{iso}$ and Ω are plotted as a function of *n* Sn NNN, with the data points coloured by *n* but shaped according to the specific NNN arrangement, as shown in Figure 5.90, new insights into the effect cation disorder and B-site arrangements have on calculated $^{119}$Sn NMR parameters are obtained. Figure 5.90a indicates that the 1,3-Sn4Zr2, 1,3,5-Sn3Zr3 and 4,6-Sn2Zr4 NNN arrangements have much larger (downfield) $^{119}$Sn $\delta_{iso}$ than the other arrangements with the same *n*. A similar observation can be made for Figure 5.90b, with the same three NNN arrangements exhibiting noticeably smaller $^{119}$Sn Ω than other arrangements for $n$ = 4, 3 or 2. The significance of this is that the 1,3-Sn4Zr2, 1,3,5-Sn3Zr3 and 4,6-Sn2Zr4 arrangements, shown

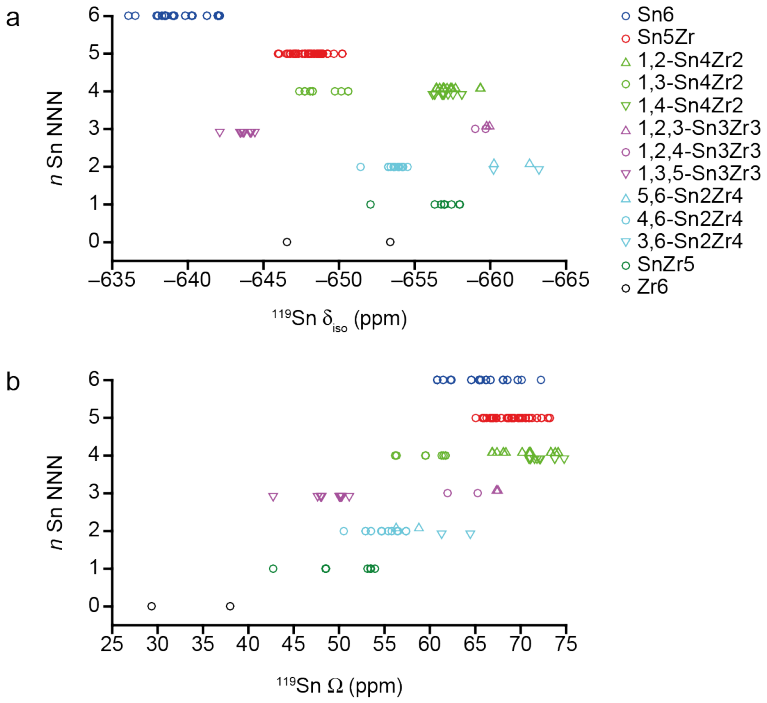


**Figure 5.90:** Plot of calculated $^{119}$Sn (a) $\delta_{iso}$ and (b) Ω as a function of *n* Sn NNN for the 26 Sn-centred cluster models of $La_2Sn_xZr_{2-x}O_7$, with the data points shaped by Sn NNN arrangement. For *n* Sn NNN = 4, 3 and 2 the data points for the different NNN arrangements have been offset slightly to facilitate comparison.

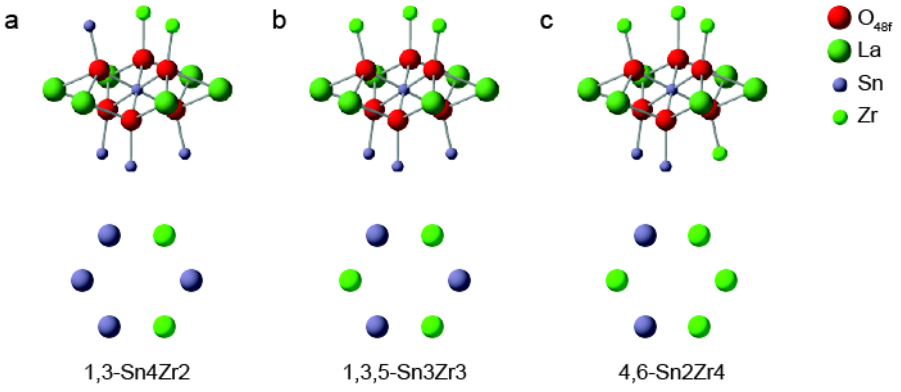


**Figure 5.91:** The local environment of the (a) 1,3-Sn4Zr2, (b) 1,3,5-Sn3Zr3 and (c) 4,6-Sn2Zr4 Sn-centred NNN arrangement, showing a two-dimensional representation of the NNN B site arrangement. In all two-dimensional representation the central Sn cation is not shown.

in Figure 5.91, represent the most asymmetrical ways of arranging the Sn and Zr cations on the six NNN B sites. In the 1,3-Sn4Zr2 arrangement, both Zr occupy neighbouring B sites on the same face of the cluster, *i.e.*, both occupy sites above (or below) the central Sn. In the 1,2-Sn4Zr2 and 1,4-Sn4Zr2

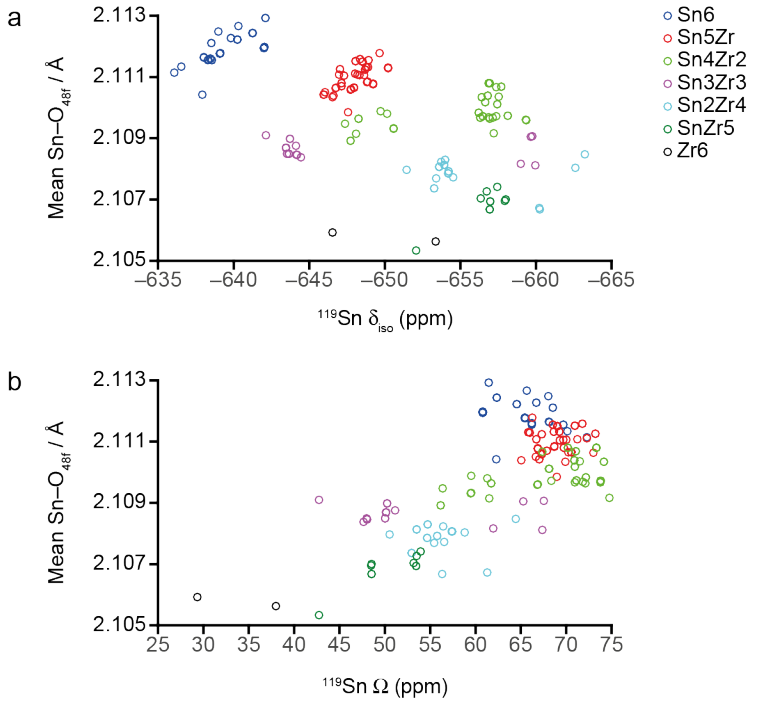


**Figure 5.92:** Plot of calculated $^{119}$Sn (a) $\delta_{iso}$ and (b) **Ω** as a function of mean Sn–$O_{48f}$ bond length for the 26 Sn-centred cluster models of $La_2Sn_xZr_{2-x}O_7$, with data points coloured by *n* Sn NNN.

arrangements, the two Zr are found on opposite faces of the cluster of atoms around the central Sn, with each triangle of NNN B-sites containing one Zr and two Sn cations. This observation also applies to the symmetrically related 4,6-Sn2Zr4 arrangement, where the two NNN Sn cations occupy adjacent sites on the same face of the cluster, *i.e.*, sites 4 and 6 in Figure 5.87, resulting in the most asymmetric arrangement of two Sn and four Zr cations. While the $^{119}$Sn $\delta_{iso}$ for the 1,3-Sn4Zr2 and 4,6-Sn2Zr4 arrangements are ~6-8 ppm higher than the other $n$ = 4 or 2 environments, the variation in $\delta_{iso}$ observed for $n$ = 3 arrangements is far larger, with a separation of ~15 ppm between the 1,3,5-Sn3Zr3 and the remaining two Sn3Zr3 arrangements. As shown in Figure 5.91, in the 1,3,5-Sn3Zr3 arrangement the set of three NNN B sites on one face of the cluster is entirely occupied by one atom type, *e.g.*, solely by Sn, with the other set of three sites occupied solely by the other atom types. In contrast, for the 1,2,3-Sn3Zr3 and 1,2,4-Sn3Zr3 arrangements, Sn and Zr are found on both faces of this cluster *i.e.*, each set of three B sites contains both Sn and Zr. Therefore, the 1,3,5-Sn3Zr3 arrangement represents

the most asymmetric distribution of Sn and Zr over the six NNN B sites.
A similar trend is observed in Figure 5.90b, indicating that calculated $^{119}$Sn Ω is also sensitive to the specific NNN B-site arrangement, with the smallest Ω corresponding to the least symmetric, *i.e.*, the 1,3-Sn4Zr2, 1,3,5-Sn3Zr3 and 4,6-Sn2Zr4 arrangements. The sensitivity of $^{119}$Sn $\delta_{iso}$ to different NNN B-site arrangements with the same *n* could help explain the broad and overlapped resonances in the experimental $^{119}$Sn MAS NMR spectra of $La_2Sn_xZr_{2-x}O_7$ (see Figure 5.85).

Calculated $^{119}$Sn $\delta_{iso}$ and Ω are plotted as a function of mean Sn–$O_{48f}$ bond length in Figure 5.92. These plots indicate that as *n* decreases, *i.e.*, as more of the B sites surrounding the central Sn are occupied by Zr, the mean Sn–$O_{48f}$ bond length also decreases. A possible explanation for this observation is the slightly larger size of $Zr^{4+}$ relative to $Sn^{4+}$. To compensate for the increased number of NNN Zr, the O species bonded to these cations will be forced closer to the smaller cation, *i.e.*, the central Sn, causing the mean Sn–$O_{48f}$ bond length to decrease. Indeed, there is a small difference in M–O (M = Sn, Zr) bond lengths in the two end member materials, with a Sn–$O_{48f}$ bond length in $La_2Sn_2O_7$[104] of 2.074 Å, but a Zr–$O_{48f}$ bond length in $La_2Zr_2O_7$[105] of 2.099 Å. Despite the slight decrease in mean Sn–$O_{48f}$ bond length with decreasing *n*, Figure 5.92 indicates that unlike $^{119}$Sn $\delta_{iso}$ and Ω, this parameter is not sensitive to the specific specific arrangement of NNN B-site cations (*i.e.*, all cation arrangements with the same *n* have a similar mean Sn–$O_{48f}$ bond length).

The Sn-centred cluster models discussed in this section provide useful insights into how the calculated $^{119}$Sn NMR parameters are affected by variations in both B-site composition and configuration, which could help facilitate the interpretation of the experimental $^{119}$Sn NMR spectra of $La_2Sn_xZr_{2-x}O_7$. In particular, it is apparent that calculated $^{119}$Sn $\delta_{iso}$ and Ω are both sensitive to the specific NNN arrangement of the B-site cations, (far more so than was observed for $Y_2Sn_xTi_{2-x}O_7$ in Section 5.5.3). Despite this observation, it is clear that further study, potentially involving the use of a

much larger set of (more realistic) structural models is required in order to understand the dependence of the calculated $^{119}$Sn NMR parameters on local structure and to facilitate the detailed interpretation of the $^{119}$Sn MAS NMR spectra of $La_2Sn_xZr_{2-x}O_7$.

### 5.6.4 SOD-generated structural models

The local structure and cation disorder in $La_2Sn_xZr_{2-x}O_7$ have also been investigated through a collaboration with Dr Ricardo Grau-Crespo at the University of Reading. As described above for $Y_2Sn_xTi_{2-x}O_7$, the SOD program[88] (see Chapter 4, Section 4.3.1) was used to generate all symmetry inequivalent structural models for a series of $La_2Sn_xZr_{2-x}O_7$ compositions. A summary of the number of structural models generated is given in Table 5.6. An initial pyrochlore structure with $Fd\bar{3}m$ space group was used to generate all SOD structures, with the only variation in these pre-geometry optimised structures being the number of Sn and Zr present in the unit cell.

The 279 $La_2Sn_xZr_{2-x}O_7$ SOD-generated structures were initially geometry optimised (by Dr Grau-Crespo), using VASP 5.[97–100] These optimisations used the PBE $E_{XC}$ functional, an $E_{cut}$ of 520 eV (38 Ry), a k-point sampling for the gamma point only and PAW pseudopotentials,[101,102] with 11, 14, 12, and 6 valence electrons for La, Sn, Zr and O, respectively. These VASP-optimised structures were used as inputs for a second (more accurate) geometry optimisation, performed using CASTEP 16.11. For the CASTEP 16.11 geometry optimisation and subsequent calculation of NMR parameters, an $E_{cut}$ of 60 Ry, a k-point spacing of 0.04 $2\pi$ Å$^{-1}$ (see Appendix B1 for convergence testing), the PBE $E_{XC}$ functional,[94] default on-the-fly ultrasoft pseudopotentials,[95] a `geom_energy_tol` value of $1 \times 10^{-5}$ eV / atom and an `elec_energy_tol` value of $1 \times 10^{-9}$ eV / atom (see Section 5.5.4.1) were used, with relativistic effects accounted for by the ZORA. The calculated $^{119}$Sn and $^{17}$O $\sigma_{iso}$ were converted to $\delta_{iso}$ by applying the same referencing procedures used for the 26 Sn-centred cluster models (see Section 5.6.3 and Appendix B2). In this section only the magnitude of the $^{17}$O $C_Q$ is considered.

**Table 5.6:** The total number of B site configurations (W) and the number of symmetry inequivalent configurations (M) for structural models of $La_2Sn_xZr_{2-x}O_7$ generated using SOD.

| Structural formula | $x$ | B site composition | W | M |
|---|---|---|---|---|
| $La_2Sn_2O_7$ | 2.0 | Sn16 | 1 | 1 |
| $La_2Sn_{1.75}Zr_{0.25}O_7$ | 1.75 | Sn14Zr2 | 120 | 3 |
| $La_2Sn_{1.5}Zr_{0.5}O_7$ | 1.5 | Sn12Zr4 | 1820 | 22 |
| $La_2Sn_{1.25}Zr_{0.75}O_7$ | 1.25 | Sn10Zr6 | 8008 | 65 |
| $La_2SnZrO_7$ | 1.0 | Sn8Zr8 | 12870 | 97 |
| $La_2Sn_{0.75}Zr_{1.25}O_7$ | 0.75 | Sn6Zr10 | 8008 | 65 |
| $La_2Sn_{0.5}Zr_{1.5}O_7$ | 0.5 | Sn4Zr12 | 1820 | 22 |
| $La_2Sn_{0.25}Zr_{1.75}O_7$ | 0.25 | Sn2Zr14 | 120 | 3 |
| $Y_2Zr_2O_7$ | 0.0 | Zr16 | 1 | 1 |
| Total | | | 32768 | 279 |

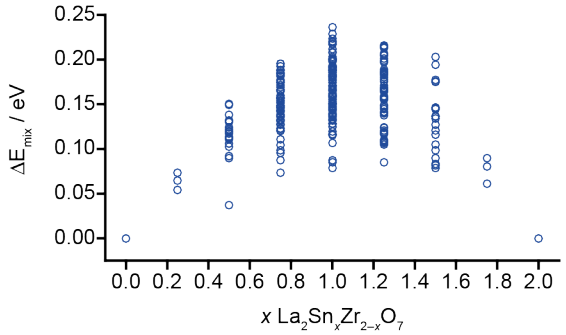


**Figure 5.93:** Plot of relative energy of mixing ($\Delta E_{mix}$) as a function of Sn composition, $x$, for the 279 structural models of $La_2Sn_xZr_{2-x}O_7$.

As discussed in Section 5.5.5.1, the relative energy of mixing ($\Delta E_{mix}$) for the fully optimised structural models was determined from the total energy values from the CASTEP 16.11 NMR calculations for the pyrochlore end members, $La_2Sn_2O_7$ and $La_2Zr_2O_7$. As shown in Figure 5.93, the $\Delta E_{mix}$ for all structural models are positive, although it should be noted this does not account for any entropic effects for the mixed-metal materials. Based on $\Delta E_{mix}$ for the $x$ = 0.25 and 1.75 structural models, it appears that it is very slightly

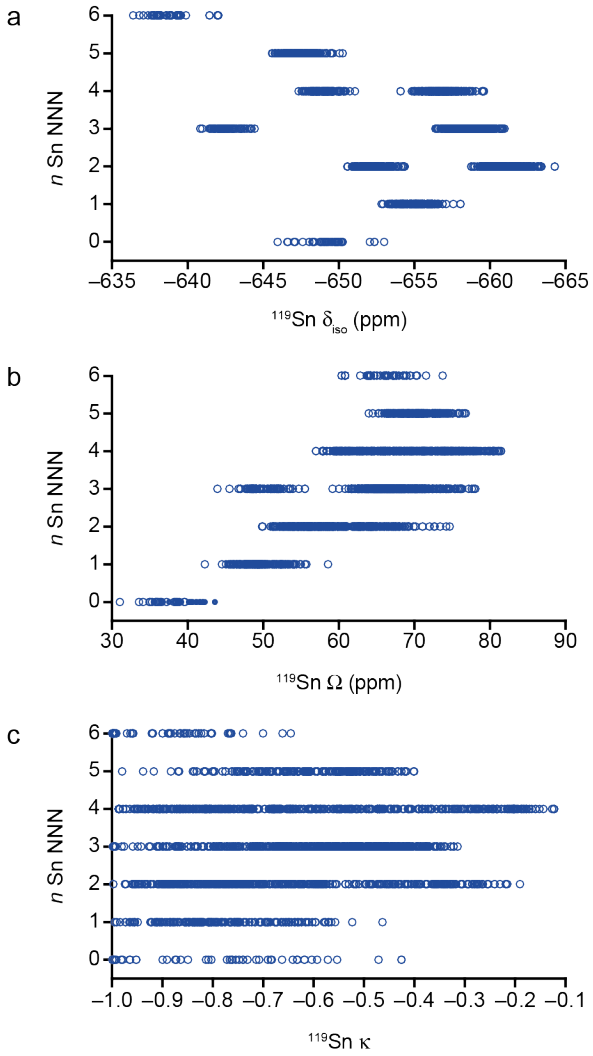


**Figure 5.94:** Plot of calculated $^{119}$Sn (a) $\delta_{iso}$, (b) Ω and (c) κ as a function of *n* Sn NNN for the structural models of $La_2Sn_xZr_{2-x}O_7$.

more energetically favourable to substitute a small amount of Sn into $La_2Zr_2O_7$, compared to substitute an equal amount of Zr into $La_2Sn_2O_7$, than *vice versa*. There is an energy gap of ~0.05 eV between one of the $La_2Sn_{0.5}Zr_{1.5}O_7$ ($x$ = 0.5) models and the remaining 21 structures, with this lowest energy structure corresponding to the most 'clustered' arrangement of Sn possible, with three Sn cations adopting a *n* Sn NNN = 3 environment around a central fourth cation. Compared to $Y_2Sn_xTi_{2-x}O_7$ (see Section 5.5.5.3), in total, $\Delta E_{mix}$ for the $La_2Sn_xZr_{2-x}O_7$ models spans a smaller range, indicating that the structural (and thus energy), variations may be less significant in this series.

Figure 5.94 shows the calculated $^{119}$Sn $\delta_{iso}$, Ω and κ for the SOD-generated structural models of $La_2Sn_xZr_{2-x}O_7$ plotted as a function of *n* Sn NNN. Figure 5.94a shows that $^{119}$Sn $\delta_{iso}$ initially decreases (moves upfield) as *n* decreases, before this trend reverses when $n < 2$. As seen for the Sn-centred cluster models (see Figure 5.88a), Sn species with $n = 4$, 3 and 2 are each split into two groups, with this most apparent for Sn3Zr3. Figure 5.94a indicates that several *n* Sn NNN environments have overlapping regions of $^{119}$Sn $\delta_{iso}$, explaining why only a maximum of three broadened resonances are observed in the $^{119}$Sn MAS NMR spectra. Figure 5.94b indicates that there is significant overlap in the values of calculated $^{119}$Sn Ω observed, particularly for environments with high *n*, with more significant decreases in Ω observed for $n < 3$. Figure 5.94b also shows that $^{119}$Sn Ω is sensitive to the arrangement of the NNN cations, with Sn species with $n = 3$ split into two distinct groups, with the centre of each group separated by ~15-20 ppm. As seen previously for the Sn-centred cluster models, Figure 5.94c confirms there is no correlation between $^{119}$Sn κ and *n*. As shown in Figure 5.95, it is clear that the specific arrangement of Sn and Zr on the six NNN B sites has a significant effect on both $^{119}$Sn $\delta_{iso}$ and Ω. The calculated $^{119}$Sn NMR parameters for Sn with 1,3-Sn4Zr2, 1,3,5-Sn3Zr3 or 4,6-Sn2Zr4 arrangements (see Figure 5.91) are noticeably different, in agreement with the observations from the Sn-centred cluster models discussed above.

In an attempt to rationalise the variations in $^{119}$Sn $\delta_{iso}$ and Ω with the change in *n* Sn NNN, Figures 5.96 and 5.97 plot the dependence of these NMR parameters on the mean and the range (*i.e.*, the difference between the longest and the shortest Sn–$O_{48f}$ bond lengths) of Sn–$O_{48f}$ bond lengths, respectively. Figure 5.96 shows decreasing *n* results in a slight decrease in the mean Sn–$O_{48f}$ bond length. However, all three arrangements for the $n = 4$, 3 and 2 environments have very similar mean Sn–$O_{48f}$ bond lengths despite the differences observed in $\delta_{iso}$ and Ω with the range in Sn–$O_{48f}$ bond length is considered, as shown in Figure 5.97. The difference in the calculated NMR parameters clearly does not result in differences in the Sn–$O_{48f}$ bond lengths.

Although there is little difference in the mean or range of Sn–$O_{48f}$ bond lengths for environments with the same *n*, it is clear from Figure 5.98 that different arrangements of B-site cations do have noticeably different mean Sn–Sn interatomic distances. The 1,3-Sn4Zr2, 1,3,5-Sn3Zr3 and 4,6-Sn2Zr4 arrangements exhibit a higher (most downfield) $^{119}$Sn $\delta_{iso}$, a lower $^{119}$Sn Ω and the shorter Sn–Sn interatomic distances when compared to the other *n* = 4, 3 or 2 NNN arrangements, respectively. The inverse relationships can be seen in Figure 5.99, where $^{119}$Sn $\delta_{iso}$ and Ω are plotted as a function of the mean Sn–Zr interatomic distance. The differences in $^{119}$Sn $\delta_{iso}$, a lower $^{119}$Sn Ω for the 1,3-Sn4Zr2, 1,3,5-Sn3Zr3 and 4,6-Sn2Zr4 highlighted above correlate with longer mean Sn–Zr distances. Figures 5.98 and 5.99 indicate that the 1,3-Sn4Zr2, 1,3,5-Sn3Zr3 and 4,6-Sn2Zr4 arrangements cause the central Sn cation to shift closer to the NNN sites occupied by Sn and thus further from

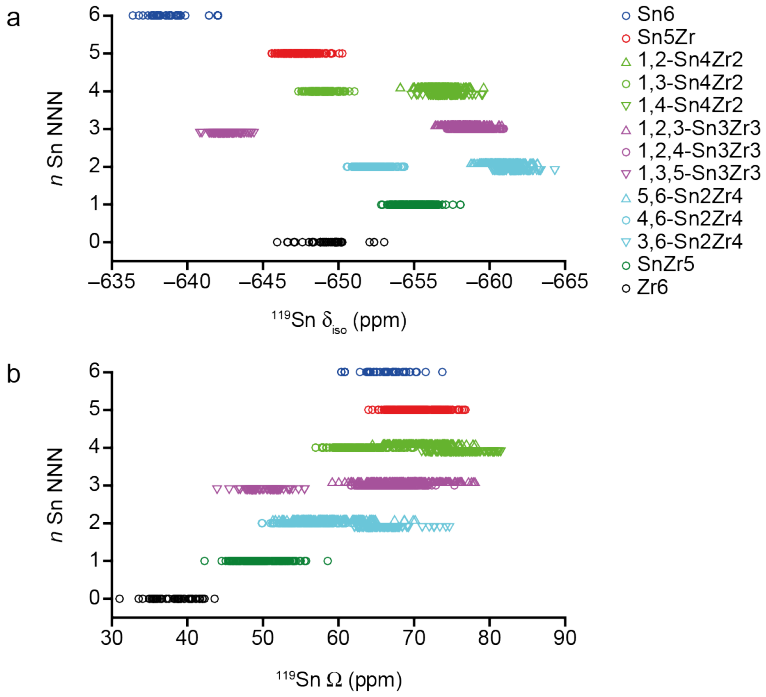


**Figure 5.95:** Plot of calculated $^{119}$Sn (a) $\delta_{iso}$ and (b) Ω as a function of *n* Sn NNN for the structural models of $La_2Sn_xZr_{2-x}O_7$, with data points shaped by Sn NNN arrangement. For *n* = 4, 3 and 2, the data points for the different arrangements have been offset slightly to facilitate comparison.

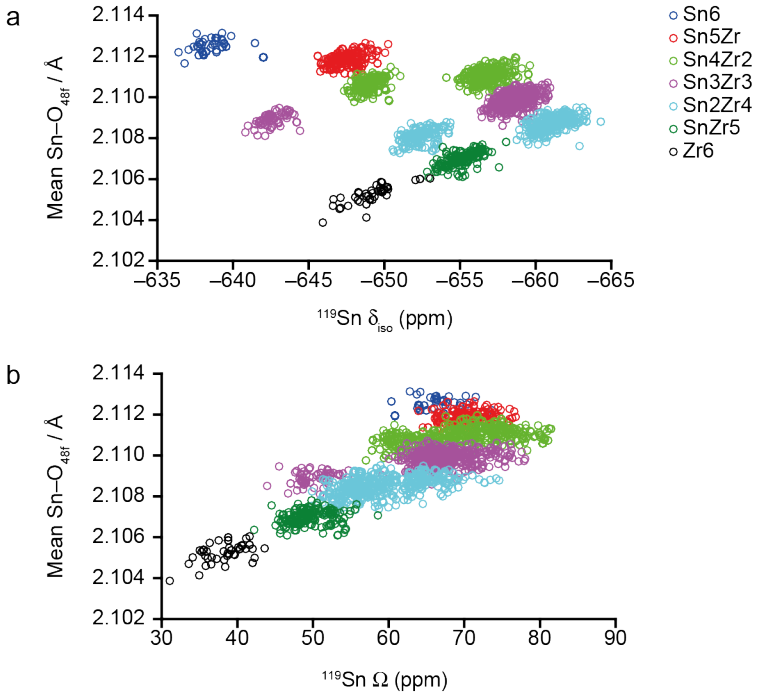


**Figure 5.96:** Plot of calculated $^{119}$Sn (a) $\delta_{iso}$ and (b) Ω as a function of the mean Sn–$O_{48f}$ bond length for the structural models of $La_2Sn_xZr_{2-x}O_7$, with data points coloured by *n* Sn NNN.

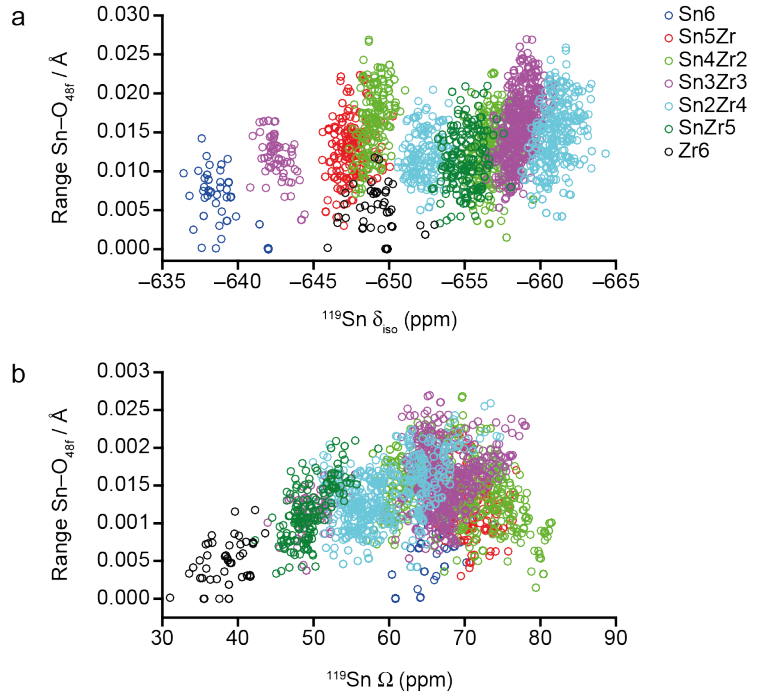


**Figure 5.97:** Plot of calculated $^{119}$Sn (a) $\delta_{iso}$ and (b) Ω as a function of the range of Sn–$O_{48f}$ bond lengths for the structural models of $La_2Sn_xZr_{2-x}O_7$, with data points coloured by *n* Sn NNN.

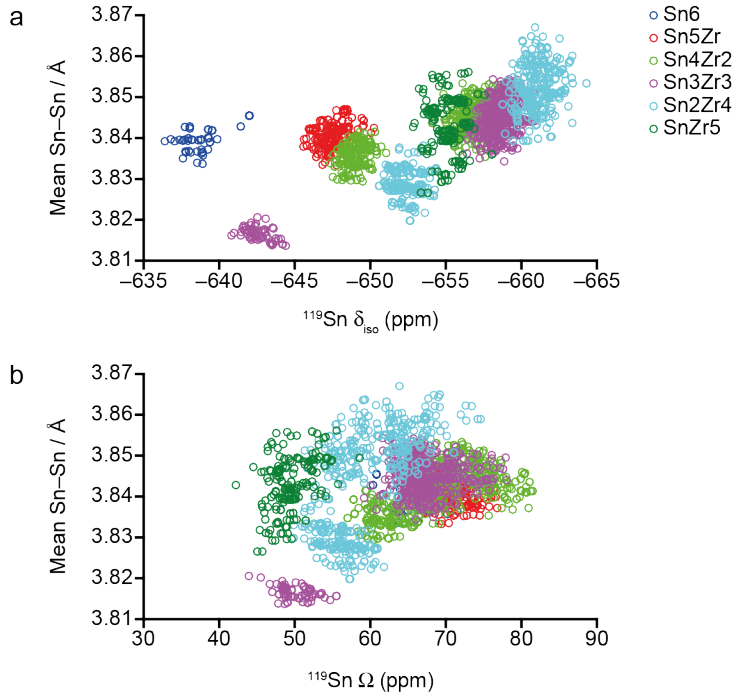


**Figure 5.98:** Plot of calculated $^{119}$Sn (a) $\delta_{iso}$ and (b) Ω as a function of mean Sn–Sn interatomic distance for the structural models of $La_2Sn_xZr_{2-x}O_7$, with data points coloured by *n* Sn NNN.

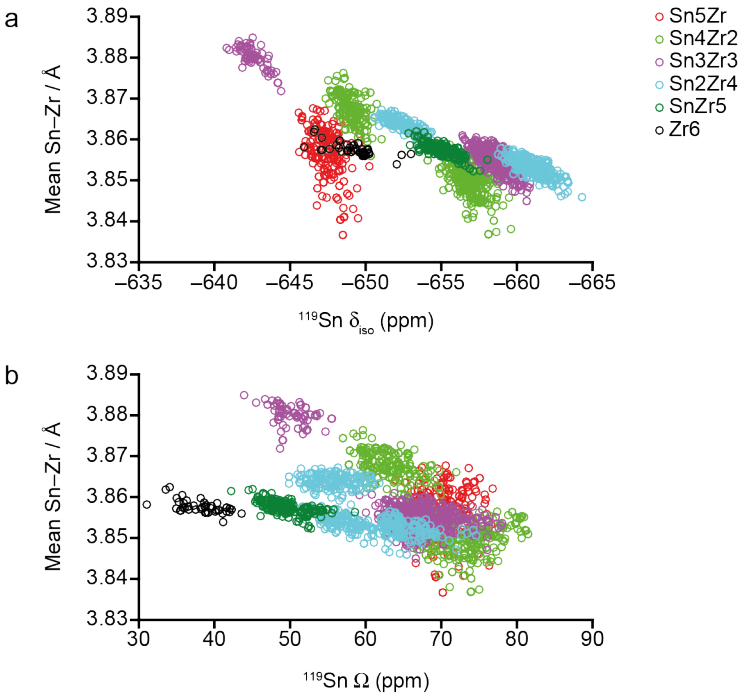


**Figure 5.99:** Plot of calculated $^{119}$Sn (a) $\delta_{iso}$, and (b) Ω as a function of mean Sn–Zr interatomic distance for the structural models of $La_2Sn_xZr_{2-x}O_7$, with data points coloured by *n* Sn NNN.

the sites occupied by Zr, relative to the other six arrangements, causing significant variations in the calculated $^{119}$Sn NMR parameters. In all of these three arrangements the smaller $Sn^{4+}$ cations are all located on the same face of the cluster of B sites around the central Sn (*i.e.*, they are only found on one of the two sets of three B sites), as shown in Figure 5.9. The central Sn is then able ot move closer to the set of B sites containing the smaller cations (shortening all Sn–Sn distances and lengthening all Sn–Zr distances). For other arrangements of the Sn cations (*i.e.*, those where Sn is found on both sets of three B sites) it is not possible for the central Sn to move such that distances to all NNN Sn species are decreased simultaneously.

Figure 5.100 plots the calculated $^{119}$Sn $\delta_{iso}$ and Ω for the structural models of $La_2Sn_xZr_{2-x}O_7$ as a function of the range (*i.e.*, difference between the largest and smallest values) of the Sn–B-site cation interatomic distance. This indicates that there is a significant difference in the range of distances depending on the specific NNN B-site cation arrangement. Indeed, the

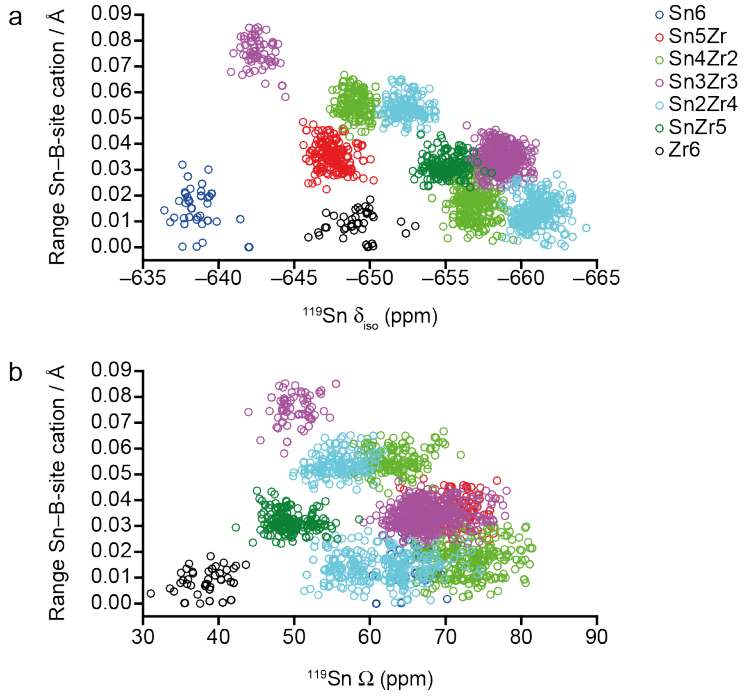


**Figure 5.100:** Plot of calculated $^{119}$Sn (a) $\delta_{iso}$ and (b) Ω as a function of the range of Sn–B-site cation interatomic distance for the structural models of $La_2Sn_xZr_{2-x}O_7$, with data points coloured by *n* Sn NNN.

largest range is observed for the NNN B-site arrangements that also exhibit the highest $^{119}$Sn $\delta_{iso}$ for a particular *n* Sn NNN environment, *i.e.* 1,3-Sn4Zr2, 1,3,5-Sn3Zr3 and 4,6-Sn2Zr4. This confirms that Sn species in these three environments move closer to the set of three B sites (*i.e.*, above or below the central Sn) that contains the largest number of the smaller (Sn) cations. The remaining $n$ = 4, 3 and 2 NNN arrangements exhibit much smaller ranges of Sn–B-site cation interatomic distance, the more even distribution of Sn and Zr over the three B sites above and below the central Sn, limiting the preference for this cation to move towards a particular set of B sites.

Following the same procedure used for the series 3 structural models of $Y_2Sn_xTi_{2-x}O_7$ (see Section 5.5.5.3), simulated spectra based on the calculated $^{119}$Sn $\delta_{iso}$ were generated for all eight Sn-containing compositions of $La_2Sn_xZr_{2-x}O_7$. Each individual Sn species was represented by a single Gaussian lineshape centred at $\delta_{iso}$ with a LB of 1.0 ppm, with the intensity scaled by the configurational degeneracy of the specific structural model in which that species was found These were then summed for all structural models with a specific composition. Figure 5.101 shows the simulated $^{119}$Sn NMR spectra alongside the experimental $^{119}$Sn MAS NMR spectra of $La_2Sn_xZr_{2-x}O_7$. Figure 5.102 shows a similar comparison, but with the simulated spectra decomposed according to *n* Sn NNN. From Figure 5.101, reasonably good agreement between the simulated and experimental $^{119}$Sn spectra is observed, with the former set of spectra containing the same number of broadened resonances for the majority of compositions.

As previously seen for the $^{119}$Sn NMR spectra of $Y_2Sn_xTi_{2-x}O_7$ (see Figure 5.77), the poorest agreement between the relative intensities of the spectral lineshapes is seen for compositions with $x$ = 1.75 and 0.25. As discussed in Section 5.5.5.3, this may well result from the use of only a single unit cell, which restricts the number of symmetry inequivalent structural models for these compositions to three. The use of a supercell could potentially improve the agreement between the simulated and experimental $^{119}$Sn NMR spectra, particularly for compositions with small numbers of Sn or Zr cations,

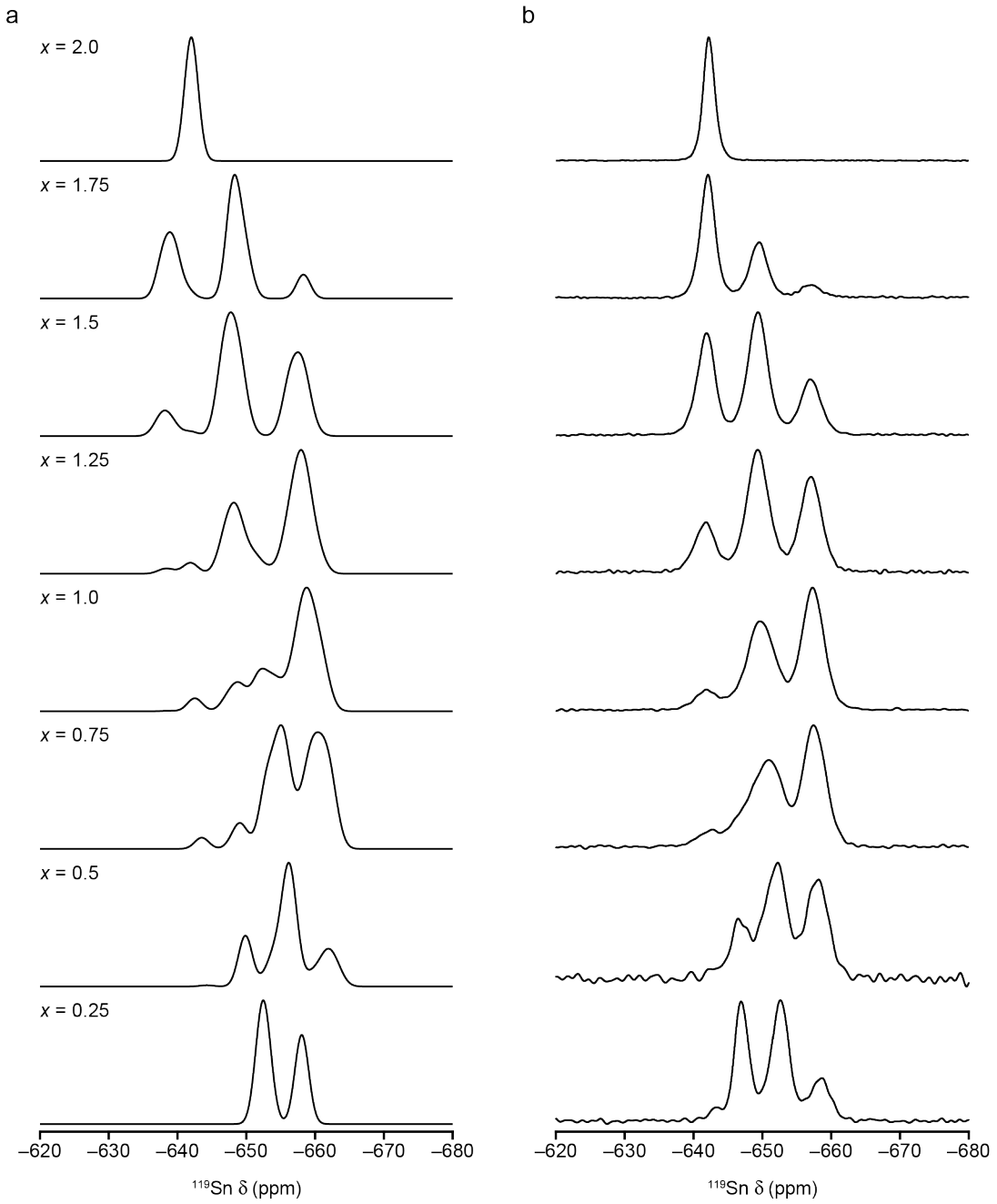


**Figure 5.101:** (a) Simulated $^{119}$Sn MAS NMR spectra for the structural models of $La_2Sn_xZr_{2-x}O_7$. (b) $^{119}$Sn (9.4 T, 14 kHz) MAS NMR spectra of $La_2Sn_xZr_{2-x}O_7$.

enabling additional environments to be considered. For example, when $x$ = 0.25 there are only two Sn species within the unit cell, with only Zr6 and SnZr5 environments possible in the compositional models (and therefore simulated spectra). The experimental $^{119}$Sn MAS NMR spectrum clearly contains a third resonance, likely corresponding to Sn2Zr4 environments, suggesting a lower level of B-site cation clustering in the real material.

As shown in Figure 5.102a, when the simulated $^{119}$Sn NMR spectra of $La_2Sn_xZr_{2-x}O_7$ are decomposed according to $n$, it is clear that for many compositions, the different NNN B-site cation arrangements for a particular $n$ environment contribute intensity to multiple spectral resonances. For

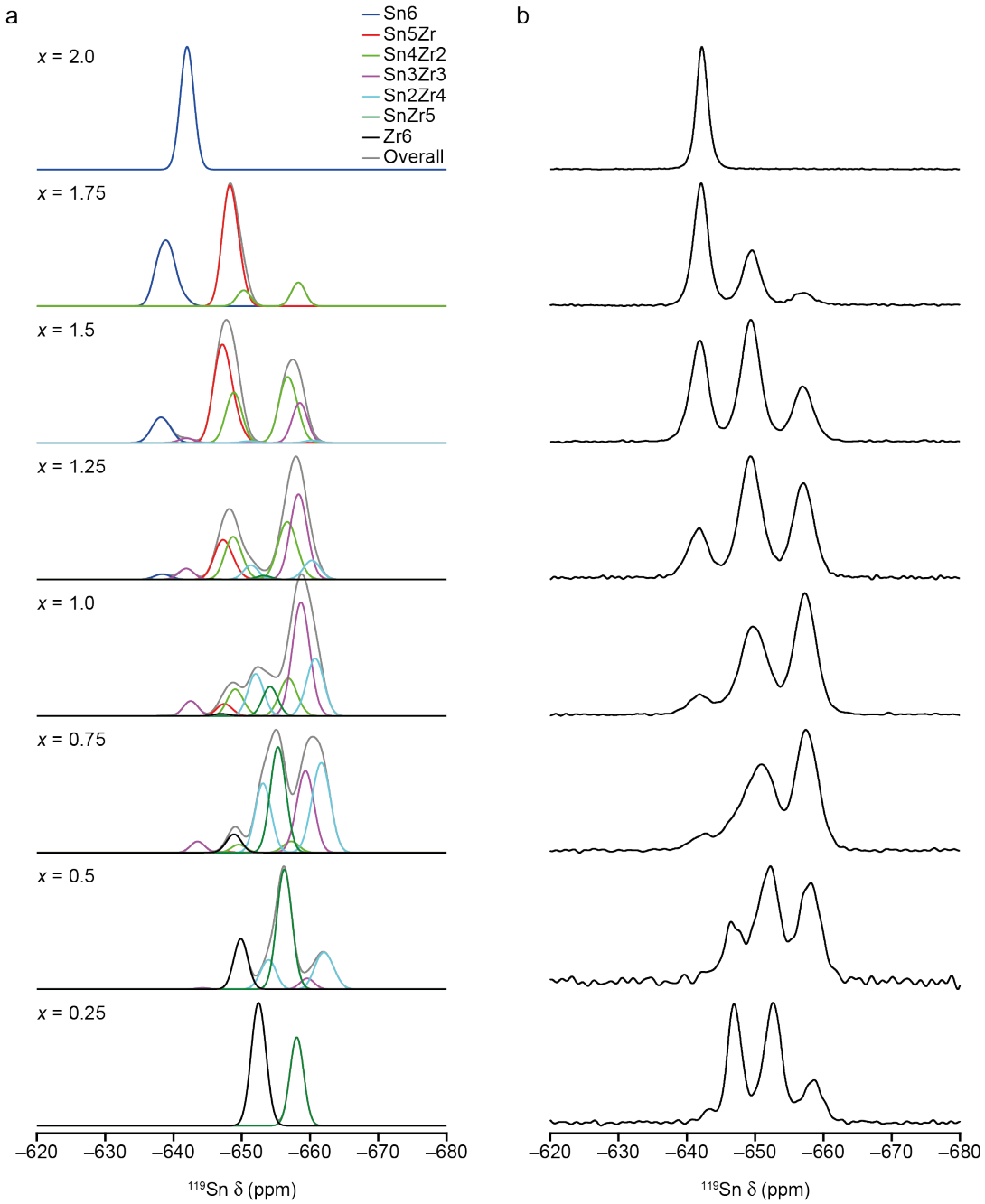


**Figure 5.102:** (a) Simulated $^{119}$Sn MAS NMR spectra for the structural models of $La_2Sn_xZr_{2-x}O_7$, decomposed according to $n$ Sn NNN. (b) $^{119}$Sn (9.4 T, 14 kHz) MAS NMR spectra of $La_2Sn_xZr_{2-x}O_7$.

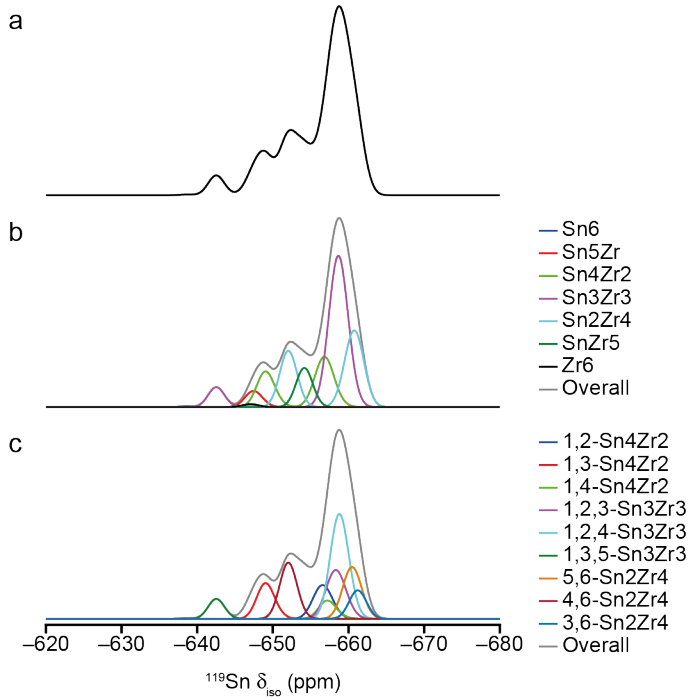


**Figure 5.103:** (a) Simulated $^{119}$Sn NMR spectrum for the structural models of $La_2SnZrO_7$. Spectra are then shown decomposed according to (b) $n$ Sn NNN and (c) the specific Sn NNN arrangements for the $n$ = 4, 3 and 2 environments.

example, when $x$ = 0.5, species with four different values of $n$ are present in the spectrum. However, signals from environments with $n$ = 3 and 2 overlap between –658 and –662 ppm, while different arrangements of cations for $n$ = 2 environments also contribute to the resonance at ~ –655 ppm. This leads to the observation of only three broadened resonances in the spectrum, in good agreement with the experimental observations. At higher $x$, the overlap of signal from environments with different $n$ result in only three broadened spectral resonances in all spectra, for example, when $x$ = 1.5 signal from $n$ = 5 and 4 environments overlap at ~ –647 ppm and signal from $n$ = 4 and 3 environments overlap at ~ –658 ppm. More generally, the environments with smaller Sn–Sn and larger Sn–Zr (relative to other environments with similar $n$), *i.e.*, 1,3-Sn4Zr2, 1,3,5-Sn3Zr3 and 4,6-Sn2Zr4 result in significant signal that overlaps with resonances at much higher shift.

The simulated $^{119}$Sn NMR spectra of $La_2SnZrO_7$ was investigated in more detail, as shown in Figure 5.103,where it is separated according to $n$ (Figure 5.103b) and into the nine individual B-site cation arrangements for the

Sn4Zr2, Sn3Zr3 and Sn2Zr4 (*i.e.*, $n$ = 4, 3 and 2) environments (Figure 5.103c). From Figure 5.103b it is clear that the $^{119}$Sn $\delta_{iso}$ for Sn species with different $n$ Sn NNN environments exhibit considerable overlap, with Sn with $n$ = 4, 3 and 2 contributing to multiple resonances, making it impossible to assign spectral lineshapes to specific values of $n$. Figure 5.103c (where the simulated $^{119}$Sn NMR spectrum of $La_2SnZrO_7$ is decomposed so only intensity from $n$ = 4, 3 and 2 environments, coloured according to the specific B-site cation arrangement is shown) shows that six of the nine arrangements have very similar $^{119}$Sn $\delta_{iso}$, leading to an intense resonance at this point in the spectrum. In contrast, the 1,3-Sn4Zr2, 1,3,5-Sn3Zr3 and 4,6-Sn2Zr4 arrangements, all of which have significantly higher (more downfield) $^{119}$Sn $\delta_{iso}$, each have a reasonably well-defined range of $\delta_{iso}$ that leads to additional resonances being observed, and leading to an overall lineshape that generally agrees well with experiment (see Figure 5.101). Therefore, while Sn species with 1,3-Sn4Zr2, 1,3,5-Sn3Zr3 and 4,6-Sn2Zr4 NNN B-site arrangements may yield distinctive ranges of calculated $^{119}$Sn $\delta_{iso}$, for a particular value of $n$, the significant spectral overlap with signal from Sn with different $n$ means that signals from these environments cannot be assigned directly.

The calculated $^{119}$Sn NMR parameters for the structural models of $La_2Sn_xZr_{2-x}O_7$ (see Figure 5.94 to 5.103) provide important insights into the relationship between NMR parameters and local geometry, with the results agreeing well with those observed for the Sn-centred cluster models (see Section 5.6.3). In contrast to $Y_2Sn_xTi_{2-x}O_7$ (see Section 5.5.5.3), calculated $^{119}$Sn $\delta_{iso}$ and (to a lesser extent) $\Omega$ are sensitive to changes in NNN B-site arrangement, with Sn species with 1,3-Sn4Zr2, 1,3,5-Sn3Zr3 or 4,6-Sn2Zr4 environments exhibiting far higher $\delta_{iso}$ than any other arrangement with similar $n$. The simulated $^{119}$Sn NMR spectra of $La_2Sn_xZr_{2-x}O_7$ also aid interpretation of the experimental $^{119}$Sn MAS NMR spectra, with reasonably good agreement seen for most compositions. Decomposition of the simulated $^{119}$Sn NMR spectrum of $La_2SnZrO_7$ according to the nine specific $n$ = 4, 3 and 2 NNN B-site

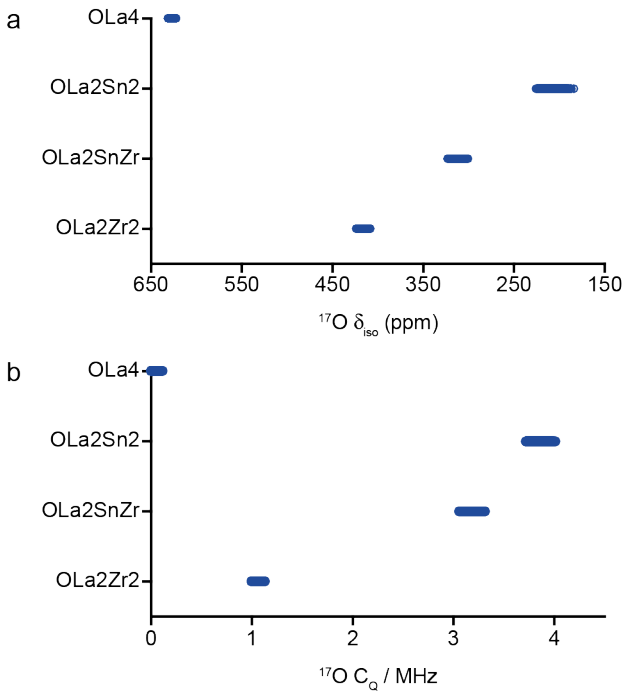


**Figure 5.104:** Plot of calculated $^{17}$O (a) $\delta_{iso}$ and (b) $C_Q$ as a function of O environment for the structural models of $La_2Sn_xZr_{2-x}O_7$.

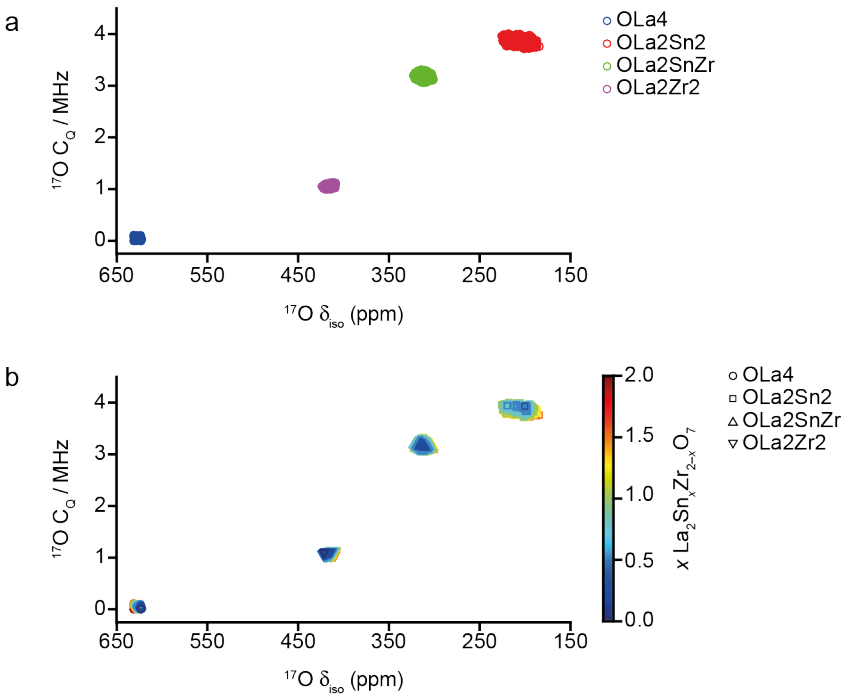


**Figure 5.105:** Plot of calculated $^{17}$O $\delta_{iso}$ as a function of $C_Q$ for the structural models of $La_2Sn_xZr_{2-x}O_7$, with the data points (a) coloured by the type of O environment and (b) coloured by $x$ $La_2Sn_xZr_{2-x}O_7$.

arrangements reveals both the extent of the overlap in $^{119}$Sn $\delta_{iso}$ for six of the arrangements, and also highlights the distinctly different $\delta_{iso}$ seen for the 1,3-Sn4Zr2, 1,3,5-Sn3Zr3 and 4,6-Sn2Zr4 arrangements resulting from the movement of the central Sn cation closer to the set of three NNN B-sites occupied by Sn in these three arrangements. These observations indicate that although a full assignment of the $^{119}$Sn MAS NMR spectra of $La_2Sn_xZr_{2-x}O_7$ is not possible, comparison with the simulated $^{119}$Sn NMR spectra facilitates a more detailed understanding of the experimental spectra and insight into the environments that may be present.

To probe the relationship between $^{17}$O NMR parameters and local geometry, and to potentially gain insights that could assist in the interpretation and assignment of the experimental $^{17}$O MAS NMR spectra of $La_2Sn_xZr_{2-x}O_7$ (see Figure 5.86), the calculated $^{17}$O $\delta_{iso}$ and $C_Q$ parameters for the 279 structural models have been analysed. From Figures 5.104a and 5.104b it is clear that each type of O local environment (*i.e.*, OLa4, OLa2Sn2, OLa2SnZr and

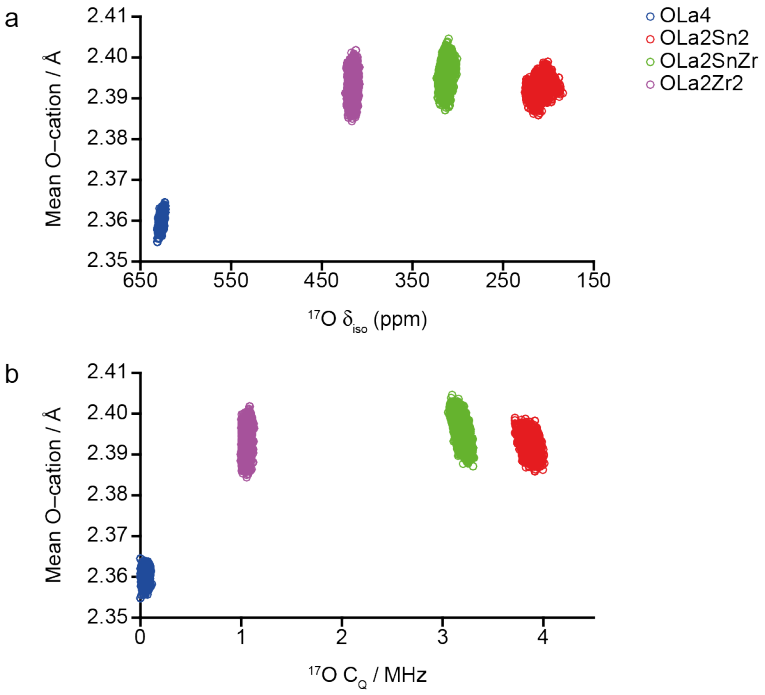


**Figure 5.106:** Plot of calculated $^{17}$O (a) $\delta_{iso}$ and (b) $C_Q$ as a function of mean O–cation bond length for the structural models of $La_2Sn_xZr_{2-x}O_7$, with data points coloured by the type of O environment.

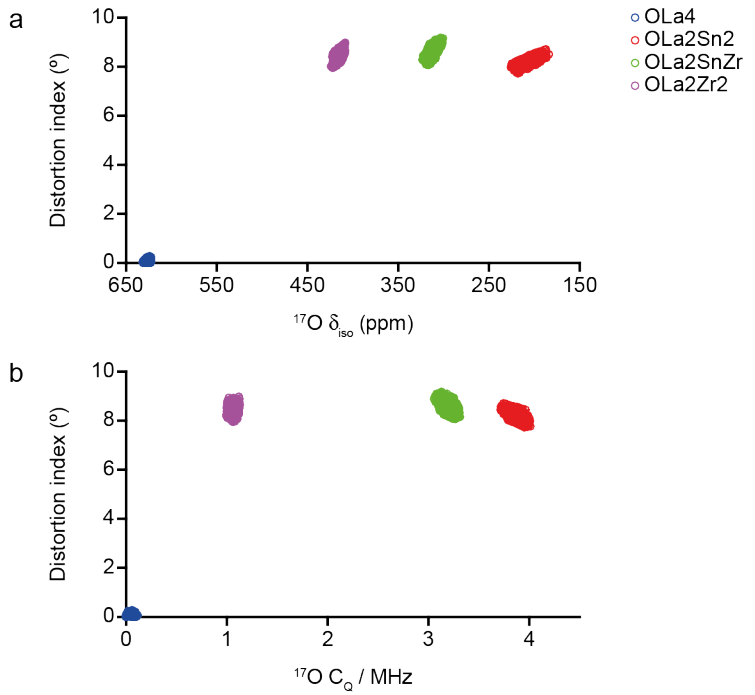


**Figure 5.107:** Plot of calculated $^{17}$O (a) $\delta_{iso}$ and (b) $C_Q$ as a function of the distortion index for the structural models of $La_2Sn_xZr_{2-x}O_7$, with data points coloured by the type of O environment.

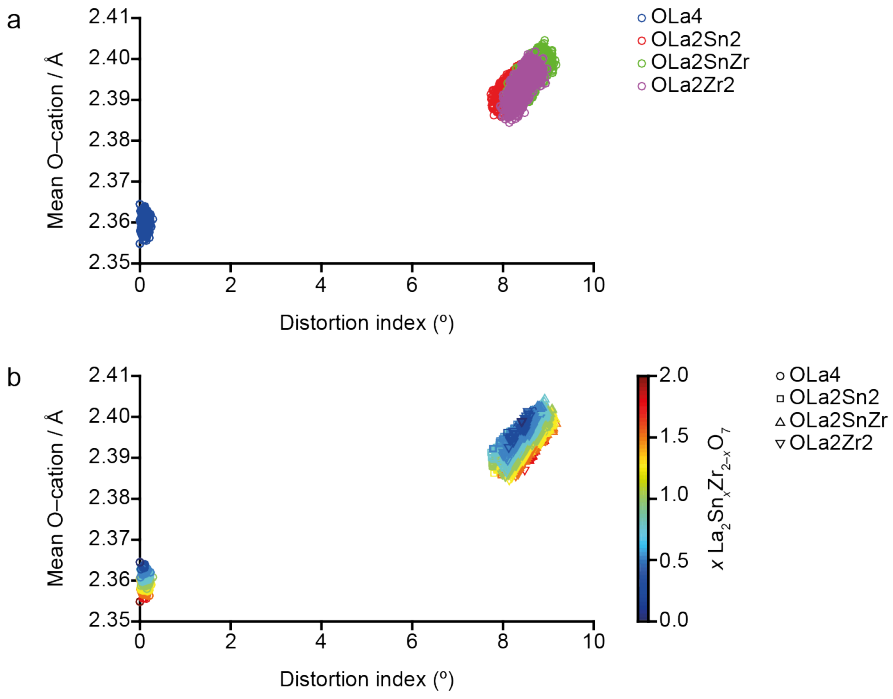


**Figure 5.108:** Plot of distortion index against mean O–cation bond length for the structural models of $La_2Sn_xZr_{2-x}O_7$, with data points coloured by (a) the type of O environment and (b) by $x$ $La_2Sn_xZr_{2-x}O_7$.

OLa2Zr2) have a well-defined range of both $^{17}O$ $\delta_{iso}$ and $C_Q$, with the OLa2Sn2 environment exhibiting the largest range in both parameters. The highly symmetrical OLa4 environment exhibits a very narrow range of $^{17}O$ $\delta_{iso}$ and (as expected) very small $C_Q$ values. In contrast, due to the more covalent nature of the Sn–O bond, the largest $^{17}O$ $C_Q$ is observed for the OLa2Sn2 environment (despite the less symmetric nature of the OLa2SnZr coordination environment), with increasing Zr content leading to a reduction in this parameter. A similar trend is observed for $Y_2Sn_xTi_{2-x}O_7$, where the OY2Sn2 environment exhibited resulted in the largest $^{17}O$ $C_Q$ value (see Section 5.5.5.3).

As shown in Figure 5.105, a plot of calculated $^{17}O$ $C_Q$ against $^{17}O$ $\delta_{iso}$ highlights how distinct the four types of O local environments are. Figure 5.105b, where the data points are coloured according to $x$ (*i.e.*, $La_2Sn_xZr_{2-x}O_7$ composition) shows that some $^{17}O$ $\delta_{iso}$ are slightly affected by a change in B-site cation composition. As Zr content increases (*i.e.*, as $x$ decreases) the $^{17}O$ $\delta_{iso}$ for the OLa4 environment decreases (moves upfield) slightly, something also observed in the $^{17}O$ MAS NMR spectra of $La_2Sn_xZr_{2-x}O_7$ (see Figure 5.86), whereas the $^{17}O$ $\delta_{iso}$ for the OLa2Sn2, OLa2SnZr and OLa2Zr2 local environment seem relatively unaffected by a change in composition.

Figures 5.106 and 5.107 show that both the mean O–cation bond length and the distortion index (describing the tetrahedral coordination of the O) are dependent on the particular type of O local environment, with OLa4 species exhibiting noticeably shorter mean bond lengths and much smaller distortion indices than the other three environment types. The substitution of Sn, and the more covalent O–Sn interaction, causes movement of the central O resulting in shorter O–Sn bond lengths, and larger O–La/Zr bond lengths and an overall increase in the mean O–cation distance. The similar size and ionicity of La and Zr means that the effect is comparable for the OLa2Sn2, OLa2SnZr and OLa2Zr2 environments, resulting in similar mean O–cation distances and similar distortion indices in each case, as shown in Figure 5.108a. Figure 5.108b shows that a decrease in $x$ (*i.e.*, a decrease in the total Sn

content of the unit cell in which a particular species is found), results in generally larger mean O–cation bond lengths and smaller distortion indices for the OLa2Sn2, OLa2SnZr and OLa2Zr2 environments. This is likely to result from the larger size of $Zr^{4+}$ (relative to $Sn^{4+}$), and the resulting overall expansion of the unit cell as the Zr content increases.

From this analysis it is clear that the calculated $^{17}O$ NMR parameters for the 279 structural models are particularly sensitive to changes in the local coordination environment in $La_2Sn_xZr_{2-x}O_7$. All four types of O environments, *i.e.*, OLa4, OLa2Sn2, OLa2SnZr and OLa2Zr2 have very distinct regions of calculated $^{17}O$ $\delta_{iso}$ and different $^{17}O$ $C_Q$, making it straightforward to assign the resonances in the experimental $^{17}O$ NMR spectra in Figure 5.86. The very small $C_Q$ exhibited by the OLa4 species results from the more symmetrical coordination environment, and more ionic nature of the O–La interactions. In contrast, the substitution of Sn on the neighbouring sites (and the corresponding increase in the covalency of the bonds) results in higher $C_Q$ values. It is clear the variation in $C_Q$ between OLa2Sn2, OLa2SnZr and OLa2Zr2 environments arises from the different electron distribution, rather than larger changes in geometry (*i.e.*, bond distances or angles, as measure by O–cation distances and distortion indices), as these are similar for the three environments. The significant variation in the $^{17}O$ NMR parameters with coordinating atoms suggests the $^{17}O$ NMR spectroscopy could be a vital tool in the study of disordered ceramics, assuming the challenges of uniform isotropic enrichment (to address the low natural abundance) can be overcome.

### 5.6.5 Summary

This section has illustrated how solid-state NMR parameters are a sensitive probe of the variation in local geometry and, more specifically, B-site cation disorder in $La_2Sn_xZr_{2-x}O_7$, with first-principles calculations capable of providing insights that can aid interpretation and assignment of experimental $^{119}Sn$ and $^{17}O$ MAS NMR spectra. As the significant overlap

between signals arising from different types of Sn species causes the $^{119}$Sn MAS NMR spectra of $La_2Sn_xZr_{2-x}O_7$ (see Figure 5.85) to be particularly challenging to assign, the importance of first-principles calculations to provide insight into the types of species that may be present (and perhaps more importantly, the conclusions that cannot simply be assumed on the basis of chemical shift) cannot be understated. Within this study two approaches for generating structural models to represent the range of local Sn and O environments in $La_2Sn_xZr_{2-x}O_7$ has been investigated.

Initially, a series of Sn-centred cluster models were generated by systematically varying the *n* Sn NNN environment of a single Sn cation in a pyrochlore unit cell to provide an example of each type of local chemical environment that might be encountered. Despite the simplicity of this approach, the calculated $^{119}$Sn NMR parameters were able to provide insight into the interpretation of the experimental spectra, and help to explain the origin of the broader lines observed, and the similarity in resonance positions even for materials with very different compositions. Although small decreases in $^{119}$Sn $\delta_{iso}$ are seen when Zr is first substituted onto the NNN sites, subsequent increases in the Zr content increases $\delta_{iso}$ leading to a very similar set of resonance positions being observed. The calculations were able to demonstrate that a significant change in $\delta_{iso}$ was observed for particular cation arrangements (*i.e.*, 1,3-Sn4Zr2, 1,3,5-Sn3Zr3 and 4,6-Sn2Zr4) when $n$ = 4, 3 and 2, leading to much higher $\delta_{iso}$ than for other arrangements with similar *n* and the additional overlap of spectral resonances. However, the restriction in the long-range environments for the cluster models (and the inability to model the intensity of the spectral resonances) ultimately limits the information available by this approach.

The use of SOD to generate a complete set of unique cation arrangements for nine specific $La_2Sn_xZr_{2-x}O_7$ compositions offers not only the ability to confirm the tentative conclusions determined from the simple cluster models, but the ability to, firstly, investigate in more detail the dependence of the NMR parameters on the local geometry and, secondly, to model the predicted

intensity of the spectral resonances and facilitate overall comparison to experiment. This approach provides a more realistic set of structural models and enables the effects of changes in the longer-range environment to be evaluated. The calculated NMR parameters supported the conclusions obtained from the simple cluster models, helping to explain the overlap of the spectral resonances seen experimentally. The much larger number of models enabled a more detailed understanding of the effect of cation distribution on the local geometry, and ultimately, on the NMR parameters. The much higher shifts seen for 1,3-Sn4Zr2, 1,3,5-Sn3Zr3 or 4,6-Sn2Zr4 environments was shown to be linked not to a variation in the Sn–O bond lengths, but to the changes in Sn–Sn and Sn–Zr interatomic distances that result from the displacement of the central Sn cation towards the set of three B sites on which the smaller $Sn^{4+}$ NNN cations are exclusively located. The ability to consider the configurational degeneracy of all atomic arrangements enabled the spectral intensities to be predicted and facilitated the understanding of the complex experimental lineshapes. While good overall agreement was obtained in most cases, the small difference in intensities between experiment and simulation, particularly when there is a small number of Sn (or Zr) cations within the unit cell, suggests that the real material do contain a low level clustering of like cations on length scales larger than the unit cell, and that supercells might be required to model experimental spectra more accurately.

The calculated $^{17}O$ NMR parameters for the SOD-generated structural models of $La_2Sn_xZr_{2-x}O_7$ confirm these are extremely sensitive to the coordinated cations, and confirm the assignment of the experimental spectra unambiguously. The significant variation in parameters for different types of O environment suggest that $^{17}O$ NMR spectroscopy will be an excellent probe of disordered ceramics. The very low $C_Q$ observed for the OLa4 environment results from the symmetric nature of the coordination environment, but significantly larger values of $C_Q$ were observed for O species bound to Sn. Consideration of the local geometry (bond distances and distortion indices) revealed that these arise not from significant distortions in the local geometry (*i.e.*, OLa2Sn2, OLa2SnZr and OLa2Zr2 have

very similar mean O–cation distances and distortion indices, most likely as a result of their very similar sizes), but from the covalency of the Sn–O bonds, and the resulting differences in electron distribution.

Considering the in-depth investigation presented in this section, it is concluded that, as for the $Y_2Sn_xTi_{2-x}O_7$ series (see Section 5.5), the most effective strategy for generating structural models capable of representing the range of local environments resulting from configurational B-site cation disorder in $La_2Sn_xZr_{2-x}O_7$ is the use of SOD. This approach is capable of identifying every symmetry inequivalent B-site cation arrangement (within the specified system size), and perhaps, more importantly, determining the corresponding configurational degeneracies, allowing not only a comparison of NMR parameters, but also simulated NMR spectra to be directly compared to their experimental counterparts. This facilitates spectral interpretation and assignment, prevents incorrect and simplified conclusions being drawn and provides insight into the cation distribution. As computational hardware improves and DFT methodology becomes more advanced this might represent the best approach for modelling compositional disorder in solids in the future.

## 5.7 $Y_2Zr_2O_7$ and $Y_2Hf_2O_7$: probing cation disorder and anion randomisation using NMR spectroscopy and first-principles calculations

### 5.7.1 Introduction

This section focuses on exploring preliminary computational approaches to model defect fluorite materials, which have considerably higher levels of disorder than the mixed-metal pyrochlores discussed in Sections 5.5 and 5.6. As described in Section 5.1.2, defect fluorites exhibit disorder on both the cation and anion sub lattices, with mixing of cations and disorder of the anions and oxygen vacancies, with each anion site having a fractional occupancy of 0.875. This increase in disorder increases significantly

the challenge of structural characterisation by either XRD or NMR spectroscopy. As a result, first-principles calculations could represent a valuable additional tool for understanding the structure of defect fluorite materials and aiding in the interpretation of experimental measurements. In this section, the ability for simple computational models to provide insight into the interpretation of experimental NMR spectra of two defect fluorites, $Y_2Zr_2O_7$ and $Y_2Hf_2O_7$, is investigated. The first of these materials has been studied previously using $^{89}Y$ NMR spectroscopy, as part of a comprehensive study into the phase distribution, phase composition and disorder in $Y_2(Sn,Zr)_2O_7$.[79] As in Sections 5.5 and 5.6, the ultimate aim is to explore if computation can be used to construct a series of structural models that can adequately represent the range of local environments present in $Y_2Zr_2O_7$ and $Y_2Hf_2O_7$, and use the predicted NMR parameters to help guide assignment of the corresponding $^{89}Y$ and $^{17}O$ MAS NMR spectra of these two defect fluorite materials.

## 5.7.2 Experimental NMR spectra

As described in Section 5.4, the $^{89}Y$ and $^{17}O$ MAS NMR spectra of $Y_2Zr_2O_7$ and $Y_2Hf_2O_7$ were acquired by Miss Arantxa Fernandes using Bruker Avance III spectrometers equipped with a 14.1 T wide-bore magnet at the Solid-State NMR Facility at the University of St Andrews.

### 5.7.2.1 $^{89}Y$ MAS NMR spectra

The $^{89}Y$ MAS NMR spectra of $Y_2Zr_2O_7$ and $Y_2Hf_2O_7$ are shown in Figure 5.109. Both spectra contain three broad resonances, which can be attributed to six-, seven- and eight-coordinate Y, with an increase in coordination number resulting in a more upfield (smaller) chemical shift.[80] A summary of the coordination number, $^{89}Y$ $\delta_{iso}$ and relative intensity (in %) for the resonance in the $^{89}Y$ MAS NMR spectra shown in Figure 5.109 is given in Table 5.7. From Figure 5.109, it is apparent that Y in both $Y_2Zr_2O_7$ and $Y_2Hf_2O_7$ preferentially adopts a higher coordination number, with only a

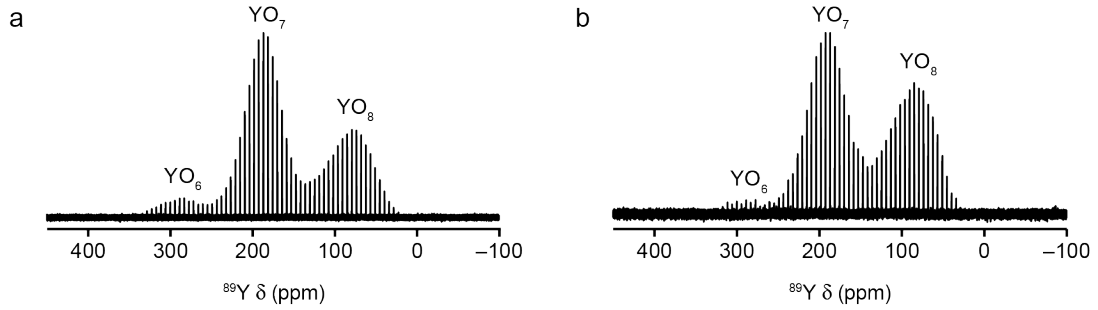


**Figure 5.109:** $^{89}$Y (14.1 T, 14 kHz) MAS NMR spectra of (a) $Y_2Zr_2O_7$ and (b) $Y_2Hf_2O_7$, acquired using a CPMG pulse sequence.

**Table 5.7:** Coordination number (CN), $^{89}$Y $\delta_{iso}$ and relative intensities (%) of the resonances observed in the $^{89}$Y MAS NMR spectra of $Y_2Zr_2O_7$ and $Y_2Hf_2O_7$, shown in Figure 5.109.

| $Y_2Zr_2O_7$[79,a] | | | $Y_2Hf_2O_7$[106,a,b] | | |
|---|---|---|---|---|---|
| CN | $^{89}$Y $\delta_{iso}$ (ppm) | Intensity (%) | CN | $^{89}$Y $\delta_{iso}$ (ppm) | Intensity (%) |
| 6 | 290.0 | 5.6 | 6 | 279.9 | 2.1 |
| 7 | 185.0 | 64.9 | 7 | 190.7 | 46.8 |
| 8 | 78.0 | 29.5 | 8 | 85.7 | 51.1 |

[a] $^{89}$Y $\delta_{iso}$ and relative intensities for $Y_2Zr_2O_7$ and $Y_2Hf_2O_7$ are from Ref. 76 and 100, respectively.

[b] Data taken from page 318 of Ref. 100, with the incorrect $YO_8$ % intensity of 51.0 corrected to 51.1

small proportion of six-coordinate Y observed, particularly in $Y_2Hf_2O_7$. Based on the relative intensities given in Table 5.7, the average coordination number of Y in $Y_2Zr_2O_7$ and $Y_2Hf_2O_7$ is 7.24 and 7.49, respectively. As the average cation coordination number in a defect fluorite phase is 7 (as with the pyrochlore), it follows that the average coordination number of Zr in $Y_2Zr_2O_7$ and Hf in $Y_2Hf_2O_7$ must be 6.76 and 6.51, respectively. This means that in both $Y_2Zr_2O_7$ and $Y_2Hf_2O_7$, there is preferential association of vacancies with Zr/Hf, and O prefer to occupy anion sites around the larger $Y^{3+}$ cation. Due to the broadening of the resonances in the $^{89}$Y MAS NMR spectra of both defect fluorite materials, other than the relative ratio of six-, seven- and eight-coordinate Y, little additional structural information (*e.g.*, on the NNN environments) can be easily extracted.

### 5.7.2.2 $^{17}$O MAS NMR spectra

From the $^{17}$O MAS NMR spectra of $Y_2Zr_2O_7$ and $Y_2Hf_2O_7$ shown in Figure 5.110, it is clear that the highly disordered nature of the defect fluorite phase has a significant effect on the appearance of the NMR spectra. This is especially apparent if the NMR spectra shown in Figure 5.110 are compared to the $^{17}$O MAS NMR spectra of $Y_2Sn_xTi_{2-x}O_7$ (Figure 5.9) and $La_2Sn_xZr_{2-x}O_7$ (Figure 5.86), both of which contain a maximum of four, relatively sharp resonances. Despite both $Y_2Zr_2O_7$ and $Y_2Hf_2O_7$ adopting a defect fluorite phase, Figure 5.110 shows that the $^{17}$O NMR spectra of the two materials are quite different, with the lineshape for $Y_2Hf_2O_7$ exhibiting several distinct peaks, whereas in $Y_2Zr_2O_7$, the individual resonances appear far more overlapped. The difference in average coordination number for Y, and thus Zr and Hf in $Y_2Zr_2O_7$ and $Y_2Hf_2O_7$, could also affect the appearance of the range of corresponding $^{17}$O MAS NMR spectra, through the expected ratios of the range of O environments *i.e.*, OY4, OY3Zr, OY2Zr2, OYZr3 and OZr4 in $Y_2Zr_2O_7$ and OY4, OY3Hf, OY2Hf2, OYHf3 and OHf4 in $Y_2Hf_2O_7$. The average Y coordination numbers (determined from the percentage intensities shown in Table 5.7) suggest that $Y_2Hf_2O_7$ should contain a slightly greater proportion of Y-rich environments, relative to $Y_2Zr_2O_7$, where the average Y coordination number is closer to seven. Regardless of the reasons for the differences in the $^{17}$O MAS NMR spectra of $Y_2Zr_2O_7$ and $Y_2Hf_2O_7$, it is clear that both NMR spectra are challenging to interpret, emphasising the importance of using first-principles calculations to guide spectral interpretation.

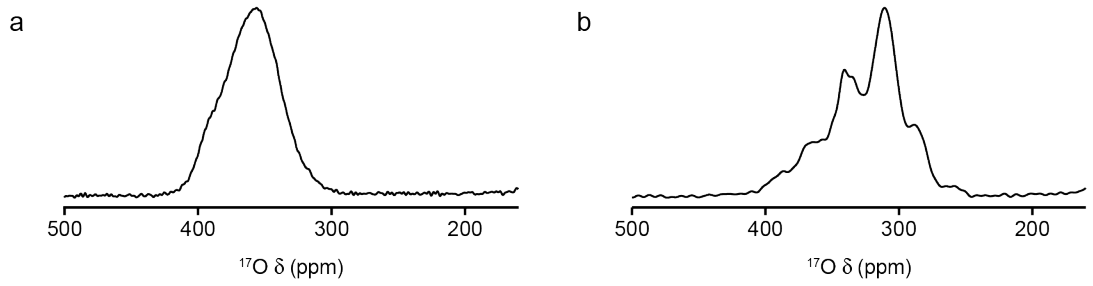


**Figure 5.110:** $^{17}$O (14.1 T, 21 kHz) MAS NMR spectra of (a) $Y_2Zr_2O_7$ and (b) $Y_2Hf_2O_7$.

### 5.7.3 Models with cation mixing and randomised anion positions

As described in Section 4.3.1, using simple statistics (see Equation 4.1) it is possible to determine the total number of atomic arrangements in a material given a known number of well-defined crystallographic sites. A 2 × 2 × 2 supercell of the defect fluorite structure contains the same number of atoms as in a pyrochlore unit cell, *i.e.*, 32 cation sites, occupied by 16 Y and 16 Zr (or Hf), and 64 anion sites, 56 occupied by O, leaving 8 vacant. This would give ~601 million potential cation arrangements and 4.43 billion anion arrangements, leading to a total of over $2.66 \times 10^{18}$ possible structures. Even though many of these arrangements will be symmetry related, considering every inequivalent structure is still unfeasible. In contrast to the pyrochlore systems discussed in Sections 5.5 and 5.6, the number of possible defect fluorite structures is too large even for the SOD approach. In order to provide insight into the NMR parameters and ultimately help assign the $^{89}$Y and $^{17}$O NMR spectra of $Y_2Zr_2O_7$ and $Y_2Hf_2O_7$, the only option is to consider a much smaller subset of structures.

In a similar process to that used to generate the $Y_2Sn_xTi_{2-x}O_7$ structures with randomised cation positions in Section 5.5.4, an automated script was used to generate a set of 30 $Y_2Zr_2O_7$ possible defect fluorite structures within a 2 × 2 × 2 supercell of an $AO_2$ fluorite structure,[107] containing 32 cation and 64 anion sites. For each structural model, 16 cation sites were randomly occupied by Y, with Zr placed on the remaining 16 sites. Simultaneously, 8 out of the 64 anion sites were randomly assigned to be vacant, with the remaining 56 occupied by O. The 30 $Y_2Zr_2O_7$ structural models were then geometry optimised using CASTEP 8.0. However, many of these structures started far from equilibrium, and optimisation was a two-step process. Firstly, the EDFT SCF solver was used for a maximum of 50 optimisation iterations, before the output from this first calculation was taken and optimised further using the DM SCF solver. The 30 geometry optimised $Y_2Zr_2O_7$ structures were then used as the initial input for 30 $Y_2Hf_2O_7$ structures, with all Zr replaced by Hf

before re-geometry optimising using the DM SCF solver.

All NMR parameters calculations for the 30 $Y_2Zr_2O_7$ and 30 $Y_2Hf_2O_7$ were performed using CASTEP 8.0, with an $E_{cut}$ of 60 Ry, a k-point spacing of 0.04 $2\pi$ Å$^{-1}$ (see Appendix A1 for convergence testing), the PBE $E_{XC}$ functional,[94] default on-the-fly ultrasoft pseudopotentials,[95] a `geom_energy_tol` value of $1 \times 10^{-5}$ eV / atom atom and an `elec_energy_tol` value of $1 \times 10^{-9}$ eV / atom (see Section 5.5.4.1), with ZORA correction applied. Experimental $\delta_{iso}$ and calculated $\sigma_{iso}$ for a series of Y- and O-containing simple compounds were used to reference $^{89}$Y and $^{17}$O calculated isotropic shieldings, as described in Appendix C1. In this section only the magnitude of the $^{17}$O $C_Q$ is considered.

As a result of the randomisation of the anion vacancies, the defect fluorite structural models contain examples of five-, six-, seven- and eight-coordinate Y species, while the $^{89}$Y MAS NMR spectra of $Y_2Zr_2O_7$ and $Y_2Hf_2O_7$ (see Figure 5.110) suggest only the latter three environments are present in any

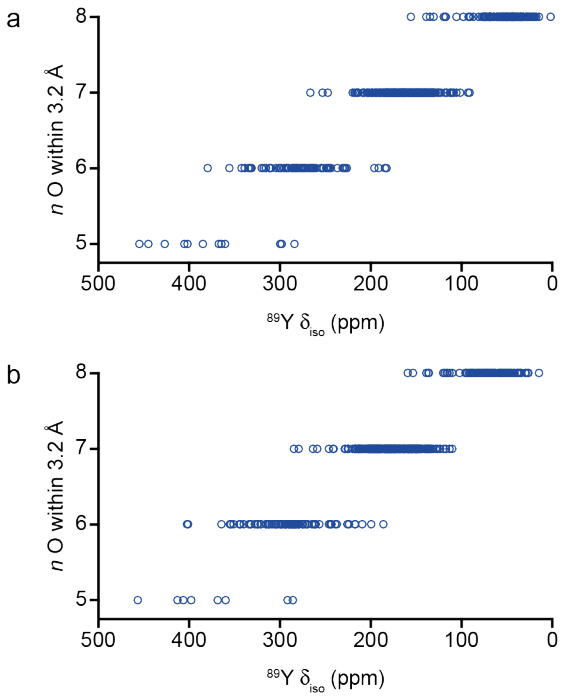


**Figure 5.111:** Plot of calculated $^{89}$Y $\delta_{iso}$ as a function of the number of O ($n$) within 3.2 Å of each Y for the 30 structural models of (a) $Y_2Zr_2O_7$ and (b) $Y_2Hf_2O_7$.

significant amount (and with a much lower amount of six-coordinate Y). Following geometry optimisation, the $Y_2Zr_2O_7$ and $Y_2Hf_2O_7$ structures span energy ranges of 5.35 and 5.42 eV, respectively. The lowest energy structural model of $Y_2Zr_2O_7$ contains two six-coordinate, twelve seven-coordinate and two eight-coordinate Y, whereas the lowest energy model for $Y_2Hf_2O_7$ has one, thirteen and two six-, seven- and eight-coordinate Y, respectively, with neither structure containing any five-coordinate Y. These lowest energy structures have average Y coordination numbers of 7.0, and 7.06, for $Y_2Zr_2O_7$ and $Y_2Hf_2O_7$, respectively. These values are lower than the average coordination numbers determined from the experimental $^{89}$Y MAS NMR spectra (see Table 5.7).

In contrast to the pyrochlore structure, where the ordered vacancies ensure that Y is exclusively eight-coordinate, the randomisation of the vacancies within a defect fluorite structure, and the subsequent additional structural flexibility this imparts, poses a difficulty in the determination of the Y-coordination number owing to the larger variation in the Y–O interatomic distances. In this thesis, the coordination number of an Y species is defined by the number of O (*n* O), within 3.2 Å. As shown in Figure 5.111, when calculated $^{89}$Y $\delta_{iso}$ is plotted as a function of the coordination number (as defined above), despite significant overlap in the ranges observed as the number of coordinated O species *n*, increases, a decrease (a move upfield) in the average $^{89}$Y $\delta_{iso}$ is observed for both $Y_2Zr_2O_7$ and $Y_2Hf_2O_7$. This confirms the assignment of the experimental $^{89}$Y MAS NMR spectra in Figure 5.109.

Figure 5.112 plots $^{89}$Y $\delta_{iso}$ against $^{89}$Y $\Omega$, and reveals that, in general, $\Omega$ increases slightly, with an increase in $^{89}$Y $\delta_{iso}$ meaning that Y with the lower coordination numbers exhibit largest $\Omega$. The few Y with $\Omega$ above 600 ppm also have the largest $\delta_{iso}$ and are all five-coordinate Y species that result from higher-energy structural models. In addition, Figure 5.113 shows that, a decrease in $^{89}$Y $\delta_{iso}$ is generally associated with an increase in mean Y–O bond length, with Y species with $n = 8$, *i.e.*, the Y with the most steric crowding, exhibiting the longest mean Y–O bond length.

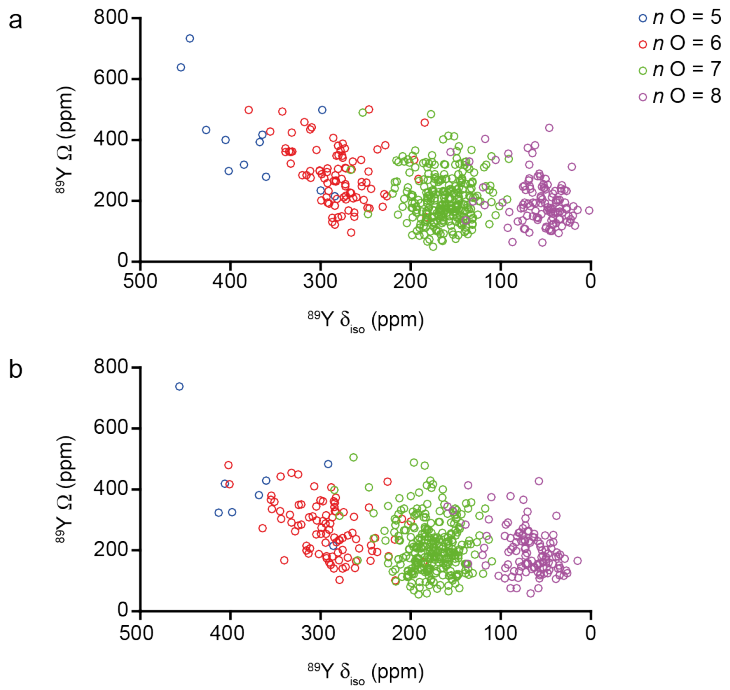


**Figure 5.112:** Plot of calculated $^{89}Y$ $\delta_{iso}$ against Ω for the 30 structural models of (a) $Y_2Zr_2O_7$ and (b) $Y_2Hf_2O_7$, with data points coloured by the number, *n*, of O within 3.2 Å of each Y.

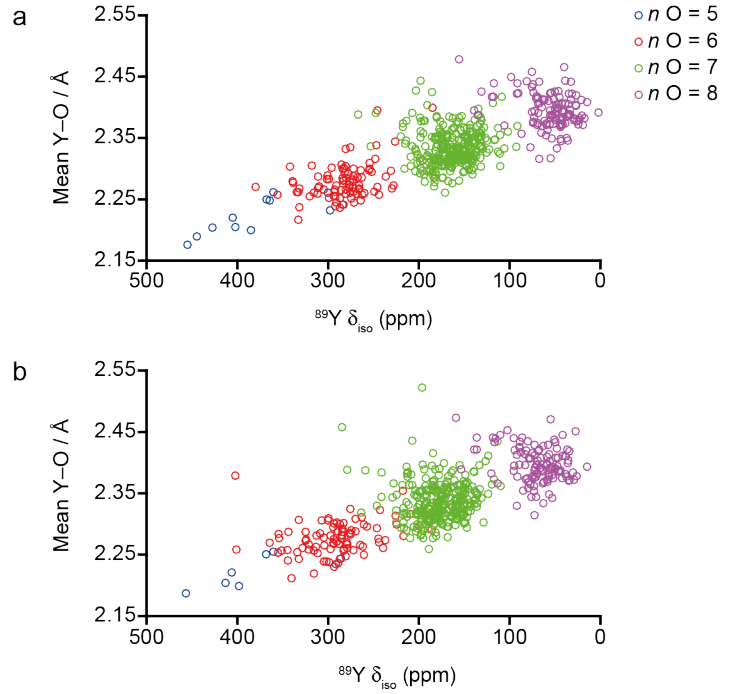


**Figure 5.113:** Plot of calculated $^{89}Y$ $\delta_{iso}$ as a function of mean Y–O bond length for the 30 structural models of (a) $Y_2Zr_2O_7$ and (b) $Y_2Hf_2O_7$, with data points coloured by the number, *n*, of O within 3.2 Å of each Y.

The calculated $^{89}$Y NMR parameters for $Y_2Zr_2O_7$ and $Y_2Hf_2O_7$ reveal that, even for these highly disordered materials, $^{89}$Y $\delta_{iso}$ is a sensitive probe of changes in local geometry and coordination environment, with a strong correlation with the number of coordinated O atoms and a weaker correlation with the mean Y–O bond length. However, limited structural information about the longer-range structure is easily accessible from the Y spectra, owing to the broader lineshapes that result from the increased levels of disorder.

In an attempt to understand the effect that changes in the local structure has on $^{17}$O NMR parameters, and whether the resonances seen in the experimental $^{17}$O MAS NMR spectra can be assigned, the calculated $^{17}$O $\delta_{iso}$ and $C_Q$ for the 30 $Y_2Zr_2O_7$ and 30 $Y_2Hf_2O_7$ structural models were considered. Figure 5.114 shows that a large range of $^{17}$O $\delta_{iso}$ is observed for the O species, regardless of the coordinated atoms. The overlap is much more pronounced for $Y_2Zr_2O_7$, in good agreement with lineshapes seen in the experimental $^{17}$O NMR spectra in Figure 5.110. As shown in Figure 5.114b, despite the overlap

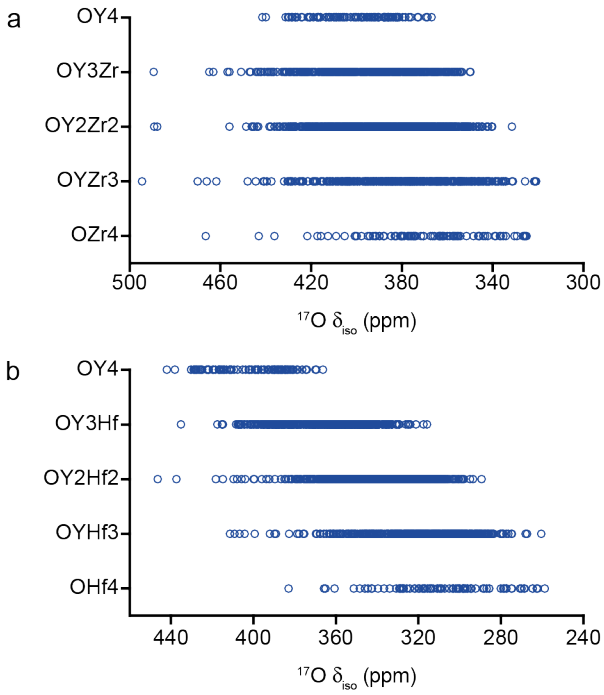


**Figure 5.114:** Plot of calculated $^{17}$O $\delta_{iso}$ as a function of O environment for the 30 structural models of (a) $Y_2Zr_2O_7$ and (b) $Y_2Hf_2O_7$.

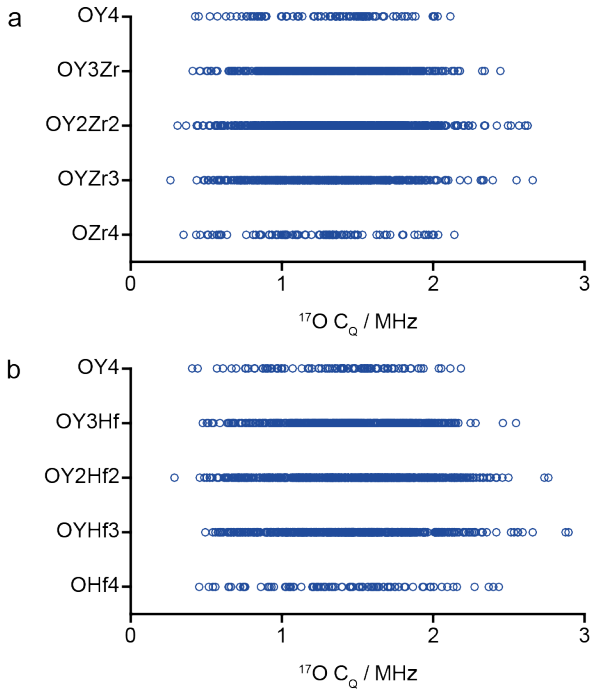


**Figure 5.115:** Plot of calculated $^{17}$O $C_Q$ as a function of O environment for the 30 structural models of (a) $Y_2Zr_2O_7$ and (b) $Y_2Hf_2O_7$.

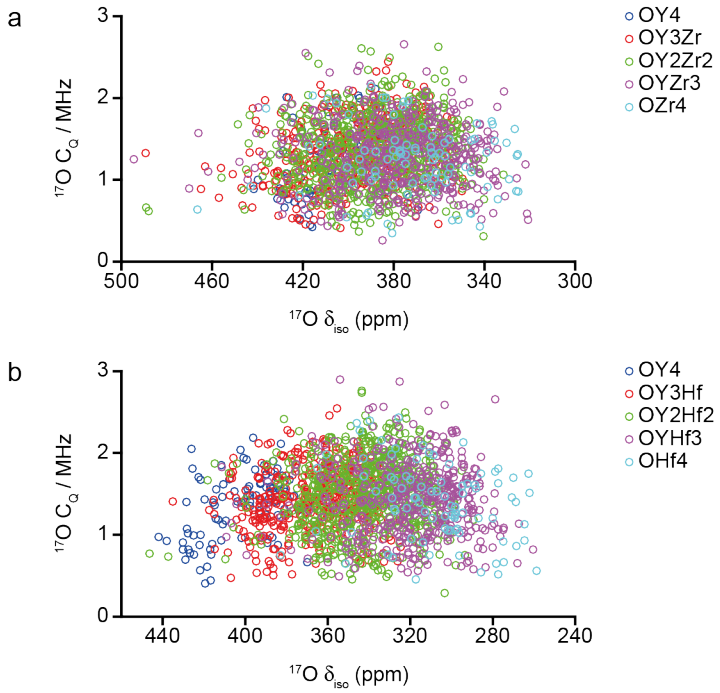


**Figure 5.116:** Plot of calculated $^{17}$O $\delta_{iso}$ against $C_Q$ for the 30 structural models of (a) $Y_2Zr_2O_7$ and (b) $Y_2Hf_2O_7$, with the points coloured by O environment.

in the ranges of shifts seen for different O environments, there is a clear decrease (more upfield) in $^{17}O$ $\delta_{iso}$ with a decrease in the number of Y coordinated to each O. Figure 5.115 shows that very similar (and small) $^{17}O$ $C_Q$ are found for all O species in both $Y_2Zr_2O_7$ and $Y_2Hf_2O_7$, with Figure 5.116 showing little correlation between $^{17}O$ $\delta_{iso}$ and $C_Q$ for either material.

The dependence of the $^{17}O$ NMR parameters on two different structural parameters (mean O–cation bond length and distortion index) was also investigated. Figures 5.117 to 5.120 show calculated $^{17}O$ $\delta_{iso}$ and $C_Q$ for the structural models of both $Y_2Zr_2O_7$ and $Y_2Hf_2O_7$, plotted as functions of the two structural parameters. No correlation is observed between the $^{17}O$ $C_Q$ with either the mean O–cation bond length or the distortion index for $Y_2Zr_2O_7$ or $Y_2Hf_2O_7$. There is perhaps a weak correlation between $^{17}O$ $\delta_{iso}$ and the mean O–cation bond length, and a slightly stronger dependence of this parameter on the distortion index. These effects are most easily seen for $Y_2Hf_2O_7$ in Figure 5.117b and 5.119b. This suggests that the changes in shift

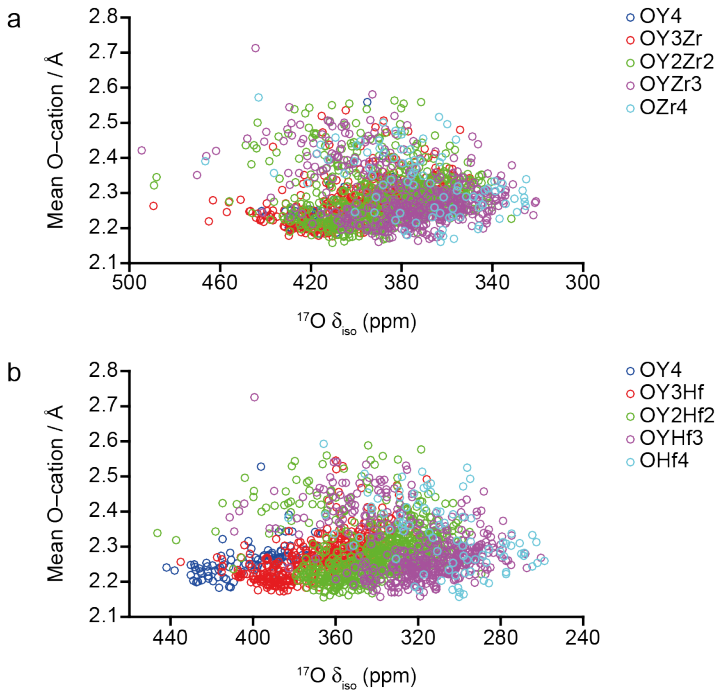


**Figure 5.117:** Plot of calculated $^{17}O$ $\delta_{iso}$ as a function of mean O–cation bond length for the 30 structural models of (a) $Y_2Zr_2O_7$ and (b) $Y_2Hf_2O_7$, with data points coloured by O environment.

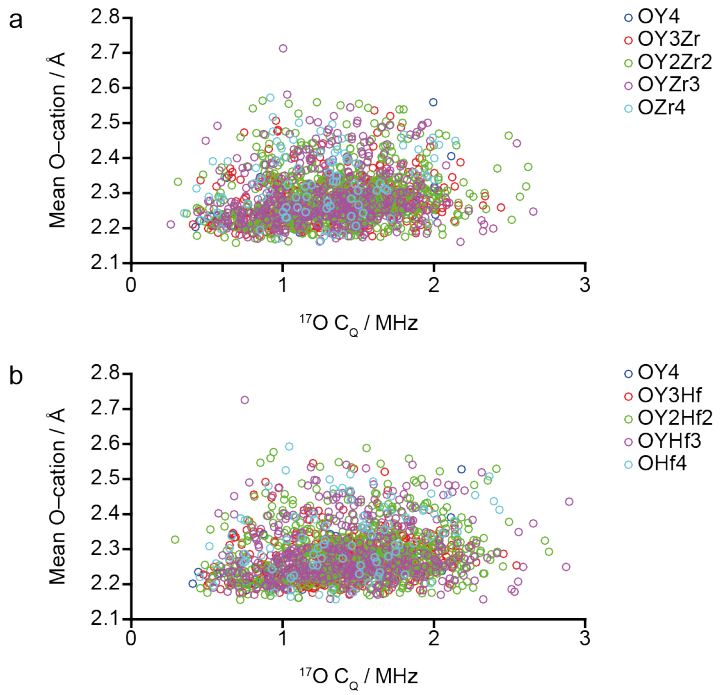


**Figure 5.118:** Plot of calculated $^{17}O$ $C_Q$ as a function of mean O–cation bond length for the 30 structural models of (a) $Y_2Zr_2O_7$ and (b) $Y_2Hf_2O_7$, with data points coloured by O environment.

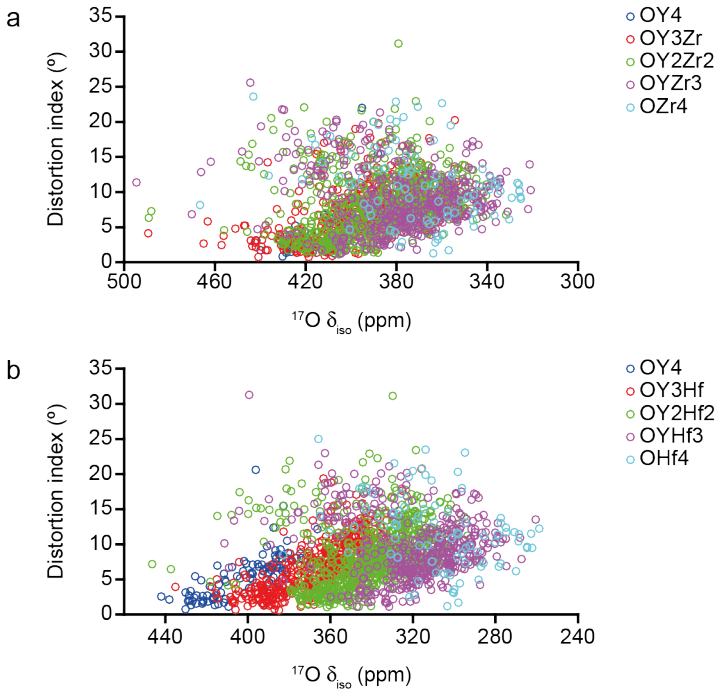


**Figure 5.119:** Plot of calculated $^{17}O$ $\delta_{iso}$ as a function of distortion index for the 30 structural models of (a) $Y_2Zr_2O_7$ and (b) $Y_2Hf_2O_7$, with data points coloured by O environment.

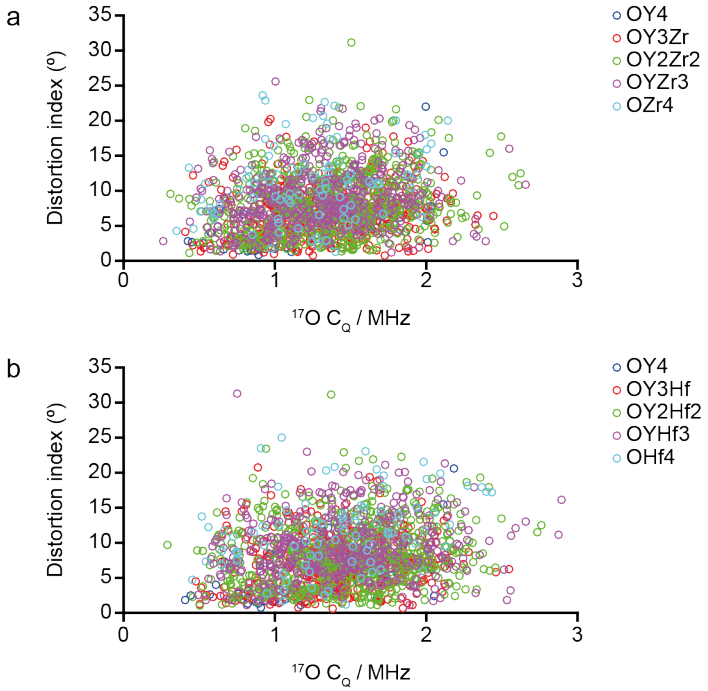


**Figure 5.120:** Plot of calculated $^{17}O$ $C_Q$ as a function of distortion index for the 30 structural models of (a) $Y_2Zr_2O_7$ and (b) $Y_2Hf_2O_7$, with data points coloured by O environment.

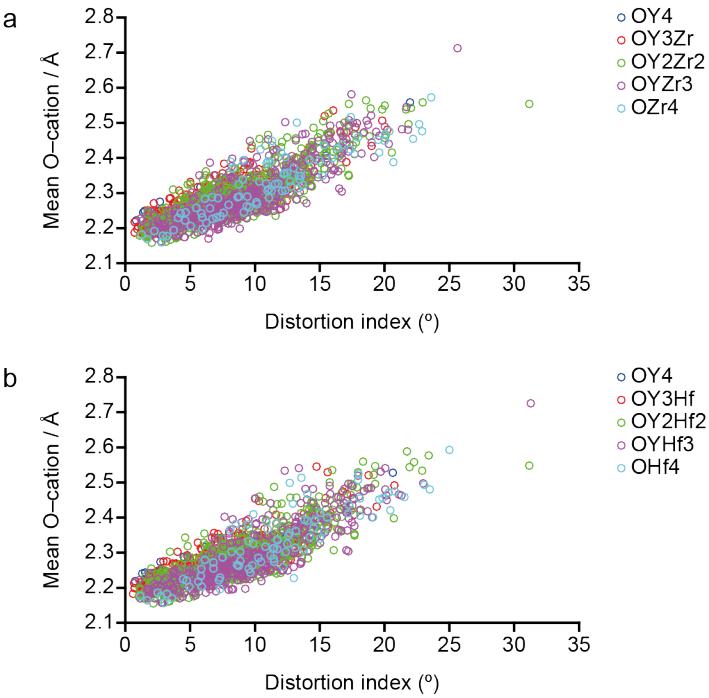


**Figure 5.121:** Plot of distortion index as a function of mean O–cation bond length for the 30 structural models of (a) $Y_2Zr_2O_7$ and (b) $Y_2Hf_2O_7$, with data points coloured by O environment.

for O species with different numbers of Y and Zr/Hf cations coordinated do not result from any significant changes in local structure, but probably arise from the small difference in electronegativity. There is however a strong correlation between the mean O–cation bond length and distortion index for both $Y_2Zr_2O_7$ and $Y_2Hf_2O_7$ as shown in Figure 5.121, with a longer mean O–cation bond length exhibited by O species that have a more distorted local geometry, *i.e.*, a larger distortion index.

Figures 5.114 to 5.121 highlight that there appears to be little structural difference in the O local environments in $Y_2Zr_2O_7$ and $Y_2Hf_2O_7$ when the coordinating cations are varied. This variation therefore results in only small changes to the NMR parameters, with a small decrease in shift observed with an increase in the number of coordinated Zr (or Hf), and very small $C_Q$ values observed in all cases. The small changes predicted will result in significant overlap of resonances from different local O environments, particularly for $Y_2Zr_2O_7$ and may well hinder the assignment of the spectral resonances and the extraction of detailed structural information. The slightly larger shift changes seen for $Y_2Hf_2O_7$ agree well with the higher resolution seen in the experimental $^{17}O$ MAS NMR spectrum (Figure 5.110b). Given the presence of more, well resolved signals, in this spectrum it is tempting to try and assign these to particular types of O environment.

Figure 5.110b shows that six distinct components can be identified in the $^{17}O$ MAS NMR spectrum of $Y_2Hf_2O_7$, at ~387 (2%), ~364 (11%), ~337 (29%), ~310 (46%). ~288 (11%) and ~260 (1%) ppm,[103] while only five local environments (OY4, OY3Hf, OY2Hf2, OYHf3 and OHf4) are expected. Additional experimental results[103] (not shown here) confirm that the lineshapes do not result from significant quadrupolar broadening (in agreement with the low predicted $C_Q$ values), there is no contribution of the satellite transitions to the spectrum, none of the signals result from impurity phases and no signals result from surface –OH species (which can potentially be a problem if enrichment is particularly surface limited). Additionally, for samples of $Y_2Hf_2O_7$, varying the $^{17}O$ enrichment temperature or time seems to have very little effect on the appearance of the $^{17}O$ MAS NMR spectral ineshape. Figure

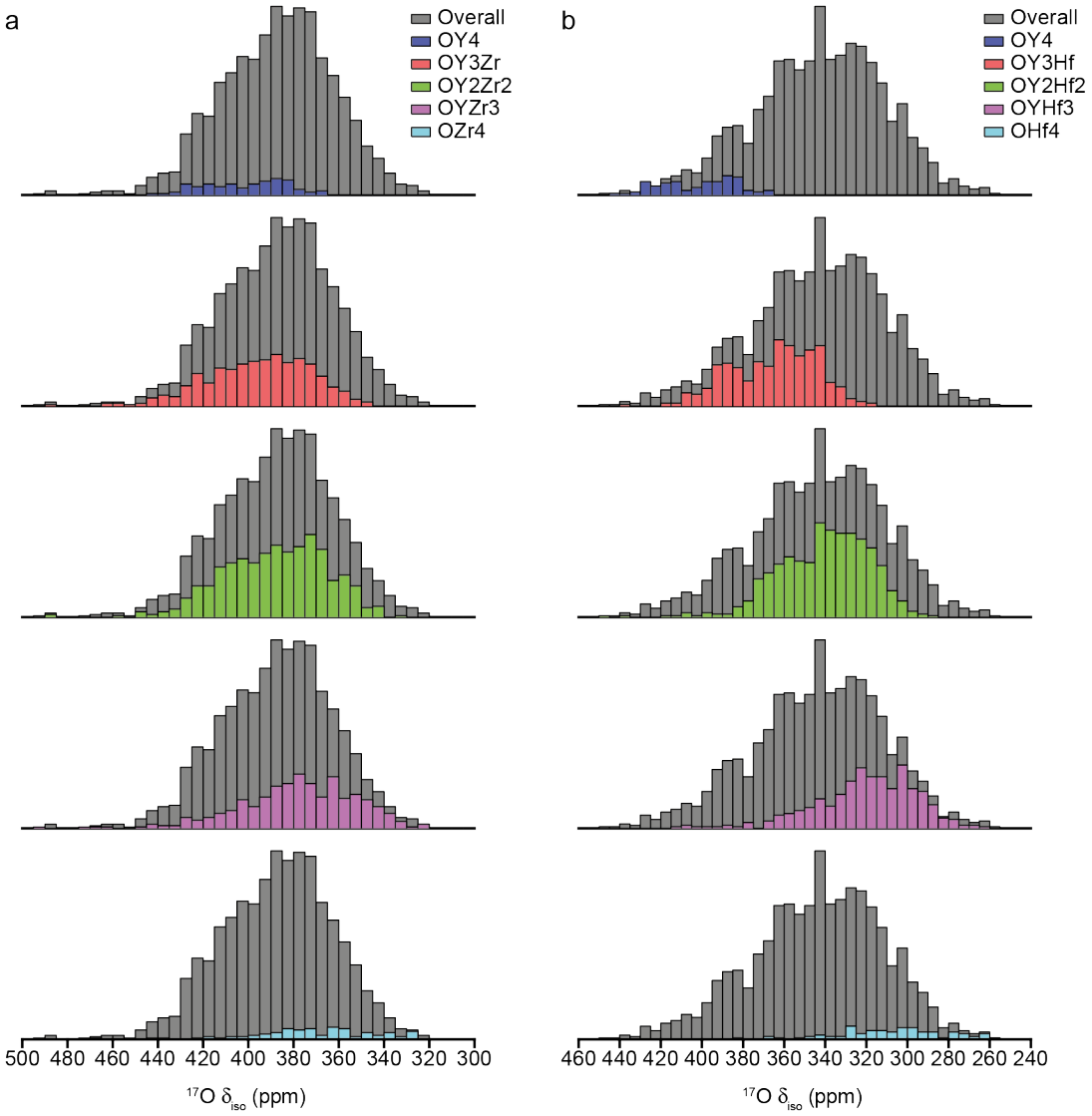


**Figure 5.122:** Calculated $^{17}$O $\delta_{iso}$ for the 30 structural models of (a) $Y_2Zr_2O_7$ and (b) $Y_2Hf_2O_7$, represented as histograms, separated according to O environment.

5.122 plots (simply as a histogram) the calculated $^{17}$O $\delta_{iso}$ for the 30 structural modes of $Y_2Zr_2O_7$ and $Y_2Hf_2O_7$. This shows that there is significant overlap between the ranges of signals seen for the different O environments, for both $Y_2Zr_2O_7$ and $Y_2Hf_2O_7$, although there is a more noticeable change in the average $^{17}$O $\delta_{iso}$ for $Y_2Hf_2O_7$, with each additional Hf bonded to O resulting in a 20-30 ppm decrease in $\delta_{iso}$. However, the broad range of shifts seen for all five O environments in $Y_2Hf_2O_7$, suggests that, it would not be possible (or sensible) to try and assign resonances to an individual type of O

environment, precluding a more detailed understanding of cation or anion disorder. Although the structures considered represent only a very small number of (likely high energy) potential structural models for this complex system, the preliminary results presented here suggest that significant computational effort (and expense) to generate a much larger set of structural models would likely not be justified.

### 5.7.4 Summary

This section has explored the use of first-principles calculations to investigate the effects of cation and anion disorder in $Y_2Zr_2O_7$ and $Y_2Hf_2O_7$, on the predicted NMR parameters. The ultimate aim of such work would be to use these predicted parameters to assist interpretation and guide assignment of the experimental ($^{89}Y$ and $^{17}O$) MAS NMR spectra of these two defect fluorite materials. Although the SOD approach has proved invaluable for the investigation of the more ordered $Y_2Sn_xTi_{2-x}O_7$ and $Y_2Sn_xZr_{2-x}O_7$ pyrochlores, discussed in Sections 5.5.5 and 5.6.4, respectively, the sheer number of possible structural models that result from the extensive cation and anion disorder makes any method that attempts to produce all possible atomic arrangements impractical. As a result, the preliminary work here employed a less sophisticated method of generating structural models using an in-house script to randomise the occupancy of 32 cation sites by the 16 Y and 16 Zr (or Hf), while simultaneously randomising the 8 vacancies on the 64 potential anion sites. Using this method, 30 $Y_2Zr_2O_7$ structural models were generated and subsequently used to make an equivalent number of $Y_2Hf_2O_7$ models.

The calculated $^{89}Y$ $\delta_{iso}$ for the structural models was shown to be sensitive to the Y coordination number, decreasing (moving upfield) as the number of O surrounding the Y increased, aiding assignment of the signals seen in the $^{89}Y$ MAS NMR spectra of $Y_2Hf_2O_7$ and confirming the previous assignment for $Y_2Zr_2O_7$.[79] The large range of shifts seen for each coordination number was not analysed in any further detail (*i.e.*, to understand the effects of NNN

cations). While such an investigation may be possible, a larger set of structural models should perhaps be considered before such a task was undertaken. The $^{17}O$ NMR parameters for the 30 structural models of $Y_2Zr_2O_7$ and $Y_2Hf_2O_7$ were also investigated. Although small changes in $\delta_{iso}$ were observed as the number of Y and Zr (or Hf) coordinated to the O varied, significant overlap of the shift ranges was observed, particularly for $Y_2Zr_2O_7$, in agreement with the broad lines seen in the experimental $^{17}O$ NMR spectra. A greater change in shift was predicted for $Y_2Hf_2O_7$, moving upfield as the number of Hf surrounding the O species increased, helping to explain the more well resolved resonances seen experimentally. However, representing the calculated $^{17}O$ $\delta_{iso}$ as histograms, it becomes apparent that there is still significant overlap of the shifts seen for different O environments, and their intensity at any one point in the spectrum could well result from O in multiple different O environments. This helps to explain the presence of six resonances in the experimental spectrum, when only five types of local environment are possible. Detailed analysis of the structural models reveals very little changes in local structure (*i.e.*, mean O–cation bond length or distortion index) between the different O species, perhaps explaining the small changes in the NMR parameters observed. However, this work suggests that deconvolution and assignment of individual resonances is not possible even for $Y_2Hf_2O_7$.

While the 30 $Y_2Zr_2O_7$ and $Y_2Hf_2O_7$ structural models provide some insight into the appearance of the experimental $^{89}Y$ and $^{17}O$ MAS NMR spectra, in order to better understand the local structure of these and other highly disordered materials, it is apparent that a more effective strategy for generating relevant and realistic structural models must be developed. The structural models discussed in this section clearly only represent the first tentative steps along the path that leads to this goal. The challenge will become much greater when substitution of other atoms (*e.g.*, Sn or Ti) is also considered (although it is likely that the structural changes in those system might be much more significant) It is clear that methods for the efficient generation of a large number of symmetry unique models are required, and

that these might be most effectively used if information from experiment (*e.g.*, the known coordination number of Y or of other substituted atoms) could be used in determining which models are most relevant.

Potential approaches for generating a single, or series of, structural models for $Y_2Zr_2O_7$ or $Y_2Hf_2O_7$ and other related defect fluorite materials, could involve using Pair Distribution Function (PDF)[108,109] XRD analysis to identify the various interatomic distances that describe the short-range connectivity seen for the material. This information could then be used as a constraint for a reverse Monte-Carlo (RMC)[110,111] modelling algorithm to output potential three-dimensional atomic configurations (*i.e.*, input structural models). As described above, additional experimental information, such as the average coordination number for Y and other cation species, determined from MAS NMR spectra could also be used in the RMC simulation, increasing the probability of the generated structural models that more accurately represent the disordered materials under investigation. However, irrespective of the modelling approaches is considered in the future, this investigation underlines the need for realistic structural models, if first-principles calculations are to provide insight into local structure and thus assist the assignment of experimental NMR spectra for disordered materials.

## 5.8 Outlook

This chapter has investigated the extent to which first-principles calculations can assist in the interpretation and assignment of solid-state NMR spectra, and ultimately providing insight into the local structure of disordered ceramic materials. It has been shown that the usefulness of such calculations is heavily influenced by the ability to efficiently generate one or more structural models that can represent the local environments present in a disordered material. While simple substitution might provide initial insight into the interpretation of an experimental spectrum, more sophisticated approaches are required to ensure that the effects of longer-range structural changes on the NMR parameters can be accurately assessed. The importance of performing a rigorous geometry optimisation of structural models prior to

the calculation of NMR parameters has also been highlighted, with the need for an accurate `elec_energy_tol` parameter proving particularly crucial to the accuracy and repeatability of calculations performed using CASTEP.

The different degrees of structural disorder exhibited by the inorganic materials discussed in this chapter, *i.e.*, B-site cation disorder in $Y_2Sn_xTi_{2-x}O_7$ and $La_2Sn_xZr_{2-x}O_7$ pyrochlores and disorder on both the cation and anion sublattice in $Y_2Zr_2O_7$ and $Y_2Hf_2O_7$, has led to structural models being generated using a variety of approaches. The approach taken depends both on the type of disorder displayed by a material, and on the level of detail that is required to understand experimental measurements or to extract information on local structure. While simple substitution to produce local clusters allowed the relationships between calculated multinuclear NMR parameters and systematic changes in local structure in $Y_2Sn_xTi_{2-x}O_7$ or $La_2Sn_xZr_{2-x}O_7$ to be probed, only a small number of models are considered, with little variation in the longer-range structure, likely representing a significant oversimplification of the real pyrochlore materials. In contrast, the series of SOD-generated $Y_2Sn_xTi_{2-x}O_7$ and $La_2Sn_xZr_{2-x}O_7$ structural models facilitates a comprehensive investigation into the effect of B-site cation disorder on the local structure and on the calculated $^{89}Y$, $^{119}Sn$ and $^{17}O$ NMR parameters, with the full simulation of $^{89}Y$ and $^{119}Sn$ MAS NMR spectra enabling direct comparison between experimental and computation. Due to the combinatorial nature of the structural disorder exhibited by $Y_2Zr_2O_7$ and $Y_2Hf_2O_7$, the investigation into these defect fluorites materials proved more challenging, both computationally, but more importantly, conceptionally, given the lack of a clear initial structural model or modelling procedure. Despite this, even using a small number of structural models, first-principles calculations were able to provide new insights into the changes in local geometry and predicted NMR parameters for both $Y_2Zr_2O_7$ and $Y_2Hf_2O_7$, although neither the $^{89}Y$ or $^{17}O$ MAS NMR spectra could be confidently assigned (other than identifying the presence of six-, seven- and eight-coordinate Y from the $^{89}Y$ MAS NMR spectra), indicating that further study into these materials is required.

It is hoped that in the future, limitations in computing power and access to HPC facilities will increase, potentially making it more routine to generate a much larger number of structural models. Despite this, for particularly complex systems, such as defect fluorites, there may still be limits to the insightfulness of analysis, even if significantly larger sets of structural models are considered. Future improvements in DFT, including more accurate exchange-correlation functionals and pseudopotentials will hopefully result in better agreement between predicted and experimental NMR parameters, and help considerably in the use of calculations to compliment NMR experiments. The investigations presented in this chapter aim to serve as a guide for those studying the structure or physical properties of disordered inorganic materials using first-principles calculations, with the emphasis clearly on identifying the most effective and appropriate methods for modelling system that exhibit some form of configurational disorder.

## 5.9 References


1. B. C. Chakoumakos, *J. Solid State Chem.*, 1984, **53**, 120–129.
2. M. T. Weller, R. W. Hughes, J. Rooke, C. S. Knee, and J. Reading, *Dalt. Trans.*, 2004, **0**, 3032–3041.
3. B. J. Wuensch, K. W. Eberman, C. Heremans, E. M. Ku, P. Onnerud, E. M. E. Yeo, S. M. Haile, J. K. Stalick, and J. D. Jorgensen, *Solid State Ionics*, 2000, **129**, 111–133.
4. M. A. Subramanian, G. Aravamudan, and G. V. Subba Rao, *Prog. Solid State Chem.*, 1983, **15**, 55–143.
5. R. W. G. Wyckoff, *The Analytical Expression of the Results of the Theory of Space Groups*, Carnegie Institution of Washington, Washington, 2nd edn., 1930.
6. H. Arnold, M. I. Aroyo, E. F. Bertaut, H. Burzlaff, G. Chapuis, W. Fischer, H. D. Flack, A. M. Glazer, H. Grimmer, B. Gruber, T. Hahn, H. Klapper, E. Koch, P. Konstantinov, V. Kopsky, D. B. Litvin, L.-V. A., U. Muller, K. Momma, U. Shmueli, B. Souvignier, J. C. H. Spence, P. M. De Wolf, H. Wondratschek, and H. Zimmermann, *International Tables*

*for Crystallography, Volume A: Space-Group Symmetry*, Wiley, 6th edn., 2016.

7. A. K. Cheetham, B. E. F. Fender, and M. J. Cooper, *J. Phys. C Solid State Phys.*, 1971, **4**, 3107–3121.
8. F. Brisse and O. Knop, *Can. J. Chem.*, 1968, **46**, 859–873.
9. J. K. Brandon and H. D. Megaw, *Philos. Mag. A J. Theor. Exp. Appl. Phys.*, 1970, **21**, 189–194.
10. N. Ishizawa, F. Marumo, T. Kawamura, and M. Kimura, *Acta Crystallogr. Sect. B*, 1973, **31**, 1912–1915.
11. M. Gasperin, *Acta Crystallogr. Sect. B*, 1975, **31**, 2129–2130.
12. H. W. Schmalle, T. Williams, A. Reller, A. Linden, and J. G. Bednorz, *Acta Crystallogr. Sect. B*, 1993, **49**, 235–244.
13. E. J. Harvey, S. E. Ashbrook, G. R. Lumpkin, and S. A. T. Redfern, *J. Mater. Chem.*, 2006, **16**, 4665–4674.
14. A. Fernandes, D. McKay, S. Sneddon, D. M. Dawson, S. Lawson, R. Veazey, K. R. Whittle, and S. E. Ashbrook, *J. Phys. Chem. C*, 2016, **120**, 20288–20296.
15. E. Reynolds, P. E. R. Blanchard, Q. Zhou, B. J. Kennedy, Z. Zhang, and L. Y. Jang, *Phys. Rev. B*, 2012, **85**, 132101.
16. L. Kong, Z. Zhang, M. de los Reyes, I. Karatchevtseva, G. R. Lumpkin, G. Triani, and R. D. Aughterson, *Ceram. Int.*, 2015, **41**, 5309–5317.
17. Z. Zhang, M. Avdeev, M. de los Reyes, G. R. Lumpkin, B. J. Kennedy, P. E. R. Blanchard, S. Liu, A. Tadich, and B. C. C. Cowie, *J. Phys. Chem. C*, 2016, **120**, 26465–26479.
18. F. X. Zhang and S. K. Saxena, *Chem. Phys. Lett.*, 2005, **413**, 248–251.
19. F. X. Zhang, M. Lang, U. Becker, R. C. Ewing, and J. Lian, *Appl. Phys. Lett.*, 2008, **92**, 011909–011912.
20. Z. Zhang, S. C. Middleburgh, M. de los Reyes, G. R. Lumpkin, B. J. Kennedy, P. E. R. Blanchard, E. Reynolds, and L. Y. Jang, *J. Phys. Chem. C*, 2013, **117**, 26740–26749.
21. K. Matsuhira, K. Hinatsu, K. Tenya, and Sakakibara T., *J. Phys. Condens. Matter*, 2000, **12**, L649–L656.
22. J. S. Gardner, M. J. P. Gingras, and J. E. Greedan, *Rev. Mod. Phys.*, 2010, **82**, 53–107.

23. M. C. Hatnean, R. Sibille, M. R. Lees, M. Kenzelmann, V. Ban, V. Pomjakushin, and G. Balakrishnan, *J. Phys. Condens. Matter*, 2017, **29**, 75902.
24. A. M. Srivastava, *Mater. Res. Bull.*, 2002, **37**, 745–751.
25. H. Yamamura, H. Nishino, K. Kakinuma, and K. Nomura, *Solid State Ionics*, 2003, **158**, 359–365.
26. B. P. Mandal, S. K. Deshpande, and A. K. Tyagi, *J. Mater. Res.*, 2008, **23**, 911–916.
27. J. A. Díaz-Guillén, A. F. Fuentes, M. R. Díaz-Guillén, J. M. Almanza, J. Santamaría, and C. León, *J. Power Sources*, 2009, **186**, 349–352.
28. A. V. Shlyakhtina, K. S. Pigalskiy, D. A. Belov, N. V. Lyskov, E. P. Kharitonova, I. V. Kolbanev, A. B. Borunova, O. K. Karyagina, E. M. Sadovskaya, V. A. Sadykov, and N. F. Eremeev, *Dalt. Trans.*, 2018, **47**, 2376–2392.
29. K. Kimura, Y. Ohta, and S. Nakatsuji, *J. Phys. Conf. Ser.*, 2012, **400**, 32040.
30. C. Sun and U. Stimming, *J. Power Sources*, 2007, **171**, 247–260.
31. N. Mahato, A. Banerjee, A. Gupta, S. Omar, and K. Balani, *Prog. Mater. Sci.*, 2015, **72**, 141–337.
32. L. Malavasi, C. A. J. Fisher, and M. S. Islam, *Chem. Soc. Rev.*, 2010, **39**, 4370–4387.
33. H. Y. Playford, D. R. Modeshia, E. R. Barney, A. C. Hannon, C. S. Wright, J. M. Fisher, A. Amieiro-Fonseca, D. Thompsett, L. A. O'Dell, G. J. Rees, M. E. Smith, J. V. Hanna, and R. I. Walton, *Chem. Mater.*, 2011, **23**, 5464–5473.
34. S. H. Oh, R. Black, E. Pomerantseva, J.-H. Lee, and L. F. Nazar, *Nat. Chem.*, 2012, **4**, 1004–1010.
35. M. M. Gentleman and D. R. Clarke, *Surf. Coatings Technol.*, 2005, **200**, 1264–1269.
36. R. Vassen, M. O. Jarligo, T. Steinke, D. E. Mack, and D. Stöver, *Surf. Coatings Technol.*, 2010, **205**, 938–942.
37. J. W. Fergus, *Metall. Mater. Trans. E*, 2014, **1**, 118–131.
38. S. Mahade, N. Curry, S. Bjorklund, N. Markocsan, P. Nylen, and R. Vassen, *Surf. Coatings Technol.*, 2017, **318**, 208–216.

39. W. J. Weber, R. C. Ewing, C. R. A. Catlow, T. Diaz de la Rubia, L. W. Hobbs, C. Kinoshita, H. Matzke, A. T. Motta, M. Nastasi, E. K. H. Salje, E. R. Vance, and S. J. Zinkle, *J. Mater. Res.*, 1998, **13**, 1434–1484.
40. R. C. Ewing, *Can. Mineral.*, 2001, **39**, 697–715.
41. R. C. Ewing, W. J. Weber, and J. Lian, *J. Appl. Phys.*, 2004, **95**, 5949–5971.
42. B. D. Begg, N. J. Hess, W. J. Weber, R. Devanathan, J. P. Icenhower, S. Thevuthasan, and B. P. McGrail, *J. Nucl. Mater.*, 2001, **288**, 208–216.
43. G. R. Lumpkin, *Elements*, 2006, **2**, 365–372.
44. R. Perriot, P. P. Dholabhai, and B. P. Uberuaga, *Phys. Chem. Chem. Phys.*, 2016, **18**, 22852–22863.
45. *Radioactive Wastes in the UK: A Summary of the 2016 Inventory*, Department for Business, Energy and Industrial Stratergy (BEIS) and the Nuclear Deccommissioning Authority (NDA), ISBN: 978-1-905985-36-4, 2016.
46. I. W. Donald, B. L. Metcalfe, and R. N. J. Taylor, *J. Mater. Sci.*, 1997, **32**, 5851–5887.
47. W. J. Weber, R. C. Ewing, C. A. Angell, G. W. Arnold, A. N. Cormack, J.-M. Delaye, D. L. Griscom, L. W. Hobbs, A. Navrotsky, D. L. Price, A. M. Stoneham, and M. C. Weinberg, *J. Mater. Res.*, 1997, **12**, 1946–1978.
48. M. I. Ojovan and W. E. Lee, *Metall. Mater. Trans. A*, 2011, **42**, 837–851.
49. A. E. Ringwood, *Safe disposal of high level nuclear wastes: A new strategy*, Canberra, 1978.
50. A. E. Ringwood, S. E. Kesson, N. G. Ware, W. Hibberson, and A. Major, *Nature*, 1979, **278**, 219–223.
51. A. E. Ringwood, S. E. Kesson, N. G. Ware, W. O. Hibberson, and A. Major, *Geochem. J.*, 1979, **13**, 141–165.
52. W. E. Lee, M. I. Ojovan, M. C. Stennett, and N. C. Hyatt, *Adv. Appl. Ceram.*, 2006, **105**, 3–12.
53. G. R. Lumpkin, *J. Nucl. Mater.*, 2001, **289**, 136–166.
54. R. F. Cook, B. R. Lawn, T. P. Dabbs, K. D. Reeve, E. J. Ramm, and J. L. Woolfrey, *J. Am. Ceram. Soc.*, 1982, **65**, c172–c173.
55. K. L. Smith, G. R. Lumpkin, M. G. Blackford, R. A. Day, and K. P. Hart, *J. Nucl. Mater.*, 1992, **190**, 287–294.

56. B. D. Begg, E. R. Vance, and S. D. Conradson, *J. Alloys Compd.*, 1998, **271**, 221–226.
57. Y. Zhang, M. W. A. Stewart, H. Li, M. L. Carter, E. R. Vance, and S. Moricca, *J. Nucl. Mater.*, 2009, **395**, 69–74.
58. Y. Zhang, D. J. Gregg, L. Kong, M. Jovanovich, and G. Triani, *J. Nucl. Mater.*, 2017, **490**, 238–241.
59. R. C. Ewing, W. J. Weber, and F. W. Clinard, *Prog. Nucl. Energy*, 1995, **29**, 63–127.
60. I. Farnan and E. K. H. Salje, *J. Appl. Phys.*, 2001, **89**, 2084–2090.
61. I. Farnan, E. Balan, C. J. Pickard, and F. Mauri, *Am. Mineral.*, 2003, **88**, 1663–1667.
62. G. Deissmann, S. Neumeier, G. Modolo, and D. Bosbach, *Mineral. Mag.*, 2012, **76**, 2911–2918.
63. J. E. Mendel, R. D. Nelson, R. P. Turcotte, W. J. Grey, M. D. Merz, F. P. Roberts, W. J. Weber, J. J. H. Westsik, and D. E. Clark, *A state-of-the-art review of materials properties of nuclear waste forms*, Pacific Northwest Laboratory, (PNL-3802), Washington, 1981.
64. R. C. Ewing, J. Lian, and L. M. Wang, *Mater. Res. Soc. Symp. Proc.*, 2003, 792, R2.1.
65. S. X. Wang, B. D. Begg, L. M. Wang, R. C. Ewing, W. J. Weber, and K. V. Govidan Kutty, *J. Mater. Res.*, 1999, **14**, 4470–4473.
66. K. E. Sickafus, L. Minervini, R. W. Grimes, J. A. Valdez, M. Ishimaru, F. Li, K. J. McClellan, and T. Hartmann, *Science*, 2000, **289**, 748–751.
67. G. R. Lumpkin, K. L. Smith, M. G. Blackford, K. R. Whittle, E. J. Harvey, S. A. T. Redfern, and N. J. Zaluzec, *Chem. Mater.*, 2009, **21**, 2746–2754.
68. J. Lian, K. B. Helean, B. J. Kennedy, L. M. Wang, A. Navrotsky, and R. C. Ewing, *J. Phys. Chem. B*, 2006, **110**, 2343–2350.
69. C. P. Grey, M. E. Smith, A. K. Cheetham, C. M. Dobson, and R. Dupree, *J. Am. Chem. Soc.*, 1990, **112**, 4670–4675.
70. D. R. Lide, *CRC Handbook of Chemistry and Physics, Internet Version*, CRC Press, 2005.
71. S. E. Ashbrook, K. R. Whittle, G. R. Lumpkin, and I. Farnan, *J. Phys. Chem. B*, 2006, **110**, 10358–10364.

72. R. Dupree and M. E. Smith, *Chem. Phys. Lett.*, 1988, **148**, 41–44.
73. S. Reader, M. R. Mitchell, K. E. Johnston, C. J. Pickard, K. R. Whittle, and S. E. Ashbrook, *J. Phys. Chem. C*, 2009, **113**, 18874–18883.
74. M. R. Mitchell, D. Carnevale, R. Orr, K. R. Whittle, and S. E. Ashbrook, *J. Phys. Chem. C*, 2012, **116**, 4273–4286.
75. R. Orr, M. J. Duer, and S. E. Ashbrook, *J. Magn. Reson.*, 2005, **174**, 301–309.
76. R. Orr and M. J. Duer, *J. Magn. Reson.*, 2006, **181**, 1–8.
77. C. P. Grey, C. M. Dobson, A. K. Cheetham, and R. J. B. Jakeman, *J. Am. Chem. Soc.*, 1989, **111**, 505–511.
78. M. R. Mitchell, S. W. Reader, K. E. Johnston, C. J. Pickard, K. R. Whittle, and S. E. Ashbrook, *Phys. Chem. Chem. Phys.*, 2011, **13**, 488–497.
79. S. E. Ashbrook, M. R. Mitchell, S. Sneddon, R. F. Moran, M. de los Reyes, G. R. Lumpkin, and K. R. Whittle, *Phys. Chem. Chem. Phys.*, 2015, **17**, 9049–9059.
80. K. Kawata, H. Maekawa, T. Nemoto, and T. Yamamura, *Solid State Ionics*, 2006, **177**, 1687–1690.
81. M. De Los Reyes, K. R. Whittle, Z. Zhang, S. E. Ashbrook, M. R. Mitchell, L. Y. Jang, and G. R. Lumpkin, *RSC Adv.*, 2013, **3**, 5090–5099.
82. S. E. Ashbrook and M. E. Smith, *Chem. Soc. Rev.*, 2006, **35**, 718–735.
83. N. Kim and C. P. Grey, *J. Solid State Chem.*, 2003, **175**, 110–115.
84. J. L. Palumbo, T. A. Schaedler, L. Peng, C. G. Levi, and C. P. Grey, *J. Solid State Chem.*, 2007, **180**, 2175–2185.
85. C. Bonhomme, C. Gervais, F. Babonneau, C. Coelho, F. Pourpoint, T. Azaïs, S. E. Ashbrook, J. M. Griffin, J. R. Yates, F. Mauri, and C. J. Pickard, *Chem. Rev.*, 2012, **112**, 5733–5779.
86. S. E. Ashbrook and D. McKay, *Chem. Commun.*, 2016, **52**, 7186–7204.
87. R. F. Moran, D. M. Dawson, and S. E. Ashbrook, *Int. Rev. Phys. Chem.*, 2017, **36**, 39–115.
88. R. Grau-Crespo, S. Hamad, C. R. A. Catlow, and N. H. De Leeuw, *J. Phys. Condens. Matter*, 2007, **19**, 256201.
89. M. R. Mitchell, *PhD Thesis: Investigation of Structure and Disorder in inorganic Solids Using Solid-State NMR*, University of St Andrews, St Andrews, 2012.

90. O. Knop, F. Brisse, and L. Castelliz, *Can. J. Chem.*, 1969, **47**, 971–990.
91. S. J. Clark, M. D. Segall, C. J. Pickard, P. J. Hasnip, M. I. J. Probert, K. Refson, and M. C. Payne, *Z. Kristallogr.*, 2005, **220**, 567–570.
92. J. R. Yates, C. J. Pickard, M. C. Payne, and F. Mauri, *J. Chem. Phys.*, 2003, **118**, 5746.
93. T. F. G. Green and J. R. Yates, *J. Chem. Phys.*, 2014, **140**, 234106.
94. J. P. Perdew, K. Burke, and M. Ernzerhof, *Phys. Rev. Lett.*, 1996, **77**, 3865–3868.
95. J. R. Yates, C. J. Pickard, and F. Mauri, *Phys. Rev. B*, 2007, **76**, 24401.
96. S. Sturniolo, T. F. G. Green, R. M. Hanson, M. Zilka, K. Refson, P. Hodgkinson, S. P. Brown, and J. R. Yates, *Solid State Nucl. Magn. Reson.*, 2016, **78**, 64–70.
97. G. Kresse and J. Hafner, *Phys. Rev. B*, 1993, **47**, 558–561.
98. G. Kresse and J. Hafner, *Phys. Rev. B*, 1994, **49**, 14251–14269.
99. G. Kresse and J. Furthmüller, *Phys. Rev. B*, 1996, **54**, 11169–11186.
100. G. Kresse and J. Furthmüller, *Comput. Mater. Sci.*, 1996, **6**, 15–50.
101. P. E. Blöchl, *Phys. Rev. B*, 1994, **50**, 17953–17979.
102. G. Kresse and D. Joubert, *Phys. Rev. B*, 1999, **59**, 1758–1775.
103. A. Fernandes, R. F. Moran, S. Sneddon, D. M. Dawson, D. McKay, G. P. M. Bignami, F. Blanc, K. R. Whittle, and S. E. Ashbrook, *RSC Adv.*, 2018, **8**, 7089–7101.
104. B. J. Kennedy, *Physica. B*, 1998, **241**, 303–310.
105. Y. Tabira, R. L. Withers, T. Yamada, and N. Ishizawa, *Z. Kristallogr.*, 2001, **216**, 92–98.
106. S. Sneddon, *PhD Thesis: Characterisation of Inorganic Materials using Solid-State NMR Spectroscopy*, University of St Andrews, St Andrews, 2016.
107. M. Glerup, O. F. Nielsen, and F. W. Poulsen, *J. Solid State Chem.*, 2001, **160**, 25–32.
108. B. E. Warren, *Phys. Rev.*, 1934, **45**, 657–661.
109. D. A. Keen and A. L. Goodwin, *Nature*, 2015, **521**, 303–309.
110. R. L. McGreevy and L. Pusztai, *Mol. Simul.*, 1988, **1**, 359–367.
111. R. L. McGreevy, *J. Phys. Condens. Matter*, 2001, **13**, R877–R913.

# Chapter 6: Investigating proton disorder in hydrous wadsleyite, an inner-Earth mineral

## 6.1 Introduction

In order to better understand the chemical and physical properties of the inner Earth, detailed structural studies of the minerals that comprise it are becoming increasingly important.[1] As shown in Figure 6.1, the Earth's mantle is predominantly composed of magnesium silicate minerals with the general formulas $(Fe,Mg)_2SiO_4$ and $(Fe,Mg)SiO_3$, where the increasing temperatures and pressures associated with increasing depth cause phase transitions.[2] In the last two decades, it has been shown that the nominally anhydrous minerals (NAMs) found in the Earth's mantle can accommodate significant amounts of hydrogen, typically in the form of hydroxyl groups (–OH), and commonly referred to as incorporated "water", believed to be associated with lattice defects.[3–5] Due to the immense volume of the Earth's mantle, even a low concentration of water incorporated in NAMs could translate to vast subterranean reservoirs, far larger than the amount of water in the Earth's oceans and atmosphere combined.[4–7] It is clear therefore, that the physical and chemical properties of the mantle can be affected by not only the presence, but also by the distribution, of this incorporated water. Indeed, hydrous minerals have lower melting points than their anhydrous equivalents, with hydrogen incorporation increasing the susceptibility of a mineral to structural distortion. It has also been suggested that the presence of water in the mantle can affect tectonic plate movement, seismic activities and subduction processes,[8–10] in addition to having an impact on the electrical conductivity of the Earth's upper mantle.[11–13]

Elucidating the structure of hydrous silicate minerals found in the Earth's upper mantle can be extremely challenging. For example, although XRD and neutron diffraction techniques can give information on the long-range order of the lattice, determining the extent, or even the existence, of dynamics or disorder is often very challenging, particularly in systems where the level of

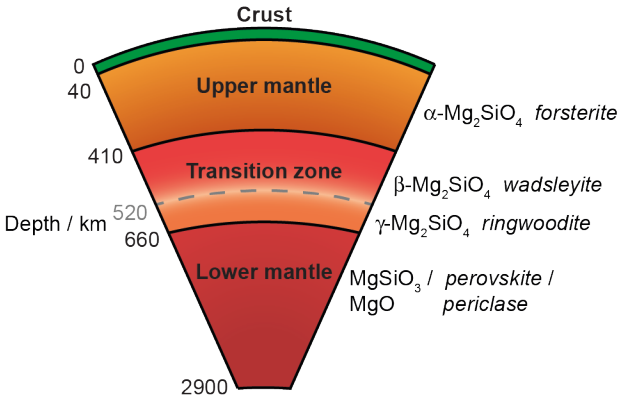


**Figure 6.1:** Schematic of the Earth's mantle, showing the principal mineral components.

hydration is low, *i.e.*, non-stoichiometric amounts of hydrogen, are present, limiting the insights afforded by these approaches.[1] Another analytical technique used to investigate the structure of hydrous inner-Earth minerals is Fourier transform infra-red (FTIR) spectroscopy, which uses the stretching frequency of the hydroxyl bonds to infer the O–H bond lengths and orientations, from which potential structural models or features can be constructed.[14,15]

With its ability to probe local structure and dynamics, without the need for long-range order, solid-state NMR spectroscopy has proven to be a powerful technique for elucidating the structure of disordered materials,[16,17] making it an ideal approach for structure determination of hydrous inner-Earth minerals. Despite the apparent insights into local structure that NMR spectroscopy provides, the characterisation of hydrous mantle minerals is far from a straightforward or routine process. Firstly, the natural isotopic abundance of many of the key constituents of mantle minerals is very low, which can make the acquisition of useful NMR spectra challenging. For example, the natural abundance of $^{17}$O, $^{25}$Mg and $^{29}$Si, three commonly studied NMR-active nuclei, are 0.038, 10.00 and 4.685%, respectively.[1] In addition, most natural samples of mantle minerals (which are often extremely rare) contain Fe, leading to large paramagnetic interactions that limit the structural insight that can be extracted from NMR spectra. To circumvent this, synthetic Fe-free variants of hydrous, high-pressure mantle minerals can be produced (often involving isotopically enriched reagents to

facilitate subsequent NMR studies). However, this procedure can be extremely challenging, typically requiring extremely high temperatures and pressures, limiting the sample volume available as the pressure increases. For example, at a pressure of ~5 GPa, a piston-cylinder apparatus can produce ~100 mg of sample, while a multi-anvil press, capable of generating pressures up to ~25 GPa typically yields less than 10 mg of sample. Synthetic pressures above 25 GPa, usually resulting in less than 1 mg of sample being produced, necessitate the use of a diamond anvil cell.[1]

An approach that is continuing to garner interest due to its proven ability to aid in the interpretation of NMR spectra is the use of first-principles calculations that include periodic boundary conditions, allowing crystalline materials (rather than discrete clusters or molecules) to be considered. By using the GIPAW method,[18] such calculations are able to predict solid-state NMR parameters with ever increasing accuracy and efficiency. As a result, it is becoming increasingly desirable to investigate the structure of materials by combining both experimental measurements and predicted NMR parameters, as the latter is able to provide valuable information relating to structure and disorder (both static and temporal), which can help guide the interpretation of NMR spectra that are often too complex to accurately assign directly.[16,19–22]

As hydrous inner-Earth minerals are often disordered, elucidating the structure and, in particular, identifying the preferential site(s) that hydrogen atoms occupy, is experimentally challenging. While XRD can often struggle to accurately determine the location of hydrogen atoms, the complex lineshapes typically observed in the NMR spectra of hydrous minerals means that this approach, although usually very sensitive to subtle changes in local structure, also struggles to provide detailed structural information on hydrous minerals. As a result of these challenges, it is possible that a combined approach (where a number of techniques are used) may be the most promising strategy for investigating the structure of these important minerals in a way that provides new insights and a deeper understanding of the hydration mechanism and the different local environments that result.

## 6.2 Fe-free wadsleyite

Fe-free wadsleyite, β-$Mg_2SiO_4$, is a high-pressure silicate mineral and the Mg end member of the β-$(Mg,Fe)_2SiO_4$ solid solution, believed to be one of the principal components of the transition zone, a region of the Earth's mantle between depths of ~410 and ~530 km.[23,24] As shown in Figure 6.2a, this mineral has orthorhombic symmetry and adopts the *Imma* space group, with a single unit cell containing sixteen Mg, eight Si and thirty two O atoms, *i.e.*, 8 $Mg_2SiO_4$ units.[25] β-$Mg_2SiO_4$ contains one, three and four distinct Si, Mg and O crystallographic sites, respectively, with a detailed view of the four-coordinate (tetrahedral) Si and six-coordinate (octahedral) Mg sites shown in Figure 6.2b. The single Si site is found in a pyrosilicate ($Si_2O_7$) unit, containing a bridging O2 site and two crystallographically distinct non-bridging (terminating) silicate oxygen sites, O3 and O4. The remaining oxygen, O1, is not bonded directly to Si, but is instead surrounded by five $Mg^{2+}$ cations (four Mg3 and one Mg2), leading to this site being classified as 'underbonded' relative to typical divalent O species.

Wadsleyite is believed to be capable of accommodating up to 3.3 wt% $H_2O$ in the form of hydroxyls. This is a higher hydration level than any other upper mantle mineral, meaning that hydrous wadsleyite could represent a vast water reservoir deep within the Earth.[6,7,26] Hydrogen incorporation is widely accepted to be achieved through the formation of cation vacancies in NAMs.[27–29] The hydration of wadsleyite is believed to be charge balanced by the removal of $Mg^{2+}$ cations, *i.e.*, by the creation of Mg vacancies, with a sample containing the maximum hydration level of 3.3 wt% $H_2O$, corresponding to the exchange of four $H^+$ for two $Mg^{2+}$ per unit cell. As β-$Mg_2SiO_4$ contains three crystallographically distinct $Mg^{2+}$ sites, hydration introduces ambiguity relating to the specific site(s) where cation vacancies are created. In addition, as $H^+$ do not occupy a known crystallographic site within the structure, being too small to effectively stabilise the vacant six-coordinate $Mg^{2+}$ site, many experimental techniques will find it challenging to identify the location and/or orientation of the hydroxyls formed during

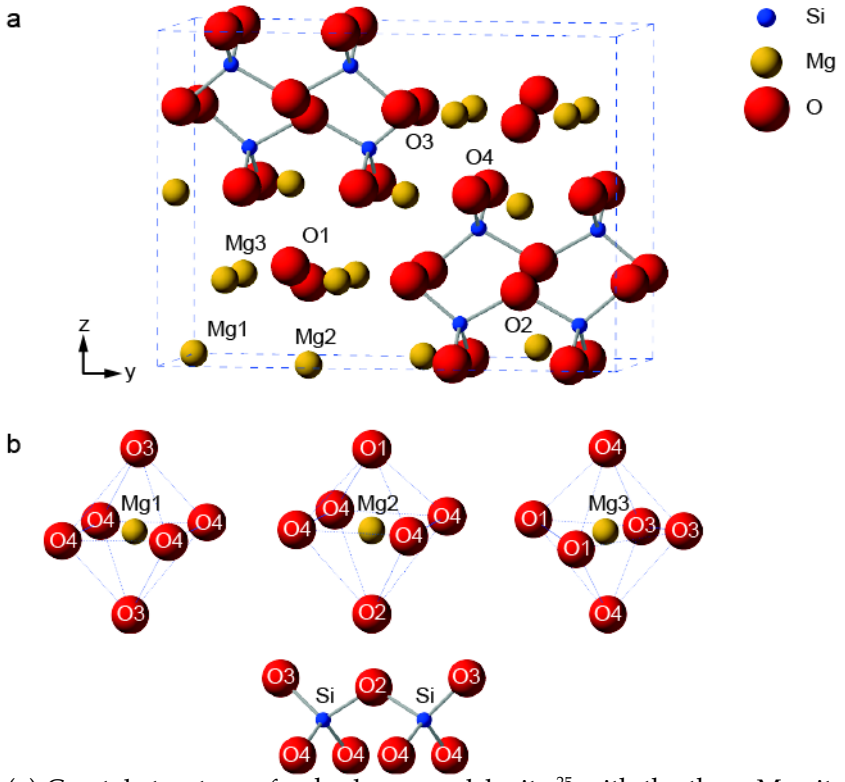


**Figure 6.2:** (a) Crystal structure of anhydrous wadsleyite,[25] with the three Mg sites and four O sites labelled. (b) Detailed view of the Mg sites and the single Si site in the pyrosilicate ($Si_2O_7$) unit, with the associated O sites labelled.

the hydration of wadsleyite. Therefore, the ambiguity in both the location and relation of $Mg^{2+}$ vacancies and the location of the incorporated $H^+$ means that hydrous wadsleyite will exhibit structural disorder. Due to this, although several possible hydration mechanisms have been proposed (as discussed in Section 6.3), a definitive mechanism for the hydration of wadsleyite is yet to be universally accepted, and the detailed structure of this mineral is still unknown.

## 6.3 Previous work

The structure and specific hydration mechanism leading to hydrous wadsleyite have previously been investigated using a range of both theoretical and/or experimental techniques,[6,7,30–46] with the focus predominantly on β-$Mg_2SiO_4$, the Fe-free end member of the solid solution. As a result of its underbonded character (being surrounded by five $Mg^{2+}$ and

no $Si^{4+}$), several theoretical studies have identified O1 (see Figure 6.2a) as the most likely O site at which protonation occurs.[6,7,30–34] Relying on simple ionic constraints, Smyth created a theoretical structural model of β-$Mg_2SiO_4$ containing 3.3 wt% $H_2O$, concluding that the most stable structure consists of protonated O1 sites, with hydroxyl bonds orientated parallel to the *c*-axis of the unit cell (leading to no direct hydrogen bonding), with $H^+$ incorporation charge balanced by the removal of the closest Mg2 cations,[7] These cations were chosen for removal in order to minimise charge separation and because Mg2 represents a high-symmetry, low multiplicity site.[7] In a separate study, Downs determined the electrostatic potential surface for β-$Mg_2SiO_4$,[35] using the structure derived from the single-crystal XRD data of Horiuchi and Sawamoto,[25] finding a broad energy minimum near O1, suggesting this represents a possible protonation site, in agreement with the model of hydrous wadsleyite proposed by Smyth.[7] Downs also identified low electrostatic potential minima above and below the bonding plane of the O2 site, effectively suggesting that protonation is likely to occur at both the O1 and O2 sites. Using electrostatic potentials, Ross *et al.* found that all four O sites exhibit possible hydrogen docking sites, although it was suggested that protonation at the O3 or O4 sites only occurred if $H^+$ incorporation was accompanied by the removal of $Mg^{2+}$ cations from neighbouring Mg1, Mg2 or Mg3 sites.[36] However, in these studies, neither the presence nor the position of Mg vacancies, necessary to charge balance the incorporation of protons, were directly included in the proposed structural models.

In a study using first-principles DFT calculations, Tsuchiya and Tsuchiya identified possible structures for hydrous wadsleyite with chemical formulas $Mg_{1.875}SiH_{0.25}O_4$ and $Mg_{1.75}SiH_{0.5}O_4$, corresponding to systems containing 1.65 and 3.3 wt% $H_2O$, respectively.[34] After geometry optimisation, the lowest energy structural models (generated by manually removing Mg cations and placing protons on nearby O sites), consisted of unit cells with monoclinic symmetry and protonation of O1 species, charge balanced by Mg3 site vacancies, with the hydroxyls aligned along the edges of the octahedron of oxygen atoms surrounding the Mg3 vacancy. Although this contradicts

conclusions from previous theoretical investigations,[7,35,36] it does agree with several XRD-based studies into the structure of hydrous wadsleyite.[37–40] In an investigation into the structure of wadsleyite containing 3.3 wt% $H_2O$, Kudoh *et al.*, suggested that hydrogen is incorporated around an Mg3 vacancy, with Raman and FTIR spectroscopy confirming the presence of hydroxyls and valence sum calculations based on the refined bond lengths in the sample implying protonation occurs at the O1 site.[37] However, in a later publication, using XRD, Kudoh and Inoue showed that in samples with high levels of hydration, vacancies at different Mg sites are formed, with hydrous wadsleyite containing 3.3 wt% $H_2O$ (*i.e.*, $Mg_{1.75}SiH_{0.5}O_4$) exhibiting fractional occupancies of 100%, 92% and 76%, for the Mg1, Mg2 and Mg3 sites, respectively.[38] Small Fourier peaks were also found at an interstitial tetrahedral void, termed the "Si2" site, believed to represent the migration of a small amount of $Si^{4+}$, and having a fractional occupancy of 0.07 in $Mg_{1.75}SiH_{0.5}O_4$. Migration to the interstitial Si2 site was only observed when the cation occupying the adjacent Mg3 site was removed, allowing the $Si^{4+}$ cation to move without causing face sharing between neighbouring $SiO_4$ and $MgO_6$ polyhedra. In contrast, although an XRD study by Holl *et al.* showed a strong preference for O1 hydroxyls to be formed in samples of wadsleyite containing between 0.005 and 1.66 wt% $H_2O$, only Mg3 site vacancies were detected.[39] In a similar XRD-based investigation into the structure and compressibility of a wadsleyite sample containing 2.8 wt% $H_2O$, Ye *et al.* reported a significant reduction in the Mg3 site occupancy, suggesting that hydration is charge balanced solely by the removal of $Mg^{2+}$ cations from this site.[40] An increase in the bond lengths surrounding the O1 site in the hydrous wadsleyite sample led Ye *et al.* to conclude that this is the preferential protonation site at this hydration level.

Using neutron time-of-flight single-crystal Laue diffraction to investigate the position of $H^+$ in a sample of wadsleyite containing 1.36 wt% $H_2O$, Purevjav *et al*. concluded that only vacancies on the Mg3 site were formed, with this site exhibiting a fractional occupancy of 0.895(1) and 0.898(1) at 100 and 295 K, respectively.[41] In this study, the authors also identified that $H^+$ are most likely located on O1, with the hydroxyl bonds orientated along the O1···O4

edges of the octahedron surrounding the vacant Mg3 site, in good agreement with the DFT analysis of Tsuchiya and Tsuchiya.[34] Similarly, preferential protonation site(s) and possible cation vacancy ordering in a series of wadsleyite samples containing between ~50 and ~10,600 ppm (~1.06 wt%) $H_2O$ have been investigated by Jacobsen *et al.*, in which a combination of single-crystal XRD and FTIR spectroscopy were used.[42] Only vacancies on the Mg3 site were identified using XRD, with the fractional occupancy of this site decreasing as the hydration level increased. In the FTIR spectra of these hydrous wadsleyite samples, all the main bands from the hydroxyl stretching region were attributed to O1 protonation.[42] This interpretation of the FTIR spectra was supported by the XRD data, which showed a systematic shortening of several hydrogen bonded O···O octahedral edges surrounding an Mg3 vacancy, an observation that was attributed to a reduction in O···O repulsion forces following protonation of O sites near a $Mg^{2+}$ cation vacancy. In a later study, Deon *et al.* used FTIR spectroscopy, single-crystal XRD and electron microprobe analysis (EMPA) to identify the location of hydroxyls in hydrous wadsleyite, concluding that hydrogen incorporation is charge balanced exclusively by the removal of Mg3 cations, with the preferential protonation location being the O1 sites directly surrounding the $Mg^{2+}$ vacancy.[43] However, in contrast to previous studies,[42] through analysing the electron density map Deon *et al.* suggested that protonation also occurs along the O1···O4 and O3···O4 edges of the vacant Mg3-centred octahedron, *i.e.*, that not only the O1 site is protonated.[43] In a study in which single-crystal XRD, neutron power diffraction and Raman spectroscopy were used, the structure and distribution of deuterons in a wadsleyite sample containing ~1.6 wt% $^2H_2O$ ($^2H$ = D) was investigated.[44] Both X-ray and neutron diffraction data indicated a fractional occupancy of the Mg3 site in the sample, consistent with previous diffraction-based studies.[37–41] Indeed, single-crystal XRD analysis showed the Mg1 and Mg3 sites as having fractional occupancies of 0.991(3) and 0.879(2), respectively, with an interstitial "Si2" site with fractional occupancy 0.012(2) also identified, supporting the observations made by Kudoh and Inoue.[38] Using difference Fourier maps based on the unit cell of anhydrous wadsleyite,

Sano-Furukawa *et al.*[44] also found that deuterons are located on O1 sites, with the hydroxyl bond aligned along the O1···O4 edge of the octahedron surrounding the Mg3 site vacancy.

As NMR spectroscopy does not rely on long-range atomic ordering to probe the local structure of solids, this technique has previously been used to identify different local environments in minerals,[47–52] and, more generally, has proved able to detect and classify structural disorder in a wide range of materials.[16,17,20,53–55] Along with FTIR spectroscopy, Kohn *et al.* applied $^{1}$H MAS NMR spectroscopy to study wadsleyite samples containing between 0.8 and 1.5 wt% $H_2O$.[45] The FTIR spectra of these hydrous samples indicated that 14 of 17 protonation sites (identified based on the different O···O distances and combinations of spatially close oxygen atoms in the crystal structure of orthorhombic wadsleyite containing 3.3 wt% $H_2O$, derived from XRD analysis),[37] are occupied. The $^{1}$H MAS NMR spectrum of hydrous wadsleyite containing 1.5 wt% $H_2O$ presented by Kohn *et al*. exhibits a complex lineshape with intensity between 11 and 1 ppm that the authors attribute to the overlap of six separate resonances, with a resonance at 4.2 ppm accounting for the majority of the intensity. Based on the complexity of the $^{1}$H MAS NMR lineshape, in combination with FTIR spectra analysis, Kohn *et al.* concluded that in the sample of wadsleyite containing 1.5 wt% $H_2O$, all four crystallographic O sites are protonated, with the preferential formation of O1 hydroxyls being an indication that protonation is not totally disordered, *i.e.*, that hydrogen is not randomly distributed across all four O sites.

A more recent study by Griffin *et al.* showed how multinuclear ($^{1}$H, $^{2}$H, $^{17}$O, $^{25}$Mg and $^{29}$Si) solid-state NMR spectroscopy in combination with first-principles calculations could be used to perform a detailed investigation into the structure of Fe-free wadsleyite samples containing ~3 wt% $H_2O$ or $^{2}H_2O$.[46] In contrast to previous work by Smyth,[7] where structural models with Mg2 vacancies were suggested to be the most favourable, Griffin *et al*. found that the closest agreement between predicted NMR parameters for a small number of candidate structures with experimental NMR spectra for hydrous

wadsleyite, occurred when the structural models contained Mg3 vacancies, with poorer agreement seen for those with Mg2 vacancies.[46] The $^{1}$H MAS NMR spectrum of wadsleyite containing ~3 wt% $H_2O$ was interpreted as consisting of at least four major resonances, at 8.6, 6.7, 3.4 and 1.1 ppm, with the signal at 3.4 ppm (attributed to protonation of the O1 site), clearly the most prominent feature, comprising ~64% of the total intensity. However, the presence of multiple peaks in the $^{1}$H and $^{2}$H MAS NMR spectra suggests that protonation also occurs at other O sites, likely leading to the formation of silanol (Si–OH) groups, which are also evident from $^{1}$H-$^{17}$O and $^{1}$H-$^{29}$Si heteronuclear correlation NMR experiments.[46] Based on the interpretation of the experimental NMR spectra, and assisted by the predicted NMR parameters for a series of structural models, Griffin *et al.* concluded that ~20% of all protonation could occur at silicate oxygen (O2, O3 or O4) sites, meaning that silanol defects could be more prominent than previous studies have suggested.[34,37,40–42,44]

In this chapter, an NMR crystallographic approach (involving XRD, solid-state NMR spectroscopy and first-principles calculations) is used to investigate the structure of Fe-free wadsleyite containing 1.65 and 3.30 wt% $H_2O$, systems referred to in this chapter as semi- and fully-hydrous wadsleyite, respectively. This investigation involves using AIRSS,[56,57] – a structure searching approach introduced in Section 4.3.2, and discussed further in Section 6.6.1 – to generate a series of candidate structures, in which a variety of protonation sites and combinations of hydroxyl bond orientations were explored. To facilitate comparison with the experimental NMR spectra, the NMR parameters for a subset (with the specific selection criteria discussed in the relevant Sections) of the AIRSS-generated candidates were calculated, with the level of agreement between calculated and experimental NMR parameters allowing the accuracy of the generated structural models to be evaluated. The $^{25}$Mg MAS NMR spectra of anhydrous wadsleyite and a sample containing ~3 wt% $H_2O$ appear very similar,[46] suggesting that this nucleus provides less insight into the structure of hydrous wadsleyite. As a result, neither the experimental nor the calculated $^{25}$Mg NMR parameters for hydrous wadsleyite are discussed further in this

chapter. This chapter highlights how first-principles calculations can assist the interpretation of the complex NMR spectra observed for hydrous wadsleyite. Indeed, the combined strategy presented in this chapter has enabled multinuclear NMR spectra of hydrous wadsleyite (which often consist of several overlapping resonances), to be decomposed and signals assigned to specific local environments, allowing a structural picture of hydrous wadsleyite, more detailed than previously reported, to be determined.

The work presented in this chapter aims to build on the research previously published by Griffin *et al.*,[46] and has resulted in the publication of two papers.[58,59] In addition to the structural investigation of hydrous wadsleyite using a combination of random structure searching and NMR spectroscopy, a major aim of this work was to highlight more generally the effectiveness of this combined approach for the study of disordered materials

## 6.4 Acknowledgements

The anhydrous and hydrous wadsleyite samples discussed in this chapter were synthesised by the group of Dr Andrew Berry at the Australian National University. Anhydrous β-$Mg_2Si^{17}O_4$ (containing 35% enriched $^{17}O$) was synthesised from α-$Mg_2Si^{17}O_4$ at 16 GPa and 1873 K for 1 hour, using a MA8-type multiple anvil apparatus, as described by Ashbrook *et al.*[60] β-$Mg_{1.77}SiH_{0.46}{}^{17}O_4$ (~3 wt% $H_2{}^{17}O$) and β-$Mg_{1.77}Si^2H_{0.46}O_4$ (~3 wt% $^2H_2O$) were synthesised from the relevant amounts of starting materials, $SiO_2$ and $Mg(OH)_2$, enriched in $^{17}O$ and/or $^2H$ as required. As described by Griffin *et al.* in 2013,[46] these samples were equilibrated at either 1100 °C and 14 GPa or 1200 °C and 14.5 GPa for 1-3 hours, using a split-cylinder 6-8 Kwai-type multi-anvil apparatus.

All solid-state NMR spectra shown in this chapter were acquired by either Dr John Griffin or Dr Daniel Dawson at the UK High-Field Solid-State NMR Facility, at the University of Warwick, using a Bruker Avance III 850 MHz

(20.0 T) spectrometer, or at the University of St Andrews, using a Bruker Avance III 600 MHz (14.1 T) spectrometer. The NMR spectra acquired by Dr John Griffin, which represent the majority of the spectra discussed in this chapter, have previously been published.[46] Specific experimental details are given at the relevant points in the text (see Section 6.5).

Professor Chris Pickard and his research group at the University of Cambridge (previously at University College London) are thanked for the initial generation of a series of structural models for semi-hydrous wadsleyite using the AIRSS program.[56,57]

Dr David McKay, a postdoctoral research fellow in the Ashbrook group at the University of St Andrews, is also thanked for his assistance in planning and performing AIRSS and CASTEP calculations, as well as for his help in developing Python scripts to analyse output data from the first-principles calculations.

Thanks must also go to Dr Simone Sturniolo for developing Soprano,[61] a Python library developed and maintained by the CCP-NC (the EPSRC combined computational project in NMR Crystallography). The Soprano library was used to categorise AIRSS-generated models based on energies and a set of structural parameters, thereby creating subsets of models that were subsequently investigated in more detail.

## 6.5 Experimental NMR spectra

The NMR spectra discussed in this section have previously been published.[46] However, as they are integral to the investigation presented in this chapter, spectra for samples of anhydrous and hydrous wadsleyite are included to facilitate comparison between predicted and experimental NMR measurements throughout this chapter.

### 6.5.1 Anhydrous Fe-free wadsleyite

The 20.0 T $^{17}$O MAS and STMAS spectra of anhydrous wadsleyite are shown in Figures 6.3a and 6.3b, respectively. Figure 6.3a exhibits a sharp resonance at 38 ppm corresponding to the O1 species which, due to its symmetric local environment, shows a very small quadrupolar coupling constant, in good agreement with previous studies carried out using lower field strengths.[60,62] The signal between 40 and 80 ppm in Figure 6.3a can then be assigned to the three silicate O species (O2, O3 and O4), which all have much larger quadrupolar interactions and appear significantly overlapped at this fieldstrength. Figure 6.3b shows that improved resolution of the O species is observed in the STMAS NMR spectrum, with the O1 and O2 sites

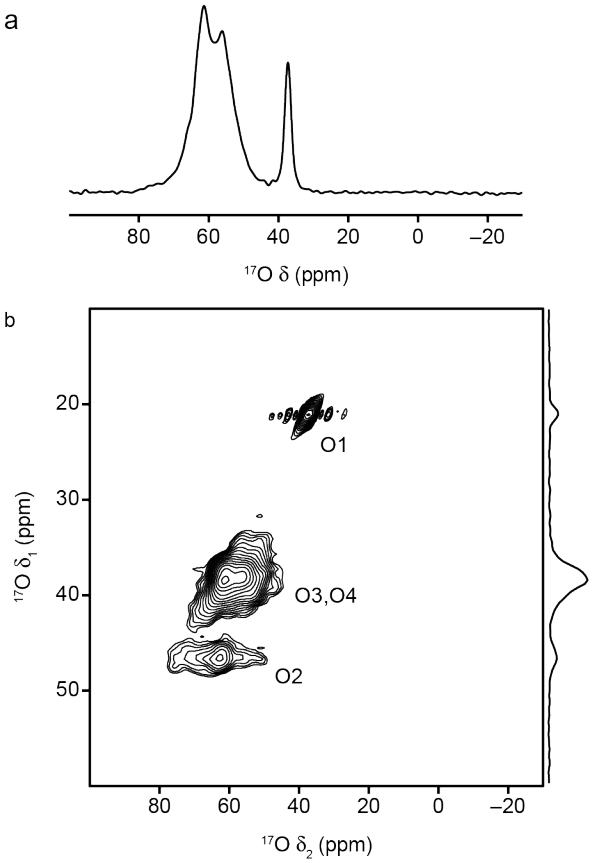


**Figure 6.3:** $^{17}$O (20.0 T, 30 kHz) (a) MAS and (b) split-$t_1$ shifted-echo STMAS NMR spectra of anhydrous wadsleyite. In (a), 360 transients were averaged, each separated by a recycle interval of 30 s. In (b), 1280 transients separated by a recycle interval of 1 s were averaged for each of 164 $t_1$ increments of 43.06 μs, with an echo duration of 1.8 ms. The figures have been modified from those presented by Griffin *et al*.[46]

**Table 6.1:** Experimental $^{17}O$ chemical shifts, $\delta_{iso}$ and quadrupolar couplings, $C_Q$, for the four crystallographically distinct O sites in anhydrous wadsleyite.

| O site | Relative site population | $^{17}O$ $\delta_{iso}$[49] (ppm) | $^{17}O$ $C_Q$[49] / MHz |
|---|---|---|---|
| O1 | 1 | 38(1) | - |
| O2 | 1 | 76(1) | 4.9(2) |
| O3 | 2 | 66(1) | 4.4(1) |
| O4 | 4 | 65(1) | 3.8(1) |

clearly separated in the $\delta_1$ dimension. However, despite this improvement in resolution, there is little separation of the O3 and O4 sites. In previous studies, performed at lower magnetic fields, the O3 and O4 silicate species could be separated and assigned, with O3 exhibiting a slightly higher chemical shift.[60,62] Table 6.1 summarises the experimentally determined $^{17}O$ NMR parameters for the four O sites in anhydrous wadsleyite.

Figure 6.4 shows the $^{29}Si$ MAS NMR spectrum of anhydrous wadsleyite, which contains a single peak at ~79 ppm, characteristic of a pyrosilicate. This spectrum confirms there is a single crystallographically distinct Si site in anhydrous wadsleyite,[25] in good agreement with previous studies of this transition zone mineral using $^{29}Si$ NMR spectroscopy.[62–65]

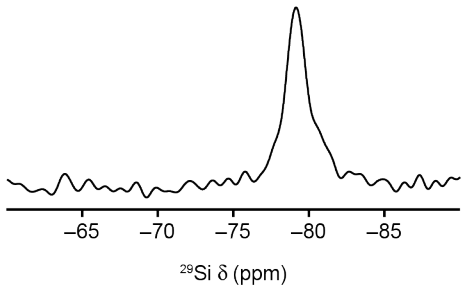


**Figure 6.4:** $^{29}Si$ (14.1 T, 20 kHz) MAS NMR spectrum of anhydrous wadsleyite, resulting from the averaging of 135 transients each separated by a recycle interval of 120 s. This figure has been modified from that presented by Griffin *et al.*[46]

### 6.5.2 Hydrous Fe-free wadsleyite

The $^{1}$H MAS NMR spectrum of β-$Mg_{1.77}SiH_{0.46}{}^{17}O_4$ (*i.e.*, a hydration level equivalent to ~3 wt% $H_2{}^{17}O$), a sample referred to as "wads-H" by Griffin *et al.*,[46] is shown in Figure 6.5a, with the $^{1}$H $\delta_{iso}$ and relative intensities shown in Table 6.2. The spectrum consists of a complex lineshape with the majority of intensity appearing between 10 and 0 ppm. A possible fit, containing four separate resonances, is also shown. The most intense feature in the $^{1}$H MAS NMR spectrum at 3.4 ppm, as well as signal appearing upfield as a shoulder at ~1 ppm are in the chemical shift range consistent with Mg–OH groups,[66–68] suggesting that these resonances result from protonated O1 environments (as O1 is the only non-silicate O site in wadsleyite). The intensity of the two resonances at ~4 and ~1 ppm indicates that the most common hydration mechanism in wadsleyite likely involves the protonation of O1. However, the two resonances with $^{1}$H $\delta_{iso}$ of 8.6 and 6.7 ppm, jointly account for ~17% of the total intensity in the $^{1}$H MAS NMR spectrum. The chemical shifts of these two signals are too high to likely correspond to Mg–OH-type environments, meaning they could correspond instead to environments resulting from the protonation of silicate O sites, *i.e.*, the formation of silanol (Si–OH) environments.

A two-dimensional $^{1}$H DQ MAS NMR spectrum of wads-H (which shows the correlations between homonuclear dipolar-coupled spins, allowing species that are in close spatial proximity to be identified) is shown in Figure 6.5b. The $^{1}$H DQ MAS spectrum clearly shows the presence of several distinct H environments, indicating protons are located on multiple (and potentially different combinations of) O sites in wads-H. Figure 6.5b shows that the region of intensity at ~4 ppm in the $\delta_{SQ}$ dimension, clearly results from the overlap of signal from two similar, yet distinct $^{1}$H environments. However, from the significant spread of intensity along the diagonal (where $\delta_{DQ} = 2\,\delta_{SQ}$) it can be inferred that a distribution of Mg–OH environments exist in wads-H. Figure 6.5b also shows a number of $^{1}$H correlations, with the region of

**Table 6.2:** Experimental $^{1}$H chemical shifts, $\delta_{iso}$, and relative intensities for the four resonances in the $^{1}$H MAS NMR spectrum of wads-H, shown in Figure 6.5a, based on the fit to this spectrum.[46]

| H site | $^{1}$H $\delta_{iso}$[46] (ppm) | Relative intensity[46] (%) |
|---|---|---|
| 1 | 1.1 | 19 |
| 2 | 3.4 | 64 |
| 3 | 6.7 | 10 |
| 4 | 8.6 | 7 |

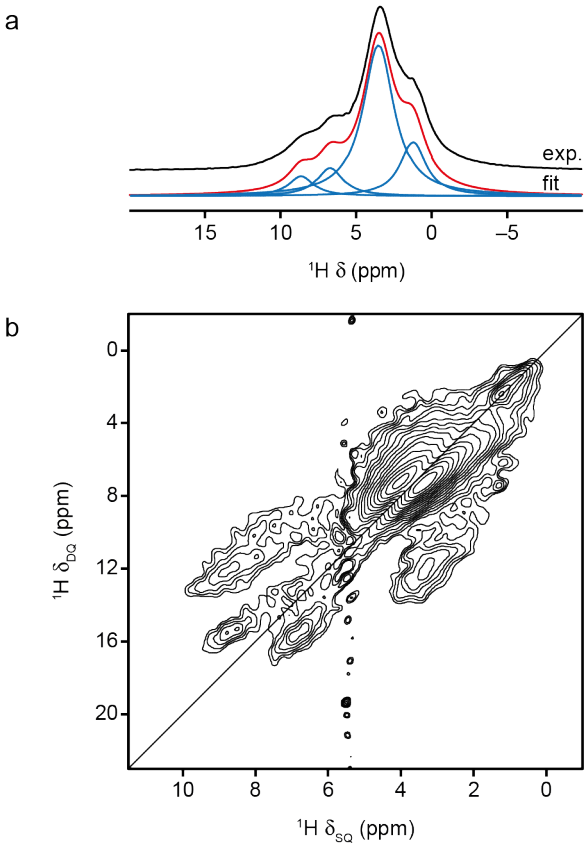


**Figure 6.5:** (a) $^{1}$H (14.1 T, 30 kHz) MAS NMR spectrum of wads-H resulting from the averaging of 16 transients each separated by a recycle interval of 10 s. A possible fit of the experimental spectrum is shown below the MAS lineshape in red, with the four individual components shown in blue. (b) Rotor-synchronised $^{1}$H (14.1 T, 30 kHz) DQ MAS NMR spectrum of wads-H recorded using two cycles of BABA recoupling. The spectrum is a result of the averaging of 32 transients, separated by a recycle interval of 2 s, for each of 100 $t_1$ increments of 33.33 μs, with the $\delta_{DQ} = 2\delta_{SQ}$ axis is shown by a diagonal line. The figures have been modified from those presented by Griffin *et al*.[46]

signal between ~2 and ~4 ppm in the $\delta_{SQ}$ dimension, clearly correlating with

resonances at a much higher chemical shift (downfield in the $\delta_{SQ}$ dimension), suggesting that Mg–OH and Si–OH environments are in close proximity. Additional correlations between resonances with $^{1}$H $\delta_{SQ}$ > 6 ppm suggests that interactions between multiple environments, none of which are Mg–OH *i.e.*, interactions between potential silanol environments, are present. Although it is not possible to confidently assign the $^{1}$H resonances to species based on specific O site(s) from the information in Figure 6.5, these spectra do confirm that multiple H environments (including both Mg–OH and Si–OH) are present.

The $^{17}$O MAS and STMAS NMR spectra of wads-H are shown in Figure 6.6a and 6.6b, respectively. By comparing Figure 6.6a with the $^{17}$O MAS NMR spectrum of anhydrous wadsleyite (in Figure 6.3a), it is clear that they appear similar, with both containing a sharper resonance at ~40 ppm resulting from the O1 and a broader region of signal corresponding to silicate (O2-O4) oxygens, respectively. However, there is significant broadening of the signal at higher shift upon hydration, perhaps indicating that a distribution of environments are present. The expansion in Figure 6.6a reveals the presence of a third, much broader resonance, absent in the $^{17}$O MAS NMR spectrum of anhydrous wadsleyite. The lower chemical shift and larger quadrupolar coupling of this resonance is typical of protonated O sites in silicates, environments that have been shown to have $^{17}$O $C_Q$ as large as 7-8 MHz.[69–71] From Figure 6.6a it is also clear that the intensity of the resonance assigned to O1 decreases significantly upon hydration which, combined with the presence of the broader hydroxyl resonance, suggests that significant protonation must occur at this O site, in good agreement with the observation of the intense $^{1}$H resonance at δ of 4 ppm in Figure 6.5a.

As shown in Figure 6.6b, the hydroxyl resonance clearly appears in the $^{17}$O STMAS NMR spectrum, at $\delta_1 \approx 20$ ppm. By comparing the appearance of this STMAS spectrum with a triple-quantum MAS NMR spectrum of wads-H, Griffin *et al.* were able to confirm that the width (in both the $\delta_1$ and

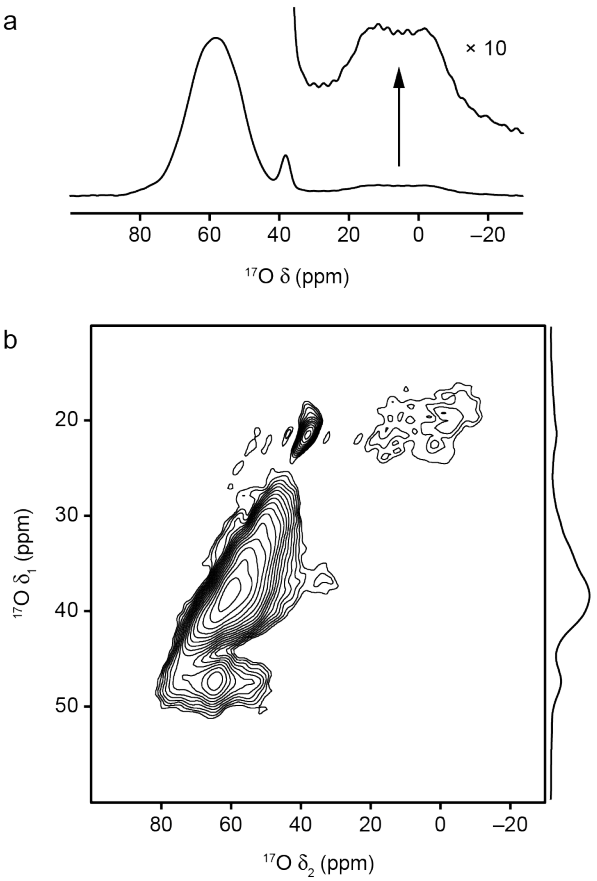


**Figure 6.6:** $^{17}$O (20.0 T, 30 kHz) (a) MAS and (b) split-$t_1$ shifted-echo STMAS NMR spectrum of wads-H. In (a), the spectrum is the result of averaging 360 transients each separated by a recycle interval of 30 s. In (b), 512 transients separated by a recycle interval of 1 s were averaged for 128 $t_1$ increments of 43.06 μs, with an echo duration of 1.8 ms. The figures have been modified from those presented by Griffin *et al.*[46]

$\delta_2$ dimensions) of the resonances is due to H species exhibiting positional, not dynamic, disorder.[46] This confirms that wads-H contains several different hydroxyl environments, in agreement with the interpretation of the $^1$H MAS and DQ MAS spectra shown in Figure 6.5, confirming its disordered nature.

Figure 6.7a shows the $^1$H-$^{17}$O CP MAS NMR spectrum of wads-H, where signal is transferred from H to nearby O species. By choosing a sufficiently short contact time, it is possible to selectively "edit" the spectrum such that only hydroxyl O species appear. Figure 6.7a contains two distinct regions of signal, an intense resonance at low $^1$H and $^{17}$O chemical shift, and a second, much weaker resonance appearing downfield. As shown in Figure 6.7b, the

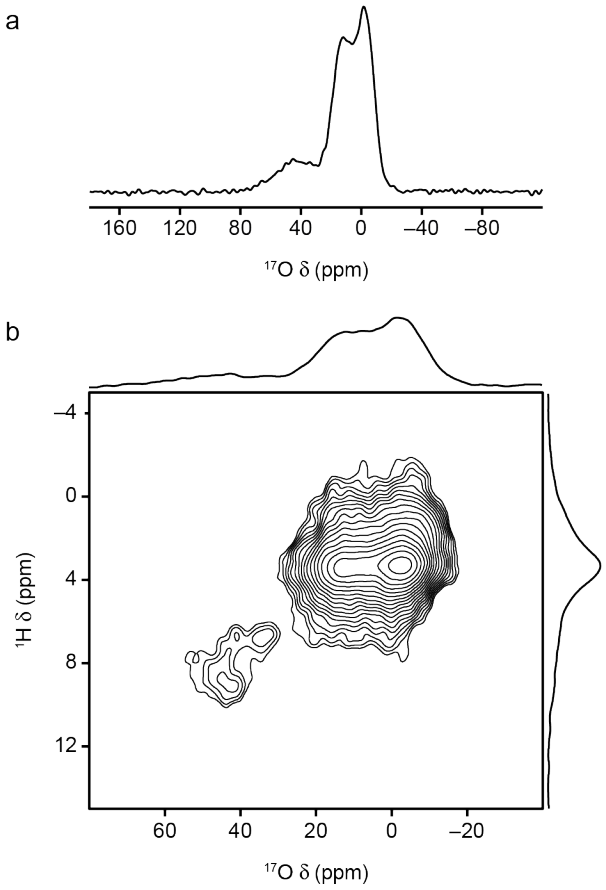


**Figure 6.7:** (a) $^{1}$H-$^{17}$O (20.0 T, 30 kHz) CP MAS NMR spectrum of wads-H, resulting from the averaging of 3752 transients each separated by a recycle interval of 1.5 s. (b) H-$^{17}$O (20.0 T, 30 kHz) CP HETCOR NMR spectrum of wads-H, resulting from the averaging of 400 transients separated by a recycle interval of 1.5 s for each of the 90 $t_1$ increments of 33.33 μs. In both spectra polarisation transfer was achieved using a contract time of 500 μs. The figures have been modified from those presented by Griffin *et al*.[46]

$^{1}$H-$^{17}$O CP HETCOR NMR spectrum of wads-H also contains two correlation peaks, with one significantly more intense than the other. The most intense feature is the result of O species with $^{17}$O δ between 20 and 0 ppm correlating with protons with $^{1}$H $\delta < 5$ ppm, suggesting this results from Mg–OH environments The second, less intense correlation arises from the correlation between O species at higher shift and $^{1}$H with $\delta > 5$ ppm. The work of Griffin *et al*. suggested that this results from the presence of Si–OH environments, and supported this conclusion by predicting NMR parameters for a series of hydrous wadsleyite structural models, constructed from a 2 × 1 × 1 supercell of anhydrous wadsleyite, where protons were manually placed in chemically

sensible positions around an Mg1, Mg2 or Mg3 vacancy.[46]

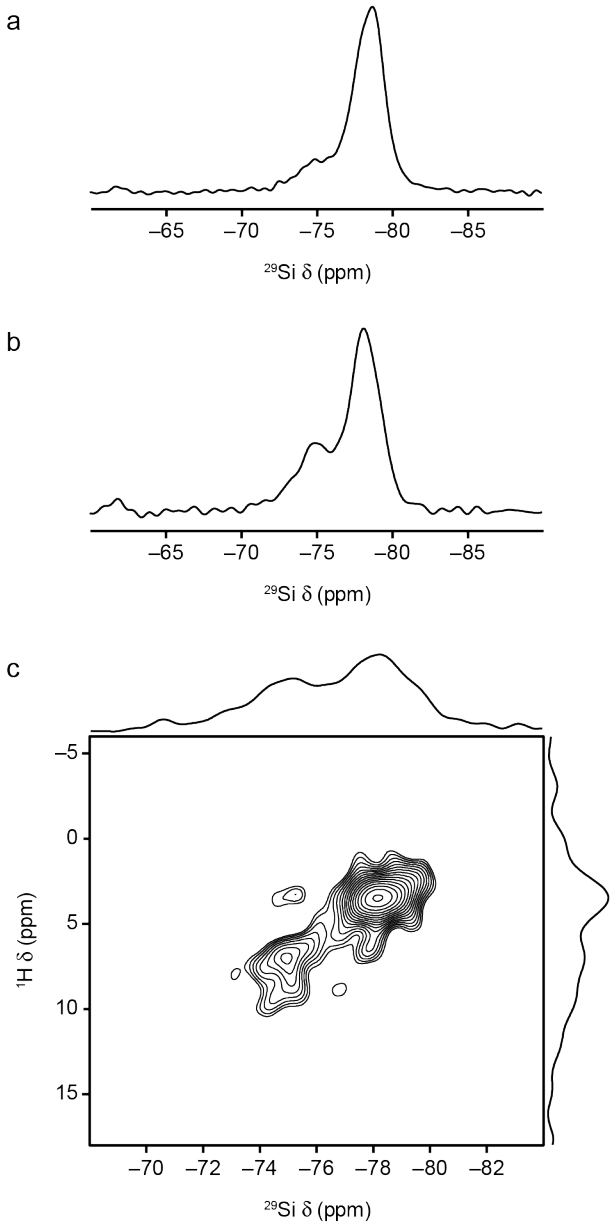


**Figure 6.8:** (a) $^{29}$Si (14.1 T, 30 kHz) MAS NMR spectrum of wads-H, resulting from the averaging of 1576 transients each separated by a recycle interval of 120 s. (b) $^{1}$H-$^{29}$Si (14.1 T, 12.5 kHz) CP MAS NMR spectrum of wads-H, resulting from the averaging of 2400 transients each separated by a recycle interval of 3 s, with a contact pulse duration of 6 ms. (c) $^{1}$H-$^{29}$Si (14.1 T, 20 kHz) CP HETCOR NMR spectrum of wads-H, resulting from the averaging of 2720 transients each separated by a recycle interval of 1.5 s for each of the 28 $t_1$ increments of 50 μs, with polarisation transfer achieved using a contact pulse duration of 1 ms. The figures have been modified from those presented by Griffin *et al.*[46]

The presence of Si–OH groups was also confirmed in the work of Griffin *et al.*[46] using $^{29}$Si NMR, as shown in Figure 6.8a. The $^{29}$Si MAS NMR spectrum of wads-H resembles the equivalent spectrum of anhydrous wadsleyite (see Figure 6.4), each with a resonance at $\delta \approx -79$ ppm. In addition to this signal, Figure 6.8a also contains a weaker resonance at $^{29}$Si $\delta \approx -75$ ppm, not seen in the spectrum of anhydrous wadsleyite. The corresponding $^{1}$H-$^{29}$Si CP MAS NMR spectrum of wads-H (Figure 6.8b) shows that the intensity of the $^{29}$Si peak at approximately –75 ppm increases significantly relative to the upfield resonance, confirming that the former likely results from Si–OH environments. The $^{1}$H-$^{29}$Si CP HETCOR NMR spectrum of wads-H in Figure 6.8c, shows that the Si species at –75 ppm correlate with $^{1}$H with $\delta > 5$ ppm, confirming Si–OH environments are present. The correlation peak between $^{1}$H and $^{29}$Si with $\delta$ of 4 and –79 ppm, respectively, likely represents the interaction of protons in Mg–OH (protonated O1) environments with non-protonated Si species in nearby pyrosilicate units.

## 6.6 Investigating the structure of semi-hydrous wadsleyite

### 6.6.1 AIRSS-generated structural models

In this chapter, Fe-free semi-hydrous wadsleyite refers to β-$Mg_2SiO_4$ containing 1.65 wt% $H_2O$, a hydration level that is equivalent to the incorporation of two $H^+$ per unit cell, charge balanced in each case by the removal of one $Mg^{2+}$ cation. In contrast to the work presented by Griffin *et al.*, where a small set of hydrous wadsleyite structural models were generated manually *i.e.*, by placing H atoms in manually chosen, chemically sensible locations, for the investigation carried out here, AIRSS,[56,57] an inherently unbiased approach for generating structural models, has been used. Although AIRSS has been used to probe the structure of a number of different systems, including organic molecules, potential battery materials, and high-pressure phases of water and hydrogen,[57,72–74] the work presented in

this chapter represents the first time this random structure searching approach, in combination with both experimental and predicted NMR parameters, has been applied to the structure elucidation of a disordered inorganic mineral.

Using an anhydrous Fe-free wadsleyite unit cell[25] (containing 8 $Mg_2SiO_4$ formula units) as the input structure, AIRSS was used to randomly position two H atoms within the structure. Hydration is achieved by substituting one Mg for two H, with each H atom sequentially placed on the (now vacant) Mg site before being allowed to move randomly anywhere within a sphere with radius given by the manually chosen variable POSAMP. In this work POSAMP was chosen to be 3.0 Å, in an attempt to minimise the charge

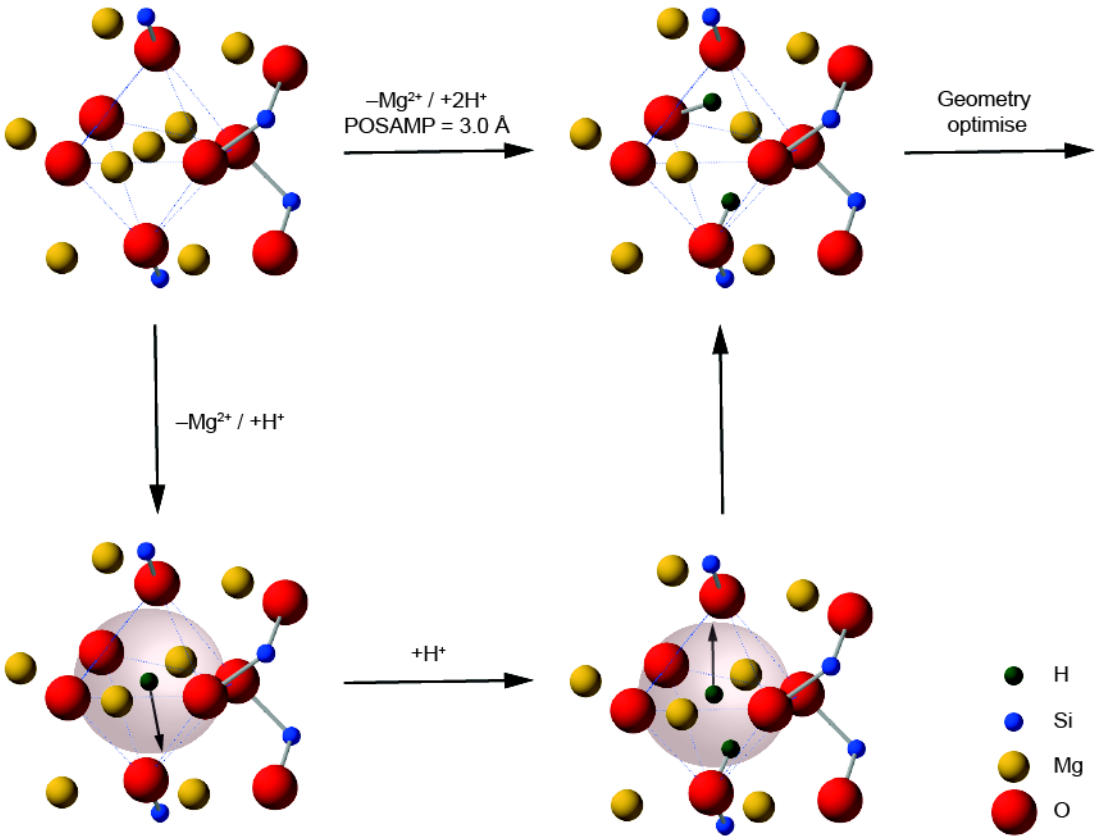


**Figure 6.9:** Schematic showing a Mg3 site centred 7.0 Å cluster of the anhydrous wadsleyite structure, illustrating the AIRSS process, in which one $Mg^{2+}$ cation is replaced by two $H^+$ cations, following which the structure is geometry optimised using DFT. The grey sphere represents the POSAMP (predetermined to have radius of 3.0 Å), where the two $H^+$ cations can be randomly placed.

separation (caused by the removal of a $Mg^{2+}$ cation), and to limit search space. During the AIRSS process the unit cell dimensions and the positions of all Mg, Si and O atoms are fixed, *i.e.*, only the positions of the substituted H are randomised. Figure 6.9 shows a schematic of the general AIRSS process used to generate the 223, 245 and 819 structural models of semi-hydrous Fe-free wadsleyite containing one Mg1, Mg2 and Mg3 vacancy per unit cell, respectively. These AIRSS-generated structural models were then geometry optimised using CASTEP 7.01,[75] with an $E_{cut}$ of 25 Ry, a k-point spacing of 0.1 $2\pi$ $Å^{-1}$, the PBE $E_{XC}$ functional[76] and the default ultrasoft pseudopotentials.[77] In this optimisation step the position of all H, Mg, Si and O atoms were allowed to vary, but the unit cell dimensions were fixed to those for anhydrous wadsleyite.[25] Although previous studies have shown that poor sampling of the Brillouim zone (determined by the number of k-points) can lead to unphysical structures,[57] computational efficiency was favoured over accuracy during this initial geometry optimisation process.

Figure 6.10 shows the three series of geometry optimised semi-hydrous wadsleyite structures, *i.e.*, structural models with Mg1, Mg2 or Mg3 vacancies, ranked according to their relative enthalpy. The lowest enthalpy structure in each series was set to $\Delta H = 0.0$ eV. Each of the three series consists of several low enthalpy "plateaus" of structural models, suggesting that structures with the same or very similar protonation arrangements have been identified multiple times, a strong indicator that the PES has been sampled thoroughly. Figure 6.11 shows a combined plot of the enthalpies for structural models from all three series, indicating that the structural model representing the "global" enthalpy minimum is found with a Mg3 vacancy. It should also be noted that, a significant number of structures in this series exhibit a lower $\Delta H$ than the structural models with the lowest enthalpy from the series generated with a Mg1 or Mg2 vacancy.

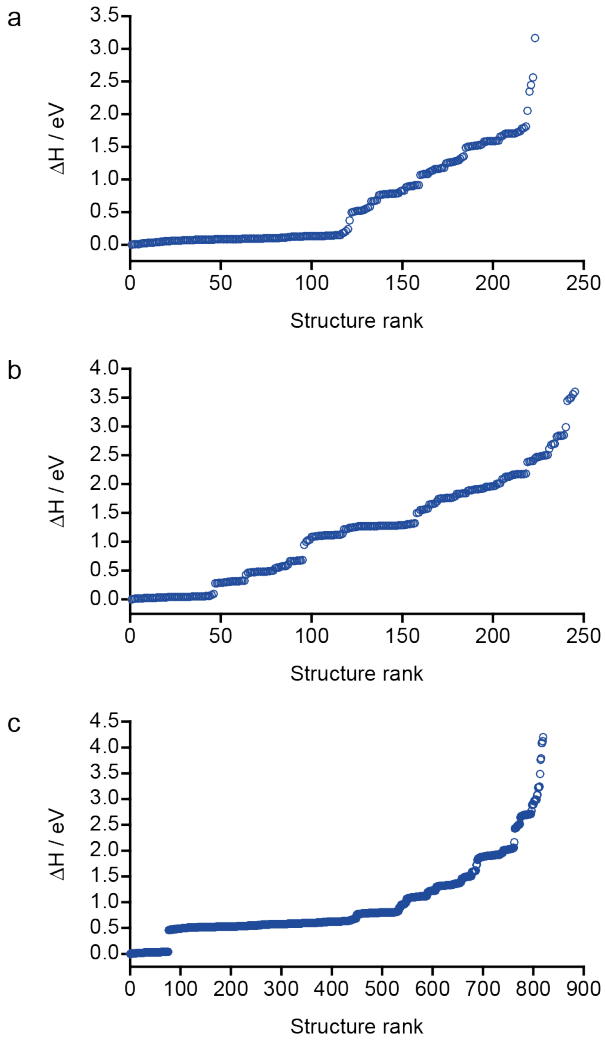


**Figure 6.10:** Plot showing the relative enthalpy (ΔH) of the (a) 223, (b) 245 and (c) 819 semi-hydrous wadsleyite structural models with an (a) Mg1, (b) Mg2 and (c) Mg3 vacancy.

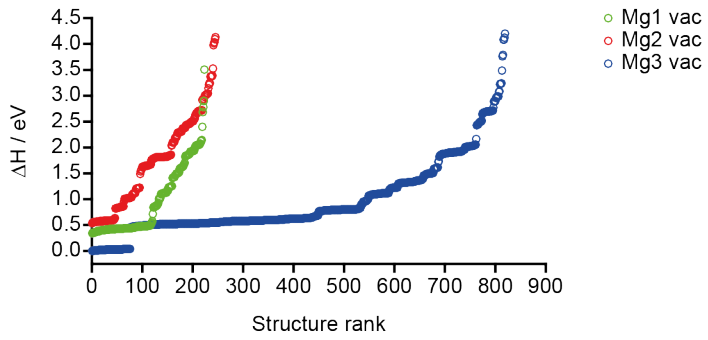


**Figure 6.11:** Plot showing the relative enthalpy (ΔH) of all semi-hydrous wadsleyite structural models, ranked relative to the lowest enthalpy AIRSS-generated structure, with the data points coloured by Mg site vacancy.

### 6.6.2 Mg3 vacant structural models

Based on ΔH for the AIRSS-generated structural models of semi-hydrous Fe-free wadsleyite (see Figure 6.11), and considering the tentative literature consensus regarding the mechanism by which hydration of this mineral occurs (see Section 6.3),[34,39–44,46] a more in-depth investigation into the stable and metastable protonation arrangements adopted by the structural models with Mg3 vacancies was performed. This series consists of 819 structures, in which the protons are overwhelmingly located on O species directly surrounding the Mg3 vacancy, with only 11 out of the 819 AIRSS-generated structures containing a proton outside this octahedron of O sites, specifically 1 × O2, 4 × O3 and 6 × O4 hydroxyls. As investigating all 819 structures would require significant computational resource, a much smaller subset of structures was identified, with ΔH used as the selection criteria. This subset consisted of the 25 lowest enthalpy structures, then one structure for each of a series of enthalpy increments (δΔH): $\delta\Delta H = 0.002$ eV up to $\Delta H = 0.5$ eV; $\delta\Delta H = 0.005$ eV for $0.5 < \Delta H < 0.6$ eV; $\delta\Delta H = 0.05$ eV for $0.6 < \Delta H < 1.0$ eV and $\delta\Delta H = 0.1$ eV for structures with $\Delta H > 1.0$ eV, leading to a total of 103 selected structural models, as shown in Figure 6.12. Although a large number of low enthalpy structures are selected using this ΔH based approach, the subset also includes a number of enthalpically less stable structural models, therefore ensuring that the PES of the system is well sampled. Prior to the calculation of NMR parameters, all 103 structures were further geometry optimised using a higher level of accuracy (subsequently termed "fully-optimised" models). All first-principles calculations were performed using CASTEP 7.01, with $E_{cut}$ of 60 Ry and a k-point spacing of 0.04 $2\pi$ Å$^{-1}$ (see Appendix D1 for convergence testing), the PBE $E_{XC}$ functional,[76] the default ultrasoft pseudopotentials,[77] a `geom_energy_tol` value of $1 \times 10^{-4}$ eV / atom and an `elec_energy_tol` value of $1 \times 10^{-5}$ eV / atom. The position of H, Mg, Si and O atoms, and the unit cell dimensions were allowed to vary during the geometry optimisation. As described in Chapter 3, a reference shielding ($\sigma_{ref}$) is used to convert calculated isotropic shieldings ($\sigma_{iso}$) to isotropic shifts

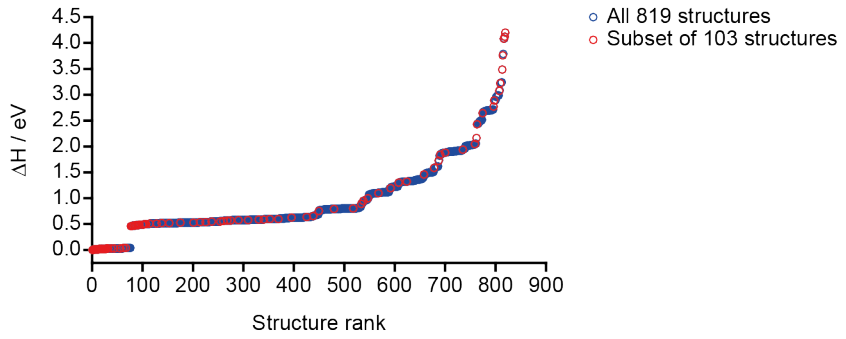


**Figure 6.12:** Plot showing the relative enthalpy (ΔH) of all 819 semi-hydrous wadsleyite structural models with a Mg3 vacancy, shown in blue, and the subset of 103 structural models chosen for further analysis, shown in red.

($\delta_{iso}$). Reference shieldings of 31.03, 249.22 and 320.11 ppm were used for $^{1}$H, $^{17}$O and $^{29}$Si, determined by comparing the experimental $\delta_{iso}$ and calculated $\sigma_{iso}$ values for brucite[78] ($^{1}$H) and anhydrous wadsleyite[25] ($^{17}$O and $^{29}$Si). In this section, only the magnitude of the $^{2}$H and $^{17}$O $C_Q$ values is considered. Calculated NMR parameters were analysed using in-house Python scripts extending the CCP-NC MagresPython module.[79]

Figure 6.13a shows the 103 selected semi-hydrous wadsleyite structural models ranked by ΔH following the second, more accurate geometry optimisation. While the second geometry optimisation step only causes the ΔH of the low enthalpy structures to decrease slightly, more significant variation in proton positions within the less stable structures often leads to a greater decrease in ΔH. Even though this subset consists of only 103 structures, Figure 6.13a shows that structures with ΔH < 1.0 eV again fall into several well-defined plateaus, indicating that many of the low enthalpy structures closely resemble one another, *i.e.*, that all the low enthalpy structures can be represented by a finite number of protonation arrangements. The four protonation arrangements with the lowest enthalpy (termed motifs **1**-**4**) are shown in Figure 6.13b. The structure with the lowest enthalpy motif **1** (ΔH = 0.0 eV), corresponds to the protonation of the two O1 species surrounding the Mg3 vacancy, with the protons hydrogen bonded to O4 species, causing the hydroxyl bonds to align parallel with the O1···O4

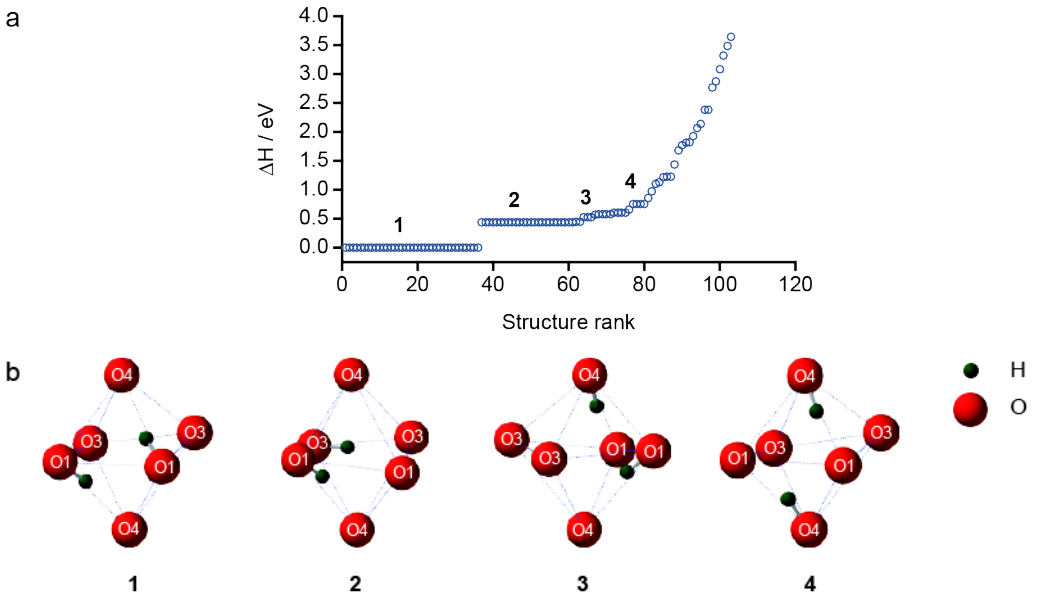


**Figure 6.13:** (a) Plot showing the relative enthalpy (ΔH) of the 103 semi-hydrous wadsleyite structural models, following the second geometry optimisation. (b) Representative structures of the four lowest enthalpy protonation motifs showing **1**, two O1 hydroxyls, **2**, one O1 and one O3 hydroxyl, **3**, one O1 and one O4 hydroxyl, and **4**, two O4 hydroxyls.

edges of the octahedron, in good agreement with results from some of the previous investigations.[38,40,43,44,46] As both H are hydrogen bonded to a different O4 species, the hydroxyl bonds in motif **1** appear staggered, with a dihedral angle (*d*[HOOH]) of 104°. The second plateau of structures (ΔH ≈ 0.5 eV) are represented by motif **2**, which consists of protons on neighbouring O1 and O3 sites, hydrogen bonded to O4 and O3 sites, respectively, leading to a much smaller dihedral angle. By comparing ΔH for motifs **1** and **2**, the formation of a silanol (Si–OH) group, *i.e.*, the protonation of an O3 rather than an O1 site, is associated with a significant enthalpic penalty of ~0.5 eV. This is perhaps because the non-protonated O1 site in motif **2** is even more underbonded than in anhydrous wadsleyite, as now only four $Mg^{2+}$ cations surround it, whereas in motif **1**, both formally underbonded O1 sties surround the Mg3 vacancy are protonated.

As shown in Figure 6.13c, motif **3** consists of O1–H···O4 and O4–H···O1 hydrogen bonding arrangements, with the protonation of an O4, rather than an O3 site resulting in another (but less significant) enthalpy increase of ~0.1

eV, with this plateau appearing at ΔH ≈ 0.6 eV. By comparing ΔH for motifs **1**, **2** and **3**, the order of protonation site enthalpic stability is clearly H–O1 > H–O3 > H–O4, with this trend seemingly correlating with the variation in hydroxyl bond length. While O1 hydroxyls exhibit a bond length of ~0.99 Å, there is a ~0.02 and ~0.04 Å bond length increase observed for O3 and O4 hydroxyls, respectively, indicating that higher enthalpy structures tend to have longer hydroxyl bonds. Structures such as motif **4**, which contain two silanol (either O3 or O4) groups are less enthalpically stable, with ΔH more than 0.8 eV above structures consisting solely of Mg–OH (O1) hydroxyls, *i.e.*, motif **1**.

The magnitude of the enthalpic penalty associated with creating a silanol group rather than protonating an O1 site, *i.e.*, the ~0.5 eV ΔH jump seen for motif **2** relative to motif **1**, is believed to be a direct result of the size and explicit periodicity of the structural models used. In these specific AIRSS-generated structures, protonation arrangements in which at least one O1 site is not protonated result in at best, a 1:1 ratio between Mg–OH and Si–OH environments. This potentially explains why a large enthalpy increase is seen for motif **2**, where 50% of all protons in the periodically (*i.e.*, infinitely repeating) structural model are located on non-optimum O3 pyrosilicate sites. Although it has not been attempted in this investigation, increasing the size of the structural model would reduce the *relative* enthalpy penalty associated with the protonation of a single pyrosilicate O site, as in a larger cell (with the same overall hydration level) the formation of one silanol group would not result in the Mg–OH to Si–OH 1:1 ratio discussed above. For example, a 2 × 2 × 2 supercell containing 64 $Mg_2SiO_4$ formula units, the same hydration level, *i.e.*, 1.65 wt% $H_2O$, would consist of 8 Mg site vacancies and 16 hydroxyls. If only a single silanol was formed, with the remaining protons located on the preferential O1 sites, this structural model would exhibit a 15:1 ratio of Mg–OH to Si–OH environments, meaning silanol groups would only contribute 6.25% of protonation, compared to 50% in the single unit cell discussed above. In addition, as the Mg–OH to Si–OH ratio increases (*i.e.*, O1 site protonation dominates), there would also be an

entropy increase associated with the formation of a silanol group. This suggests that despite having a high enthalpy penalty in the structural models presented in this study, silanol defects could contribute make up a small proportion of overall protonation in semi-hydrous wadsleyite structures dominated by Mg–OH (protonated O1) environments. The presence of a small proportion of silanol groups *i.e.*, silanol defects within a sea of Mg–OH groups in semi-hydrous wadsleyite agrees with several studies,[43,45] including the multinuclear NMR investigation of Griffin *et al.*.[46]

The calculated $^{1}$H, $^{2}$H, $^{17}$O and $^{29}$Si NMR parameters for the 103 semi-hydrous wadsleyite structures are presented, with the hope that these predicted measurements will help to interpret the previously published experimental NMR spectra for a sample of almost fully-hydrous wadsleyite.[46] Figure 6.14 shows plots of the variation in $^{1}$H $\delta_{iso}$ and $^{2}$H $C_Q$ as a function of the covalent hydroxyl (H–O) or hydrogen (O···H) bond length, with strong correlations seen in all four plots, agreeing with studies that have previously identified strong relationships between these geometrical and NMR parameters.[67,80–82] Figure 6.14a shows that increased H–O bond length results in an increase (*i.e.*, downfield shift) in $^{1}$H $\delta_{iso}$, with the reverse relationship observed in Figure 6.14b, where a decrease in the hydrogen bond length (indicating that the hydroxyl bond length has increased) leads to an increase in $^{1}$H $\delta_{iso}$. Similarly, Figure 6.14c indicates that $^{2}$H $C_Q$ is strongly dependant on the interatomic distances between H and the two nearest O species, *i.e.*, the hydroxyl and hydrogen bond distances. Figures 6.14c and 6.14d indicate that an increase in the hydroxyl bond length (and therefore a decrease in the hydrogen bond length) results in a decrease in $^{2}$H $C_Q$. The five points that lie slightly below the trendline in Figure 6.14c represent proton environments in structural models with high $\Delta H$ ($\Delta H > 1.1$ eV) where the hydroxyl bonds are orientated away from the Mg3 vacancy, *i.e.*, pointing towards O species not within the octahedron directly surrounding the cation site vacancy.

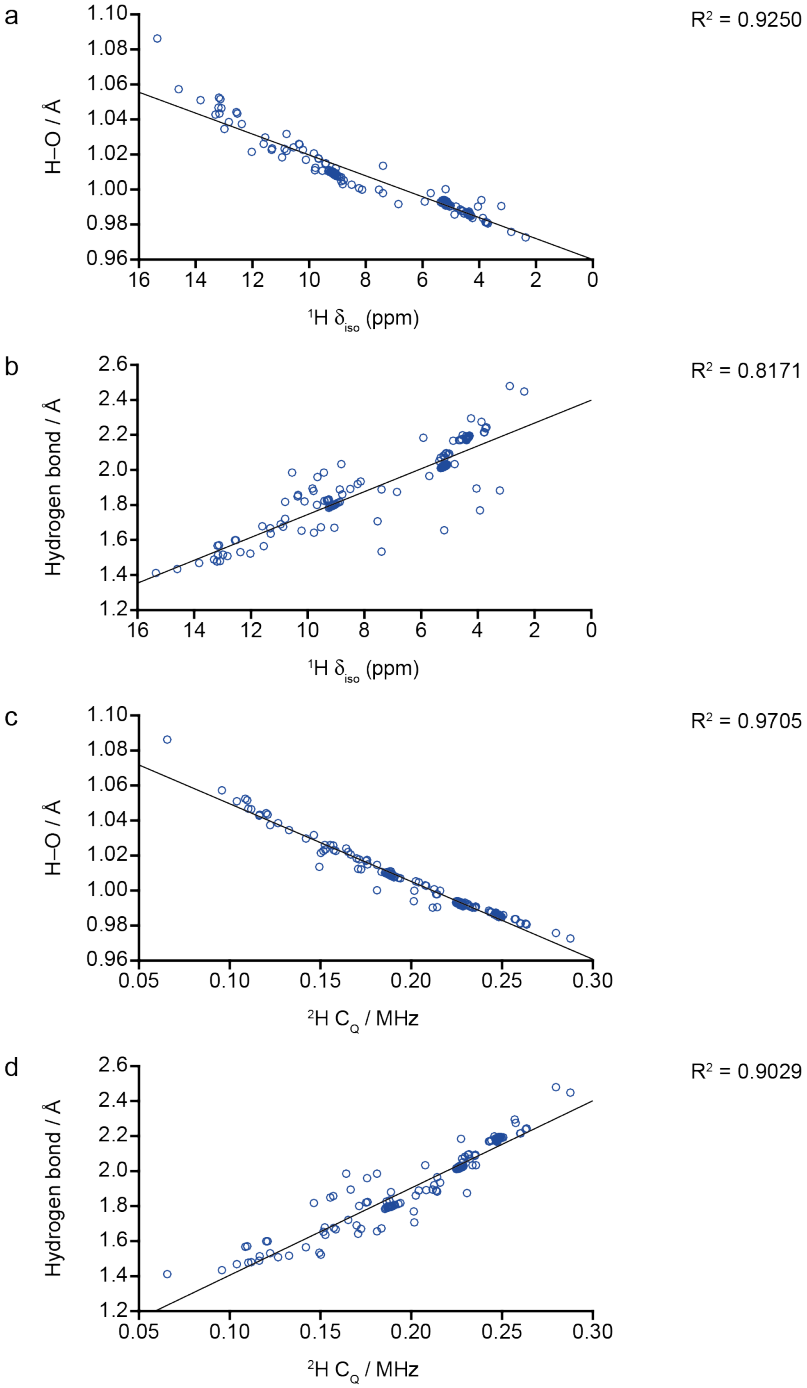


**Figure 6.14:** Plot of calculated (a and c) H–O bond length and (b and d) hydrogen-bond (H-bond) length, against (a and b) $^{1}H$ $\delta_{iso}$ and (c and d) $^{2}H$ $C_Q$ for the 103 fully-optimised semi-hydrous wadsleyite structural models.

As shown in Figure 6.15, once the data points from the plots of hydroxyl bond length against either $^{1}H$ $\delta_{iso}$ or $^{2}H$ $C_Q$ (see Figures 6.14a and 6.14c) are coloured according to the general type of hydroxyl environment (*i.e.*, Mg–

OH or Si–OH), it is apparent that each results in reasonably well-defined regions of $^{1}H$ $\delta_{iso}$ and $^{2}H$ $C_Q$. In general, Mg–OH hydroxyls, formed by the protonation of O1 species, exhibit calculated $^{1}H$ $\delta_{iso}$ values below 6 ppm and $^{2}H$ $C_Q$ values above 0.2 MHz, with the only exceptions to this resulting from protonated O1 sites in structures with very high ΔH. In contrast, silanol hydroxyls tend to exhibit larger $^{1}H$ $\delta_{iso}$ and smaller $^{2}H$ $C_Q$ values, with significantly wider ranges in both parameters seen for these hydroxyl environments. From Figure 6.15b it is also clear that all five of the data points that lie below the trendline in Figure 6.14c are caused by high enthalpy structures, exhibiting a H–O1 hydroxyl bond that is orientated away from the Mg3 vacancy (see Figure 6.15c).

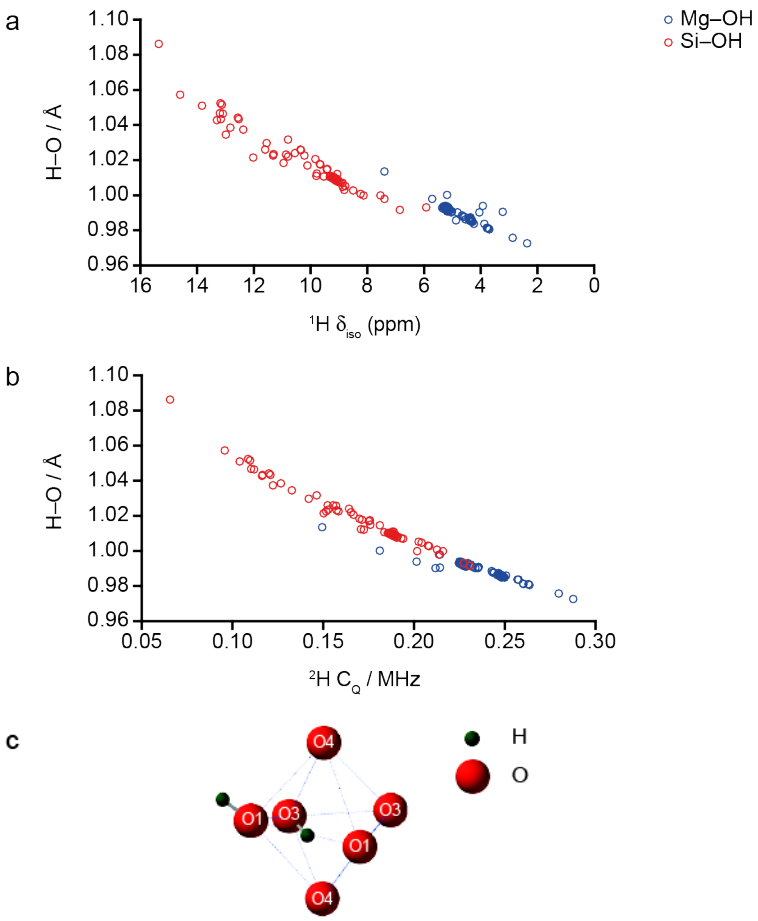


**Figure 6.15:** Plot of calculated H–O bond length against (a) $^{1}H$ $\delta_{iso}$ and (b) $^{2}H$ $C_Q$ for the 103 fully-optimised semi-hydrous wadsleyite structural models, with the data points coloured by chemical type of hydroxyl. (c) Representative high enthalpy structural model containing an O1 hydroxyl group that is orientated away from the Mg vacancy.

Figures 6.16a and 6.16b show the data plotted in Figures 6.14a and 6.14c, respectively, with the data points in each now coloured by the specific site of protonation site rather than the general chemical type of hydroxyl environment (see Figure 6.15). From Figure 6.16, it is clear that while protonated O1 sites tend to result in $^{1}H$ $\delta_{iso}$ and $^{2}H$ $C_Q$ with reasonably well-defined ranges, making it fairly simple to separate Mg–OH from Si–OH environments based on these NMR parameters, the same cannot be said for protonation of the individual O sites within the pyrosilicate unit. Both Figure 6.16a and 6.16b show that there is significant overlap between the hydroxyl bond lengths, $^{1}H$ $\delta_{iso}$ and $^{2}H$ $C_Q$ values for H located on O3 and O4 sites; overlap that prevents these protonation of these two hydroxyl sites from being clearly distinguished by their respective NMR parameters. The only apparent difference between O3 and O4 hydroxyls is that the H–O3 bond length tends to be slightly shorter (as discussed above), meaning that H bonded to O3 species tend to have slightly smaller $^{1}H$ $\delta_{iso}$ and slightly larger $^{2}H$ $C_Q$ values relative to H located on O4 sites.

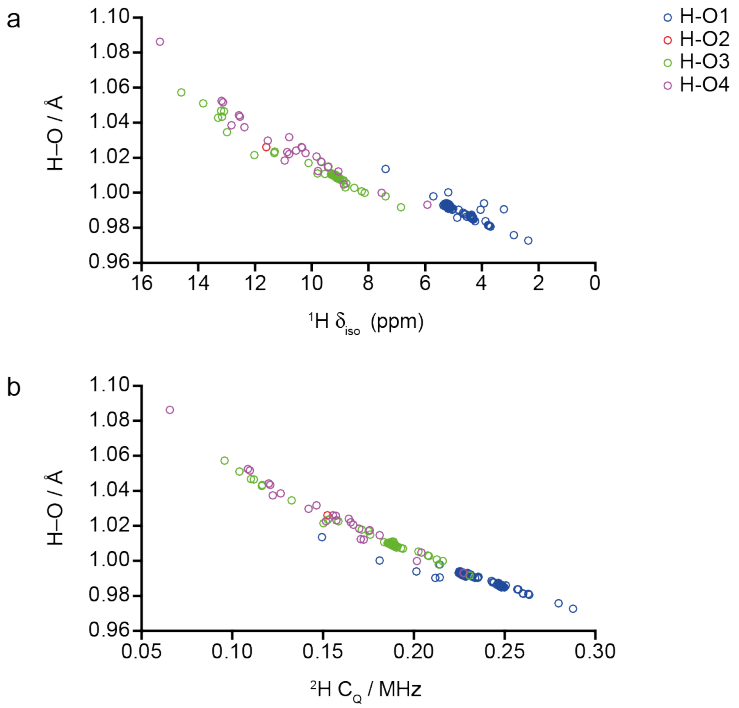


**Figure 6.16:** Plot of calculated H–O bond length against (a) $^{1}H$ $\delta_{iso}$ and (b) $^{2}H$ $C_Q$ for the 103 fully-optimised semi-hydrous wadsleyite structural models, with the data points coloured by the O site at which protonation occurs.

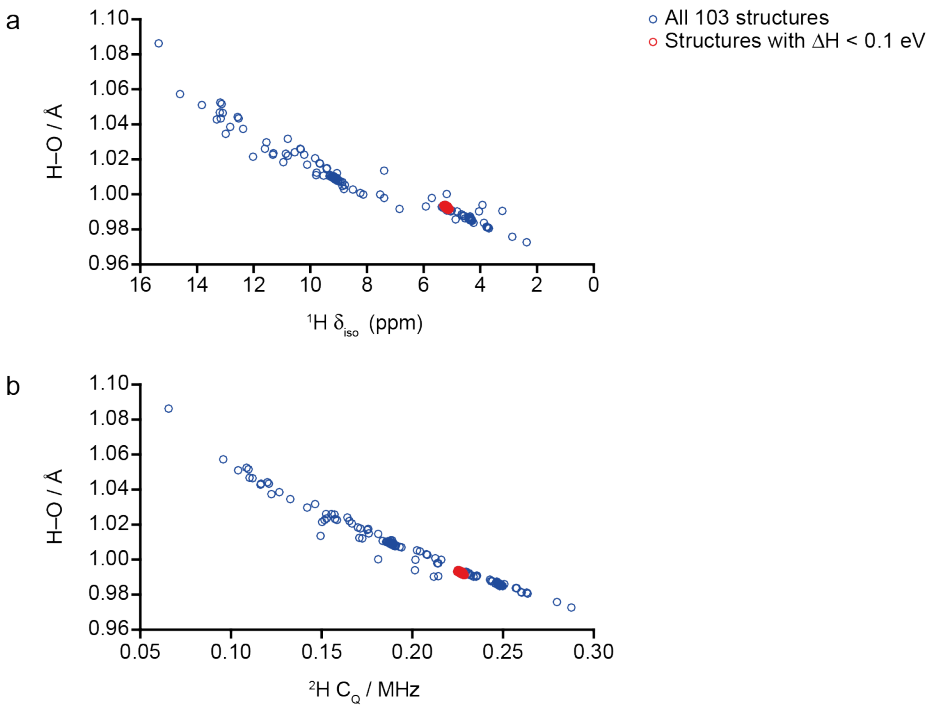


**Figure 6.17:** Plot of calculated H–O bond length against (a) $^{1}H$ $\delta_{iso}$ and (b) $^{2}H$ $C_Q$ for the 103 fully-optimised semi-hydrous wadsleyite structural models, with the data points coloured by a cut off in ΔH. The blue data points represent all 103 structures, *i.e.*, where no ΔH is applied, whereas the red data points represent only the structures with ΔH < 0.1 eV, *i.e.*, the structures that resemble motif **1**.

While the $^{1}H/^{2}H$ NMR parameters for all 103 fully-optimised semi-hydrous wadsleyite structures result in strong correlations between both $^{1}H$ $\delta_{iso}$ and $^{2}H$ $C_Q$ and the hydroxyl bond length, as shown in Figure 6.1, a very different picture results when only the data points corresponding to the structures that adopt the lowest enthalpy protonation arrangement, motif **1**, *i.e.*, structures with ΔH < 0.1 eV are considered. Figure 6.17a shows that all protons in structural models that resemble motif **1**, where H are covalently bonded exclusively to O1 species, have $^{1}H$ $\delta_{iso}$ values of ~5 ppm, whereas Figure 6.17b indicates that all calculated $^{2}H$ $C_Q$ values for these low enthalpy structures are ~0.23 MHz.

Figure 6.18 shows the calculated hydroxyl bond length plotted separately against $^{1}H$ $\delta_{iso}$ and $^{2}H$ $C_Q$, with the blue data points representing the entire set of 103 fully-optimised semi-hydrous structures and the red data points

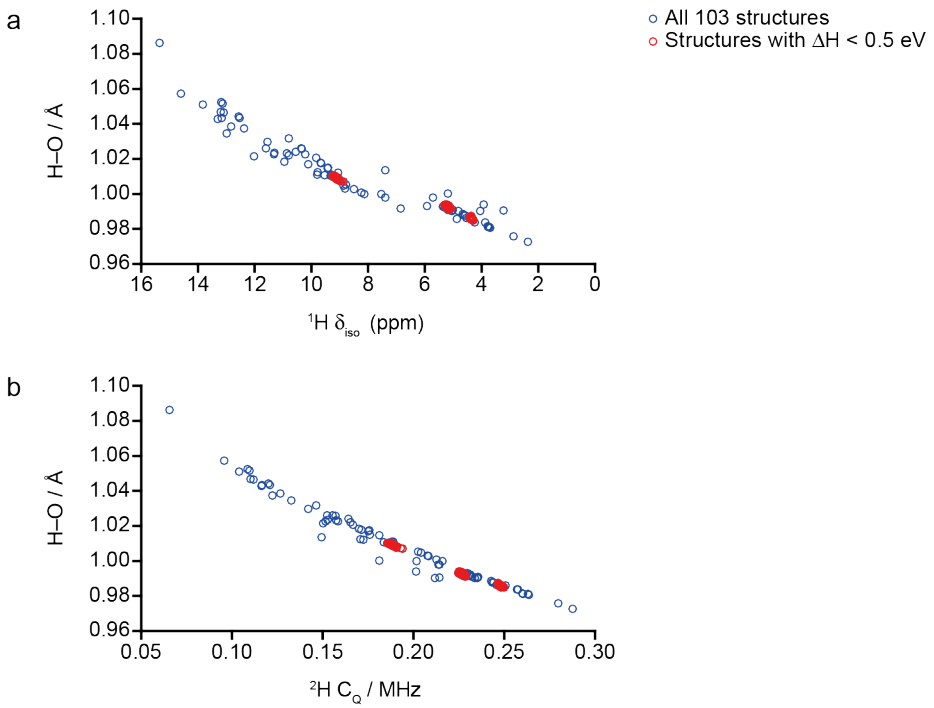


**Figure 6.18:** Plot of calculated H–O bond length against (a) $^{1}$H $\delta_{iso}$ and (b) $^{2}$H $C_Q$ for the 103 fully-optimised semi-hydrous wadsleyite structural models, with the data points coloured by a cut off in ΔH. The blue data points represent all 103 structures, *i.e.*, where no ΔH is applied, whereas the red data points represent only the structures with ΔH < 0.5 eV, *i.e.*, the structures that resemble motifs **1** and **2**.

corresponding to the structures with ΔH < 0.5 eV. This restriction results in a subset of structures that only represent either motifs **1** or **2**, meaning only protonated O1 and O3 sites are present. From Figure 6.18a, the protons in these structural models containing motifs **1** and **2** are split into three distinct clusters of data points with $^{1}$H $\delta_{iso}$ values of approximately 9, 5 and 4 ppm. Based on Figure 6.17, the O1 site hydroxyls in motif **1** are known to exhibit $^{1}$H $\delta_{iso}$ of ~5 ppm, meaning that the remaining two clusters of red points at ~9 and ~4 ppm represent the H–O3 and H–O1 hydroxyls, respectively, in the metastable motif **2** structures. The considerable difference between the bond lengths of O1 and O3 hydroxyls (H–O1 < H–O3) in the motif **2** structures results in a ~5 ppm change in $^{1}$H $\delta_{iso}$, allowing the H–O1 and H–O3 environments to be distinguished. This large chemical shift difference is a result of the change in hydrogen and hydroxyl bond lengths (decreasing and increasing, respectively), from those in structural models containing motif **1**.

The higher $^{1}$H $\delta_{iso}$ seen for protons bonded to O3 species has previously been observed experimentally,[46] although (owing to the very small number of manually chosen structural models used in the previous work) the resonance in question (with $^{1}$H $\delta_{iso}$ = 6.7 ppm) was not explicitly assigned to O3 site hydroxyls, but merely to Si–OH groups in general. The three clusters of data points in Figure 6.18a at ~9, ~5 and ~4 ppm can be attributed to three of the resonances in the $^{1}$H MAS NMR spectrum of wads-H (see Figure 6.5a) with $^{1}$H $\delta_{iso}$ of 6.7, 3.4 and 1.1 ppm,[46] respectively.

Although a good qualitative agreement is observed between computation and experiment, the values of the predicted $^{1}$H $\delta_{iso}$ for the three hydroxyl environments described above do not agree exactly with those observed experimentally for wads-H.[46] A potential explanation for this is the differing hydration levels in the calculations (1.65 wt% $H_2O$) and experiment (~3 wt% $H_2O$), with previous work indicating that varying hydration level can affect the preferential protonation sites (and potentially their chemical shifts).[45] It is also possible that limitations in the accuracy of the DFT approach employed, specifically the $E_{XC}$ functional and the pseudopotentials used, contribute to the differences observed between experimental and predicted $^{1}$H $\delta_{iso}$ values. The method used to determine the referencing shielding could also be contributing to the level of agreement between the predicted $^{1}$H $\delta_{iso}$ for the H–O1 hydroxyls in motif **1** and the H–O1/H–O3 hydroxyls in motif **2**, as the predicted $^{1}$H chemical shifts for the 103 fully-optimised structural models span a much larger range than is seen experimentally, and appear offset (*i.e.*, at a higher $^{1}$H $\delta_{iso}$) relative to the experimental $^{1}$H measurements. In an attempt to improve the comparison between predicted and experimental $^{1}$H $\delta_{iso}$ values, an alternative (and hopefully more relevant) reference shielding approach is used in subsequent investigations (see Section 6.6.3). Although the $^{1}$H $\delta_{iso}$ for the three clusters of red data points in Figure 6.18a do not overlay precisely with the three experimental NMR resonances, the qualitative agreement is still reasonable. As a result, based on the strong linear relationship between calculated H–O bond length and $^{1}$H $\delta_{iso}$, and on

the observation that O4 site hydroxyls tend to, in general (and especially when structures with very high ΔH are not considered), have longer bond lengths than H–O3 hydroxyls, the fourth, and least intense resonance in the $^{1}$H MAS NMR spectrum of wads-H reported by Griffin *et al.*,[46] with $^{1}$H $\delta_{iso}$ = 8.6 ppm (see Figure 6.5a), can then be tentatively assigned to H–O4 hydroxyls.

In an attempt to more clearly distinguish between H–O3 and H–O4 hydroxyls, the calculated $^{17}$O NMR parameters for the 103 fully-optimised structural models were also considered, with a plot of $^{17}$O $C_Q$ against $^{17}$O $\delta_{iso}$ for the protonated O species, with the data points coloured by O site, is shown in Figure 6.19a. This shows that protonated O1 species exhibit the lowest (*i.e.*, most upfield) calculated $^{17}$O $\delta_{iso}$ and the largest $C_Q$. The five blue data points with $^{17}$O $\delta_{iso}$ > 40 ppm result from hydroxyl bonds orientated away from the Mg3 vacancy (see Figure 6.15c). While there is a clear difference in $^{17}$O $\delta_{iso}$ between Mg–OH and Si–OH environments, the ranges of $^{17}$O NMR parameters for the three silanol O species (H–O2, H–O3 and H–O4, respectively) are far more overlapped. From Figure 6.19b, a plot of calculated $^{17}$O $C_Q$ against $^{17}$O $\delta_{iso}$ for all protonated and non-protonated O species in the 103 structures, it can be seen that irrespective of O site, protonation leads to an increase in $^{17}$O $C_Q$, with this change being most noticeable for O1 species, where $C_Q$ increases from ~1-2 to ~5-8 MHz upon protonation. Protonation also leads to Mg–OH groups exhibiting a large upfield shift in $^{17}$O $\delta_{iso}$ relative to non-protonated O1 species. The significant increase in $^{17}$O $C_Q$ and upfield shift in $\delta_{iso}$ that results from protonation suggests that only O1 site hydroxyls contribute to the broad resonance in the $^{17}$O MAS NMR spectrum of wads-H shown in Figure 6.6a, with all silanol environments exhibiting much higher (more downfield) $^{17}$O $\delta_{iso}$ values.

Plots of $^{1}$H $\delta_{iso}$ against $^{17}$O $\delta_{iso}$ for the 103 semi-hydrous wadsleyite structures are shown in Figure 6.20, with Figure 6.20a showing that the two chemical

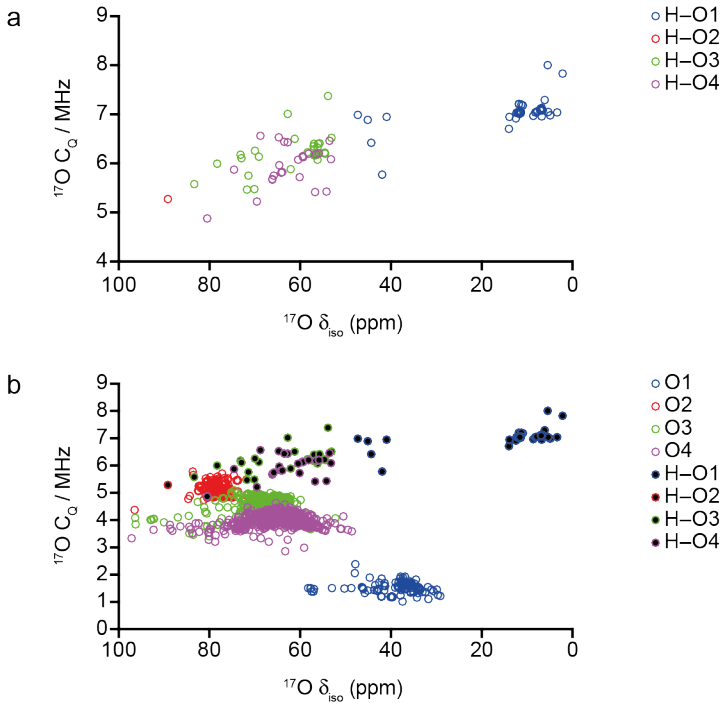


**Figure 6.19:** Plot of calculated $^{17}$O $C_Q$ against $^{17}$O $\delta_{iso}$ for (a) hydroxyl O species only, and (b) all protonated and non-protonated O species for the 103 fully-optimised semi-hydrous wadsleyite structural models, with the data points coloured by O environment.

types of hydroxyl environment, *i.e.*, Mg–OH and Si–OH have distinct parameters. However, when, as in Figure 6.20b, the data points are coloured by specific protonation site, significant overlap between both the $^{1}$H and $^{17}$O $\delta_{iso}$ values for O3 and O4 hydroxyls is observed, indicating that confident distinction of these two silanol environments is not possible. From Figure 6.20c, where the shape and colour of the data points denote the protonation site and $\Delta H$ of the structure, respectively, it is clear that when all 103 structures are considered, the ranges in $^{1}$H and $^{17}$O $\delta_{iso}$ are much larger than those seen experimentally.[46] However, when only structures with $\Delta H < 1.0$ eV (denoted by blue data points) are considered, the ranges observed for both $^{1}$H and $^{17}$O $\delta_{iso}$ decrease significantly.

The calculated $^{29}$Si NMR parameters for the 103 semi-hydrous wadsleyite structures were also considered, with Figure 6.21 showing plots of $^{1}$H $\delta_{iso}$ against $^{29}$Si $\delta_{iso}$ for all H–Si interatomic distances less than 4.0 Å, with the data

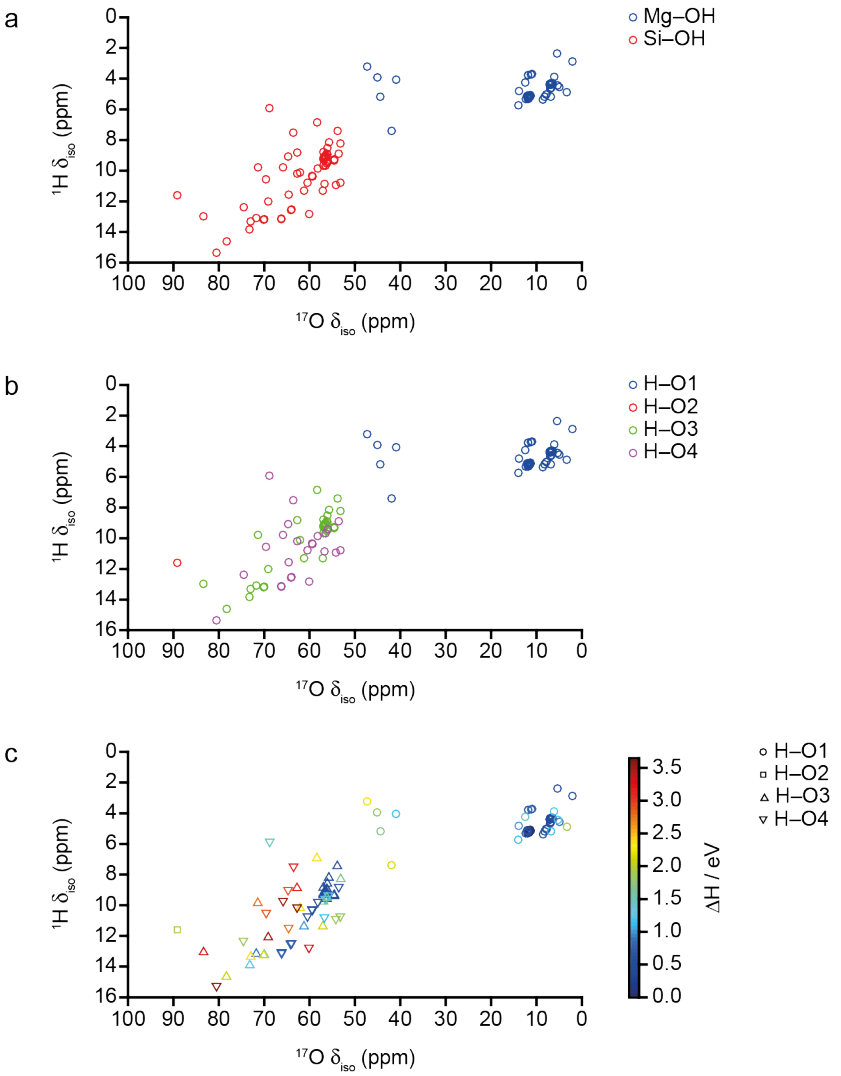


**Figure 6.20:** Plot of calculated $^{1}$H $\delta_{iso}$ against $^{17}$O $\delta_{iso}$ for all 103 fully-optimised semi-hydrous wadsleyite structural models, with the data points coloured by (a) chemical type of hydroxyl, (b) the O site at which protonation occurs, and (c) ΔH, with the data points shaped by the O site at which protonation occurs).

points coloured by the chemical type of hydroxyl (*i.e.*, Mg–OH or Si–OH) environment. In Figure 6.21a, where the $^{1}$H and $^{29}$Si $\delta_{iso}$ for all 103 structures are considered, significant scatter is observed. However, in Figure 6.21b, where only structures with ΔH < 0.1 eV (*i.e.*, those that resemble motif **1**) are considered, the data points fall into three distinct clusters, with $^{1}$H $\delta_{iso}$ ≈ 5 ppm and $^{29}$Si $\delta_{iso}$ ≈ –77.5, –78.5 and –79.5 ppm, respectively, corresponding to H located on O1 sites (Mg–OH groups), interacting with three different Si in nearby pyrosilicate units, which supports the assignment made by

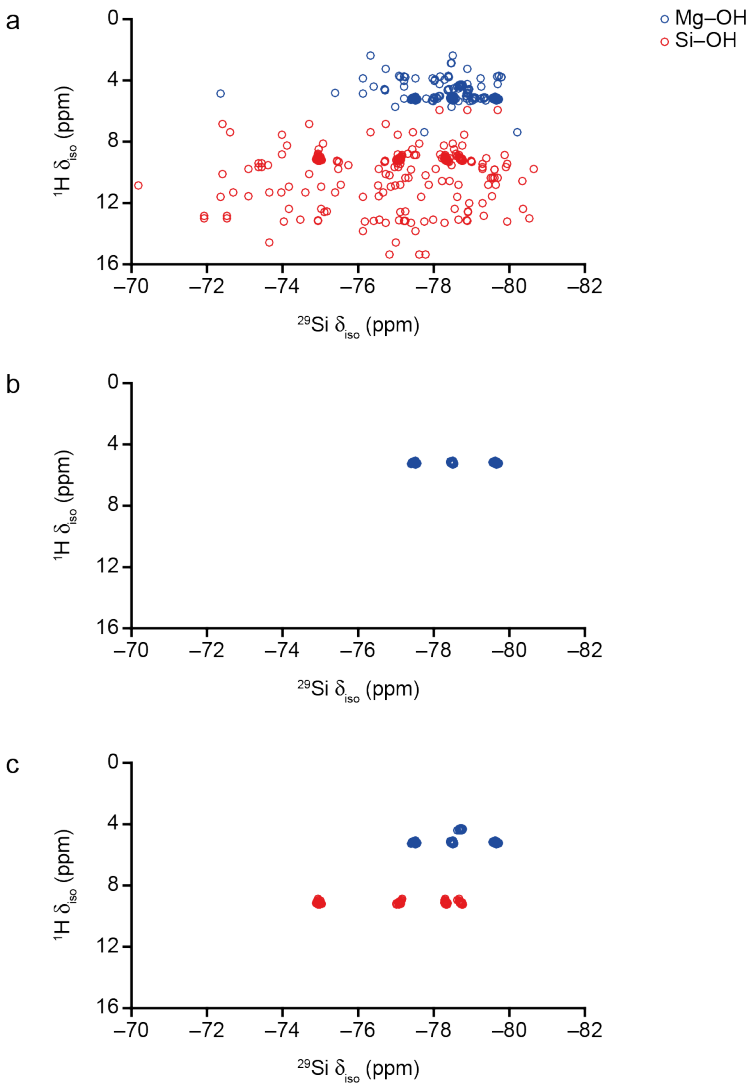


**Figure 6.21:** Plot of calculated $^{1}$H $\delta_{iso}$ against $^{29}$Si $\delta_{iso}$ for (a) all 103 fully-optimised semi-hydrous wadsleyite structural models, with the data points coloured by chemical type of hydroxyl. Only $^{1}$H-$^{29}$Si correlations between H and Si with interatomic distances (H–Si) less than 4.0 Å are shown, with a ΔH cut-off of (b) 0.1 eV and (c) 0.5 eV applied.

Griffin *et al.*[46] of the intense correlation peaks in the $^{1}$H-$^{29}$Si CP HETCOR NMR spectrum of wads-H, shown in Figure 6.8c. In Figure 6.21c, only the $^{1}$H and $^{29}$Si $\delta_{iso}$ for structures with $\Delta H < 0.5$ eV (corresponding to structures resembling motifs **1** and **2**), are shown. The inclusion of motif **2** leads to the appearance of five additional clusters. The data points at $^{1}$H $\delta_{iso} \approx 4$ ppm correspond to the H–O1 hydroxyls in motif **2** structures, while the cluster of points at $^{1}$H and $^{29}$Si $\delta_{iso} \approx 9$ ppm and –75 ppm, respectively, corresponds to H–O3 protons in the same motif **2** structures, correlating to Si less than 2.5 Å

away, meaning this is a correlation between neighbouring H and Si in the same silanol group. The chemical shifts observed for this cluster indicate that as the H–Si interatomic distance decreases, both $^{1}$H and $^{29}$Si $\delta_{iso}$ increase, in agreement with observations made previously by Griffin *et al.*[46] The three clusters at $^{1}$H $\delta_{iso} \approx 9$ ppm and $^{29}$Si $\delta_{iso} \approx -77.0$, –78.3 and –78.7 ppm, respectively, represent correlations between $^{1}$H in Si–OH groups (H–O3 hydroxyls) and non-protonated Si species in nearby pyrosilicate units. It should be noted that these correlation peaks are not observed in the spectra in Ref. 46 (at least at the contour levels shown).[46] It is possible that this is due to differences in the relaxation parameters for the different hydroxyl environments, with evidence in the literature suggesting that due to fast $T_{1\rho}$ relaxation, silanol environments in minerals are often underrepresented in NMR spectra.[70,83]

AIRSS and first-principles calculations of NMR parameters have been used to generate, and subsequently analyse 819 semi-hydrous Fe-free wadsleyite structures containing a Mg3 vacancy. The structures with the lowest ΔH, represented by motif **1**, contain two protonated O1 sites, with the hydroxyl bonds orientated along the O1···O4 edge of the vacant Mg3 octahedron, in agreement with previous studies.[38,40,43,44,46] Structures that are represented by motifs **2** or **3**, which contain a single silanol group exhibit higher ΔH, with those containing no O1 site hydroxyls (*i.e.*, no Mg–OH groups), such as motif **4**, even less enthalpically stable. Although the NMR parameters for only a subset of 103 structures were calculated, the agreement with the experimental NMR measurements for wadsleyite containing ~3 wt% $H_2O$[46] has proved sufficiently good to allow tentative assignment of several spectral resonances. Calculated $^{1}$H $\delta_{iso} > 6$ ppm appear to be a result of the increased hydroxyl bond length exhibited by silanol hydroxyls compared to H–O1 species. The calculated $^{1}$H $\delta_{iso}$ was used to assign the most intense resonance in the $^{1}$H MAS NMR spectrum of wads-H (see Figure 6.5a), with $^{1}$H $\delta_{iso} \approx 3.4$ ppm to H–O1 hydroxyls, with the resonances at 6.7 and 8.6 ppm tentatively assigned to hydroxyls on O3 and O4, respectively.

While the low enthalpy structures identified in this study *i.e.*, the structures that adopt motifs **1**-**3**, allow the $^{1}$H MAS NMR spectrum of wads-H to be understood and assigned reasonably well, these three motifs do not account for all of the correlations present in the $^{1}$H DQ MAS NMR spectrum of wads-H (see Figure 6.5b). Although a hydrous wadsleyite phase comprised of motifs **1**-**3** will result in H–O1/H–O1, H–O1/H–O3 and H–O1/H–O4 correlations, which based on the assignment of Figure 6.5a, appear to be present in Figure 6.5b, correlations between two silanol hydroxyls, *i.e.*, H–O3/H–O3, H–O3/H–O4 or H–O4/H–O4 hydroxyls, are only observed in the structures with higher ΔH structures. This suggests that a hydrous wadsleyite comprised solely of the three lowest motifs identified in this study does not agree with all of the information provided by the $^{1}$H DQ MAS NMR spectrum of wads-H,[46] indicating that, either, a change in hydration level has a significant effect on the structure of hydrous wadsleyite (as suggested by Kohn *et al.*[45]), or, that the current structural picture obtained in this work is incomplete.

### 6.6.3 Mg1, Mg2 and Mg3 vacant structural models

The investigation discussed in the previous section undoubtedly provides new insights into the structure of hydrous wadsleyite, yet still represents a study with rather limited scope. In this section, a more extensive expansive AIRSS-based study of this system is presented, in which all the AIRSS-generated semi-hydrous structures containing a Mg1, Mg2 or Mg3 vacancy (see Section 6.6.1) are considered. Rather than using ΔH to select a subset of structures for further analysis (which can introduce bias, with the selection scheme discussed in Section 6.6.2 leading to the overrepresentation of structures with low ΔH), here a *k*-means clustering approach, as implemented in the Soprano Python library,[61] was used. This approach involved using a set of parameters, termed "genes" to divide a dataset (*i.e.*, a series of structures) into *k* groups, or "clusters", each comprised of members which are determined to be similar according to a normalized set of general (*i.e.* ΔH) and system-specific genes. In an iterative process, *k* data points are

first chosen at random and neighbouring data points (neighbouring in *n*-dimension vector space) become members of those clusters, after which the central data point of each cluster is set to that closest to the cluster mean and the cluster members refined according to their distances from the mean data point. In this case, the end goal of *k*-means clustering is to separate the AIRSS-generated structures into *k* sets of similar structures, from which one representative can be identified for further study, without the need to consider the remaining cluster members. The specific genes used to cluster the AIRSS-generated structures in this work were ΔH (relative to the lowest enthalpy semi-hydrous wadsleyite structure with a Mg3 vacancy); hydroxyl O type; Mg vacancy type; H–H interatomic distance; H–vacancy distance; hydroxyl (H–O) bond length; hydrogen bond length and the magnitude of the combined hydroxyl orientation vector, $\left\|\overrightarrow{\mathrm{OH}}\right\|$. This last parameter is defined as the sum of unit vectors placed along the two hydroxyls bonds, leading to values between 0 and 2, with the two extremes representing anti-parallel and parallel hydroxyl bonds, respectively. A detailed description of the *k*-means clustering approach used to select the subset of semi-hydrous wadsleyite structures for more detailed study is given in Appendix D2. Using this approach, of the original 1287 semi-hydrous wadsleyite structures, a total of 88 structures were selected for further study, consisting of 32, 7 and 49 with a Mg1, Mg2 and Mg3 vacancy, respectively.

Prior to the calculation of NMR parameters, all 88 structures were geometry optimised using a higher level of accuracy, after which they are considered "fully optimised". All first-principles calculations were performed using CASTEP 8.0, with $E_{cut}$ of 60 Ry and a k-point spacing of 0.04 $2\pi$ Å$^{-1}$ (see Appendix D1 for convergence testing), the PBE $E_{XC}$ functional,[76] the default ultrasoft pseudopotentials,[77] a `geom_energy_tol` value of $1 \times 10^{-5}$ eV / atom, an `elec_energy_tol` value of $1 \times 10^{-9}$ eV / atom, the TS SEDC scheme[84] and with the ZORA correction applied.[85,86] The position of H, Mg, Si and O atoms, and the unit cell dimensions were allowed to vary during the geometry optimisation. A description of the referencing procedure used for $^{1}$H, $^{17}$O and

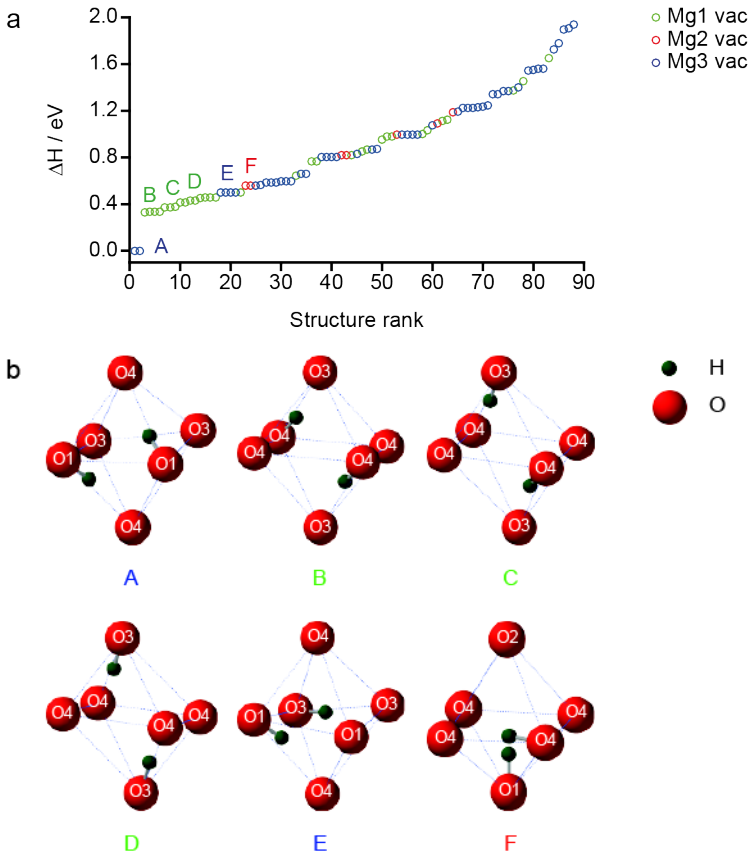


**Figure 6.22:** (a) Plot showing the relative enthalpy (ΔH) of the 88 semi-hydrous wadsleyite structural models following the second geometry optimisation, with the data points coloured by Mg site vacancy. (b) Representative structures of the six lowest enthalpy protonation motifs (**A**-**F**) with labels coloured by the Mg vacancy.

$^{29}$Si $\sigma_{iso}$, which involved comparing the experimental $\delta_{iso}$ and calculated $\sigma_{iso}$ for hydrous wadsleyite itself (for $^{1}$H), or three polymorphs of $Mg_2SiO_4$ (for $^{17}$O and $^{29}$Si) is given in Appendix D4. In this section, only the magnitude of the $^{2}$H and $^{17}$O $C_Q$ values is considered. Calculated NMR parameters were analysed using in-house Python scripts extending the CCP-NC MagresPython module.[79]

The enthalpy of the 88 semi-hydrous wadsleyite structures (ranked relative to the most enthalpically stable member of this set) is shown in Figure 6.22a, with motifs **A**-**F**, shown in Figure 6.22b, representing the six lowest enthalpy proton arrangements. The structure with the lowest ΔH structure, *i.e.*, motif **A**, consists of two protonated O1 species with hydroxyl bonds aligned

parallel to the O1···O4 edges of the octahedron of O surrounding the Mg3 vacancy, a structure consistent with the ground state identified in Section 6.6.2. Motifs **B**-**D** represent structures with ΔH between 0.3 and 0.4 eV which, as shown in Figure 6.22b, exhibit one of three protonation arrangements surrounding an Mg1 vacancy, Motifs **B**, **C** and **D** each contain two protonated pyrosilicate O sites, specifically, two O4 in **B**, one O3 and one O4 in **C**, and two O3 in **D**, with all hydroxyl bonds orientated parallel to the edges of the octahedron defining the Mg1 vacancy. Motif **E** (ΔH ≈ 0.5 eV) represents structures with O1–H···O4 and O3–H···O3 protonation environments surrounding an Mg3 vacancy. While in Section 6.6.2 (where only structures with a Mg3 vacancy were considered), this proton arrangement was identified as being the semi-hydrous wadsleyite structure with the second lowest enthalpy, here, motifs **B**-**D** all exhibit lower ΔH than **E**. Motif **F** (ΔH ≈ 0.6 eV) represents the most stable structure with an Mg2 vacancy and contains O1 and O4 hydroxyls, the latter of which points towards a neighbouring O4 species. In contrast to all structures with lower ΔH, only one of the hydroxyl bonds in motif **F** is aligned parallel to the O···O edge of the octahedron, with the O1 hydroxyl instead orientated more towards the centre. In motif **F**, the closest O4 to the H–O1 proton is 2.07 Å away, indicating that this environment exhibits a weak hydrogen bonding interaction, which could be contributing to the higher ΔH of this structure. Only one out of the 88 structures contains a protonated O2 species, a structure found to have ΔH ≈ 1.1 eV, with O1 and O2 hydroxyls surrounding a Mg2 vacancy, in contrast to some previous studies,[35,36,45] significant protonation occurring at this site seems unlikely.

Plots of calculated covalent H–O bond length against $^{1}H$ $\delta_{iso}$ and $^{2}H$ $C_Q$ are shown in Figure 6.23, with the data points coloured by the chemical type of hydroxyl environment *i.e.*, Mg–OH or Si–OH in Figures 6.23a and 6.23b, and coloured by the O site at which protonation occurs in Figures 6.23c and

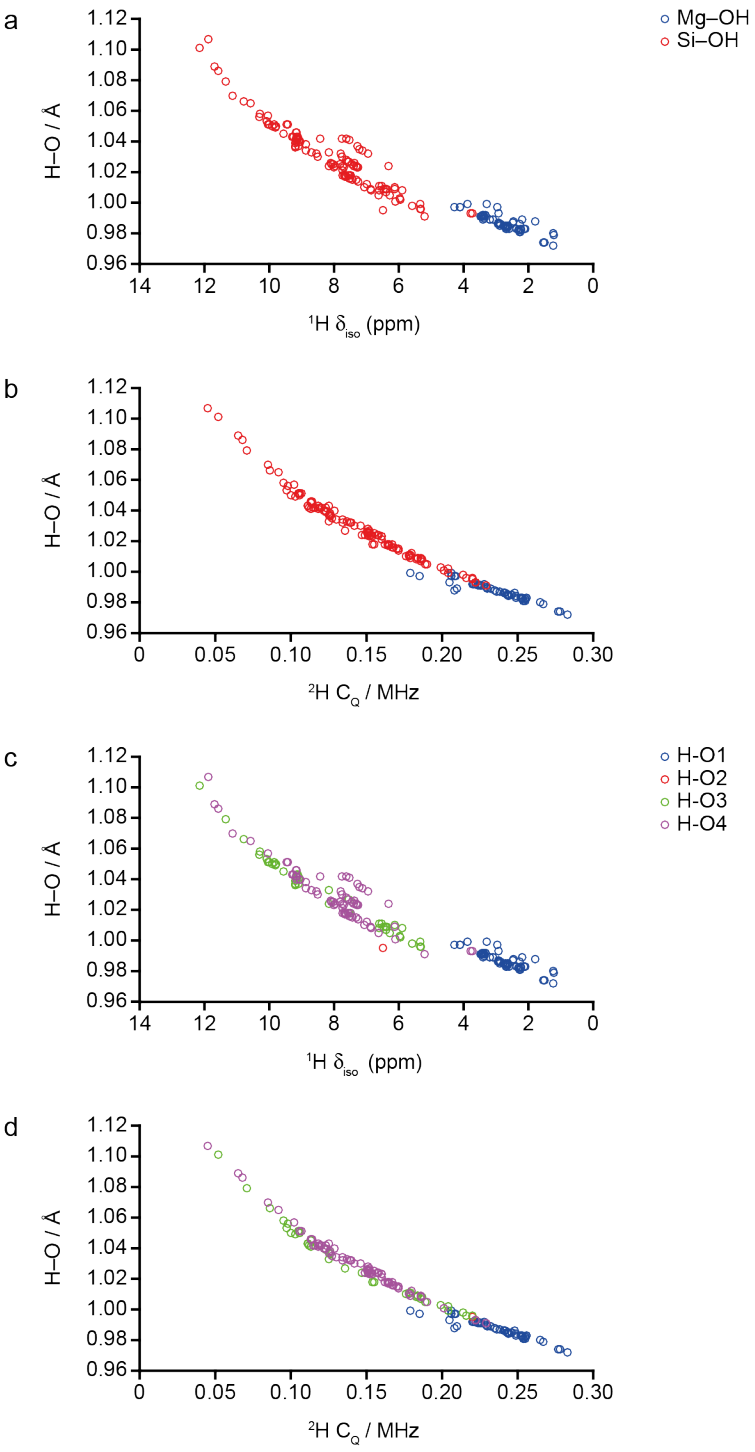


**Figure 6.23:** Plot of calculated H–O bond length against (a and c) $^{1}H$ $\delta_{iso}$ and (b and d) $^{2}H$ $C_Q$ for the 88 semi-hydrous wadsleyite structural models, with the data points coloured by (a and b) chemical type of hydroxyl and (c and d) the O site at which protonation occurs.

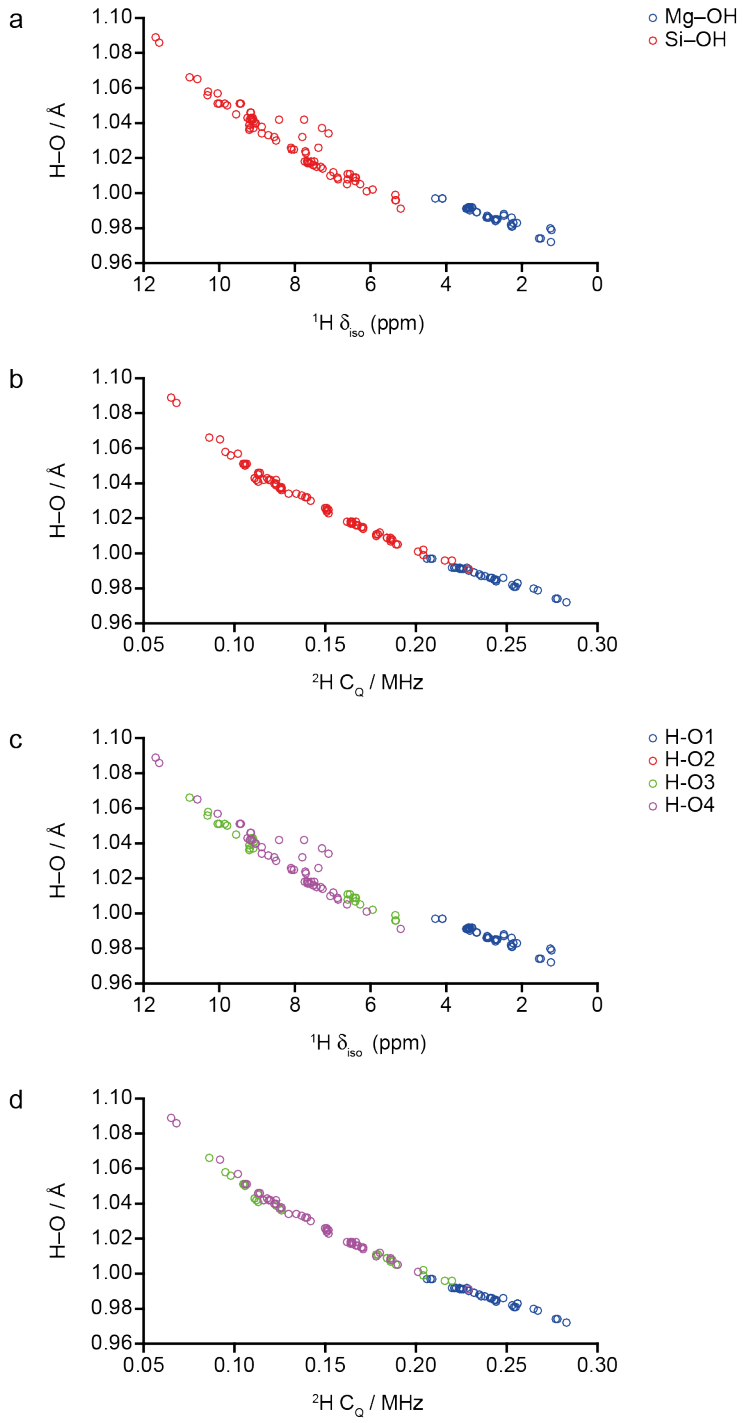


**Figure 6.24:** Plot of calculated H–O bond length against (a and c) $^{1}H$ $\delta_{iso}$ and (b and d) $^{2}H$ $C_Q$ for the semi-hydrous wadsleyite structural models with $\Delta H < 1.0$ eV, with the data points coloured by (a and b) chemical type of hydroxyl and (c and d) the O site at which protonation occurs.

6.23d. As shown in Section 6.6.2, strong correlations are seen in all four plots, with an increase in H–O bond length resulting in an increase in $^{1}H$ $\delta_{iso}$ and a

decrease in $^{2}$H $C_Q$. The NMR parameters for Mg–OH and Si–OH environments appear to exhibit reasonably well-defined ranges, with the former tending to exhibit more upfield shifted $^{1}$H $\delta_{iso}$ and larger $^{2}$H $C_Q$ compared to protons in silanol environments. As shown in Figure 6.24, when only structures with $\Delta H < 1.0$ eV are considered, the separation between Mg–OH and Si–OH environments become more pronounced, with H–O1 protons exhibiting $^{1}$H $\delta_{iso} < 5$ ppm and silanol protons having $^{1}$H $\delta_{iso} > 5$ ppm. In addition, when only the structures with low $\Delta H$ are considered (see Figure 6.24), the overall ranges of calculated $^{1}$H $\delta_{iso}$ and $^{2}$H $C_Q$ values decrease. However, Figures 6.24c and 6.24d show that even when high $\Delta H$ structures are omitted, there is little distinction between H–O3 and H–O4 environments, with both as the $^{1}$H $\delta_{iso}$ and $^{2}$H $C_Q$ ranges showing significant overlap.

As shown in Figure 6.25, a plot of calculated $^{17}$O $C_Q$ against $^{17}$O $\delta_{iso}$ for the 88 structures closely resembles the equivalent plot for the 103 structures with a Mg3 vacancy discussed in Section 6.6.2 (*i.e.*, Figure 6.19b), with protonation of any O site resulting in an increase in $C_Q$ and an upfield shift in $\delta_{iso}$, and with O1 species exhibiting the largest change in NMR parameters upon protonation. The four data points for H–O1 with $^{17}$O $\delta_{iso} > 35$ ppm contain hydroxyl bonds that are orientated away from the Mg vacancy in structures with high $\Delta H$ (see Figure 6.15c). The assertion made in Section 6.6.2, that the

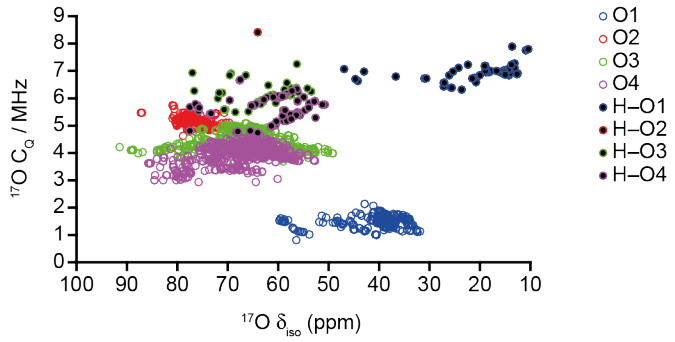


**Figure 6.25:** Plot of calculated $^{17}$O $C_Q$ against $^{17}$O $\delta_{iso}$ for all protonated and non-protonated O in the 88 semi-hydrous wadsleyite structural models, with the data points coloured by O environment.

broad resonance with low intensity in the $^{17}O$ MAS NMR spectrum of wads-H[46] (see Figure 6.6a) can be assigned to protonated O1 species, is supported by Figure 6.24, which shows that the majority of protonated O1 sites have $^{17}O$ $\delta_{iso} < 30$ ppm, with silanols exhibiting much higher $\delta_{iso}$. However, Figure 6.25 indicates that due to the similarities in $^{17}O$ $\delta_{iso}$ and $C_Q$ values for protonated O3 and O4 species, a confident distinction between these two silanol environments is not possible.

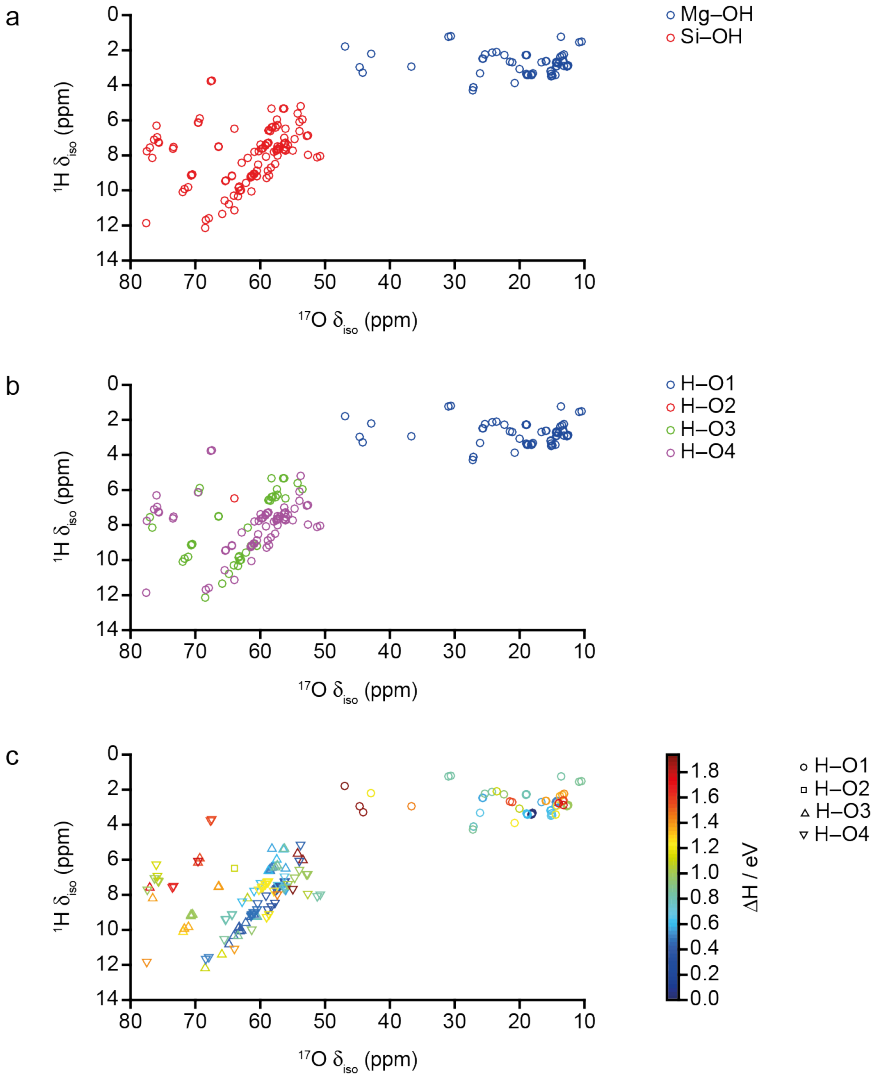


**Figure 6.26:** Plot of calculated $^1H$ $\delta_{iso}$ against $^{17}O$ $\delta_{iso}$ for all 88 semi-hydrous wadsleyite structural models, with the data points coloured by (a) chemical type of hydroxyl, (b) the O site at which protonation occurs and (c) ΔH, with the data points shaped by the O site at which protonation occurs.

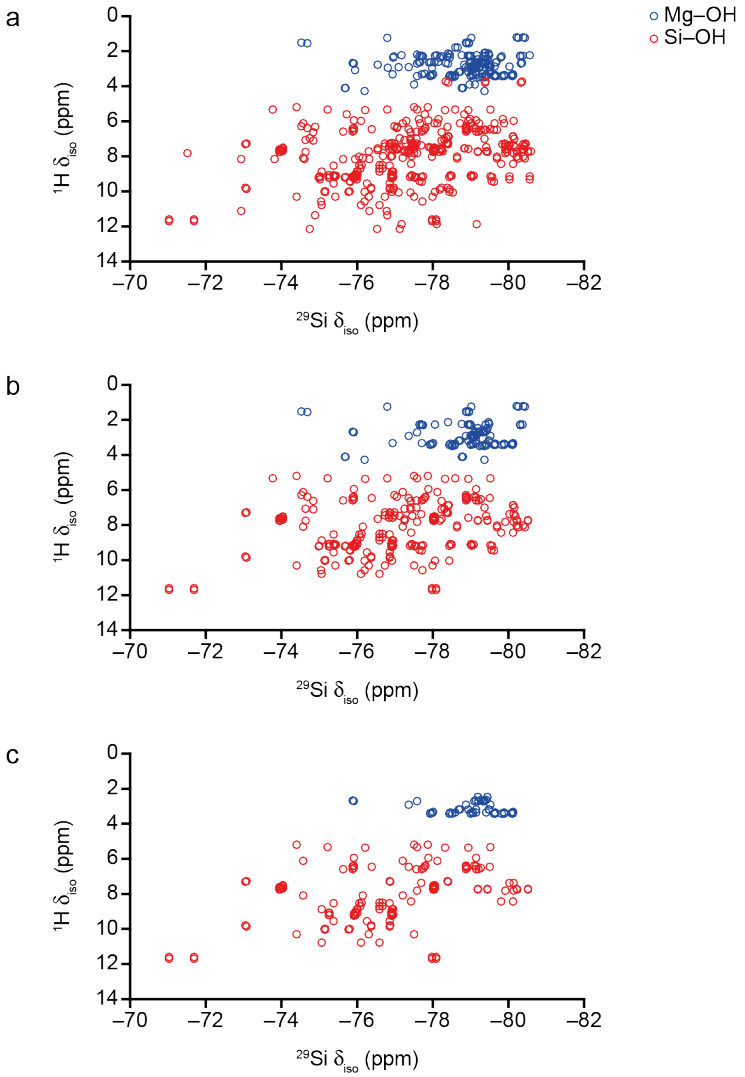


**Figure 6.27:** Plot of calculated $^{1}$H $\delta_{iso}$ against $^{29}$Si $\delta_{iso}$ for (a) all 88 semi-hydrous wadsleyite structural models, with the data points coloured by chemical type of hydroxyl. Only $^{1}$H-$^{29}$Si correlations between H and Si with interatomic distances (H–Si) less than 4.0 Å are shown, with a ΔH cut-off of (b) 1.0 eV and (c) 0.5 eV applied.

Plots of $^{1}$H $\delta_{iso}$ against $^{17}$O $\delta_{iso}$ for the 88 semi-hydrous wadsleyite structures are shown in Figure 6.26, with each bearing a close resemblance to the corresponding plots for the structures discussed in Section 6.6.2 (see Figure 6.20), with Figure 6.26a confirming that Mg–OH and Si–OH environments have well-defined $^{1}$H and $^{17}$O $\delta_{iso}$ ranges. Figure 6.26b indicates that even when the data points are coloured according to protonation site, no clear distinction between O3 and O4 site hydroxyl environments exists, as the $^{1}$H and $^{17}$O $\delta_{iso}$ ranges for these silanol groups are too similar and overlapped.

When, as in Figure 6.26c, the ΔH of structures is also considered, the range of $\delta_{iso}$ observed (especially for $^{17}O$) decreases noticeably. If only structures with ΔH < 1.0 eV are considered, a ~10 ppm range of $^{1}H$ $\delta_{iso}$ (from ~12 to ~2 ppm) is observed, showing reasonable agreement with the shift range seen experimentally,[46] where, as shown in Figure 6.5a, the majority of $^{1}H$ intensity appears between 10 and 0 ppm.

To investigate whether a clearer distinction between different protonation environments is possible, the calculated $^{1}H$ $\delta_{iso}$ values were plotted against $^{29}Si$ $\delta_{iso}$ for the 88 semi-hydrous structures, as shown in Figure 6.27a, with the data points coloured according to general chemical type of hydroxyl environment (*i.e.*, Mg–OH or Si–OH), In Figure 6.27, only $^{1}H$-$^{29}Si$ $\delta_{iso}$ correlations for H–Si interatomic distances less than 4.0 Å are considered. While significant scatter in both $^{1}H$ and $^{29}Si$ $\delta_{iso}$ for the Mg–OH and Si–OH environments (especially for silanol groups) is apparent from Figure 6.27a, where all 88 structures are considered, when only structures with ΔH < 1.0 eV or < 0.5 eV, are considered, as shown in Figures 6.26b and 6.26c, respectively, the degree of scatter is reduced. In Figure 6.27c, the points with $^{1}H$ $\delta_{iso}$ ≈ 3-4 ppm correspond to H in Mg–OH (*i.e.*, H–O1) environments, correlating with Si in surrounding pyrosilicate units. The cluster of points with $^{1}H$ $\delta_{iso}$ > 5 ppm and $^{29}Si$ $\delta_{iso}$ ≈ –74 ppm corresponds to protons in silanol environments, correlating with the nearest Si species, *i.e.*, the closest of the two Si in the same pyrosilicate unit. These correlations show good agreement with the assignment of the $^{1}H$-$^{29}Si$ CP HETCOR spectrum of wads-H made by Griffin *et al.*,[46] as well as with the interpretation of Figure 6.21. The clusters of points with $^{1}H$ $\delta_{iso}$ > 5 ppm and $^{29}Si$ $\delta_{iso}$ < –75 ppm correspond to silanol protons correlating with non-silanol (*i.e.*, Si–O not Si–OH) Si species from adjacent pyrosilicate units. These assignments show that a decrease in H–Si interatomic distance (which is shortest when a silanol group is formed) causes an increase in both $^{1}H$ and $^{29}Si$ $\delta_{iso}$ *i.e.*, both shift downfield.

**Table 6.3:** Calculated $^{1}H$ $\delta_{iso}$ and $\Delta H$ values for motifs **A**-**F**.

| Motif | Mg site vacancy | Protonation site | $^{1}H$ $\delta_{iso}$ (ppm) | $\Delta H$ / eV |
|---|---|---|---|---|
| **A** | Mg3 | O1 | 3.4 | 0.00 |
| | | O1 | 3.4 | |
| **B** | Mg1 | O4 | 8.5 | 0.33 |
| | | O4 | 8.7 | |
| **C** | Mg1 | O3 | 10.8 | 0.37 |
| | | O4 | 8.9 | |
| **D** | Mg1 | O3 | 10.0 | 0.37 |
| | | O3 | 10.0 | |
| **E** | Mg3 | O1 | 2.7 | 0.50 |
| | | O3 | 6.4 | |
| **F** | Mg2 | O1 | 2.5 | 0.56 |
| | | O4 | 7.7 | |

As shown in Figures 6.23b, 6.26c and 6.27b, even when a 1.0 eV $\Delta H$ cut-off is applied, structures still exhibit a calculated range of $^{1}H$ $\delta_{iso}$ range (~12-2 ppm) larger than that seen experimentally (~10-0 ppm).[46] To investigate whether the agreement between calculation and experiment can be improved, a subset containing only the six lowest enthalpy structures, *i.e.*, those containingmotifs **A**-**F,** was considered, with the corresponding $^{1}H$ $\delta_{iso}$ and $\Delta H$ values given in Table 6.3. From analysis of the 103 structures with Mg3 vacancies discussed in Section 6.6.2, the three most intense resonances in the $^{1}H$ MAS NMR spectrum of wads-H,[46] shown in Figure 6.5a, at 3.4, 6.7 and 8.6 ppm result from the protonation of O1, O3 and O4 species, respectively. The H–O1, H–O3 and H–O4 hydroxyls in motif **A**, **B** and **E** (and the H–O4 hydroxyl in motif **C**) exhibit $^{1}H$ $\delta_{iso}$ in agreement with the initial assignment of the $^{1}H$ MAS NMR spectrum. Despite exhibiting similar $\Delta H$ to motif **B**, the $^{1}H$ $\delta_{iso}$ for H–O3 groups in motifs **C** and **D** are shifted significantly downfield relative to the same hydroxyl environment in motif **E**, and have higher $\delta_{iso}$ than the H–O4 groups in motif **B**. This seems to be because H–O3 groups in structures with a Mg1 vacancy, have longer hydroxyl bonds than H–O4 groups surrounding the same vacancy. H–O3 groups in motifs **C** and **D**

exhibit hydroxyl bond lengths greater than 1.05 Å, whereas H–O4 groups surrounding Mg1 vacancies (seen in motifs **B** and **C**) have hydroxyl bond lengths of ~1.03 Å, with H–O3 groups surrounding Mg3 vacancies (present in motif **E**) having even shorter hydroxyl bond lengths, of ~1.01 Å. This shows that when surrounding an Mg1 vacancy the trend in hydroxyl bond lengths is H–O3 > H–O4, this is reversed in structures with a Mg3 vacancy. Similarly, the upfield shift in $^{1}$H $\delta_{iso}$ for the H–O1 hydroxyl in motif **B** (2.7 ppm) relative to that in motif **A** (3.4 ppm), seems to be a result of a decrease in H–O1 bond length, which increases from 0.992 Å in **A** to 0.985 Å in **E**. The H–O4 hydroxyl in motif **F** (lowest enthalpy structure with a Mg2 vacancy) has a $^{1}$H $\delta_{iso}$ of 7.7. ppm, which, based on the assignment of the experimental $^{1}$H MAS NMR spectrum of wads-H,[46] discussed in Section 6.6.2, does not agree with the expected chemical shift of either H–O3 or H–O4 hydroxyls, an indication that this type of structure, *i.e.*, one with a Mg2 vacancy, is not contributing significantly to the $^{1}$H MAS NMR spectrum of wads-H.

### 6.6.4 Summary

This section has explored the use of AIRSS,[56,57] combined with first-principles solid-state NMR parameter calculations to investigate the structure of wadsleyite containing 1.65 wt% $H_2O$, *i.e.*, a hydration level referred to throughout this chapter as semi hydrous. In Section 6.6.2 a subset of 103 semi-hydrous structures with a Mg3 vacancy, selected based on ΔH, were studied, with the ground state structure, *i.e.*, motif **1**, containing two O1–H···O4 hydroxyls. The protonation of a pyrosilicate O site was found to result in a ΔH penalty, with the ΔH of motifs **1**-**3** showing that, in terms of the stability associated with protonation at different sites, the trend O1 > O3 > O4 is observed, with structures containing two silanol (Si–OH) groups, *i.e.*, motif **4**, exhibiting even higher ΔH. Investigating the predicted NMR parameters for the low enthalpy structures also allowed the three resonances in the $^{1}$H MAS NMR spectra of wads-H[46] (see Figure 6.5a) at 3.4, 6.7 and 8.6 ppm, to be tentatively assigned to H–O1, H–O3 and H–O4, respectively. However, while structures represented by motifs **1**-**3** have calculated $^{1}$H $\delta_{iso}$

values that agree reasonably well with many of the resonances in the $^{1}$H MAS NMR spectrum of wads-H, as shown in Figure 6.5b, these structures fail to account for many of the signals seen in the $^{1}$H DQ MAS NMR spectrum of this hydrous wadsleyite sample, indicating that limiting the study to only structures with a single Mg3 vacancy produces a somewhat incomplete description of the true, disordered hydrous wadsleyite system.

In Section 6.6.3 the study into the structure of semi-hydrous wadsleyite was expanded to include AIRSS-generated candidates containing an Mg1, Mg2 or Mg3 vacancy. To increase computational efficiency and avoid choosing multiple structures with the same, or a very similar, proton arrangement, a *k*-means clustering approach, as implemented in the Soprano Python library,[61] was used to identify 88 structures for additional analysis. Following a second, more accurate geometry optimisation, the ground state structure, represented by motif **A**, was found to consist of two O1–H···O4 hydroxyls surrounding an Mg3 vacancy, mirroring the ground state found in Section 6.6.2.

The calculated multinuclear NMR parameters for the 88 structures closely resemble the equivalent values exhibited by the set of 103 structures with a Mg3 vacancy, discussed in Section 6.6.2, with strong correlations between hydroxyl bond length and both $^{1}$H $\delta_{iso}$ and $^{2}$H $C_Q$ observed. The two general groups of hydroxyls, *i.e.*, Mg–OH and Si–OH were easily distinguishable, with both exhibiting reasonably well-defined ranges of $^{1}$H $\delta_{iso}$ and $^{2}$H $C_Q$. However, significant overlap was observed in ranges of $^{1}$H $\delta_{iso}$ and $^{2}$H $C_Q$ values exhibited by protons located on O3 and O4 sites, preventing these hydroxyl environments from being distinguished. The calculated $^{17}$O NMR parameters showed the same, with the distinction between Mg–OH and Si–OH hydroxyl environments being reasonably clear, but with confident distinction between different silanol environments proving challenging, even when $^{1}$H and $^{17}$O $\delta_{iso}$ were considered simultaneously. By investigating plots of $^{1}$H $\delta_{iso}$ against $^{29}$Si $\delta_{iso}$, several distinct $^{1}$H-$^{29}$Si correlations were identified, in good agreement with previous literature.[46]

The $^1$H $\delta_{iso}$ values for the H–O1, H–O3 and H–O4 hydroxyl environments in motifs **A**, **B** and **E** agree reasonably well with the experimental $^1$H MAS NMR spectrum of wads-H (see Figure 6.5a), supporting the assignment of the resonances at 3.4, 6.7 and 8.6 ppm to protonated O1, O3 and O4 sites, respectively. However, much poorer agreement is seen between the corresponding $^1$H DQ MAS NMR spectrum (either at the contour levels shown by Griffin *et al.*,[46] or the level shown in Figure 6.5b) and the calculated $^1$H $\delta_{iso}$ for motifs **A**, **B** and **E**. These three motifs will result in H–O1/H–O1 (**A**), H–O4/H–O4 (**B**) and H–O1/H–O3 (**E**) $^1$H correlations, whereas the $^1$H DQ MAS NMR spectrum published by Griffin *et al.*[46] contains signals resulting from additional $^1$H correlations. This suggests that in order to more accurately describe the local protonation environments leading to the $^1$H MAS NMR spectra shown in Figure 6.5, it seems necessary to perform an AIRSS-based investigation into a wadsleyite system with a hydration level more similar to that of the samples studed experimentally.

## 6.7 Investigating the structure of fully-hydrous wadsleyite

### 6.7.1 AIRSS-generated structural models

Wadsleyite containing 3.3 wt% $H_2O$, *i.e.*, fully-hydrous wadsleyite, can be achieved through the incorporation of four protons into a unit cell of the anhydrous structure, charge balanced by the removal of two $Mg^{2+}$ cations. The incorporation of four protons could equally be charge balanced by the removal of a single $Si^{4+}$ cation, however, Si was used in excess during the experimental synthesis of hydrous wadsleyite, reducing the chance of samples being produced with Si vacancies.[46] Although they are not discussed further in this chapter, brief discussion of the AIRSS-generated structures resulting from the removal of a $Si^{4+}$ cation is presented in Appendix E1.

**Table 6.4:** Summary of the 11 input structures created for separate AIRSS runs, including the combination of Mg site vacancies, the intervacancy distance and the number of structures generated.

| Run | Mg site vacancy combination | Intervacancy distance / Å | Number of AIRSS-generated structures |
|---|---|---|---|
| 1 | Mg1/Mg1 | 7.61 | 400 |
| 2 | Mg1/Mg3 | 2.90 | 255 |
| 3 | Mg1/Mg3 | 4.96 | 220 |
| 4 | Mg2/Mg2 | 7.61 | 260 |
| 5 | Mg2/Mg3 | 3.06 | 200 |
| 6 | Mg2/Mg3 | 4.89 | 220 |
| 7 | Mg3/Mg3 | 2.83 | 200 |
| 8 | Mg3/Mg3 | 2.85 | 200 |
| 9 | Mg3/Mg3 | 4.02 | 200 |
| 10 | Mg3/Mg3 | 5.04 | 200 |
| 11 | Mg3/Mg3 | 7.06 | 795 |
| Total | | | 3150 |

As the ground state structure of semi-hydrous wadsleyite was found to consist of two O1–H···O4 hydroxyl environments surrounding an Mg3 vacancy, particular emphasis was placed on investigating fully-hydrous candidates charge balanced by the removal of at least one Mg3 cation, although, other combinations of Mg vacancies were generated. A summary of the input structures used for the AIRSS-based study is given in Table 6.4. The same general AIRSS procedure that was used to generate the semi-hydrous wadsleyite structures was used to generate these structures (see Figure 6.9), with two protons initially placed at the site of each Mg vacancy, before their positions were allowed to vary anywhere within a sphere with radius of 3.0 Å, *i.e.*, POSAMP = 3.0 Å, while the positions of all O, Mg and Si atoms, and the unit cell vectors were fixed. These AIRSS-generated structural models were then geometry optimised using CASTEP 8.0,[75] with an $E_{cut}$ of 40 Ry, a k-point spacing of 0.1 2π $Å^{-1}$, the PBE $E_{XC}$ functional[76] and the default on-the-fly ultrasoft pseudopotentials.[77] During the geometry optimisation, the position of all H, O, Mg, and Si atoms were allowed to vary while the

unit cell dimensions were fixed. During geometry optimisation a small number of candidate structures underwent structural rearrangement in the form of Mg cation migration, leading to Mg vacancy combinations and intervacancy distances that were not initially considered, including several structures with a Mg1/Mg2 vacancies.

Figure 6.28a shows the enthalpy of all 3150 AIRSS-generated fully-hydrous wadsleyite structures, plotted against the intervacancy distance, with the data points coloured according to the Mg vacancy combination. From Figure 6.28a, the lowest enthalpy structure consists of two Mg3 vacancies ~7 Å apart, *i.e.*, two "isolated" Mg3 vacancies, in good agreement with the ground state seen for semi-hydrous wadsleyite (see Section 6.6.3). Figure 6.28b only shows the data points relating to structures with $\Delta H < 4.0$ eV, from which it is clear that all structures with a Mg1/Mg2 vacancy combination (formed through rearrangement of initial models with other vacancy combinations)

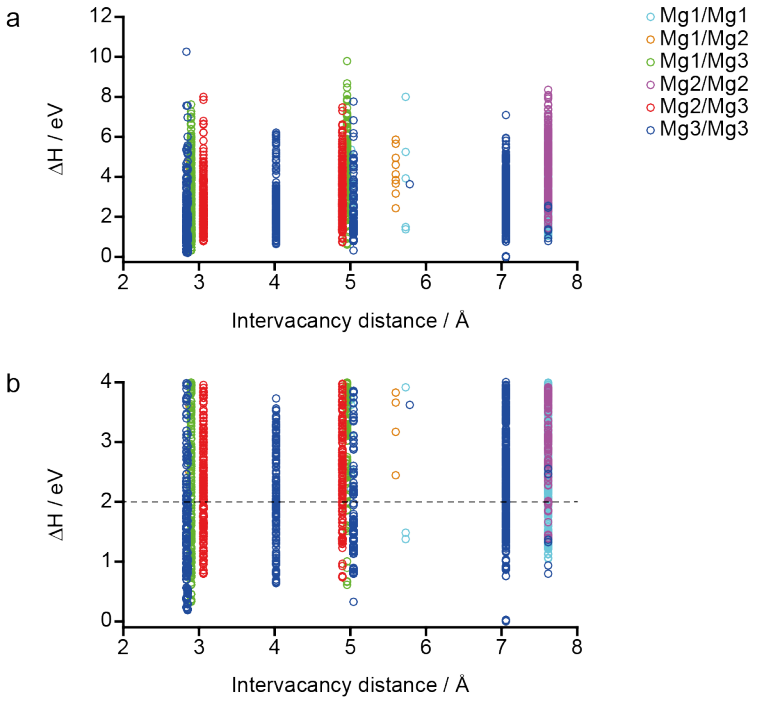


**Figure 6.28**: Plot showing the ΔH of (a) all 3150 AIRSS-generated fully-hydrous wadsleyite structural models against the intervacancy distance with the data points coloured by Mg vacancy combination. In (b) only structures with ΔH below 4.0 eV are shown, with the dashed line at ΔH = 2.0 eV represent the enthalpy cut-off used during *k*-means clustering.

are more enthalpically unstable, with $\Delta H > 2.0$ eV (a $\Delta H$ cut-off denoted by the dashed line). As for the semi-hydrous wadsleyite structures (see Section 6.6.3), the *k*-means clustering approach, as implemented in the Soprano Python library,[61] was used to identify a subset of structures for more detailed analysis. The clustering scripts used were based on those used for the semi-hydrous wadsleyite system (see Appendix D2), with the inclusion of genes to describe the Mg vacancy combination and the intervacancy distance. The latter gene was weighted so that each cluster consisted of structures with the same intervacancy distances and Mg vacancy combinations. The original genes used to cluster the semi-hydrous structures were modified to allow two Mg vacancies and four protons to be considered, including changes to the genes describing H–H interatomic distance and H–vacancy distance to consider the shortest distance for each proton. The gene describing the orientation of the hydroxyl vectors was redefined as the sum of unit vectors placed along all four hydroxyl bonds, leading to $0 \leq \left|\left|\overrightarrow{OH}\right|\right| \leq 4$, where 0 and 4 represent all four hydroxyl bonds being anti-parallel and parallel, respectively. Between the semi- and fully-hydrous wadsleyite systems, the genes representing $\Delta H$, hydroxyl (H–O) bond length, hydrogen bond length and hydroxyl O type were not changed. By applying a $\Delta H$ cut off of 2.0 eV (shown by the dashed line in Figure 6.28b), *k*-means clustering identified 199 AIRSS-generated structures for further analysis.

### 6.7.2 Post *k*-means clustering analysis

Prior to the calculation of NMR parameters, all 199 structures were geometry optimised using a higher level of accuracy, after which they are termed fully optimised. All first-principles calculations were performed using CASTEP 8.0, with $E_{cut}$ of 60 Ry and a k-point spacing of 0.04 $2\pi$ Å$^{-1}$ (see Appendix D1 for convergence testing), the PBE $E_{XC}$ functional,[76] the default ultrasoft pseudopotentials,[77] a `geom_energy_tol` value of $1 \times 10^{-5}$ eV / atom, an `elec_energy_tol` value of $1 \times 10^{-9}$ eV / atom, the TS SEDC scheme[84] and ZORA correction applied.[85,86] The position of H, Mg, Si and O atoms, as well

as the unit cell dimensions were allowed to vary during the geometry optimisation. A description of the referencing procedure used for $^{17}O$ and $^{29}Si$ $\sigma_{iso}$ is given in Appendix D4, with the referencing of $^{1}H$ $\sigma_{iso}$ described in Appendix E2. In this section, only the magnitudes of the $^{2}H$ and $^{17}O$ $C_Q$ values are considered. Calculated NMR parameters were analysed using in-house Python scripts extending the CCP-NC MagresPython module.[79]

The enthalpies of the 199 fully-optimised structures, ranked relative to the global ground state, with the data points coloured according to the Mg vacancy combination, are shown in Figure 6.29, with the four lowest enthalpy structural motifs, labelled **G**-**J**, shown in Figure 6.30. As all candidates with an Mg1/Mg2 vacancy combination had $\Delta H > 2.0$ eV (see Figure 6.28b), *i.e.*, above the $\Delta H$ cut-off used in *k*-means clustering, no structures with this particular arrangement of vacancies are represented in the set of 199 shown in Figure 6.29. Motif **G** represents the global ground state, containing two Mg3 vacancies at a distance of ~7.1 Å (allowing them to be considered isolated vacancies), with all protons covalently bonded to O1 species, leading to four O1–H···O4 hydroxyls. This ground state structure is in good agreement with Section 6.6.3, which found motif **A** (see Figure 6.22b), a structure containing O1 hydroxyls surrounding an Mg3 vacancy, to be the ground state for the semi-hydrous structures. Motif **H** ($\Delta H \approx 0.2$ eV) has two Mg3 vacancies ~2.9 Å apart, aligned with the *y* lattice vector, charge balanced by two O1-H···O4 and two O3–H···O3 hydroxyls (see Figure 6.30).

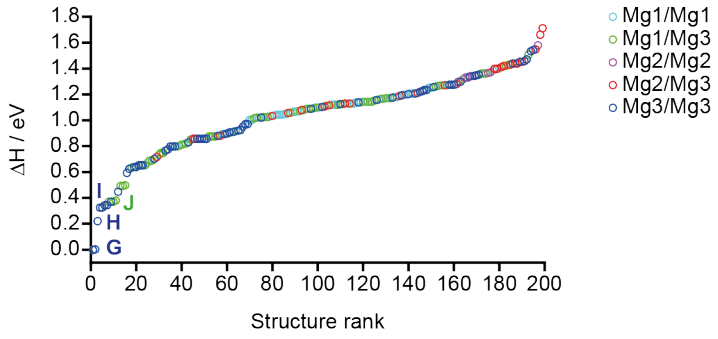


**Figure 6.29:** Plot showing the relative enthalpy of the 199 fully-hydrous wadsleyite structural models following the second geometry optimisation, with the data points coloured by Mg vacancy combination and the four lowest structural motifs labelled **G**-**J**.

Motif **I** (ΔH ≈ 0.3 eV) also has two Mg3 vacancies separated by ~2.9 Å, but with the vacancies aligned parallel to the *x* lattice vector, with the protons forming two O1–H···O4 and two O3–H···O4 hydroxyls. Unlike motif **H**, where the two Mg3 vacancies facilitate the hydrogen bonding of H–O3 hydroxyl groups to neighbouring O3 species, by separating the two

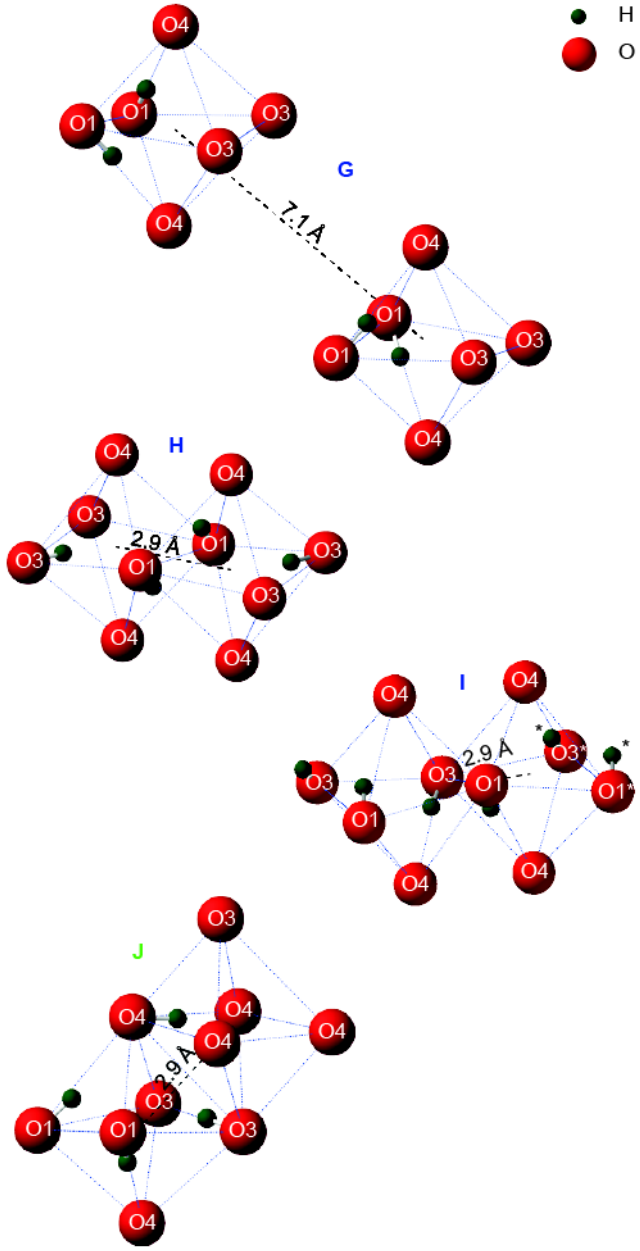


**Figure 6.30:** Representative structures of the four lowest enthalpy protonation motifs (**G**-**J**) from Figure 6.29, with labels coloured according to Mg vacancy combination. In motif **I**, the starred (*) atoms lie in the adjacent unit cell.

hydroxyls (see Figure 6.30), in **I** this is not possible, with the formation of hydroxyls on neighbouring O3 sites requiring an alternative hydrogen bonding arrangement, *i.e.*, to O4 rather than O3 species, which could be an important factor in explaining why the ΔH of **I** is ~0.1 eV above **H**. Motif **J** (ΔH ≈ 0.4 eV) represents the lowest enthalpy structure not to have two Mg3 vacancies, instead containing Mg1/Mg3 vacancies separated by ~2.9 Å. As shown in Figure 6.30, this structure contains two O1–H···O4, one O3–H···O3 and one O4–H···O4 environments, with the O1 hydroxyls surrounding the Mg3 vacancy and the O3 and O4 hydroxyls located on the edges linking the two vacant octahedra. The enthalpy increase associated with the protonation of O3 rather than O1 species, in fully-hydrous wadsleyite structures *i.e.*, the ΔH difference between motifs **G** and **H**-**J**, is far smaller than the increase caused by silanol formation in the semi-hydrous system, *i.e.*, the difference in ΔH between motifs **A** and **B**. This suggests that silanol formation (seen in motifs **H**-**J**) is stabilised when the octahedra surrounding two Mg vacancies are able to edge share, *i.e.*, when clustered, rather than isolated vacancies (the latter being the only option for the semi-hydrous wadsleyite structures investigated in Section 6.6) can be formed. As discussed in Appendix E3, the fully-hydrous wadsleyite structural model proposed by Smyth[7] was also considered, however, in comparison to the 199 AIRSS-generated structures, it was found to be have much higher enthalpy (ΔH > 2.4 eV) above the global ground state, represented by motif **G**.

Calculated hydroxyl bond lengths are plotted against both $^{1}$H $\delta_{iso}$ and $^{2}$H $C_Q$ for the 199 fully-hydrous wadsleyite structures in Figure 6.31, and show that, as seen for the semi-hydrous wadsleyite structure (see Figure 6.23), both $^{1}$H $\delta_{iso}$ and $^{2}$H $C_Q$ correlate strongly with H–O bond length. As shown in Figure 6.31a, the $^{1}$H $\delta_{iso}$ values are reasonably well-separated by the type of O site at which protonation occurs, with 92% of Mg–OH protons exhibiting $^{1}$H $\delta_{iso} < 5$ ppm and 99% of Si–OH protons having $^{1}$H $\delta_{iso} > 5$ ppm. Figure 6.31b shows that the range of $^{2}$H $C_Q$ for the two different hydroxyl environments is

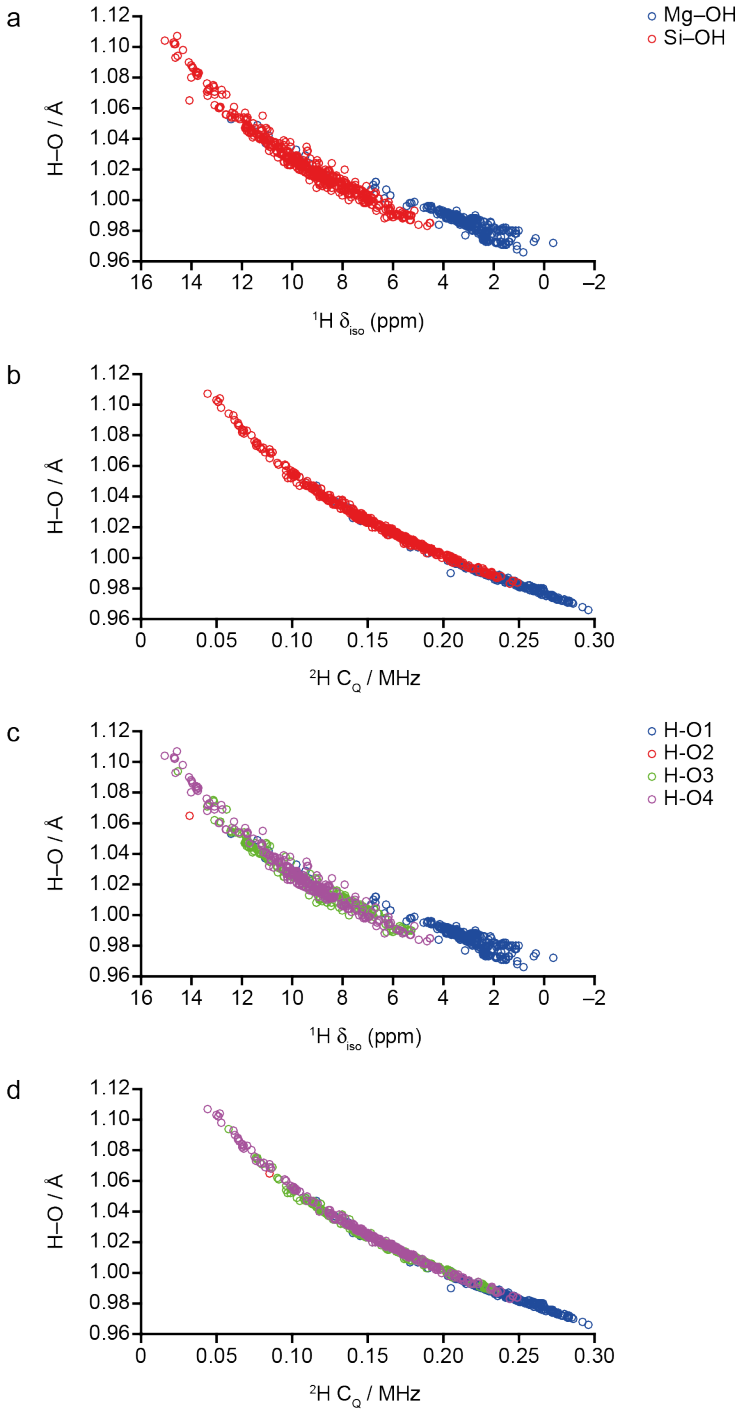


**Figure 6.31:** Plot of calculated H–O bond length against (a and c) $^{1}H$ $\delta_{iso}$ and (b and d) $^{2}H$ $C_Q$ for the 199 fully-hydrous wadsleyite structural models, with the data points coloured by (a and b) chemical type of hydroxyl and (c and d) the O site at which protonation occurs.

similarly well defined, with 94% of Mg–OH and 86% of Si–OH protons having $^{2}H$ $C_Q > 0.2$ MHz and $< 0.2$ MHz, respectively. When the specific site of protonation is considered, as in Figures 6.31c and 6.31d, the similarities in

NMR parameters for silanol (especially O3 and O4) hydroxyls, caused by their structural similarities, makes it challenging to confidently distinguish between different (non-O1) protonation sites.

By using the calculated $^{1}H$ $\delta_{iso}$ values for the 199 structures, and assuming that each proton in a structure can interact with the other three protons (irrespective of their spatial proximity), a simulated $^{1}H$ DQ spectrum (where $^{1}H$ $\delta_{DQ}$ (the sum of $^{1}H$ $\delta_{iso}$ for two $^{1}H$ species) is plotted against $^{1}H$ $\delta_{SQ}$ (the $\delta_{iso}$ of one $^{1}H$ species)) was produced, as shown in Figure 6.32. In Figure 6.32 the shape and colour of the data points represent the protonation site and H–O bond length, respectively. This plot not only emphasises the strong correlation between H–O bond length and $^{1}H$ $\delta_{iso}$, but also shows reasonable agreement with the experimental $^{1}H$ DQ MAS NMR spectrum of wads-H shown in Figure 6.5b.[46] Despite this, the many $^{1}H$ correlations between different protonation environments hinders interpretation rather than enabling a more detailed assignment of the $^{1}H$ DQ MAS NMR spectrum to be achieved.

As shown in Figure 6.33, a plot of calculated $^{17}O$ $C_Q$ against $^{17}O$ $\delta_{iso}$ for the 199 fully-hydrous wadsleyite structures closely resemble the equivalent plot for the 88 semi-hydrous wadsleyite structures (see Figure 6.25). The non-protonated O1 species clearly have the lowest $^{17}O$ $C_Q$ (< 2 MHz) and most upfield $\delta_{iso}$ (< 60 ppm) while pyrosilicate O species have larger $^{17}O$ $C_Q$ and a more downfield $\delta_{iso}$. This latter group of O species also exhibit much larger ranges of $^{17}O$ $C_Q$ and $\delta_{iso}$, of ~4 MHz and ~50 ppm, respectively. While the $^{17}O$ $\delta_{iso}$ values for O2, O3 and O4 species span a very similar range, there seems to be clearer distinction (although significant overlap is still present) between the three sites based on their $^{17}O$ $C_Q$ values, with the magnitude decreasing O2 > O3 > O4. As seen previously for the semi-hydrous wadsleyite structures (see Figure 6.15), following protonation, the largest change in $^{17}O$ NMR parameters is seen for the O1 species, with $C_Q$ increasing by ~4-6 MHz and $\delta_{iso}$ decreasing by ~30-50 ppm. Though the changes are less significant,

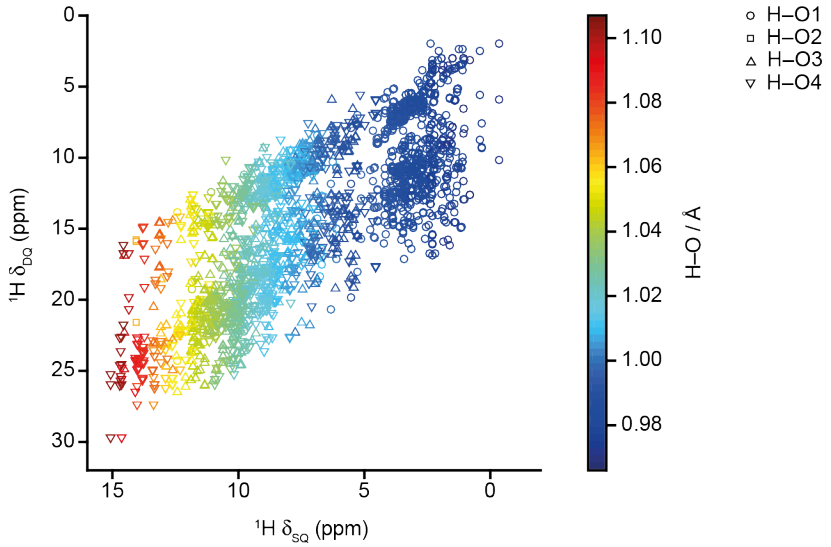


**Figure 6.32:** Plot of calculated $^1$H $\delta_{DQ}$ against $^1$H $\delta_{SQ}$ for the 199 fully-hydrous wadsleyite structural models, with the data points coloured by H–O bond length and shaped by the O site at which protonation occurs and

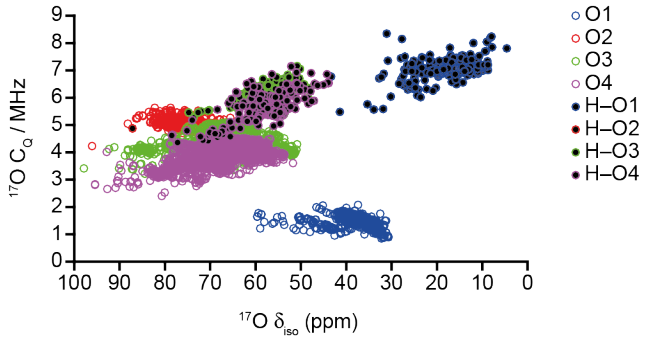


**Figure 6.33:** Plot of calculated $^{17}$O $C_Q$ against $^{17}$O $\delta_{iso}$ for all protonated and non-protonated O species in the 199 fully-hydrous wadsleyite structural models, with the data points coloured by O environment.

pyrosilicate O species also exhibit a similar increase in $^{17}$O $C_Q$ and upfield shift in $\delta_{iso}$ upon protonation. However, there is again extensive overlap in the $^{17}$O NMR parameters for protonated O3 and O4 species that hinders distinction of these two chemically and crystallographically similar sites, mirroring the overlap in $^1$H $\delta_{iso}$ and $^2$H $C_Q$ parameters seen for protons bonded to O3 and O4 species (see Figure 6.31).

Figure 6.34a shows the $^1$H $\delta_{iso}$ plotted against $^{17}$O $\delta_{iso}$ for all 199 structures,

with the data points coloured by H–O bond length. It is clear that both $^{1}$H and $^{17}$O $\delta_{iso}$ show a reasonably strong correlation with hydroxyl bond length. Based especially on $^{17}$O $\delta_{iso}$, a clear distinction between Mg–OH and Si–OH environments becomes obvious from Figure 6.34b, with a decrease of O2 > O3/O4 > O1 for both $^{1}$H and $^{17}$O, although again, no easy distinction between O3 and O4 sites can be made. As shown in Figure 6.34c, when a ΔH cut-off of 0.6 eV is applied, the observed ranges of $^{1}$H and $^{17}$O $\delta_{iso}$ decrease

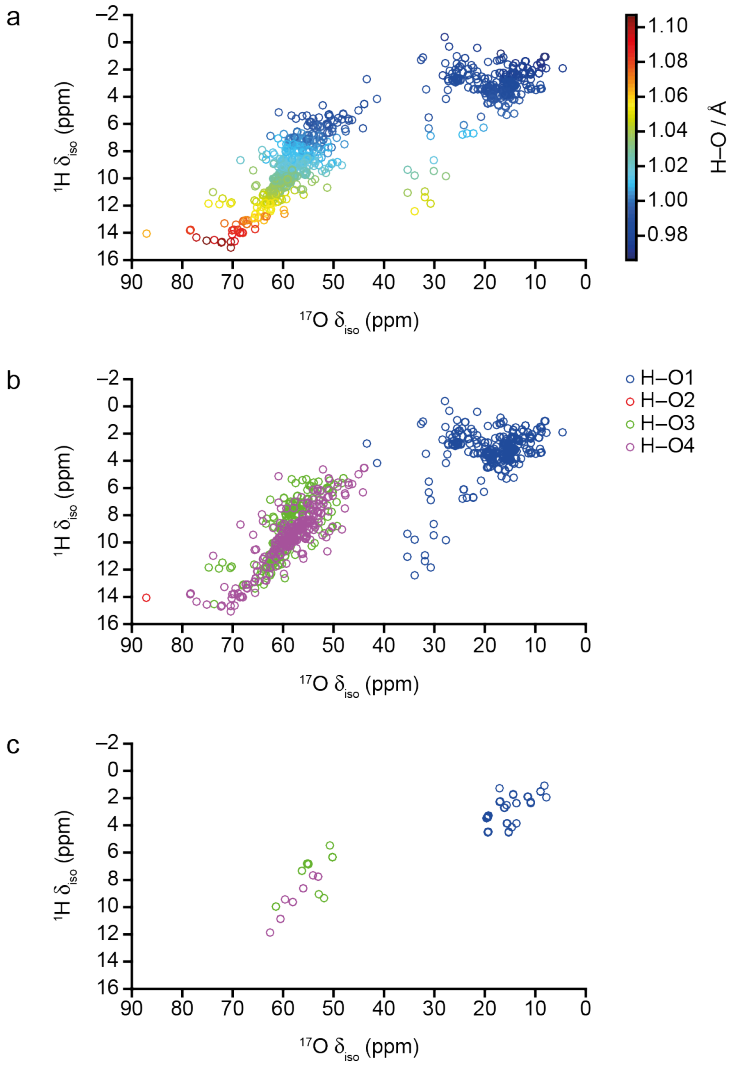


**Figure 6.34:** (a and b) Plot of calculated $^{1}$H $\delta_{iso}$ against $^{17}$O $\delta_{iso}$ for all 199 fully-hydrous wadsleyite structural models, with the data points coloured by (a) H–O bond length and (b) the O site at which protonation occurs. (c) Plot of calculated $^{1}$H $\delta_{iso}$ against $^{17}$O $\delta_{iso}$ for all fully-hydrous wadsleyite structural models with ΔH < 0.6 eV, with the data points coloured by the O site at which protonation occurs.

significantly, with Mg–OH and Si–OH hydroxyl environments even more clearly separated. However, Figure 6.34c shows that, even when only low ΔH structures are considered, distinction of signals from O3 and O4 hydroxyls is still challenging.

In an attempt to identify the protonation arrangements contributing to the structure of fully-hydrous wadsleyite, a very restricted, subset of structures with low ΔH was considered. By following the assumption that for a particular Mg vacancy combination and intervacancy distance, only the ground state protonation arrangement is likely to be observed at rom temperature, and thus contribute to the experimental NMR spectra, this subset consisted of only structures representing the four most stable Mg vacancy combinations, *i.e.*, motifs **G**, **H**, **I** and **J**. A summary of the combination of Mg vacancies, intervacancy distances, $^{1}H$ $\delta_{iso}$ and ΔH values for the four motifs is given in Table 6.5. As shown in Table 6.5, the $^{1}H$ $\delta_{iso}$ for the 16 protons in motifs **G**-**J** fall within the range seen in the experimental $^{1}H$ MAS NMR spectrum of wads-H,[46] shown in Figure 6.5a. The protons in motif **G** exhibit $^{1}H$ $\delta_{iso}$ of 3.3-3.5 ppm, overlaying well with the intense resonance at 3.4 ppm in the $^{1}H$ MAS NMR spectrum of wads-H.[46] The $^{1}H$ $\delta_{iso}$ for O3 and O4 hydroxyls in motifs **H**-**J**, appearing at 6.3-6.8 and 8.6 ppm, respectively, correlate well with the chemical shifts of the two resonances in the $^{1}H$ MAS NMR spectrum of wads-H that were tentatively assigned to silanol environments, at 6.7 and 8.6 ppm, respectively.[46] There is also a reasonable correlation between the $^{1}H$ $\delta_{iso}$ for the H–O1 hydroxyls in motifs **H** and **I** at 1.5-1.9 ppm and the resonance at 1.1 ppm in the $^{1}H$ MAS NMR spectrum of wads-H, suggesting that this resonance could represent Mg–OH (H–O1) environments that are adjacent to a silanol group, an arrangement shown above to cause a bond length contraction (relative to the neighbouring hydroxyl also being on an O1 site), which in turn causes the $^{1}H$ $\delta_{iso}$ of the H–O1 proton to move upfield (see Section 6.6.2).

**Table 6.5:** The combination of Mg vacancies, intervacancy distances, calculated $^{1}H$ $\delta_{iso}$ and $\Delta H$ values for motifs **G**-**J**.

| Motif | Mg site vacancy combination | Intervacancy distance / Å | Protonation site | $^{1}H$ $\delta_{iso}$ (ppm) | $\Delta H$ / eV |
|---|---|---|---|---|---|
| **G** | Mg3/Mg3 | 7.13 | O1 | 3.3 | 0.00 |
| | | | O1 | 3.3 | |
| | | | O1 | 3.5 | |
| | | | O1 | 3.5 | |
| **H** | Mg3/Mg3 | 2.87 | O1 | 1.9 | 0.22 |
| | | | O1 | 1.9 | |
| | | | O3 | 6.8 | |
| | | | O3 | 6.8 | |
| **I** | Mg3/Mg3 | 2.86 | O1 | 1.5 | 0.33 |
| | | | O1 | 1.5 | |
| | | | O3 | 6.3 | |
| | | | O3 | 6.3 | |
| **J** | Mg1/Mg3 | 2.88 | O1 | 2.2 | 0.37 |
| | | | O1 | 3.8 | |
| | | | O3 | 6.8 | |
| | | | O4 | 8.6 | |

Figure 6.35a shows a plot of H–O bond length against $^{1}H$ $\delta_{iso}$ for motifs **G**-**J**, from which it can be seen that distinct regions of chemical shift are exhibited by the three different protonation sites, allowing a clear distinction to be made not only between Mg–OH and Si–OH environments, but also between O3 and O4 silanol environments. As two separate clusters of H–O1 data points are observed, the 16 protons in motifs **G**-**J** actually separate into four distinct $^{1}H$ $\delta_{iso}$ regions at 1-2, 3-4, 6-7 and 8-9 ppm, closely resembling the appearance of the $^{1}H$ MAS NMR spectrum of wads-H shown in Figure 6.5a.[46] Figure 6.35b shows a plot of $^{1}H$ $\delta_{iso}$ against $^{17}O$ $\delta_{iso}$ for motifs **G**-**J**, with the data points coloured by protonation site, which again shows the clear distinction between Mg–OH and Si–OH environments. While the $^{1}H$ $\delta_{iso}$ for

H–O3 and H–O4 hydroxyls are very distinct, there is far less separation between the $^{17}O$ $\delta_{iso}$ for these two environments, with the $\delta_{iso}$ of the protonated O4 site only slightly more downfield shifted compared to the O3 sites. A plot of $^{1}H$ $\delta_{iso}$ against $^{29}Si$ $\delta_{iso}$ for motifs **G**-**J**, with the data points coloured by hydroxyl environment is shown in Figure 6.35c, from which four distinct types of $^{1}H$-$^{29}Si$ correlations were identified, with coloured ellipsoids used to distinguish between them. While the correlations denoted by the upfield blue ellipsoid and the downfield red ellipsoid have previously been

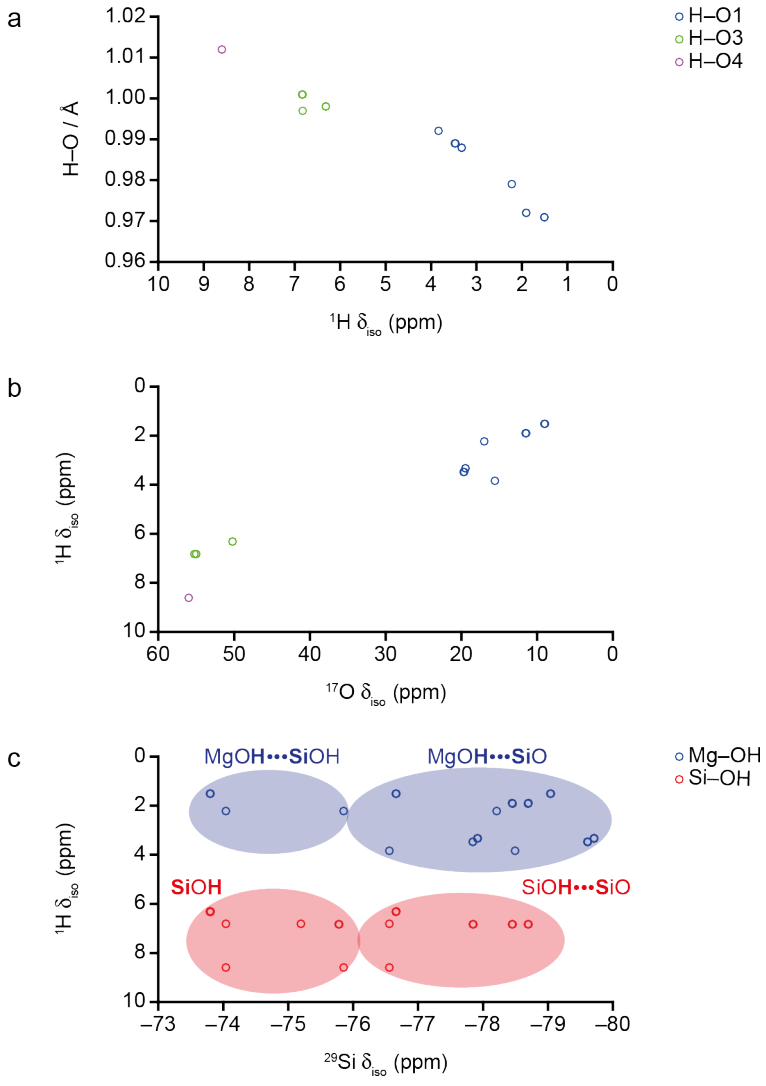


**Figure 6.35:** Plots of (a) calculated H–O bond length against $^{1}H$ $\delta_{iso}$, (b) $^{1}H$ $\delta_{iso}$ against $^{17}O$ $\delta_{iso}$ and (c) $^{1}H$ $\delta_{iso}$ against $^{29}Si$ $\delta_{iso}$ for motifs **G**-**J**, with the data points coloured by (a and b) the O site at which protonation occurs, and (c) chemical type of hydroxyl.

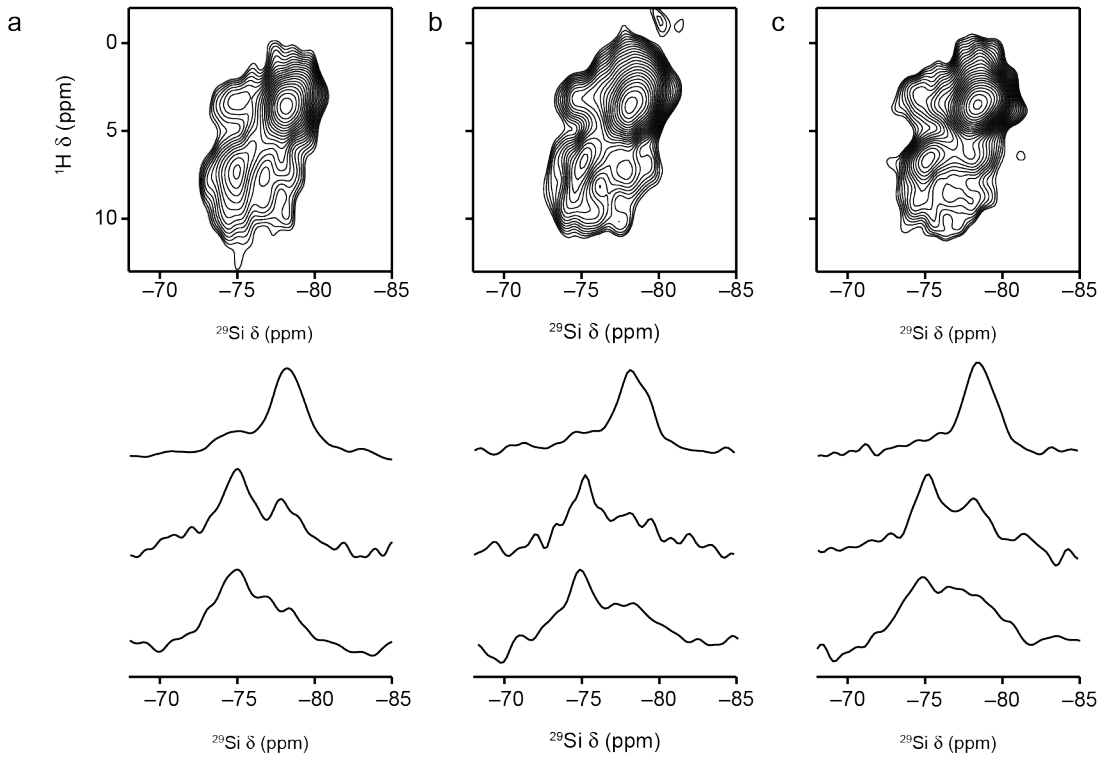


**Figure 6.36:** $^{1}$H-$^{29}$Si (14.1 T, 20 kHz) CP HETCOR NMR spectrum of wads-H, resulting from 2720 transients separated by a recycle interval of 1.5 s for each of 28 $t_1$ increments of 50 μs, with polarisation transfer achieved using a contact pulse duration of (a) 1 ms, (b) 2 ms and (c) 5 ms. Cross sections, taken parallel to $F_1$ at $^{1}$H δ of ~3.5 ppm (top), ~6.5 ppm (middle and ~8.0 ppm (bottom) are also shown.

observed in an experimental $^{1}$H-$^{29}$Si CP HETCOR experiment[46] (see Figure 6.8c), as shown in Figure 6.36, when the contact time is varied, less intense signals appear at chemical shifts consistent with the four $^{1}$H-$^{29}$Si correlations identified in Figure 6.35c.

As shown in Figure 6.37a, the calculated $^{1}$H $\delta_{iso}$ for the 16 protons in motifs **G**-**J** (see Table 6.5) were used to plot the position of signals expected in a $^{1}$H DQ spectrum, with the resulting correlations compared with those seen in the experimental $^{1}$H DQ MAS spectrum of wads-H, shown in Figure 6.37b. In Figure 6.37a blue, red and green boxes are used to highlight the predicted correlations resulting from motifs **G**, **H**/**I** and **J**, respectively, with **H** and **I** combined owing to their similarity. Motif **G**, the ground state structure results in intensity at $^{1}$H $\delta_{DQ}$ = 6.6-6.8 ppm, corresponding to $^{1}$H-$^{1}$H

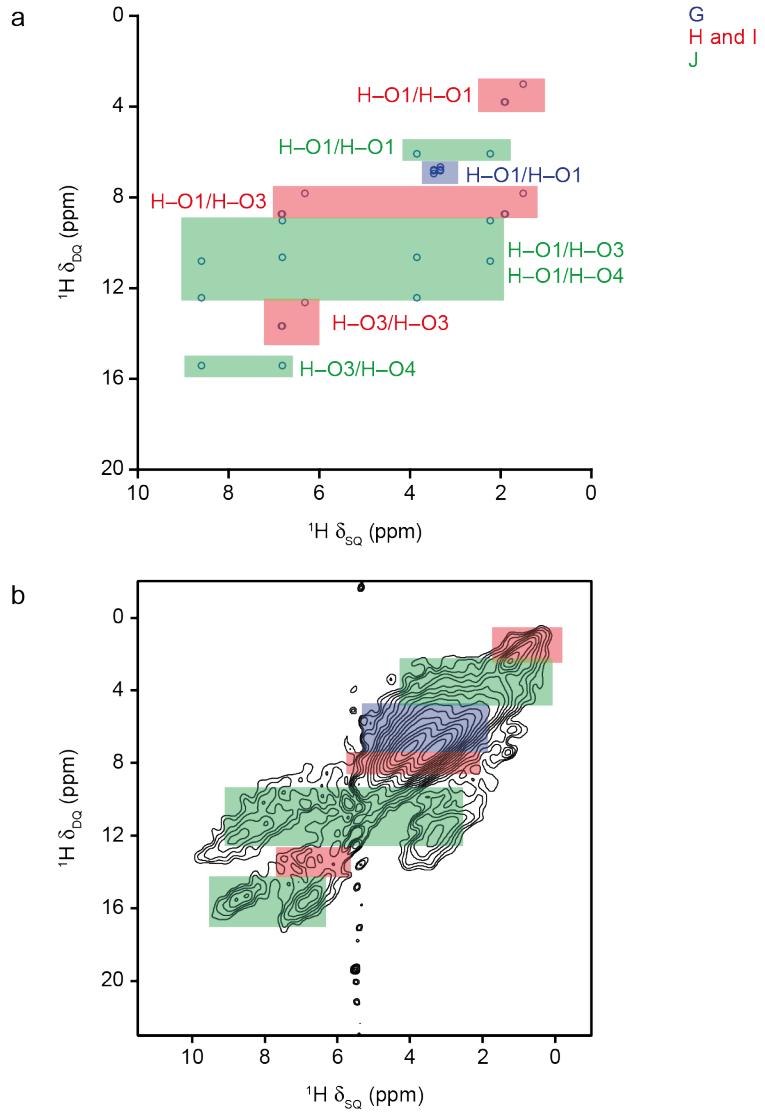


**Figure 6.37:** (a) Plot of calculated $^1$H $\delta_{DQ}$ against $^1$H $\delta_{SQ}$ for the 16 protons in structural motifs **G**-**J**, with overlaid boxes coloured by motif, with **H** and **I** are combined. (b) A rotor-synchronised $^1$H (14.1 T, 30 kHz) DQ MAS NMR spectrum of wads-H recorded using two cycles of BABA recoupling, and by averaging 32 transients separated by a recycle interval of 2 s for each of the 100 $t_1$ increments of 33.33 μs. The figure has been modified from that presented by Griffin *et al.*[46]

correlations between H–O1/H–O1 hydroxyls. Figure 6.36a shows that motifs **H** and **I** result in signals across three distinct $^1$H $\delta_{DQ}$ regions, with intensity at 3.0-3.8, 7.7-8.7 and 12.6-13.7 ppm resulting from H–O1/H–O1, H–O1/H–O3 and H–O3/H–O3 correlations, respectively. As a result of the presence of protonated O1, O3 and O4 sites, motif **J** exhibits DQ signals from a number of $^1$H-$^1$H interactions, with the $^1$H $\delta_{DQ}$ signals at 6.1, 9.1-10.7, 10.8-12.4 and

15.4 ppm resulting from H–O1/H–O1, H–O1/H–O3, H–O1/H–O4, and H–O3/H–O4 correlations, respectively. The $^{1}$H DQ signals resulting from protons in motifs **G**-**J** appear very similar to the correlations seen in the experimental $^{1}$H DQ MAS NMR spectrum of wads-H (see Figure 6.37b),[46] suggesting that the $^{1}$H-$^{1}$H correlations seen experimentally could result solely from the range of hydroxyl environments described by these four structural motifs with low ΔH.

In comparison to the subset of semi-hydrous wadsleyite structures with low ΔH (see Section 6.6.3), the predicted $^{1}$H $\delta_{iso}$ values for a set of only four fully-hydrous wadsleyite structures, *i.e.*, motifs **G**-**J**, show far better agreement with both the $^{1}$H MAS and DQ MAS NMR spectra of wads-H,[46] shown in Figure 6.5. This suggests that, somewhat counterintuitively, by only considering motifs **G**-**J**, a more accurate representation of the disordered hydrous wadsleyite system can be obtained. In addition, if it is assumed that the $^{1}$H MAS NMR spectrum of wads-H is a result of only these four motifs, the relative intensities of the resonances in this quantitative spectrum can then be used to calculate the proportion of each motif, as well as ultimately, the occupancy of each Mg site. Based on the simulated fit of the $^{1}$H MAS NMR spectrum of wads-H,[46] protons in Mg–OH and Si–OH environments account for 83 and 17% of the integrated intensity, respectively, with the resonances at 8.6 and 6.7 ppm, assigned to O4 and O3 site hydroxyls, respectively, corresponding to 7 and 10% of the total intensity. With only motif **J** containing a protonated O4 site, it follows that this motif is solely responsible for the resonance at 8.6 ppm, and that this one hydroxyl environment accounts for 7% of the total spectral intensity. As motif **J** contains three more protons, *i.e.*, one H–O3 and two H–O1 hydroxyls, this structure must account for a total of 28% of the spectral intensity, with 70% of the intensity for the peak at 6.7 ppm (which makes up 10% of the total spectral intensity) a result of the H–O3 hydroxyl from this structure. As motif **G** only contains protonated O1 sites, the remaining 30% of intensity for the peak at 6.7 ppm, which corresponds to 3% of the total spectral intensity,

**Table 6.6:** Estimated percentages of structural motifs for a fully-hydrous wadsleyite system, based on the integral intensities from the $^{1}$H MAS NMR spectrum of wads-H.[46]

| Motif | Mg site vacancy combination | Protonation site | Contribution to $^{1}$H MAS spectrum (%) | Contribution to the overall system (%) |
|---|---|---|---|---|
| **G** | Mg3/Mg3 | 4 × O1 | 66 | 66 |
| **H** | Mg3/Mg3 | 2 × O1 | 1.5 | 3 |
| | | 2 × O3 | 1.5 | |
| **I** | Mg3/Mg3 | 2 × O1 | 1.5 | 3 |
| | | 2 × O3 | 1.5 | |
| **J** | Mg1/Mg3 | 2 × O1 | 14 | 28 |
| | | 1 × O3 | 7 | |
| | | 1 × O4 | 7 | |

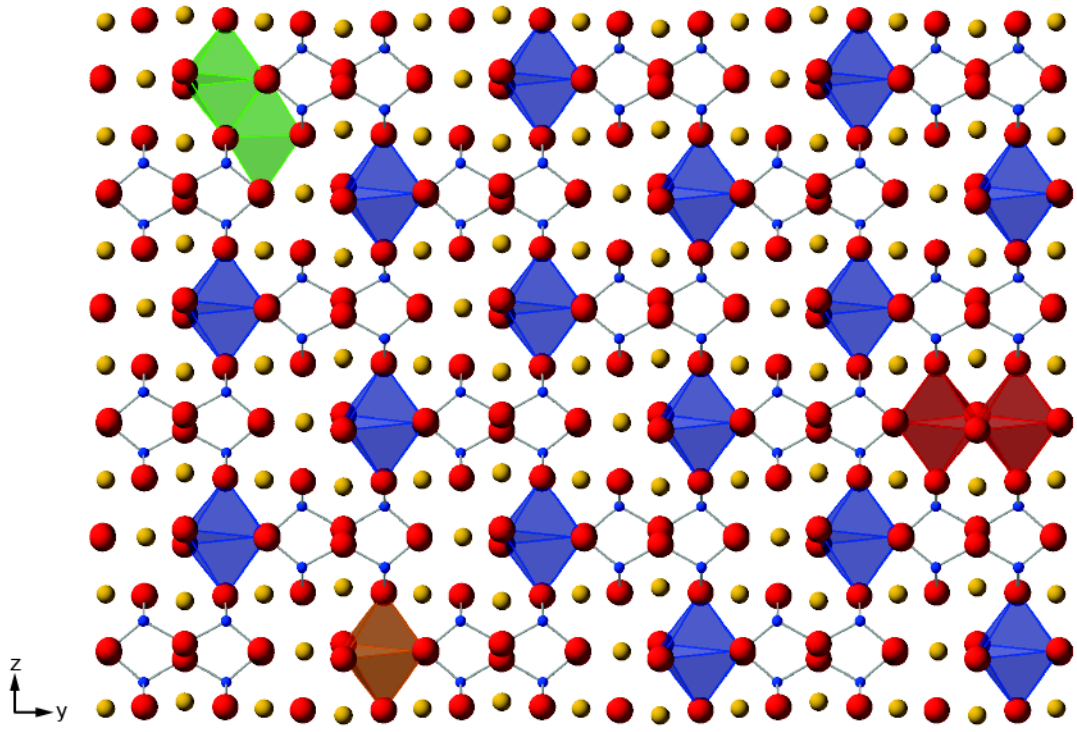


**Figure 6.38:** Schematic representation of fully-hydrous wadsleyite, showing an array of isolated Mg3 vacancies based on motif **G**, with low levels of clustered Mg3/Mg3 vacancies based on motifs **H** and **I**, and clustered Mg1/Mg3 vacancies based on motif **J**. Motifs **G**, **H**, **I** and **J**, denoted by blue, red, orange and green polyhedral, respectively, account for 66, 3, 3 and 28% of hydration defects. Note, in this orientation motif **I** appears to resemble an isolated Mg3 vacancy, however, the orange polyhedral denotes two edge sharing Mg3 vacancies aligned with the *x* lattice vector.

must come from motifs **H** and/or **I**. By assuming that each motif contributes equally to the intensity of this peak, *i.e.* 15% each, it follows that **H** and **I** each account for 3% of the overall spectral intensity, split evenly over the peaks assigned to H–O1 and H–O3 hydroxyl environments. It follows that combined, motifs **H**-**J** account for 34% of the overall intensity in the $^{1}$H MAS NMR spectrum of wads-H, meaning the remaining 66% must stem from motif **G**. As the ground state only contains H–O1 hydroxyls, this means that motif **G** accounts for ~80% *i.e.*, 66/83, of the intensity assigned to $^{1}$H in Mg–OH environments. A summary of the estimated integral intensity proportions and a breakdown of the individual motifs contribution to the overall system is given in Table 6.6.

As motifs **G**-**I** contain two Mg3 vacancies and motif **J** contains one Mg1 and one Mg3 vacancy, a structural model of fully-hydrous wadsleyite with a **G**:**H**:**I**:**J** ratio of 66:3:3:28 results in a Mg1:Mg3 vacancy ratio of 14:86 and Mg1, Mg2 and Mg3 site occupancies of 0.930, 1, and 0.785, respectively, These calculated fractional occupancies imply that the majority (66%) of vacancy defects in fully-hydrous wadsleyite arise from isolated Mg3 vacancies of the sort found in motif **G**, with clustered vacancies from a combination of motifs **H**-**J** comprising the remaining 3, 3 and 28% of the system, respectively. Figure 6.38 shows a schematic representation of the structure that would result from this ratio of different vacancy defects.

### 6.7.3 Summary

In Section 6.7.2, the AIRSS approach[56,57] was used to generate 3150 wadsleyite containing 3.3 wt% $H_2O$, *i.e.*, fully-hydrous wadsleyite candidates, each containing four protons charge balanced by the removal of two $Mg^{2+}$ cations. As shown in Table 6.4, 11 separate AIRSS runs, each based on an input structure with a unique combination of Mg vacancies and intervacancy distance combination, were performed, with structural rearrangement causing several candidates to exhibit Mg vacancy combinations (including Mg1/Mg2) that were not initially considered. Following the generation of 3150 structures, a *k*-means clustering approach

was used to identify a subset of 199 (theoretically) non-equivalent structures for more detailed analysis, involving performing a second, more accurate geometry optimisation prior to the prediction of solid-state NMR parameters.

The multinuclear NMR parameters predicted for the 199 fully-hydrous wadsleyite structures agree reasonably well with those exhibited by the 88 semi-hydrous structures discussed in Section 6.6.3, with strong correlations between hydroxyl bond length and both $^{1}H$ $\delta_{iso}$ and $^{2}H$ $C_Q$ observed. These NMR parameters also allow distinction between Mg–OH and Si–OH hydroxyl environments to be made, although, as seen in Section 6.6.3 similar and overlapping $^{1}H$ $\delta_{iso}$ and $^{2}H$ $C_Q$ ranges for H–O3 and H–O4 protons hinders any meaningful distinction between these two silanol environments. This is a limitation that the calculated $^{17}O$ NMR parameters for the 199 fully-hydrous wadsleyite structures clearly mirrors, with protonated O3 and O4 species exhibiting very similar $^{17}O$ $\delta_{iso}$ and $C_Q$ values, although protonation does change both of these parameters, with the most substantial variations seen between protonated and non-protonated O1 species.

When only the four protonation arrangements with the lowest enthalpy, *i.e.*, motifs **G**-**J**, were considered, very good agreement between the calculated $^{1}H$ $\delta_{iso}$ for the 16 protons in these structures and the signals in the $^{1}H$ MAS NMR spectrum of wads-H (see Figure 6.5a) was observed. A plot of hydroxyl bond length against $^{1}H$ $\delta_{iso}$ for the 16 protons in motifs **G**-**J** resulted in four distinct clusters of data points with $\delta_{iso}$ of 1-2, 3-4, 6-7 and 8-9 ppm, in very good agreement with the $^{1}H$ MAS NMR spectrum of wads-H,[46] which indicates that these structures contain protons in local environments similar to those observed experimentally. In addition, the various H–O1, H–O3 and H–O4 hydroxyl environments in motifs **G**-**J** result in correlations that agree well with those seen in the $^{1}H$ DQ MAS NMR spectrum of wads-H (see Figure 6.5b), which the semi-hydrous structural models discussed in Sections 6.6.2 and 6.6.3, failed to do. Using the integrated intensities for the simulated fit of the $^{1}H$ MAS NMR spectrum of wads-H,[46] shown in Figure 6.5a, and by

assuming that the NMR spectrum is a result of only these four low ΔH protonation arrangements, the contribution of motifs **G**, **H**, **I** and **J** to the overall fully-hydrous wadsleyite system were determined to be 66, 3, 3 and 28%, respectively. Based on these percentages, it was subsequently calculated that Mg1 and Mg3 vacancies account for 86 and 14% of all hydration defects, respectively, suggesting that the disordered fully-hydrous wadsleyite structure predominantly consists of defects represented by motif **G**, *i.e.*, isolated Mg3 vacancies, with clustered vacancies from a combination of motifs **H**-**J** accounting for the remaining defects.

## 6.8 Outlook

This chapter presents the use of the AIRSS approach, combined with both experimental multinuclear solid-state NMR spectroscopy and DFT-predicted NMR parameters, to investigate the structure of hydrous wadsleyite, a high-pressure silicate mineral found in the transition zone of the Earth's mantle that exhibits structural disorder in the form of hydration defects. AIRSS involved using an initial structural model of anhydrous wadsleyite, before removing one or two $Mg^{2+}$ cations per unit cell and incorporating two or four $H^{+}$ to maintain charge neutrality, a process that led to the creation of 1287 semi-hydrous and 3150 fully-hydrous wadsleyite structures, containing 1.65 and 3.3 wt% $H_2O$, respectively, with all AIRSS-generated structures geometry optimised using first-principles calculations. Initially, only the 819 Mg3 vacant semi-hydrous wadsleyite structures were considered, with ΔH used to select a subset of 103, predominantly low ΔH candidates for more detailed investigation, involving performing a second, more accurate geometry optimisation, prior to the calculation of NMR parameters. In the subsequent investigations, where semi-hydrous models with Mg1, Mg2 and Mg3 vacancies, and later, the fully-hydrous wadsleyite structures were considered, rather than relying solely on ΔH to select structures, a *k*-means clustering approach was used, leading to 88 semi-hydrous and 199 fully-hydrous structures being identified for more detailed analysis. In this investigation, using a *k*-means clustering approach to

identify structures for further analysis, rather than relying on one parameter, *i.e.*, ΔH, proved more efficient. *k*-means clustering led to the selection of structural models with unique protonation arrangements, Mg vacancy combinations and intervacancy distances, whereas basing selection purely on ΔH led to the selection of multiples models with the same, or very similar structures being identified, as a result of oversampling low ΔH structures.

The effectiveness of this investigation, into the structure of hydrous wadsleyite, a system that exhibits positional disorder, lies in the use of the AIRSS approach, which was designed to be an unbiased structure searching method. It is precisely this lack of bias in the structure generation process (in contrast to the bias imposed when computational structural models are manually generated[46,52]) that has allowed AIRSS to identify not only the ground state, but also possible metastable structures in the semi- and fully-hydrous wadsleyite systems. While this chapter outlines a reasonably comprehensive study of the hydration mechanism of wadsleyite, AIRSS could undoubtedly be used to explore this system further. One possible extension would be to consider the effect of performing an AIRSS run with an increased POSAMP, to investigate whether increasing the charge separation, *i.e.*, increasing the distance between protons and Mg vacancies, leads to new, potentially low enthalpy protonation arrangements. Similarly, AIRSS could be used to investigate the possible protonation arrangements resulting from various vacancy combinations not yet considered, such as a combination of $Mg^{2+}$ and $Si^{4+}$ vacancies. In addition, improved access to HPC resources could allow AIRSS to be applied to larger systems, *i.e.*, wadsleyite supercells, which would provide an opportunity for hydrous wadsleyite systems containing much lower hydration levels than the 1.65 and 3.3 wt% $H_2O$, respectively, studied in this chapter, to be investigated.

This chapter highlights the insights that the AIRSS approach provided into the structure of hydrous wadsleyite, a system that exhibit extensive positional disorder, occurring in the form of an unknown combination of Mg site vacancies, intervacancy distances and protonation arrangements. Based

on this, it is clear that this random structure searching approach (especially if combined with predicted and experimental solid-state NMR parameters), could be successfully applied to other systems that, dare to the presence of positional disorder, may prove challenging to investigate using more conventional experimental or computational means. Therefore, it is hoped that, through more widespread access and exposure to this approach, AIRSS-based studies into disordered materials will become more routine in the future.

## 6.9 References


1. J. M. Griffin and S. E. Ashbrook, *Annu. Rep. NMR Spectro.*, 2013, **79**, 241–332.
2. A. E. Ringwood, *Composition and Evolution of the Upper Mantle*, McGraw=Hill, New York, 1975.
3. D. R. Bell and G. R. Rossman, *Science*, 1992, **225**, 1391–1397.
4. D. L. Kohlstedt, H. Keppler, and D. C. Rubie, *Contrib. to Mineral. Petrol.*, 1996, **123**, 345–357.
5. N. Bolfan-Casanova, H. Keppler, and D. C. Rubie, *Earth Planet. Sci. Lett.*, 2000, **182**, 209–221.
6. J. R. Smyth, *Am. Mineral.*, 1987, **72**, 1051–1055.
7. J. R. Smyth, *Am. Mineral.*, 1994, **79**, 1021–1024.
8. K. Regenauer-lieb, D. A. Yuen, and J. Branlund, *Science*, 2001, **294**, 578–580.
9. E. Ohtani, L. Yuan, I. Ohira, A. Shatskiy, and K. Litasov, *J. Asian Earth Sci.*, 2018, **167**, 2–10.
10. S.-I. Karato, *Proc. Japan Acad. Ser. B*, 1995, **71**, 61–66.
11. X. Huang, Y. Xu, and S.-I. Karato, *Nature*, 2005, **434**, 746–749.
12. D. Wang, M. Mookherjee, Y. Xu, and S. Karato, *Nature*, 2006, **443**, 977–980.
13. T. Yoshino and T. Katsura, *Annu. Rev. Earth Planet. Sci.*, 2013, **41**, 605–628.
14. A. Beran and E. Libowilzky, *Rev. Mineral. Geochemistry*, 2006, **62**, 169–191.

15. W. R. Panero, J. R. Smyth, J. S. Pigott, Z. Liu, and D. J. Frost, *Am. Mineral.*, 2013, **98**, 637–642.
16. R. F. Moran, D. M. Dawson, and S. E. Ashbrook, *Int. Rev. Phys. Chem.*, 2017, **36**, 39–115.
17. P. Florian and D. Massiot, *CrystEngComm*, 2013, **15**, 8623–8626.
18. C. J. Pickard and F. Mauri, *Phys. Rev. B*, 2001, **63**, 245101.
19. C. Bonhomme, C. Gervais, F. Babonneau, C. Coelho, F. Pourpoint, T. Azaïs, S. E. Ashbrook, J. M. Griffin, J. R. Yates, F. Mauri, and C. J. Pickard, *Chem. Rev.*, 2012, **112**, 5733–5779.
20. S. E. Ashbrook and D. McKay, *Chem. Commun.*, 2016, **52**, 7186–7204.
21. T. Charpentier, *Solid State Nucl. Magn. Reson.*, 2011, **40**, 1–20.
22. S. E. Ashbrook and D. M. Dawson, *Acc. Chem. Res.*, 2013, **46**, 1964–1974.
23. T. Katsura and E. Ito, *J. Geophys. Res. Solid Earth*, 1989, **94**, 15663–15670.
24. A. E. Ringwood, *Composition and Petrology of the Earth's Mantle*, McGraw=Hill, New York, 1975.
25. H. Horiuchi and H. Sawamoto, *Am. Mineral.*, 1981, **66**, 568–575.
26. T. Inoue, H. Yurimoto, and Y. Kadoh, *Geophys. Res. Lett.*, 1995, **22**, 117–120.
27. S. D. Jacobsen, *Rev. Mineral. Geochemistry*, 2006, **62**, 321–342.
28. A. J. Berry, H. S. C. O'Neill, J. Hermann, and D. R. Scott, *Earth Planet. Sci. Lett.*, 2007, **261**, 134–142.
29. A. M. Walker, J. Hermann, A. J. Berry, and H. S. C. O'Neill, *J. Geophys. Res.*, 2007, **112**, B05211.
30. B. Winkler, V. Milman, B. Hennion, M. C. Payne, M. H. Lee, and J. S. Lin, *Phys. Chem. Miner.*, 1995, **22**, 461–467.
31. K. Wright and C. R. A. Catlow, *Phys. Chem. Miner.*, 1996, **23**, 38–41.
32. M. Haiber, P. Ballone, and M. Parrinello, *Am. Mineral.*, 1997, **82**, 913–922.
33. A. M. Walker, S. Demouchy, and K. Wright, *Eur. J. Mineral.*, 2006, **18**, 529–543.
34. J. Tsuchiya and T. Tsuchiya, *J. Geophys. Res.*, 2009, **114**, B02206.
35. J. W. Downs, *Am. Mineral.*, 1989, **74**, 1124–1129.
36. N. Ross, G. Gibbs, and K. Rosso, *Am. Mineral.*, 2003, **88**, 1452–1459.
37. Y. Kudoh, T. Inoue, and H. Arashi, *Phys. Chem. Miner.*, 1996, **23**, 461–

469.
38. Y. Kudoh and T. Inoue, *Phys. Chem. Miner.*, 1999, **26**, 382–388.
39. C. M. Holl, J. R. Smyth, S. D. Jacobsen, and D. J. Frost, *Am. Mineral.*, 2008, **93**, 598–607.
40. Y. Ye, J. R. Smyth, a. Hushur, M. H. Manghnani, D. Lonappan, P. Dera, and D. J. Frost, *Am. Mineral.*, 2010, **95**, 1765–1772.
41. N. Purevjav, T. Okuchi, N. Tomioka, X. Wang, and C. Hoffmann, *Sci. Rep.*, 2016, **6**, 34988.
42. S. D. Jacobsen, S. Demouchy, D. J. Frost, T. B. Balloran, and J. Kung, *Am. Mineral.*, 2005, **90**, 61–70.
43. F. Deon, M. Koch-Müller, D. Rhede, M. Gottschalk, R. Wirth, and S. M. Thomas, *Am. Mineral.*, 2010, **95**, 312–322.
44. A. Sano-Furukawa, T. Kuribayashi, K. Komatsu, T. Yagi, and E. Ohtani, *Phys. Earth Planet. Inter.*, 2011, **189**, 56–62.
45. S. C. Kohn, R. A. Brooker, D. J. Frost, A. E. Slesinger, and B. J. Wood, *Am. Mineral.*, 2002, **87**, 293–301.
46. J. M. Griffin, A. J. Berry, D. J. Frost, S. Wimperis, and S. E. Ashbrook, *Chem. Sci.*, 2013, **4**, 1523–1538.
47. S. E. Ashbrook, A. J. Berry, and S. Wimperis, *J. Am. Chem. Soc.*, 2001, **123**, 6360–6366.
48. S. E. Ashbrook, A. J. Berry, and S. Wimperis, *J. Phys. Chem. B*, 2002, **106**, 773–778.
49. S. E. Ashbrook, A. J. Berry, W. O. Hibberson, S. Steuernagel, and S. Wimperis, *J. Am. Chem. Soc.*, 2003, **125**, 11824–11825.
50. J. K. Moore, J. A. Surface, A. Brenner, P. Skemer, M. S. Conradi, and S. E. Hayes, *Environ. Sci. Technol.*, 2015, **49**, 657–664.
51. S. E. Ashbrook and D. M. Dawson, *Nucl. Magn. Reson.*, 2016, **45**, 1–52.
52. H. Grüninger, K. Armstrong, D. Greim, T. Boffa-Ballaran, D. J. Frost, and J. Senker, *J. Am. Chem. Soc.*, 2017, **139**, 10499–10505.
53. S. E. Ashbrook, D. M. Dawson, and J. M. Griffin, in *Local Structural Characterisation*, eds. D. W. Bruce, D. O'Hare, and R. I. Walton, John Wiley & Sons, Ltd, 2014.
54. A. Fernandes, R. F. Moran, S. Sneddon, D. M. Dawson, D. McKay, G. P. M. Bignami, F. Blanc, K. R. Whittle, and S. E. Ashbrook, *RSC Adv.*,

2018, **8**, 7089–7101.
55. S. E. Ashbrook, J. M. Griffin, and K. E. Johnston, *Annu. Rev. Anal. Chem.*, 2018, **11**, 485–508.
56. C. J. Pickard and R. J. Needs, *Phys. Rev. Lett.*, 2006, **97**, 45504.
57. C. J. Pickard and R. J. Needs, *J. Phys. Condens. Matter*, 2011, **23**, 53201.
58. R. F. Moran, D. McKay, C. J. Pickard, A. J. Berry, J. M. Griffin, and S. E. Ashbrook, *Phys. Chem. Chem. Phys.*, 2016, **18**, 10173–10181.
59. D. Mckay, R. F. Moran, D. M. Dawson, J. M. Griffin, S. Sturniolo, C. J. Pickard, A. J. Berry, and S. E. Ashbrook, *J. Am. Chem. Soc.*, 2019, **141**, 3024–3036.
60. S. E. Ashbrook, A. J. Berry, W. O. Hibberson, S. Steuernagel, and S. Wimperis, *J. Am. Chem. Soc.*, 2003, **125**, 11824–11825.
61. S. Sturniolo, *Soprano - a Python library developed by the CCP for NMR Crystallography*, https://ccp-nc.github.io/soprano/.
62. S. E. Ashbrook, A. J. Berry, W. O. Hibberson, S. Steuernagel, and S. Wimperis, *Am. Mineral.*, 2005, **90**, 1861–1870.
63. J. F. Stebbins and M. Kanzaki, *Science*, 1991, **251**, 294–298.
64. J. F. Stebbins, W. R. Panero, J. R. Smyth, and D. J. Frost, *Am. Mineral.*, 2009, **94**, 626–629.
65. J. F. Stebbins, J. R. Smyth, W. R. Panero, and D. J. Frost, *Am. Mineral.*, 2009, **94**, 905–915.
66. C. Chizallet, H. Petitjean, G. Costentin, H. Lauron-pernot, J. Maquet, C. Bonhomme, and M. Che, *J. Catal.*, 2009, **268**, 175–179.
67. X. Wue and M. Kanzaki, *J. Am. Ceram. Soc.*, 2009, **92**, 2803–2830.
68. X. Xue, M. Kanzaki, D. Turner, and D. Loroch, *Am. Mineral.*, 2017, **102**, 519–536.
69. E. R. H. van Eck, M. E. Smith, and S. C. Kohn, *Solid State Nucl. Magn. Reson.*, 1999, **15**, 181–188.
70. S. E. Ashbrook and M. E. Smith, *Chem. Soc. Rev.*, 2006, **35**, 718–735.
71. S. E. Ashbrook and S. Sneddon, *J. Am. Chem. Soc.*, 2014, **136**, 15440−15456.
72. A. J. Morris, R. J. Needs, E. Salager, C. P. Grey, and C. J. Pickard, *Phys. Rev. B - Condens. Matter Mater. Phys.*, 2013, **87**, 174108.
73. K. A. See, M. Leskes, J. M. Griffin, S. Britto, P. D. Matthews, A. Emly,

A. Van Der Ven, D. S. Wright, A. J. Morris, C. P. Grey, and R. Seshadri, *J. Am. Chem. Soc.*, 2014, **136**, 16368–16377.

74. J. M. Stratford, M. Mayo, P. K. Allan, O. Pecher, O. J. Borkiewicz, K. M. Wiaderek, K. W. Chapman, C. J. Pickard, A. J. Morris, and C. P. Grey, *J. Am. Chem. Soc.*, 2017, **139**, 7273–7286.
75. S. J. Clark, M. D. Segall, C. J. Pickard, P. J. Hasnip, M. I. J. Probert, K. Refson, and M. C. Payne, *Z. Kristallogr.*, 2005, **220**, 567–570.
76. J. P. Perdew, K. Burke, and M. Ernzerhof, *Phys. Rev. Lett.*, 1996, **77**, 3865–3868.
77. J. R. Yates, C. J. Pickard, and F. Mauri, *Phys. Rev. B*, 2007, **76**, 24401.
78. M. Catti, G. Ferraris, S. Hull, and A. Pavese, *Phys. Chem. Miner.*, 1995, 22, 200–206.
79. S. Sturniolo, T. F. G. Green, R. M. Hanson, M. Zilka, K. Refson, P. Hodgkinson, S. P. Brown, and J. R. Yates, *Solid State Nucl. Magn. Reson.*, 2016, **78**, 64–70.
80. B. Berglund and R. W. Vaughan, *J. Chem. Phys.*, 1980, **73**, 2037–2043.
81. G. A. Jeffrey and Y. Yeon, *Acta Biomater.*, 1986, **B42**, 410–413.
82. U. Sternberg and E. Brunner, *J. Magn. Reson.*, 1994, **108**, 142–150.
83. T. H. Walter, G. L. Turner, and E. Oldfield, *J. Magn. Reson.*, 1988, **76**, 106–120.
84. A. Tkatchenko and M. Scheffler, *Phys. Rev. Lett.*, 2009, **102**, 73005.
85. J. R. Yates, C. J. Pickard, M. C. Payne, and F. Mauri, *J. Chem. Phys.*, 2003, **118**, 5746.
86. T. F. G. Green and J. R. Yates, *J. Chem. Phys.*, 2014, **140**, 234106.

# Chapter 7: Conclusions and outlook

In this thesis, the use of first-principles calculations to assist NMR spectroscopic studies of disordered inorganic solids has been explored. Despite NMR spectroscopy being a sensitive probe of local structure, with no need for long-range order or periodicity, the NMR spectra of disordered materials often exhibit complex lineshapes that are challenging to interpret or assign to specific chemical environments. As a result, first-principles calculations are in many cases important and in others simply vital for the confident assignment of the NMR spectra of disordered inorganic materials, something that can ultimately lead to structure elucidation. Nevertheless, attempting to use first-principles calculations to investigate the structure of disordered materials is itself a complex task, with the main challenge being attempting to answer the deceptively simple question, "what is the best way of modelling disorder?", which does not have an obvious or definite answer or a prescribed recipe that can be easily followed.

By its very nature, disorder is an abstract concept, meaning the method by which a material that exhibits structural disorder (*i.e.*, compositional, configurational, positional, temporal, or some combination of these), can be modelled computationally is not clear. In Chapter 4, a variety of computational methods capable of modelling (with varying levels of accuracy) the structure of disordered materials were presented. This chapter highlighted the breadth of computational approaches available, ranging from generating a series of structural models by manually altering a simpler, related input structure in a systematic way, to far more sophisticated or automated approaches to generate series of related structural models. The results discussed in this thesis involved the use of a variety of computational approaches to generate models that were subsequently used to, in Chapter 5, investigate configurational disorder in pyrochlore and defect fluorite materials and, in Chapter 6, probe positional disorder of protons and vacancies in the important inner Earth mineral hydrous wadsleyite. These studies were all successful, with predicted NMR parameters for

computationally generated structural models clearly facilitating new structural insights and allowing more confident assignment of the solid-state NMR spectra for these materials. However, the success of these investigations has highlighted the importance of producing structural models that can provide an accurate description of the local and longer-range environments in the real materials being studied, as well as reinforcing how the way in which structural modelling is extremely system dependent.

In Chapter 5, the SOD program proved particularly well suited for the generation of structural models capable of representing the B-site cation disorder in $Y_2Sn_xTi_{2-x}O_7$ and $La_2Sn_xZr_{2-x}O_7$ pyrochlore solid solutions. While the predicted NMR parameters for the two sets of Y- or Sn-centred cluster models, or the models with randomised B-site cations, enabled trends between predicted NMR parameters and variations in local structure to be observed, the complete set (for a fixed composition) of SOD-generated structural models allowed a far deeper understanding of the relationship between predicted NMR and geometrical parameters to be obtained. In addition, as SOD is able to determine the configurational degeneracy of a particular B-site cation arrangement, simulation of $^{89}Y$ and $^{119}Sn$ (for $Y_2Sn_xTi_{2-x}O_7$) and $^{119}Sn$ (for $La_2Sn_xZr_{2-x}O_7$) NMR spectra could be performed, facilitating, for the first time, a way to directly compare the predicted and experimental NMR spectra for these materials. Therefore, it is concluded that for $Y_2Sn_xTi_{2-x}O_7$ and $La_2Sn_xZr_{2-x}O_7$ pyrochlores, SOD clearly represents the method of choice for generating structural models and ultimately probing the structures of these disordered materials, with the predicted NMR parameters for these models proving to be a vital tool for the interpretation of the experimental NMR spectra.

The immense number of possible atom arrangements resulting from the combination of cation disorder and randomised oxygen vacancies in $Y_2Zr_2O_7$ and $Y_2Hf_2O_7$ defect fluorites prevents the use of SOD to generate all possible structural models. Therefore a far less sophisticated, and less representative, method for modelling disorder had to be used to study these systems, with a limited number of structural models produced. As a result of the small

number of defect fluorite structural models considered, their predicted NMR parameters provided less insight into the assignment of the complicated experimental $^{89}$Y or $^{17}$O NMR spectra of $Y_2Zr_2O_7$ or $Y_2Hf_2O_7$, although it is clear that the complex spectral lineshape result from the overlap of signals from different local environments. For the future, it may be possible to use restraints from experiment (*e.g.*, the coordination numbers of different species, or information on likely NNN) to restrict the number of models that need to be considered, or at least to reduce the complexity such that more automated schemes, such as SOD, can be employed. While Chapter 5 clearly demonstrates that the combination of first-principles calculations and experimental solid-state NMR spectroscopy is a powerful approach to elucidate the structure of disordered inorganic materials, as the level of disorder increases the efficient generation of at least a subset of accurate and relevant structural models is crucial if the complex NMR spectra and, by association, the structure of these materials is to be understood.

In Chapter 6, structure searching, first-principles calculations and multinuclear solid-state NMR spectroscopy were combined to investigate the structure of Fe-free hydrous wadsleyite. Materials containing 1.65 and 3.3 wt% $H_2O$, (termed semi- and fully-hydrous wadsleyite, respectively), were considered. The protons in these hydrous systems are disordered and, owing to their small size, are not located on specific, well-defined crystallographic sites. As a result, SOD, which was used successfully in Chapter 5 to produce structural models for mixed-metal ceramics that exhibit configurational disorder, is not able to generate structures that are representative of the positional disorder in hydrous wadsleyite. Instead, the AIRSS approach, developed to be an unbiased structure searching algorithm, was used to generate 1287 and 3150 semi- and fully-hydrous wadsleyite structures, respectively. By comparing the predicted NMR parameters for a subset of AIRSS-generated semi- and fully-hydrous wadsleyite structures (subsets that were selected from the complete set of models based on either $\Delta H$, or by using a *k*-means clustering approach), with the experimental NMR spectra of hydrous wadsleyite, new insights into the mechanism by which hydration occurs, were achieved, and a new structural picture of fully-hydrous

wadsleyite proposed. It is concluded that the unbiased nature of the AIRSS approach was vital for the success of this investigation, with the generation and subsequent analysis of metastable atomic arrangements allowing a structural picture of hydrous wadsleyite that was in good agreement with the experimental NMR spectra, to be suggested.

Through the investigations presented in Chapters 5 and 6 of this thesis, it can be concluded that first-principles calculations are extremely helpful in assigning the complex experimental NMR spectra of solids, and therefore in determining the structure of disordered inorganic materials. By comparing predicted solid-state NMR parameters to experimental NMR spectra, not only can the former be used to assist spectral assignment, but this comparison also provides a way for the accuracy and relevance of one or more computationally generated structural models to be evaluated. This thesis has shown that the type (and level) of disorder exhibited by a system influences the optimum methods by which structural models can and should be generated, *i.e.*, the SOD and AIRSS approaches being better suited to investigating systems that display configurational and positional disorder, respectively, therefore, it is vital that the most appropriate structure modelling approach is employed.

In this thesis, the very idea of what it means to determine the structure of a disordered material has been questioned. While diffraction seeks to represent the position of every atom within a material using a structural picture that is averaged over time and distance, *i.e.*, some type of periodic unit cell, in contrast, NMR spectroscopists consider that the assignment of spectral resonances to specific, local chemical environments, and the understanding of the local rather than average structure, is vital. However, when considering a disordered system, in many instances, neither of these two approaches can provide the complete picture, or the level of detail required, as configurational or positional disorder can lead to diffraction-based structural descriptions being far from accurate, at a local level, while the complex NMR lineshapes exhibited by disordered materials often contain overlapping resonances that cannot be confidently assigned (or indeed

assigned at all) to specific chemical environments. In either case, significant ambiguity and/or inaccuracy can arise when the structure of a disordered inorganic material is proposed. For the systems discussed specifically in this thesis, the idea of a diffraction- or NMR-based description of a disordered inorganic material being a sufficiently detailed and accurate representation of the true system, has been questioned, with both the ceramic and hydrous minerals highlighting that an ensemble of structures, each containing a specific atomic arrangement, might be required to explain experimental observations. However, more philosophically, the challenge is to understand how many models are enough, what size of system is sufficient to model particular types of disorder and, whether it is even feasible to talk about "the structure" for complex materials. Is there a need for some sort of "picture" that involves imposing some level of periodicity, a restriction that hinders insight into the chemical reactivity (and ultimately applications and uses) of a material, which might be considered to depend on the more local structure? Similarly, the desire for an NMR spectrum to be decomposed into contributions that reflect only the local structure might not be feasible (as shown in Chapter 5) or even required for structural insight. Indeed, regardless of what set of structural models are used, can a good match between prediction and experiment for something such as an NMR spectrum ever constitute a sufficient understanding of the structure?

In this thesis first-principles calculations have been used to perform comprehensive studies of the structure of both ceramics and minerals, with the emphasis firmly placed on evaluating how effective such calculations can be in assisting the assignment of NMR spectra. It is hoped that the investigations presented in Chapters 5 and 6 will lay the groundwork for similar studies to probe the structure of ever more complex disordered materials. In the near future, based on the successful investigations of $Y_2Sn_xTi_{2-x}O_7$ and $La_2Sn_xZr_{2-x}O_7$, SOD could be used to generate structural models for a range of oxide-based materials that exhibit configurational disorder, such as pyrochlores, fluorites, garnets and perovskites. The ability to identify every symmetry inequivalent atomic arrangement for a specific composition means that SOD could alternatively be employed to investigate

the effects of configurational disorder in many microporous materials such as AlPOs, MOFs and zeolites, enabling a more detailed understanding of the structure-property relationships that underpin their applications in gas storage, catalysis and drug discovery. AIRSS (and similar structure prediction approaches) could be applied to study the effect of positional disorder in a wide range of systems, including the incorporation of hydrogen into other high-pressure silicate minerals such as forsterite ($\alpha$-$Mg_2SiO_4$) or ringwoodite ($\gamma$-$Mg_2SiO_4$), in hydrogen storage and potential battery or fuel cell materials, or alternatively, to probe the effect of introducing small molecules into framework materials in order to explore potential coordination environments. It is also possible, and exciting, to consider the prospect of combining SOD and AIRSS to investigate a system, with this union of approaches potentially well suited to the study of materials that exhibit both configurational and positional disorder.

Obviously, in many cases it is unreasonable, as well as unwise, to advocate the use of first-principles calculations in isolation, *i.e.*, in the absence of any experimental measurements by which the success or accuracy of such calculations can be quantified. However, it is hoped that this thesis shows how valuable and versatile first-principles calculations can be when they are combined with solid-state NMR spectroscopy for the study of disordered inorganic materials. Indeed, as the accuracy of first-principles calculations improves with future developments, and as experimentalists become more aware of the structural insights they can provide, it is anticipated that their use will continue to grow in popularity. In addition, improved accessibility to HPC resources will allow larger and more disordered systems to be investigated more routinely, with hardware developments possibly facilitating or even necessitating new methods of computationally modelling disordered materials to be identified. It is clear that while computation has much to offer experimentalists, no one approach can "solve everything" and that development of both experiment and computation will be required to improve structural characterisation, and ultimately, the design and control of the materials that will fuel and support our future.

# Appendices

## A $Y_2Sn_xTi_{2-x}O_7$: computational details

### A1 Convergence testing

Convergence testing was based on the $Y_2Sn_2O_7$ structure,[1] in which a series of NMR parameter calculations were performed, in which the $E_{cut}$ and k-point spacing were varied independently. While k-point spacing was varied, an $E_{cut}$ of 60 Ry was used, whereas a k-point spacing of 0.04 2π Å$^{-1}$ was used when $E_{cut}$ was varied. All NMR parameter calculations were performed using CASTEP 8.0, with ZORA correction applied. Plots of $^{89}$Y, $^{119}$Sn and $^{17}$O NMR parameters against $E_{cut}$ and k-point spacing are shown in Figures A1.1, A1.2 and A1.3, respectively. Based on the results of the convergence testing, an $E_{cut}$ of 60 Ry and a k-point spacing of 0.04 2π Å$^{-1}$ were used in the geometry optimisation and NMR parameter calculations for the cluster models of $Y_2Sn_xTi_{2-x}O_7$, discussed in Section 5.5.3.

### A2 Cluster models: referencing calculated NMR parameters

For $^{89}$Y, the reference shielding was based on the calculated isotropic chemical shielding and experimental isotropic chemical shift, averaged over the two Y sites in $Y_2O_3$,[2] as shown in Table A2.1. As $\sigma_{ref} = \sigma_{iso}^{calc} + \delta_{iso}^{exp}$, it follows that the $^{89}$Y $\sigma_{ref}$ = 2412.14 + 293.5 = 2705.64 ppm.

In order to achieve better agreement with experimental $^{89}$Y $\delta_{iso}$ values, the calculated $^{89}$Y $\delta_{iso}$ and Ω parameters for the cluster models were scaled. The calculated and experimental NMR parameters for $Y_2Sn_2O_7$ and $Y_2Ti_2O_7$, the two end members of the $Y_2Sn_xTi_{2-x}O_7$ structural models, shown in Table A2.2, were compared. By plotting experimental $^{89}$Y $\delta_{iso}$ (or Ω) against calculated $^{89}$Y

$\delta_{iso}$ (or Ω), as shown in Figure A2.1, the equations of the lines of best fit can be applied to scale calculated $^{89}$Y $\delta_{iso}$ and Ω values. Therefore, the equation

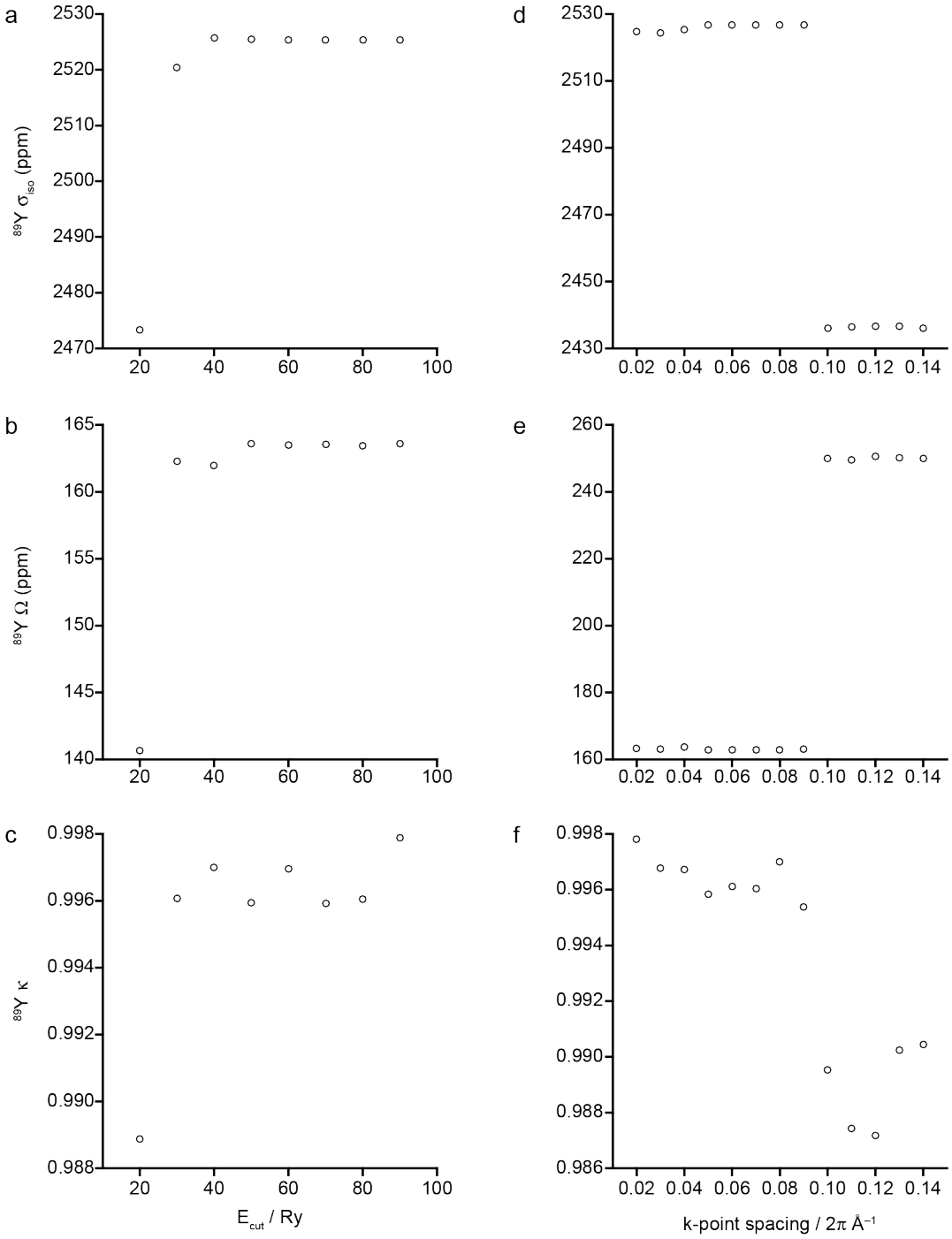


**Figure A1.1:** Convergence of $Y_2Sn_2O_7$, showing plots of calculated $^{89}$Y (a and d) $\sigma_{iso}$, (b and e) Ω and (c and f) κ, against (a-c) $E_{cut}$ and (d-f) k-point spacing, with all calculations performed using CASTEP 8.0, with ZORA correction applied.

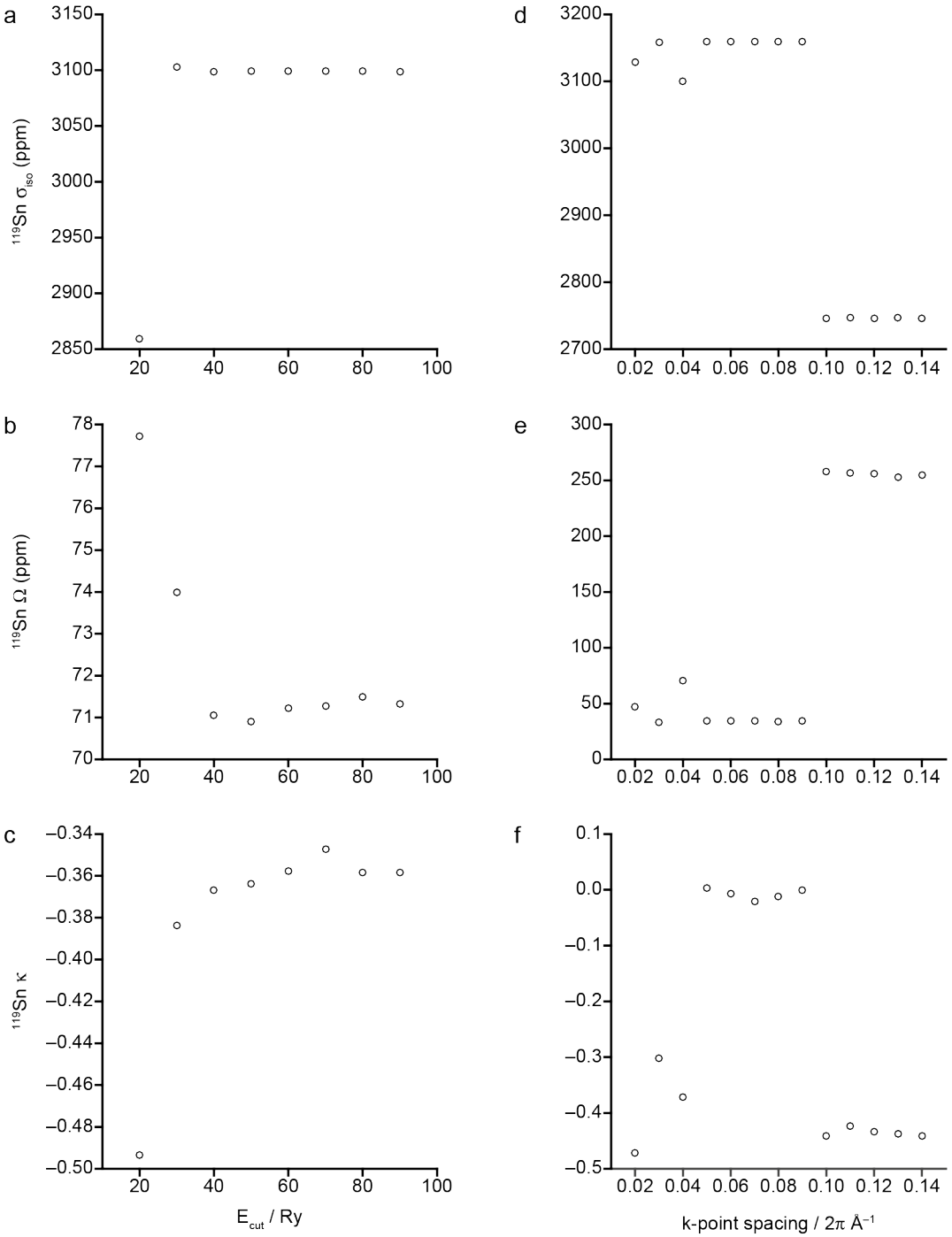


**Figure A1.2:** Convergence of $Y_2Sn_2O_7$, showing plots of calculated $^{119}$Sn (a and d) $\sigma_{iso}$, (b and e) Ω and (c and f) κ, against (a-c) $E_{cut}$ and (d-f) k-point spacing, with all calculations performed using CASTEP 8.0, with ZORA correction applied.

shown in Figure A2.1a was used to scale the calculated $^{89}$Y $\delta_{iso}$, values for the Y-centred cluster models. Similarly, the equation shown in Figure A2.1b was used to scale the calculated $^{89}$Y Ω values for the Y-centred cluster models.

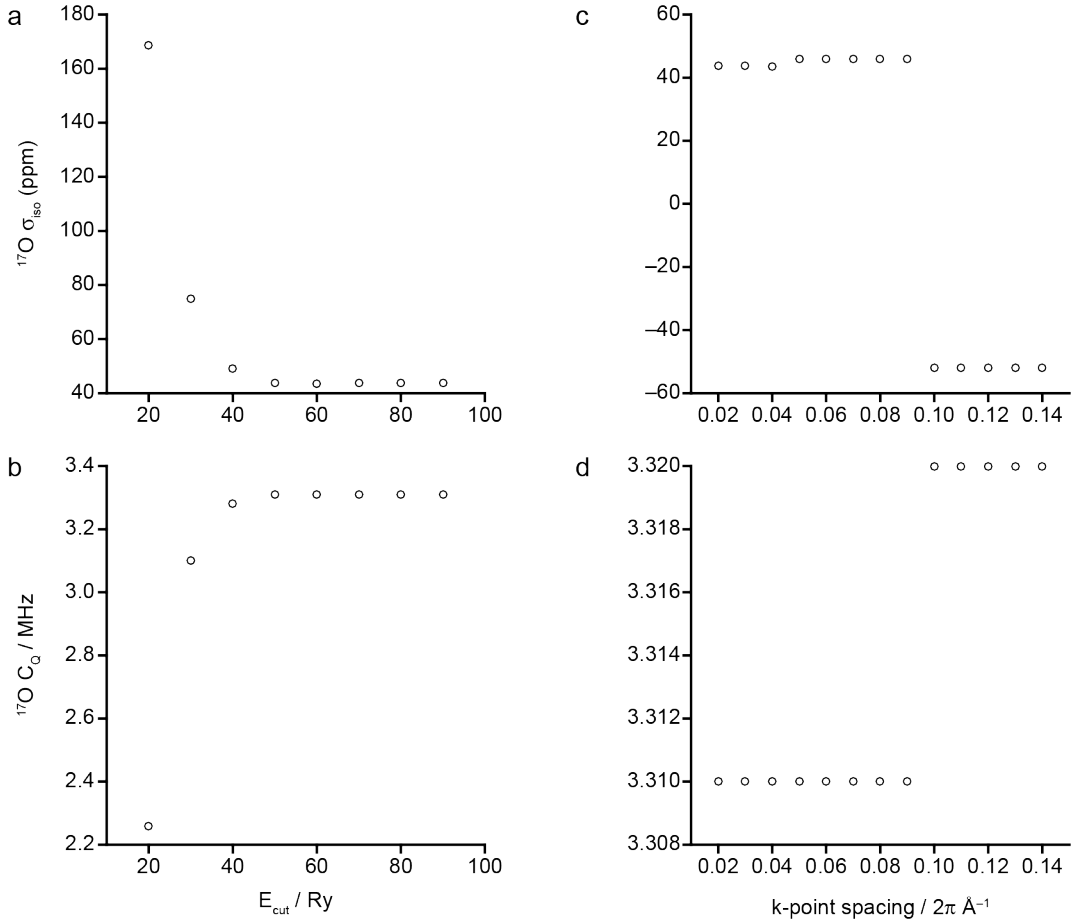


**Figure A1.3:** Convergence of $Y_2Sn_2O_7$, showing plots of calculated $^{17}O$ (a and c) $\sigma_{iso}$, and (b and d) $C_Q$, against (a and b) $E_{cut}$ and (c and d) k-point spacing, with all calculations performed using CASTEP 8.0, with ZORA correction applied.

**Table A2.1:** Experimental $^{89}Y$ isotropic chemical shift ($\delta_{iso}$) and calculated $^{89}Y$ isotropic chemical shielding ($\sigma_{iso}$) for the two Y sites in $Y_2O_3$,[2] with the average values also included.

| | Y1 (ppm) | Y2 (ppm) | Average (ppm) |
|---|---|---|---|
| Experimental $^{89}Y$ $\delta_{iso}$[3] | 273 | 314 | 293.5 |
| Calculated $^{89}Y$ $\sigma_{iso}$ | 2434.04 | 2390.24 | 2412.14 |

**Table A2.2:** Experimental and calculated $^{89}Y$ isotropic chemical shift ($\delta_{iso}$) and span ($\Omega$) values for $Y_2Sn_2O_7$ and $Y_2Ti_2O_7$.

| | Calculated | | Experimental | |
|---|---|---|---|---|
| Structure | $\delta_{iso}$ (ppm) | $\Omega$ (ppm) | $\delta_{iso}$[4] (ppm) | $\Omega$[5] (ppm) |
| $Y_2Sn_2O_7$[1] | 170.45 | 160.47 | 150 | 208 |
| $Y_2Ti_2O_7$[6] | 34.21 | 640.41 | 65 | 595 |

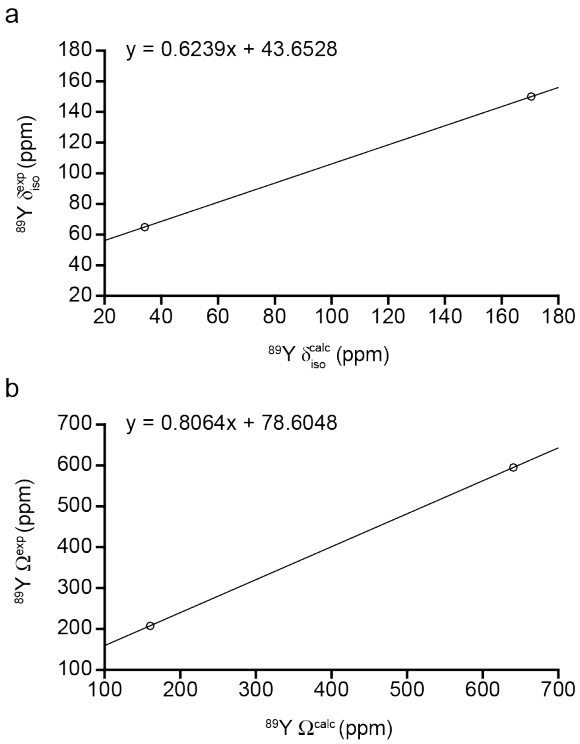


**Figure A2.1:** (a) Experimental $^{89}$Y $\delta_{iso}$ plotted against calculated $^{89}$Y $\delta_{iso}$ and (b) experimental $^{89}$Y $\Omega$ plotted against calculated $^{89}$Y $\Omega$, for $Y_2Sn_2O_7$ and $Y_2Ti_2O_7$, with the equation of the lines of best fit shown.

The $^{119}$Sn reference shielding was based on the experimental $\delta_{iso}$, –582 ppm,[7] and the calculated $\sigma_{iso}$, 3183.93 ppm, for the Sn site in $Y_2Sn_2O_7$.[1] As $\sigma_{ref} = \sigma_{iso}^{calc} + \delta_{iso}^{exp}$, it follows that the $^{119}$Sn $\sigma_{ref}$ = 3183.93 + –582 = 2601.93 ppm. This $\sigma_{ref}$ was used to reference the calculated $^{119}$Sn $\sigma_{iso}$ for the Sn-centred cluster models.

## A3 Models with randomised B-site cations: referencing calculated $^{17}$O $\sigma_{iso}$

In order to convert calculated $^{17}$O $\sigma_{iso}$ to $\delta_{iso}$ for the structural models with randomised B-site cations, the experimental and calculated $^{17}$O NMR parameters for the two O sites in both $Y_2Sn_2O_7$ and $Y_2Ti_2O_7$ were compared, with a summary of these parameters given in Table A3.1. The equation

**Table A3.1:** Experimental $^{17}O$ isotropic chemical shift ($\delta_{iso}$) and calculated $^{17}O$ isotropic chemical shielding ($\sigma_{iso}$) values for the two O sites in both $Y_2Sn_2O_7$ and $Y_2Ti_2O_7$.

| Structure | Site | $^{17}O$ $\delta_{iso}$ [8] (ppm) | $^{17}O$ $\sigma_{iso}$ (ppm) |
|---|---|---|---|
| $Y_2Sn_2O_7$ [1] | O1 | 385 | –185.88 |
| | O2 | 165 | 28.53 |
| $Y_2Ti_2O_7$ [6] | O1 | 385 | –172.17 |
| | O2 | 455 | –257.28 |

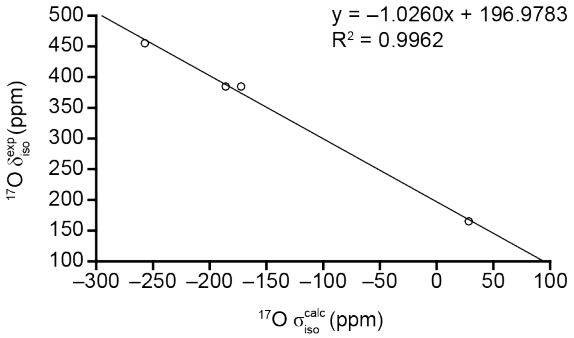


**Figure A3.1:** Plot of experimental $^{17}O$ $\delta_{iso}$ against calculated $^{17}O$ $\delta_{iso}$ for the two O sites in $Y_2Sn_2O_7$ and $Y_2Ti_2O_7$, with the equation of the lines of best fit shown.

shown in Figure A3.1, that results from plotting experimental $^{17}O$ $\delta_{iso}$ against calculated $^{17}O$ $\sigma_{iso}$, and was used to reference calculated $^{17}O$ $\sigma_{iso}$ for the structural models with randomised B-site cations.

## A4 SOD series 1: referencing calculated NMR parameters

The calculated $^{89}Y$ $\sigma_{iso}$ were converted to $\delta_{iso}$ using the calculated and experimental NMR parameters for $Y_2Sn_2O_7$ and $Y_2Ti_2O_7$, the two end members of the $Y_2Sn_xTi_{2-x}O_7$ pyrochlore series. The calculated and experimental $^{89}Y$ $\Omega$ for $Y_2Sn_2O_7$ and $Y_2Ti_2O_7$ were also used to scale the calculated $^{89}Y$ $\Omega$, in order to achieve a closer agreement with experimental measurements. The calculated and experimental $^{89}Y$ NMR parameters are shown in Table A4.1, with plots of these NMR parameters shown in Figure A4.1. The equations in Figure A4.1 were used to reference the calculated $^{89}Y$ $\sigma_{iso}$ and $\Omega$ values for the series 1 structural models.

**Table A4.1:** Experimental and calculated $^{89}$Y NMR parameters for $Y_2Sn_2O_7$ and $Y_2Ti_2O_7$.

| | Calculated | | Experimental | |
|---|---|---|---|---|
| Structure | $\sigma_{iso}$ (ppm) | $\Omega$ (ppm) | $\delta_{is}$[4] (ppm) | $\Omega$[5] (ppm) |
| $Y_2Sn_2O_7$[a] | 2537.71 | 161.49 | 150 | 208 |
| $Y_2Ti_2O_7$[a] | 2681.53 | 624.97 | 65 | 595 |

[a] Both compositional end members from series 1 are based on a $Fd\bar{3}m$ pyrochlore structure.

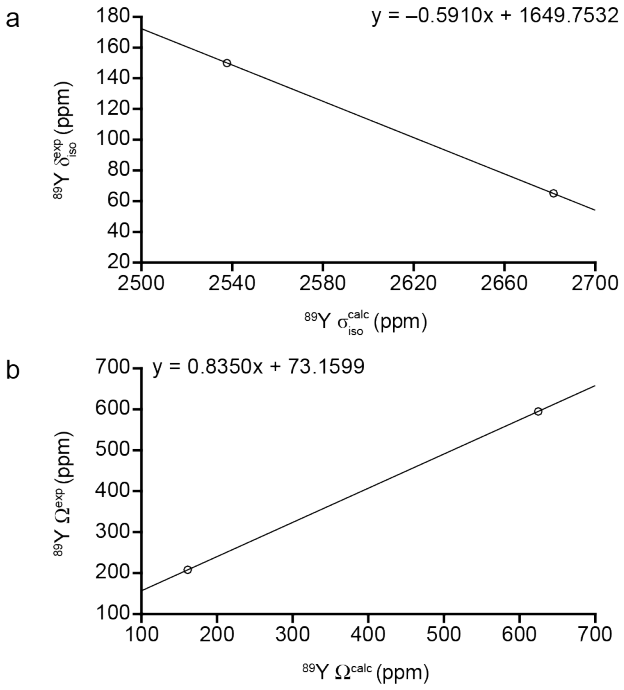


**Figure A4.1:** Plot of (a) Experimental $^{89}$Y $\delta_{iso}$ plotted against calculated $^{89}$Y $\delta_{iso}$ and (b) experimental $^{89}$Y $\Omega$ plotted against calculated $^{89}$Y $\Omega$, for the compositional end members from series 1, $Y_2Sn_2O_7$ and $Y_2Ti_2O_7$, with the equation of the lines of best fit shown.

The $^{119}$Sn reference shielding was based on the experimental $^{119}$Sn $\delta_{iso}$ –582 ppm,[7] and the calculated $^{119}$Sn $\sigma_{iso}$, 3115.28 ppm, for the Sn site in $Y_2Sn_2O_7$, the Sn-rich pyrochlore end member of the series 1 structural models. As $\sigma_{ref} = \sigma_{iso}^{calc} + \delta_{iso}^{exp}$, it follows that $^{119}$Sn $\sigma_{ref}$ = 3115.28 + –582 = 2533.28 ppm. This $\sigma_{ref}$ was used to reference the calculated $^{119}$Sn $\sigma_{iso}$ for the series 1 structural models.

# A5 SOD series 2: referencing calculated NMR parameters

The calculated $^{89}$Y $\sigma_{iso}$ were converted to $\delta_{iso}$ using the calculated and experimental NMR parameters for $Y_2Sn_2O_7$ and $Y_2Ti_2O_7$, the two end members of the $Y_2Sn_xTi_{2-x}O_7$ pyrochlore series. The calculated and experimental $^{89}$Y $\Omega$ for $Y_2Sn_2O_7$ and $Y_2Ti_2O_7$ were also used to scale the calculated $^{89}$Y $\Omega$, in order to achieve a closer agreement with experimental measurements. The calculated and experimental $^{89}$Y NMR parameters are shown in Table A5.1, with plots of these NMR parameters shown in Figure A5.1. The equations in Figure A5.1 were used to reference the calculated $^{89}$Y $\sigma_{iso}$ and $\Omega$ values for the series 2 structural models.

The $^{119}$Sn reference shielding was based on the experimental $\delta_{iso}$, –582 ppm,[7] and the calculated $\sigma_{iso}$, 3115.63 ppm, for the Sn site in $Y_2Sn_2O_7$, the Sn-rich pyrochlore end member of the series 2 structural models. As $\sigma_{ref} = \sigma_{iso}^{calc} + \delta_{iso}^{exp}$, it follows that $^{119}$Sn $\sigma_{ref}$ = 3115.63 + –582 = 2533.63 ppm. This $\sigma_{ref}$ was used to reference the calculated $^{119}$Sn $\sigma_{iso}$ for the series 2 structural models.

**Table A5.1:** Experimental and calculated $^{89}$Y NMR parameters for $Y_2Sn_2O_7$ and $Y_2Ti_2O_7$.

| | Calculated | | Experimental | |
|---|---|---|---|---|
| Structure | $\sigma_{iso}$ (ppm) | $\Omega$ (ppm) | $\delta_{iso}$[4] (ppm) | $\Omega$[5] (ppm) |
| $Y_2Sn_2O_7$[a] | 2537.70 | 161.17 | 150 | 208 |
| $Y_2Ti_2O_7$[a] | 2677.54 | 631.33 | 65 | 595 |

[a] Both compositional end members from series 2 are based on a $Fd\bar{3}m$ pyrochlore structure.

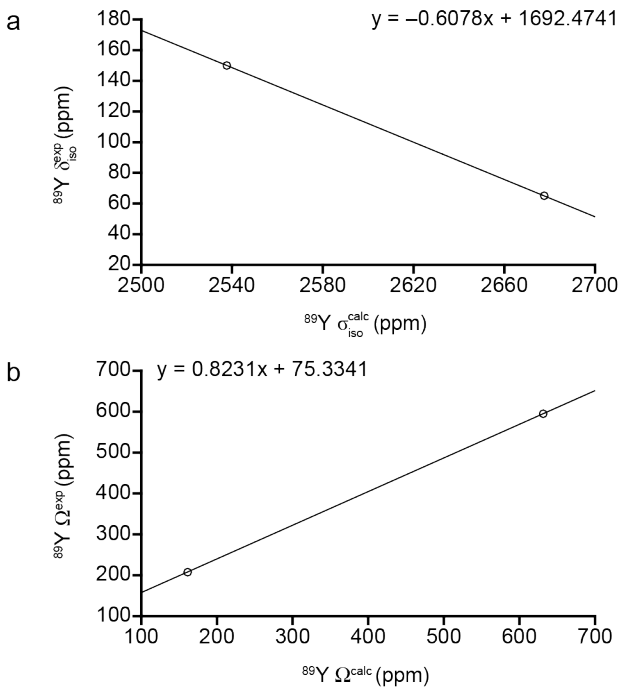


**Figure A5.1:** Plot of (a) Experimental $^{89}Y$ $\delta_{iso}$ plotted against calculated $^{89}Y$ $\delta_{iso}$ and (b) experimental $^{89}Y$ $\Omega$ plotted against calculated $^{89}Y$ $\Omega$, for the compositional end members from series 2, $Y_2Sn_2O_7$ and $Y_2Ti_2O_7$, with the equation of the lines of best fit shown.

## A6 SOD series 3: referencing calculated NMR parameters

The calculated $^{89}Y$ $\sigma_{iso}$ were converted to $\delta_{iso}$ using the calculated and experimental NMR parameters for $Y_2Sn_2O_7$ and $Y_2Ti_2O_7$, the two end members of the $Y_2Sn_xTi_{2-x}O_7$ pyrochlore series. The calculated and experimental $^{89}Y$ $\Omega$ for $Y_2Sn_2O_7$ and $Y_2Ti_2O_7$ were also used to scale the calculated $^{89}Y$ $\Omega$, in order to achieve a closer agreement with experimental measurements. The calculated and experimental $^{89}Y$ NMR parameters are shown in Table A6.1, with plots of these NMR parameters shown in Figure A6.1. The equations in Figure A6.1 were used to reference the calculated $^{89}Y$ $\sigma_{iso}$ and $\Omega$ values for the series 3 structural models.

**Table A6.1:** Experimental and calculated $^{89}$Y NMR parameters for $Y_2Sn_2O_7$ and $Y_2Ti_2O_7$.

| | Calculated | | Experimental | |
|---|---|---|---|---|
| Structure | $\sigma_{iso}$ (ppm) | $\Omega$ (ppm) | $\delta_{iso}$[4] (ppm) | $\Omega$[5] (ppm) |
| $Y_2Sn_2O_7$[a] | 2535.57 | 160.47 | 150 | 208 |
| $Y_2Ti_2O_7$[a] | 2671.40 | 640.05 | 65 | 595 |

[a] Both compositional end members from series 3 are based on a $Fd\bar{3}m$ pyrochlore structure.

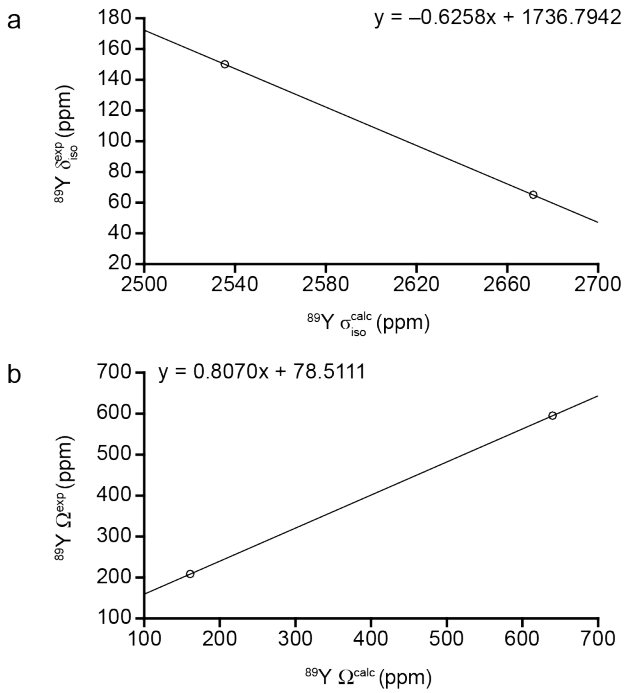


**Figure A6.1:** Plot of (a) Experimental $^{89}$Y $\delta_{iso}$ plotted against calculated $^{89}$Y $\delta_{iso}$ and (b) experimental $^{89}$Y $\Omega$ plotted against calculated $^{89}$Y $\Omega$, for the compositional end members from series 3, $Y_2Sn_2O_7$ and $Y_2Ti_2O_7$, with the equation of the lines of best fit shown.

The $^{119}$Sn reference shielding was based on the experimental $\delta_{iso}$, –582 ppm,[7] and the calculated $\sigma_{iso}$, 3184.49 ppm, for the Sn site in $Y_2Sn_2O_7$, the Sn-rich pyrochlore end member of the series 3 structural models. As $\sigma_{ref} = \sigma_{iso}^{calc} + \delta_{iso}^{exp}$, it follows that $^{119}$Sn $\sigma_{ref}$ = 3184.49 + –582 = 2602.49 ppm. This $\sigma_{ref}$ was used to reference the calculated $^{119}$Sn $\sigma_{iso}$ for the series 3 structural models.

In order to convert calculated $^{17}$O $\sigma_{iso}$ to $\delta_{iso}$ for the Series 3 $Y_2Sn_xTi_{2-x}O_7$ structural models, the experimental and calculated $^{17}$O NMR parameters for

**Table A6.2:** Experimental $^{17}O$ isotropic chemical shift ($\delta_{iso}$) and calculated $^{17}O$ isotropic chemical shielding ($\sigma_{iso}$) values for the two O sites in both $Y_2Sn_2O_7$ and $Y_2Ti_2O_7$.

| Structure | Site | $^{17}O$ $\delta_{iso}$ [8] (ppm) | $^{17}O$ $\sigma_{iso}$ (ppm) |
|---|---|---|---|
| $Y_2Sn_2O_7$[a] | O1 | 385 | –185.90 |
| | O2 | 165 | 27.98 |
| $Y_2Ti_2O_7$[a] | O1 | 385 | –172.52 |
| | O2 | 455 | –257.45 |

[a] Both compositional end members from series 3 are based on a $Fd\bar{3}m$ pyrochlore structure.

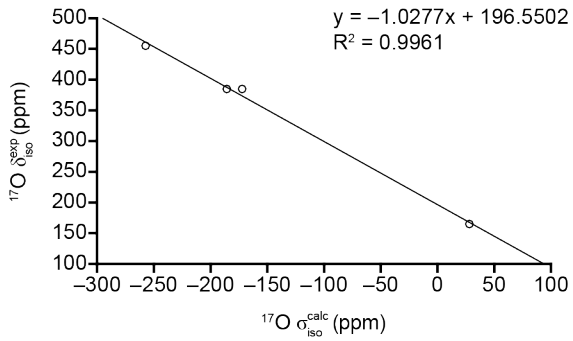


**Figure A6.2:** Plot of experimental $^{17}O$ $\delta_{iso}$ against calculated $^{17}O$ $\sigma_{iso}$ for the two O sites in $Y_2Sn_2O_7$ and $Y_2Ti_2O_7$, with the equation of the line of best fit shown.

the two O sites in both $Y_2Sn_2O_7$ and $Y_2Ti_2O_7$ were used, with a summary of these parameters given in Table A6.2 and a plot of experiment $^{17}O$ $\delta_{iso}$ against the calculated $\sigma_{iso}$ shown in Figure A6.2. The equation of the line shown in Figure A6.2 was used to reference calculated $^{17}O$ $\sigma_{iso}$ values for the series 3 structural models.

# B $La_2Sn_xZr_{2-x}O_7$: computational details

## B1 Convergence testing

Convergence testing was based on the $La_2Sn_2O_7$ structure,[9] in which a series of NMR parameter calculations were performed, in which the $E_{cut}$ and k-point spacing were varied independently. While k-point spacing was varied, an $E_{cut}$ of 60 Ry was used, whereas a k-point spacing of 0.04 $2\pi$ $Å^{-1}$ was used when $E_{cut}$ was varied. All NMR parameter calculations were performed using CASTEP 16.11, with ZORA correction applied. Plots of $^{119}Sn$ and $^{17}O$ NMR parameters against $E_{cut}$ and k-point spacing are shown in Figures B1.1 and B1.2, respectively. Based on the results of the convergence testing, an $E_{cut}$ of 60 Ry and a k-point spacing of 0.04 $2\pi$ $Å^{-1}$ were used in the geometry optimisation and NMR parameter calculations for the cluster models of $La_2Sn_xZr_{2-x}O_7$, discussed in Section 5.6.3.

## B2 Cluster models: referencing calculated NMR parameters

The $^{119}Sn$ reference shielding was based on the experimental $\delta_{iso}$, –642 ppm,[7] and the calculated $\sigma_{iso}$, 3238.52 ppm, for the Sn site in $La_2Sn_2O_7$.[9] As $\sigma_{ref} = \sigma_{iso}^{calc} + \delta_{iso}^{exp}$, it follows that $^{119}Sn$ $\sigma_{ref}$ = 3238.52 + –642 = 2596.52 ppm. This $\sigma_{ref}$ was used to reference the calculated $^{119}Sn$ $\sigma_{iso}$ for the $La_2Sn_xZr_{2-x}O_7$ cluster models.

In order to convert calculated $^{17}O$ $\sigma_{iso}$ to $\delta_{iso}$, the experimental and calculated $^{17}O$ NMR parameters for the two O sites in both $La_2Sn_2O_7$ and $La_2Zr_2O_7$ were compared, with a summary of these parameters given in Table B2.1. The equation resulting from plotting experiment $^{17}O$ $\delta_{iso}$ against calculated $^{17}O$ $\sigma_{iso}$, (see Figure B2.1) was used to reference $^{17}O$ $\sigma_{iso}$ values for the $La_2Sn_xZr_{2-x}O_7$ cluster models.

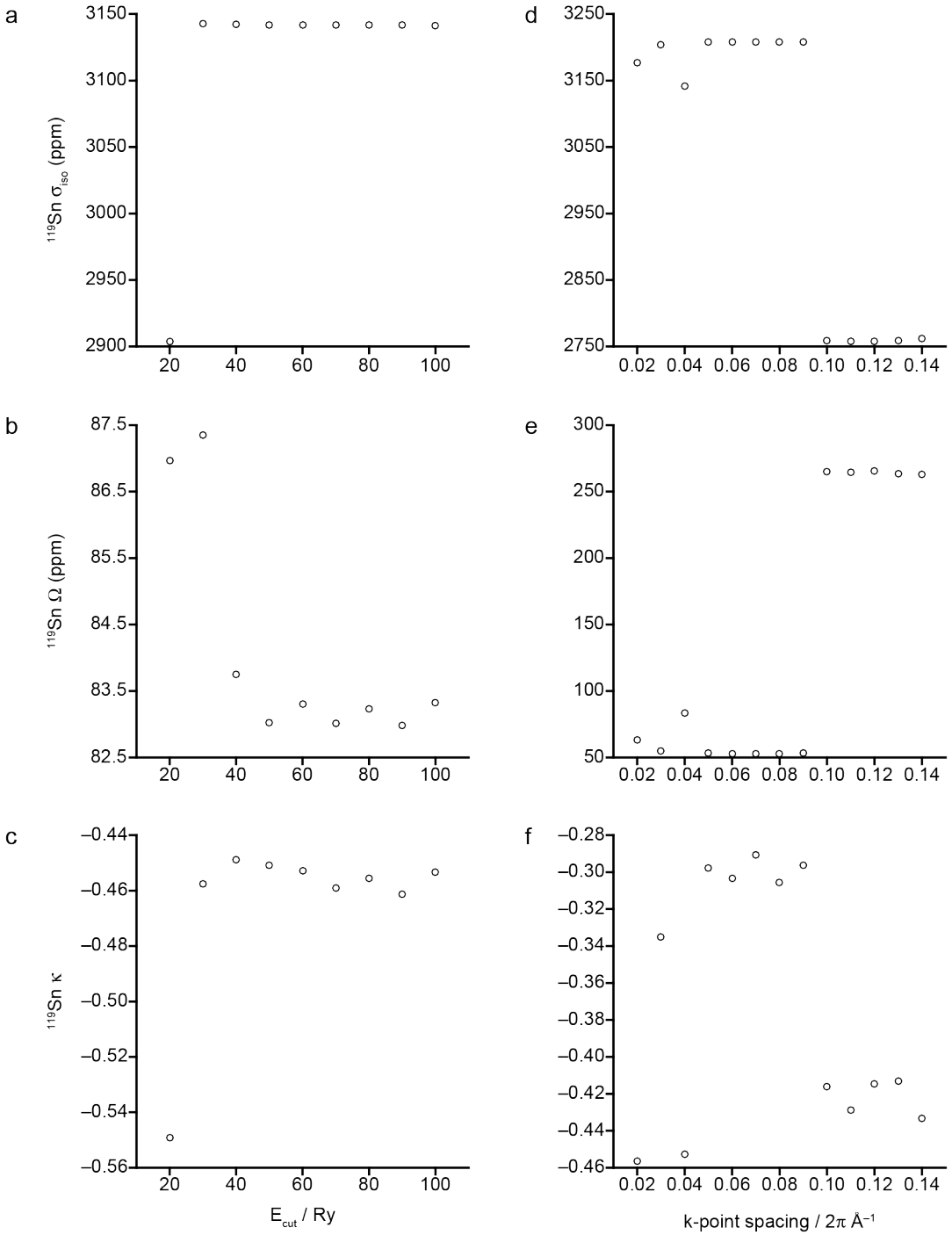


**Figure B1.1:** Convergence of $La_2Sn_2O_7$, showing plots of calculated $^{119}$Sn (a and d) $\sigma_{iso}$, (b and e) Ω and (c and f) κ, against (a-c) $E_{cut}$ and (d-f) k-point spacing. All calculations were carried out using CASTEP 16.11, with ZORA correction applied.

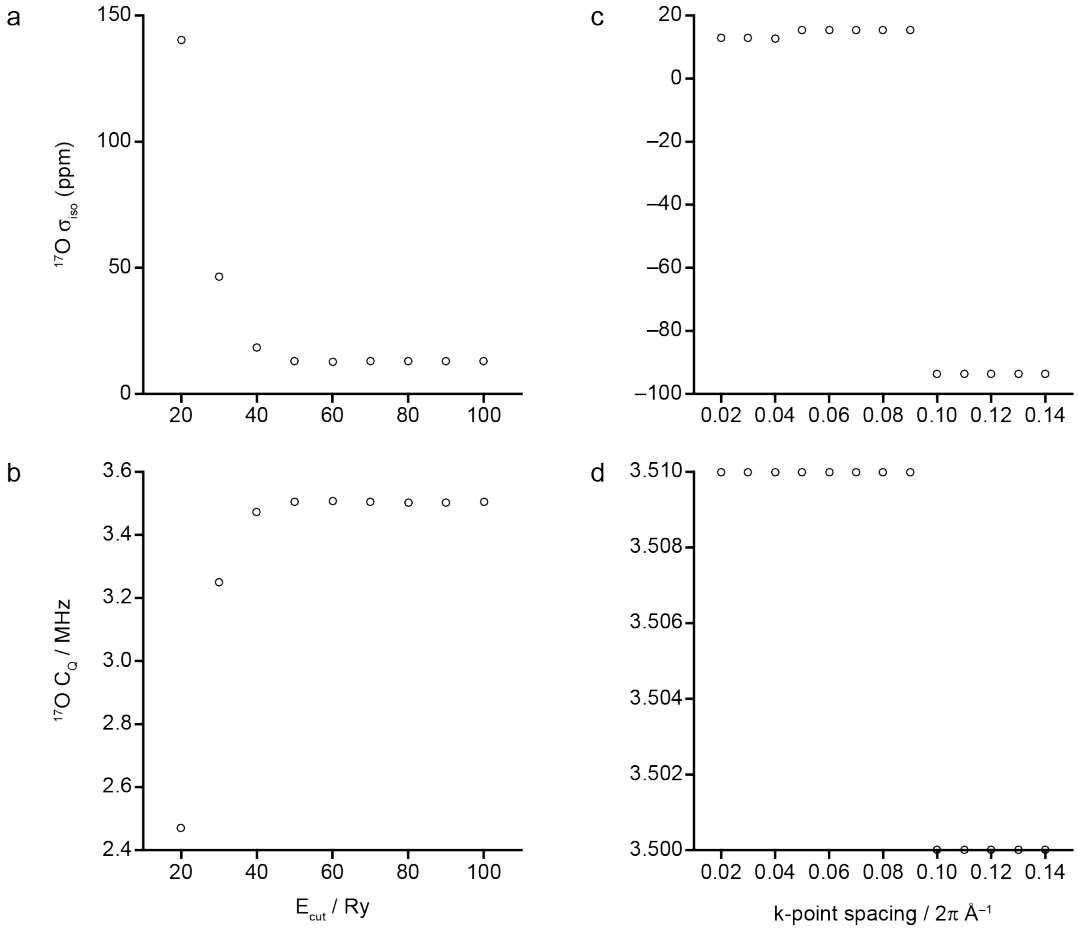


**Figure B1.2:** Convergence of $La_2Sn_2O_7$, showing plots of calculated $^{17}O$ (a and c) $\sigma_{iso}$, and (b and d) $C_Q$, against (a and b) $E_{cut}$ and (c and d) k-point spacing. All calculations were carried out using CASTEP 16.11, with ZORA correction applied.

**Table B2.1:** Experimental $^{17}O$ isotropic chemical shift ($\delta_{iso}$) and calculated $^{17}O$ isotropic chemical shielding ($\sigma_{iso}$) values for the two O sites in both $La_2Sn_2O_7$ and $La_2Zr_2O_7$.

| Structure | Site | $^{17}O$ $\delta_{iso}$ [a] (ppm) | $^{17}O$ $\sigma_{iso}$ (ppm) |
|---|---|---|---|
| $La_2Sn_2O_7$[9] | O1 | 641.50 | –321.52 |
| | O2 | 222.00 | –11.04 |
| $La_2Zr_2O_7$[10] | O1 | 626.26 | –315.56 |
| | O2 | 394.02 | –167.55 |

[a] Experimental $^{17}O$ $\delta_{iso}$ taken from the $^{17}O$ MAS NMR spectra of $La_2Sn_2O_7$ and $La_2Zr_2O_7$ recorded by Miss Arantxa Fernandes at the University of St Andrews.

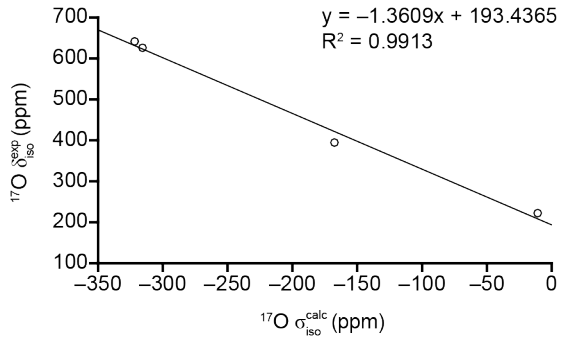


**Figure B2.1:** Plot of experimental $^{17}O$ $\delta_{iso}$ against calculated $^{17}O$ $\sigma_{iso}$ for the two O sites in both $La_2Sn_2O_7$ and $La_2Zr_2O_7$, with the equation of the line of best fit shown.

# C $Y_2Zr_2O_7$ and $Y_2Hf_2O_7$: computational details

## C1 Referencing $^{89}Y$ and $^{17}O$ $\sigma_{iso}$

The calculated $^{89}Y$ $\sigma_{iso}$ for the 30 $Y_2Zr_2O_7$ and 30 $Y_2Hf_2O_7$ structural models were referenced by comparing the experimental $^{89}Y$ $\delta_{iso}$ and calculated $^{89}Y$ $\sigma_{iso}$ for a series of Y-containing compounds, with a summary of the relevant NMR parameters given in Table C1.1, with a plot of experimental $^{89}Y$ $\delta_{iso}$ against calculated $\sigma_{iso}$, shown in Figure C1.1. The equation in Figure C1.1 was used to reference calculated $^{89}Y$ $\sigma_{iso}$ for the $Y_2Zr_2O_7$ and $Y_2Hf_2O_7$ structural models.

**Table C1.1:** Calculated $^{89}Y$ isotropic chemical shielding ($\sigma_{iso}$) and experimental $^{89}Y$ isotropic chemical shift ($\delta_{iso}$) for a series of Y-containing compounds. All structures were geometry optimised prior to NMR parameters being calculated, with all calculations performed using CASTEP 8.0, with ZORA correction applied for the calculation of NMR parameters.

| Compound | $^{89}Y$ $\sigma_{iso}$ (ppm) | $^{89}Y$ $\delta_{iso}$ (ppm) |
|---|---|---|
| $Y_2O_3$[2] | 2431.58 | 273[3] |
| | 2387.83 | 314[3] |
| $Y_2Sn_2O_7$[1] | 2535.20 | 150[4] |
| $Y_2Ti_2O_7$[6] | 2671.45 | 65[4] |
| $YAlO_3$[11] | 2440.90 | 215[3] |
| $YF_3$[12] | 2779.02 | –112[13] |
| $Y_3Al_5O_{12}$[14] | 2442.96 | 222[3] |
| $YScO_3$[15] | 2418.51 | 263.1[15] |
| α-$Y_2Si_2O_7$[16] | 2515.32 | 170.8[17] |
| | 2552.22 | 132.9[17] |
| | 2596.45 | 95.1[17] |
| | 2637.91 | 37.7[17] |
| β-$Y_2Si_2O_7$[18] | 2483.58 | 207.3[17] |
| γ-$Y_2Si_2O_7$[16] | 2491.91 | 198.9[17] |

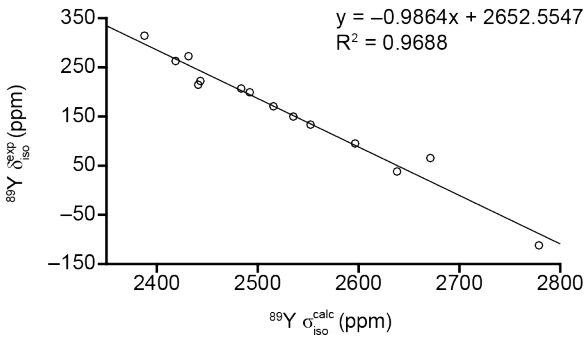


**Figure C1.1:** Plot of experimental $^{89}Y$ $\delta_{iso}$ against calculated $^{89}Y$ $\sigma_{iso}$ for the compounds listed in Table C1.1, with the equation of the line of best fit shown.

The calculated $^{17}O$ $\sigma_{iso}$ for the 30 $Y_2Zr_2O_7$ and 30 $Y_2Hf_2O_7$ structural models were referenced by comparing the experimental $^{17}O$ $\delta_{iso}$ and calculated $^{17}O$ $\sigma_{iso}$ for a series of O-containing compounds, with a summary of the relevant NMR parameters given in Table C1.2, with a plot of experimental $^{17}O$ $\delta_{iso}$ against calculated $\sigma_{iso}$, shown in Figure C1.2. The equation in Figure C1.2 was used to reference calculated $^{17}Y$ $\sigma_{iso}$ for the $Y_2Zr_2O_7$ and $Y_2Hf_2O_7$ structural models.

**Table C1.2:** Calculated $^{17}O$ isotropic chemical shielding ($\sigma_{iso}$) and experimental $^{17}O$ isotropic chemical shift ($\delta_{iso}$) for a series of O-containing compounds. All structures were geometry optimised prior to NMR parameters being calculated, with all calculations performed using CASTEP 8.0 with ZORA correction applied for the calculation of NMR parameters.

| Compound | $^{17}O$ $\sigma_{iso}$ (ppm) | $^{17}O$ $\delta_{iso}$ (ppm) |
|---|---|---|
| α-Cristobalite[19] | 220.72 | 37.2[20] |
| α-Quartz[21] | 217.92 | 40.8[20] |
| $MgSiO_3$ (perovskite)[22] | 129.17 | 108[23] |
| $MgSiO_3$ (akimotoite)[24] | 135.37 | 106[23] |
| α-$Mg_2SiO_4$[25] | 203.19 | 48[26–28] |
| | 184.78 | 64[26–28] |
| | 187.57 | 61[26–28] |
| β-$Mg_2SiO_4$[29] | 214.38 | 38[28,30] |
| | 169.41 | 76[28,30] |
| | 180.29 | 66[28,30] |

| | | |
|---|---|---|
| | 182.35 | 65[28,30] |
| γ-$Mg_2SiO_4$[31] | 181.46 | 63[28] |
| $SrTiO_3$ (perovskite)[32] | –281.27 | 465[33] |
| $BaZrO_3$ (perovskite)[34] | 170.54 | 376[33] |
| $LiNbO_3$[35] | –222.50 | 449.9[a] |
| $LaAlO_3$[36] | 69.11 | 170.2[33] |
| $Y_2Sn_2O_7$[1] | –185.90 | 385[8] |
| | 28.37 | 165[8] |
| $Y_2Ti_2O_7$[6] | –172.17 | 385[8] |
| | –257.48 | 455[8] |
| $Y_2O_3$[2] | –155.84 | 356[37] |
| $TiO_2$ (rutile)[38] | –398.38 | 591[37,39] |
| $CaTiO_3$[40] | –267.89 | 448[33] |
| | –259.18 | 443.4[33] |
| $CaZrO_3$[40] | –136.54 | 336[33] |
| | –128.51 | 329[33] |
| BeO[41] | 231.67 | 26[42] |
| MgO[43] | 197.80 | 47[42] |
| SrO[44] | –206.25 | 390[42] |
| BaO[45] | –456.42 | 629[42] |
| $La_2O_3$[46] | –304.92 | 582.4[33] |
| | –194.38 | 466.5[33] |
| $HfO_2$[47] | –51.46 | 267[48] |
| | –115.02 | 336[48] |
| $MgSiO_3$ (clinoenstatite)[49] | 211.02 | 41[50] |
| | 203.64 | 45[50] |
| | 200.69 | 51[50] |
| | 196.17 | 54[50] |
| | 188.88 | 64[50] |
| | 176.40 | 75[50] |

[a] $^{17}O$ $\delta_{iso}$ for $LiNbO_3$ determined from analysis of an MQ MAS spectrum.

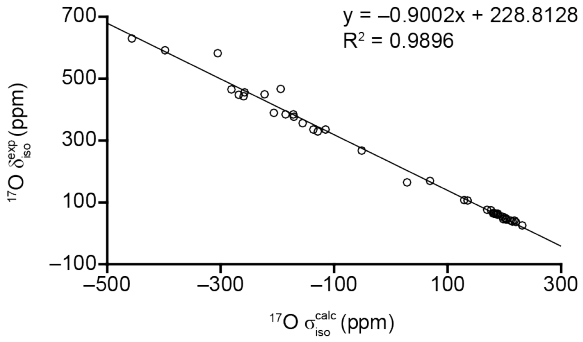


**Figure C1.2:** Plot of experimental $^{17}O$ $\delta_{iso}$ against calculated $^{17}O$ $\sigma_{iso}$ for the compounds listed in Table C1.2, with the equation of the line of best fit shown.

# D Semi-hydrous wadsleyite: computational details

## D1 CASTEP 7.01 convergence testing

Convergence testing was based on brucite ($Mg(OH)_2$)[51] for $^1$H, and anhydrous wadsleyite ($\beta$-$Mg_2SiO_4$)[29] for $^{17}$O and $^{29}$Si. A series of NMR parameter calculations were performed, in which the $E_{cut}$ and k-point spacing were varied independently. While k-point spacing was varied, an $E_{cut}$ of 60 Ry was used, whereas a k-point spacing of 0.04 2$\pi$ Å$^{-1}$ was used when $E_{cut}$ was varied. All NMR parameter calculations were performed using CASTEP 7.01. Plots of $^1$H $\sigma_{iso}$ and $^2$H $C_Q$ against $E_{cut}$ and k-point spacing are shown in Figure D1.1, while plots of $^{17}$O $\sigma_{iso}$, $^{17}$O $C_Q$ and $^{29}$Si $\sigma_{iso}$ against $E_{cut}$ and k-point spacing are shown in Figure D1.2, Based on the results of the convergence testing, an $E_{cut}$ of 60 Ry and a k-point spacing of 0.04 2$\pi$ Å$^{-1}$ were used in the geometry optimisation and NMR parameter calculations for the subset of Mg3 vacant semi-hydrous wadsleyite structures discussed in Section 6.6.2.

## D2 *k*-means clustering

The Soprano Python library,[52] was used to implement the *k*-means clustering approach, used to select subsets of AIRSS-generated Mg1, Mg2 and Mg3 vacant semi-hydrous structures for more detailed study. The clustering of Mg1, Mg2 and Mg3 vacant structures was performed separately, leading to three separate sets of structures being selected. The specific genes used to cluster the AIRSS-generated semi-hydrous structures were, $\Delta$H (relative to the lowest enthalpy semi-hydrous Mg3 vacant structure); hydroxyl O type; vacancy type; H–H interatomic distance; H–vacancy distance; hydroxyl (H–O) bond length; hydrogen-bond (H-bond) length and magnitude of the combined hydroxyl orientation vector, $\left\|\overrightarrow{OH}\right\|$. This parameter is defined as the sum of unit vectors placed along the two hydroxyls bonds, leading to values between 0 and 2 ($0 \leq \left\|\overrightarrow{OH}\right\| \leq 2$), with the

two extremes representing anti-parallel and parallel hydroxyl bonds, respectively. The position of the Mg site vacancy was formally defined as the fractional coordinates of the Mg cation removed from the anhydrous wadsleyite structure, determined to be a reasonable approximation as the unit cell was fixed during the AIRSS process, with the positions of atoms heavier than H exhibiting little change during the initial geometry optimisation. Genes based on ΔH, protonated O type and $\left\|\overrightarrow{OH}\right\|$ were found to cluster structures well, where, a change in O type having a large effect on ΔH, and with a range of $\left\|\overrightarrow{OH}\right\|$ values found for even a small enthalpy range. All other genes, *i.e.*, H–H interatomic distance, H–vacancy distance, H–O

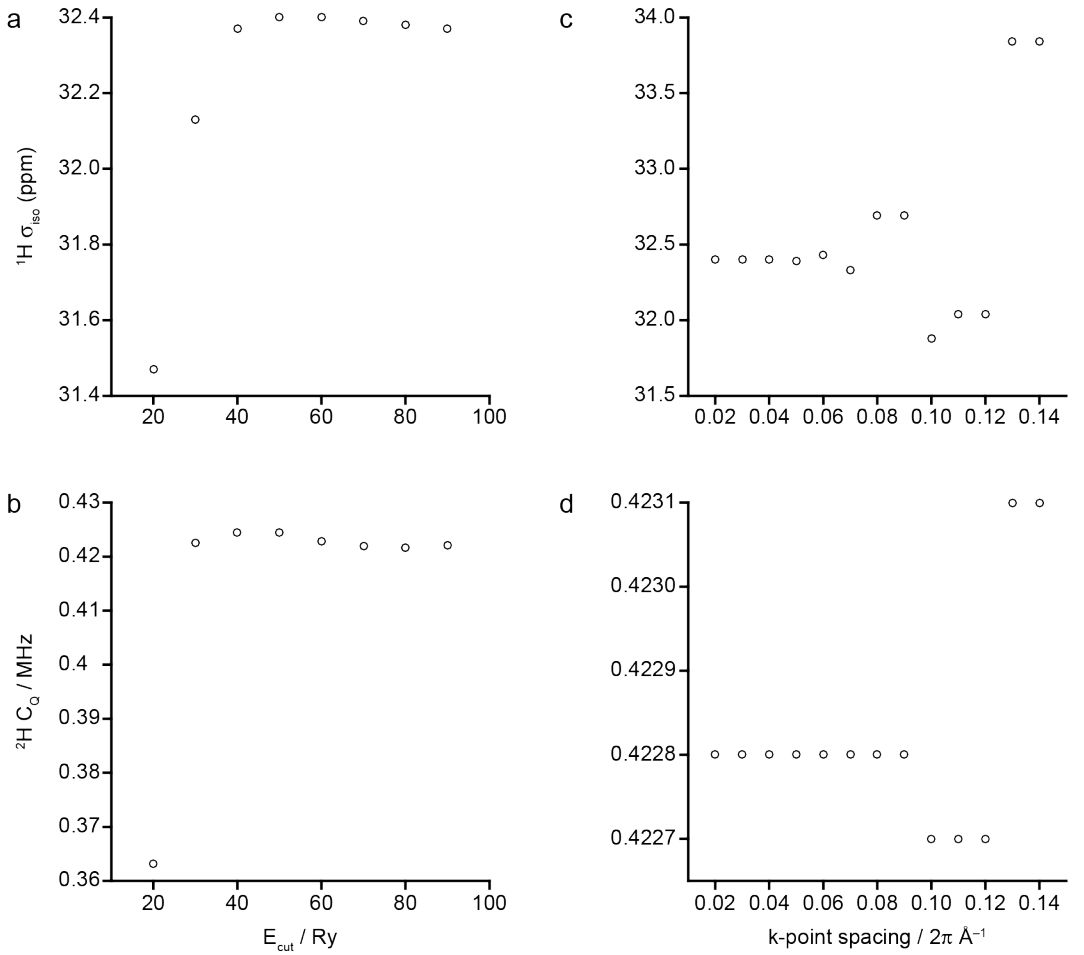


**Figure D1.1:** Convergence of brucite, showing plots of calculated (a and c) $^1$H $\sigma_{iso}$ and (b and d) $^2$H $C_Q$ against (a and b) $E_{cut}$ and (c and d) k-point spacing, with all calculations performed using CASTEP 7.01.

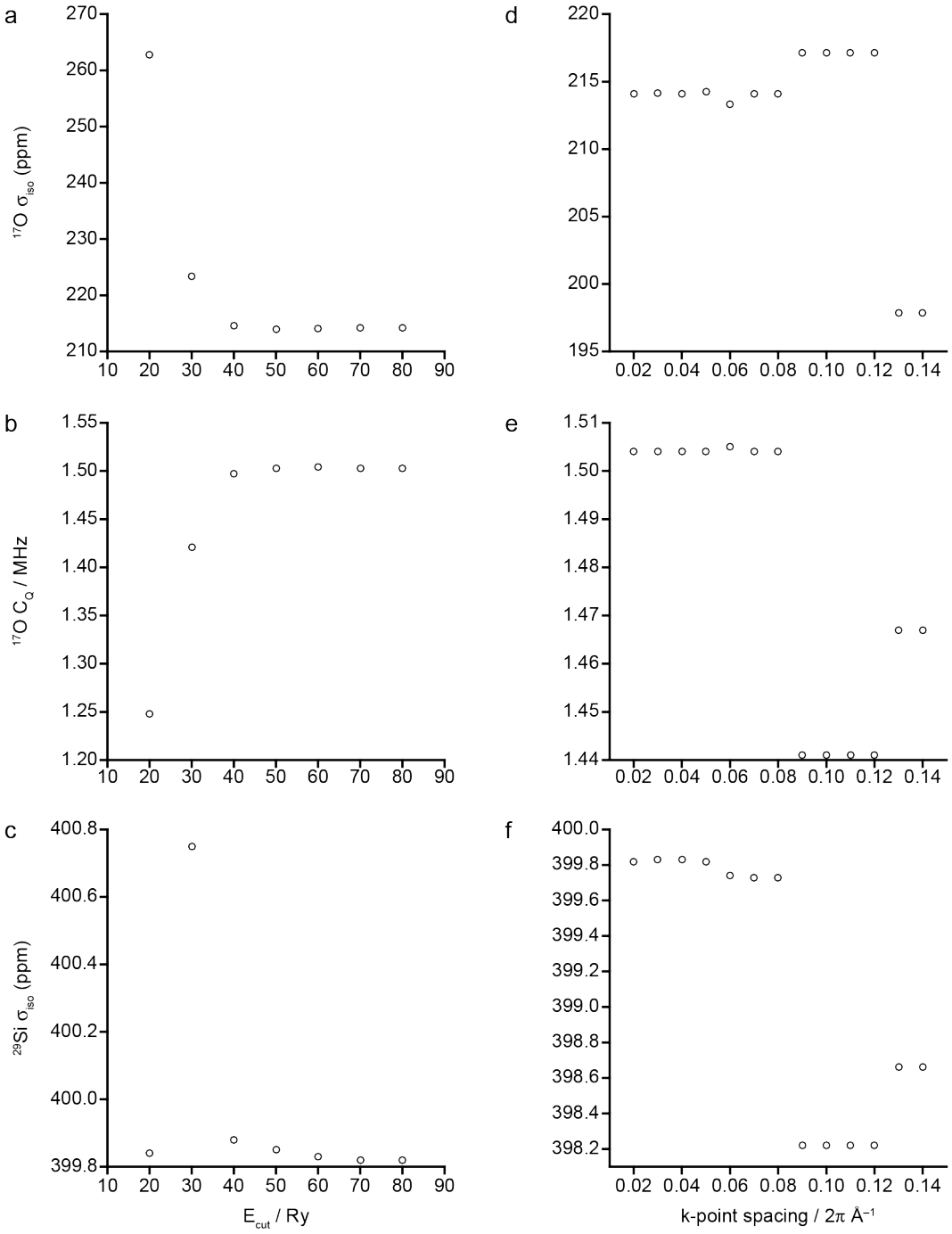


**Figure D1.2:** Convergence of anhydrous wadlseyite, showing plots of calculated (a and d) $^{17}$O $\sigma_{iso}$, (b and e) $^{17}$O $C_Q$ and (c and f) $^{29}$Si $\sigma_{iso}$, against (a-c) $E_{cut}$ and (d-f) k-point spacing, with all calculations performed using CASTEP 7.01.

bond length and H-bond length showed consistent values over large enthalpy range and thus were not useful in clustering.

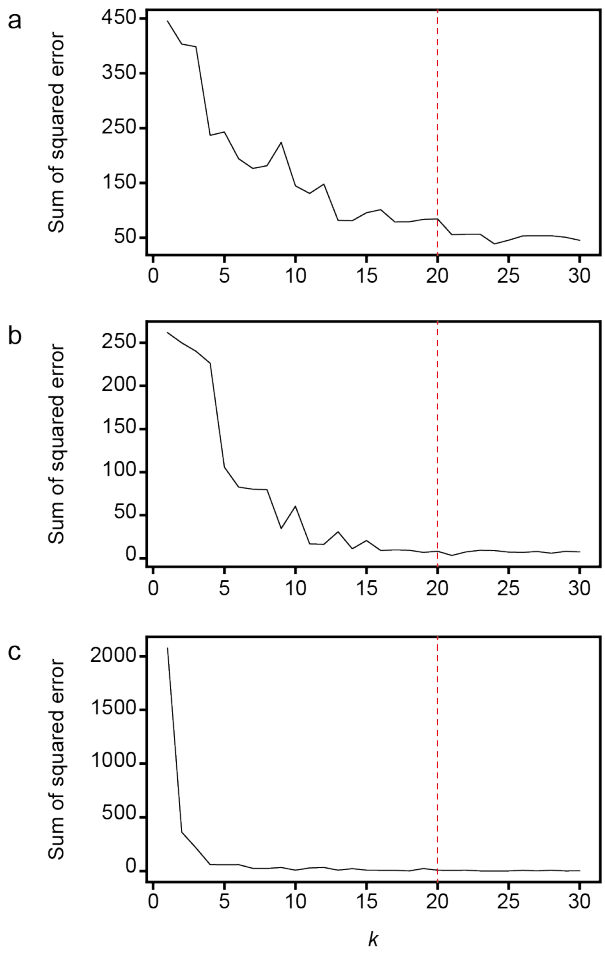


**Figure D2.1:** Convergence plots of *k*-means clustering quantities, where the sum of squared errors is plotted against *k* for the set of 819 AIRSS-generated Mg3 vacant semi-hydrous wadsleyite structures. Plots show the convergence of (a) ΔH, (b) $\left|\left|\overrightarrow{\mathrm{OH}}\right|\right|$, and (c) O type, with the dashed line indicating the maximum value of *k* chosen for this dataset.

The required number of clusters, *k*, was determined by plotting the sum of squared errors within each cluster against *k*, a plot which will reach unity when *k* equals the number of structures in the series, *i.e.*, when $k = N$. A maximum value of *k* was chosen such that the sum of squared errors within each cluster is well converged. Figure D2.1 illustrates this convergence process for the series of Mg3 vacant semi-hydrous wadsleyite structures.

The quality of clustering was evaluated by plotting each cluster as a Gaussian function according to a specific gene,

$$f(x|\mu,\sigma) = e^{-\left(\frac{x-\mu}{\sigma}\right)^2}, \quad (1)$$

$$f(x|\mu,\sigma) = e^{-\left(\frac{x-\mu}{0.1+\sigma}\right)^2}, \quad (2)$$

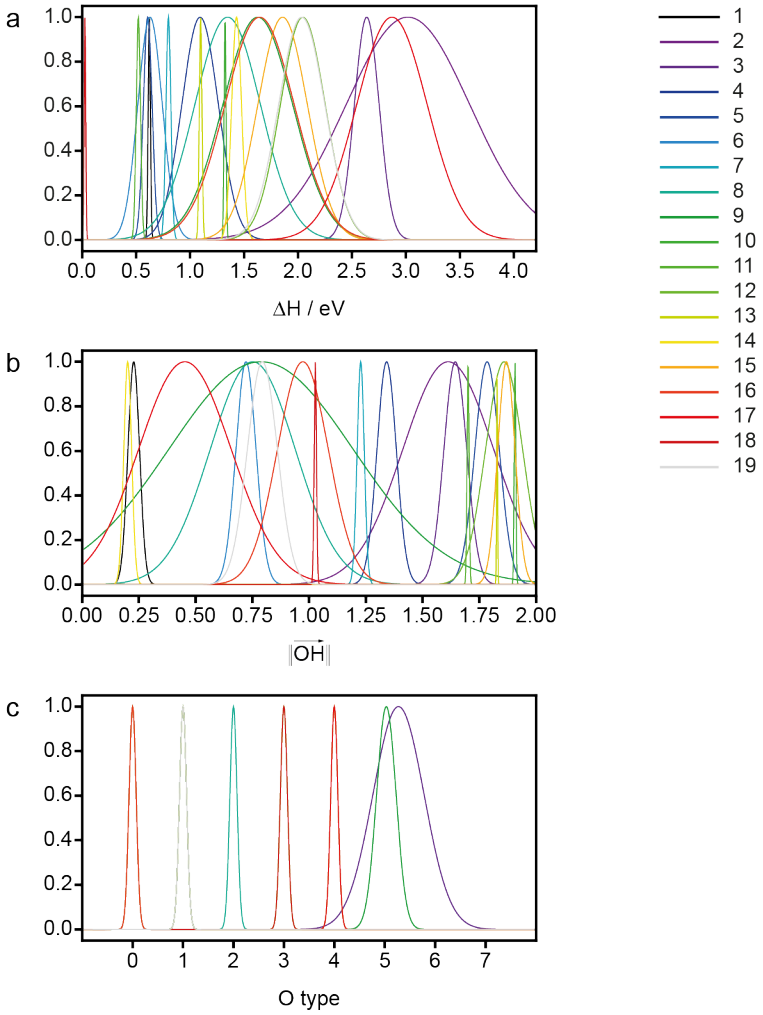


**Figure D2.2:** Gaussian representation of (a) ΔH, (b) $\left|\left|\overrightarrow{OH}\right|\right|$, and (c) O type genes within each of 19 *k*-means clusters found for the set of 819 AIRSS-generated Mg3 vacant semi-hydrous wadsleyite structures, with the Gaussian curves coloured by cluster number.

where x represents the ΔH, $\left|\left|\overrightarrow{OH}\right|\right|$ or O type for a specific structure, μ is the mean of that gene for all structures in the cluster to which the structure in questions belongs, and σ is the standard deviation of that gene in the cluster.

Equation D.1 was used for ΔH and $\left\|\overrightarrow{OH}\right\|$ genes and D.2 was used for the O type, since a value of $\sigma = 0$ was possible and would not be visible. In the case of the ΔH gene, the aim was to have narrow Gaussians at low ΔH and broad Gaussians at high ΔH (see Figure D2.2a), as the low ΔH structures would be better candidates for further study. Due to the discrete nature of the O type, this gene was weighted highly in an attempt to ensure that each cluster contained structures with a common hydroxyl O type, as shown in Figure D2.2b, in which the majority of Gaussians are narrow.

The *k*-means clustering is used to inform the selection of structures for further study, with the lowest ΔH structure selected. Clusters were then pre-filtered based on a ΔH cut-off, set at the ΔH value where the enthalpy profile changed from a series of plateaus to a steep increase in enthalpy. A ΔH cut-off of 1.4 eV was selected for the Mg1 and Mg2 vacant series, with a cut-off of 2.0 eV used for the Mg3 vacant series, with the enthalpy profile and cut-off for the latter series shown in Figure D2.3.

All clusters with a mean ΔH above 2.0 eV were discarded, with the median ΔH structure taken from each of the remaining clusters. The width of the Gaussians for the ΔH and $\left\|\overrightarrow{OH}\right\|$ genes was then used to inform whether

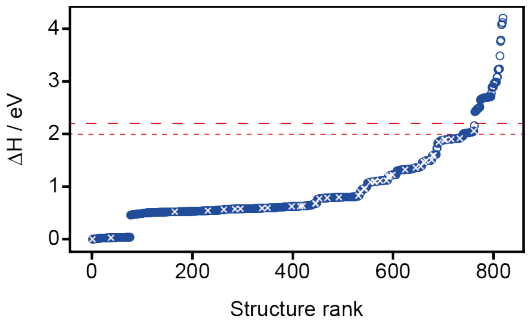


**Figure D2.3:** Plot of ΔH against structure rank for the 819 Mg3 vacant semi-hydrous wadsleyite structures (blue circles), showing *k*-means cluster-selected structures (white crosses), with the dashed lines at 2.0 and 2.2 eV representing the cluster mean ΔH cut-off and the percentile ΔH cut-off, respectively.

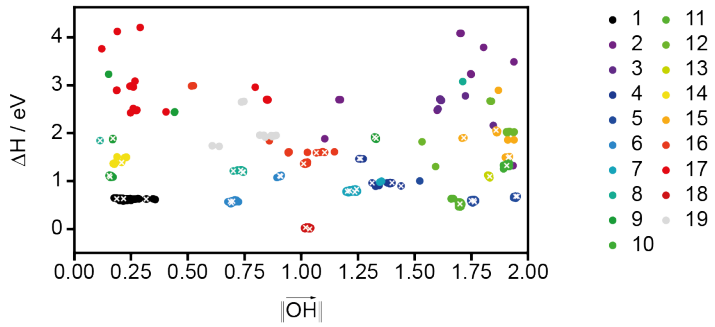


**Figure D2.4:** Plot of ΔH against $\left\|\overrightarrow{OH}\right\|$, for the 819 Mg3 vacant semi-hydrous wadsleyite structures, with the data points coloured by cluster number and the selected structures represented by white crosses.

additional structures should be selected. A cluster was defined as being broad if its width covered > 5% of the whole series, in which case, structures at the 5$^{th}$ and 95$^{th}$ percentile were also selected, providing these structures fall within the enthalpy cut-off. As shown in Figure D2.4, this resulted in the selection of a maximum of five structures per cluster (if the cluster is broad in terms of both ΔH and $\left\|\overrightarrow{OH}\right\|$). This *k*-means clustering approach was used to select a total of 88 structures, 32, 7 and 49 of which contained an Mg1, Mg2 and Mg3 vacancy, respectively.

## D3 CASTEP 8.0 convergence testing

Convergence testing was based on brucite ($Mg(OH)_2$)[51] for $^1$H, and anhydrous wadsleyite (β-$Mg_2SiO_4$)[29] for $^{17}$O and $^{29}$Si. A series of NMR parameter calculations were performed, in which the $E_{cut}$ and k-point spacing were varied independently. While k-point spacing was varied, an $E_{cut}$ of 60 Ry was used, whereas a k-point spacing of 0.04 2π Å$^{-1}$ was used when $E_{cut}$ was varied. All NMR parameter calculations were performed using CASTEP 8.0. Plots of $^1$H $\sigma_{iso}$ and $^2$H $C_Q$ against $E_{cut}$ and k-point spacing are shown in Figure D3.1, while plots of $^{17}$O $\sigma_{iso}$, $^{17}$O $C_Q$ and $^{29}$Si $\sigma_{iso}$ against $E_{cut}$ and k-point spacing are shown in Figure D3.2, Based on the results of the convergence testing, an $E_{cut}$ of 60 Ry and a k-point spacing of 0.04 2π Å$^{-1}$ were used in the geometry optimisation and NMR parameter calculations for the subset of

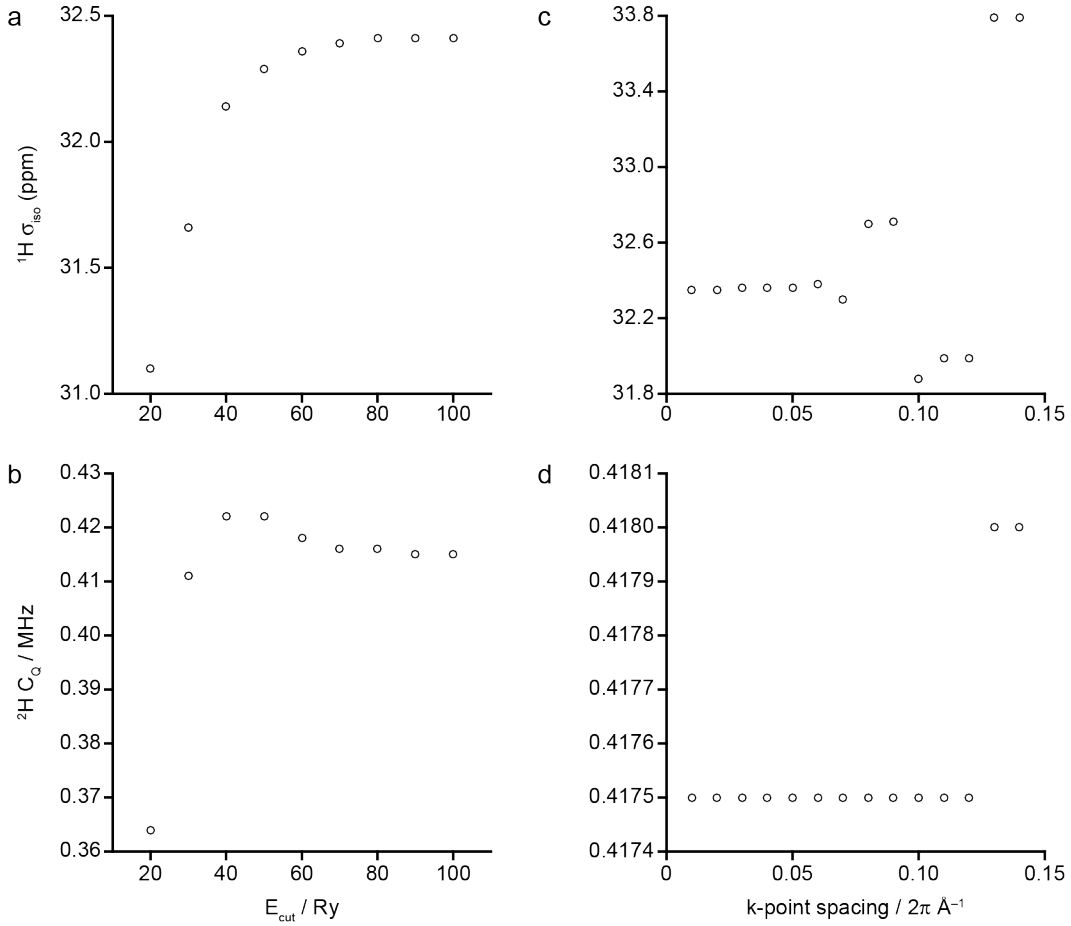


**Figure D3.1:** Convergence of brucite, showing plots of calculated (a and c) $^1$H $\sigma_{iso}$ and (b and d) $^2$H $C_Q$ against (a and b) $E_{cut}$ and (c and d) k-point spacing, with all calculations performed using CASTEP 8.0.

semi- and fully-hydrous wadsleyite structures discussed in Sections 6.6.3 and 6.7, respectively.

## D4 Referencing $^1$H, $^{17}$O and $^{29}$Si $\sigma_{iso}$

Table D4.1 and D4.2 show the $^{17}$O and $^{29}$Si calculated isotropic chemical shielding ($\sigma_{iso}$) and experimental isotropic chemical shift ($\delta_{iso}$) for three polymorphs of $Mg_2SiO_4$, forsterite ($\alpha$-$Mg_2SiO_4$), wadsleyite ($\beta$-$Mg_2SiO_4$) and ringwoodite ($\gamma$-$Mg_2SiO_4$). The initial geometries of the structural models were geometry optimised prior to the calculation of NMR parameters using

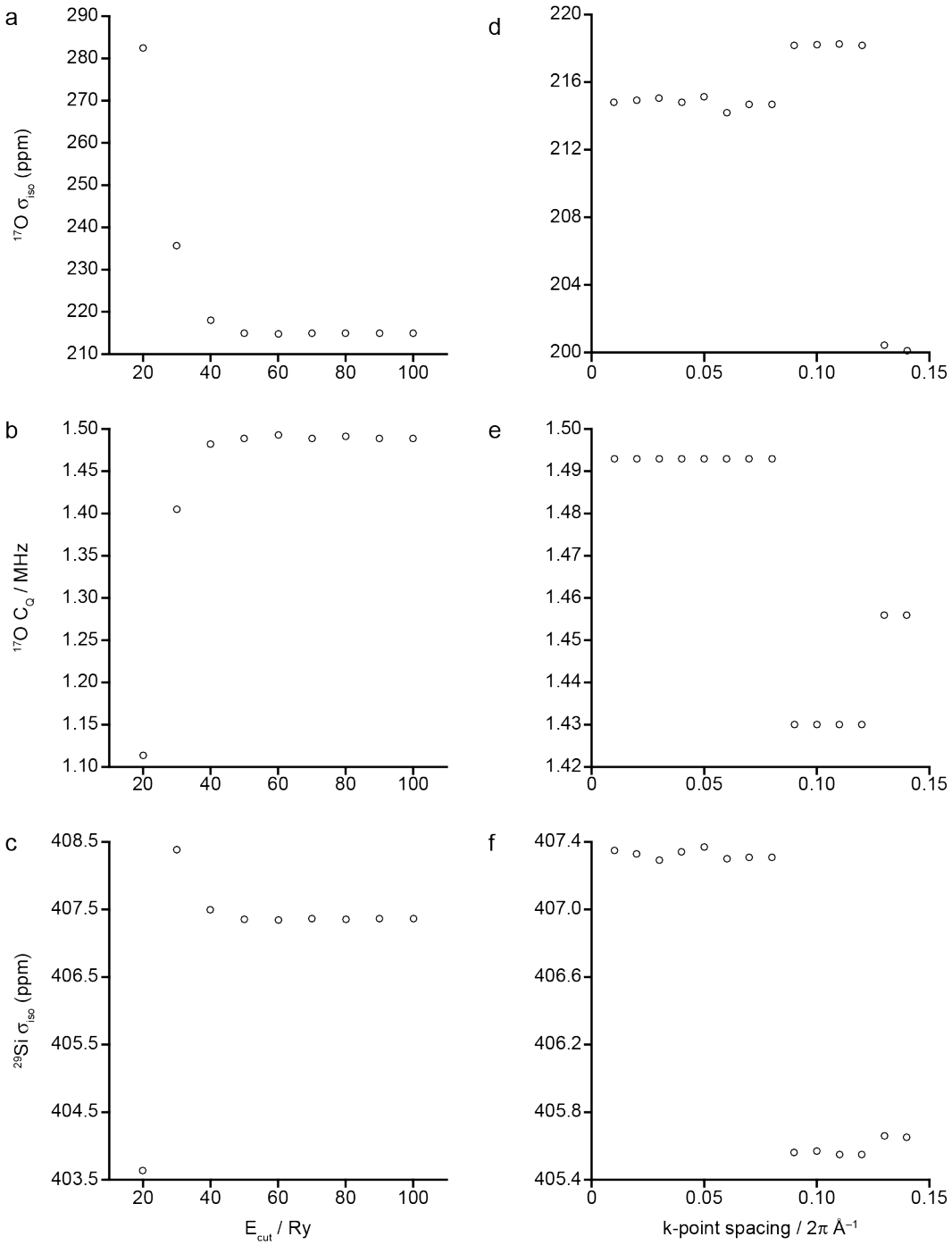


**Figure D3.2:** Convergence of anhydrous wadlseyite, showing plots of calculated (a and d) $^{17}$O $\sigma_{iso}$, (b and e) $^{17}$O $C_Q$ and (c and f) $^{29}$Si $\sigma_{iso}$, against (a-c) $E_{cut}$ and (d-f) k-point spacing, with all calculations performed using CASTEP 8.0.

CASTEP 8.0. Figure D4.1a and D4.1b plot $\delta_{iso}$ against $\sigma_{iso}$ for the three $Mg_2SiO_4$ polymorphs, with both showing good linear correlations. Therefore, the equations shown in Figure D4.1a and D4.1b were used to reference the

**Table D4.1:** $^{17}O$ calculated isotropic chemical shielding ($\sigma_{iso}$) and experimental isotropic chemical shift ($\delta_{iso}$) for forsterite ($\alpha$-$Mg_2SiO_4$), wadsleyite ($\beta$-$Mg_2SiO_4$) and ringwoodite ($\gamma$-$Mg_2SiO_4$).

| Compound | $^{17}O$ $\sigma_{iso}$ (ppm) | $^{17}O$ $\delta_{iso}$ (ppm) |
|---|---|---|
| $\alpha$-$Mg_2SiO_4$[25] | 203.69 | 48[26–28] |
| | 184.66 | 64[26–28] |
| | 188.00 | 61[26–28] |
| $\beta$-$Mg_2SiO_4$[29] | 214.01 | 38[28,53] |
| | 181.94 | 76[28,53] |
| | 181.37 | 66[28,53] |
| | 183.48 | 65[28,53] |
| $\gamma$-$Mg_2SiO_4$[31] | 183.12 | 63[28] |

**Table D4.2:** $^{29}Si$ calculated isotropic chemical shielding ($\sigma_{iso}$) and experimental isotropic chemical shift ($\delta_{iso}$) for forsterite ($\alpha$-$Mg_2SiO_4$), wadsleyite ($\beta$-$Mg_2SiO_4$) and ringwoodite ($\gamma$-$Mg_2SiO_4$).

| Compound | $^{29}Si$ $\sigma_{iso}$ (ppm) | $^{29}Si$ $\delta_{iso}$ (ppm) |
|---|---|---|
| $\alpha$-$Mg_2SiO_4$[25] | 387.40 | –61.9[54] |
| $\beta$-$Mg_2SiO_4$[29] | 406.11 | –79.0[28,55,56] |
| $\gamma$-$Mg_2SiO_4$[31] | 408.23 | –82.0[28] |

$^{17}O$ and $^{29}Si$ calculated isotropic chemical shielding values, respectively, for the 88 semi-hydrous wadsleyite structures selected for further study.

As there are limited examples in the literature of hydrous high-pressure silicate minerals with accurate experimental isotropic chemical shift information as well as well-defined structures, finding an approach for referencing calculated $^1H$ $\sigma_{iso}$ for the 88 semi-hydrous wadsleyite structures is challenging. It was therefore decided that calculated $^1H$ $\sigma_{iso}$ values would be referenced using experimental and calculated NMR parameters for hydrous wadsleyite itself. Based on the AIRSS-based study presented in Section 6.6.2, several resonances in the $^1H$ MAS NMR spectrum of wads-H, a sample of wadsleyite containing ~3 wt% $H_2O$,[56] have been tentatively assigned. It was concluded that the resonances that appear at 3.4, 6.7 and 8.6 ppm correspond

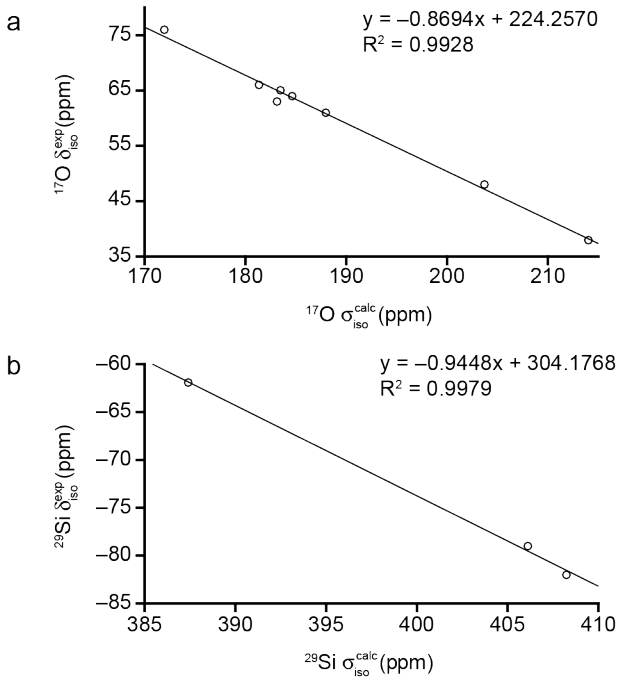


**Figure D4.1:** Plot of (a) $^{17}O$ and (b) $^{29}Si$ experimental $\delta_{iso}$ against calculated $\sigma_{iso}$ for forsterite ($\alpha$-$Mg_2SiO_4$), wadsleyite ($\beta$-$Mg_2SiO_4$) and ringwoodite ($\gamma$-$Mg_2SiO_4$).

to the protonation of O1, O3 and O4 sites, respectively. $^1H$ $\sigma_{iso}$ referencing is based on the semi-hydrous wadsleyite structures assigned to the $^1H$ resonances at 3.4 and 8.6 ppm (corresponding to O1 and O4 site hydroxyls, respectively), were used. Where more than one of a particular protonation arrangement is observed, *i.e.*, when both protons are located on O1 sites, the average $^1H$ $\sigma_{iso}$ value is used. Table D4.3 shows the calculated $^1H$ $\sigma_{iso}$ values for the selected AIRSS-generated semi-hydrous wadsleyite structures. The equation shown in Figure D4.2 was used to reference the $^1H$ $\sigma_{iso}$ for the 88 semi-hydrous wadsleytie structures discussed in Section 6.6.3.

**Table D4.3:** $^1H$ calculated isotropic chemical shielding ($s_{iso}$) and experimental isotropic chemical shift ($d_{iso}$) for the two semi-hydrous wadsleyite structures chosen to reference $^1H$ $\sigma_{iso}$ for structures with this hydration level.

| Mg site vacancy | Protonation motif | Protonation site | $^1H$ $\sigma_{iso}$ (ppm) | $^1H$ $\delta_{iso}$[56] (ppm) | $\Delta H$ / eV |
|---|---|---|---|---|---|
| Mg3 | 2 × H–O1 | O1 | 25.38 | 3.4 | 0.00 |
| Mg1 | 2 × H–O4 | O4 | 18.67 | 8.6 | 0.33 |

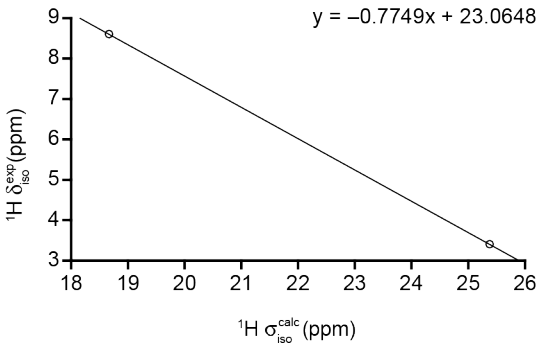


**Figure D4.2:** Plot of experimental $^1H$ $\delta_{iso}$ against calculated $\sigma_{iso}$ for the selected AIRSS-generated semi-hydrous wadsleyite structures used to reference the $\sigma_{iso}$ values for the 88 structures with the same hydration level, discussed in Section 6.6.3.

# E Fully-hydrous wadsleyite: computational details

## E1 Fully-hydrous wadsleyite structures with a Si vacancy

Fully-hydrous wadsleyite structural models, each containing a single $Si^{4+}$ vacancy, were generated by using the AIRSS approach to add four H atoms to a unit cell of anhydrous wadsleyite,[29] producing 251 structures, with the enthalpy profile of these structures shown in Figure E1.1a. The enthalpy rank shows that the AIRSS-generated structures fall into two well-defined regions, where 142 have $\Delta H < 0.04$ eV, with the remaining 109 structures exhibiting $\Delta H > 0.27$ eV. The lowest enthalpy structures contain all four H on the tetrahedron of O atoms that directly surround the Si vacancy, with the protonation motif for the lowest enthalpy structure ($\Delta H = 0.0$ eV), which contains O2–H···O4, O3–H···O4, O4–H···O3 and O4–H···O4 hydroxyl environments, is shown in Figure E1.1b. In all the structures with $\Delta H > 0.27$ eV, at least one H atom is located on an O atom outside of the four that directly surround the Si vacancy.

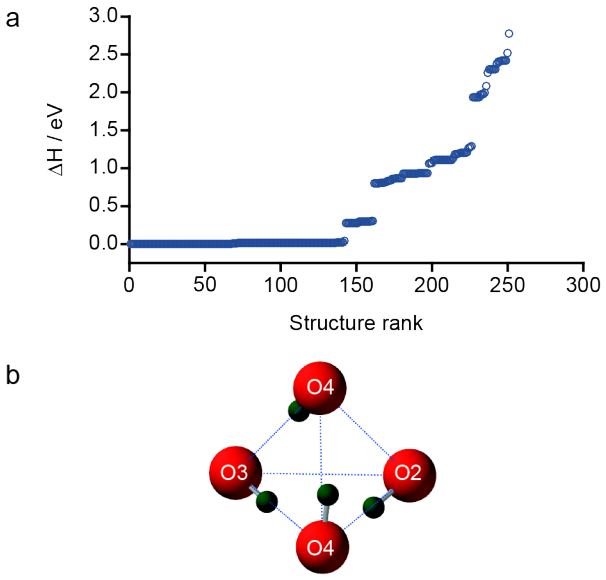


**Figure E1.1:** (a) Plot of relative enthalpy ($\Delta H$) of the 251 fully-hydrous wadsleyite structural models with a Si vacancy. (b) Representative structure of the lowest enthalpy fully-hydrous wadsleyite protonation motif with a Si vacancy.

In order to compare hydration mechanisms featuring a Si vacancyagainst those with two Mg vacancies, a balanced reaction, interchanging these materials was constructed. The formula for a unit cell of fully-hydrous wadsleyite containing a Si vacancy is $Mg_{16}Si_7O_{32}H_4$, with the formula for the structure containing two Mg vacancies being $Mg_{14}Si_8O_{32}H_4$. As shown in Equation 3, using stishovite[57] and akimotoite,[24] polymorphs of $SiO_2$ and $MgSiO_3$, respectively, these two materials can be stoichiometrically balanced.

$$Mg_{14}Si_8O_{32}H_4 + 2MgSiO_3 \rightarrow Mg_{16}Si_7O_{32}H_4 + 3SiO_2, \quad \Delta H = +1.16 \text{ eV} . \quad (3)$$

Equation 3 shows that formation of $Mg_{16}Si_7O_{32}H_4$ (and stishovite) from akimotoite and $Mg_{14}Si_8O_{32}H_4$ has an enthalpic cost of +1.16 eV, suggesting that experimentally, fully-hydrous wadsleyite containing Si vacancies is unlikely to occur.

## E2 Referencing $^1H$ $\sigma_{iso}$

The calculated $^1H$ $\sigma_{iso}$ values for the 199 AIRSS-generated fully-hydrous wadsleyite structures selected for further study were referenced using the calculated isotropic chemical shielding ($\sigma_{iso}$) and experimental isotropic chemical shift ($\delta_{iso}$) values for hydrous wadsleyite itself. $^1H$ $\sigma_{iso}$ referencing is based on the fully-hydrous wadsleyite structures assigned to the $^1H$ resonances at 3.4 and 8.6 ppm, corresponding to O1 and O4 site hydroxyls, respectively. Where more than one of a particular protonation arrangement is observed, *i.e.*, when all four protons are located on O1 sites, the average $^1H$ $\sigma_{iso}$ value is used. Table E2.1 shows the calculated $^1H$ $\sigma_{iso}$ values for the two selected fully-hydrous wadsleyite structures. The equation shown in Figure E2.1 was used to reference $^1H$ $\sigma_{iso}$ values for the 199 fully-hydrous wadsleytie structures discussed in Section 6.7.

**Table E2.1:** $^{1}$H calculated isotropic chemical shielding ($s_{iso}$) and experimental isotropic chemical shift ($d_{iso}$) for the two fully-hydrous wadsleyite structures chosen to reference $^{1}$H $\sigma_{iso}$ for structures with this hydration level.

| Mg site vacancy | Protonation motif | Protonation site | $^{1}$H $\sigma_{iso}$ (ppm) | $^{1}$H $\delta_{iso}$[56] (ppm) | ΔH / eV |
|---|---|---|---|---|---|
| Mg3/Mg3 | 4 × H–O1 | O1 | 26.05 | 3.4 | 0.00 |
| Mg1/Mg3 | 2 × H–O1 | O4 | 20.63 | 8.6 | 0.37 |
| | 1 × H–O3 | | | | |
| | 1 × H–O4 | | | | |

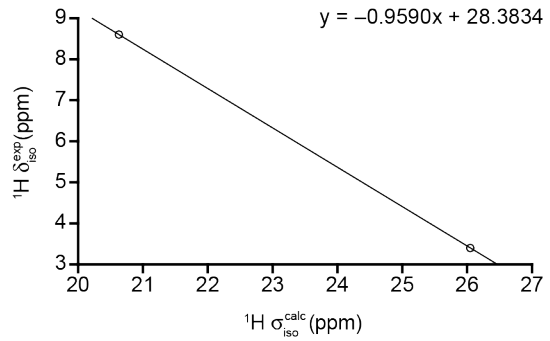


**Figure E2.1:** Plot of experimental $^{1}$H $\delta_{iso}$ against calculated $\sigma_{iso}$ for the selected AIRSS-generated fully-hydrous wadsleyite structures used to reference the $\sigma_{iso}$ values for the 199 structures with the same hydration level, discussed in Section 6.7.

## E3 The Smyth fully-hydrous wadsleyite structural model

The enthalpic stability of the fully-hydrous wadsleyite structural model proposed by Smyth,[58] relative to the AIRSS-generated structures presented in Chapter 6 of this thesis, was investigated. Smyth generated this structural model was generated using simple ionic constraints, and as shown in Figure E3.1, it consists of protonated O1 sites, with the H–O1 hydroxyls aligning parallel to the *c* axis (rather than with the O···O edge of the vacancy centred octahedron), with hydration charge balanced by the removal of two Mg2 site cations. From Figure E3.2, which shows the ΔH of the Smyth structure (following geometry optimisation), alongside the 199 AIRSS-generated structures identified using a *k*-means clustering approach, it is clear that the Smyth structure (ΔH ≈ 2.45 eV) is enthalpically unstable, with a

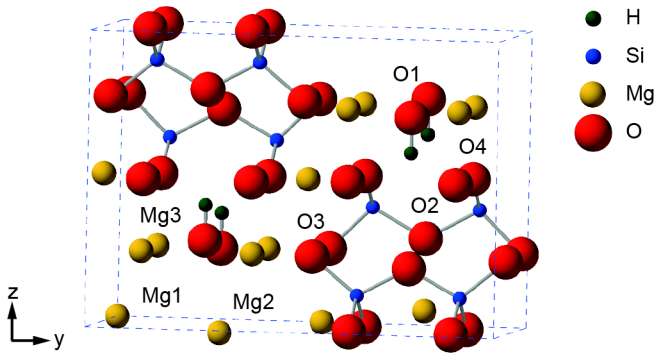


**Figure E3.1:** The structural model of fully-hydrous wadsleyite proposed by Smyth.[58]

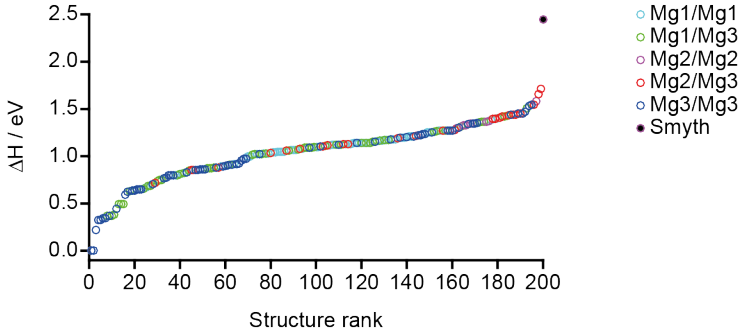


**Figure E3.2:** Plot showing the relative enthalpy (ΔH) of the Smyth structural model,[58] alongside the 199 *k*-means cluster-selected fully-hydrous wadsleyite structural models, with the data points coloured by Mg vacancy combination.

ΔH far higher than any of the *k*-means cluster-selected structures with two Mg2 vacancies. The highly unstable nature of this model, relative to the AIRSS-generated equivalents, could be due to the hydroxyl orientation proposed by Smyth, which prevents the formation of protonation environments with strong hydrogen bonding.

# F References


1. F. Brisse and O. Knop, *Can. J. Chem.*, 1968, **46**, 859–873.
2. M. G. Paton and E. N. Maslen, *Acta Crystallogr.*, 1965, **19**, 307–310.
3. P. Florian, M. Gervais, A. Douy, D. Massiot, and J.-P. Coutures, *J. Phys. Chem. B*, 2001, **105**, 379–391.
4. C. P. Grey, M. E. Smith, A. K. Cheetham, C. M. Dobson, and R. Dupree, *J. Am. Chem. Soc.*, 1990, **112**, 4670–4675.
5. M. R. Mitchell, D. Carnevale, R. Orr, K. R. Whittle, and S. E. Ashbrook, *J. Phys. Chem. C*, 2012, **116**, 4273–4286.
6. O. Knop, F. Brisse, and L. Castelliz, *Can. J. Chem.*, 1969, **47**, 971–990.
7. C. P. Grey, C. M. Dobson, A. K. Cheetham, and R. J. B. Jakeman, *J. Am. Chem. Soc.*, 1989, **111**, 505–511.
8. N. Kim and C. P. Grey, *J. Solid State Chem.*, 2003, **175**, 110–115.
9. B. J. Kennedy, *Physica. B*, 1998, **241**, 303–310.
10. Y. Tabira, R. L. Withers, T. Yamada, and N. Ishizawa, *Z. Kristallogr.*, 2001, **216**, 92–98.
11. R. Diehl and G. Brandt, *Mater. Res. Bull.*, 1975, **10**, 85–90.
12. A. K. Cheetham and N. Norman, *Acta Chem. Scand. A*, 1974, **28**, 55–60.
13. J. Wu, T. J. Boyle, J. L. Shreeve, J. W. Ziller, and W. J. Evans, *Inorg. Chem.*, 1993, **32**, 1130–1134.
14. F. Euler and J. A. Bruce, *Acta Crystallogr.*, 1965, **19**, 971–978.
15. K. E. Johnston, M. R. Mitchell, F. Blanc, P. Lightfoot, and S. E. Ashbrook, *J. Phys. Chem. C*, 2013, **117**, 2252–2265.
16. M. D. Dolan, B. Harlan, J. S. White, M. Hall, S. T. Misture, S. C. Bancheri, and B. Bewlay, *Powder Diffr.*, 2008, **23**, 20–25.
17. A. I. Becerro, A. Escudero, P. Florian, D. Massiot, and M. D. Alba, *J. Solid State Chem.*, 2004, **177**, 2783–2789.
18. G. J. Redhammer and G. Roth, *Acta Crystallogr. Sect. C Cryst. Struct. Commun.*, 2003, **59**, 103–106.
19. R. T. Downs and D. C. Palmer, *Am. Mineral.*, 1994, **79**, 9–14.
20. M. Profeta, F. Mauri, and C. J. Pickard, *J. Am. Chem. Soc.*, 2003, **125**, 541–548.

21. R. M. Hazen, L. W. Finger, R. J. Hemley, and H. K. Mao, *Solid State Commun.*, 1989, **72**, 507–511.
22. N. Ross and R. M. Hazen, *Phys. Chem. Miner.*, 1990, **17**, 228–237.
23. S. E. Ashbrook, A. J. Berry, D. J. Frost, A. Gregorovic, C. J. Pickard, J. E. Readman, and S. Wimperis, *J. Am. Chem. Soc.*, 2007, **129**, 13213–13224.
24. H. Horiuchi and M. Hirano, *Am. Mineral.*, 1982, **67**, 788–793.
25. J. R. Smyth and R. M. Hazen, *Am. Mineral.*, 1973, **58**, 588–593.
26. S. E. Ashbrook, A. J. Berry, and S. Wimperis, *Am. Mineral.*, 1999, **84**, 1191–1194.
27. S. E. Ashbrook, A. J. Berry, and S. Wimperis, *J. Am. Chem. Soc.*, 2001, **123**, 6360–6366.
28. S. E. Ashbrook, A. J. Berry, W. O. Hibberson, S. Steuernagel, and S. Wimperis, *Am. Mineral.*, 2005, 90, 1861–1870.
29. H. Horiuchi and H. Sawamoto, *Am. Mineral.*, 1981, **66**, 568–575.
30. S. E. Ashbrook, A. J. Berry, W. O. Hibberson, S. Steuernagel, and S. Wimperis, *J. Am. Chem. Soc.*, 2003, **125**, 11824–11825.
31. S. Sasaki, C. T. Prewitt, Y. Sato, and E. Ito, *J. Geophys. Res.*, 1982, **87**, 7829–7832.
32. Y. A. Abramov, V. G. Tsirelson, V. E. Zavodnik, S. A. Ivanov, and I. D. Brown, *Acta Crystallogr. Sect. B*, 1995, **51**, 942–951.
33. T. J. Bastow, P. J. Dirken, M. E. Smith, and H. J. Whitfield, *J. Phys. Chem.*, 1996, **100**, 18539–18545.
34. T. Pagnier, I. Charrier-Cougoulic, C. Ritter, and G. Lucazeau, *Eur. Phys. J. App. Phys.*, 2000, **9**, 1–9.
35. S. C. Abrahams, J. M. Reddy, and J. L. Bernstein, *J. Phys. Chem. Solids*, 1966, **27**, 997–1012.
36. H. Lehnert, H. Boysen, J. Schneider, F. Frey, D. Hohlwein, P. Radaelli, and H. Ehrenberg, *Z. Kristallogr.*, 2000, **215**, 536–541.
37. E. Oldfield, C. Coretsopoulos, S. Yang, L. Reven, H. C. Lee, J. Shore, O. H. Han, E. Ramli, and D. Hinks, *Phys. Rev. B*, 1989, **40**, 6832–6849.
38. W. H. Baur and A. A. Khan, *Acta Crystallogr. Sect. B*, 1971, **27**, 2133–2139.
39. T. J. Bastow, A. F. Moodie, M. E. Smith, and H. J. Whitfield, *J. Mater. Chem.*, 1993, **3**, 697–702.

40. H. J. A. Koopmans, G. M. H. van de Velde, and P. J. Gellings, *Acta Crystallogr. Sect. C Cryst. Struct. Commun.*, 1983, **39**, 1323–1325.
41. J. W. Downs, F. K. Ross, and G. V. Gibbs, *Acta Crystallogr. Sect. B*, 1985, **41**, 425–431.
42. L. Turner, S. E. Chung, and E. Oldfield, *J. Magn. Reson.*, 1985, **324**, 316–324.
43. V. G. Tsirelson, a. S. Avilov, Y. a. Abramov, E. L. Belokoneva, R. Kitaneh, and D. Feil, *Acta Crystallogr. Sect. B Struct. Sci.*, 1998, **54**, 8–17.
44. M. C. Verbraeken, E. Suard, and J. T. S. Irvine, *J. Mater. Chem.*, 2009, **19**, 2766–2770.
45. W. Z. Gerlach, *Zeitschrift für Phys.*, 1922, **9**, 184–192.
46. L. Marsella and V. Fiorentini, *Phys. Rev. B*, 2004, **69**, 172103.
47. R. Ruh and P. W. R. Corfield, *J. Am. Ceram. Soc.*, 1970, **53**, 126–129.
48. T. J. Bastow, M. E. Smith, and H. J. Whitfield, *J. Mater. Chem.*, 1996, **6**, 1951–1955.
49. Y. Ohashi, *Phys. Chem. Miner.*, 1984, **10**, 217–229.
50. S. E. Ashbrook, A. J. Berry, and S. Wimperis, *J. Phys. Chem. B*, 2002, **106**, 773–778.
51. M. Catti, G. Ferraris, S. Hull, and A. Pavese, *Phys. Chem. Miner.*, 1995, 22, 200–206.
52. S. Sturniolo, *Soprano - a Python library developed by the CCP for NMR Crystallography*, https://ccp-nc.github.io/soprano/.
53. S. E. Ashbrook, A. J. Berry, W. O. Hibberson, S. Steuernagel, and S. Wimperis, *J. Am. Chem. Soc.*, 2003, **125**, 11824–11825.
54. M. Mági, E. Lippmaa, A. Samoson, G. Engelhard, and A.-R. Grimmer, *J. Phys. Chem.*, 1984, **88**, 1518–1522.
55. J. F. Stebbins and M. Kanzaki, *Science*, 1991, **251**, 294–298.
56. J. M. Griffin, A. J. Berry, D. J. Frost, S. Wimperis, and S. E. Ashbrook, *Chem. Sci.*, 2013, **4**, 1523–1538.
57. W. Sinclair and A. E. Ringwood, *Nature*, 1978, **272**, 714–715.
58. J. R. Smyth, *Am. Mineral.*, 1994, **79**, 1021–1024.